Imperial College London
Department of Mechanical Engineering

Experimental Characterization of Frictional Hysteresis for Nonlinear Dynamic Analysis of Jointed Structures

Alfredo Fantetti

A thesis submitted to Imperial College London for
the degree of Doctor of Philosophy and the Diploma of Imperial College

February 2022

Preface

This dissertation is the result of work carried out by the author in the Dynamics Group of the Department of Mechanical Engineering at Imperial College London in the period between October 2017 and December 2020. The work was supervised by the main supervisor Dr. Christoph Schwingshackl and the second supervisor Prof. David Nowell. The work was funded by the European Union's Horizon 2020 research and innovation programme under the Marie Skłodowska-Curie grant agreement No 721865 - "models, EXperiments and high PERformance computing for Turbine mechanical Integrity and Structural dynamics in Europe" (EXPERTISE). The work in Chapter 5 resulted in the award of the first price in the 2020 "Young Stress Analyst Competition" by the British Society for Strain Measurement (BSSM). The work in Chapters 4, 5 and 7 resulted in the bestowal of the "Innovation in Tribology 2021 Award" by the Institute of Physics (IOP). Some of the work described herein has contributed to the following publications:

1. A Fantetti, S Mariani, L Pesaresi, D Nowell, F Cegla, C Schwingshackl, "Ultrasonic Monitoring of Friction Contacts during Shear Vibration Cycles", Mechanical Systems and Signal Processing, 161 (2021).

2. A Fantetti, LR Tamatam, M Volvert, I Lawal, L Liu, L Salles, M Brake, C Schwingshackl, D Nowell, "The impact of fretting wear on structural dynamics: Experiment and Simulation", Tribology International, 138 (2019): 111-124.

3. V Gimpl, A Fantetti, S Klaassen, C Schwingshackl, D Rixen, "Contact stiffness of jointed interfaces: a comparison of dynamic substructuring techniques with frictional hysteresis measurements", Mechanical System and Signal Processing, accepted.

4. J Yuan, A Fantetti, E Denimal, S Bhatnagar, L Pesaresi, C Scwinghsackl, L Salles, "Propagation of Uncertainties from Friction Interfaces in Nonlinear Dynamics of Turbine Blades with Underplatform Dampers", Mechanical System and Signal Processing, 156 (2021).

5. L Pesaresi, A Fantetti, F Cegla, L. Salles, C. Schwingshackl, "On the use of ultrasound waves to monitor the local dynamics of friction joints", Experimental Mechanics, 60 (2020): 129-141.

6. A Fantetti, C Schwingshackl, "Effect of Friction on the Structural Dynamics of Built-up Structures: An Experimental Study", Proceedings of ASME Turbo Expo 2020, 2020.

7. A Fantetti, C Pennisi, S Zucca, D Botto, C Schwingshackl, "Comparison of nonlinear dynamic contact interface parameters measured from two different friction rigs", International Conference on Noise and Vibration Engineering, 2020.

8. S Bhatnagar, J Yuan, A Fantetti, E Denimal, L Salles, "Quantification of Uncertainties in Nonlinear Vibrations of Turbine Blades with Underplatform Dampers", International Conference on Noise and Vibration Engineering, 2020.

9. F Tubita, A Fantetti, L Blanc, F Thouverez, "Effect of fretting-wear on dynamic analysis. Comparison between experimental results and numerical simulations for a vibratory friction rig", IX International Conference on Computational Methods for Coupled Problems in Science and Engineering, 2021.

Statement of Originality

I declare that the contents of this thesis are entirely my own work, unless otherwise stated, and that any additional sources of information have been duly cited.

Copyright Declaration

The copyright of this thesis rests with the author. Unless otherwise indicated, its contents are licensed under a Creative Commons Attribution-Non Commercial 4.0 International Licence (CC BY-NC). Under this licence, you may copy and redistribute the material in any medium or format. You may also create and distribute modified versions of the work. This is on the condition that: you credit the author and do not use it, or any derivative works, for a commercial purpose. When reusing or sharing this work, ensure you make the licence terms clear to others by naming the licence and linking to the licence text. Where a work has been adapted, you should indicate that the work has been changed and describe those changes. Please seek permission from the copyright holder for uses of this work that are not included in this licence or permitted under UK Copyright Law.

Acknowledgements

Throughout the writing of this dissertation and during the years of my PhD, I have been supported and guided by several people that I want to thank.

First of all, I want to thank my enthusiastic supervisor, Dr. Christoph Schwingshackl, for all the guidance (and patience) he has provided over the years and for everything he has taught me, which has been invaluable towards my development as an independent researcher. I will always be grateful to him. I also want to thank my second supervisor Prof. David Nowell, for the fruitful and enjoyable discussions throughout the PhD and for constantly motivating and supporting me. I am thankful to the European Union for funding my PhD research and providing me with all the financial support for my personal and career development.

I would also like to express my special appreciation to Dr. Loic Salles, who has extensively supported me with numerous technical advice and with the use of FORSE. Likewise, I thank Dr. Luke Muscutt for all his tolerance in explaining how things work in the lab and helping me in setting up experimental testing. Thanks are also due to Dr. Fred Cegla, who provided me with guidance and equipment for performing the ultrasonic experiments; to Dr. Richard Setchfield, for his technical expertise and guidance provided during my 3-month internship in Rolls-Royce plc; to Prof. Teresa Berruti, my master thesis supervisor, for making me aware of this great PhD opportunity. If I applied for this job, which changed my life, it is thanks to her; to Prof. Stefano Zucca and Prof. Daniele Botto for their guidance and inspiration during and after my 3-month secondment in Politecnico di Torino; to Prof. Daniel Rixen, for providing essential guidance within the substructuring experimental study; to Prof. Daniele Dini and Pawel Orzlowski for providing access to the Tribology Group facilities.

A special mention goes to Peter Higgs, our fantastic administrator for always solving any financial and logistic problem we, students, encountered during our journeys. Thank you for your infinite patience (and for proofing my thesis!).

Special thanks go as well to my colleagues/mentors/friends Luca Pesaresi and Stefano Mariani. They have both been essential for improving my knowledge and my self-awareness as a researcher. Of course, I want to thank all my colleagues, now friends, from Imperial College, with whom I shared this amazing experience. I also express my gratitude to my colleagues from the EXPERTISE programme and all my other friends in London (special mention to Gema, Fasulla and the Pizzetta crew). I shared with them truly the best moments throughout my PhD. A special thanks also to the great master students I supervised within my PhD, with whom I created strong connections: Cristiana, Luca and Verena.

Finally, I want to dedicate this thesis to my family, for their unconditional love and support. I know they will always be there for me.

Abstract

Modern high-value jointed structures such as aero-engines are carefully designed and optimized to prevent failure and maximise durability. During operation, these structures are subjected to high-frequency vibrations that, uncontrolled, might lead to loss of performance, higher maintenance and, in the worst-case scenario, catastrophic failures due to high cycle fatigue. Accurate dynamics predictions are therefore needed to achieve safer designs. Often, challenges in obtaining such predictions are introduced by the presence of friction between the thousands of components in contact. Despite the considerable research efforts over the past decades, the effects of friction on the dynamics are not yet fully understood, due to the complex mechanisms that govern the interface behaviour. As a result, fully validated and predictive modelling approaches are not available and expensive physical testing is still required to assess the performance and reliability of new designs.

The aims of this PhD research are thus to i) provide a better understanding of the friction mechanisms, ii) quantify their effects on the dynamic response of jointed structures and iii) validate/upgrade state-of-the-art measuring and modelling approaches for nonlinear dynamic analysis. For those purposes, an extensive round robin test was performed on two high-frequency friction rigs of different institutions to measure a wide range of hysteresis loops. Novel experiment-based contact laws were discovered to be used in simulations. Simultaneously with the hysteresis measurements, ultrasonic measurements were performed to monitor the vibrating contact interfaces in real time, providing unprecedented insights into the friction mechanisms. These experimental methods were also employed to monitor the dynamic behaviour of the friction rigs, leading to an improved understanding of the effects of friction on the dynamics. The knowledge thus gained was used to propose upgrades for state-of-the-art modelling approaches, which were then validated by comparing new simulations with experimental measurements.

Contents

Preface i

Abstract v

1 Introduction 1

1.1 Thesis outline 4

2 Literature review 7

2.1 Nonlinear dynamic analysis of jointed structures 7

2.2 The physics of the hysteresis loop and its contact parameters 10

2.2.1 Physics of the friction coefficient 13

2.2.2 Physics of the contact stiffness 16

2.3 Contact models used for nonlinear dynamic analysis 18

2.3.1 Static friction models 19

2.3.2 Dynamic friction models 19

2.4 Analytical and numerical methods for contact parameter estimations 24

2.5 Experimental methods for contact parameter estimations 28

2.5.1 Local contact hysteresis measurements 29

2.5.2 Local contact ultrasonic measurements 30

2.5.3 Global dynamics measurements 32

2.6 Summary of the literature review 32

3 Evaluation of the existing high-frequency friction rig 35

3.1 Description of the friction rig . . . 35

3.2 Sensitivity study for the accuracy of the contact parameters extraction method . 37

3.2.1 Tangential contact stiffness extraction method . . . 37

3.2.2 Friction coefficient extraction method . . . 39

3.3 Sources of uncertainty . . . 41

3.3.1 Uncertainty in the measured normal load . . . 41

3.3.2 Uncertainty in the measured displacement . . . 45

3.3.3 Uncertainty in the measured friction force . . . 46

3.4 Conclusions . . . 46

4 Measuring contact parameters with the traditional hysteresis technique: round robin test including rigs of different institutions 49

4.1 Round robin test description . . . 50

4.2 Measurements at Imperial College London . . . 57

4.2.1 Evolution of the contact parameters with wear . . . 59

4.2.2 Repeatability of the tests . . . 66

4.2.3 Tangential contact stiffness . . . 71

4.2.4 Friction coefficient . . . 80

4.3 Measurements at Politecnico di Torino . . . 82

4.3.1 Evolution of the contact parameters with wear . . . 84

4.3.2 Repeatability of the tests . . . 87

4.3.3 Tangential contact stiffness . . . 90

4.3.4 Friction coefficient . . . 95

4.4 Comparison of results from the two friction rigs . . . 98

4.4.1 Guidelines for providing accurate input contact parameters for nonlinear dynamic analysis of jointed structures . . . 103

4.5 Conclusions . . . 107

5 Monitoring frictional hysteresis with the ultrasound technique 109

5.1 Experimental setup with ultrasound . . . 110

5.2 Ultrasonic tests under stuck conditions and different normal loads . . . 112

5.2.1 Hysteresis loop measurements . . . 112

5.2.2 Ultrasonic measurements . . . 113

5.2.3 Comparison between contact stiffnesses obtained from hysteresis loops and ultrasonic measurements . . . 115

5.3 Ultrasonic tests under varying sliding conditions and fixed normal load . . . 119

5.3.1 Hysteresis loop measurements . . . 120

5.3.2 Mean ultrasound values: dependence on relative displacement . . . 121

5.3.3 Variations in the ultrasound measurement: effect of friction regimes . . . 123

5.4 Conclusions . . . 127

6 Effect of frictional hysteresis on the structural dynamics 129

6.1 Description of the rig dynamic behaviour . . . 130

6.2 Effects of hysteresis loops on the dynamics . . . 132

6.2.1 Effect of normal load . . . 132

6.2.2 Effect of displacement amplitude and excitation force . . . 134

6.2.3 Effect of wear . . . 137

6.3 Effects of the dynamics on hysteresis loops . . . 139

6.4 Dynamic substructuring technique to extract tangential contact stiffness . . . 142

6.5 Conclusions . . . 145

7 Validation of modelling approaches for nonlinear dynamic analysis: friction rig test case 147

7.1 Quasi-static contact simulations . . . 148

7.1.1 FEM simulations: effect of the bulk deformation . . . 149

7.1.2 BEM simulations: effect of wear and surface topography . . . 151

7.2 Nonlinear dynamics simulations . . . 159

7.2.1 Imperial friction rig: effect of wear . . . 159

7.2.2 Underplatform damper rig: effect of contact stiffness load dependency and uncertainty quantification . . . 162

7.3 Conclusions . . . 169

8 Validation of modelling approaches for nonlinear dynamic analysis: industrial test case 171

8.1 Industrial test case: aero-engine turbine bladed disk sector . . . 172

8.2 Modelling approach . . . 176

8.2.1 Normal load distribution and nominal area of contact . . . 178

8.2.2 Friction coefficient and contact stiffness load dependence . . . 178

8.3 Simulation results . . . 181

8.3.1 Frequency shift predictions - Effect of contact bedding patterns and k_t sensitivity . . . 181

8.3.2 Amplitude predictions - Comparison with strain gauge data . . . 185

8.3.3 Effect of the friction coefficient . . . 188

8.3.4 Effect of the grid density of contact nodes . . . 190

8.4 Summary of results . . . 191

8.5 Conclusions . . . 192

9 Guidelines for improved nonlinear dynamic analysis 195

9.1 Guidelines for improving measuring approaches . . . 195

9.2 Guidelines for improving modelling approaches . . . 199

10 Conclusions and future work 205

Bibliography 211

Appendix A High-frequency friction rigs to measure hysteresis loops 229

Appendix B Digital Image Correlation to investigate the stiffness of the friction rig in the normal direction 233

Appendix C Evolution of contact interfaces with wear 235

Appendix D FE analysis to characterize the ultrasonic wave propagation 238

Appendix E FE analysis to estimate the specimen tangential bulk deformation 241

Appendix F FE simulations to quantify the effect of the surface topography 243

Appendix G Supplementary data for the simulations of chapter 8 250

List of Tables

2.1 Summary of analytical and numerical methods. 28

4.1 Operating regimes of Imperial and PoliTO friction rigs. 52

4.2 Test matrix summary. In red highlighted the reference test for each rig (used for repeatability studies). 54

4.3 μ and k_t steady state (or end of test) values of the three repeatability tests of Figs. 4.38 and 4.39. 88

4.4 μ and K_T values to be used in nonlinear dynamic analysis for steel on steel contacts plus uncertainty bands. p [MPa] is the normal load divided by the worn area of contact. Also K_T [N/μm/mm^2] is normalised by the worn area of contact. See Figs. 4.50 and 4.51 for the supporting data. See section 7.1 for the numerical modelling. 103

5.1 Summary of test loading conditions for the vibration tests under stuck conditions. 113

5.2 Summary of test loading conditions for the tests under different displacement amplitudes and constant normal load. 121

6.1 2 DOFs lumped model of the friction rig. 132

7.1 Bouc-Wen parameters used to replicate experimental trends of the test of section 6.2.3. 161

7.2 Uncertainty parameters used for the LHS based on the experimental data from chapter 4. 167

8.1 Number of nodes for each combination of bedding patterns and grid densities. The table also shows the information on the nominal areas, which is needed for the caclulation of the normal load distribution, as discussed in section 8.2.1. 177

8.2 Summary of frequency shifts with respect to the undamped case (simulations and experiments) and contact conditions for modes low EO/mode 2, high EO/mode 3 and high EO/mode 4, for the full contact case and outer edge contact case v2, both with the grid density 40*3 and k_t load-dependence. 185

8.3 Summary of normalised strain amplitudes of two strain gauges for each mode. The experimental amplitudes are not directly comparable, since they are based on measurements of a single blade, and not averaged over the whole test set. 188

8.4 Computational time for different grid densities and contact bedding patterns. The computational time is normalised to the datum approach – 40*3 full contact case - and refers to simulations of the high EO/mode 3 with the k_t load dependence law as those shown in the Appendix G. Note that the two shown bedding patterns have a different total number of nodes, for the same grid density, as a result of their different nominal areas of contact, as shown in Table 8.1. 191

9.1 Summary of experimental methods. 196

A.1 Main features of the Imperial, Politecnico and Oxford friction rigs. 229

List of Figures

1.1 The Trent XWB aero engine from Rolls-Royce [6] and an example of friction joints. 2

1.2 Friction hysteresis loop, the load-deflection curve resulting from the vibrating motion of two contact interfaces. μ is the friction coefficient, T is the friction force during gross slip, N is the normal load and k_t is the tangential contact stiffness. 3

1.3 Thesis structure. 4

2.1 Most common mechanical joints in aero-engines. 8

2.2 a) Blades equipped with an underplatform damper [19]; b) Close view of the underplatform damper; c) Experimental FRFs measured at constant centrifugal load (960 N) and increasing excitation force [19]. 8

2.3 Standard practice for nonlinear dynamic analysis of jointed structures (left part of the image) with emphasis on the contact modelling methods (right part of the image). 11

2.4 A typical hysteresis loop: a) physical meaning; b) Force and displacement vs time. μ is the friction coefficient, T_{sl} is the friction force during gross slip, N is the normal load and k_t is the tangential contact stiffness. 13

2.5 Multi-physics phenomena involved in friction [62]. 16

2.6 Contact stiffness versus normal load: a-b-c) Hysteresis measurements [74, 80, 83]; d-e-f) Ultrasound measurements [66, 71, 73]; g) Contact resonance measurements [84]; h-i) Finite Element Method predictions [72, 78]. 17

2.7 Constitutive models of friction. 18

2.8 Static (velocity-based) friction models. 19

2.9 Macroslip contact models: a) Jenkins element; b) Jenkins element with variable normal load; c) 2D contact model with uncoupled tangential motions; d) 2D contact model with coupled tangential motions; e) Quasi-3D contact model. 20

2.10 Microslip models: a) Iwan element and its hysteresis loop; b) Bouc-Wen hysteresis loops [103]; c) Conceptualization of LuGre model. 22

3.1 a) Specimen details; b) Photo of the friction rig [201]. 36

3.2 Friction rig scheme. 36

3.3 Fitting lines used for the extraction of the contact parameters. Two red lines fit the stick part of the loop and two blue lines fit the friction limits. 38

3.4 Sensitivity study on the tangential contact stiffness: a-c) hysteresis loops with different number of points chosen for the linear fitting and corresponding k_t values (k_{tL} and k_{tR} are the stiffnesses estimated from the left and right stick regions respectively); d) k_t values for different combinations of points used for the fitting. 39

3.5 Sensitivity study on the friction coefficient (a-b) energy μ and (c-d) standard μ: a) Minimum and maximum reference positions for the sliding amplitude estimation for the energy friction coefficient calculation; b) Energy friction coefficient for sliding amplitudes estimated at different positions; c) Minimum and maximum reference limit points for the fitting of the friction limits; d) Standard friction coefficient estimated from friction limits fitted to points limited by different reference positions. 40

3.6 a) Abaqus structural model; b-c) Reaction forces (in blue and red) due to a tangential load of 100 N (in yellow). Case b) is with the top push rod free to move vertically at its top connection with the pneumatic actuator; case c) is with the top push rod constrained vertically at its top connection with the pneumatic actuator. When the tangential load of 100 N is applied in the opposite direction (not shown here), the arms bend upwards and backwards, and all reaction forces are equal and opposite. 42

3.7 a) Upgraded rig setup to measure the normal load fluctuations during a vibration cycle; b-e) Normal load and friction force measurements during one vibration cycle at 100 Hz excitation. . . 43

3.8 Normal load fluctuations for an increasing displacement amplitude. 44

3.9 Displacement sources of uncertainty: a) Tilting due to non-ideal clamping and bulk deformation; b) Rotation induced by bending moment; c) Impact of the laser point positions on the contact stiffness estimation: laser measurement points on both specimens and arms. 45

3.10 Sources of uncertainty in the friction force measurement. Horizontal forces equilibrium. 47

4.1 PoliTO friction rig: (a) overall view; (b) floating self-aligning specimen support; (c) mobile specimen support excited my means of the shaker [170]. 51

4.2 a-b) Rigid body contact approach of Imperial rig; c-e) Self-aligning contact approach of PoliTO rig [170]. 51

4.3 a) Specimens of PoliTO rig [170]: contact occurs on the two legs; b) specimens of Imperial rig [169]: one-patch square contact. 52

4.4 a) Test Matrix: tests with both colours were performed on both rigs; b) Specimens of Imperial (from left to right 1 mm^2, 5 mm^2 and 10 mm^2); c) Specimens of PoliTO (from left to right 5 mm^2, 10 mm^2 and 40 mm^2). 53

4.5 a) Scan of the unworn contact interface of an Imperial specimen; b) Profile of the unworn contact interface; c) Photo and scan of a fully worn contact interface of an Imperial specimen. 55

4.6 a) Scan, photo and profile of the worn contact interface of a PoliTO specimen (the contact is on the two worn spots). 56

4.7 a) Typical evolution of the contact stiffness during a 2.5 hours long test, and identification of the steady state values. The specimen interface at the end of the test is also shown; b) Violin plot of the steady state values of the test in a). The white marker indicates the median of the data; the black marker indicates the interquartile range (between the 1^{st} and 3^{rd} quartiles); the blue shaded area includes all sample points. 57

4.8 Overview of contact interfaces and hysteresis loops for tests conducted on specimens with a 1 mm^2 nominal area of contact at Imperial. Columns are normal loads and rows are displacement amplitudes. 58

4.9 Overview of contact interfaces and hysteresis loops for tests conducted on specimens with a 5 mm^2 nominal area of contact at Imperial. Columns are normal loads and rows are displacement amplitudes. . . . 58

4.10 Overview of contact interfaces and hysteresis loops for tests conducted on specimens with a 9 mm^2 nominal area of contact at Imperial. Columns are normal loads and rows are displacement amplitudes. . . . 59

4.11 Typical evolution of hysteresis loops on tests performed on the Imperial rig: a) 2D plot; b) 3D plot. Values for the Test n. IC2: 87 N normal load, 24.5 μm displacement amplitude, 1 mm^2 nominal area of contact, 100 Hz excitation frequency and 2.5 hours of running, total hysteresis cycles=900000, material=stainless steel, temperature=25°C. . . . 60

4.12 Typical evolution of contact parameters of Imperial specimens (beginning of the steady state highlighted with a vertical red dashed line - the interface photo shows the worn area of contact at the end of the test): a-b) Friction coefficient, μ, (linear and log scale); c-d) Tangential contact stiffness (linear and log scale - k_{tL} and k_{tR} are the contact stiffnesses of left and right stick portions of the hysteresis loops, as defined in section 3.2.1). Values for the Test n. IC2: 87 N normal load, 24.5 μm displacement amplitude, 1 mm^2 nominal area of contact, 100 Hz excitation frequency and 2.5 hours of running, total hysteresis cycles=900000, material=stainless steel, temperature=25°C. 61

4.13 Typical evolution of the contact interface of Imperial specimens with wear: a) unworn contact and stiffness contributions; b) stiffness contributions in the worn contact. $k_{topography}$ is the stiffness due to asperities and waviness; k_{bulk} is the stiffness due to the deformation of the bulk around the interface. k_2 disappears due to the material removal with wear. Note that this is only a simplified and qualitative representation. . . . 62

4.14 Evolution of tangential contact stiffness (k_{tL} and k_{tR} are the contact stiffnesses of left and right stick portions of the hysteresis loops, as defined in section 3.2.1 - the interface photos show the worn areas of contact at the end of the test - the hysteresis loops are the loops at the end of the tests): a) Tests performed at 1 μm displacement amplitude; b) Tests performed at 24.5 μm displacement amplitude. Values for the Tests n. IC32-27: 150 N normal load, 1 μm and 24.5 μm displacement amplitude respectively, 5 mm^2 nominal area of contact, 100 Hz excitation frequency and 2.5 hours of running, total hysteresis cycles=900000, material=stainless steel, temperature=25°C. . . . 63

4.15 Evolution of the friction coefficient with wear for tests performed over different running times at 60 N normal load, 20 μm displacement amplitude, 100 Hz excitation frequency and 1 mm^2 nominal area of contact stainless steel specimens at room temperature. . . . 64

4.16 8 different tests: a-b) Evolution of tangential contact stiffness with wear in log and linear scale respectively; c) End-of-test worn areas of contact – all specimens had a nominal area of contact of 1 mm^2; d) Tangential contact stiffness values at the end of tests versus the worn area of contact at the end of tests. Tests performed over different running times at 60 N normal load, 20 μm displacement amplitude, 100 Hz excitation frequency. . . . 64

4.17 Worn surface images highlighting the material transfer between the top and bottom specimens for different test couples. The contact interfaces of the bottom specimens were opened and flipped to help the overlap comparison [20]. . . . 67

4.18 Repeatability study. Three tests performed with the same loading conditions but different specimen pairs: a-b) Energy friction coefficient, μ, (linear and log scale); c-d) Tangential contact stiffness, k_t, (linear and log scale). Values for the Tests n. IC1-8-12: 87 N normal load, 14 μm displacement amplitude, 1 mm^2 nominal area of contact, 100 Hz excitation frequency and 2.5 hours of running, total hysteresis cycles=900000, material=stainless steel, temperature=25°C. . . . 68

4.19 Hysteresis loop during chattering. Taken from the Test n. IC1 at the 30^{th} minute (see Fig. 4.18 for the time evolution). . . . 68

4.20 Violin plots of the steady state values for the Tests n. IC1-IC8-IC12: 87 N normal load, 14 μm displacement amplitude, 1 mm^2 nominal area of contact, 100 Hz excitation frequency and 2.5 hours of running, total hysteresis cycles=900000, material=stainless steel, temperature=25°C. . . . 69

4.21 Assembly test: a) Friction coefficient during operations 2-3-4-5-6-7 (see the text for detailed info on each operation); b) Friction coefficient during operations 8-9; c) Tangential contact stiffness during operations 2-3-4-5-6-7 (see the text for detailed info on each operation); d) Tangential contact stiffness during operations 8-9. Test conditions: 87 N normal load, 14 μm displacement amplitude, 1 mm^2 nominal area of contact, 100 Hz excitation frequency and 2.5 hours of running, total hysteresis cycles=900000, material=stainless steel, temperature=25°C. 70

4.22 Qualitative summary trends: a) Tangential contact stiffness steady state values, k_t, of the round robin test on the Imperial friction rig; b) Worn area normalised tangential contact stiffness steady state values, K_T; c) Worn areas of contact at the end of each test, plus example photos of worn areas at the end of tests for the 9 mm^2 nominal area of contact case (for which a fully worn area could not establish at the end of the test). 72

4.23 Violin plots of the steady state values of the tangential contact stiffness, k_t, of every round robin test on the Imperial friction rig. Each violin corresponds to a different test for one normal load, displacement amplitude and nominal area of contact. The legends indicate the mean and standard deviation of the steady state values of each test. The figure titles indicate the worn areas of the three tests and the energy dissipated when the steady state was reached (note that in most of the tests the steady state was not reached, and the energy represents the energy towards the end of the test). Chattering is often observed during tests at 17 N normal load and that is why the standard deviation is quite large in those tests. 73

4.24 Worn area normalised K_T versus contact pressure obtained by dividing the normal load by the worn area. Each point in the Figure corresponds to a different test of the round robin matrix with a different worn area of contact (green and red tests are from the round robin test, while blue tests are those shown in section 4.2.1). Note that, although some tests were performed with the same normal load, they have different contact pressures due to their different worn areas. The experimental fit is also shown (Eq. 4.1). 74

4.25 Violin plots of the steady state values of the worn area normalised tangential contact stiffness, K_T, of every round robin test on the Imperial friction rig. Each violin corresponds to a different test for one normal load, displacement amplitude and nominal area of contact. The legends indicate the mean and standard deviation of the steady state values of each test. The figure titles indicate the worn areas of the three tests and the energy dissipated when the steady state was reached (note that in most of the tests the steady state was not reached, and the energy represents the energy towards the end of the test). Chattering is often observed during tests at 17 N normal load and that is why the standard deviation is quite large in those tests. Note that tests performed at 1 mm^2 are not normalised by the worn area of contact, because no wear marks were present at the end of the tests. 75

4.26 a) Hysteresis loops measured at different displacement amplitudes at 100 Hz excitation frequency within the same test; b) k_t as a function of the displacement amplitude from hysteresis loops shown in a). Note that k_t is the slope measured right after the load reversal in each hysteresis loop. Test conditions: 87 N normal load, 1 mm^2 nominal area of contact, 100 Hz excitation frequency, steady state reached after 2.5 hours of running at 30 μm displacement amplitude and then loops measured at different displacement amplitudes, material=stainless steel, temperature=25°C. . . . 77

4.27 a) Hysteresis loops measured at different displacement amplitudes at 30 Hz excitation frequency within the same test; b) Hysteresis loops measured at different sliding distances at 100 Hz excitation frequency within the same test; c) k_t as a function of the displacement amplitude from hysteresis loops shown in a) and b); d) k_t as a function of the peak velocity, given by the displacement amplitude multiplied by the excitation frequency, from hysteresis loops shown in a) and b). Test conditions: 87 N normal load, 14 μm displacement amplitude, 1 mm^2 nominal area of contact, 30 Hz or 100 Hz excitation frequency, steady state reached after 2.5 hours of running and then loops measured at different displacement amplitudes, material=stainless steel, temperature=25°C. 78

4.28 a) Hysteresis loops measured at different displacement amplitudes at 100 Hz excitation frequency within the same test; b) Instantaneous contact stiffness versus the tangential relative displacement. The blue squares represent the k_t evaluated after load reversal (i.e. the k_t shown in Fig. 4.27c). The red circles indicate the peaks in the instantaneous k_t for the different loops; c) Instantaneous contact stiffness versus the instantaneous relative velocity. The red circles indicate the peaks in the instantaneous k_t for the different loops. Test conditions: 87 N normal load, 14 μm displacement amplitude, 1 mm^2 nominal area of contact, 100 Hz excitation frequency, steady state reached after 2.5 hours of running and then loops measured at different displacement amplitudes, material=stainless steel, temperature=25°C. 79

4.29 Friction coefficient steady state values of the round robin test on the Imperial friction rig. 80

4.30 Violin plots of the steady state values of the friction coefficient of every round robin test on the Imperial friction rig. Each violin corresponds to a different test for one normal load, displacement amplitude and nominal area of contact. The legends indicate the mean and standard deviation of the steady state values of each test. The figure titles indicate the worn areas of the three tests and the energy dissipated when the steady state was reached. Chattering was often observed during tests at 17 N normal load and that is why the standard deviation is quite large in those tests. 81

4.31 Overview of contact interfaces and hysteresis loops for tests conducted on specimens with a 5 mm^2 nominal area of contact at PoliTO. Columns are normal loads and rows are displacement amplitudes. The red dots indicate the position of the laser measurement location since the displacement could only be measured on one of the two contact legs during the experiment. . . . 82

4.32 Overview of contact interfaces and hysteresis loops for tests conducted on specimens with a 10 mm^2 nominal area of contact at PoliTO. Columns are normal loads and rows are displacement amplitudes. The red dots indicate the position of the laser measurement location since the displacement could only be measured on one of the two contact legs during the experiment. . . . 83

4.33 Overview of contact interfaces and hysteresis loops for tests conducted on specimens with a 40 mm^2 nominal area of contact at PoliTO. Columns are normal loads and rows are displacement amplitudes. The red dots indicate the position of the laser measurement location since the displacement could only be measured on one of the two contact legs during the experiment. . . . 83

4.34 Typical evolution of contact parameters of PoliTO specimens: a) Hysteresis loops; b) Friction coefficient; c) Tangential contact stiffness (k_{tL} and k_{tR} are the contact stiffnesses of left and right stick portions of the hysteresis loops, as defined in section 3.2.1). Vertical lines indicate the beginning of the steady state; the photo shows the specimen interfaces at the end of the test with a full worn area of contact. Values for the Test n. TO14: 87 N normal load, 14 μm displacement amplitude, 5 mm^2 nominal area of contact, 175 Hz excitation frequency and 2.5 hours of running. 85

4.35 Example of post-processing issues in the k_t estimations occurring in few PoliTO tests with very large k_t (>300 N/μm). Test n. TO5: 87 N normal load, 14 μm displacement amplitude, 10 mm^2 nominal area of contact, 175 Hz excitation frequency and 6 hours of running. 86

4.36 Tangential contact stiffness evolution for the Test n. TO25 (17 N normal load, 14 μm displacement amplitude, 5 mm^2 nominal area of contact, 175 Hz excitation frequency and 2.5 hours of running). Vertical lines indicate the beginning of the steady state for k_t left and right; the photo shows the specimen interfaces at the end of the test. 86

4.37 a) Evolution of hysteresis loops for the Test n. TO10 performed at 1 μm displacement amplitude on the PoliTO friction rig. The photo shows the specimen interfaces at the end of the test (no wear present); b) k_t evolution in time. Vertical lines indicate the beginning of the steady state (k_{tL} and k_{tR} are the contact stiffnesses of left and right stick portions of the hysteresis loops, as defined in section 3.2.1); c) Details of hysteresis loops at measured at different times to assess the difference between k_t left and right. Values for the Test n. TO10: 87 N normal load, 1 μm displacement amplitude, 5 mm^2 nominal area of contact, 175 Hz excitation frequency and 2.5 hours of running. 88

4.38 Repeatability study for specimens with 5 mm^2 nominal area of contact. Three tests performed with the same loading conditions but different specimen pairs: a-b) Friction coefficient, μ, (linear and log scale). The photos show the specimen interfaces at the end of the test with a full worn area of contact; c-d) Tangential contact stiffness, k_t, (linear and log scale). Values for the Tests n. TO30-14-18: 87 N normal load, 14 μm displacement amplitude, 5 mm^2 nominal area of contact, 175 Hz excitation frequency and 2.5 hours of running, total hysteresis cycles=1575000, material=stainless steel, temperature=25°C. 89

4.39 Repeatability study for specimens with 40 mm^2 nominal area of contact. Three tests performed with the same loading conditions but different specimen pairs: a-b) Friction coefficient, μ, (linear and log scale). The photos show the specimen interfaces at the end of the test (the red dots indicate the laser measurement location); c-d) Tangential contact stiffness, k_t, (linear and log scale). Values for the Tests n. TO32-33-45: 87 N normal load, 14 μm displacement amplitude, 40 mm^2 nominal area of contact, 175 Hz excitation frequency and 2.5 hours of running, total hysteresis cycles=1575000, material=stainless steel, temperature=25°C. 89

4.40 a) Tangential contact stiffness steady state values, k_t, of the round robin test on the PoliTO friction rig; b) Worn area normalised tangential contact stiffness steady state values, K_T; c) Worn areas of contact at the end of each test, plus photos of worn areas at the end of tests for the 40 mm^2 nominal area of contact case. 90

4.41 Violin plots of the steady state values of the tangential contact stiffness, k_t, of every round robin test on the PoliTO friction rig. Each violin corresponds to a different test for one normal load, displacement amplitude and nominal area of contact. The legends indicate the mean and standard deviation of the steady state values of each test. The figure titles indicate the worn areas of the three tests and the energy dissipated when the steady state was reached (note that in most of the tests the steady state was not reached, and the energy represents the energy towards the end of the test). 91

4.42 Violin plots of the steady state values of the worn area normalised tangential contact stiffness, K_T, of every round robin test on the PoliTO friction rig. Each violin corresponds to a different test for one normal load, displacement amplitude and nominal area of contact. The legends indicate the mean and standard deviation of the steady state values of each test. The figure titles indicate the worn areas of the three tests and the energy dissipated when the steady state was reached (note that in most of the tests the steady state was not reached, and the energy represents the energy towards the end of the test). Tests with unmeasured worn areas are not presented. 92

4.43 a) Hysteresis loops measured at different sliding distances at 175 Hz excitation frequency within the same test; b) k_t as a function of the displacement amplitude from hysteresis loops shown in a). Note that k_t is the slope measured right after the load reversal in each hysteresis loop. Test conditions: 87 N normal load, 10 mm^2 nominal area of contact, 175 Hz excitation frequency, steady state reached after 2.5 hours of running at 50 μm and then loops measured at different displacement amplitudes, material=stainless steel, temperature=25°C. 93

4.44 Evolution of the tangential contact stiffness of two tests performed on the PoliTO friction rig under the same loading conditions (87 N normal load, 14 μm displacement amplitude, 10 mm^2 nominal area of contact): a) Test n. TO6, k_t is very low because the displacement is measured on the leg not in contact (see red dot); b) Test n. TO3, k_t is larger because the contact is concentrated on the measured leg too. k_{tL} and k_{tR} are the contact stiffnesses of left and right stick portions of the hysteresis loops, as defined in section 3.2.1. 94

4.45 Boxplots of the tangential contact stiffness steady state (or end-of-test) values versus the worn areas of contact at the end of the tests on the PoliTO friction rig: a) Tests n. TO3-45-5 performed under the same loading conditions (87 N normal load, 14 μm displacement amplitude, 10 mm^2 nominal area of contact); b) Tests n. TO30-5-32 performed under the same loading conditions (87 N normal load, 14 μm displacement amplitude) and different nominal areas of contact (5, 10 and 40 mm^2); c) Tests n. TO26-22-31 performed under the same loading conditions (254 N normal load, 14 μm displacement amplitude) and different nominal areas of contact (5, 10 and 40 mm^2); d) Tests n. TO42-12-37 performed under the same loading conditions (254 N normal load, 50 μm displacement amplitude) and different nominal areas of contact (5, 10 and 40 mm^2). The red dots represent the location of the laser measurement. 95

4.46 Friction coefficient steady state values of the round robin test on the PoliTO friction rig. 96

4.47 Steady state hysteresis loops measured on the PoliTO friction rig under 175 Hz excitation frequency, 50 μm displacement amplitude, room temperature and: a) 17 N normal load (Test n. TO44); b) 254 N normal load (Test n. TO37). 96

4.48 Violin plots of the steady state values of the friction coefficient of every round robin test on the PoliTO friction rig. Each violin corresponds to a different test for one normal load, displacement amplitude and nominal area of contact. The legends indicate the mean and standard deviation. The figure titles indicate the worn areas of the three tests and the energy dissipated when the steady state was reached. 97

4.49 Steady state (or end-of-test) values for the 5 and 10 mm^2 nominal areas of contact. μ values refer to the standard friction coefficient and k_t values refer to the tangential contact stiffness of the left part of the hysteresis loops. The energy indicates the energy dissipated when a steady state in the contact parameter was reached. The worn areas of contact at the end of tests performed at 14 μm of displacement amplitude are also shown (red dots indicate the laser measurement location). 99

4.50 Tangential contact stiffness steady state values. Each point in the Figure corresponds to a different test of the round robin matrix with a different worn area of contact: a) Worn area normalised K_T versus contact pressure (normal load divided by the worn area). Note that, although some tests were performed with the same normal load, they have different contact pressures due to their different worn areas. The experimental fit on the Imperial tests is also shown (see Eq. 4.1); b) Worn area normalised K_T versus normal load; c) Un-normalised k_t versus normal load. 101

4.51 Friction coefficient steady state values plotted versus the normal load. Each point in the Figure corresponds to a different test of the round robin matrix. 102

5.1 Specimen designed to accommodate an ultrasonic transducer: a) Photo; b) Scheme; c) Specimens' top view. Shear waves are polarized in the y-direction [263]. 110

5.2 a) Simplified scheme of the ultrasonic experimental setup (note that the exact position of the ultrasonic transducers T/R#1 and R#2 is that shown in Fig. 5.1b); b) Incident signal characteristics [263]. 111

5.3 Vibration tests under stuck conditions: a) Hysteresis loops measured in stuck condition at different normal loads; b) Tangential contact stiffness extracted from hysteresis loops, k_t, as a function of the normal load [263]. 113

5.4 1000 peaks in the transmitted signals: a) Static test; b) Stick test at 0.4 μm displacement amplitude for some normal loads from the measurements of Fig. 5.3 [263]. 114

5.5 Vibration tests under stuck conditions: a) Reflected and b) Transmitted signals as a function of the normal load [263]. 115

5.6 Vibration tests under stuck conditions: a) Reflection coefficients obtained from values of Fig. 5.5a; b) Tangential contact stiffness obtained from the reflection coefficient by using Eq. 2.13 (Tattersall formulation) [263]. 116

5.7 Vibration tests under stuck conditions - each point corresponds to a different normal load: a) k_t from hysteresis loops vs k_{us} from ultrasonic reflection or b) k_t from hysteresis loops vs ultrasonic transmitted signal [263]. 117

5.8 Vibration tests under stuck conditions: comparison of tangential contact stiffness from hysteresis loop, k_t; from ultrasonic reflection measurements, k_{us}; and from Eq. 5.1, k_{eq}, which includes the interface contribution (i.e. k_{us}) and the bulk deformation contribution (i.e. stiffness k_{bulk} obtained from the FE model of the Appendix E) [263]. 118

5.9 Tests under different displacement amplitudes and constant normal load: a) Hysteresis loops; b) Tangential contact stiffness extracted after load reversal for each hysteresis loop [263]. 120

5.10 Tests under different displacement amplitudes and constant normal load - transmitted signal within hysteresis loops: a) Time history of the transmission within 10 consecutive hysteresis loops measured at different displacement amplitudes; b) Standard deviation from mean transmission within the hysteresis loops measured at different displacement amplitudes [263]. 122

5.11 Tests under different displacement amplitudes and constant normal load: a) Reflected and b) Transmitted signals as a function of the displacement amplitude [263]. 122

5.12 Tests under different displacement amplitudes and constant normal load - each point corresponds to different hysteresis loops with different displacement amplitudes: a) k_t from hysteresis loops vs k_{US} from ultrasound reflection or b) k_t from hysteresis loops vs transmitted signal [263]. . . . 123

5.13 a) Ultrasonic transmission (in colorbar) within the hysteresis loops measured at different displacement amplitudes (1, 3, 10 and 30 μm respectively). The respective ultrasound time histories are shown in Fig. 5.10a; b) Ultrasonic transmission plotted versus the relative displacement to better identify peaks and drops [263]. 124

6.1 Hammer test campaign to evaluate the rig dynamic behaviour: a) moving mass alone; b) moving arm freely suspended on one end and attached to the moving mass on the other end; c) assembly with a very large normal load, which guaranteed a full stuck configuration [169]. 130

6.2 Effect of the normal load on hysteresis loops measured at a 100 Hz harmonic excitation. The transition from stick to microslip to gross slip is visible as the normal load decreases [169]. 133

6.3 FRFs of the friction rig obtained from hammer tests performed at different normal loads and 100 N of excitation impacts [169]. 134

6.4 Effect of displacement amplitude on hysteresis loops (blue plots) and excitation force (orange plots). φ is the phase between the excitation force and the displacement. The resonant frequency of the first mode decreases from 200 Hz to 40 Hz as the displacement amplitude increases [169]. . 135

6.5 FRFs obtained from the linear 2 DOFs model of the friction rig shown in Fig. 6.1c. Different values of k_3 stiffness were obtained by fitting the hysteresis loops to straight lines. In the background, the experimental FRFs of Fig. 6.3 are shown to see the overlap of the resonant frequencies with those numerical [169]. 136

6.6 Evolution of the rig dynamics: a) 7N normal load; b) 60N normal load. Hysteresis loops are only indicative [20]. 138

6.7 a) Typical hysteresis loop recorded at a 100 Hz harmonic excitation, 60 N normal load and 14 μm of sliding amplitude. Oscillations in the gross slip region are visible; b) friction force time signal and static arm scheme [169]. 140

6.8 a) FRF of the static arm from an hammer test at 60 N of normal load and 100 N of excitation impact; b) experimental setup [169]. 140

6.9 a) Hysteresis loops measured at two slightly different excitation frequencies; b) friction forces fft [169]. 141

6.10 Visualisation of substructures coupling. The assembly AJB consists of two substructures A and B and the joint J. The two substructures are coupled with a flexible joint, indicating a "weak interface", e.g. the joint consists of springs and dampers and is assumed to be massless [272]. . . . 143

6.11 DS contact stiffness estimation over the investigated frequency range [272]. 144

6.12 a) Fully stuck hysteresis loop at 100 Hz; b) Example of elliptical hysteresis loop measured in the 192-218 Hz frequency range [272]. 144

7.1 Typical evolution of the contact interface of Imperial specimens with wear: a) unworn contact and stiffness contributions; b) stiffness contributions in the worn contact. $k_{topography}$ is the stiffness due to asperities and waviness of the real (non-smooth, non-flat) surface topography; k_{bulk} is the stiffness due to the bulk deformation of the (upper-bound) smooth and flat interface. 149

7.2 a) Photo of one specimen; b) Specimen held by the holders; c) Side view of the specimen close to the contact interface; d) FE mesh of the specimens and points of measured displacement. . . . 150

7.3 Displacement field of the deformed specimens under a 100 N tangential load (only the component in the sliding direction). Most of the deformation occurs in the portion highlighted with the red circle. Bulk stiffness values, k_{bulk}, are shown at different locations. The further the measurement points, the lower the k_{bulk}. 150

7.4 a) Curvature of the real specimen contact interface. When the mating specimen is oriented orthogonally, the resulting equivalent contact is a curved (spherical) contact; b) Rendering of the curved ideal unworn contact interface (33.2 mm curvature); c) Rendering of the curved contact interface with a 33.2 mm curvature and a flat portion at the tip that represents an ideal flat worn area of 0.34 mm^2. 153

7.5 BEM predictions for the (a-b-c) ideal unworn interface and the (d-e-f) 0.34 mm^2 "ideal" worn interface: a-b/d-e) normal and tangential pressure distributions; c/f) Hysteresis loops. 154

7.6 k_t versus worn areas of contact: comparison of experimental data from Fig. 4.16 and BEM predictions with ideal worn areas set up as in Fig. 7.4c. Also the k_{bulk} obtained from the FE simulation of Fig. 7.3 are shown. 154

7.7 Real surface data: a-b) Specimens A and B; c) Specimen B with best orientation to match specimen A (correlation coefficient of 0.84 in this case); d-e) Specimens A and B after cross-correlation and cropping; f) Height difference of the two specimen interfaces used as input in the BEM solver. 157

7.8 k_t versus worn areas of contact: comparison of experimental data from Fig. 4.16 and BEM predictions with ideal and real worn areas. 158

7.9 Relative height of the two contact interfaces for the test with a 0.44 mm^2 worn area of contact. A reference plane is plotted to show where the worn area would lie. The peaks and valleys that pass through the plane are probably due to missing wear debris that leads to a wrong relative height calculation. 158

7.10 Comparison between numerical and experimental results for the test of section 6.2.3: a) numerical loops; b) numerical loops vs experimental loops; c) friction coefficient vs energy dissipated (wear function defined in Table 7.1); d) contact stiffness vs energy dissipated (wear function defined in Table 7.1) [20]. 162

7.11 Numerical FRFs, before and after wear, based on the input hammer excitation of the test 1: a) 7 N normal load; b) 60 N normal load. Compare with the experimental FRFs in Fig. 6.6 [20]. . . 163

7.12 Photo of the underplatform damper rig [19]. 163

7.13 Comparison of experimental FRFs [19] and numerical FRFs predicted for different k_t on the UPD rig. 166

7.14 Comparison of amplitude response from the updated PCE models and experimental data from the UPD rig [278]. . . . 168

8.1 a) FE model of the high-pressure turbine bladed disk sector used in the analysis (IP-free version); b) FE model of the damper (IP-free version); c-d) Close-up of the blade-damper assembly. . . . 172

8.2 Strain gauge locations for the vibration test and corresponding mode shapes. . . . 174

8.3 Engine order components of strain gauge experimental data for the four modes of interest. . . . 175

8.4 a) Most common contact marks on the damper; b) kinematics blade/damper due to the centrifugal load. . . . 175

8.5 Six contact bedding patterns used in the simulation and three grid densities (shown in different colours – red, green and blue). . . . 177

8.6 a) Contact pressure on each damper face as a function of the rotating speed; b) tangential contact stiffness dependency on the contact pressure, measurements from chapter 4 and ref. [85]; c) tangential contact stiffness as a function of the rotational speed; d) global contact stiffness as a function of the rotational speed. . . . 179

8.7 Low EO/mode 2 (1E) simulations for the six bedding patterns and the node grid density 40*3: a) K_T=30000 N/mm^3 for all the bedding patterns – this leads to lower global k_t for bedding patterns with lower nominal areas of contact; b) k_t=3701 N/μm for all the bedding patterns – this case is needed to investigate the effect of the patterns alone. . . . 182

8.8 Low EO/mode 2 (1E) simulations for the six bedding patterns and the node grid density 40*3: a) k_t load dependence case; b) k_t load dependence case and response normalised by the scaling factor of exciting forces. . . . 183

8.9 Low EO/mode 2 (1E) contact states at resonance for the k_t load-dependent simulations with grid density 40*3: a) Full contact bedding pattern; b) OuterEdgeContactv2 bedding pattern; c) Convex contact bedding pattern. Note that the 2D damper view is deformed to protect intellectual property. . . . 184

8.10 Low EO/mode 2 (1E) energy dissipated at resonance for the k_t load-dependent simulations with grid density 40*3: a) Full contact bedding pattern; b) Real contact bedding pattern v2; c) Convex contact bedding pattern. Energy dissipated over frequency range: d) Full contact bedding pattern; e) OuterEdgeContactv2 bedding pattern; f) Convex contact bedding pattern. Note that the 2D damper view is deformed to protect intellectual property. . . . 184

8.11 Low EO/mode 2 (1E) strain amplitudes. Comparison between strain gauge data and simulations for three bedding patterns with node grid density 40*3. . . . 186

8.12 Friction coefficient sensitivity: simulations for the three modes (a-b-c) and outer edge contact v2 case, grid density 40*3, k_t load-dependence. . . . 189

8.13 Friction coefficient sensitivity for low EO/mode2, outer edge contact v2 case, grid density 40*3, k_t load-dependence: a-c, Contact conditions; d-f, Energy dissipated. Note that the 2D damper view is deformed to protect intellectual property. . . . 190

8.14 Grid density sensitivity. Full contact and outer edge contact v2 cases with k_t load dependence. Hz shifts are referred to the undamped resonance, while amplitudes are referred to the full contact bedding pattern with K_T=30000 N/mm^3. . . . 191

A.1 Politecnico di Torino friction rigs: a) sphere-on-flat test rig [14, 86]; b) flat-on-flat test rig [170]. . 230

A.2 a) University of Oxford - Linear motion test rig [80]; b) “Hook” feature in the hysteresis loops [229]; c) Schematic diagram of wear–scar interaction types [229]. . . . 232

A.3 a) University of Oxford - Torsional motion test rig [229]; b) Two contact configurations; c) Hysteresis loops for the two contact configurations [229]. 232

B.1 a) Typical photo of the side view of moving and static arms used for the DIC study. In blue and orange highlighted the point locations used for the analysis; b) Normal stiffness on the point locations highlighted in a); c) Rig deformation for three different normal loads visualised with 500 scaling magnification. 234

C.1 Wear volume as a function of energy dissipated at the contact. Test conditions: excitation frequency=100Hz, normal load=60 N, nominal area of contact=$1mm^2$, material=Stainless Steel, temperature=25°C. 236

C.2 Hilbert analysis to capture the evolution of the first natural frequency during test 5: a) Time signal at the end of the test; b) Hilbert envelope of the filtered signal; c-d) Amplitude dependencies of natural frequency and damping ratio obtained from the Hilbert envelopes [20]. 237

D.1 Colour-coded magnitude of displacements measured at two simulation times for the "bonded contact model". a) The red area shows the extent of the modelled sensor patch. b-c) Section cuts in the y-z and z-x planes, respectively, after 3μs from the wave being generated. 240

D.2 a) Comparison between experimental and numerical signals obtained for the "no contact model" (both signals normalized to the peak of their envelopes). b) Comparison between numerical signals obtained for "no contact" (same as red signal in (a)) and "bonded contact" models, both signals being normalized to the envelope peak of the former. 240

E.1 a) FE mesh of the specimens and points of measured displacement; b) Bulk stiffness values, k_{bulk}, at different locations. The further the measurement points, the lower the k_{bulk}. 242

F.1 a) Specimen photo and surface data to show the curvature; b) Specimen FE model; c) Rendering of the curved contact interfaces of the two specimens in contact. 245

F.2 a) Specimen held by the holders; b) Side view of the specimen close to the contact interface; c) Full set of FE nodes; d) Reduced set of FE nodes. 246

F.3 Pressure distribution and specimen interfaces for the nominally flat specimens at 87 N normal load and 14 μm displacement amplitude. Results given at different wear cycles. 247

F.4 k_t as a function of the number of cycles for the nominally flat specimens and different normal loads. 247

F.5 Pressure distribution and specimen interfaces for the curved specimens at 87 N normal load and 14 μm displacement amplitude. Results given at different wear cycles. 248

F.6 a) k_t as a function of the number of cycles for the curved specimens and different normal loads; b) k_t as a function of the energy dissipated for the curved specimens and different normal loads. 249

G.1 High EO/mode 3 (1T) simulations for the six bedding patterns and node grid density 40*3: a) k_t=30000 N/mm^3; b) k_t=3701 N/μm (case needed to investigate the effect of the patterns alone). 251

G.2 High EO/mode 3 (1T) simulations for the six bedding patterns and node grid density 40*3: a) k_t load dependence case; b) k_t load dependence case and response normalised by the scaling factor of exciting forces. 251

G.3 High EO/mode 3 (1T) contact states at resonance for the k_t load dependent simulations with grid density 40*3: a) Full contact bedding pattern; b) OuterEdgeContactv2 bedding pattern; c) Convex contact bedding pattern. Energy dissipated at resonance for: d) Full contact bedding pattern; e) OuterEdgeContactv2 bedding pattern; f) Convex contact bedding pattern. 252

G.4 High EO/mode 4 (2F) simulations for the six bedding patterns and node grid density 40*3: a) k_t=30000 N/mm^3; b) k_t=3701 N/μm (case needed to investigate the effect of the patterns alone). 253

G.5 High EO/mode 4 (2F) simulations for the six bedding patterns and node grid density 40*3: a) k_t load dependence case; b) k_t load dependence case and response normalised by the scaling factor of exciting forces. 254

G.6 High EO/mode 4 (2F) contact states at resonance for the k_t load dependent simulations with grid density 40*3: a) Full contact bedding pattern; b) OuterEdgeContactv2 bedding pattern; c) Convex contact bedding pattern. Energy dissipated at resonance for: d) Full contact bedding pattern; e) OuterEdgeContactv2 bedding pattern; f) Convex contact bedding pattern. 255

G.7 High EO/mode 3 (1T) strain amplitudes. Comparison between strain gauge data and simulations for two bedding patterns with node grid density 40*3. 256

G.8 High EO/mode 4 (2F) strain amplitudes. Comparison between strain gauge data and simulations for two bedding patterns with node grid density 40*3. 257

G.9 Low EO/mode 1 (1F) strain amplitudes: a) Comparison between strain gauge data and simulations. The outer edge bedding pattern has node grid density 40*3 and k_t load dependence; b) the contact conditions at resonance. 258

G.10 Combined analysis of low EO/mode 1 (1F) and high EO/mode 4 (2F). a) Comparison between strain gauge data and simulations for the outer edge bedding pattern with node grid density 40*3 and k_t load dependence; b) Close-up of the combined analysis simulation resonance. 259

G.11 a) Combined analysis of low EO/mode 1 (1F) and high EO/mode 4 (2F), with excitation 50 times larger than what was used in Figure 37; b) contact conditions at resonance. 259

G.12 Combined analysis of low EO/mode 1 (1F) and high EO/mode 4 (2F). Effect on high EO/mode 4. 260

Chapter 1

Introduction

"CO2 levels today are at a level not seen since 3 million years ago when there were trees on Antarctica ... and that is why we are pledged here in the UK to deliver net zero carbon emissions by 2050."

UK Prime Minister Boris Johnson launches the next United Nations Climate Conference, Feb 2020 [1]

"Aviation has to play its full part in delivering a zero carbon future ... innovating and introducing new, low carbon technologies, from new engine and aircraft designs to ground-breaking sustainable aviation fuels."

Neil Robinson, the chair of UK Sustainable Aviation, Feb 2020 [2]

To achieve the zero-carbon target in aviation, new aero-engine designs will have to be lighter and more flexible. With lighter designs, new challenges appear for the safe operation of the aircraft, such as increased vibration levels. Uncontrolled, vibrations might lead to loss of performance, higher maintenance and large stresses in components that compromise the integrity of the entire engine. A great deal of research is currently being conducted in industry and academia to accurately predict such unwanted vibrations. There is currently no fully-predictive modelling approach, and expensive physical testing is still required to validate the new designs. Predictive capabilities are limited, partly due to the presence of friction between the thousands of components in contact (e.g. friction dampers, bolted joints, dove-tail or fir-tree joints as shown in Fig. 1.1). Beyond their primary function of joining components, guaranteeing the structural integrity and potentially sealing, friction contacts are often the main source of damping in the assembly, due to the energy dissipation at the interfaces, and as such largely influence the nonlinear dynamic response [3–5]. The introduced damping is beneficial as it reduces vibration amplitudes that could lead to high cycle fatigue failures, but is also detrimental since it introduces wear that leads to degradation of components with consequently increased maintenance requirements. The understanding of these friction mechanisms is of importance for more accurate predictive capabilities.

Despite the good progress already achieved, the understanding of the friction mechanisms and the prediction of their effects on the dynamics of jointed structures are still considered as a "grand challenge", as discussed during a series of workshops organized in the last 15 years by the joint mechanics community [7–9]. Even the physics' Nobel Laureate Wolfgang

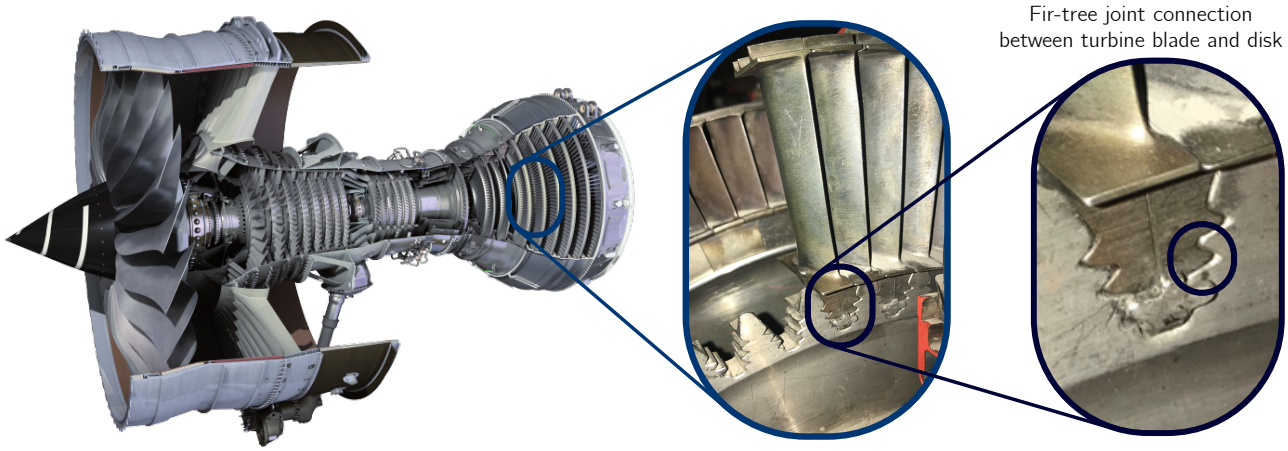


Figure 1.1: The Trent XWB aero engine from Rolls-Royce [6] and an example of friction joints.

Pauli once said, "*God made the bulk; surfaces were invented by the devil*", as quoted in [10]. He did not refer to nonlinearities introduced by the joints, but his quote perfectly catches the essence of the problem: surface contact interactions are extremely difficult to understand and model due to their complexity. One of the challenges is the multidisciplinarity of the problem, which involves different research fields, such as tribology, contact mechanics and nonlinear dynamics, whose combined knowledge is required to advance the understanding of such interfacial dissipation and dynamical system responses. In addition, jointed structures are computationally challenging to analyse due to the resolution of length scales, ranging from the micro-scale to capture the dissipative phenomena up to the macro-scale to capture the global vibration of the contacting components. The length scales of the resulting model must therefore span several orders of magnitude, leading to significant computational challenges, unless simplified modelling approaches are employed.

A series of modelling approaches, hereafter referred to as nonlinear dynamic analysis, has been developed in the years to overcome those challenges and model the nonlinear frictional behaviour of joints [3]. Many of the current approaches base their predictive capabilities on the discretisation of the contact interfaces and on the use of hysteresis loops to capture the underlying friction mechanisms across the interface [11–13]. Hysteresis loops are the cyclic load-deflection curves that plot the friction force against the relative displacement occurring between two oscillating contact interfaces (see Fig. 1.2). These curves are the common basis for many of the modelling approaches for nonlinear dynamic analysis [14] since they can represent to a reasonable degree the underlying physics of the contacting interfaces, for example by capturing stick, microslip, gross slip and separation contact states. Although these approaches have been validated against global response data, leading to a high level of confidence in their overall capabilities, the physics-based modelling of the interface mechanisms remains a large unknown due to a lack of high-quality validation data from the contact interfaces. It is in fact challenging to capture what is happening locally in the interface during high-frequency vibration cycles without interfering with the contact interface itself. This lack of validation data prevents the development of fully-validated and predictive modelling approaches. As a result, expensive physical testing is required to assess the performance and reliability of new designs.

The object of this PhD research is therefore to improve current modelling approaches by providing more reliable and detailed input contact parameters for the contact models and improving

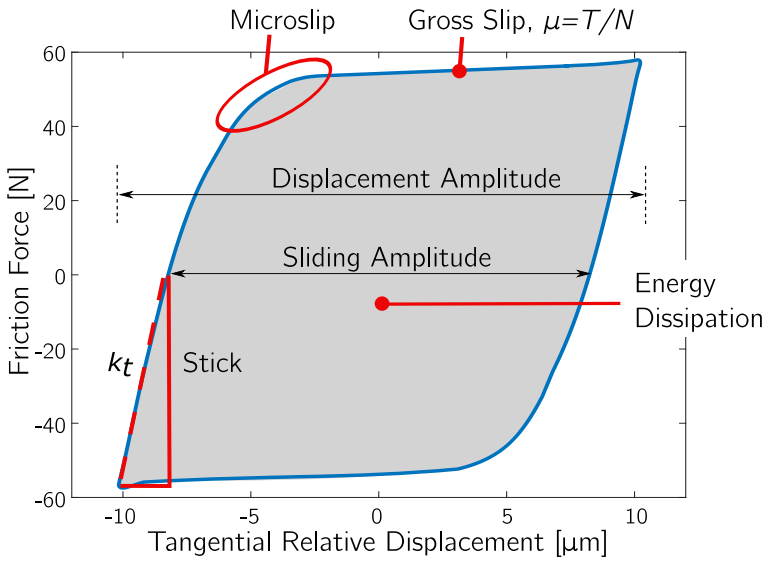


Figure 1.2: Friction hysteresis loop, the load-deflection curve resulting from the vibrating motion of two contact interfaces. μ is the friction coefficient, T is the friction force during gross slip, N is the normal load and k_t is the tangential contact stiffness.

the understanding of the effects of those parameters on the nonlinear dynamic response. This is achieved with an extensive experimental investigation by using a high-frequency friction rig that measures hysteresis loops. The obtained understanding is then used to perform upgraded simulations for nonlinear dynamic analysis, which are validated against experimental data. The goals of this PhD thesis are summarised as follows:

1. Provide a better understanding of the underlying physics of the contact parameters used in nonlinear dynamic analysis and identify and quantify any missing parameters.
   To be achieved with experiments on contact and friction.

2. Provide a better understanding of the effects of those contact parameters on the nonlinear dynamic response of jointed structures.
   To be achieved with experiments on nonlinear dynamics.

3. Identify any shortcomings in state-of-the-art modelling and measuring approaches for nonlinear dynamic analysis and upgrade and/or validate them.
   To be achieved with experiments and simulations on contact and nonlinear dynamics.

With this PhD research, the understanding of friction mechanisms is improved together with their effects on the dynamic response of jointed structures. Findings are potentially applicable to all joint types, although the main focus here is on friction dampers. Missing features in state-of-the-art modelling approaches are identified and their impact on the dynamic response predictions is highlighted. This improved understanding takes a step towards the ultimate community goal of providing a fully-validated nonlinear model of turbomachinery components required for safer and cleaner aero-engine designs.

1.1 Thesis outline

This thesis structure is shown in Fig. 1.3 and the chapters are briefly described below.

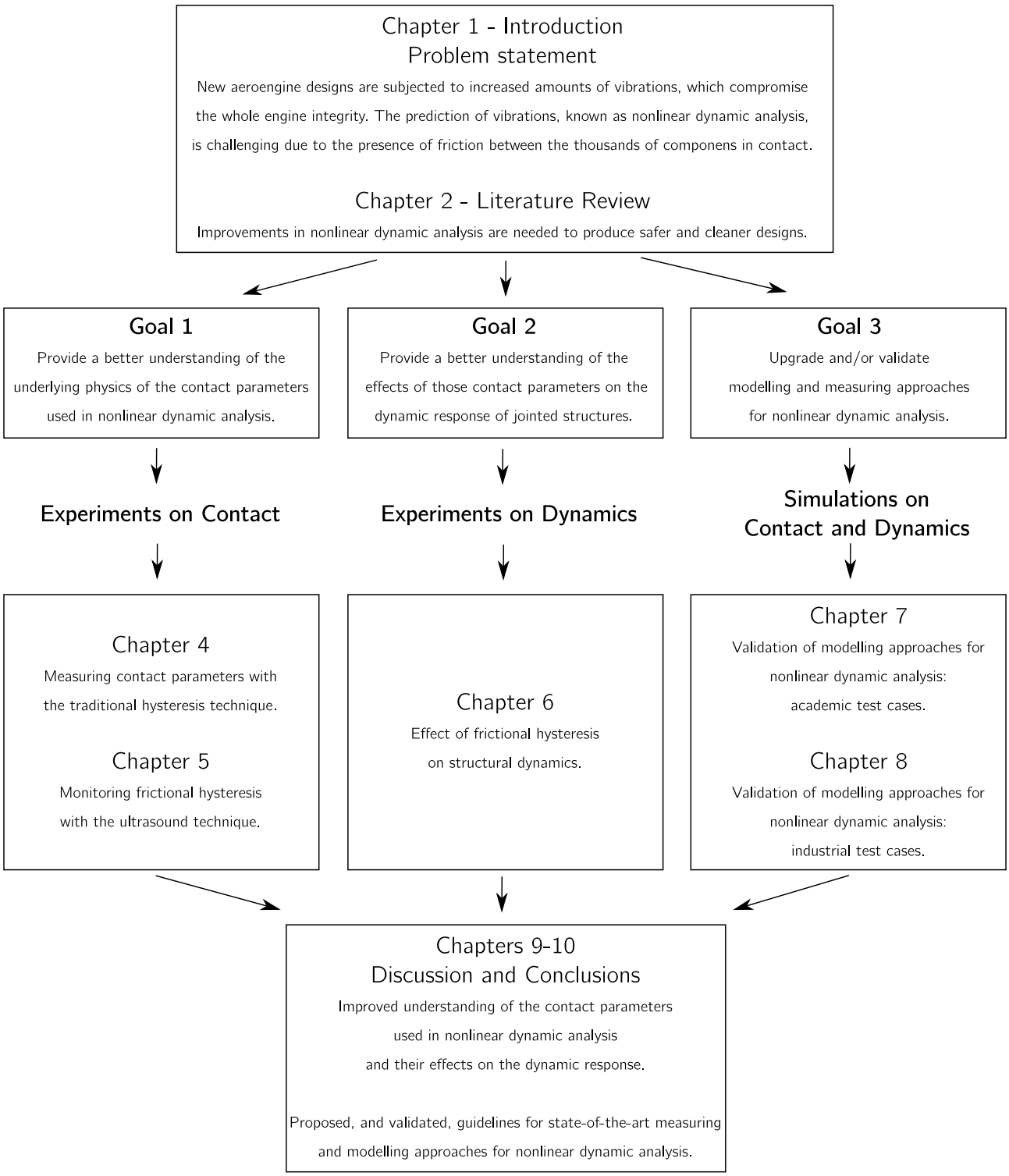


Figure 1.3: Thesis structure.

Ch.2: Literature Review. A critical review of the modelling approaches for nonlinear dynamic analysis of jointed structures is presented. An overview is also provided of the physics

of the contact parameters with a description of the measuring and modelling techniques used for their estimation.

Ch.3: Evaluation of the existing high-frequency friction rig. This PhD work is mainly experimental and focuses on a high-frequency friction rig built to measure hysteresis loops. Detailed static and dynamic analyses of the friction rig are presented together with the post-processing methods to extract contact parameters for nonlinear dynamic analysis.

Ch.4: Measuring contact parameters with the traditional hysteresis technique: round robin test including rigs of different institutions. An extensive round robin test between the two high-frequency friction rigs of Imperial College London and Politecnico di Torino was conducted to measure a multitude of hysteresis loops. Measurements provided several novel insights into the physics of the contact parameters and resulted in guidelines proposed to improve current modelling approaches.

Ch.5: Monitoring frictional hysteresis with the ultrasound technique. The round robin hysteresis measurements were based on information coming only from the outer edge of the contact, where the displacement was measured. The behaviour of the central part of the contact was instead unknown, thus limiting the completeness of the measurements. Therefore, another experimental method was used to access the central part of the contact during vibration: the ultrasound technique, which was used simultaneously with the hysteresis measurements to monitor the vibrating contact in real time. Unprecedented insights are provided on some physical aspects of the friction mechanisms and hysteresis and ultrasonic measurements are cross-validated.

Ch.6: Effect of frictional hysteresis on the structural dynamics. Previous chapters have improved the understanding of the physics of input contact parameters for nonlinear dynamic analysis. In this chapter, such understanding is used to investigate the effect of the contact parameters on the dynamics in order to provide suggestions to improve existing measuring and modelling approaches for nonlinear dynamic analysis.

Ch.7: Validation of modelling approaches for nonlinear dynamic analysis: academic test cases. The improved understanding from previous chapters is used here to upgrade state-of-the-art modelling approaches for nonlinear dynamic analysis by introducing, for example, the effect of wear, normal load and surface topography in the simulations. Two academic test cases are used, the high-frequency friction rig and an underplatform damper rig at Imperial College. Two sets of simulations are performed: contact simulations employing finite element and boundary element methods, and nonlinear dynamics simulations employing time and frequency domain solvers. Predictions are validated against the experimental measurements presented in the previous chapters.

Ch.8: Validation of modelling approaches for nonlinear dynamic analysis: industrial test cases. During the final year of this PhD project, a 3-month secondment was organised at Rolls-Royce Plc to apply and transfer the developed knowledge to improve the industrial approaches for nonlinear dynamic analysis. For this purpose, an aero-engine turbine bladed disk sector equipped with underplatform dampers was used for improved nonlinear dynamics predictions that were compared against existing measured data.

Ch.9: Guidelines for improved nonlinear dynamic analysis. Findings from previous chapters are put into context and discussed. Guidelines are proposed i) to increase the reliability

of the measuring approaches employed for the extraction of the contact parameters and ii) to improve modelling approaches for nonlinear dynamic analysis.

Ch.10: Conclusions. Overall conclusions are presented together with recommendations for future research directions and best industrial practices.

Chapter 2

Literature review

This literature review provides an overview of the modelling approaches for nonlinear dynamic analysis of jointed structures. The review is divided into five sections. First, the most common mechanical joints are presented together with their effects on the dynamics of jointed structures. State-of-the-art approaches for nonlinear dynamic analysis are also summarised. Then, an overview of the physics of input contact parameters for nonlinear dynamic analysis is presented. After that, an overview is given of the contact models used for nonlinear dynamic analysis. The last two sections describe how to estimate the input contact parameters for those contact models, with modelling and experimental methods respectively.

2.1 Nonlinear dynamic analysis of jointed structures

In turbomachinery assemblies, thousands of friction contacts are present. Figure 2.1 shows the most common mechanical joints found in aero-engines, such as blade root contacts in turbine blades [15–17]. Another source of friction is the presence of friction dampers, which are devices purposely designed to take advantage of energy dissipation. These devices are small metal masses placed in different locations within the turbine assembly and dissipate energy through frictional interactions with the mating components. Friction dampers are relatively inexpensive and easy to replace. Figure 2.2a-b shows the most common type of friction damper, the underplatform damper [11, 13, 18]. Centrifugal forces, generated by the disk rotation, push the damper against the blade platforms. During vibrations, a sliding motion takes place between the damper and the blade platform, thus leading to energy dissipation that reduces the vibration amplitudes.

These contacts have a heavy impact on the dynamic response in terms of shifts in resonant frequency and changes in vibration amplitude [20–22]. Such changes might induce unwanted stresses in the structure, which could eventually lead to high cycle fatigue failures of components [15, 23]. Therefore, predicting the local frictional response is an essential step to get more accurate dynamic response simulations. The dynamic response is studied by analysing the frequency response functions (FRFs) of the structure, which are the characteristic frequency-dependent responses of the system subjected to harmonic excitation. In the case of turbine assemblies, the excitation comes mainly from fluid flows impacting on the blades, which in turn start to vibrate.

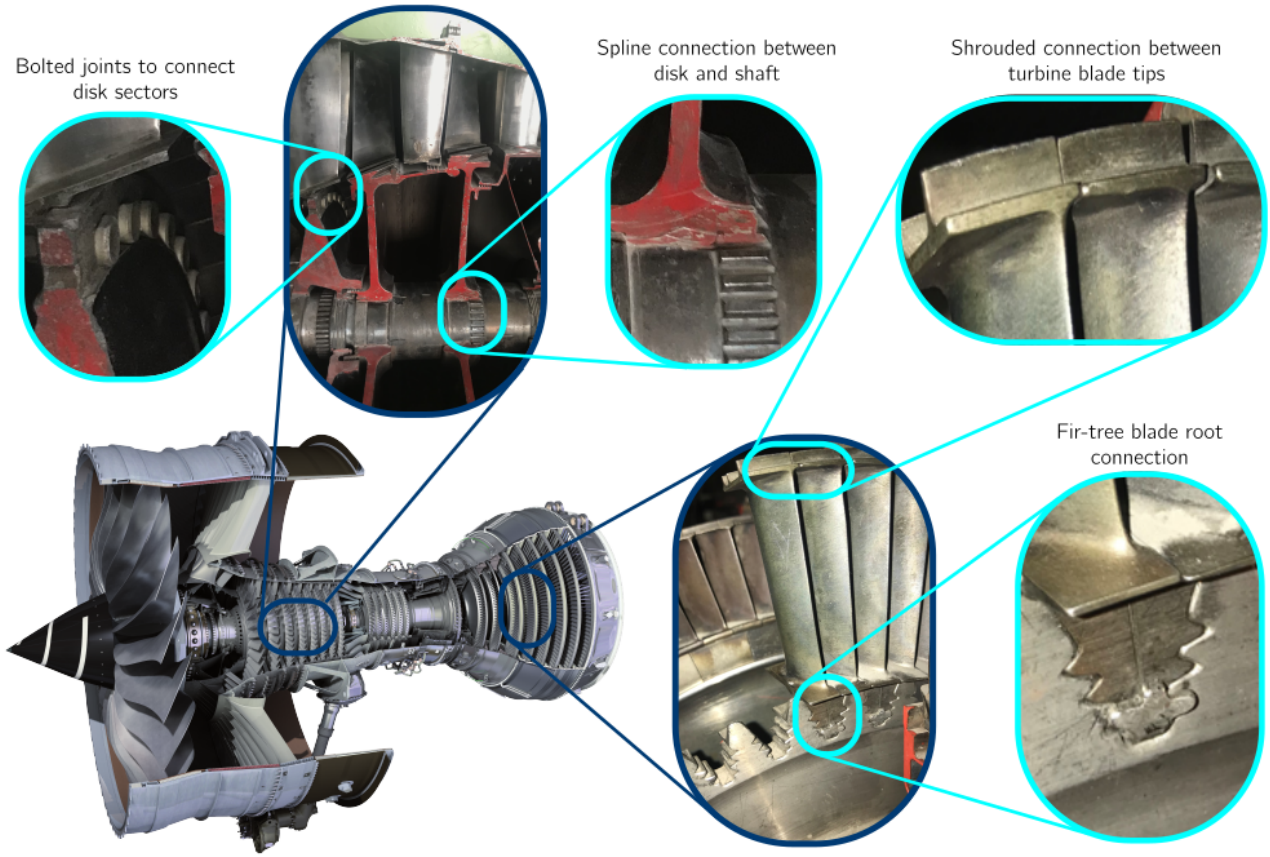


Figure 2.1: Most common mechanical joints in aero-engines.

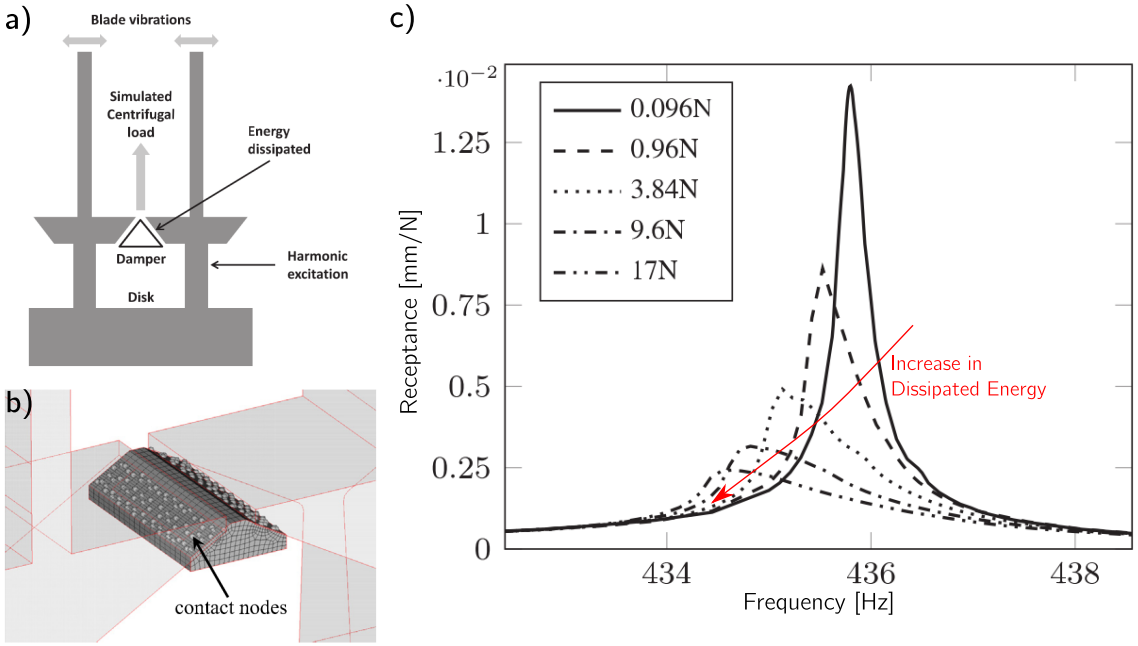


Figure 2.2: a) Blades equipped with an underplatform damper [19]; b) Close view of the underplatform damper; c) Experimental FRFs measured at constant centrifugal load (960 N) and increasing excitation force [19].

To understand the effect of frictional interactions on the FRFs of the structure, an example from the literature is reported in Fig. 2.2c, which shows the nonlinear dynamic response of two blades equipped with an underplatform damper [19]. The experimental setup is shown in Fig. 2.2a: a constant centrifugal load pushes the damper against the blade platform and a harmonic excitation is applied to the blade base. Figure 2.2c shows the experimental FRFs measured at the blade tip. Two aspects are evident from the Figure: 1) the peak amplitudes of the FRFs decrease with increased excitation. This occurs because the relative sliding motion between damper and blade platform increases as the blade is subjected to larger excitations. This results in a larger amount of dissipated energy with a consequent reduction in the vibration amplitude[1]; 2) the natural frequency decreases with the increasing excitation because the damper moves more relatively to the platform, thus reducing the structural stiffness.

This example shows the significant impact that friction has on the structural dynamic behaviour. It strongly damps vibration amplitudes and shifts natural frequencies. These changes make the system dynamic response nonlinear because the response does not scale linearly with the excitation, but it changes nonlinearly. This nonlinearity is quite difficult to model since the physics of the frictional mechanisms is not well understood yet. In addition, a significant amount of uncertainty is also introduced by other factors, such as mistuning [13, 25, 26], wear [20], manufacturing tolerances, mounting [17], etc. For all these reasons, the impact of friction joints on the dynamics is yet quite complicated to predict.

A standard approach for nonlinear dynamic analysis of jointed structures has been defined in a recently published book within the joint mechanics community [27] and is summarised in Fig. 2.3. This approach consists of modelling the individual components with Finite Elements (FE) and connecting the contacting interfaces of mating components with contact elements that simulate the friction mechanisms by means of hysteresis loops. Three stages are defined for this approach:

1. **Nonlinear static analysis.** Once the contact interfaces of the mating components have been discretised with FE, as the friction damper of Fig. 2.2b, a nonlinear static analysis is performed to determine the contact pressure distributions. In this way, normal forces are estimated on each FE node of the contact interface. In addition, it is also possible to identify if any gap between the nodes is present. This information is required as input for the following step, which is the contact interface modelling.

2. **Contact interface modelling.** This step consists in defining the contact models that describe the friction mechanisms by means of the hysteresis loops. A summary of these contact models is given in section 2.3. The most common solution to connect nodes of two contacting interfaces is by employing "contact elements" [28], which are elements that represent the constitutive equations of the contact model. Contact elements are applied between either individual pairs of contacting nodes ("node-to-node" contact elements [29]) or between pairs of contact patches, which are larger portions of interfaces constituted by more individual contact nodes approximated by a single master node. In this case, the elements are called "patch-to-patch" contact elements [30] and they have the advantage of reducing the total number of interface degrees of freedom as they only connect a few master nodes to approximate the whole interface. Contact elements need different inputs

[1]Note that damping will only increase up to a maximum value for a given excitation amplitude, see e.g. [24]. Above the optimal excitation amplitude, damping will decrease and vibration amplitudes will consequently increase.

depending on the contact model they represent and provide as output the nonlinear friction force for any given input relative displacement occurring between the nodes they connect. When plotting the output friction force versus the input relative displacement, hysteresis loops are obtained.

3. **Nonlinear dynamic analysis.** After the contact model has been implemented, the nonlinear dynamic analysis is run. This analysis consists of solving the set of dynamic balance equations that represent the structure. The equations are formulated as follows:

$$M\ddot{\mathbf{x}}(t) + C\dot{\mathbf{x}}(t) + K\mathbf{x}(t) = \mathbf{F_{ex}}(t) - \mathbf{F_{nl}}(t, \mathbf{x}, \dot{\mathbf{x}}) \tag{2.1}$$

Where M, C, and K are the mass, damping and stiffness matrices of the system respectively. These matrices are extracted from the FE models of the individual components. $\mathbf{x}$ is the displacement vector of the degrees of freedom (DOFs) of the FE models. Displacements, $\mathbf{x}$, are the unknown solutions to be estimated by solving the equations. $\dot{\mathbf{x}}$ and $\ddot{\mathbf{x}}$ are velocity and acceleration respectively. $\mathbf{F_{ex}}$ is the vector of external forces acting on the turbine assembly, such as harmonic excitation forces due to gas flows and centrifugal loads due to rotation. $\mathbf{F_{nl}}$ is the vector of nonlinear friction forces predicted by the contact models mentioned before.

The system of equations (2.1) can be solved by following two different classes of methods: time-domain methods [31–33] and frequency-domain methods [34–38]. A summary of these methods is given in [39]. Time-domain methods directly integrate the equations of motion in time employing numerical integration schemes. These methods allow for the study of transient events such as shock/impulse loading or non-harmonic excitation. Frequency-domain methods allow only for the prediction of the steady-state response since they simplify the initial set of differential equations. The simplification consists in assuming that both excitation and system response are periodic and, for this reason, frequency-domain methods are considerably faster in computations compared to time-domain ones. Amongst frequency-domain methods, the most common is the (multi)-harmonic balance method [34]. Although frequency-domain methods are faster, time-domain methods are more versatile as they allow for the description of generic types of excitation (and not only harmonic excitation). A comparison between the two methods has recently been assessed for a jointed structure in [40, 41].

The described standard approach is summarized in Fig. 2.3, where more details are given with regards to the contact modelling methods. There are three methods to estimate the input contact parameters for the contact models: analytical, numerical and experimental methods, which are described in the following sections. First, the next section provides an overview of the physics of the hysteresis loop and its main characterising contact parameters.

2.2 The physics of the hysteresis loop and its contact parameters

In this section, a critical review of the physics of hysteresis loops is presented together with a detailed description of the contact parameters that characterise them. Before presenting this review, it is useful to clarify the distinction between definitions of *contact* and *friction*:

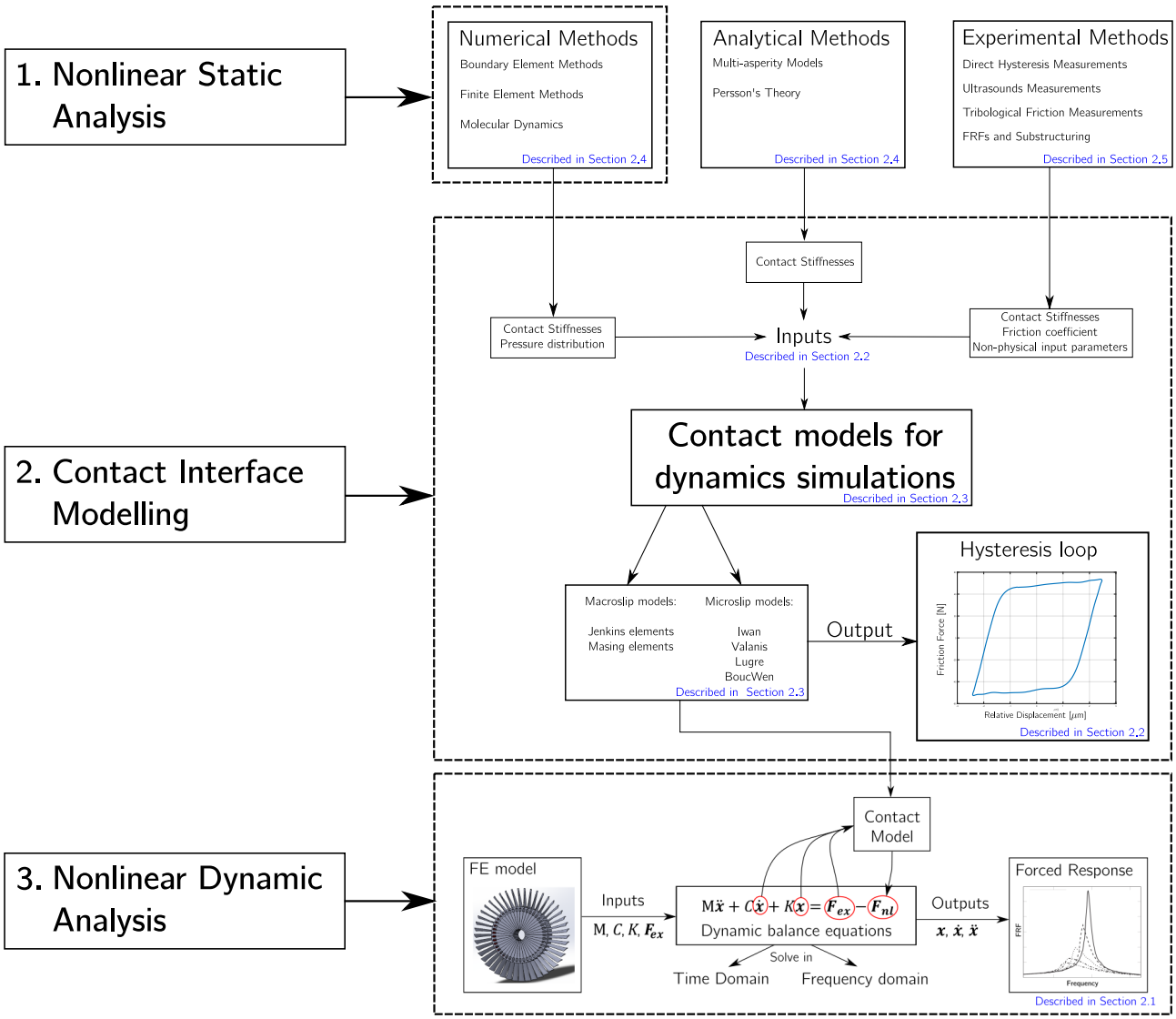


Figure 2.3: Standard practice for nonlinear dynamic analysis of jointed structures (left part of the image) with emphasis on the contact modelling methods (right part of the image).

Contact is a state of physical touching and it occurs when two bodies get in touch. Contact may occur in the normal direction (if two bodies are pressed by normal forces) or in the tangential direction (if the two bodies experience tangential forces). Normal contact problems are well known and described in the literature [42]. Tangential contact problems are more complex to describe as they involve friction.

Friction is the resistance that one surface or object encounters when moving over another. Friction occurs whenever relative sliding motion takes place between two surfaces and is the cause of energy dissipation due to the force transmitted at the contact. This force is called friction force (denoted as F_{nl}, T or Q depending on the notation) and is a nonlinear function of the relative displacement between the two contacting interfaces. A plot of friction force versus relative displacement does not always display a straight line, but often displays a "loop", known as the hysteresis loop.

The hysteresis loop plays a central role in the modelling of contact and friction since it provides information on the macroscopic behaviour of the two surfaces in contact. It is the cyclic load-

deflection curve obtained when plotting the friction force against the relative displacement occurring between two oscillating contact interfaces. From the hysteresis loop, it is possible to extract three important pieces of information: the friction coefficient, the tangential contact stiffness and the energy dissipated at the contact. The latter has to be predicted by contact models as accurately as possible for nonlinear dynamic analysis. Figure 2.4a shows a typical hysteresis loop, which is characterised by the following contact regimes:

- *Stick regime* occurs right after the reversal of motion, ①→② or ④→⑤. In this regime, the friction force is linearly related to the relative displacement by the tangential contact stiffness k_t. The tangential contact stiffness is evaluated from the slope of this linear behaviour and is due to the elastic deformation of the micro-asperities at the contact interfaces [43] and to the bulk elastic deformation at the macroscopic contact scale [44]. The contact stiffness is an important parameter to predict since it might strongly affect the resonant frequencies of the system [21].

- *Microslip* occurs during the transition between the stick regime and the gross slip regime, ②→③ or ⑤→⑥, and is due to a partial slip at the contact interfaces because a portion of the area of contact is still stuck (i.e. asperities elastically deform) and the remaining portion starts to slip. It appears with a progressive flattening of the friction force, which becomes approximately constant during gross slip [45]. For accurate modelling of this behaviour, a dense discretization of the interface is required to distinguish between portions in stick and portions in gross slip.

- *Gross slip* occurs when the whole contact experiences a full relative sliding motion, ③→④ or ⑥→①. An approximately constant friction force is transmitted and is equal to the friction limit μN, where μ is the friction coefficient and N is the normal load. Due to this constant friction force, the hysteresis loop dissipates energy, which is quantified by the area inside the loop itself. This dissipated energy is an important parameter to predict since it affects the damping of the system and the wear of components. The gross slip regime is also referred to as macroslip.

- *Separation* occurs when the normal load becomes zero and contact interfaces detach. In that case, no friction force is transmitted, but energy could still be dissipated due to impacts. The hysteresis loop will consequently show a 0 N friction force because the interfaces are not in contact (not shown in the Figure).

It is important to be able to accurately predict these contact regimes, as they strongly affect the dynamic response of jointed structures in terms of both stiffness and damping. For example, the higher the degree of slipping, the higher the damping because more energy is dissipated due to the friction force (i.e. the area of the loop is larger)[2]. The increase in the degree of slipping also reduces the stiffness of the system as the linear relationship ($T = k_t \cdot x$) does not hold anymore. Figure 2.4b also shows the time signals of friction force and relative displacement. The friction force looks like a square wave since, during gross slip, it reaches the almost constant friction limit. The relative displacement instead varies rapidly during the gross slip and smoothly during the stick regime since the contact is almost completely stuck. In the following two sections, the physics of friction coefficient and contact stiffness respectively is described more in detail.

[2]Note that damping will only increase up to a maximum value for a given excitation amplitude, see e.g. [24]. Above the optimal excitation amplitude, damping will decrease and vibration amplitudes will consequently increase.

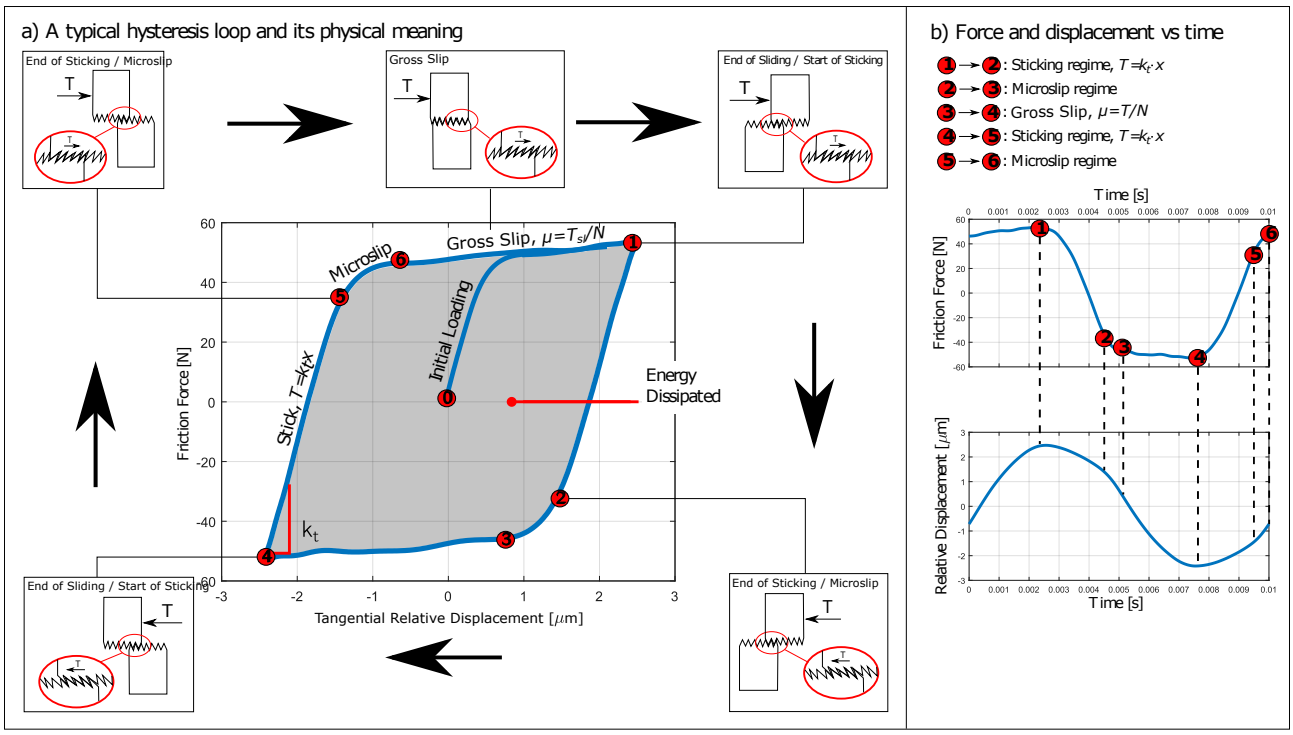


Figure 2.4: A typical hysteresis loop: a) physical meaning; b) Force and displacement vs time. μ is the friction coefficient, T_{sl} is the friction force during gross slip, N is the normal load and k_t is the tangential contact stiffness.

2.2.1 Physics of the friction coefficient

The study of friction has a long history [46]. The first recorded scientific study on friction is attributed to Leonardo Da Vinci (1452-1519), who about half a millennium ago formulated the earliest basic statements on friction [47]. These statements agree with the two laws of friction defined 200 years later by the independent work of Amontons (1699) [48]:

1. **Amontons' first law.** $T = \mu N$, the force of friction T is directly proportional to the applied load N (via the coefficient of friction μ)[3].

2. **Amontons' second law.** The force of friction is independent of the "nominal" area of contact.[4]

Later on, in 1785, Coulomb confirmed and extended these findings [54], and introduced the third law of friction stating that kinetic friction is generally lower than static friction and also independent of sliding velocity. Coulomb conducted a systematic work on friction by investigating the influence of several variables on the phenomenon, including the nature of materials in contact, the normal load, the role of asperities and the time of repose. Due to this systematic work, the Amontons' first law is often referred to as Coulomb friction law, whilst it should be called the Amontons-Coulomb law of friction.

[3]The symbol μ was only later introduced by Euler in 1750 [49], and the concept of a "coefficient of friction" was described explicitly for the first time by Kotelnikov [50], although he did not use that exact terminology.

[4]Friction is dependent on the true area of contact. Nevertheless, the concept of true area of contact will only be introduced 250 years later in the 20$^{\text{th}}$ century [51–53].

The presented laws are based on direct experimental observations, but their physical origin is not fully understood yet. Modern theories of friction are not able to predict accurate values of friction coefficients and even the most recent contact models still lie on such laws defined centuries ago. The physical origin of friction has been described in the centuries by adopting three main approaches [46]:

1. Mechanistic approach, based on the concept of the interlocking of asperities.
2. Adhesive approach, based on the concept of cohesive forces arising at the contact.
3. Modern theories based on combined adhesive, deformation and ploughing actions, with the latter two referring respectively to the plastic deformation of asperities and ploughing of wear particles.

The mechanistic approach was adopted by Amontons and Coulomb who believed that friction occurred due to the interlocking of asperities. Friction was considered as the force required to pull a rough surface over the asperities of the mating component. The major criticism of this view is the exclusion of the description of energy dissipation mechanisms. In fact, the potential energy required to pull one asperity over the other should be gained back when the asperity goes down again. In the same century, the adhesion concept was proposed too. Desanguiler (1734) [55] was the first to argue that cohesive forces were arising at the contact thus contributing to the mechanisms of friction. Unfortunately, this theory was discarded at first, since it did not satisfy the second Amontons' law that defined friction as independent of the area of contact.

These two approaches to describe the origin of friction were mutually exclusive since the adhesion approach supposed friction to be area dependent, while the mechanistic approach did not. Amontons and others had demonstrated that the resistance generated by asperity interactions was independent of the area of contact, and thus this latter view was in accordance with the laws of friction. For this reason, the mechanistic approach dominated most of the analyses on friction until the nineteenth century, when the adhesion concept faced a remarkable development. In the period between 1938 and 1940 a series of experiments, conducted by Holm [51], Bowden and Tabor [52] and Ernst and Merchant [53], revealed that a substantial difference existed between the nominal area of contact and the true area of contact. The experiments were based on the conduction of electricity between contacting bodies and showed that the real area of contact is indeed much smaller than the nominal one, at the point that Bowden said "...Putting two solids together is rather like turning Switzerland upside down and standing it on Austria - the area of intimate contact will be small" [56].

This striking finding brought Bowden and Tabor [57] to pursue the idea of adhesion as the source of friction. They showed that the friction force was proportional to the real area of contact by explaining that when two asperities come into contact, they weld together due to the adhesion between the two materials. The area of contact A_r between asperities increases until it becomes able to support the normal load N, thus generating a stress p_m:

$$N = p_m A_r \tag{2.2}$$

p_m was vaguely described by Bowden and Tabor as the "yield pressure of the softer metal", and it is generally approximated with the hardness of the softer material, which is about three

times larger than the yield strength. Once the asperities come into contact, they form welded junctions. When sliding takes place, work is required to shear such junctions until the junction's shear strength τ is reached:

$$T = \tau A_r \tag{2.3}$$

Bowden and Tabor assumed that the junction's shear strength is approximately similar to the bulk material's one. During sliding, new micro-welded junctions are formed and broken continuously. This process leads to energy dissipation, and it increases linearly with the true area of contact. From Eq. 2.2 and 2.3, the formula for the coefficient of friction is obtained:

$$\mu = \tau / p_m \tag{2.4}$$

Although adhesion is widely accepted as a significant player in the phenomenon of friction, this theory presented some major limitations [46]:

1. For most metals, the adhesion theory predicts lower friction coefficients than those measured experimentally. According to this theory, μ should be equal to about 0.16 for all metals, because $\tau \sim \sigma_i/2$ and $p_m \sim 3\sigma_i$, where σ_i is the metal yielding strength. Therefore, according to Eq. 2.4, $\mu \sim 0.16$. This prediction is not in good agreement with experimentally obtained friction coefficients.

2. If adhesion is the main source of friction, then a pull-off force is expected when the contacting bodies are detached. This resistance does not occur in most practical cases. However, a probable reason for it is that when two contacting surfaces detach, elastic stresses are released thus breaking the adhesion bonds.

3. This theory does not account for the effect of roughness on friction.

For the above reasons, more advanced theories have been proposed, which included novel physical explanations on the origin of friction. Bowden and Tabor improved their original theory in 1964 [58] by considering the frictional resistance as the sum of two terms, the shearing due to adhesion and the ploughing effect generated by hard asperities and wear particles. When a hard asperity or wear particle penetrates in a mating softer material, it ploughs out a groove by plastic flow. To displace the particle further, a resistance is generated that results in a larger coefficient of friction. In 1981, a more comprehensive theory has been proposed by Suh and Sin [59]. They stated that friction is driven by three major factors, namely adhesion μ_a, deformation μ_d and ploughing μ_p, according to $\mu = \mu_a + \mu_d + \mu_p$, where:

- μ_a is due to the adhesion forces and is in the range 0 - 0.4, where low values are experienced in well-lubricated surfaces, while the highest values occur for identical materials with no contamination or oxide layers. Suh and Sin stated also that in most cases adhesion may not be the dominant factor.

- μ_d is due to the plastic deformation of asperities and is the major source for the static friction coefficient being in the range 0.43 - 0.75. During sliding, the actual contribution of asperity deformation is expected to be quite small instead, since frictional resistance is mainly generated by ploughing and adhesion effects.

- μ_p is due to the ploughing of wear particles and is in the range 0 - 0.4. Low values are experienced when wear particles are absent or when a soft material slides against a harder

material (in fact the particles would penetrate in the softer material and just slide over the harder one). High values are associated with similar mating materials because wear particles may penetrate both their surfaces, thus increasing the resistance to sliding. Wear particles are often referred to in the literature as third body, which has been extensively investigated in the past 40 years [60, 61].

Despite the remarkable advances in the field, a great deal of research is still being conducted to improve the understanding of the physics of friction. A predictive model for the coefficient of friction is not available yet. The main challenge is related to the fact that friction is a complex system with multi-physics and multi-scale aspects, and therefore it cannot be considered as a scalar property. A recent review from the tribology research community emphasized the multi-scale aspects of friction and, more in general, of tribological problems [62]. Predictive models should bridge length scales from atomistic levels to mesoscale levels. The multi-physics aspects include plasticity, thermal dissipations, chemical interactions, material pairings, contact geometry and load histories among others, as shown in Fig. 2.5. For the above-mentioned reasons the modelling of friction remains largely empirical and, consequently, the values for the friction coefficient are mainly obtained from experiments.

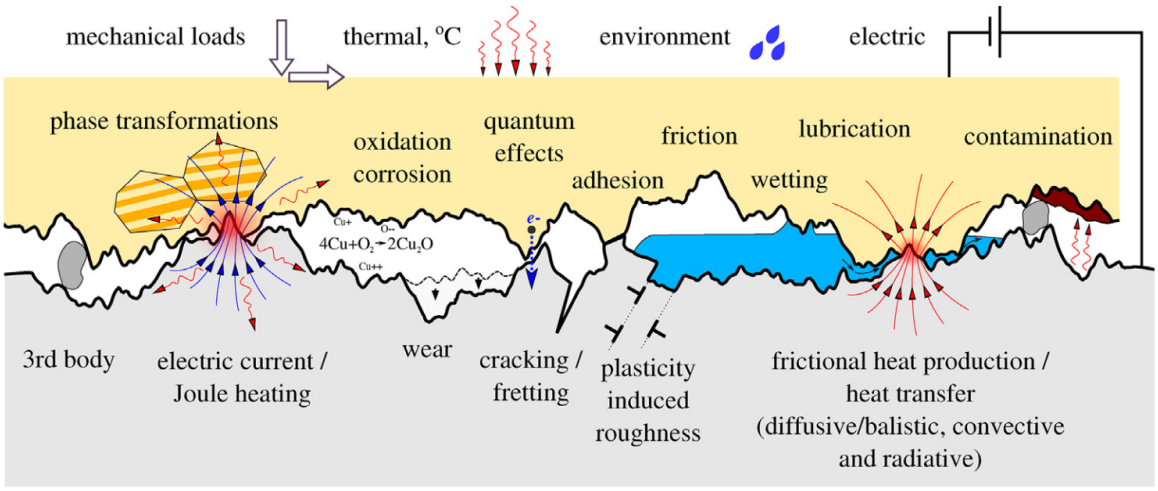


Figure 2.5: Multi-physics phenomena involved in friction [62].

2.2.2 Physics of the contact stiffness

The contact stiffness linearly relate changes in the load with changes in the relative displacement between the contact interfaces. It can be defined in both normal and tangential directions. Its physical origin is attributed to the elastic deformation of the micro-asperities at the contact interfaces [43, 63] and to the bulk elastic deformation at the macroscopic contact scale [44, 64]. When the tangential deformation becomes large enough, asperities will deform plastically and the slipping phenomenon is likely to occur, thus giving rise to friction dissipation.

The contact stiffness depends on multiple variables including normal load, surface roughness, wear and area of contact. Several experimental studies investigated the influence of most of these variables. For example, a large variety of experiments has been conducted to investigate the influence of the normal load on the contact stiffness [65–83]. A comparison between these different studies is shown in Fig. 2.6. The different experimental techniques employed for these

estimations are described in detail in section 2.5. The contact stiffness increases with increasing normal loads due the changes in number and size of contact spots. At light loads, the contact stiffness is low because only a few asperities are in contact and, therefore, the amount of elastic interactions that generate the contact stiffness is limited. As the load increases, more asperities come into contact rapidly, thus contributing to increases in the contact stiffness. At moderate/high loads the contact becomes homogeneously spaced over the whole area, and further increases in the normal load do not affect the contact stiffness to a great extent as the number of new contacts is much reduced.

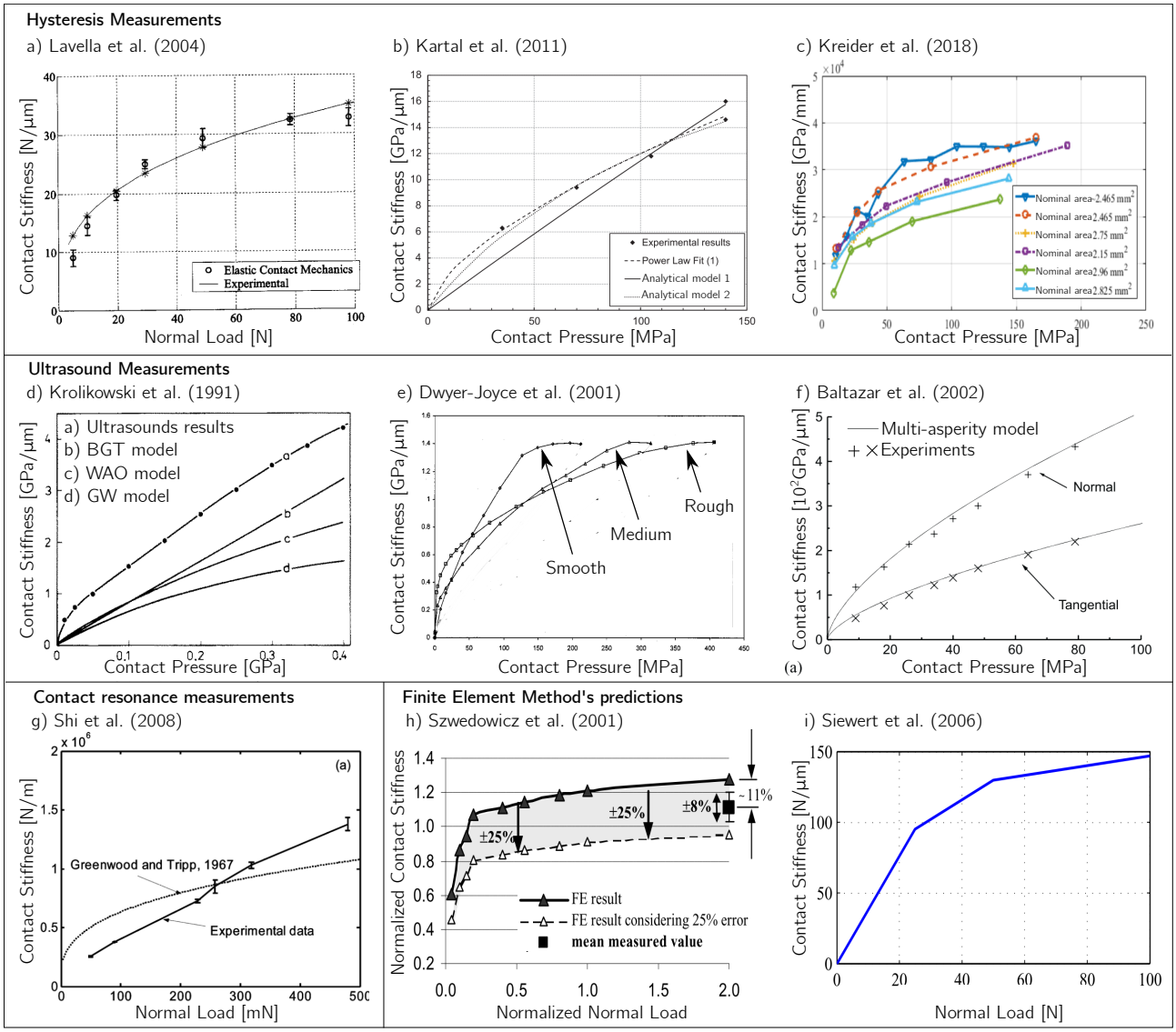


Figure 2.6: Contact stiffness versus normal load: a-b-c) Hysteresis measurements [74,80,83]; d-e-f) Ultrasound measurements [66,71,73]; g) Contact resonance measurements [84]; h-i) Finite Element Method predictions [72,78].

Also the effect of roughness has been investigated in some of these studies, see e.g. Fig. 2.6e [71]. As expected, smooth profiles lead to higher contact stiffness values for the same normal load, since less load is required to increase the number of contact points. Instead, rough profiles lead to lower contact stiffnesses since the asperity tips largely contribute to the softening of the contact. Only a few studies have instead investigated the evolution of the tangential contact stiffness with wear [80,85–87], finding that the contact stiffness increases with hysteresis cycles

until it reaches an asymptotic value. This probably occurs because, at the beginning of the tests, interfaces are not compliant, and only after several wear cycles, the compliance increases thus contributing to the increase in the contact stiffness. A detailed investigation focused on the evolution of the contact stiffness with wear has not been proposed yet.

Finally, also the effects of the nominal area of contact have been investigated. It has been confirmed by Finite Element simulations that the contact stiffness increases with the increasing nominal area of contact [72,80] and, in fact, it is a common practice to express it in a normalized form divided by the nominal contact area. However, experimental studies that investigate this relationship are few [80], and no detailed investigations are present in the current literature.

2.3 Contact models used for nonlinear dynamic analysis

The previous section has described the physics of the hysteresis loop and its characterising parameters. Here, an overview is given of the contact models used to replicate hysteresis loops for nonlinear dynamic analysis. A throughout review of these models is given in [88]. Models of friction are divided into two main branches [4,28] as shown in Fig. 2.7: static friction models (also known as velocity-based friction models) and dynamic friction models (also known as state-based friction models). The latter are those used in nonlinear dynamic analysis, since they are dependent on the dynamic history. Instead, velocity-based friction models are independent of loading history, as they are explicitly expressed in terms of the system's velocity.

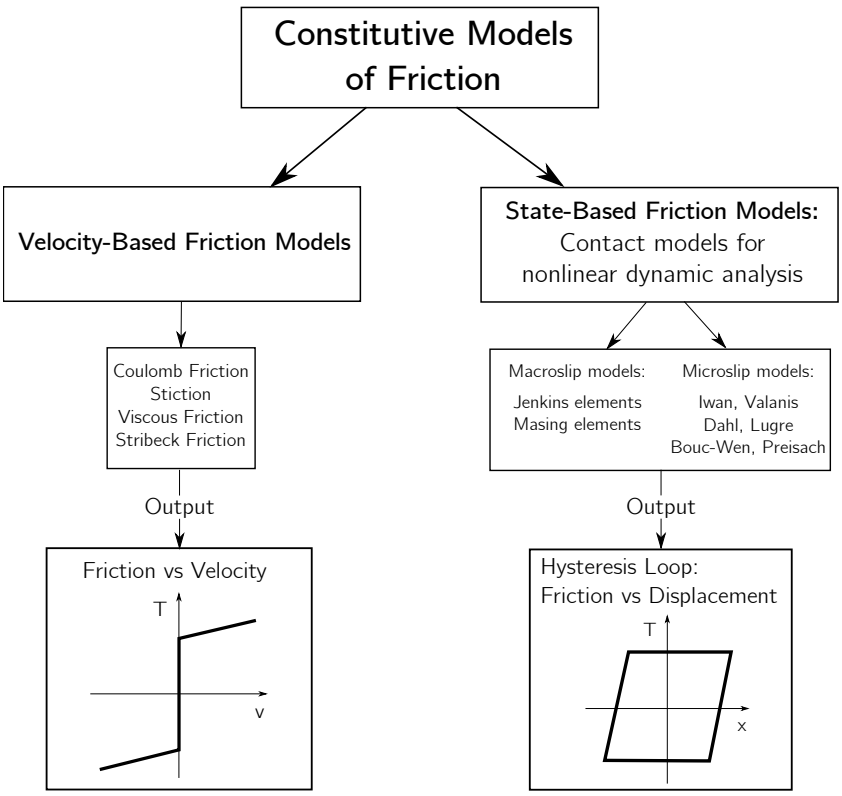


Figure 2.7: Constitutive models of friction.

2.3.1 Static friction models

Static (velocity-based) friction models are shown in Fig. 2.8. They are divided in the following four types [28]:

- Coulomb friction: This model is only constituted by the Amontons-Coulomb friction law $T = \mu N$, with the sign of the force T being opposite to the sliding relative velocity v.
- Stiction: This model considers a difference between the static friction coefficient μ_s and the kinetic friction coefficient μ_k, with the latter being smaller. The interfaces are stuck until $T \leq \mu_s N$. Then, when full sliding occurs, the friction force reduces to $T = \mu_k N$.
- Viscous friction: This model is associated with lubrication and it adds a vicous effect to the Amontons-Coulomb friction law, according to $T = \mu N + cv$, where c is the viscous coefficient and v is the sliding relative velocity. The viscousness of the fluid increases the friction resistance as the velocity increases.
- Stribeck friction: This model is an improved way of representing lubricated contacts. For low velocities, T is close to static friction; for medium velocities, T decreases to a local minimum; for high velocities T increases again due to fluid viscosity, according to:

$$T = \left(\mu_k N + (\mu_s - \mu_k) N e^{-(v/v_s)^{\delta_s}}\right) sign(v) + cv \tag{2.5}$$

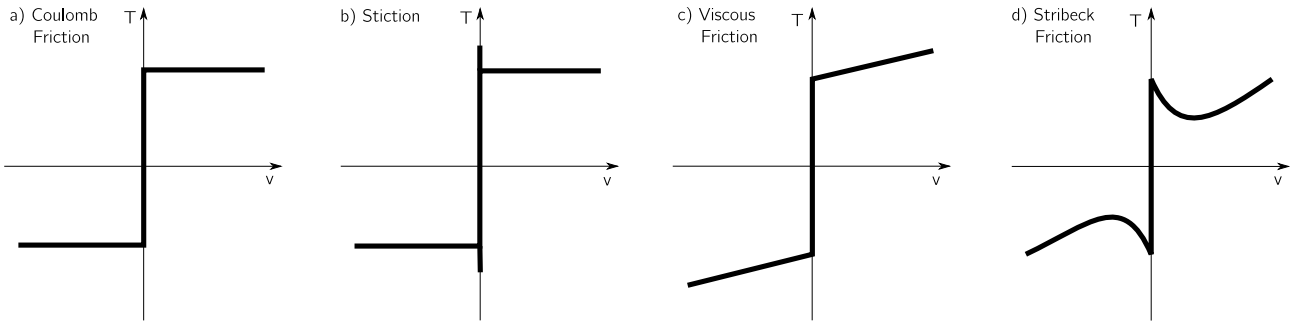


Figure 2.8: Static (velocity-based) friction models.

2.3.2 Dynamic friction models

Dynamic friction models are the contact models used to replicate hysteresis loops for nonlinear dynamic analysis. These contact models are state-based, which means that they require a specific state variable that records the state of the model at previous time-steps (this is the feature needed to replicate hysteresis loops). Such models can be classified into macroslip models and microslip models:

- Macroslip models are related to the original Amontons-Coulomb's friction law ($T = \mu N$) and are capable of better capturing the real physics behind the contact interactions.
- Microslip models can predict more accurate hysteresis loops at the price of neglecting some physical features of the contact.

Macroslip models

Macroslip models describe the gross slip regime of the hysteresis loop without accounting for the microslip regime (i.e. the regime in which a portion of the contact interfaces slips, while the remaining one is stuck). These models are based on the so-called Jenkins elements that are attributed to Jenkins [89], who studied material stress-strain relationships, and are also known as friction slider elements (see Fig. 2.9a). The friction slider is constituted by an elastic spring in series with a Coulomb element. The Coulomb element follows the Amontons-Coulomb law ($T = \mu N$), and the elastic spring, also known as tangential contact stiffness, relates the force linearly to the displacement ($T = k_t x$). This element is able to generate hysteresis loops, without describing the microslip regime of the hysteresis loop. Although the Jenkins element does not include a microslip description, it can still model this phenomenon quite well. In fact, if the contact interfaces are modelled with enough FE nodes coupled by different Jenkins elements, some pairs of nodes would be in slip regime and some of them would be in stick regime. Therefore, some portion of the contact interfaces would slip and some would be stuck, thus replicating the microslip regime.

The Jenkins element is able to describe a 1D tangential force with a fixed normal load. To improve such model, two modifications could be performed: the addition of a normal contact stiffness to include a varying normal load, and the addition of another tangential contact stiffness to describe a 2D tangential force in the plane, as shown in Fig. 2.9.

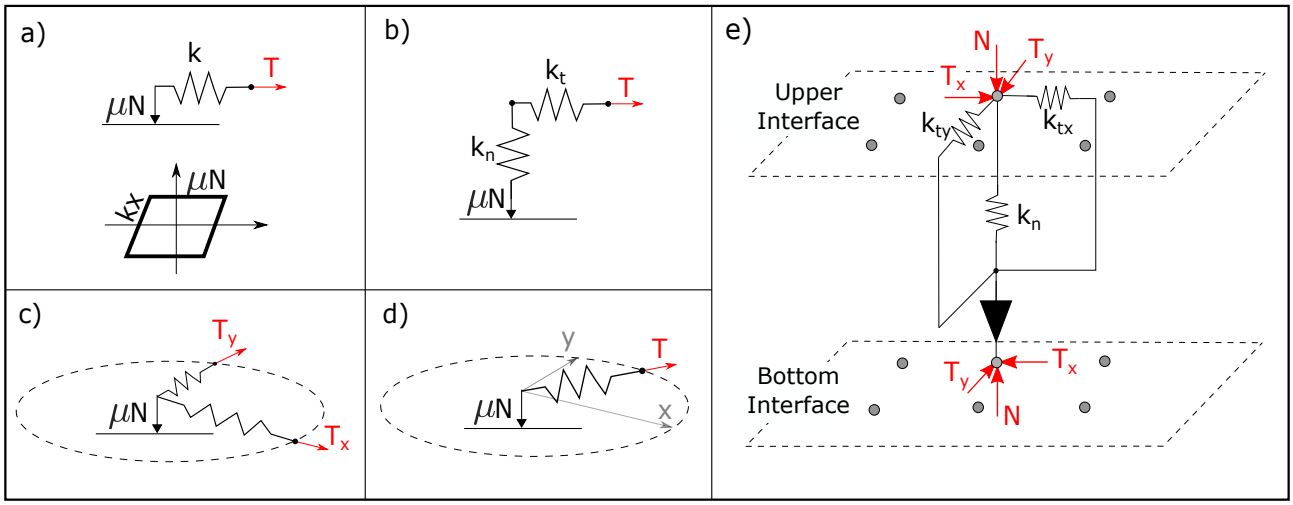


Figure 2.9: Macroslip contact models: a) Jenkins element; b) Jenkins element with variable normal load; c) 2D contact model with uncoupled tangential motions; d) 2D contact model with coupled tangential motions; e) Quasi-3D contact model.

The first to use Jenkins elements for dynamic simulations was Griffin in 1980 [90] although he did not use this term to refer to the contact elements. Griffin used a 1D Jenkins element with a constant normal load and later he improved the model with other researchers: in 1986 [91], including a normal motion that varyied in-phase with the tangential motion, and in 1991 [92], including an approximate description of the 2D tangential motion. Later, in 1998, Yang and Menq proposed three more comprehensive contact models: 1) a contact model with 2D tangential motion and constant normal load [93]. A similar model was proposed in 1996 too [35]. This model is a 2D Jenkins model, also known as Masing element [28]; 2) a contact model with 1D tangential motion and variable normal load [94] and 3) a 3D contact model [95] that

described a 2D coupled tangential motion with a variable normal load. The variable normal load, N, was linearly dependent on the relative normal motion, n, by means of a normal contact stiffness, $N = k_n \cdot n$. Although the coupled tangential motion is more complete, it is a common practice in turbomachinery dynamic simulations to account for uncoupled tangential motions [23] by means of "quasi-3D" contact models. These models simplify the tangential motion by using two uncoupled contact stiffnesses along the two tangential directions [93], see e.g. applications in [22, 36, 96]. However, the full 3D contact models are recently used more and more, with one the latest formulations being implemented within the nonlinear code FORSE [97] by the Vibration University Centre at Imperial College London. Multiple examples are present in the literature of applications of macroslip Jenkins models for nonlinear dynamic analysis [19,22,41,98,99]. A visual representation of all those macroslip contact models is given in Fig. 2.9. In short, three contact conditions might occur between two nodes connected by a macroslip contact element:

- *Stick*: The tangential force transmitted between the two nodes is below the friction limit ($T < \mu N$) and it changes linearly with the relative displacement ($T = k_t x$).
- *Slip*: The tangential force reaches the friction limit ($T = \mu N$), and the two nodes start to slide.
- *Separation*: The two nodes are not in contact anymore, and therefore both normal load and tangential force are zero.

These models have the advantage of being constituted by physical parameters (i.e. μ, k_t and k_n), which could be determined experimentally, or predicted with analytical or numerical methods.

Microslip models

Microslip models can describe the microslip regime of the hysteresis loops and thus are able to replicate loops quite similar to the experimental ones. For this reason, microslip models do not require a fine spatial discretization of the contact interfaces, as they can capture the microslip behaviour with few "patch-to-patch" contact elements. The drawback of such models is that most of the parameters required as input are non-physical and therefore can only be obtained with a tuning of the model to the experimental results. In addition, these models often consider a constant normal load in time, and, if they account for normal load variations, computational difficulties tipically arise, especially in the case of separation [23]. The most common microslip models used for dynamic simulations are [23]: Iwan [100,101], Bouc-Wen [102,103], Dahl [104], LuGre [105], Preisach [106,107] and Valanis models [108].

Iwan Model. This is one of the most used microslip models for dynamic simulations. This model was first proposed by Iwan in 1966 [100] for descibing metal elastoplasticity. Iwan defined the model as composed of a series of Jenkins elements, as shown in Fig. 2.10a. Later, in 2005, Segalman adapted the model for the desciprion of mechanical joint interactions, defining the well-known Four-parameter Iwan model [101]. The four parameters $\{K_T, F_S, \chi, \beta\}$ allow for the description of the distribution of the Jenkins elements and are described as follows: K_T is the tangential stiffness, F_S is the force required to start slipping, χ is the exponent of the energy dissipation per cycle and β is the ratio of Jenkins elements that slip before macroslip to those

that silp at marcoslip. The last two parameters are more difficult to obtain, since they do not have a proper physical origin. Mathematically, the constitutive form of the model is:

$$F(t) = \int_0^\infty \rho(\phi)[u(t) - x(t,\phi)]d\phi \tag{2.6}$$

where F and u are the friction force and displacement acting on the Iwan element, $\rho(\phi)$ is the distribution of Jenkins elements with strength ϕ and x is the displacement of single Jenkins elements. The distribution of Jenkins elements $\rho(\phi)$ is quite difficult to characterize and it depends on the four model parameters $\{K_T, F_S, \chi, \beta\}$. A typical hysteresis loop from Iwan elements is shown in Fig. 2.10a.

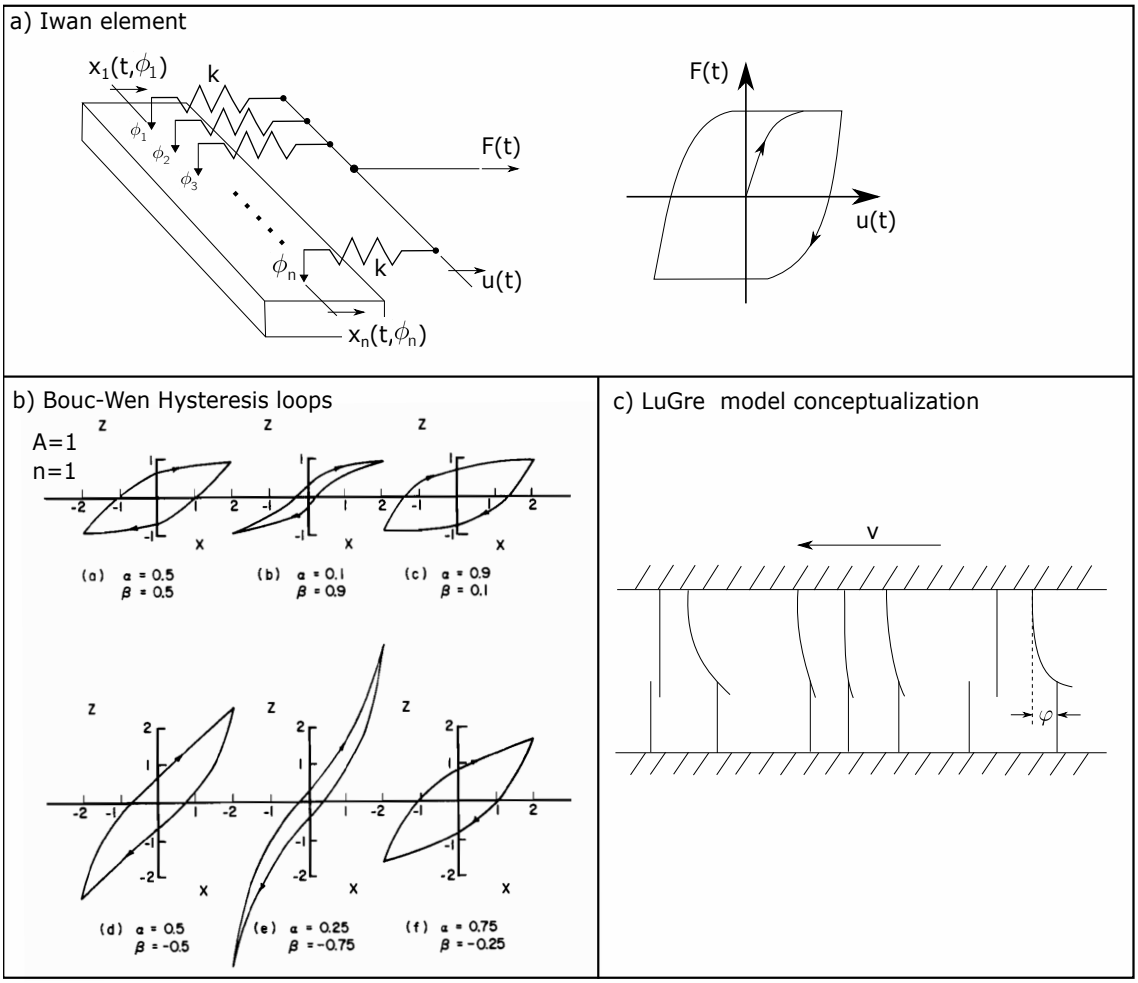


Figure 2.10: Microslip models: a) Iwan element and its hysteresis loop; b) Bouc-Wen hysteresis loops [103]; c) Conceptualization of LuGre model.

Bouc-Wen Model. This model was first developed by Bouc [102] in 1971 and then extended by Wen in 1976 [103]. The Bouc-Wen model consists of a set of first-order nonlinear differential equations that for a given input displacement generate an output restoring force. By plotting this force versus the displacement, an hysteresis loop is obtained, which can be accommodated to a real hysteresis by changing a set of four input parameters $\{\alpha, \beta, A, n\}$. As for the Iwan model, this set of parameters is nonphysical, thus making their proper identification quite

challenging. Mathematically, the Bouc-Wen model is expressed as:

$$F(u, \dot{u}) = g(u, \dot{u}) + z(u, t) \tag{2.7}$$

where u and $\dot{u}$ are the relative displacement and velocity, g is a nonhysteretic component and z is the hysteretic component, which is defined by the following equation:

$$\dot{z} = -\alpha|\dot{u}|sign(z)|z^n| - \beta\dot{u}|z^n| + A\dot{u} \tag{2.8}$$

The set of input parameters $\{\alpha, \beta, A, n\}$ must be determined through parameter identification techniques as in the case of Iwan models. These parameters strongly affect the shape of the hysteresis loops, as shown in Fig. 2.10b. The Bouc-Wen model can replicate arbitrary hysteresis loops and therefore it has a wide field of applications, among which only few are related to bolted joints. In particular, Oldfield et al. in 2005 [109] modelled a bolted joint in three different ways: a high fidelity finite element analysis with a Coulomb friction model, a contact discretization in which Jenkins elements were used and, finally, a contact discretization in which a Bouc-Wen model was used. The results obtained with the Jenkins and Bouc-Wen elements were compared to the results of the Finite Element Anlayisis. The comparison showed that the Bouc-Wen model is able to represent the hysteresis loop in an aggragate manner, while the Jenkins elements can provide a more accurate representation of the contact behaviour.

It is worth mentioning the research carried out by Guo et al. (2008) [110], in which they proposed a Bouc-Wen model adapted to replicate friction phenomena. They reformulated the original equations substituting the four non-physical parameters with four physical parameters defined as follows:

$$\begin{aligned} z_0 &= \left(\tfrac{A}{\beta+\gamma}\right)^{\frac{1}{n}}, \qquad & \rho &= \tfrac{A}{z_0} > 0, \\ \sigma &= \tfrac{\beta}{\beta+\gamma} \geq 0, \qquad & \xi &= \tfrac{z}{z_0} \in [-1; 1] \end{aligned}$$

This formulation leads to a normalized Bouc-Wen variable ξ which varies in $[-1; 1]$. This variable ξ is simply a normalized hysteresis loop that varies between the force limits -1 and 1 (when there is full sliding). The general Bouc-Wen model expressed in Eq. 2.7 can be rewritten as:

$$\begin{cases} z = z_0\xi \\ \dot{\xi} = \rho(1 - (\sigma sgn(\dot{x})sgn(\xi) + 1 - \sigma)\,|\xi|^n)\dot{x} \end{cases} \tag{2.9}$$

which is equivalent to its original form. Furthermore, the friction component can be rewritten as:

$$\mathbf{F_f}(\mathbf{x}, \dot{\mathbf{x}}) = z_0\boldsymbol{\xi}(\boldsymbol{\xi}, \boldsymbol{x}, \dot{\boldsymbol{x}}) \tag{2.10}$$

The advantage of writing the Bouc-Wen model as in Eq. 2.9 is that the parameters can now be physically linked. In fact, z_0 defines the friction limit μN, where μ is the friction coefficient and N is the normal load applied to the system. ρ plays the role of the contact stiffness and is equal to $\frac{k_t}{\mu N}$, where k_t is the experimental contact stiffness. $n \geq 1$ controls the microslip region and σ, the global shape of the hysteresis loop. This formulation facilitates modelling as the physical parameters are more intuitive than the non-physical parameters used in a traditional formulation.

LuGre Model. The LuGre model was proposed in 1995 by the two research groups of Lund and Grenoble [105] and it is based on the Dahl model previously developed in 1976 [104]. The LuGre model is also known as the bristle model, since it is a representation of contact between bristles (see Fig. 2.10c), which approximate the asperity elastic interactions. In fact, each

bristle deflects like a spring and gives rise to the friction force. For simplicity, one set of bristles is considered rigid and the other elastic. The model is defined by the following set of differential equations:

$$\begin{aligned} F &= (\sigma_0\varphi + \sigma_1\dot{\varphi} + \sigma_2 v)N = \mu(\varphi, \dot{\varphi}, v)N \\ \dot{\varphi} &= v - \sigma_0 N \frac{||v||}{g(v)}\varphi, \qquad \varphi(t=0) = \varphi_0 \\ g(v) &= \mu N + (\mu_s - \mu)Ne^{-(v/v_s)^2} \end{aligned} \tag{2.11}$$

where F is the frictional force, v is the relative sliding velocity and φ is the average bristle deflection. σ_0 is the bristle stiffness and σ_1 and σ_2 describe the dynamic friction velocity dependence. μ is the coefficient of friction, and the function $g(v)$ accounts for the stiction and Stribeck effects. The LuGre model can replicate realistic hysteresis loops as it describes presliding displacement, stick-slip phenomenon and it accounts also for the Stribeck effect. In addition, this model allows for analytical studies, which are not possible with other discontinuous models [4].

Valanis Model. This model was proposed by Valanis in 1971 [111] to describe endochronic plasticity. In fact, the plastic hysteretic behaviour of materials can be associated with the frictional hysteretic behaviour of sliding interfaces. The model is described by a first order differential equation [108], from which an equivalent formulation is obtained to describe the "transfer" behaviour of a joint connection [4]:

$$\dot{F} = \frac{E_0\dot{u}[1 + \frac{\lambda}{E_0}sign(\dot{u})(E_t u - F)]}{1 + \kappa\frac{\lambda}{E_0}sign(\dot{u})(E_t u - F)} = \dot{F}(u, \dot{u}, F) \tag{2.12}$$

where F and u are the friction force and relative displacement, and λ, E_0 and E_t are material parameters, which in the case of joint connections assume the following physical meanings: E_0 describes the slope of the hysteresis stick regime and E_t describes the slope of the slip regime. The parameter κ controls the mircoslip regime. The Valanis model has been used to model friction in bolted joints [112,113] and more recently to model even underplatform dampers [11]. The advantage of using a Valanis model is that all the parameters are physical and therefore the tuning with experimental results is faster.

2.4 Analytical and numerical methods for contact parameter estimations

The most important input parameters for the above mentioned contact models are the friction coefficient and tangential contact stiffness. As already shown in Fig. 2.3, they can be obtained by using three different methods: analytical, numerical and experimental methods. This section describes the analytical and numerical methods, while a summary of the experimental methods is given in section 2.5.

Analytical methods

Analytical methods are used to describe the normal and tangential approach between contacting interfaces. These methods are the fastest in computation since do not require intense iterations

to get the solution. However, they lie on quite restrictive assumptions, which make their usage limited to a few real cases. Analytical methods are classified into two major classes: multi-asperity models and Persson's theory. Before presenting these two major classes, it is worth mentioning the fundamental study that Hertz conducted in 1882 [114]. The Hertzian theory analytically describes the local stresses generating as two elastic solids with smooth surfaces come into contact under imposed normal loads. The deformation field is also calculated by minimizing the elastic deformation energy. Further developments of the original Hertzian equations resulted in the modern and more advanced contact models that are described below.

Multi-asperity Models also known as micromechanical models, lie on the pioneering work of Greenwood and Williamson (GW) proposed in 1966 [43]. The study aimed to model the normal approach of nominally flat, but rough surfaces, and to calculate the resulting force and the true area of contact. GW considered the interfaces constituted by a series of asperities that were treated as i) spheres with the same curvature radius but different height distributions and ii) distant enough between each other to not exhibit any interaction. The deformation of the spheres was given by the Hertzian theory [114]. The GW model predicts that a linear relationship exists between the normal load and the true area of contact. The average separation δ between the interfaces is predicted, thus leading to a calculation of the normal contact stiffness ($k_n = N/\delta$). In the years, generalizations were applied to the original GW model to describe more contact situations, (see e.g. [115–117]), with the Bush, Gibson and Thomas (BGT) theory [115] being one of the most advanced. Eventually, multi-asperity models were improved to the point that most recent formulations are semi-analytical and semi-numerical, especially to account for the asperity interaction effects [118–120].

The original GW model describes the normal approach of rough surfaces thus providing normal contact stiffness predictions. However, also the tangential relative motion was studied in the years. After the fundamental study of Hertz on the contact between elastic bodies [114], Cattaneo [121] and Mindlin [122] developed independently the elastic solution for two smooth spheres in contact under both normal and tangential loading. These studies allowed for the prediction of the tangential contact stiffness. Later in 1955, Johnson [123] undertook an experimental investigation of the displacement between bodies loaded tangentially and confirmed Mindlin predictions. However, Cattaneo and Mindlin's pioneering studies did not consider the role of roughness. In the following years, also the roughness was taken into account to solve elastic tangential problems, although most of the studies adopted numerical methods rather than analytical ones [63, 69, 124–127]. Multi-asperity models have been extensively compared with experimental measurements due to their relative simplicity and computational attractiveness. Some of these comparisons are presented in Fig. 2.6a-b-d-f-g and show a quite good agreement, although the models needed to undergo a calibration based on the experimental results.

Persson's Theory was proposed by Persson in 2001 [128]. This theory is based on completely different assumptions than those proposed by GW. Persson modelled the probability distribution of the contact pressure with a diffusion-type equation, without modelling asperities. The model was obtained in the limit of full contact, and was later extended to partial contacts [129]. As in the case of the GW model, Persson's theory predicts that the true contact area evolves linearly with the normal load, although the proportionality coefficient is different for the two methods. Moreover, Persson also predicted that the relation is linear only until the normal load becomes large enough that the true area of contact approaches the nominal area

of contact. The linearity predicted by Persson holds for realistic pressure and area intervals, while that predicted by multi-asperity models is only valid for vanishingly small contact areas.

The two methods have been compared extensively in the literature, often using numerical methods as a frame of reference (see e.g. [117, 119, 129–132]). The main conclusions of such comparisons are the followings [133]: i) despite assumptions of asperity-based models are quite limiting, such models are still extensively used due to their relative simplicity and computational attractiveness; ii) Persson's theory can rather successfully predict the pressure distribution and can less nicely predict the true contact area; iii) both methods are qualitatively effective (i.e. they predict a meaningful relationship between the true area of contact and the normal load), but they encounter problems in providing accurate quantitative predictions.

Numerical methods

Numerical methods also predict normal and tangential relative motions between two contacting interfaces subjected to external loading. These methods give more accurate predictions than analytical methods and also allow for the study of more general contact situations. However, numerical methods often encounter convergence problems and require major computational efforts. Numerical methods are divided into three major classes: Boundary Element Methods (BEM) [134], Finite Element Methods (FEM) [135] and Molecular Dynamics (MD) [136].

Boundary Element Methods (BEM) discretize only the contact interfaces without modelling the bulk of the contacting bodies [134]. The interfaces are discretized in a grid of finite-dimensional "boundary elements" with different average heights. The core of BEM is the use of the so-called Green's functions [137] to describe the load-displacement relationships of the boundary elements subjected to contact forces. The final deformed contact configuration is given by the integral convolution of all the contact tractions. The main assumption of BEM is that the solid is locally considered as a flat half-space. As already stated, only the interface is discretized and not the bulk of the contacting bodies. One of the earliest applications of BEM to a contact problem was proposed in 1981 [138]. Later, this method has been extensively used to describe the contact behaviour of rough surfaces, and its main applications and formulations were recently illustrated in [139]. BEM can be used to estimate contact stiffness values, as done in [63, 140] or even in nonlinear dynamic solvers to model the evolution of the contact interfaces with wear [141–143].

Relevant to this PhD research is the work of Armand et al. [141–143], who developed a multiscale approach to evaluate the effect of fretting wear and surface roughness on the nonlinear dynamic response of jointed structures subjected to vibration cycles. Their approach successfully coupled a multiharmonic balance solver used for the dynamics predictions to a contact solver based on the Boundary Element Method [144] used for a refined contact analysis and a more accurate evaluation of the local contact parameters for the nonlinear dynamic analysis. Two different time scales were used, a fast one for dynamics and a slow one for contact. Similarly two space scales were introduced to allow a refined mesh for the contact analysis, while keeping a coarser mesh for the dynamics. As a result of this, surface roughness could be directly included in the contact analysis, allowing a more physical description of the wear evolution. Their results demonstrated the sensitivity of the nonlinear dynamic response to changes at the contact interface; the wear patterns led to a redistribution of the contact pressure, which,

in turn, changed the underlying nonlinear mechanisms at the interface from sliding at the edges only to sliding over a larger part of the contact interface. Although their proposed multiscale approach is a powerful tool to accurately predict the nonlinear dynamic response of an assembled structure over its lifetime, their study was only a preliminary attempt to model the effects of fretting wear on the dynamic forced response of jointed structures. The poor experimental knowledge still limits our understanding of how joints deteriorate. This issue is therefore addressed in this PhD research with both experimental (see chapters 4 and 6) and numerical (see chapters 7 and 8) investigations.

Finite Element Methods (FEM) have been historically developed for the structural modelling, but due to their versatility they have also been employed for the description of contact problems [145,146], including even interactions between rough surfaces [147,148]. FE methods discretize both contact interfaces and the bulk of contacting bodies, thus making it possible to describe more general contact situations. FE methods are based on the minimization of the total potential energy of the system. The interface contacting nodes are related by "constraint conditions", which define the actual gaps between the nodes. These constraint conditions are described using two main approaches: Lagrange multipliers, which lead to exact solutions, and penalty methods, which lead to approximate solutions. A detailed description of such approaches is presented in [135]. An application of FEM to obtain contact stiffness values was presented in [72] for a damper/blade contact. The contact stiffness was predicted for different normal loads and results were compared to experiments showing a reasonable agreement (see Fig. 2.6h). A similar study also investigated the effects of normal loads on the contact stiffness using FEM [78] and the results are shown in Fig. 2.6i.

Molecular Dynamics (MD) was first proposed in the late 1950s [136,149] within the field of theoretical physics and then expanded to account for several physical, chemical and mechanical phenomena, including the contact between rough surfaces [130]. MD is carried out at the nanoscale level since it discretizes the contact interfaces as a grid of atoms. Atoms' interactions are described with potential functions (also known as Force Fields) such as Lennard-Jones [150] and Morse [151] potentials. MD can capture the dynamics at the atomistic level and therefore the real physics of the contact interactions. Unfortunately, MD requires significant computational resources that restrict the fields of application to small volumes (less than a cubic micrometre) and small time scales (less than microseconds) [62]. Among the different MD approaches, the Green's function MD (GFMD) [152] is extensively used in tribology applications as it allows to consider just the atoms of the contacting interfaces [153]. As an example of application, a recent study used MD to obtain values for the friction coefficient of a lubricated contact [154]. The predicted friction coefficients were in agreement with experimental results from previous studies, indicating that molecular dynamics is an effective method to provide friction coefficient estimations.

A summary of the main characteristics of the presented analytical and numerical methods is given in Table 2.1. For a more detailed description of such methods, the following recent review papers are a good starting point [62,133]. These methods have also been compared in the recent contact-mechanics challenge [42], in which a well-defined normal contact problem had to be solved. The results of the challenge showed that all the models were able to predict qualitatively the solution, with the numerical methods providing the most accurate results. However, quantitative predictions were not fully predictive due to the following reasons:

- The complex nature of the contact problems: multi-scale and multi-physics aspects must be taken into account for correct predictions. A future research direction would be to couple different approaches across the scales, in a single modelling framework, to capture the multi-scale and multi-physics aspects.
- The complexity of model validation: in most cases, contact interfaces are not accessible for direct measurements and, therefore, model validations through experiments are difficult to carry out.

The contact stiffness is in general only roughly estimated, while the friction coefficient can be predicted with MD simulations, which, however, are still infeasible for industrial applications due to large computational requirements. As a result, experimental measurements must be performed to provide accurate input parameters for the nonlinear dynamic analysis of jointed structures.

Table 2.1: Summary of analytical and numerical methods.

	Input	**Output**	**Advantages**	**Disadvantages**
Multi Asperity Models	Statistical height distribution of asperities	True area of contact, Separation vs load	Fast computation	Not accurate enough, not versatile, based only on asperities
Persson's Theory	Surface roughness power spectrum	True area of contact, Separation vs load	Fast computation	Not accurate enough, less versatile than numerical methods
BEM	Discretization of the interface	True area of contact, Separation vs load, Pressure distribution	Accurate, faster than FEM	Less versatile than FEM
FEM	Discretization of the interface and the bulk	True area of contact, Separation vs load, Pressure distribution	Versatile, accurate	Demanding computation, complex FE
MD	Atoms' distribution, and potentials	Atoms' kinematics Friction coefficient	Might capture the real physics	Demanding computation, only nanoscale problems

2.5 Experimental methods for contact parameter estimations

Experimental methods are the major source for providing input contact parameters for nonlinear dynamic analysis and can be classified into three classes:

- Local contact hysteresis measurements, based on the recording of hysteresis loops to extract the coefficient of friction and the contact stiffness. In addition to hysteresis measurements, also unidirectional experiments can be used to measure the coefficient of friction.
- Local contact ultrasound measurements, based on acoustic waves propagating through contacting components to extract the contact stiffness.

- Global dynamics measurements, based on experimentally measuring frequency response functions (FRFs) and then matching predicted FRFs by tuning contact parameters used in numerical models.

2.5.1 Local contact hysteresis measurements

Hysteresis measurements are considered the most reliable method to provide input contact parameters for nonlinear dynamic analysis [14] since current simulation approaches for such analyses require the replication of the hysteresis loops to solve the dynamics equilibrium equations. The measurement of a hysteresis loop requires two pieces of information: the friction force transmitted between two sliding components and their relative tangential displacement[5]. In general, forces are measured with force transducers and displacements are measured relatively close to the contact interface, on the edges of the contacting components, with contact or non-contact measuring techniques.

One of the first measurements of hysteresis loops dates back to 1951, when Mindlin et al. [155] measured hysteresis between lenses with convex surfaces. Their findings agreed with the theoretical results of the Cattaneo-Mindlin theory [121, 122]. Later, in 1955, Johnson [123] confirmed the theories with an experimental investigation on hard steel spheres in contact with hard steel rollers. After these pioneering studies, several research groups conducted a variety of experiments to measure hysteresis loops [69, 70, 156–168]. Most of these studies were mainly concerned with the friction coefficient only or performed measurements at low excitation frequencies. Fewer rigs instead were purposely designed to provide input contact parameters for nonlinear dynamic analysis by recording data at higher frequencies [18, 80, 169–175]. Those rigs provide accurate displacement measurements with optical non-contact techniques based on either Laser Doppler vibrometer (LDV) measurements [18, 169, 170, 172] or digital image correlation (DIC) with high-speed cameras [80, 176–182]. DIC is a well-established technique to measure displacement fields [176]. It consists of acquiring high-resolution images during experiments and post-processing them to extract the field of deformation of the surfaces. Both LDV and DIC measurements have been used to monitor the motion of the boundaries of friction joint interfaces during a vibration cycle. Some of these rigs were described and compared in a survey of 2018 [14], including the high-frequency friction rig in the Dynamics Group at Imperial College. That rig is the focus of this PhD research and is accurately described in chapter 3. Other rigs are briefly described in the Appendix A, together with a summary of their main experimental measurements.

Despite a series of measurements having been published at different institutions, a complete study of high-frequency data is still missing thus limiting the knowledge of the friction mechanisms at high frequencies. In addition, due to a lack of direct comparisons, the reliability of these high-frequency friction rigs remains unknown and there is no standardized approach for conducting measurements. The joint mechanics community has been talking for a long time about comparing contact interface parameters measured from those friction rigs, so to provide more confidence in the data sets used for nonlinear dynamic analysis. This PhD research partly addresses this issue, since chapter 4 shows a round robin test campaign performed between the two high-frequency friction rigs of Imperial College London and Politecnico di Torino.

[5]Note that normal load measurements are also required to extract values for the friction coefficient.

In addition to hysteresis loop measurements, many other methods exist to measure the coefficient of friction because μ is relatively easy to measure (only normal load and friction force need to be measured). Bowden and Tabor [58] listed some of the many tribological methods, including pin on disc, weights hanging on a pulley, tilting of inclined planes, deflection of a pendulum or a spring and so on. Thanks to the huge number of experiments carried out during the past centuries there is a list of values of the friction coefficient for a large variety of material pairings obtained in different conditions (e.g. different sliding velocities or temperatures). Other friction analyses are related to earthquakes, which have long been recognized as being the result of stick-slip frictional instabilities [183, 184]. However, hysteresis measurements give more pieces of information for nonlinear dynamic analysis and, therefore, are the main focus of this PhD research.

A mention is given in this section to other experimental techniques used to study sliding contacts, such as non-contact techniques based on direct optical measurements [185–190], which successfully observed changes in the real area of contact at the onset of slip, but only on the contact of transparent materials. The requirement of at least one transparent medium to allow optical access makes these approaches non-applicable for common metal to metal dry friction joints. For this reason, hysteresis measurements are the most used for nonlinear dynamic analysis. However, the main limitation of hysteresis measurements is that measurement points are not located exactly on the interface but tens of micrometres far from it, on the side of the contacting components. Therefore, they only provide one- or two-dimensional information from the edge of the contact interface, without providing any insight into the behaviour of the central part of the contact. The information on the full contact behaviour is then still relying on numerical models to predict what is happening inside, with only a few validation data coming from experimental evidence at the edges.

2.5.2 Local contact ultrasonic measurements

An alternative method to access the central part of contact interfaces is the use of active ultrasound and/or acoustic emissions (i.e. passive ultrasound). Previous studies have used acoustic emissions [191–194] measured in the near field around the contact to detect the onset of slipping. The main challenges for dynamic applications would be to isolate the frictional noise from other sources of noise in the test (structural vibration, shaker etc.) and to localise the slipping area. In contrast to this, active ultrasound has been mainly used to study tribological contacts under static or quasi-static conditions [195], providing e.g. detailed information on the contact stiffness [66, 68, 73, 76, 81, 196–199].

Ultrasonic techniques use acoustic waves at frequencies above the human audible range (20 kHz). They are traditionally used for crack detection, material property characterisation and imaging, but have also been used to study contact interface properties [65, 68, 195]. In this latter application, a transducer, usually piezoelectric, generates ultrasonic waves (longitudinal or shear) that travel through the host medium by pushing and pulling atoms, until reaching the contact interface. At the contact interface, some of the wave energy is transferred to the mating surface and some is reflected depending on, among other things, the degree of contact between the two contacting surfaces. When two rough surfaces are pressed together, contact occurs at the asperity peaks. Ultrasound passes through the contacting regions but is almost entirely reflected at the air-filled gaps. This reflection is due to the large acoustic impedance mismatch between structural materials and air. The amount of transmission/reflection can

be therefore used to study the contact properties of the interface. For example, changes in reflection and transmission are linked to variations in the contact stiffness of the interface, since such stiffness appears in the stress/strain equilibrium boundary conditions that govern the sound wave propagation at the interface [65, 200]. Tattersall [200] derived the relationships for the reflection, while Kendall and Tabor [65] derived them for the transmission. When the materials across the interface are identical, their derived relationships are the following for reflection and transmission respectively:

$$R = \frac{1}{\sqrt{1 + 4K_{US}^2/(2\pi f Z)^2}} \tag{2.13}$$

$$T = \frac{2}{\sqrt{4 + (2\pi f Z)^2/K_{US}^2}} \tag{2.14}$$

where K_{US} is the ultrasonically estimated contact stiffness per unit area expressed in N/mm^3 (either normal or tangential depending on whether longitudinal or shear ultrasonic waves are used respectively), f is the frequency of the ultrasonic wave [Hz], and $Z = \rho c$ is the acoustic impedance of the material, where ρ is the density [kg/m^3] and c is the velocity of the ultrasonic wave [m/s] in the material. R and T are respectively the reflection and transmission coefficients. These coefficients vary between 0 and 1 and indicate the degree of ultrasonic reflection/transmission at the contact. They are obtained by dividing the measured reflection/transmission by the possible maximum reflection/transmission for the investigated experimental setup. By experimentally measuring those coefficients, it is possible to quantify the contact stiffness, K_{US}.

Most of the ultrasonic studies improved the physical understanding of static contacts [195], providing e.g. detailed information on the contact stiffness [66, 68, 73, 76, 81, 196–199], but only a few have attempted to use ultrasound to investigate sliding or dynamic contacts [65, 196, 201–204], with the pioneering work of Kendall and Tabor [65] being one of the first. They acquired ultrasonic waves in a pin-on-disc setup, finding that the ultrasound transmission increases with sliding because of the junction growth phenomenon. A further step in the ultrasonic investigation of sliding contacts has been achieved with two studies [196, 201] that performed a direct comparison between ultrasound measurements and hysteresis loops. Mulvihill et al. [196] used ultrasound to monitor quasi-static contacts undergoing sliding while simultaneously measuring hysteresis loops with the DIC technique. They confirmed the hypothesis made by Kim et al. [76] that the ultrasound technique measures an elastic stiffness due to asperity loading and unloading cycles induced by the travelling ultrasonic wave. This ultrasonically measured stiffness is always larger than that obtained from hysteresis loops with DIC or laser measurements [196, 201], most probably because the latter also includes the bulk deformation in addition to the asperity contribution [71] since the measurement points are not located directly on the interface, but tens of micrometres far from it. Although Mulvihill et al. [196] studied sliding contacts, their measurements were performed under quasi-static conditions. A study in which the ultrasound technique has been used simultaneously with high-frequency hysteresis loops is the work of Pesaresi et al. [201], who observed that this technique is sensitive to the evolution of contact interfaces during sliding. This technique has also been investigated within this PhD research, as discussed in detail in chapter 5.

2.5.3 Global dynamics measurements

The measurement of dynamic forced responses is an indirect experimental method to obtain information on the coefficient of friction and the contact stiffness. Both friction coefficient and contact stiffness are tuned in numerical models to match predicted forced responses against the experimental responses of systems with friction contacts. This indirect technique to find contact parameters is used for structures with mechanical joints [67,84,171,205–211], Hertzian contacts [77,82,212–214] or for turbomachinery simulations [78], especially in the case of friction dampers [19,21,72,99,215–218]. Most of these studies either calibrated the numerical responses to match the experimental ones or investigated the effects of variations of contact stiffness and friction coefficient on the global dynamic forced response.

Among those techniques, it is worth mentioning a relatively recent technique used to extract information on the contact parameters: the joint identification technique [219], which is based on the dynamic substructuring idea [220]. This technique is based on the assumption that the effect of the joints can be obtained by the difference between the dynamic properties of the assembly and its individual subcomponents. FRF measurements of assembly and individual components are needed for this purpose. This technique is valid if the measurement noise is negligible but, in real applications, results are strongly influenced by noise. Some applications of dynamic substructuring to systems with friction can be found in [221–223], while for a deeper investigation, an extensive review on dynamic substructuring is provided in [220]. As an example, Tol and Özgüven [223] extracted contact stiffness values of a bolted joint using the joint identification technique and then used such contact stiffness estimations to predict FRFs. It is to be noted that most of the existing studies on joint identification techniques validated the contact parameter estimations by an indirect comparison with FRFs. However, a direct comparison of the extracted contact parameters against local interface data has never been proposed. This limits the reliability of these techniques.

2.6 Summary of the literature review

This literature review has presented:

1. An overview of approaches for nonlinear dynamic analysis, with details on the most common mechanical joints in turbomachinery structures and their effects on the system dynamic response.
2. An overview of the physics of the hysteresis loop and its two main characterising contact parameters, friction coefficient and contact stiffness.
3. An overview of the contact models used to replicate hysteresis loops for nonlinear dynamic analysis.
4. An overview of the analytical, numerical and experimental methods used to estimate the input contact parameters for those models.

The main conclusion of this overview is that frictional contacts are a major source of uncertainty for the correct prediction of the nonlinear dynamic behaviour of jointed structures. This

is due to the poor understanding of the physics of friction and contact parameters used as input in nonlinear dynamic analysis. The dependency of such parameters on external factors, such as loading conditions and materials, is not fully understood yet due to the challenges in accessing contact interfaces during vibration. Consequently, modelling approaches are not fully predictive and input contact parameters are still mainly provided by expensive and time-consuming physical testing. Several experimental methods exist to extract contact parameters for nonlinear dynamic analysis. Each of those methods captures different aspects of the physics of friction and only a few studies have attempted to use them simultaneously on the same structure for cross-validation. Such cross-validation is required to improve the current understanding of the contact parameters and ultimately lead to the development of fully-predictive modelling methods.

This PhD research addresses this issue by using the high-frequency friction rig of Imperial College as a test case for the cross-validation of the hysteresis, ultrasound and dynamics measurements methods. Chapter 4 shows a throughout round robin test campaign between two high-frequency friction rigs of different institutions to assess the reliability of hysteresis measurements. Chapter 5 shows the simultaneous acquisition of ultrasonic data with hysteresis loops, while chapter 6 shows dynamics measurements on the friction rig. Eventually, existing modelling approaches for nonlinear dynamic analysis are upgraded based on the discoveries from those experiments (chapters 7 and 8).

Chapter 3

Evaluation of the existing high-frequency friction rig

This chapter describes the high-frequency friction rig used in this work for the measurement the input contact parameters for nonlinear dynamic analysis. The friction rig has been built in 2012 in the Dynamics Group of Imperial College London [224] and has been used to measure hysteresis loops, from which friction coefficient and tangential contact stiffness are extracted. Although the friction rig has been used to extract such parameters for several years, recent understanding and experience with the rig have raised some questions on how to use the extracted parameters more accurately. Here, the most recent understanding of the friction rig is presented together with a method to accurately extract the contact parameters from the measured loops.

3.1 Description of the friction rig

The existing friction rig is shown in Fig. 3.1a and generates a unidirectional oscillating sliding motion between two cylindrical specimens with a flat-on-flat square contact as those shown in Fig. 3.1b. A simplified scheme of the rig is shown in Fig. 3.2. The two cylindrical specimens are held respectively by a static arm and a moving arm. The moving arm is hinged on a moving mass that is excited by means of an electrodynamic shaker, which generates a harmonic excitation. The moving mass is required to provide inertia to the system, so that the displacement remains relatively linear (sinusoidal), while only the transmitted friction force becomes nonlinear. This mass is connected to the ground by means of two leaf springs that are very flexible, thus allowing large horizontal displacements. A spring-loaded knife-edge connection hinges moving arm and moving mass, ensuring a free rotation of the moving arm around the mass. This free rotation is needed to guarantee that the normal load applied on the opposite end of the moving arm is fully transmitted to the static arm. Note that the knife edge is connected to the moving arm via 12 springs that pre-load the knife edge with 400 N normal force, which is considered large enough to minimize the edge stiffness non-linearity potentially induced during vibration loading and unloading cycles, such that it can be assumed as a linear joint. The static arm is fixed to a grounded mass by means of three dynamic load cells, which measure the friction force transmitted at the contact. The top specimen slides over the bottom one, which is clamped to

the static arm. Contact between specimens is ensured at all times by means of a pneumatic actuator that generates a normal load. The load is transmitted via a pushrod from the actuator to the top specimen. A second push rod, positioned below the bottom specimen, is used to avoid large bending moments and deflections of the static arm.

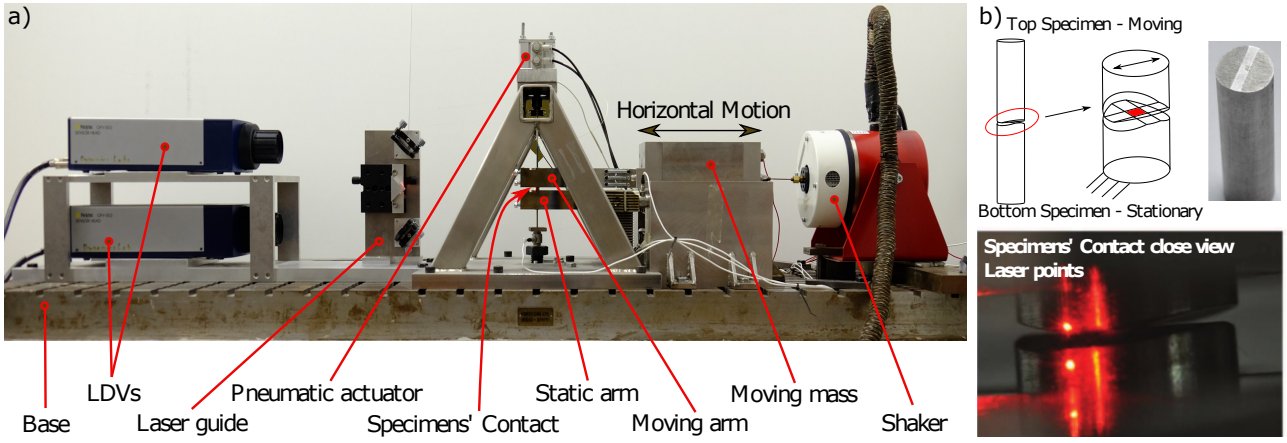


Figure 3.1: a) Specimen details; b) Photo of the friction rig [201].

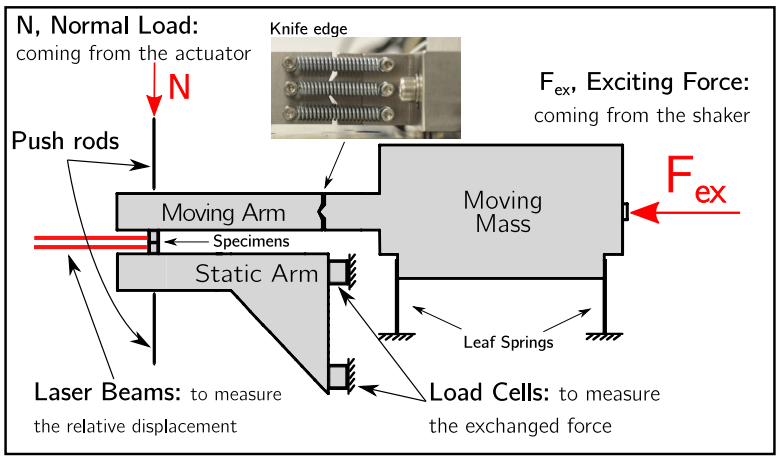


Figure 3.2: Friction rig scheme.

The four main signals recorded by the friction rig are measured as follow:

- Relative displacement: two single point Laser Doppler Vibrometers (Polytec OFV-503) are used to measure the specimens' velocities. The velocity is integrated and the relative displacement is obtained by difference. Laser points are focused very close to the contact interfaces (less than 1 mm away) by means of mirror laser guides, as shown in Fig. 3.1b. Such a close position to the contact should provide accurate displacement measurements without large influences from the bulk material deformation.

- Friction force: three dynamic load cells (Dytran 1051V3) connect the static arm to the ground as shown in Fig. 3.2. It is assumed that the friction force transmitted at the contact is then fully transmitted to the load cells since the static arm has a minimum amount of dynamics involved.

- Normal load: a static load cell (Omega LCM202) is placed under the pneumatic actuator (SMC ECQ2) and measures the normal load generated by the actuator. The actuator is controlled with an automatic pressure valve (SMC ITV0030) that adjusts the air pressure according to the user commands.
- Excitation force: a dynamic load cell (Dytran 1051V3) measures the harmonic excitation coming from the shaker (Data Physics GW-V20/PA100E) that is attached to the moving mass. Excitation frequency and amplitude are controlled in the LabView environment.

A well-controlled sliding motion is achievable by means of a displacement control system that varies the excitation force of the shaker. Usually, experiments are performed under a harmonic excitation of 100 Hz since experience has shown that this frequency leads to high-quality hysteresis loops. Normal loads can be applied up to 500 N and a maximum relative sliding distance of 150 μm can be achieved with the available excitation force at resonance excitation.

Specimens are 8 mm-diameter cylinders with a flat rectangular contact interface. As shown in Fig. 3.1a, they are rotated about their axis such that the two flat rectangular surfaces become orthogonal, thus generating a squared nominal contact area. The nominal area of contact can reach up to 25 mm^2.

In summary, the friction rig is controlled by three input signals (i.e. normal load, excitation force and excitation frequency) and measures two output signals (i.e. relative displacement and friction force). All signals are conveyed to a National Instruments PXI-1042 chassis and regulated with a control system, designed in the LabView environment, which allows for instantaneous monitoring of the hysteresis loops. As a reference, a typical hysteresis loop measured from the friction rig has been shown and described in section 2.2.

3.2 Sensitivity study for the accuracy of the contact parameters extraction method

The friction rig is used to measure hysteresis loops, from which friction coefficient and tangential contact stiffness are extracted. A Matlab code has been written in this research to automate the extraction of those parameters, for increased robustness and efficiency. This extraction can be a source of uncertainty in addition to the uncertainty coming from the experiments and therefore a sensitivity study has been performed and described in this section. Figure 3.3 shows a typical post-processed hysteresis loop. The code works by fitting four lines to the hysteresis loop, i.e. two red lines that fit the stick part of the loop and two blue lines that fit the friction limits. From those lines, the contact parameters are extracted as follows.

3.2.1 Tangential contact stiffness extraction method

The tangential contact stiffness is calculated as the gradient of the stick portion of the loop from the point of motion reversal to the point where the force is equal to zero, which is far enough from the beginning of the microslip region. Fig. 3.3 shows, with red circles, the points

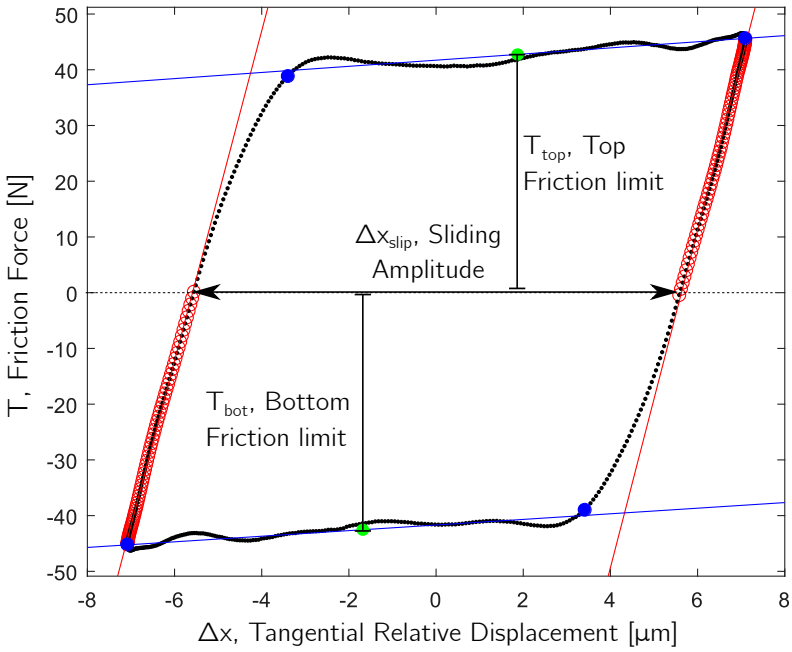


Figure 3.3: Fitting lines used for the extraction of the contact parameters. Two red lines fit the stick part of the loop and two blue lines fit the friction limits.

used for the linear fitting in the stick region of the hysteresis loop. The value of the slope of the fitted red line is the tangential contact stiffness.

The accuracy of this extraction method was tested on an individual hysteresis loop by changing the number of points used for the fitting and estimating the contact stiffness. In particular, the number of "start" points (right after the motion reversal) was changed as well as the number of "end" points (when the friction force is zero). Fig. 3.4a-c show some example loops in which points were added and subtracted, with the corresponding tangential contact stiffness values. For every combinaion of added/subtracted points, the contact stiffness was extracted from the fitting. The k_t values thus obtained are summarised in Fig. 3.4d, where k_{tL} and k_{tR} are respectively the k_t from left and right stick portions of the hysteresis loops.

The following conclusions are drawn from the Figure:
1) The k_t values (for the considered hysteresis loop) were all within 28.27 and 31.80 N/μm, with a maximum relative standard deviation of 0.9%, being much lower than the deviation due to experimental noise, as it will be shown in chapters 4 and 5. The low relative standard deviation indicates that this extraction technique is robust since it is not much sensitive to the number of points used for the fitting.

2) The k_t is more sensitive to changes in the endpoints than changes to the start points. This is expected since the endpoints are closer to the microslip region and therefore tend to reduce more the slope of the fitted line.

3) k_{tR} is slightly larger than k_{tL}. This is probably due to a slight difference in the normal load of the two friction limits, which is discussed in the following section 3.3.1. However, this effect is acceptable since the change is below 2%.

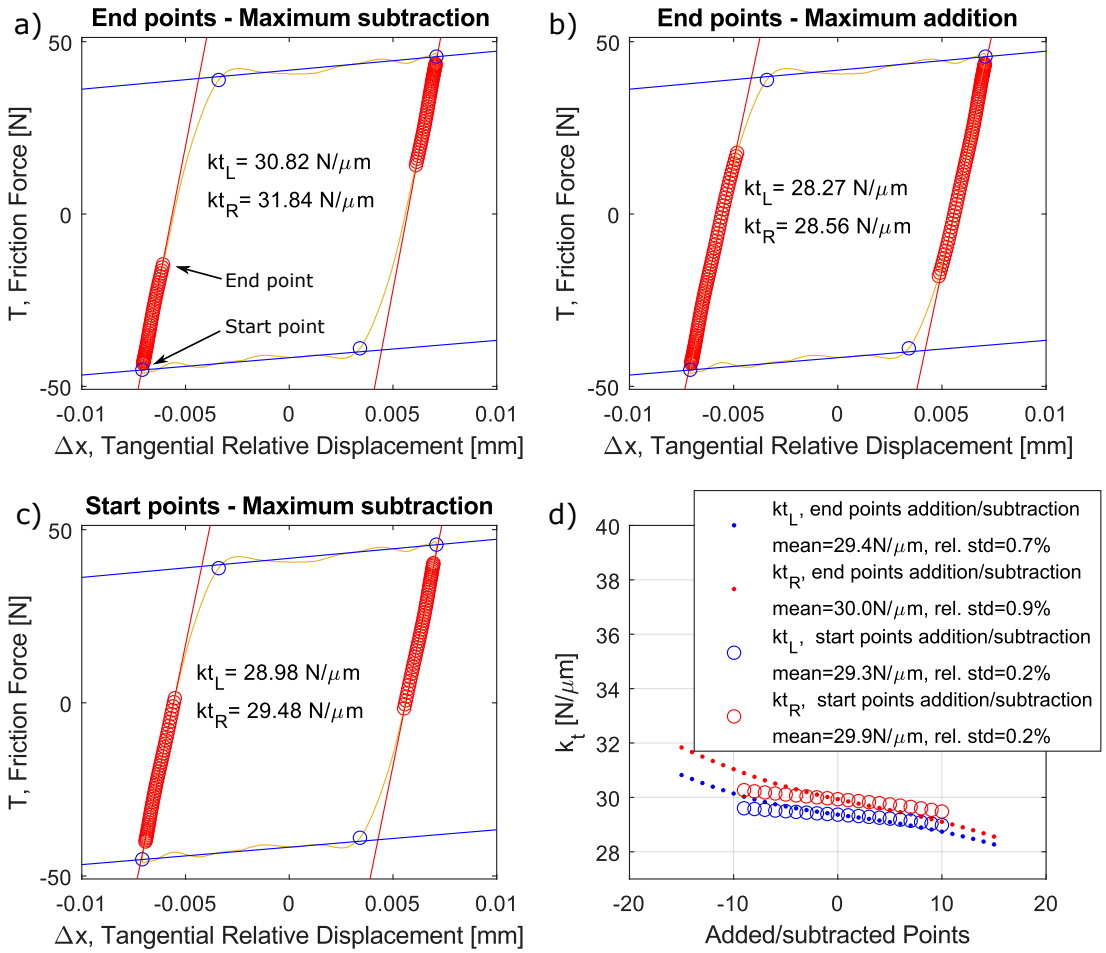


Figure 3.4: Sensitivity study on the tangential contact stiffness: a-c) hysteresis loops with different number of points chosen for the linear fitting and corresponding k_t values (k_{tL} and k_{tR} are the stiffnesses estimated from the left and right stick regions respectively); d) k_t values for different combinations of points used for the fitting.

3.2.2 Friction coefficient extraction method

The friction coefficient is calculated with two methods, the energy method and the standard method. Both methods are used in this research since some studies in the literature use only the first method and others only the second. In this way, results could be compared to more studies. The methods are described as follows:

1) Energy loss formula [170], $\mu = E/(2N\Delta x_{slip})$, where E is the energy dissipated within the hysteresis loop (equal to the area inside the loop, i.e. the integral of the friction force over the relative displacement), N is the normal load and Δx_{slip} is the sliding amplitude evaluated between the two points with zero friction force as shown in Fig. 3.3.

2) Standard friction coefficient with the equation $\mu = (T_{top} + T_{bot})/2N$, where T_{top} and T_{bot} are the (absolute) average top and bottom friction limits as shown in Fig. 3.3.

Since this extraction can be a source of uncertainty in addition to the uncertainty coming from the experiments, a sensitivity study was performed to investigate both methods accuracy. For method 1 (energy friction coefficient), the normal load is known and constant, and it is measured during the test; the energy dissipated is estimated by the integral of the friction force versus

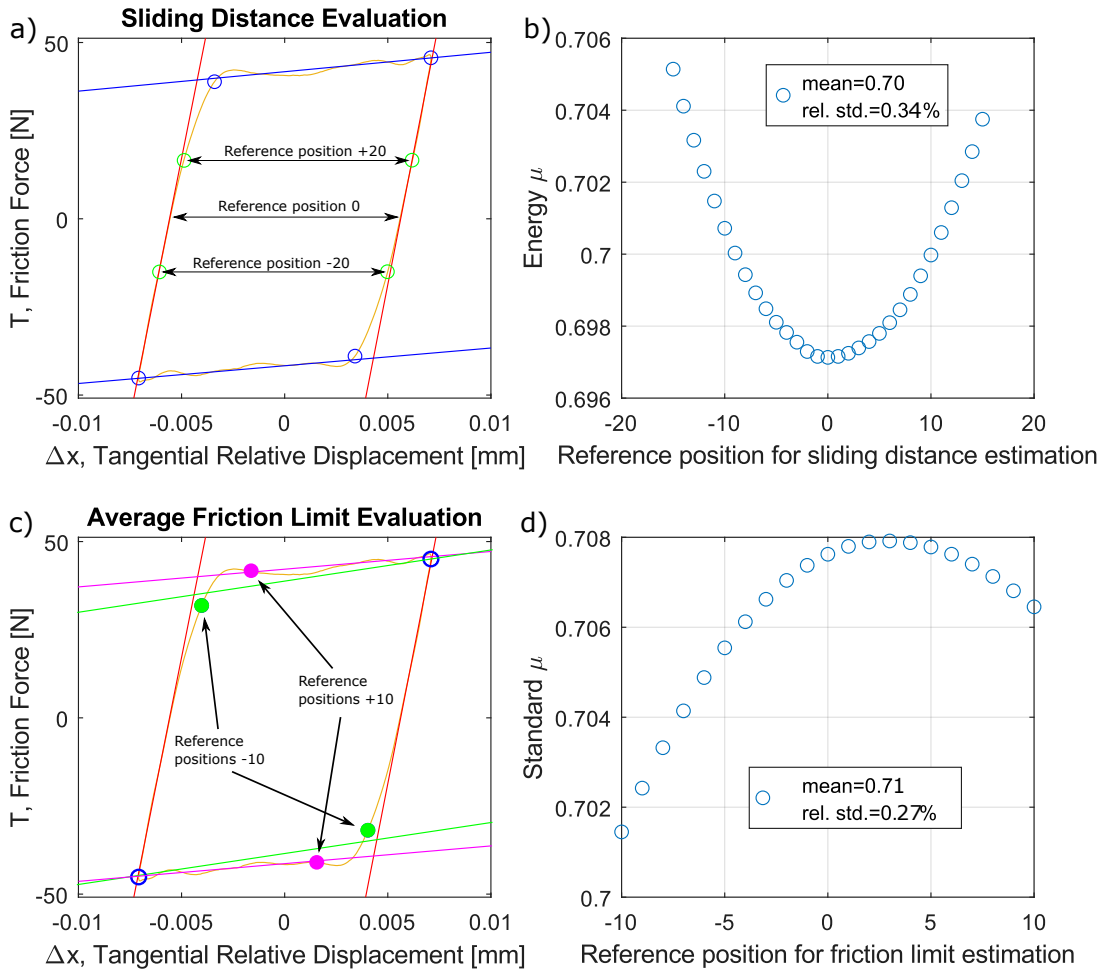


Figure 3.5: Sensitivity study on the friction coefficient (a-b) energy μ and (c-d) standard μ: a) Minimum and maximum reference positions for the sliding amplitude estimation for the energy friction coefficient calculation; b) Energy friction coefficient for sliding amplitudes estimated at different positions; c) Minimum and maximum reference limit points for the fitting of the friction limits; d) Standard friction coefficient estimated from friction limits fitted to points limited by different reference positions.

the relative displacement; therefore, the only term that can be affected by uncertainty in the extraction method is the sliding amplitude, which is estimated from the relative displacement of the two points of the hysteresis loop where the friction force is zero. A sensitivity study was performed to investigate how much this term varies if different points are used slightly above or below the 0 N friction force as shown in Fig. 3.5a. Figure 3.5b shows the result of such investigation with the *energy* μ estimated from different sliding amplitudes. Even for the extreme sliding amplitudes (reference positions +20 and -20 of Fig. 3.5a), values do not differ much with a relative standard deviation of only 0.34%. It is concluded that this extraction method is robust and not much affected by the sliding amplitude extraction process.

For method 2 (standard friction coefficient), the uncertainty might only come from the average friction limits T_{top} and T_{bot}. The friction limits are estimated by line fitting all the points between the two blue circles at the top in Fig. 3.3 for the top friction limit and all the points between the two blue circles at the bottom for the bottom friction limit. The average value is extracted for each line (resulting in T_{top} and T_{bot} of Fig. 3.3) and is then divided by the normal load to estimate the friction coefficient. For this method, the sensitivity is performed

by changing the position of the limit circles used for the line fitting of the friction limits. Figure 3.5c shows the limit reference positions of the limit circles used for the line fitting. The resulting *standard* μ values are shown in Fig. 3.5d. Also for this method, the standard deviation is quite low, only 0.27%, thus indicating that this extraction technique is robust as well. More details on the differences between different friction coefficient estimation methods can be found in the following review [167]. Note that a feature of the analysed hysteresis loops is the increasing friction force during gross slip, which is not perfectly constant as expected from the Amontons-Coulomb law of friction. This non-constant behaviour has been described in previous studies [229] and is discussed with more details in section 4.2.

In conclusion, the sensitivity study presented in this section showed that the relative standard deviation is below 0.9% for the contact stiffness extraction and below 0.5% for the friction coefficient extraction. Since the variability for both contact parameters is reasonably low, it is concluded that the developed method is reliable and robust.

3.3 Sources of uncertainty

The rig can generate high-quality hysteresis loops since it has been designed to minimise the effect of all the joints. However, sources of uncertainty might still be present due to the complex nature of the experiment. In particular, three questions arose from previous uses, which have never been addressed in detail: **a)** is the normal load kept constant during the whole experiment? **b)** is the measured relative displacement the same as the actual relative displacement occurring between the contact interfaces? **c)** is the measured force on the load cells the same as the transmitted friction force at the contact?

To address some of these questions and to investigate the possible sources of uncertainty, a detailed analysis of the rig kinematics was performed and described as follows.

3.3.1 Uncertainty in the measured normal load

Continuous contact of the specimens is ensured by applying a normal load with a pneumatic actuator. However, during vibration, both moving and static arms might move upwards and downwards due to some flexibility in the test rig, thus affecting the normal load distribution at the contact. To investigate this aspect, a simplified two-dimensional structural model of the friction rig was created in Abaqus, as shown in Fig. 3.6a. Such a simplified model was chosen to understand qualitatively the load paths in the friction rig since a quantitative analysis was not required at this stage. The model represents the moving and static arms by means of about 1000 beam elements. The moving arm is free to move horizontally and is constrained with a hinge at its right side (to simulate the free rotation due to the knife-edge). On its left side, the moving arm is connected to the static arm by means of the clamped specimens. Specimens are glued in this simplified model since the modelling of the friction behaviour is not the aim of this preliminary study. The top push rod, which transmits the normal load, is hinged in both ends (on the top where the connection with the pneumatic actuator would be, and on the bottom with the moving arm). The static arm is grounded at the dynamic load cell locations and is also connected to the hinged bottom pushrod.

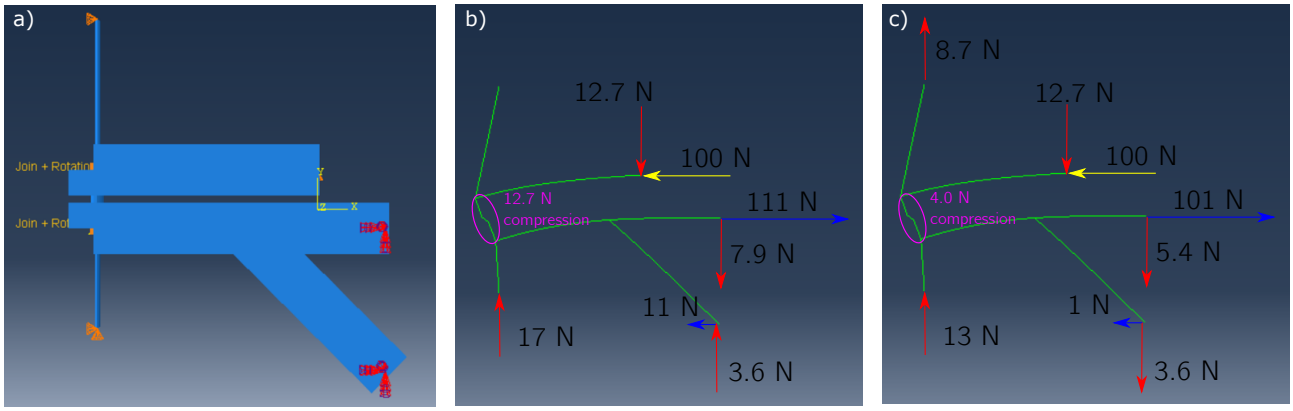


Figure 3.6: a) Abaqus structural model; b-c) Reaction forces (in blue and red) due to a tangential load of 100 N (in yellow). Case b) is with the top push rod free to move vertically at its top connection with the pneumatic actuator; case c) is with the top push rod constrained vertically at its top connection with the pneumatic actuator. When the tangential load of 100 N is applied in the opposite direction (not shown here), the arms bend upwards and backwards, and all reaction forces are equal and opposite.

Static analysis was performed by applying a 100 N tangential load that acts on the location where the exciting load from the shaker would be. This was done to model the maximum tangential excitation load observed during the vibration cycle and to understand if the upwards and downwards motion is mainly induced by that tangential load. For this reason, the normal load was not applied at this stage. Figure 3.6b and c show the results of such analysis for two different boundary conditions on the top stinger. In both simulations, a clear bending is observable, as expected, since the 100 N excitation (yellow arrow) is on a different axis than the opposite reaction forces measured on the static arm load cells (blue arrows), and therefore a moment is generated. This moment generates bending but, more importantly, it generates a compressive force in the contact. Figure 3.6b shows with a purple circle that the compressive force for the 100 N tangential load is 12.7 N, meaning that the contact experiences a larger normal load when that tangential load is applied. Instead, when the 100 N tangential load is reversed, the moving arm moves back to the right (not shown in the Figure). As a result, tension is generated at the specimen contact since the opposite moment tends to open the contact. The overall difference in the contact normal load is 25.4 N when the rig is in the two opposite configurations (12.7 N compression in one direction and 12.7 N tension in the other direction). In other words, the normal load at the contact is 25.4 N larger when the tangential load is applied in one direction than when it is applied on the other. This value is quite large (25.4% of the tangential load) and might induce large uncertainty in the extraction of the contact parameters. This effect cannot be captured by the static load cell that measures the normal load on top of the stingers since that cell, due to its static nature, can only measure an averaged normal load throughout every hysteresis loop.

To quantify experimentally this effect, two dynamic load cells were mounted above and below the top and bottom push rods respectively as shown in Fig. 3.7a. The two dynamic load cells made it possible to measure the normal load variations during the vibration cycles as predicted by the Abaqus structural simulations[1]. Figure 3.7b-d-e also show the results of such measurements, by plotting the measured normal loads and friction force versus the tangen-

[1]The vertical motion of the friction rig has also been quantified with the Digital Image Correlation technique, as shown in the Appendix B and is recalled for a model update in chapter 6, section 6.1.

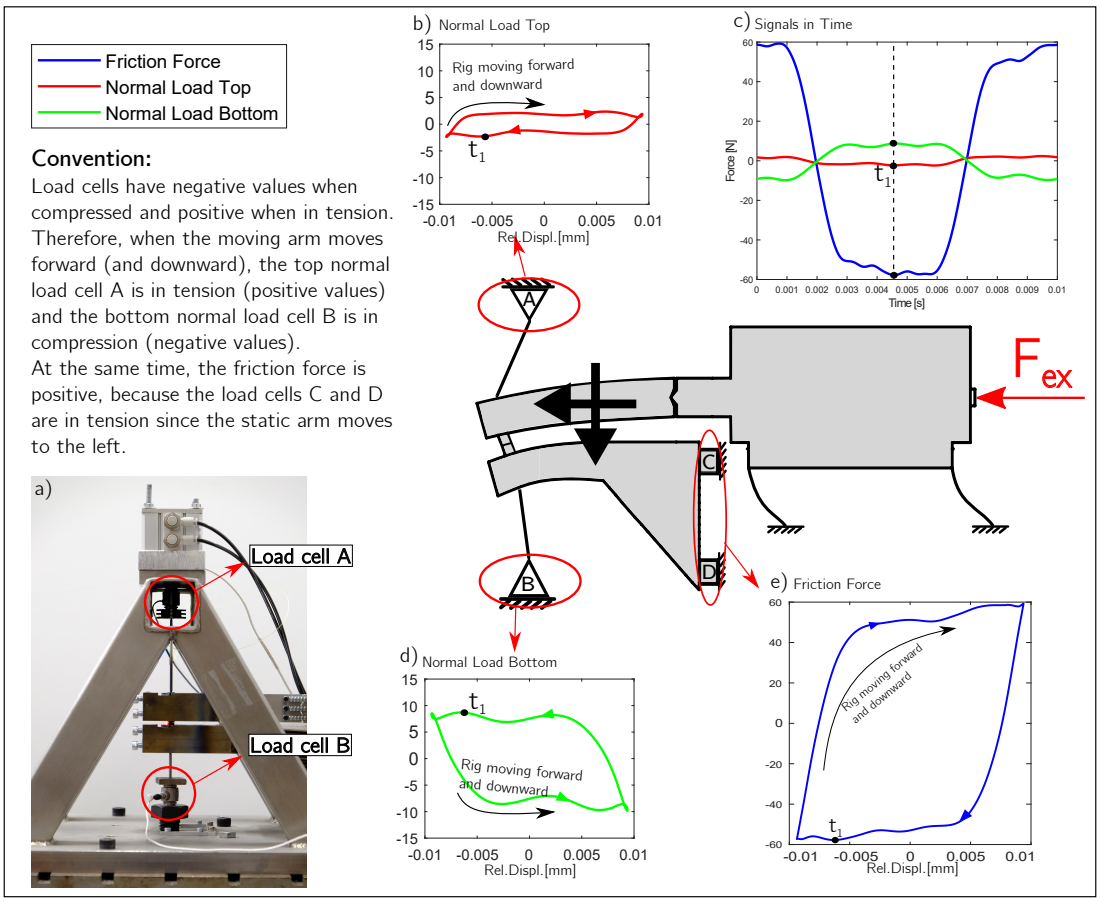


Figure 3.7: a) Upgraded rig setup to measure the normal load fluctuations during a vibration cycle; b-e) Normal load and friction force measurements during one vibration cycle at 100 Hz excitation.

tial relative displacement of the specimens. As predicted, variations in the normal loads are measured during the vibration cycle. Notably, the normal loads generate hysteresis loops in phase with the hysteresis loop of the friction force, meaning that the normal load is maintained constant during the gross slip regime, while it varies when the specimens are in the sticking regime. This is expected because, when the specimens are stuck together, the arms act as a whole piece and therefore when they move forward, they also move downward (this happens because of the bending moment in the arms induced by excitation and reaction forces). This downward motion loads the bottom normal load cell and unloads the upper load cell. Then, when the specimen starts to slide, the normal load is maintained constant and the moving arm just moves forward and does not bend further. The same, and opposite, behaviour appears when the arm moves backwards and upward (not shown in the Figure).

This explanation is also supported by Fig. 3.8, where hysteresis loops are shown for different displacement amplitudes. In Fig. 3.8a, the displacement amplitude is low and the contact is stuck with the normal load fluctuating linearly. Instead, in the other graphs, the normal load varies when the contacts are stuck, but remains constant once the specimens start to slide. Note that the measurements on the top and bottom load cells are out of phase (i.e. they have a different inclination) since when one is in compression, the other is in tension.

Figure 3.8 also shows that the variation in the normal load of the bottom load cell is larger than the variation in the top load cell. This difference can be explained by looking at Fig.

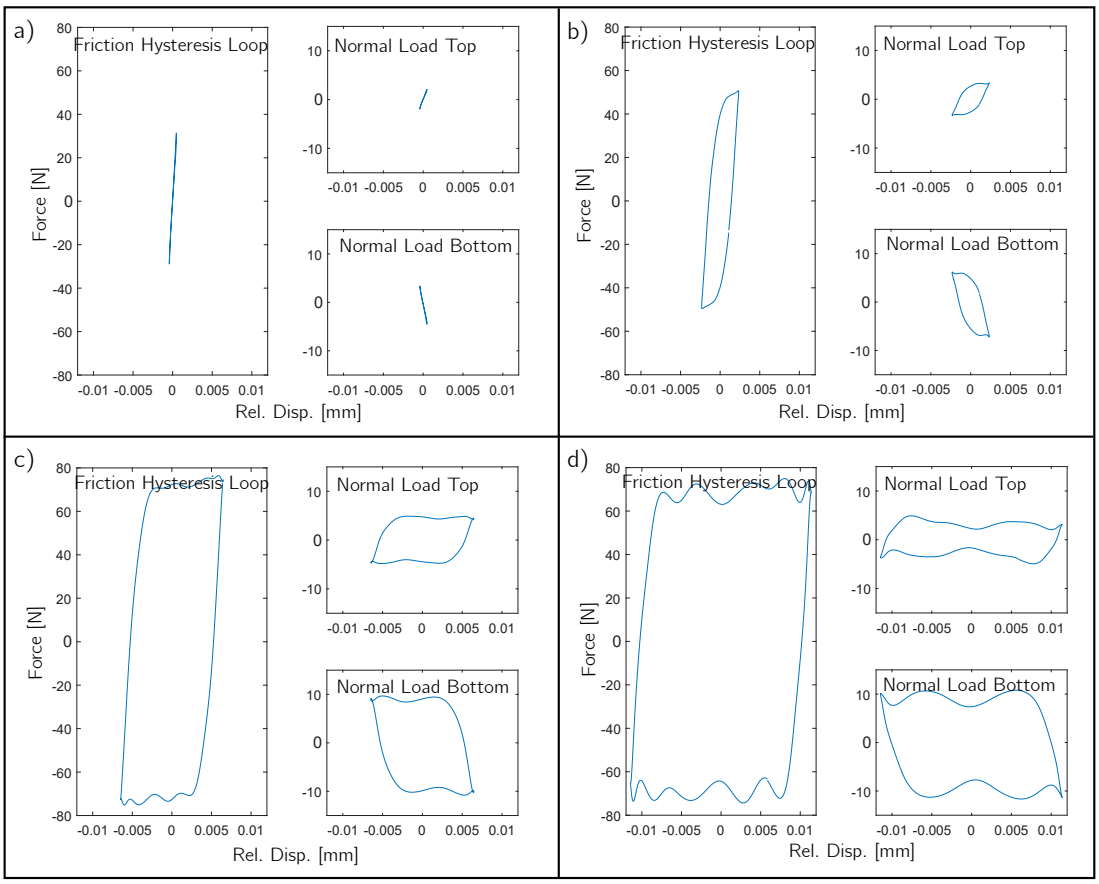


Figure 3.8: Normal load fluctuations for an increasing displacement amplitude.

3.6c, which shows that the normal load resulting from the bending is not distributed solely on the top and bottom push rods (8.7 N and 13 N respectively), but it is also transferred on the hinge of the moving arm and on the grounded connections of the static arm (12.7 N and 9 N respectively). Because of this load distribution in the rig, the normal load taken by the top load cell is reduced as compared to that taken by the bottom load cell. As a result, it is not possible to use top and bottom load cell normal load measurements to get exact indications on the real normal load variation at the contact, since part of that normal load is distributed on the other components of the rig[2].

These variations in the normal load have been measured here for the first time and must be investigated in detail since they might induce some uncertainty in the extraction of the contact parameters. The estimation of the friction coefficient, μ, is not much affected by the normal load variation because μ is extracted by using the gross slip portion of the hysteresis loops and Fig. 3.7b-d showed that, during the gross slip regime, the normal load does not change. In addition, the friction coefficient is estimated from the relative difference in the friction limits, as detailed in section 3.2, and thus any overall load variation is compensated. The contact stiffness might instead be affected by the variation in the normal load since this contact parameter is strongly dependent on the normal load as already shown in section 2.2.2. However, measurements in the following chapters (e.g. chapter 5, section 5.3.3) will show that this effect is negligible even

[2]An alternative way to obtain a quantitative estimation of the normal load variation in the contact is by means of ultrasonic measurements, which can directly access the contact. They were therefore applied to the friction rig within an extensive experimental campaign, which is the focus of chapter 5. Those measurements confirmed and quantified such normal load variations within the vibration cycles.

for the contact stiffness.

3.3.2 Uncertainty in the measured displacement

The measured relative displacement between the two specimens largely depends on the position of the two laser measurement points. The closer the laser points to the contact, the more accurate the measurement. Two main sources affect this measurement:

- Specimens' clamping and bulk deformation (Fig. 3.9a): The specimen-arm clamping, being non-ideal, does not ensure a perfect alignment between the specimen and the arm, resulting in a slight specimens' tilting. In addition, the two specimens bend when a load is applied, thus adding their bulk deformation effect in the displacement measurement.
- Arms' rotation (Fig. 3.9b): As shown in the previous section, a bending moment is present, which also induces an additional rotation motion to the specimens.

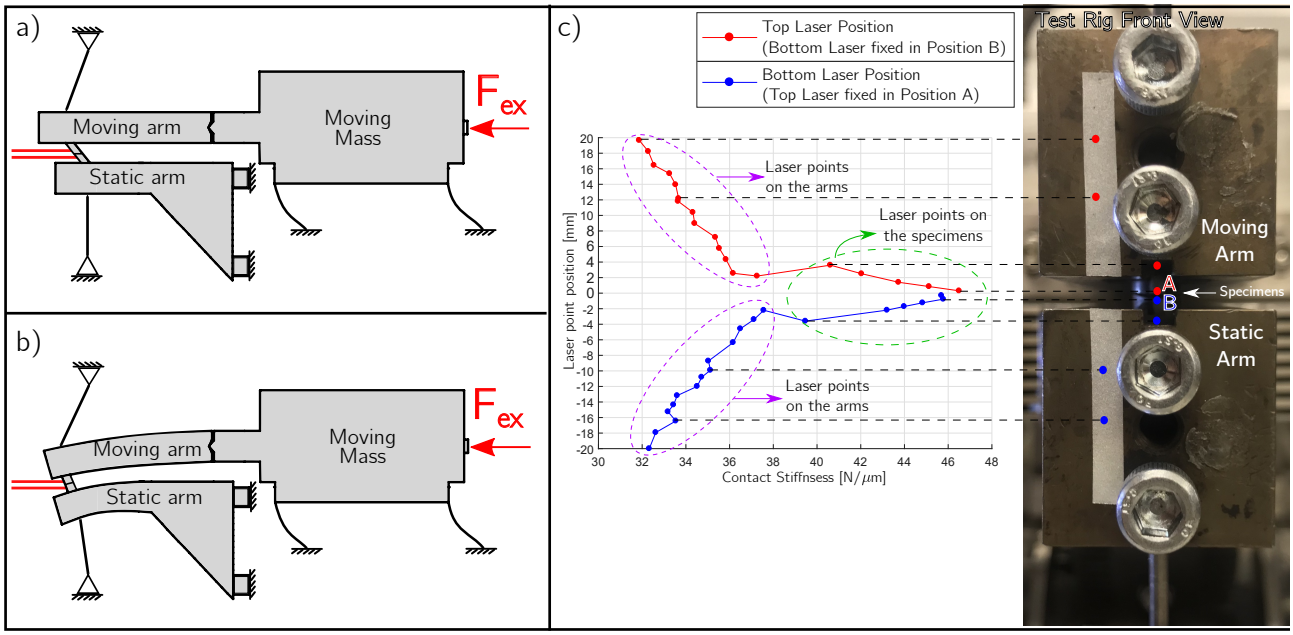


Figure 3.9: Displacement sources of uncertainty: a) Tilting due to non-ideal clamping and bulk deformation; b) Rotation induced by bending moment; c) Impact of the laser point positions on the contact stiffness estimation: laser measurement points on both specimens and arms.

This displacement uncertainty was evaluated with several hysteresis measurements recorded with both lasers pointing at different locations along the vertical direction. The results of this investigation are presented in Fig. 3.9c, where a plot is shown of the contact stiffness values versus the laser points position. The test was run for a couple of 304 steel specimens with a nominal contact area of about 2 mm^2. The normal load was 50 N, and the excitation frequency was 100 Hz. Hysteresis loops were recorded that showed a gross slip regime and the contact stiffness was estimated from the slope of the stick portion of the loop, following the extraction method described in section 3.2. First, the top laser point was moved while the bottom one was kept fixed at location B and then, the bottom laser point was moved while the top one was kept fixed at location A. Two different trends appear (circled in violet and green) and they

depend on whether the laser points are located directly on the specimens or the arms. In both cases, the contact stiffness decreases linearly with the increasing laser distance, as expected. The minimum relative distance that can be achieved during the measurement is about half a millimetre and, if the laser point relative distance is increased by about 1 mm, the contact stiffness is reduced from 46.5 N/μm to 45 N/μm, i.e. it is reduced by only the 3%, which is considered acceptable.

When the laser points are moved on the specimens (green circle) rather than on the arms (purple circles), the contact stiffness varies much more markedly with the increasing laser point distance. This suggests that the specimens' tilting and bulk deformation have a larger influence than the rotation of the arms due to the bending. Their contribution was quantified experimentally with the ultrasonic measurements of chapter 5, section 5.2.3, and numerically with the finite element simulations of chapter 7, section 7.1.1).

To further investigate the uncertainty in the displacement, a previous study [83] on the friction rig is recalled in which laser measurements were compared to Digital Image Correlation (DIC) measurements. Results of that investigation showed a very good agreement between recorded displacements with the two methods, confirming the accuracy of the laser setup in capturing the relative motion of the specimens. The agreement also demonstrated that the DIC technique is a powerful tool to measure vibration amplitudes in the order of micrometers. DIC would even allow to measure the normal relative motion at the same time of the tangential one, and therefore it is an effective technique to obtain information on the normal contact stiffness, as shown more in detail with a preliminary study performed during this PhD project and shown in the Appendix B.

3.3.3 Uncertainty in the measured friction force

The friction force transmitted at the contact is the sum of four components, as shown in Fig. 3.10. R_1 and R_2 correspond to the actual forces measured by the dynamic load cells, R_3 is the tangential force taken by the pushrod and $m\ddot{x}$ is the inertia force of the static arm. The uncertainty might come from R_3 and $m\ddot{x}$ since it is assumed that they are both negligible and therefore the friction force can be directly obtained from the measured forces $R_1 + R_2$. R_3 is assumed to be negligible since the pushrod is a pin joint, free to rotate at both ends, and therefore cannot transmit large tangential forces that are normal to its orientation. $m\ddot{x}$ is also assumed to be negligible since this arm stays almost entirely still during vibration (thus not generating large accelerations).

3.4 Conclusions

This chapter described the high-frequency friction rig used in this study for the extraction of the input contact parameters for nonlinear dynamic analysis. An automated method was developed to automate the extraction of such contact parameters. Its accuracy was evaluated with a sensitivity study. Results showed that the developed method is robust and reliable and can provide accurate estimations for both friction coefficient and tangential contact stiffness.

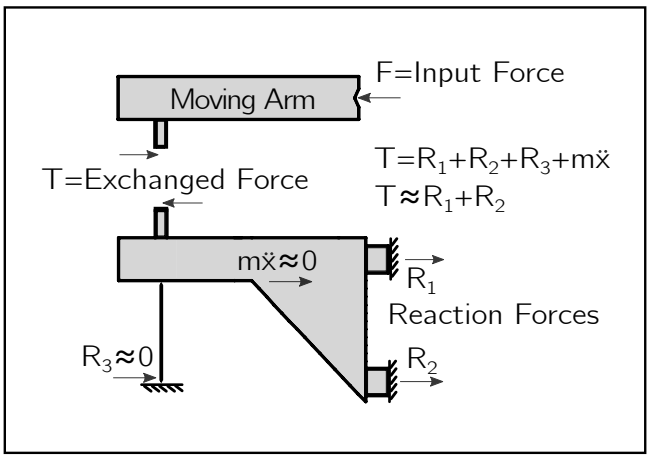


Figure 3.10: Sources of uncertainty in the friction force measurement. Horizontal forces equilibrium.

Detailed studies were also performed to improve the understanding of the kinematic behaviour of the friction rig, so to assess and quantify the amount of uncertainty in the measurements of normal load, relative displacement and friction force. With regards to the normal load, it was found that the asymmetry of excitation and reaction forces generates a bending moment, which leads to a change in the normal load during the vibration cycle. This change in the normal load can induce uncertainty in the extraction of the friction coefficient and the tangential contact stiffness. To evaluate the impact of such uncertainty on the reliability of the results, ad-hoc measurements will be performed in future chapters. With regards to the measured displacement, it was shown that the laser measurement location does not affect k_t estimations to a large extent. Finally, the friction force seems to be less affected by sources of uncertainty other than the load cell intrinsic noise.

Based on these findings and the improved confidence in the reliability of the friction rig, the next chapter shows an extensive experimental hysteresis loop measurement campaign designed to improve the physical understanding of the input contact parameters for nonlinear dynamic analysis of jointed structures.

Chapter 4

Measuring contact parameters with the traditional hysteresis technique: round robin test including rigs of different institutions

One of the goals of this PhD research is to improve the physical understanding of the contact parameters used as input in the nonlinear dynamic analysis of jointed structures. Due to a lack of validation data and to the complexity of the underlying physics, current modelling approaches for nonlinear dynamic analysis are not capable yet of providing estimations with the accuracy and reliability required for industrial applications. Therefore, contact parameters are usually extracted experimentally from hysteresis loops (measured preferably at high frequencies if data is to be used for dynamic analyses). Several test rigs have been developed at different institutions to measure high-frequency hysteresis loops [80, 169, 170, 172–175, 225], and a series of measurements published, but a comprehensive study of high-frequency data is still missing. Due to a lack of direct comparisons, the reliability of these friction rigs remains unknown and there is no standardized approach for conducting measurements. In addition, these friction rigs do not often cover a wide loading range and, thus, the confidence in the measured parameters is to be considered low. The joint mechanics community has therefore been talking for a long time about comparing contact parameters measured from those friction rigs to provide more confidence in the data sets used for nonlinear dynamic analysis.

This chapter addresses this issue by presenting a comprehensive study on hysteresis measurements based on a purposely designed round robin test that includes the two high-frequency friction rigs of Imperial College London and Politecnico di Torino, hereafter referred to as Imperial and PoliTO respectively. The round robin test consisted of recording, on the two rigs, comparable hysteresis loops by manufacturing specimen pairs from the same batch of raw stainless steel and investigating a wide range of test conditions, including varying normal loads, displacement amplitudes and nominal areas of contact. A comprehensive set of values of friction coefficient and tangential contact stiffness is obtained and mapped for practical use in the structural dynamics community - this experimental data will be published open access in due course to be accessible and reusable in a clear format by other researchers. New insights into the physics are also given and recommendations are provided to improve contact models used for nonlinear dynamic analysis.

A huge amount of experiments has been performed to complete the round robin test. The author wishes to acknowledge the work of Cristiana Pennisi, a master student who did her master thesis project under the author supervision. Cristiana performed part of the experiments on the friction rig of PoliTO. Preliminary measurements of this round robin test were published within the 2020 International Conference on Noise and Vibration Engineering [226].

4.1 Round robin test description

The round robin test was designed to directly compare data obtained from the two different high-frequency friction rigs of Imperial [169] and PoliTO [170]. The friction rig of Imperial has been described in detail in chapter 3, while the friction rig of PoliTO [170] is described in this section (more details are given in the Appendix A, flat-on-flat rig [170]). The two rigs are shown in Fig. 3.1a and Fig. 4.1 respectively. Although their setup is quite different, the general idea behind the measurement is similar. Both rigs are excited harmonically with a shaker and generate an oscillating sliding motion between two contacting specimens, one mobile and one fixed. The relative displacement between the specimens is measured with laser doppler vibrometers pointing very close to the contact interface to minimise the bulk deformation compliance. The friction force transmitted at the contact is measured with dynamic load cells mounted on the fixed block. It is possible to measure the relative displacement down to 0.05 μm thanks to the high accuracy of the laser doppler vibrometers. These rigs present two main design differences:

- Contact approach: rigid alignment vs self-alignment. The Imperial rig employs a classic rigid body contact approach, which means that only one degree of freedom is free when the two specimens are brought into contact. In the case of the Imperial rig, one specimen is restrained and the other specimen is mobile. The mobile specimen can approach the restrained specimen only along the pre-defined normal direction. By using this technique, the area of contact strongly relies on the tolerance of the specimen contact interfaces, which, if not perfectly parallel to each other, will most likely give a point/line contact as shown in Fig. 4.2a. To transform the initial point contact into a flat distributed contact, a transient is required during which the point contact extends to surface contact due to wear (see Fig. 4.2b). This approach leads to easy mounting and assembly, but it requires high-tolerance interfaces to guarantee a full distributed flat contact, at least at the beginning of the test. If high-tolerance interfaces are not achievable, a certain running-in is required to establish a distributed contact. To address this issue, the PoliTO rig instead employs a self-alignment system of the specimens, which avoids the possibility of point contacts. This is achieved by introducing some flexibility in the fixed specimen employing free rotation as shown in Fig. 4.2c-e, where the contact self-adjusts until it becomes uniformly distributed (more information can be found in [170]). A disadvantage of this contact approach is that the mounting procedure is more challenging and time-consuming than the procedure of a rigid approach.

- Contact geometry: one-leg contact vs two-leg contact. Because of the self-aligning system, PoliTO specimens employ a two-leg contact interface, as shown in Fig. 4.3a, while the Imperial rig employs a simpler one-patch square contact interface, as shown in Fig. 4.3b. Both contacts are nominally flat.

These two design differences led to several advantages and measurement challenges, which are discussed in the comparison a the end of this chapter. Finally, Table 4.1 shows a comparison of the operating regimes of the rigs.

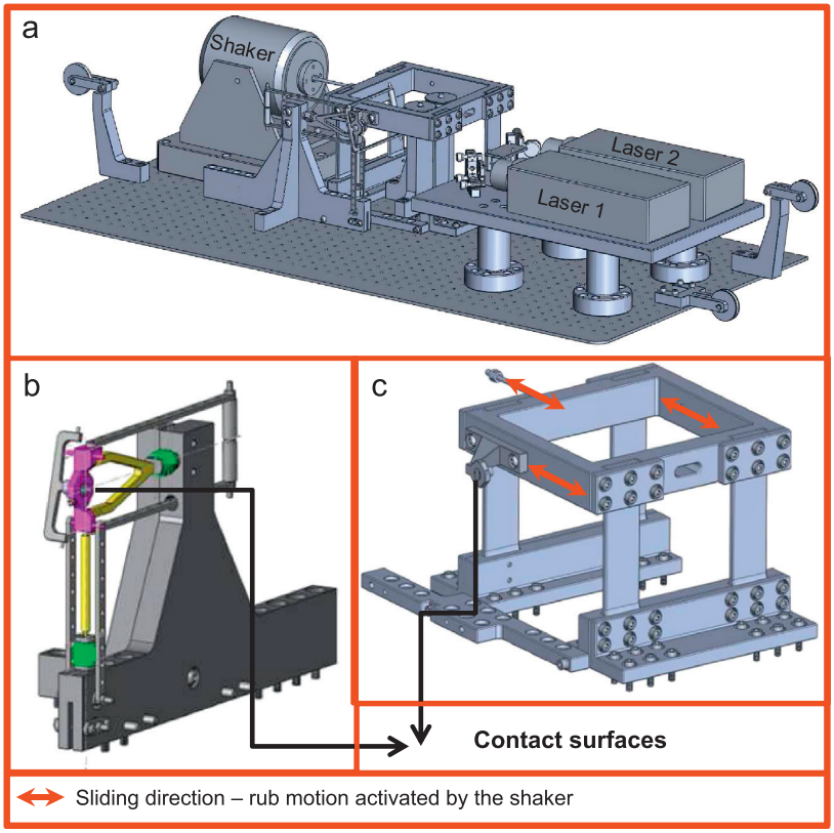


Figure 4.1: PoliTO friction rig: (a) overall view; (b) floating self-aligning specimen support; (c) mobile specimen support excited my means of the shaker [170].

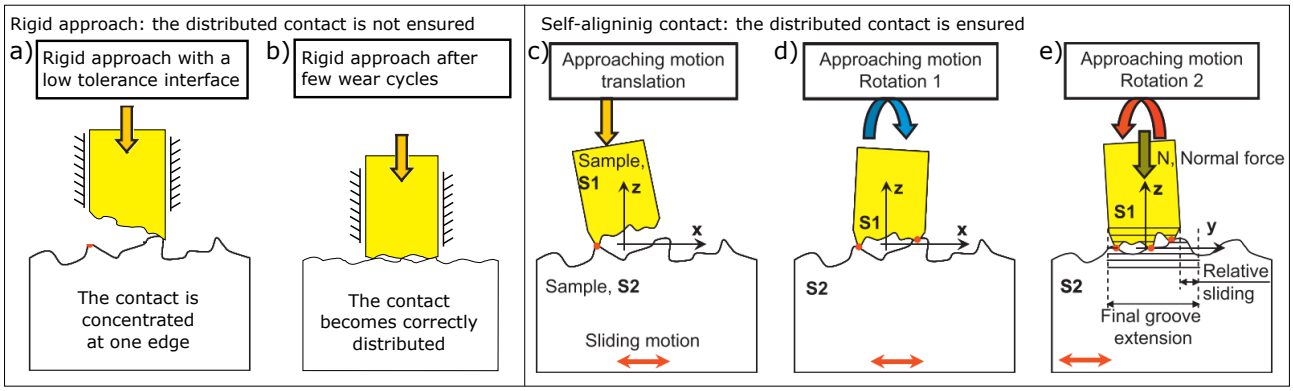


Figure 4.2: a-b) Rigid body contact approach of Imperial rig; c-e) Self-aligning contact approach of PoliTO rig [170].

Experimental plan

A large matrix of tests was designed to record hysteresis loops at room temperature for a wide range of loading conditions, chosen based on the compatibility of the rigs but also to expand

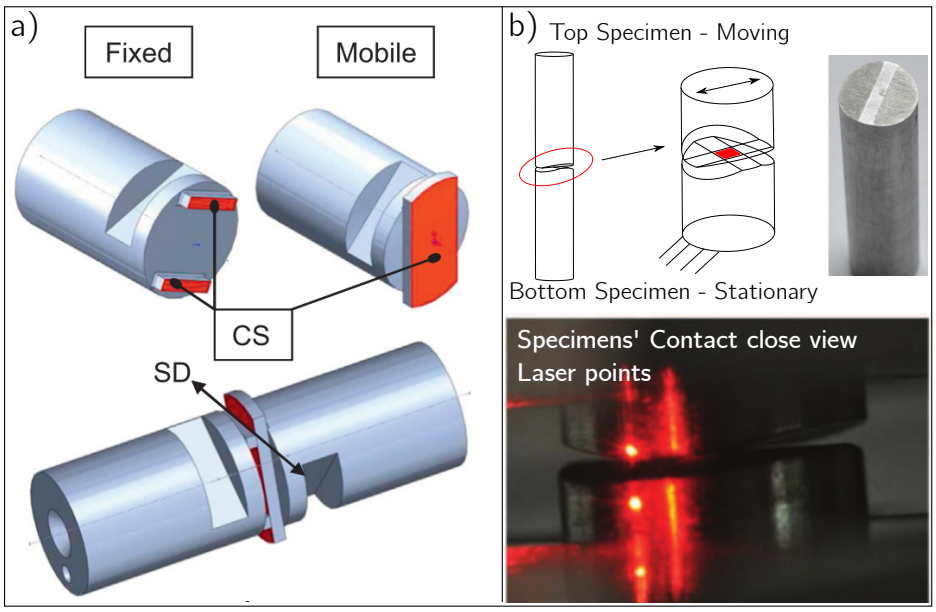


Figure 4.3: a) Specimens of PoliTO rig [170]: contact occurs on the two legs; b) specimens of Imperial rig [169]: one-patch square contact.

Table 4.1: Operating regimes of Imperial and PoliTO friction rigs.

	Imperial	**PoliTO**
Operating frequency	100 Hz	175 Hz
Displacement amplitude at the operating frequency	0.5 - 25 μm	0.5 - 50 μm
Nominal contact area	1 - 25 mm^2	5 - 50 mm^2
Nominal contact pressure	up to 500 MPa	up to 50 MPa

the test range beyond what each rig could do. The experimental matrix is shown in Fig. 4.4a and consists of four normal loads (17, 87, 150 and 253 N), four displacement amplitudes (1, 14, 25 and 50 μm) and four nominal areas of contact (1, 5, 10 and 40 mm^2). In order to explore the widest possible experimental space, each rig was tested at the extreme loading conditions that it could achieve. As a result, there was only an overlap for 10 loading combinations (circles with both green and red colours). The ranges of normal loads and displacement amplitudes were chosen to measure hysteresis loops in all the different contact regimes, namely full stick, microslip and gross slip. The two rigs operate at slightly different excitation frequencies (100 Hz and 175 Hz), which correspond to the optimal excitation frequencies of each rig. A preliminary analysis was performed to investigate the effect of the excitation frequency. That analysis was not conclusive since results were heavily dependent on the different rig dynamics and, therefore, it was decided to only focus the initial round robin on the optimal excitation frequencies. Those excitation frequencies also resulted in different sliding velocities of the specimens (obtained by multiplying the excitation frequency by the displacement amplitude). The displacement amplitudes were chosen to also have a match in velocities (achieved for the case at 2.45 mm/s, 24.5 μm for Imperial and 14 μm for PoliTO, as shown in Table 4.2). Note that, in academic test rigs with damper/blade contacts, velocities are in the range 2-5 mm/s, see e.g. [19]. Velocities

are lower in other types of joints, e.g. bolted joints or blade root contacts, since the relative motion is much lower in those cases. In the designed test matrix, the lowest achievable velocity was 0.2 mm/s, which corresponds to the velocity of a stuck contact under a 100 Hz excitation.

Finally, the selected range of nominal areas of contact was chosen to check for the scalability of the results, but also to understand what is the best way of modelling frictional contacts in dynamics simulations (e.g. if it is better to discretise the interfaces with many 1 mm^2 contact patches or with fewer 40 mm^2 patches). Note that the maximum achievable nominal area of contact for Imperial specimens was 9 mm^2 and not 10 mm^2 as planned. This slight difference was assumed to not affect the results since a full worn area of contact was never reached in the case of 9 mm^2 due to the very large area extension, as described in detail in section 4.2.

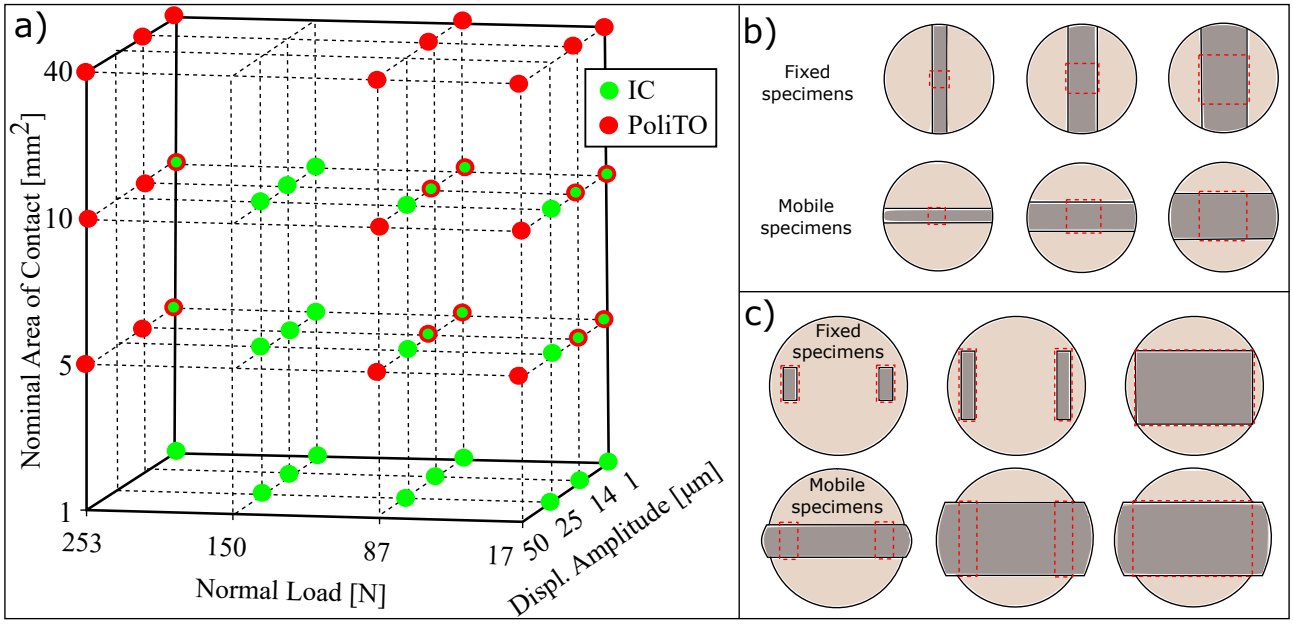


Figure 4.4: a) Test Matrix: tests with both colours were performed on both rigs; b) Specimens of Imperial (from left to right 1 mm^2, 5 mm^2 and 10 mm^2); c) Specimens of PoliTO (from left to right 5 mm^2, 10 mm^2 and 40 mm^2).

For every load combination, a new unworn specimen pair was used and run for 2.5 consecutive hours to achieve a proper running in and investigate the evolution with wear. In addition, a reference loading combination, highlighted in red in Table 4.2, was chosen on each rig for a repeatability study consisting of three tests performed with different specimen pairs to investigate the repeatability of the experiments. Before and after every test, scans of the contact interfaces were acquired with the Alicona Infinite Focus instrument at PoliTO and with the Olympius LEXT® OLS5000 3D Laser Confocal Microscope at Imperial. In this way, the condition of each specimen interface could be visually assessed before the experiments to ensure that the interface did not have scratches or imperfections. In fact, although specimens were all manufactured from the same batch of raw 304 stainless steel to guarantee comparability of the material, two different companies manufactured them in the UK and Italy, resulting in slightly different contact surface topographies[1]. In the case of Imperial, specimen interfaces were carefully hand-polished after the manufacturing by using two different grades of sand pa-

[1]The surface topography, also known as surface texture, surface finish or surface profile, is the local deviation of a surface from a perfectly flat plane. It is characterised by the roughness, the waviness and the form, which define the shape of the surface at different length scales.

Table 4.2: Test matrix summary. In red highlighted the reference test for each rig (used for repeatability studies).

	Units	Imperial	PoliTO
Material	-	Stainless steel 304	Stainless steel 304
Type of contact	-	flat-on-flat (one leg)	flat-on-flat (two legs)
Type of contact approach	-	rigid body	self-alignment
Temperature	-	room temp.	room temp.
Nominal areas of contact	[mm^2]	1 / 5 / 10	5 / 10 / 40
Normal loads	[N]	17 / 87 / 150 / 254	17 / 87 / 254
Min and max contact pressures	[MPa]	1.7 - 254	0.4 - 51
Excitation frequency	[Hz]	100	175
Displacement amplitudes	[μm]	1 / 14 / 24.5	1 / 14 / 50
Average sliding velocity	[mm/s]	0.1 / 1.4 / 2.45	0.18 / 2.45 / 8.75
Interface roughness	[μm]	0.5	5
Running time	[hours]	2.5	2.5

per: first, 800 grit for coarse and bulk material removal to reach the desired contact width and, then, 2500 grit for smooth and finer surface finish, leading to a roughness value R_a of about 0.5 μm. The hand polishing process led to slightly curved contact interfaces since material got removed at the sides first due to the rubbing on the sanding paper. An example interface is shown in the optical scan of Fig. 4.5a, colour from green on the sides to red in the centre. Note that the z-axis is magnified and better shown with Fig. 4.5b by means of the profile of the interface. The curvature was quantified by an equivalent radius of 33.2 mm, which is relatively large compared to the small interface width of only 1 mm. The curvature results in a bump of about 4 μm height, thus negligible compared to the width but very repeatable in every specimen. Although negligible, the bump was very helpful for ensuring high repeatability in the experiments since it led to an initial point contact at the centre of the interface at the beginning of the test (the specimen interfaces could be associated with two crossed cylinders of radius 33.2 mm). This feature was important for the tests performed at Imperial, whose rig employs the rigid body contact approach that makes more difficult contact self-alignment. Thanks to this unintentional curvature, the problem was partially resolved. Note that, even though at the beginning of the test the contact is concentrated at the centre of the interfaces, after repeated wear cycles the curvature would eventually wear out and the contact would fully distribute over the whole nominal contact interface, as shown in Fig. 4.5c. Scans like this one have been performed on each specimen after every test to evaluate the extension of the wear at the interface.

In the case of the PoliTO specimens, there was no manual sanding process, but the interfaces were provided by the manufacturer with a flat interface without any curvature and with some machining marks that led to a larger initial roughness value R_a of 5 μm. A typical interface

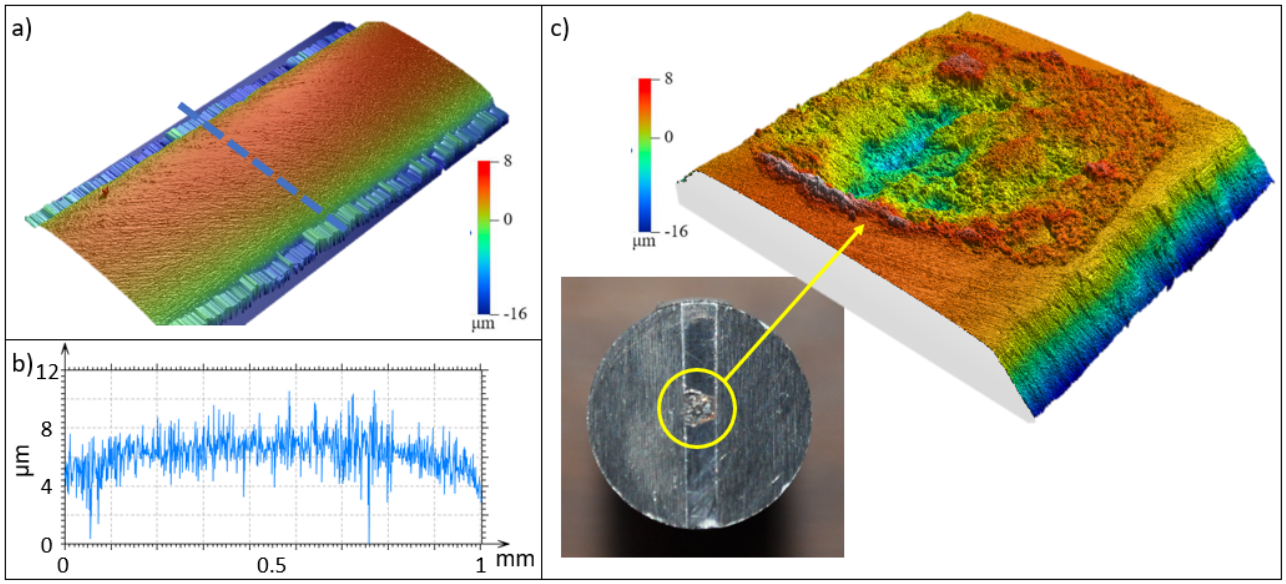


Figure 4.5: a) Scan of the unworn contact interface of an Imperial specimen; b) Profile of the unworn contact interface; c) Photo and scan of a fully worn contact interface of an Imperial specimen.

after the test is shown in Fig. 4.6, where the machining marks are visible outside the contact area while, inside the contact area (on the location of the two legs of the mating specimen), a significant amount of material is missing due to wear. Although the initial roughness values are quite different between Imperial and PoliTO specimens, hysteresis measurements will show that the initial roughness wears away quickly during the early stage of the test. This is evident in both Imperial and PoliTO specimens, from Fig. 4.5c and Fig. 4.6, where the amount of wear is of a much larger length scale than the initial roughness. Different starting roughnesses could however affect the evolution of the contact parameters and interfaces. This aspect should be investigated in future extensions of the round robin.

Data post-processing

The large experimental matrix and the completion of all the tests resulted in more than 100 specimen pairs being tested and more than 300 hours of testing. At an average excitation frequency of 140 Hz, this corresponds to roughly 150 million recorded hysteresis loops. For each specimen pair, rigs were run continuously for 2.5 hours to achieve a proper running in[2] and investigate the evolution with wear, thus generating more than 1.5 million hysteresis loops per test. Since recording all this data was infeasible because of storage limits, loops were continuously recorded only during the first 5 seconds of each test and then recorded at a gradually decreasing rate. This was done because, as will be shown in this chapter, hysteresis loops strongly vary at the beginning of the test and, consequently, all of them need to be recorded to accurately capture the evolution of contact parameters with wear. After the first 5 seconds, loops were recorded with a gradually decreasing rate until the 50^{th} minute, after which

[2]Note that few test have been conducted for longer times, up to 15 hours, to verify that the contact conditions did not vary significantly after the 2.5 hours. Since no major changes were observed, it was decided to maintain the test length to 2.5 hours.

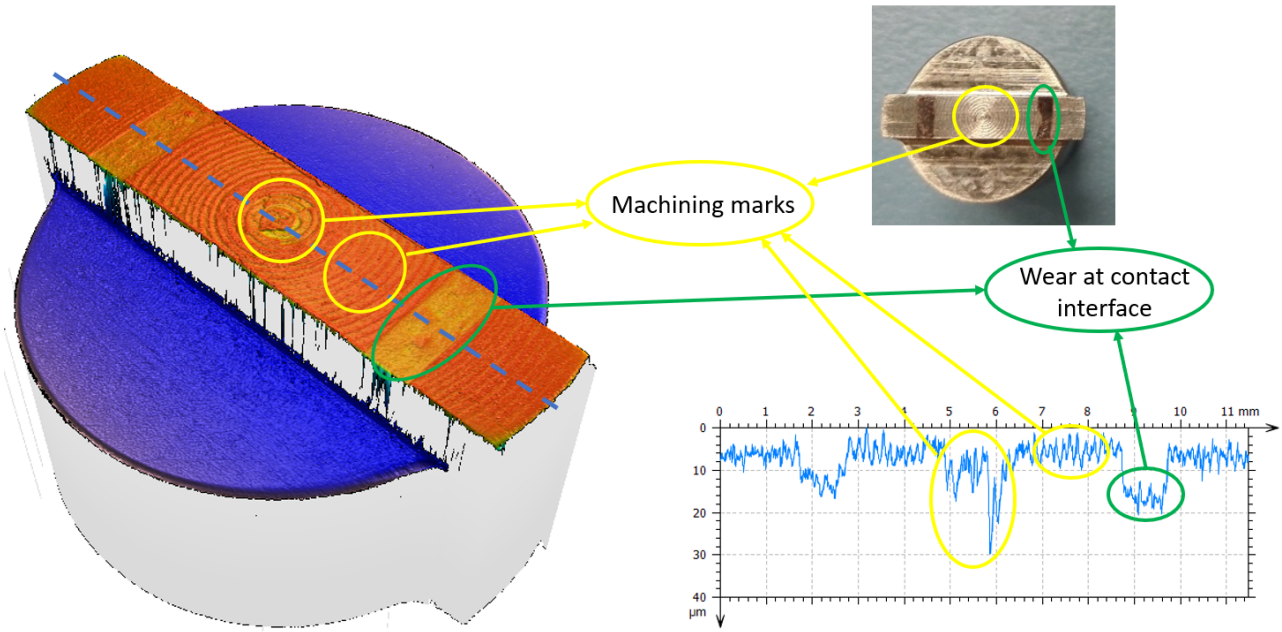


Figure 4.6: a) Scan, photo and profile of the worn contact interface of a PoliTO specimen (the contact is on the two worn spots).

only 10 consecutive hysteresis loops were recorded every 5 minutes. For every hysteresis loop, the following parameters were extracted:

- Friction coefficient, μ, calculated with the two methods described in section 3.2.
- Tangential contact stiffness, k_t, calculated as the gradient of the stick portion of the loop from the reversal up until the force is equal to zero, as described in section 3.2.
- Energy dissipated, evaluated as the area inside the loop, i.e. the integral of the friction force over the relative displacement.

The extraction was automated with the Matlab code described in section 3.2 that reads each individual hysteresis loop and extracts automatically the contact parameters. After the extraction, the contact parameters were plotted as a function of time to visualise their evolution during the whole test and to identify if any steady state existed. An example of a typical trend is shown in Fig. 4.7a. In case a steady state existed, its beginning was marked manually (as indicated by the vertical red dashed line) and a statistical analysis was performed on the steady state values. Violin plots [227, 228] were used to plot the statistical distribution of the steady state values. Violin plots include all the data that is in a box plot, namely a (white) marker for the median of the data; a (black) marker indicating the interquartile range (between the 1^{st} and 3^{rd} quartiles); and possibly all sample points if the number of samples is not too high. Violin plots are a superset of box plots, and give a much richer understanding of the data distribution, while not taking more space. As an example, Fig. 4.7b shows the violin plot of the steady state values of the test in Fig. 4.7a. Violin plots of all the tests performed within the round robin will be compared to understand their intrinsic uncertainty. This statistical analysis is performed for both friction coefficient and contact stiffness.

In addition to this analysis, scans of the contact interfaces were also used to estimate the worn area of contact with the Digital Surf Mountains® software, by selecting the black worn spots

and evaluating their extension (as the worn spot in Fig. 4.7a). The worn area of contact is needed to normalise the contact stiffness, as better shown in the following sections. For every test, the total cumulative energy dissipated was also calculated and correlated to the amount of wear estimated from the worn areas. The total cumulative energy dissipated is evaluated as the sum of the energy dissipated within each measured hysteresis loop.

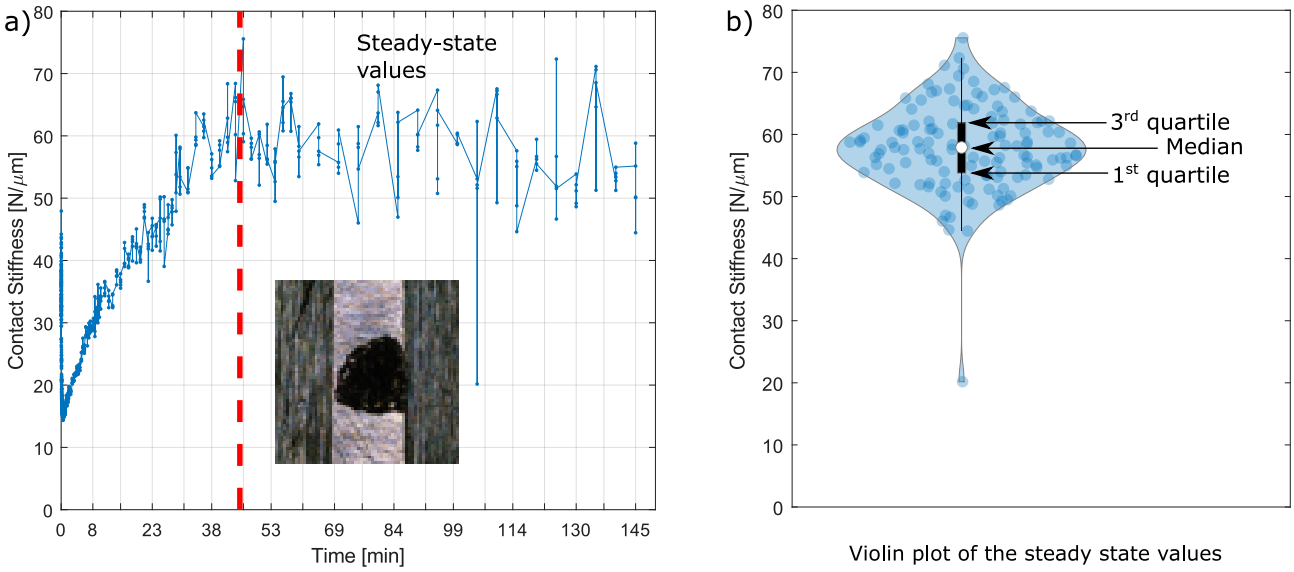


Figure 4.7: a) Typical evolution of the contact stiffness during a 2.5 hours long test, and identification of the steady state values. The specimen interface at the end of the test is also shown; b) Violin plot of the steady state values of the test in a). The white marker indicates the median of the data; the black marker indicates the interquartile range (between the 1^{st} and 3^{rd} quartiles); the blue shaded area includes all sample points.

4.2 Measurements at Imperial College London

This section shows a summary of the measurements performed on the Imperial rig. As mentioned in the previous section, a 2.5-hour test was performed for each loading combination with new specimen pairs. A general overview for every test is shown through Figs. 4.8-4.9-4.10. The Figures show the end-of-test contact interfaces and the end-of-test hysteresis loops for all the loading combinations and specimens with nominal areas of contact of 1, 5 and 9 mm^2 respectively. Note that, in the rest of the chapter, tests performed at Imperial are named consecutively IC1, IC2 etc.

Hysteresis loops strongly change as the displacement amplitude increases (loops from the top row to bottom row), shifting from being fully stuck[3] at 1 μm to being in gross slip at 14 and 24.5 μm. Also the normal load strongly affects the shape of the hysteresis loops (columns from left to right). For loops in gross slip, the friction limit, μN, increases with the normal load, as expected. For fully stuck loops, the gradient increases with the normal load since the contact

[3]Note that a full stuck regime is never achievable in practice since a small part of the contact interface will always exhibit microslip. However, at very low displacement amplitudes, the portion of the interface in microslip is assumed to be negligible compared to the major remaining portion of the interface in a stuck condition.

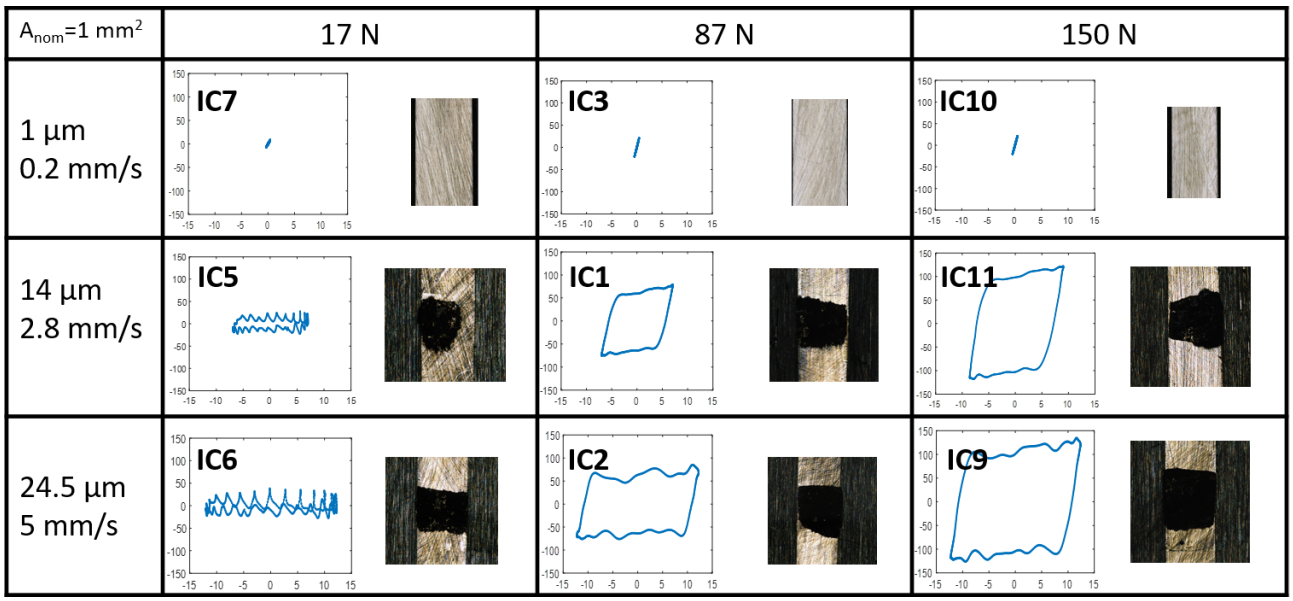


Figure 4.8: Overview of contact interfaces and hysteresis loops for tests conducted on specimens with a 1 mm^2 nominal area of contact at Imperial. Columns are normal loads and rows are displacement amplitudes.

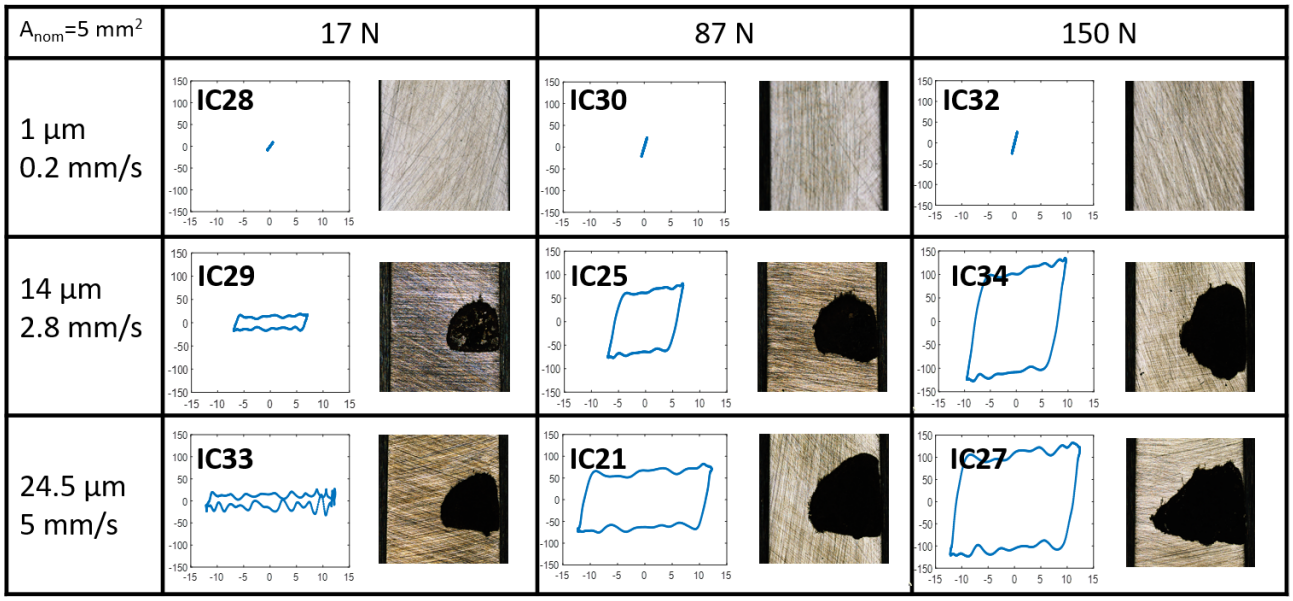


Figure 4.9: Overview of contact interfaces and hysteresis loops for tests conducted on specimens with a 5 mm^2 nominal area of contact at Imperial. Columns are normal loads and rows are displacement amplitudes.

stiffness (which is obtained from the gradient) is normal load dependent, as already known in the literature, see e.g. section 2.2.2. In addition, at the very low normal loads of 17 N, loops that are in gross slip, 14 μm and 24.5 μm, present a large number of oscillations and appear to be quite noisy. These oscillations are due to the chattering phenomenon, which occurs when the normal load is so low that specimens are more prone to lift-off. In fact, as the normal load increases, this effect disappears. More details on this phenomenon are given in section 4.2.2. Another feature present in most of the hysteresis loops is the increasing friction force observed during the gross slip stage, as opposed to the expected constant Amontons-Coulomb

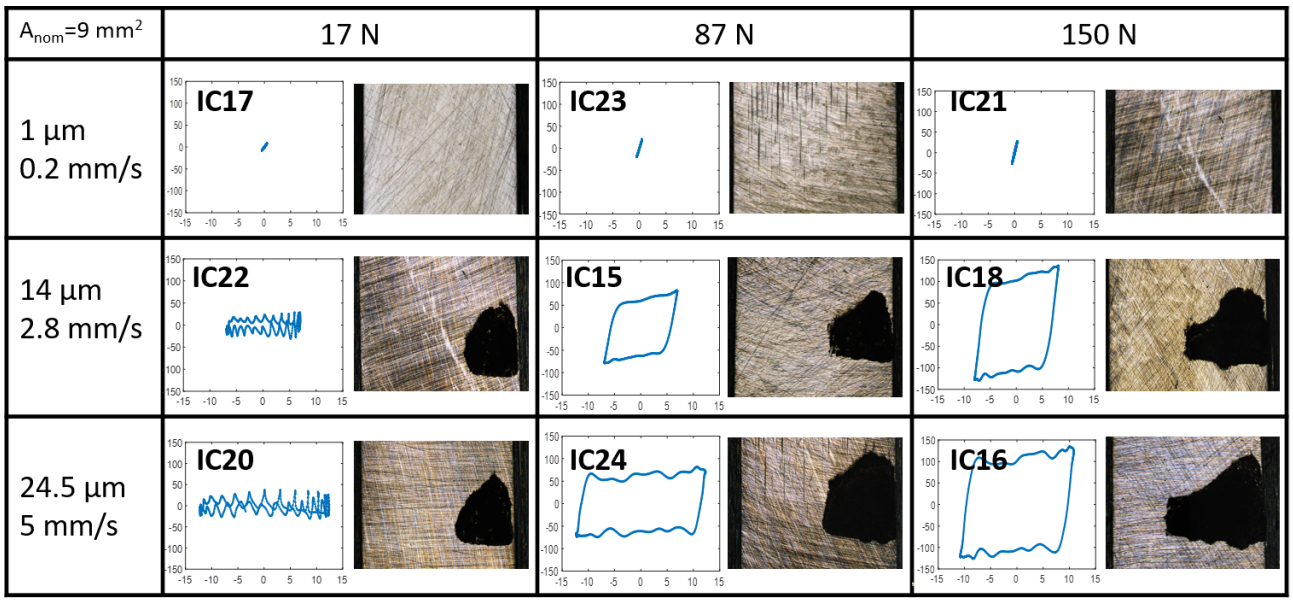


Figure 4.10: Overview of contact interfaces and hysteresis loops for tests conducted on specimens with a 9 mm^2 nominal area of contact at Imperial. Columns are normal loads and rows are displacement amplitudes.

friction force. In a previous study [229], this behaviour has been attributed to local wear scar interaction effects during the reciprocating sliding (e.g. interference of local interlocking peaks and troughs on the worn surfaces). Since this effect has already been studied in that previous study, it was decided to focus here on the understanding of the other physical aspects of the hysteresis loops.

The Figures also show the contact interfaces at the end of each test. In the stick tests, 1 μm, the interfaces do not present any visible wear mark, suggesting that a negligible amount of energy is dissipated during the full stick regime. At larger sliding distances, black spots appear indicating that worn areas have developed. These worn areas are larger when the normal load is larger since each loop dissipates more energy at larger normal loads (due to the larger area inside the loop). Note that a full worn area of contact is only reached in the specimens with the lowest 1 mm^2 nominal area of contact, while specimens with 5 and 9 mm^2 nominal areas never reached a full worn extension. Longer tests would have been required to dissipate more energy and thus wear out interface material to a larger extent. This, however, was not the main scope of the round robin test campaign. Finally, note that, especially in tests with 5 and 9 mm^2 nominal areas, the contact always occurred on the right side of the specimen interface. This slight misalignment is due to the non-ideal connection between the moving arm and the moving mass. However, this feature did not create major issues since it was very repeatable within the different assemblies and tested specimen pairs.

4.2.1 Evolution of the contact parameters with wear

The evolution of hysteresis loops over time for a typical test on the Imperial rig is shown in Fig. 4.11 (Test n. IC2: 87 N normal load, 24.5 μm displacement amplitude, 1 mm^2 nominal area of contact - the trend is similar for other tests with loops in gross slip). The Figure shows a significant increase of the sliding friction limit, μN, with hysteresis cycles. Since

the normal load, N, remained constant during the whole test, this implies that the friction coefficient, μ, has increased over time as the samples became worn. Fig. 4.12a-b shows the evolution of μ in time in linear and log scale. μ rapidly increased within the first thousands of hysteresis cycles from an initial value of 0.1 to a steady state value of 0.74 (see log scale plot). The energy dissipated to reach the steady state was approximately 84 J, obtained as the cumulative sum of the energy dissipated within each hysteresis loop[4]. It is important to know the cumulative energy dissipated since it makes it possible to compare results obtained in different test conditions (e.g. 1 hour of testing performed at 24.5 μm displacement amplitude would lead to more energy dissipated, and hence more wear, than a 1-hour test performed at 1 μm of displacement amplitude). The cumulative energy dissipated will be therefore used to compare measurements from the two friction rigs.

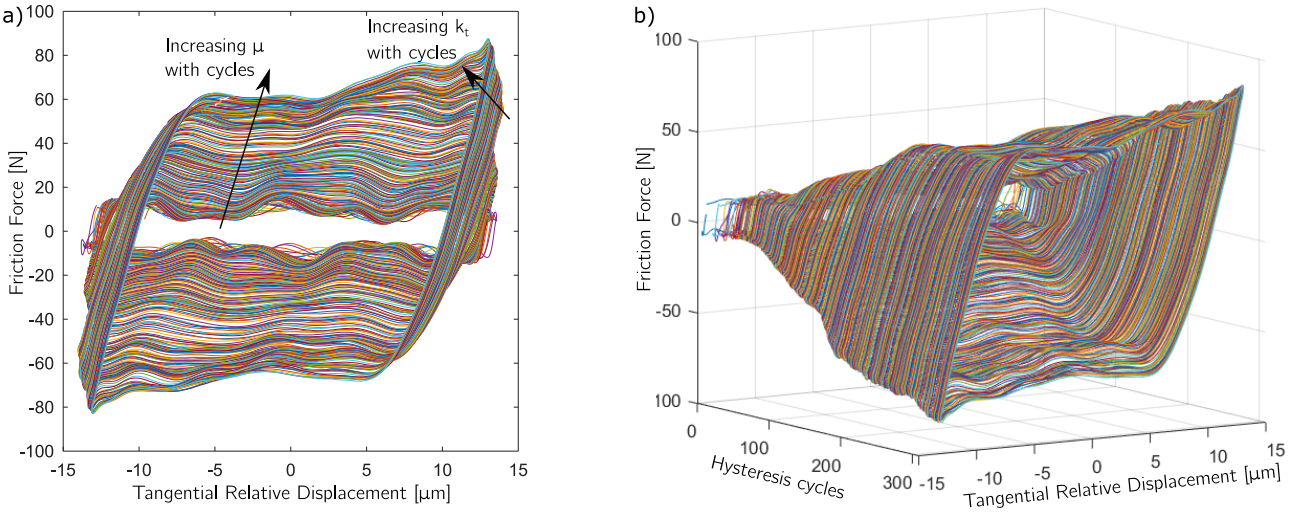


Figure 4.11: Typical evolution of hysteresis loops on tests performed on the Imperial rig: a) 2D plot; b) 3D plot. Values for the Test n. IC2: 87 N normal load, 24.5 μm displacement amplitude, 1 mm^2 nominal area of contact, 100 Hz excitation frequency and 2.5 hours of running, total hysteresis cycles=900000, material=stainless steel, temperature=25°C.

The rapid increase in μ at the start of the test and its convergence to a stable value agree with previously observed trends for fretting [87,174,175,230–246]. The physical reason for this rapid increase in μ has been attributed to the removal of initial oxide layers on the interfaces [244–249]. This removal results in a metal-to-metal contact and/or metal-to-wear particles contact that contribute to the increase in μ in terms of both adhesive and ploughing components, as defined in section 2.2.1. The steady state reached after the initial hysteresis cycles has been attributed to a balance between the generation and ejection of wear debris from the contact [248].

With regards to the tangential contact stiffness, k_t, fewer studies have investigated its evolution with wear [20,80,85–87,226], finding that the contact stiffness increases with hysteresis cycles until it reaches an asymptotic value. It is clear from Fig. 4.11a that k_t increases with the hysteresis cycles since the gradient of the stick portion of the loops increases. This increasing trend is better illustrated in Fig. 4.12c-d (with linear and log scales). k_t values show scatter at the beginning of the test and, only after a dozen of cycles, values converge to a low value of about 20 N/μm (see log scale plot). Then, k_t slowly increases until slowly approaching a

[4]Although not all the loops were measured due to storage limits, the total energy dissipated was computed assuming that the shape of the non-measured loops was the same as the last measured loop in each recording phase.

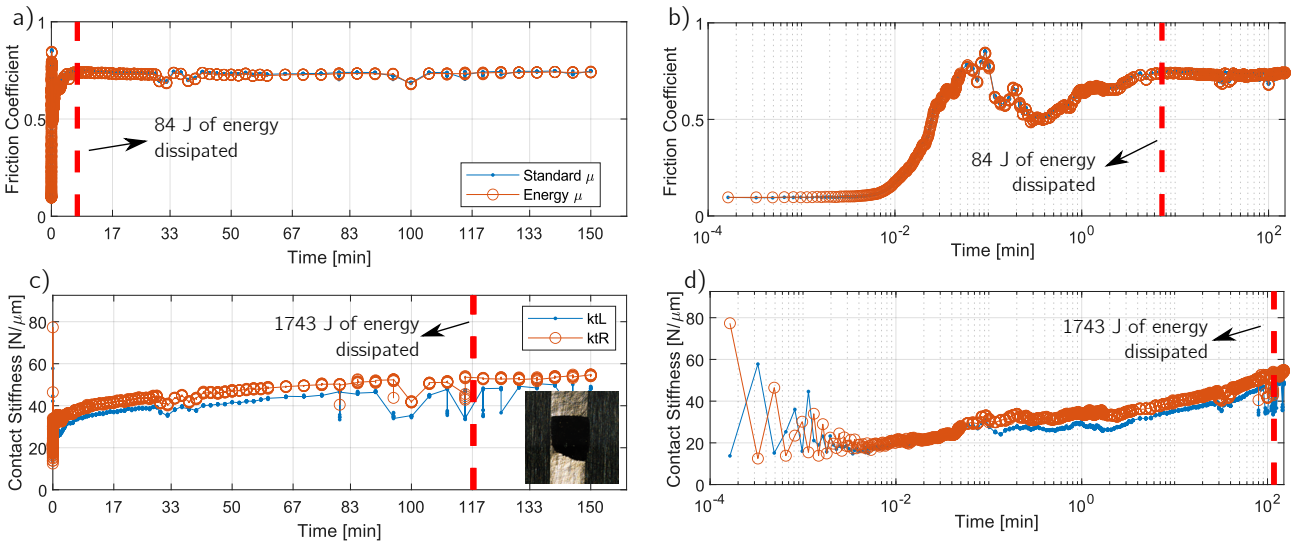


Figure 4.12: Typical evolution of contact parameters of Imperial specimens (beginning of the steady state highlighted with a vertical red dashed line - the interface photo shows the worn area of contact at the end of the test): a-b) Friction coefficient, μ, (linear and log scale); c-d) Tangential contact stiffness (linear and log scale - k_{tL} and k_{tR} are the contact stiffnesses of left and right stick portions of the hysteresis loops, as defined in section 3.2.1). Values for the Test n. IC2: 87 N normal load, 24.5 μm displacement amplitude, 1 mm^2 nominal area of contact, 100 Hz excitation frequency and 2.5 hours of running, total hysteresis cycles=900000, material=stainless steel, temperature=25°C.

steady state asymptote at roughly 53 N/μm (calculated as described in section 4.1), after 1743 J of cumulative energy dissipated at the contact (that is more than 20 times larger than the energy required to reach a steady μ).

The initial scatter probably occurs because, during the first dozen of cycles, new asperities get into contact for the first time leading to different elastic resistance to deformation (and hence different k_t values). Convergence to a low k_t value is reached around 10^{-2} minutes, corresponding to roughly 60 hysteresis cycles (see log scale plot). This convergence is reached at the same time when the friction coefficient starts to increase due to the removal of the initial oxide layers (see Fig. 4.12b). This suggests that oxide layers contribute to the observed scatter. Then, k_t slowly increases, until reaching a steady state. This slow increase is probably due to the increase in the worn area of contact, which evolves from the initial point contact, due to the curved shape of a 2 μm bump, to a more distributed contact at the end of the test. The initial curved contact was already shown in Fig. 4.5 and is now recalled with the simplified representation in Fig. 4.13a, which shows how the measured k_t is defined as the combination of three stiffnesses in series resulting from the bulk material around the interface, k_{bulk1} and k_{bulk2}, and the waviness of the contacting interfaces, $k_{topography}$, which are curved in this case. The bulk stiffness contributions become dominant as the laser measurement distance increases since, at larger measurement distances, the measured relative displacement is larger, thus resulting in a lower stiffness. Instead, the surface topography contribution stays the same regardless of the laser measurement distance. In this simplified representation, the curved part of the contact has a stiffness contribution $k_{topography1}$, and its removal with wear leads to a more conformal and less compliant contact with a higher final stiffness value, $k_{topography2}$, as shown in Fig. 4.13b. Note that roughness also plays a role in the k_t definition, but it is not represented in this simplified model. The relative importance of waviness and roughness contributions has been

quantified with the quasi-static contact simulations shown in chapter 7. Those simulations also demonstrated and confirmed the experimental hypothesis that the observed increase in k_t with wear is due to a change from the initially curved contact to the more distributed worn contact.

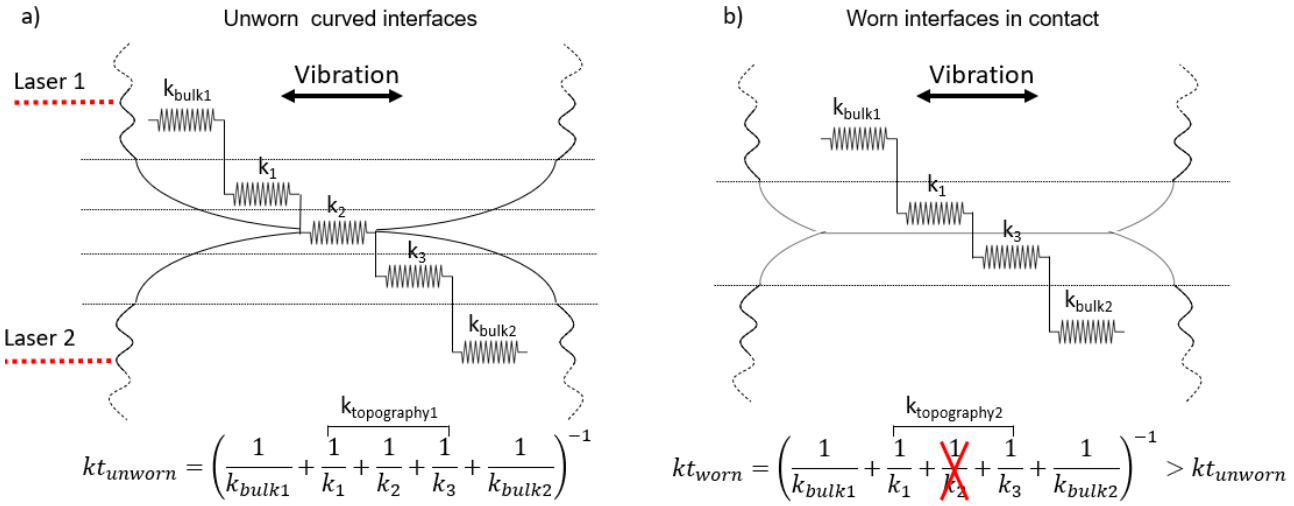


Figure 4.13: Typical evolution of the contact interface of Imperial specimens with wear: a) unworn contact and stiffness contributions; b) stiffness contributions in the worn contact. $k_{topography}$ is the stiffness due to asperities and waviness; k_{bulk} is the stiffness due to the deformation of the bulk around the interface. k_2 disappears due to the material removal with wear. Note that this is only a simplified and qualitative representation.

The hypothesis described above suggests that the steady state in the k_t should be reached when the area of contact reaches the maximum extension. For this reason, the k_t increase is slower than that of μ, because the worn area requires more energy to evolve as compared to the lower energy required for the removal of the contaminated layer that leads to the μ increase. To confirm this hypothesis, Fig. 4.14 shows two tests performed at different displacement amplitudes, 1 μm and 24.5 μm respectively, and their corresponding end-of-test contact interfaces. The test performed at 1 μm displacement amplitude does not show any sign of wear, due to the null amount of energy dissipation within the stuck loops, and indeed its k_t is constant during the whole test. Instead, the test performed at 24.5 μm displacement amplitude shows a clear increase in the k_t value associated with the increase in the worn area of contact due to the energy dissipated within the gross slip hysteresis loops. The k_t value approaches an asymptote since the worn area of contact is almost fully extended (the drop observed at 98 minutes could be due to a temporary loss of the laser focus or to some temporary unbalance in the wear debris formation/ejection). To quantify the relationship between k_t and worn area, the round robin test plan was updated to include a new set of measurements, which are described in the following section.

Worn area of contact test

The new set of measurements consisted of running 8 different specimen pairs under the same loading conditions, but over different periods (respectively 1 sec, 2 sec, 1 min, 5 min, 8 min, 30 min, 1 hr and 2.5 hrs). After each test, interfaces were scanned to monitor the evolution of the worn area of contact and link it to the contact parameters. Specimens had a 1 mm^2 nominal area of contact and the normal load was maintained constant at 60 N for all tests,

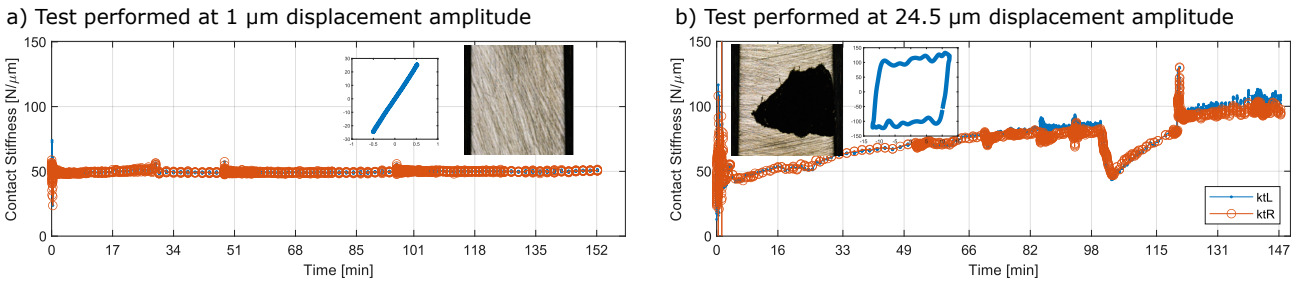


Figure 4.14: Evolution of tangential contact stiffness (k_{tL} and k_{tR} are the contact stiffnesses of left and right stick portions of the hysteresis loops, as defined in section 3.2.1 - the interface photos show the worn areas of contact at the end of the test - the hysteresis loops are the loops at the end of the tests): a) Tests performed at 1 μm displacement amplitude; b) Tests performed at 24.5 μm displacement amplitude. Values for the Tests n. IC32-27: 150 N normal load, 1 μm and 24.5 μm displacement amplitude respectively, 5 mm^2 nominal area of contact, 100 Hz excitation frequency and 2.5 hours of running, total hysteresis cycles=900000, material=stainless steel, temperature=25°C.

which resulted in a nominal pressure of 60 MPa. The excitation frequency was 100 Hz and the displacement amplitude was set to 20 μm, which ensured hysteresis loops in a gross slip regime.

Values of μ and k_t were extracted from the measured hysteresis loops. Figure 4.15 shows the evolution of the friction coefficient with wear for such tests. Results are plotted versus the cumulative energy dissipated, which has been obtained by summing the area inside each recorded hysteresis loop (since loops could not all be recorded due to storage issues, the total energy dissipated was computed assuming that the shape of the non-measured loops was the same of the last measured loop in each recording phase). As already observed in previous tests, μ rapidly increases within the first seconds. It starts from an initial average value of 0.15 (relative standard deviation of 30%) to a rather repeatable maximum peak value of 1.1. This peak has been associated with mutual polishing of the mating surfaces, which attain a mirror finish [59]. As a result of the mirror finish, the friction coefficient decreases owing to the decrease in ploughing because wear particles cannot anchor on a polished surface. The steady state is reached at 0.93 (relative standard deviation of 0.5%) after tens of thousands of cycles. The same trend has already been observed and described with Fig. 4.12. Not only steady state values are repeatable, but also the rapid increase during the transient is repeatable.

The evolution of k_t with wear is shown in Fig. 4.16a-b in log and linear scale respectively with respect to the energy dissipated. As already shown with Fig. 4.12, a great amount of scatter characterizes the measurements at the beginning of the tests (see Fig. 4.16a). This is probably attributable to the large variability of the contact that initially establishes only between a few random points. Even small motions would therefore largely affect the contact condition. After hundreds of cycles (i.e. in less than 5 seconds) the scatter disappears, and a clearer trend is observed for every test, probably due to the increased conformity. k_t reaches a local maximum, then it decreases and finally it starts again to increase, eventually tending to an asymptotic value for cumulative energy larger than 1000 J (i.e. after 1.5 hrs in Fig. 4.16b). k_t more than doubles from the average minimum value of 24 N/μm to the asymptotic steady state of about 48 N/μm.

With regards to the energy dissipated, also in these tests, μ reaches the steady state by dissipating low amounts of energy, 50 J, which is at least 20 times less compared to the k_t steady

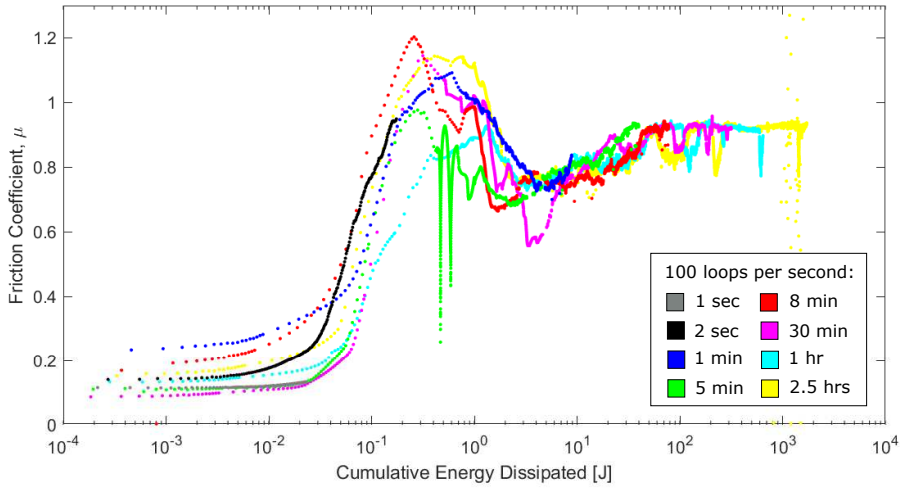


Figure 4.15: Evolution of the friction coefficient with wear for tests performed over different running times at 60 N normal load, 20 μm displacement amplitude, 100 Hz excitation frequency and 1 mm^2 nominal area of contact stainless steel specimens at room temperature.

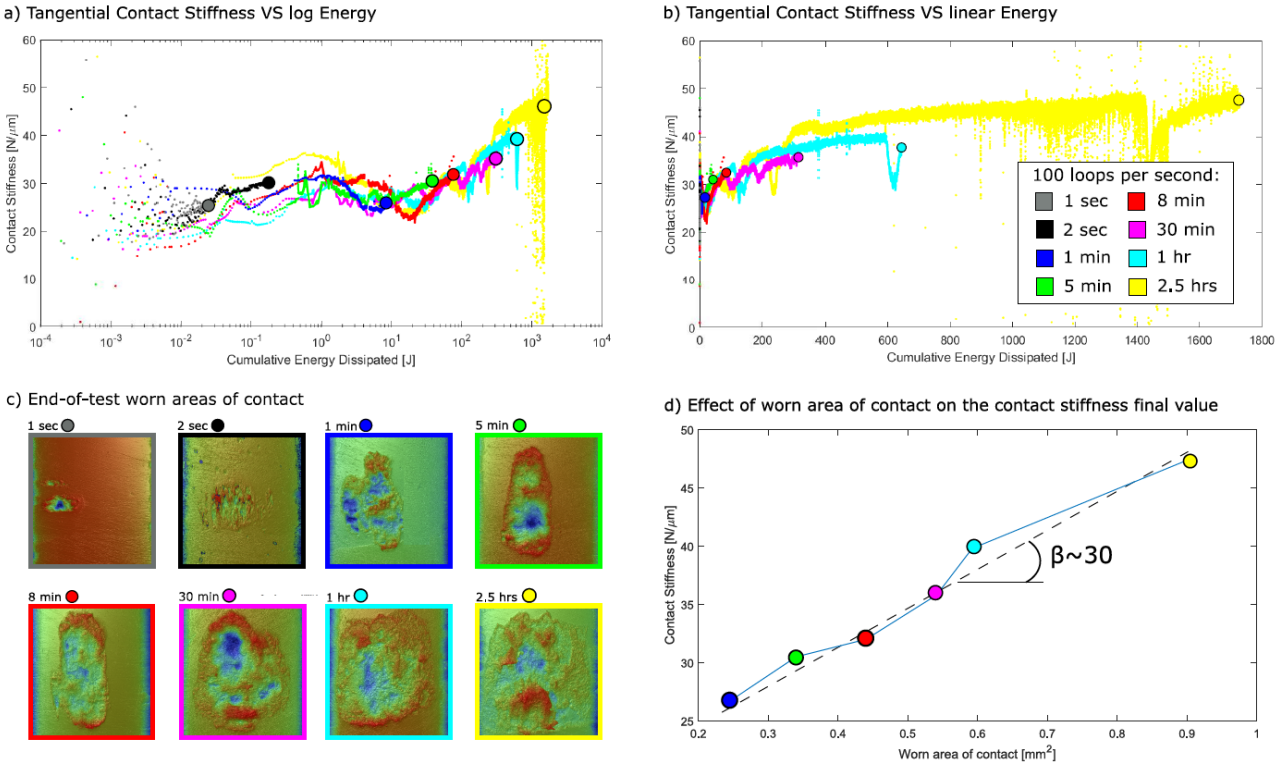


Figure 4.16: 8 different tests: a-b) Evolution of tangential contact stiffness with wear in log and linear scale respectively; c) End-of-test worn areas of contact – all specimens had a nominal area of contact of 1 mm^2; d) Tangential contact stiffness values at the end of tests versus the worn area of contact at the end of tests. Tests performed over different running times at 60 N normal load, 20 μm displacement amplitude, 100 Hz excitation frequency.

state energy. This confirms again that, in the case of μ, the running-in may be driven by the rapid removal of initial surface layers of the material, while, in the case of k_t, the steady state is probably attained when conformity due to wear is reached over the whole nominal area of contact. This hypothesis is supported by the evolution of the worn areas of contact shown in

Fig. 4.16c for the different specimen pairs. For the longer runs, the worn area of contact is larger, leading in fact to larger values of k_t. Fig. 4.16d plots the k_t values at the end of the tests versus the respective end-of-test worn areas of contact. As a reminder, the worn area of contact was estimated from the optical scans of the contact interfaces by selecting the extension of the worn spots and evaluating their area. Figure 4.16d shows that a linear relationship exists between k_t and worn area, with the slope "β" equal to 30 N/μm/mm^2. This is a novel finding, not reported in previous studies. It is in fact common practice in nonlinear dynamic analysis to normalise the k_t by the nominal area of contact (which is the same in the case of the tests here presented). Fig. 4.16d instead suggests that, contrary to what is commonly done, k_t should be normalized by the "worn" area of contact rather than by the nominal one. This behaviour can be explained by the increased interaction of the wear scars, which add elastic resistance to the tangential relative motion, thus increasing k_t. In addition, the worn area of contact leads to larger stiffnesses since the initial curved (more compliant) material is removed, as explained previously with Fig. 4.13. When the "worn" area of contact approaches the nominal area of contact, a steady state in k_t is reached. Only in cases of fully distributed wear, the normalization by the nominal area of contact would be correct. For the 2.5 hours test of Fig. 4.16b-c, the worn area of contact covers almost completely the nominal area of contact of 1 mm^2, thus leading to a k_t quite close to the asymptotic value. The effects of wear on the evolution of the contact interfaces are further explored in the following section.

Evolution of contact interfaces with wear

The results presented in this section were obtained during a group project within the 2018 Nonlinear Dynamics of Coupled Structures and Interfaces (ND-CSI) Summer School organised at Imperial College [250] as part of the EXPERTISE programme, which funded this PhD project. The group was made up of five PhD students and everyone contributed equally to the work, including the author. Results of that project were published in [20] and are reported here in a brief summary. During the group project, a series of wear tests was performed on the Imperial friction rig by using different specimen pairs at room temperature (loading conditions: 60 N normal load, 100 Hz excitation frequency, 14 and 22 μm, displacement amplitude, 1 mm^2 nominal area of contact, running times longer than 5 hours). After each fretting test, the contact interfaces were surrounded by red debris resulting from the oxidation of the fretted metal. This debris was removed by cleaning the specimens in an ultrasonic bath. The clean interfaces were then scanned with the optical interferometer. A summary of the worn interfaces from all wear tests is provided in Fig. 4.17, where material transfer spots between coupled specimens are highlighted (for more details on the tests, the reader is referred to [20]). The highlighted areas provide a clear indication of material transfer between top and bottom specimens, suggesting that the dominant wear mechanism is adhesive. The material transfer took place at both smaller and larger displacement amplitudes and also over short and long duration wear tests. The location and number of transfer areas appear random at a first glance and do not show a clear pattern. However, tests 1 and 2 (shorter displacement amplitude) present smaller and distributed transfer areas, while tests 3, 4 and 5 (larger displacement amplitude) present larger transfer areas. This is probably attributable to the fact that for a larger displacement amplitude the small wear scars merge into larger ones, since the transferred material can be pushed further.

In addition to that, some of the worn profiles show the typical "W-shaped" wear scar (see e.g. wear tests 3 and 5 in Fig. 4.17), which has been observed in many other studies [80, 231, 237, 242, 251–255], although only one of them involved a flat-on-flat contact arrangement [80].

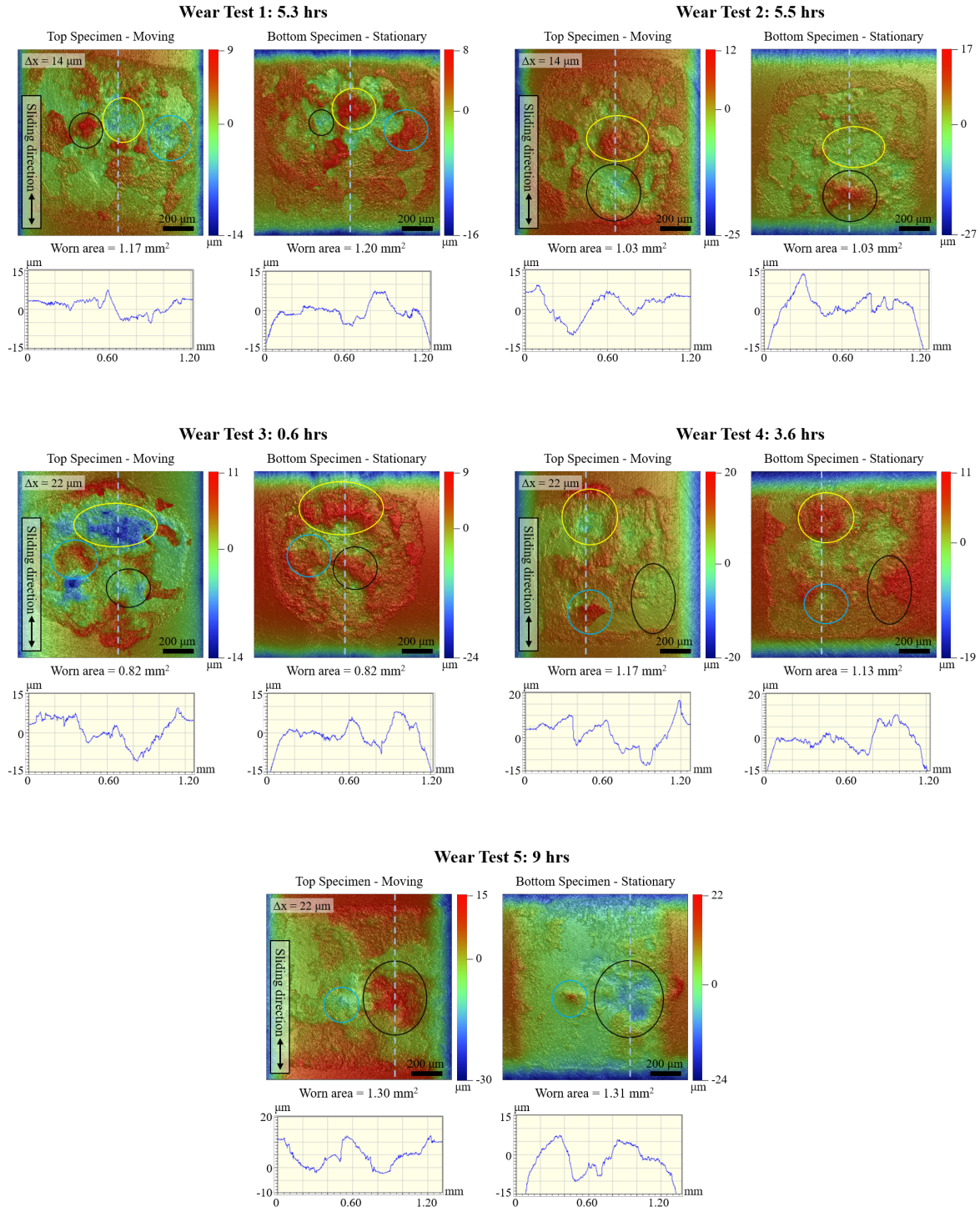


Figure 4.17: Worn surface images highlighting the material transfer between the top and bottom specimens for different test couples. The contact interfaces of the bottom specimens were opened and flipped to help the overlap comparison [20].

This W-shape is a typical wear pattern consisting of a stick region, inside the fretted interface, surrounded by slip regions on both sides [255]. Fouvry et. al [254] investigated in detail the physics of the W-shape wear scars as opposed to the U-shape scars. They found that at lower contact pressures, a homogenized U-shaped wear scar generates as a result of abrasive wear in combination with high contact oxygenation. This oxygenation produces a thin oxide debris

layer, which induces high energy wear rates and wear volumes. Instead, at higher contact pressures, W-shaped wear scars occur. The W-shaped scars are the result of (i) adhesive wear in the center of the scar, where the contact is stuck due to the higher pressure, and (ii) abrasive wear at the edges, where the pressure is lower and debris is generated due to the more severe wear induced by the increased slipping. This kind of W-shaped wear scar is more evident in the second set of tests (3, 4 and 5) conducted for a larger displacement amplitude. This suggests that for larger displacement amplitudes the adhesive wear in the central region may be activated, while at the edges of the contact abrasive wear is dominant. The same conclusions apply to the experiments performed during the round robin test, which were conducted under the same ranges of loading conditions. A side analysis on the wear rate is also shown in the Appendix C, where the wear coefficient value is extracted and compared to reported values from the literature.

4.2.2 Repeatability of the tests

The previous section has shown that both μ and k_t were reasonably repeatable in different tests, however, it did not provide extensive details on such repeatability. This section shows two repeatability studies performed to quantify respectively i) the uncertainty induced by the manufacturing of nominally identical specimens and ii) the uncertainty induced by the specimen mounting procedure during each test.

Uncertainty induced by the manufacturing of nominally identical specimens

Three nominally identical specimen pairs were manufactured to quantify the effect of manufacturing. To do so, the classic 2.5-hour tests were performed using the reference loading conditions of the round robin matrix (namely 87 N normal load, 14 μm displacement amplitude, 1 mm^2 nominal area of contact). Figure 4.18 shows the evolution of the contact parameters for the three different specimen pairs and also the scans of the contact interfaces at the end of each test. Trends are similar to those already described in the previous section.

An interesting feature from the plots in Fig. 4.18c is the large scatter occurring between 25 and 60 minutes for all tests (visible mainly for k_t). This scatter is due to the so-called chattering, which consists of a sudden and unexpected significant amount of vibration and noise coming from the contact. This vibration results in very noisy hysteresis loops as shown in Fig. 4.19. The physics of chattering has not been investigated in detail within this thesis project and more work will be performed in future to understand how this phenomenon is triggered (and how it terminates). It could be linked to the friction-induced vibration [256, 257], which is often studied in pin-on-disk friction rigs [258] and might also occur in the here investigated friction rig. It was noted that chattering occurred only during tests with a low/medium normal load and after a certain amount of accumulated wear (loops in gross slip regime were necessary for chattering to appear). If the rig components were manually slightly impacted during the chattering vibration, the large amount of vibration eventually stopped but, after a few cycles, it started again. Occasionally, chattering stopped alone, as in the case of tests of Fig. 4.18, where loops fully stabilised after 60 minutes. Interestingly, in the case of tests of Fig. 4.18, chattering always started at about the same time after 20 minutes from the beginning of the tests. Chattering was instead never observed during tests at large normal loads (i.e. 150 N),

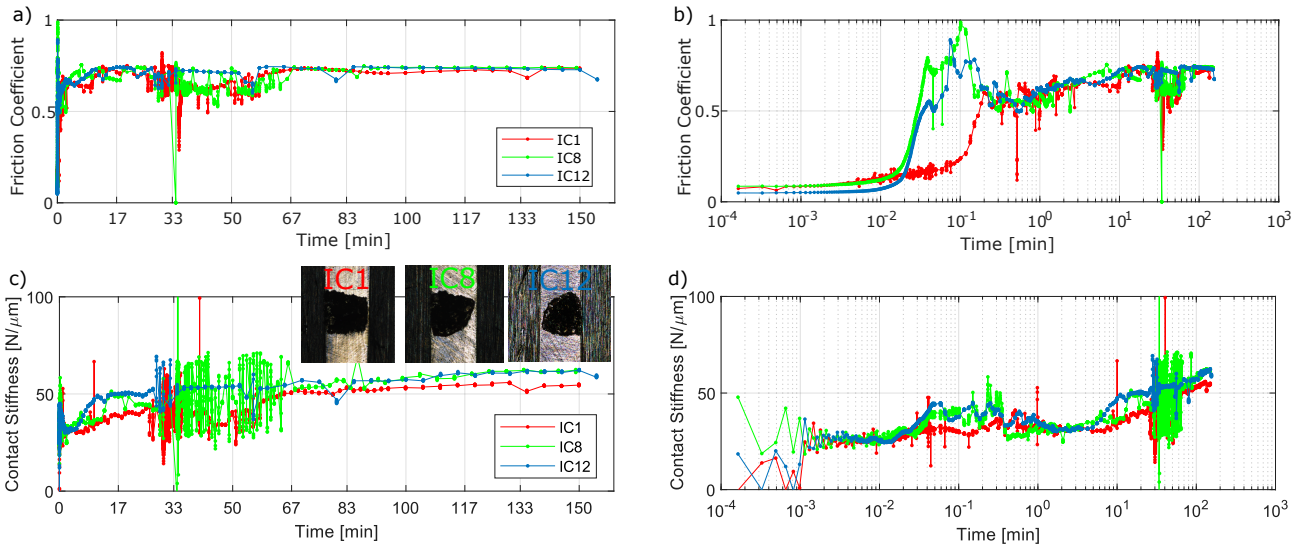


Figure 4.18: Repeatability study. Three tests performed with the same loading conditions but different specimen pairs: a-b) Energy friction coefficient, μ, (linear and log scale); c-d) Tangential contact stiffness, k_t, (linear and log scale). Values for the Tests n. IC1-8-12: 87 N normal load, 14 μm displacement amplitude, 1 mm^2 nominal area of contact, 100 Hz excitation frequency and 2.5 hours of running, total hysteresis cycles=900000, material=stainless steel, temperature=25°C.

probably because interfaces were much more compliant and less prone to vibration. Another interesting feature is that all loops in chattering presented the same frequency content at around 2600 Hz, which corresponds to the resonance of one of the vibration modes of the static arm. This strongly suggests that the origins of this phenomenon might lie in some relationships between contact properties and resonance frequencies of the system. In fact, the contact dynamics is affected by the evolving worn surface and the patterns forming on the surface. More information on the dynamics effect and the effect of resonance vibrations on the hysteresis loops are provided in chapter 6.

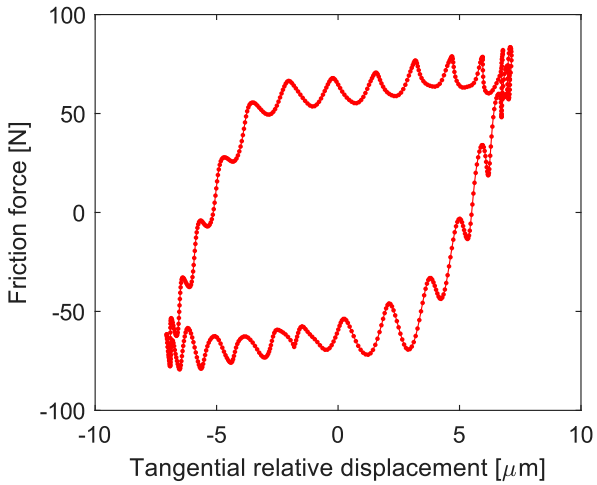


Figure 4.19: Hysteresis loop during chattering. Taken from the Test n. IC1 at the 30^{th} minute (see Fig. 4.18 for the time evolution).

Figure 4.20 shows violin plots of the steady state values of μ (values after 17 minutes) and k_t

(values after 120 minutes). Mean μ values are within 0.72-0.74, which is a relative variation below the 3%. Note that the final values of the Test n. IC1 are also around 0.73, although the mean after 17 minutes is lower due to the noisy data affected by the chattering phenomenon during the 20-60 minute range. With regards to k_t, mean values of Tests n. IC8 and IC12 are very similar (65 and 64 $N/\mu m$ respectively), while Test IC1 has a much lower mean value of 50 $N/\mu m$, which has a relative difference of 25% with the other two. This difference is much larger than that observed for μ and indicates that k_t measurements are probably more sensitive to specimen mounting and interface uncertainty, while μ is more stable.

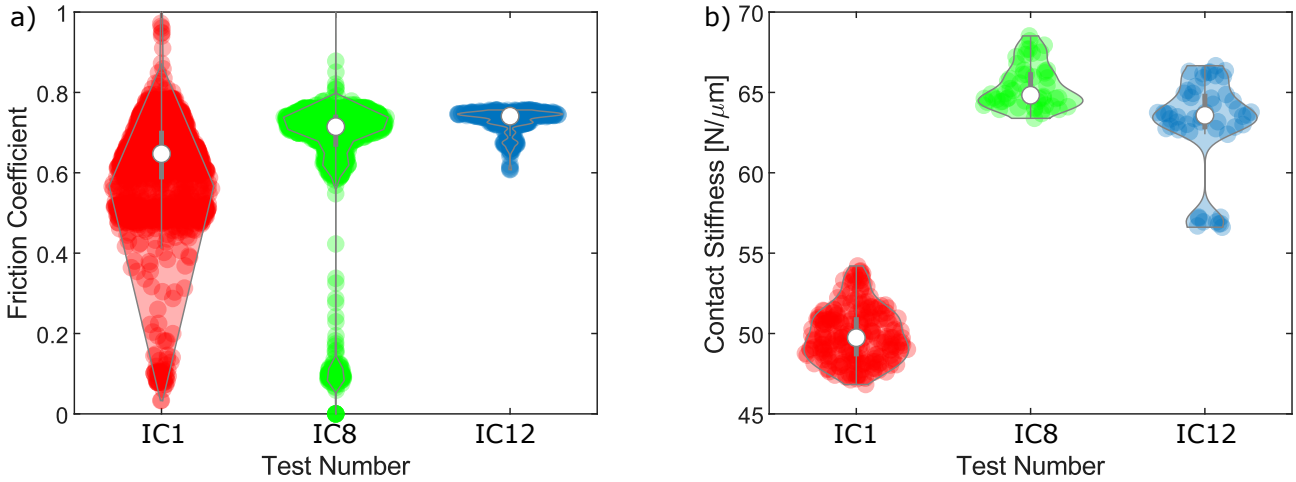


Figure 4.20: Violin plots of the steady state values for the Tests n. IC1-IC8-IC12: 87 N normal load, 14 μm displacement amplitude, 1 mm^2 nominal area of contact, 100 Hz excitation frequency and 2.5 hours of running, total hysteresis cycles=900000, material=stainless steel, temperature=25°C.

Uncertainty induced by the specimen mounting procedure

The repeatability test just shown included the effects of both using different specimen pairs and having slightly different mountings due to the non-ideal assembly process. To differentiate those two effects, a further test was performed by using only one specimen pair to quantify the effect due to the only specimen mounting. This test consisted of 9 different operations. The first operation regarded the typical 2.5 hours run at 87 N normal load and 14 μm displacement amplitude. A steady state was reached in both μ, at 0.76, and k_t, at 68 N/μm (not shown in Figures). Note that both μ and k_t values are respectively within the 3% and 25% of previously measured values. After reaching the steady state, the following eight different operations were performed to assess the repeatability of the measurements due to assembly and testing operations:

Operations 2 and 3: stop and start. The test was stopped by turning off the shaker and by maintaining the normal load at 87 N. After 1 minute, the test was restarted (same procedure performed for operations 2 and 3). Hysteresis loops were measured for 15 minutes, showing values in the range of 68.4-67.9 N/μm in k_t and 0.77 in μ (see Fig. 4.21a-c). Thus, the steady state values measured during the initial 2.5 hours test were maintained. This showed that stopping and restarting the test, without changing the normal load, does not lead to changes in the measurements.

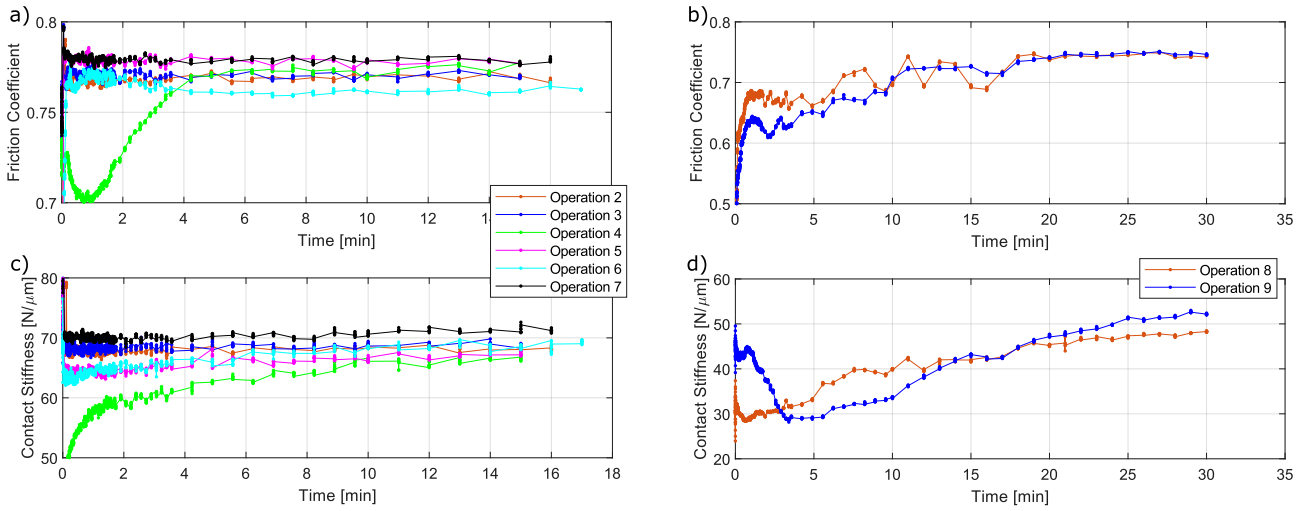


Figure 4.21: Assembly test: a) Friction coefficient during operations 2-3-4-5-6-7 (see the text for detailed info on each operation); b) Friction coefficient during operations 8-9; c) Tangential contact stiffness during operations 2-3-4-5-6-7 (see the text for detailed info on each operation); d) Tangential contact stiffness during operations 8-9. Test conditions: 87 N normal load, 14 μm displacement amplitude, 1 mm^2 nominal area of contact, 100 Hz excitation frequency and 2.5 hours of running, total hysteresis cycles=900000, material=stainless steel, temperature=25°C.

Operations 4 and 5: stop, lift-off and start. After operation 3, the test was stopped but the normal load was now removed and the moving arm was lifted off, thus opening the contact. Oxide debris was visible outside the contact but it was not removed. The contact was then closed and the normal load was applied again. The test was then restarted and loops recorded for 15 minutes. A transient appeared at the beginning in both μ and k_t (green lines in Fig. 4.21a-c) and then a steady state soon appeared in μ, but not in k_t. The end test values were similar to the previously measured values, 0.78 for μ and 66.5 N/μm for k_t. This operation showed that even if the contact is opened, similar values are measured when the contact is closed again, although a short transient is present. The same operation was repeated (operation 5). A steady state was soon reached in this case. The values at the end of the test were 0.78 for μ and 66.7 N/μm for k_t. From operations 4 and 5, it is therefore concluded that a contact opening does not lead to significant changes in the measured values. Measured values remain similar probably because the contact is not re-setted when lifting off the arm, which always goes back to the previous position since it is hinged to the knife-edge.

Operations 6 and 7: stop, lift-off, clean and start. The next operation was similar to operations 4 and 5, but this time, when the contact was opened, wear debris was fully removed by cleaning the contact with pressured air. Once cleaned, the contact was closed, the normal load applied and hysteresis loops recorded again for 15 minutes. The trends in μ and k_t are shown in cyan color in Fig. 4.21a-c. Steady states are soon reached in both cases, but values are slightly lower compared to previous operations, with μ equal to 0.76 and k_t equal to 67.7 N/μm. Operation 7 was the same as operation 6. This time, a steady state soon appeared at the beginning of the test with larger values in both μ, at 0.78, and k_t, at 70.8 N/μm. It seems that, in this case, the removal of wear debris led to an increase in the measured values compared to the previous test. Still, values are within the 3% for μ and within the 7% for k_t.

Operations 8 and 9: stop, disassembly and start. Finally, a last set of operations was performed to quantify the effect of the mounting procedure of the specimens, by stopping the test and then disassembling and reassembling the specimens in the clamping. Then, the normal load was applied and hysteresis loops were measured for 30 consecutive minutes. It was decided to run them for a longer time since changes were observed within the first 15 minutes and a more steady condition had to be reached. Results are shown in Fig. 4.21b-d for both operations 8 and 9. μ and k_t values started in both operations with a transient behaviour probably because the contact was not aligned as in the previous experiments. It is not practical to align the interfaces at the same micrometre level they were before the disassembly and even slight misalignments in the order of micrometres would lead to new contact conditions. However, μ reached a steady state at a value of 0.75 for both operations, which is in the same range of values of the previous experiments. Instead, k_t did not reach a steady state within the 30 min tests, and its end values were 48.1 N/μ and 52.8 N/μm for the two operations respectively. These values are much lower than those of previous operations, probably because a steady state was not reached yet.

In summary, this section has quantified the uncertainty introduced by different manufactured specimens and by the specimen assembly procedure. It was found that tests are reasonably repeatable when completely different specimen pairs are used. The friction coefficient shows high repeatability with a scatter in the steady state values below the 4%. The tangential contact stiffness shows instead a larger scatter, below 25%. This aspect must be considered when comparing tests performed at different loading conditions, since every test during the round robin was only performed once (except tests presented in this paragraph). The effect of different operations, such as stopping and restarting the test, was also quantified to be relatively negligible (changes below the 3% for the friction coefficient and below the 7% for the tangential contact stiffness). However, the disassembly/assembly procedures led every time to a different configuration even though the same specimens were used. Still, the total differences were below the 4% for the friction coefficient and below the 25% for the tangential contact stiffness. Note that this scatter is much higher than the scatter due to the automatised procedure developed to extract the contact parameters, which was described in chapter 3 (section 3.2). That chapter showed that the variability due to the post-processing is below 1% for both μ and k_t and, thus, it is concluded that the developed extraction method is reliable and robust as compared to the experimentally observed variability.

With this repeatability study and the wear study shown in the previous section, the reader has now a clearer understanding of the evolution of the contact parameters within individual tests. This understanding is needed to interpret the following two sections, which show detailed results of tangential contact stiffness and friction coefficient respectively, for all the loading combinations of the round robin test matrix.

4.2.3 Tangential contact stiffness

Figure 4.22a shows a qualitative summary of the steady state values of the tangential contact stiffness, k_t, for every loading combination tested during the round robin at Imperial (if a steady state was not reached, the end-of-test values were chosen instead). Details on the exact values and standard deviations are shown through violin plots in Fig. 4.23. Many trends are evident from the figures and the following sections describe them in detail.

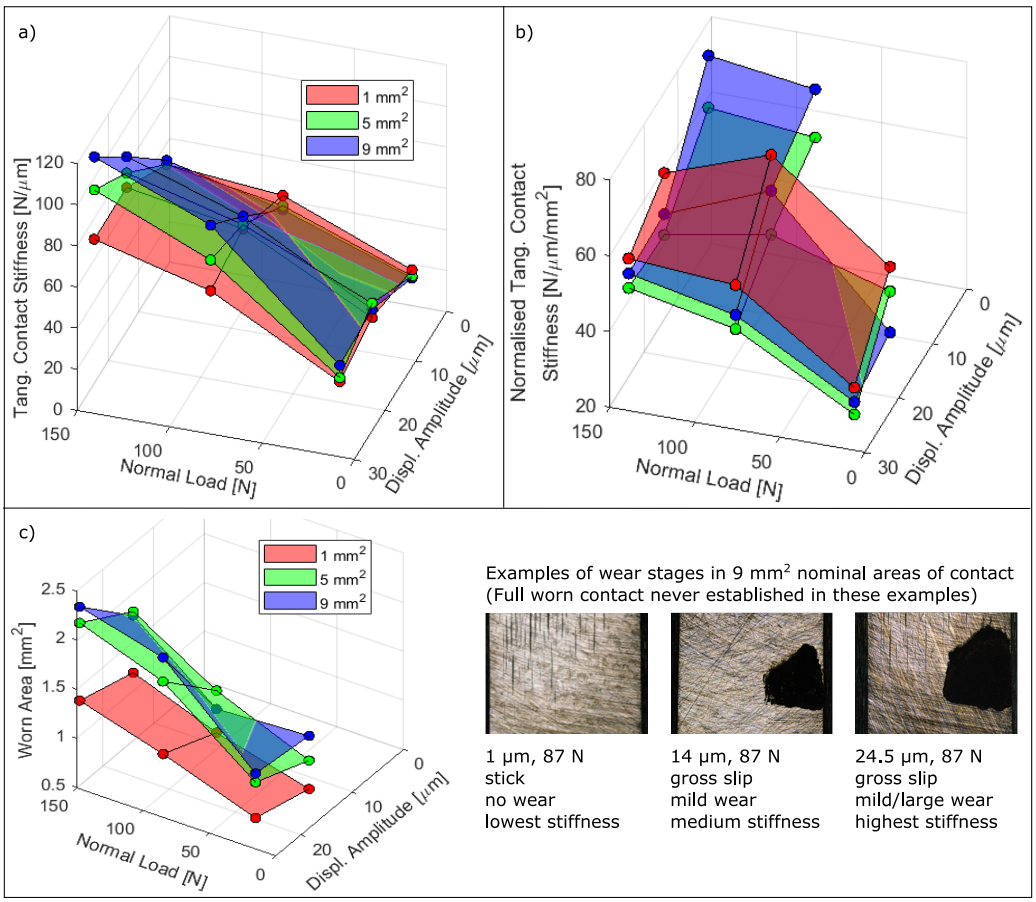


Figure 4.22: Qualitative summary trends: a) Tangential contact stiffness steady state values, k_t, of the round robin test on the Imperial friction rig; b) Worn area normalised tangential contact stiffness steady state values, K_T; c) Worn areas of contact at the end of each test, plus example photos of worn areas at the end of tests for the 9 mm^2 nominal area of contact case (for which a fully worn area could not establish at the end of the test).

Effect of normal load and worn area of contact

Firstly, it is clear that k_t strongly increases (almost fourfold) with the normal load with values rising from about 25 N/μm to 90 N/μm when the normal load increases from 17 N to 150 N, regardless of the nominal area. This trend is well known and has already been observed in a large variety of experiments [65–83]. This increase is linked to the increase in the number and size of the individual contact spots at larger normal loads, resulting in a larger real area of contact and more interactions of asperities at the interface [65, 132]. In general, the relative standard deviation of the steady state values within the individual tests is below 10%, except for the test performed at 17 N that showed the chattering phenomenon, as shown in Fig. 4.23 (Tests n. 5-29-22-6-33-20).

Note that tests performed at larger displacement amplitudes led to more energy dissipated and hence larger worn areas of contact, as confirmed with the photos of worn areas at different displacement amplitudes in Fig. 4.22c. The worn area of contact leads to larger stiffnesses as already mentioned in section 4.2.1 with Fig. 4.13 and confirmed with Figs. 4.14 and 4.16d, which clearly showed that k_t linearly increases with larger worn areas. Because of this worn

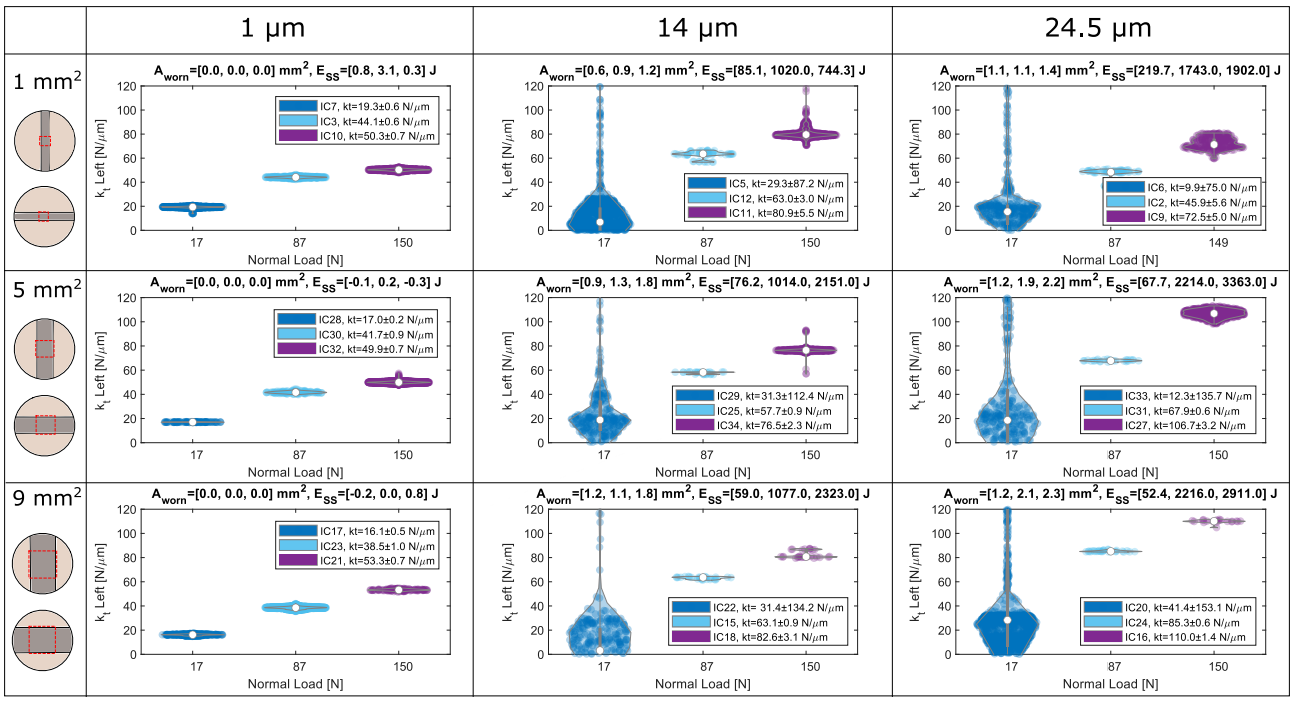


Figure 4.23: Violin plots of the steady state values of the tangential contact stiffness, k_t, of every round robin test on the Imperial friction rig. Each violin corresponds to a different test for one normal load, displacement amplitude and nominal area of contact. The legends indicate the mean and standard deviation of the steady state values of each test. The figure titles indicate the worn areas of the three tests and the energy dissipated when the steady state was reached (note that in most of the tests the steady state was not reached, and the energy represents the energy towards the end of the test). Chattering is often observed during tests at 17 N normal load and that is why the standard deviation is quite large in those tests.

area dependency, k_t was normalised by the worn area thus obtaining a normalised K_T expressed in N/μm/mm^2 (different from the small letters k_t expressed in N/μm). Note that the normalisation is done against the worn area of contact, and not the nominal area as common practice in the literature. As a reminder, the worn area of contact was estimated from the optical scans of the contact interfaces by selecting the extension of the worn spots and evaluating their area. Fig. 4.22b plots the worn area normalised K_T, while the values of worn areas of contact are shown in Fig. 4.22c. Note that the 1 μm tests did not show any wear because only a negligible amount of energy was dissipated in stuck loops. Therefore, to get the normalised K_T for those cases, the following procedure was performed: at the end of each test with a 24.5 μm displacement amplitude, the hysteresis loop was brought down to a 1 μm displacement amplitude and the k_t was extracted. In this fully-worn case, it was possible to measure k_t at 1 μm displacement amplitude but on specimens with developed full worn areas of contact. The normalised K_T in Fig. 4.22b at 1 μm was obtained in this way. Note that, even though the worn area of contact was apparently zero at the end of the fully stuck tests, a contact stiffness could still be measured since k_t ultimately depends on extension and distribution of the real area of contact. In fact, the worn area of contact is only an indicator of the region where the real area of contact is distributed. The experimental evidence presented here suggests that this indicator is adequate to approximate the distribution of the real area of contact and, hence, can be used to normalise the measured k_t.

Figure 4.22b shows that the normal load dependency still holds, with a twofold increase in

the normalised K_T within the investigated normal load range. It would be more accurate to normalise also the normal load by the worn area of contact, thus comparing normalised stiffness with pressures. This is done in Fig. 4.24 for several combinations of loading conditions. The Figure shows a quite clear trend, which is well represented by a square fit of the K_T versus the worn-area-normalised normal load with the following empirical equation:

$$K_T = K_1 * p^{\frac{1}{2}} = 6.3 * p^{\frac{1}{2}} \tag{4.1}$$

where K_1 is a coefficient equal to 6.3 obtained by fitting the experimental data. This coefficient gives a stiffness in N/μm/mm^2 when multiplied by the square root of the normal load divided by the worn area, expressed in MPa. Note that, although many experiments were performed under the same normal loads, they show different pressures since normal loads are normalised by the worn areas of contact, which differ test by test. Larger worn areas of contact lead in fact to lower pressures and hence different normalised k_t values. This aspect is important and should be accounted for in nonlinear dynamic analyses, where instead k_t values are commonly normalised by the nominal area of contact. Although this approach is more correct, it is to be noted that worn areas of contact are quite challenging to measure and/or predict. All the normalised values are also shown in Fig. 4.25 through violin plots.

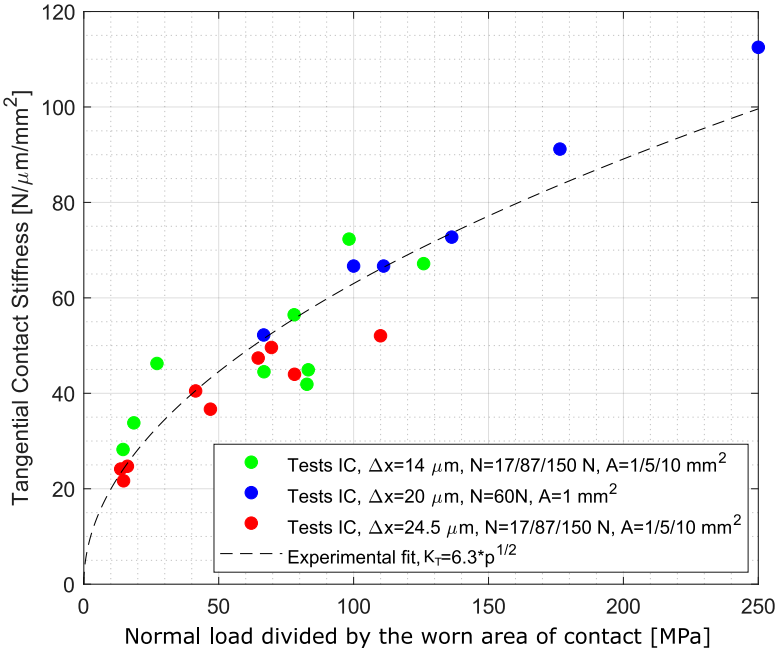


Figure 4.24: Worn area normalised K_T versus contact pressure obtained by dividing the normal load by the worn area. Each point in the Figure corresponds to a different test of the round robin matrix with a different worn area of contact (green and red tests are from the round robin test, while blue tests are those shown in section 4.2.1). Note that, although some tests were performed with the same normal load, they have different contact pressures due to their different worn areas. The experimental fit is also shown (Eq. 4.1).

Effect of the nominal area of contact

In addition to the normal load and worn area dependency, also the nominal contact area affects the results. Fig. 4.22a shows that experiments performed at the same displacement amplitude

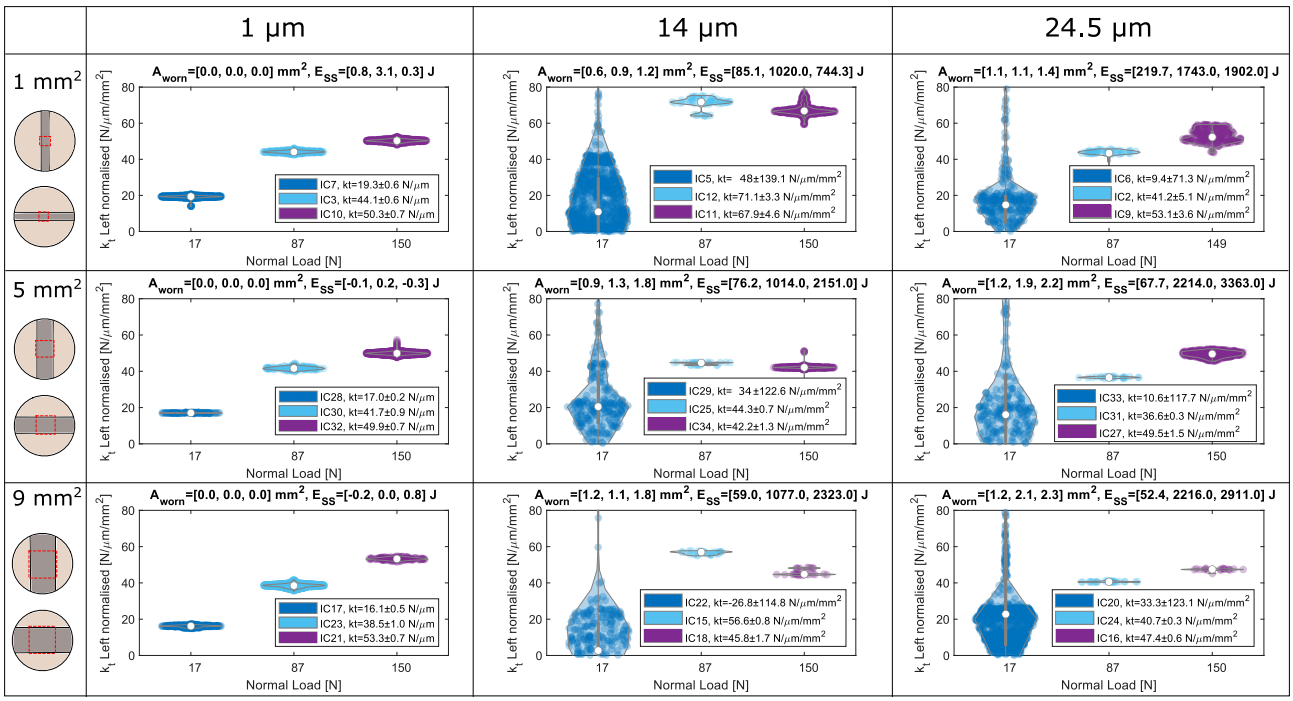


Figure 4.25: Violin plots of the steady state values of the worn area normalised tangential contact stiffness, K_T, of every round robin test on the Imperial friction rig. Each violin corresponds to a different test for one normal load, displacement amplitude and nominal area of contact. The legends indicate the mean and standard deviation of the steady state values of each test. The figure titles indicate the worn areas of the three tests and the energy dissipated when the steady state was reached (note that in most of the tests the steady state was not reached, and the energy represents the energy towards the end of the test). Chattering is often observed during tests at 17 N normal load and that is why the standard deviation is quite large in those tests. Note that tests performed at 1 mm^2 are not normalised by the worn area of contact, because no wear marks were present at the end of the tests.

and normal load, but different nominal areas of contact, lead to slightly different un-normalised k_t values. k_t values are in general larger when larger nominal areas of contact are used, with scatter up to 40%. Part of this difference is due to the larger worn areas of contact observed in the tests at larger nominal areas. However, also the normalised K_T values of Fig. 4.22b show some scatter, below 25%, at same loading conditions but different nominal areas. In contrast to what was expected, values do not match perfectly probably because:

i) Also the normal load (x-axis) should be normalised by the worn area of contact, as it was done in Fig. 4.24. In fact, the same normal load would result in a different average pressure if distributed over a different worn area of contact;

ii) Even though the normal load is normalised, surface topographies are slightly different for different nominal areas of contact. The curvature at the specimen interfaces, previously described in section 4.1, slightly changes with different nominal areas. As a result, also the contact stiffness is expected to change. This effect of the interface curvature and surface topography is investigated in detail with the numerical simulations of chapter 7, which simulate k_t values for different input surface data.

Still, the 25% scatter of the normalised K_T is lower than the 40% scatter observed in the un-

normalised k_t values (see e.g. the loading case 150 N, 24.5 μm, with un-normalised k_t values ranging from 75 N/μm to 120 N/μm, but the normalised values ranging within a narrower range 50-55 N/μm/mm^2). This reduced scatter with worn area normalised K_T values further confirms that k_t should be normalised by the actual worn area of contact rather than by the nominal area of contact, which instead is the common practice in the literature. Normalising by the nominal area of contact would be correct only when the wear is fully extended and hence the worn area of contact coincides with the nominal. To include these effects in the models, it should be known how the contact is distributed in the interfaces and correctly assign the contact stiffness values. Note that existing experimental studies on the effect of different nominal areas of contact are few [80], and no detailed investigations were found by the author in the existing literature.

Effect of the displacement amplitude

With regards to the k_t dependency on the displacement amplitude, it seems from Fig. 4.22a that k_t increases with the displacement amplitude. This increase probably occurs because larger displacement amplitudes led to more energy dissipated and hence larger worn areas of contact. In fact, the normalised K_T in Fig. 4.22b decreases as the displacement amplitude increases, on the contrary of the un-normalised k_t. This behaviour has been confirmed by performing a new experiment at 87 N, 30 μm and 1 mm^2 nominal area of contact. After reaching the steady state, several hysteresis loops were recorded at different displacement amplitudes as shown in Fig. 4.26a. k_t measurements from this test are shown in Fig. 4.26b as a function of the displacement amplitude. The displacement dependency is clear, with k_t values reducing approximately by 60% over the thirtyfold increase in displacement amplitude, nearly reaching an asymptote at the largest tested amplitude. Measurements were performed with both increasing and decreasing displacement amplitude loadings and the trend was repeatable for both loading cases. Note that, in this case, the k_t is not normalised since all measurements were performed with the same underlying worn area of contact. It has also to be noted that the values represent the k_t estimated right after the load reversal (i.e. at beginning of the stick regime), and have not to be confused with the "instantaneous" stiffness, which also decreases with increasing displacements within the hysteresis loops and becomes zero during gross slip (when the hysteresis loop shows a horizontal line). The drop in the k_t (evaluated after load reversal) with the increasing displacement amplitude has been observed in a few previous studies [20, 24, 209, 259], but no physical explanation has been provided so far.

A possible reason for this behaviour is that, at larger displacement amplitudes, also the velocity is larger and, therefore, there is more energy dissipated and heating in the contact, which could make the material more compliant. As a result, the contact stiffness would be larger. A second hypothesis is that the k_t displacement dependency originates from the so-called ageing phenomenon. The ageing results from the time of stationary contact during which the junction size at the asperity contact increases, induced by asperity creep and strengthening of bonding at asperity contacts [184, 260–262]. Optical measurements have already shown how the real area of contact slowly increases, typically logarithmically, with the time spent in contact, at rest, due to the ageing or contact rejuvenation [187, 190]. This concept can be applied to the present measurements by assuming that the stick condition is equivalent to a period of stationary resting contact. The ageing would lead to increased stiffness values during repeated (quasi-stationary) stick cycles at low displacement amplitudes (without any gross slip that would instead refresh the contact). Instead, at large displacement amplitudes, the asperities

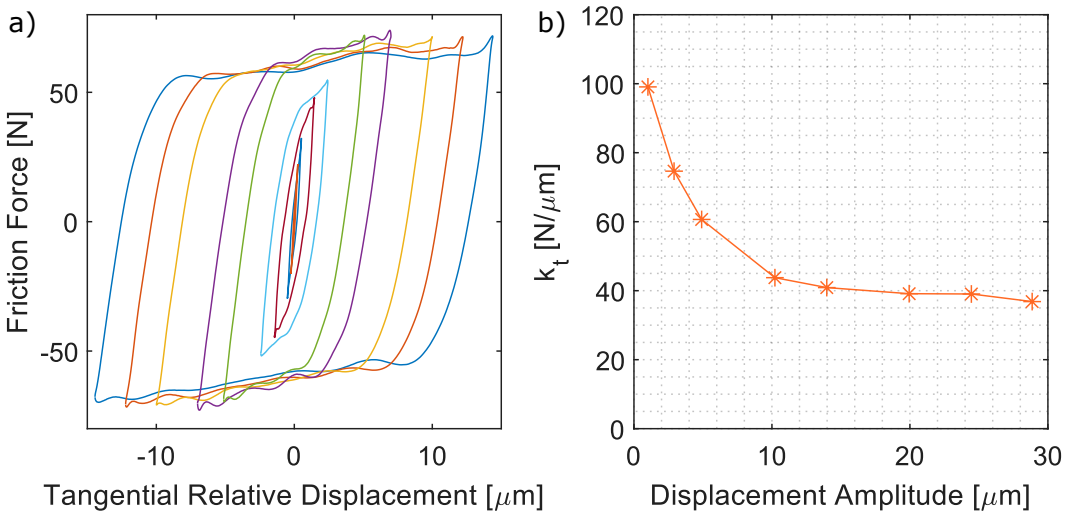


Figure 4.26: a) Hysteresis loops measured at different displacement amplitudes at 100 Hz excitation frequency within the same test; b) k_t as a function of the displacement amplitude from hysteresis loops shown in a). Note that k_t is the slope measured right after the load reversal in each hysteresis loop. Test conditions: 87 N normal load, 1 mm^2 nominal area of contact, 100 Hz excitation frequency, steady state reached after 2.5 hours of running at 30 μm displacement amplitude and then loops measured at different displacement amplitudes, material=stainless steel, temperature=25°C.

would be in stick conditions (i.e. a quasi-stationary contact) for shorter periods, thus reducing the amount of ageing and consequently resulting in lower contact stiffness. This hypothesis has been well supported by the ultrasound measurements shown in chapter 5 (see section 5.3.1 and Fig. 5.9), which resulted in a recent publication by the author [263].

This hypothesis implies that the contact stiffness depends on the time of stationary contact, which is equivalent to the time in the stick regime. This time is related to the average relative velocity of the contacting asperities, with low velocities resulting in more ageing and hence larger k_t values. Therefore, it was decided to investigate the effect of the velocity by measuring hysteresis loops at different excitation frequencies. Fig. 4.27a-b show hysteresis loops measured at several displacement amplitudes at 30 Hz and 100 Hz excitation frequencies respectively (note that the loops in 4.27b are the same of Fig. 4.26a). Fig. 4.27c shows the corresponding k_t values measured after the load reversal (i.e. at beginning of the stick regime). For both excitation frequencies, k_t decreases with increasing displacement amplitudes, however values for the different frequencies do not overlap. The reason could be that indeed this is not a displacement dependency, but rather a velocity dependency due to the ageing effect. To confirm this hypothesis, Fig. 4.27d plots the k_t as a function of the peak velocity, which is obtained by multiplying the displacement amplitude by the excitation frequency. In this case, k_t trends are much more similar, thus strongly supporting the velocity dependency.

As a further investigation, it was also evaluated the "instantaneous" k_t, which is instead the gradient between two consecutive measurement points within the hysteresis loop. The "instantaneous" k_t is shown in Fig. 4.28b as a function of the relative displacement (the corresponding hysteresis loops are shown in Fig. 4.28a). Each measurement point in the hysteresis loop has a corresponding "instantaneous" k_t value. This is an unusual representation, which has not been reported in the existing literature to the best of the author's knowledge. Some features of this plot can be explained by looking at the hysteresis loop with the largest displacement amplitude

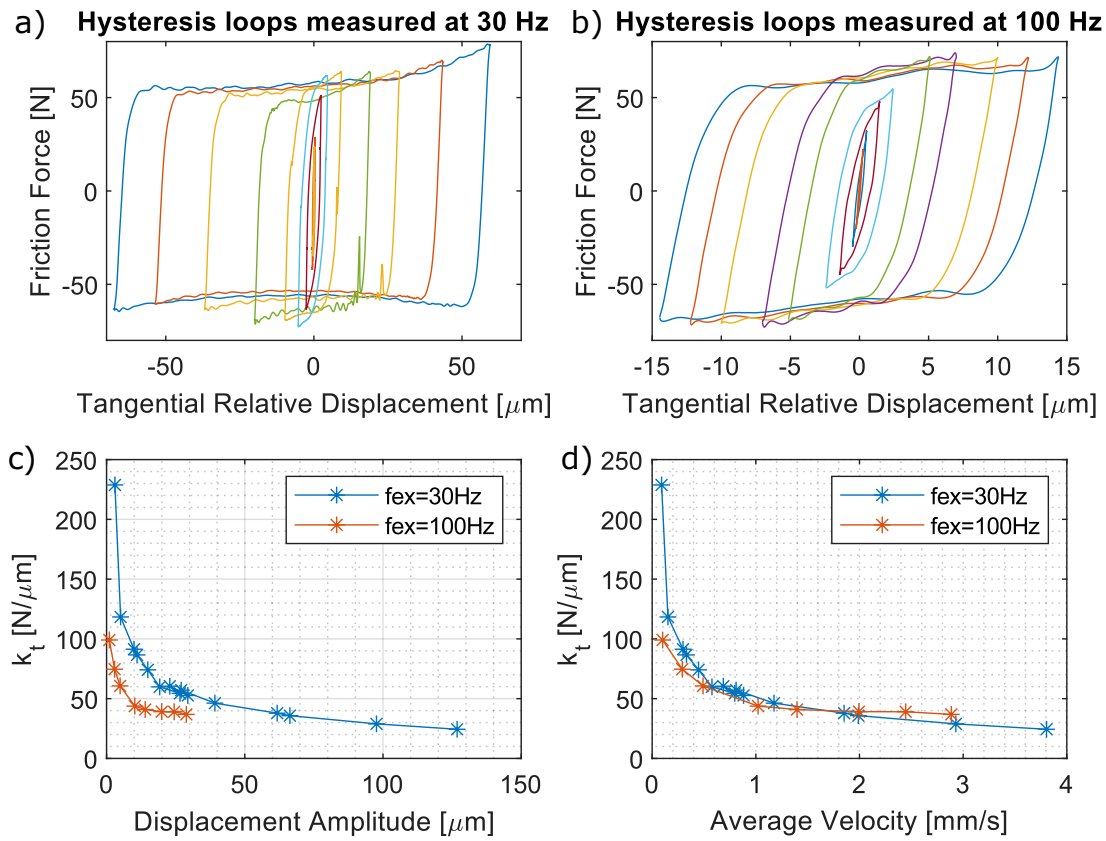


Figure 4.27: a) Hysteresis loops measured at different displacement amplitudes at 30 Hz excitation frequency within the same test; b) Hysteresis loops measured at different sliding distances at 100 Hz excitation frequency within the same test; c) k_t as a function of the displacement amplitude from hysteresis loops shown in a) and b); d) k_t as a function of the peak velocity, given by the displacement amplitude multiplied by the excitation frequency, from hysteresis loops shown in a) and b). Test conditions: 87 N normal load, 14 μm displacement amplitude, 1 mm^2 nominal area of contact, 30 Hz or 100 Hz excitation frequency, steady state reached after 2.5 hours of running and then loops measured at different displacement amplitudes, material=stainless steel, temperature=25°C.

(i.e. the external blue loop):

- Between -7 μm and 7 μm there is gross slip and indeed the "instantaneous" k_t is equal to zero on average because the loop is almost horizontal during gross slip and therefore there is no gradient between consecutive measurement points.
- At extreme displacements larger than -7 μm and 7 μm, where there is the stick regime, the "instantaneous" k_t is larger and reaches a peak right after the beginning of the stick regime. Then, the "instantaneous" k_t slowly goes towards zero, when the gross slip begins.
- Figure 4.28b also shows blue squares, which represent the average k_t value extracted for that loop (i.e. k_t of Fig. 4.27c evaluated after load reversal until the zero friction force value). This average value is in general slightly lower than the peak "instantaneous" k_t (red circles) since indeed it is the average of more consecutive "instantaneous" k_t.

By looking at the other hysteresis loops with smaller displacement amplitudes, it is clear that the peak "instantaneous" k_t increases as the displacement amplitude decreases. This is again

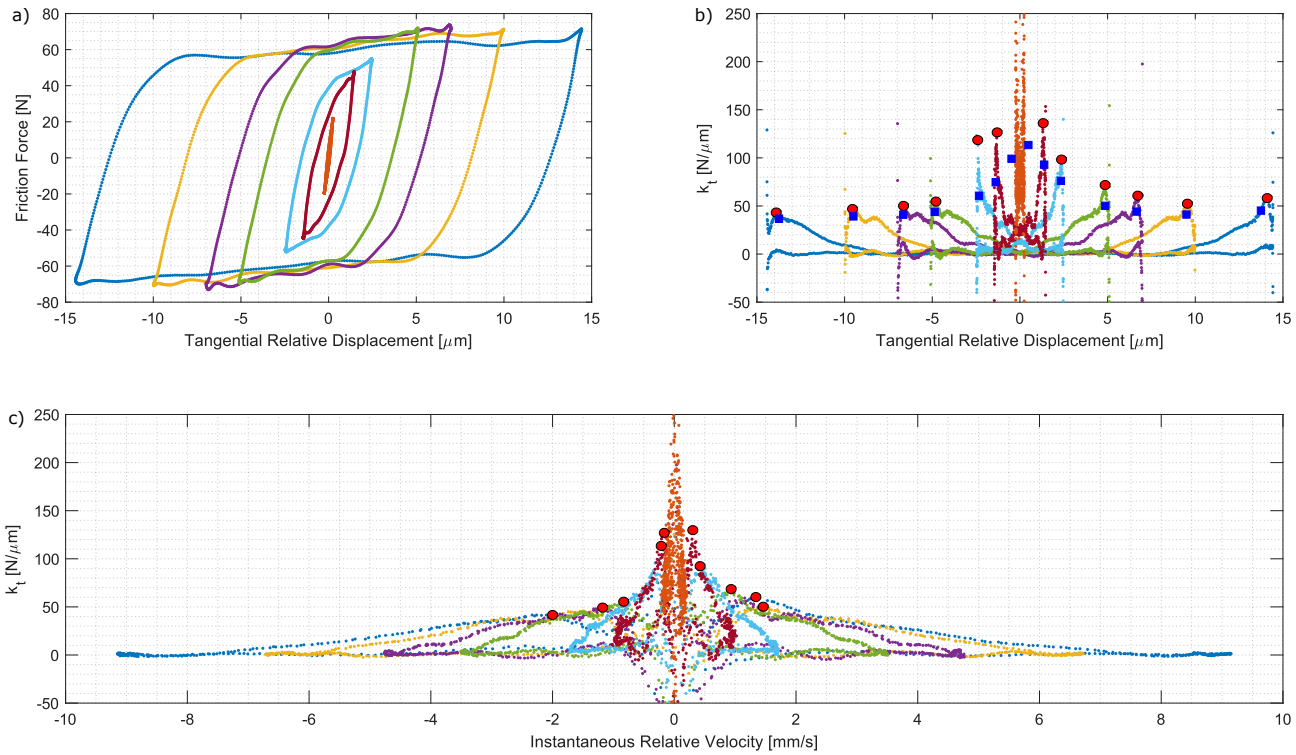


Figure 4.28: a) Hysteresis loops measured at different displacement amplitudes at 100 Hz excitation frequency within the same test; b) Instantaneous contact stiffness versus the tangential relative displacement. The blue squares represent the k_t evaluated after load reversal (i.e. the k_t shown in Fig. 4.27c). The red circles indicate the peaks in the instantaneous k_t for the different loops; c) Instantaneous contact stiffness versus the instantaneous relative velocity. The red circles indicate the peaks in the instantaneous k_t for the different loops. Test conditions: 87 N normal load, 14 μm displacement amplitude, 1 mm^2 nominal area of contact, 100 Hz excitation frequency, steady state reached after 2.5 hours of running and then loops measured at different displacement amplitudes, material=stainless steel, temperature=25°C.

supposed to be linked to the lower velocity at larger displacement amplitudes and hence to the lower time in the stick regime. This aspect is investigated with Fig. 4.28c, where the "instantaneous" k_t is plotted as a function of the instantaneous relative velocity. At the extreme velocities, the "instantaneous" k_t is equal to zero because loops are in gross slip and hence there is no gradient between two consecutive points. Instead, the peaks in the "instantaneous" k_t of the different loops seem to be related to the instantaneous velocity, since when the peaks are lower the velocity is larger. This further confirms the velocity dependence and ageing hypothesis described at the beginning of this section.

Finally, to further confirm the velocity (and hence displacement) dependency, Fig. 4.14 is recalled here. The figure showed the evolution of k_t in two tests at different displacement amplitudes. In the test at 1 μm displacement amplitude, there was no increase with time, since stuck loops did not dissipate energy and hence the worn area did not develop (as shown by the photo of the interface at the end of the test). Instead, k_t steadily increased during the test at 24.5 μm displacement amplitude since there was energy dissipation and therefore the worn area grew during the test. It is interesting to compare the values in the k_t: during the 1 μm test, k_t is constant at around 50 N/μm. This value is larger than the initial k_t of the 24.5 μm test, which was around 25 N/μm. The initial k_t measured in the 24.5 μm test is lower

because at larger displacement amplitudes, and hence larger velocities, there is less time for ageing. However, as the test progressed, the worn area increased and hence the k_t reached a larger value at the end of the test, at around 100 N/μm, which is almost fourfold the initial 25 N/μm and twofold the 50 N/μm constant value of the 1 μm test.

4.2.4 Friction coefficient

The previous section has shown a summary of the k_t steady state values from the Imperial measurements. This section shows instead the μ steady state values with Figs. 4.29 and 4.30. The Figures only show results at 14 μm and 24.5 μm and not results at 1 μm displacement amplitude since loops at 1 μm were in a full stuck condition and therefore the friction limit was not reached.

The steady state values do not vary much for the different loading conditions and nominal areas of contact, leading to an average μ steady state value of 0.74. This value could be used as a reference for 304 stainless steel material pairings operated at 100 Hz excitation at room temperature. All steady state values present a scatter below 8%. This scatter is slightly higher than the 4% scatter due to the specimen assembly procedures, as previously quantified in section 4.2.2. The remaining 4% scatter could be due to the variation in the loading conditions, although clear trends are not visible. It seems that the friction coefficient slightly decreases as the normal load increases, but this might occur because, at larger normal loads, a fully established gross slip has not been achieved within the relatively small investigated displacement amplitudes (14 μm and 24.5 μm). Displacement amplitudes and nominal areas of contact seem to not affect μ estimations to a clear extent instead. As a result, it is suggested to use a constant μ value of 0.74 as input in nonlinear dynamic analysis when 304 stainless steel material pairings are tested at room temperature. Sensitivity studies could be performed by considering the 8% scatter, which results in values ranging from 0.71 to 0.78.

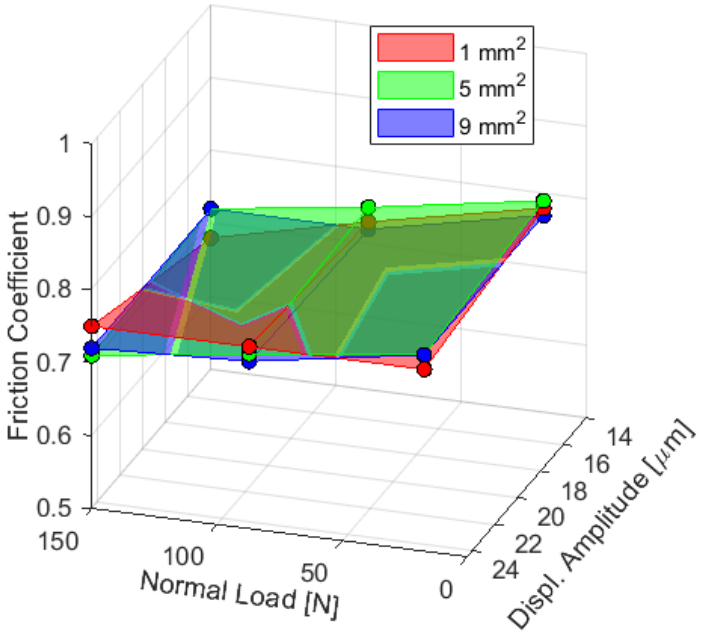


Figure 4.29: Friction coefficient steady state values of the round robin test on the Imperial friction rig.

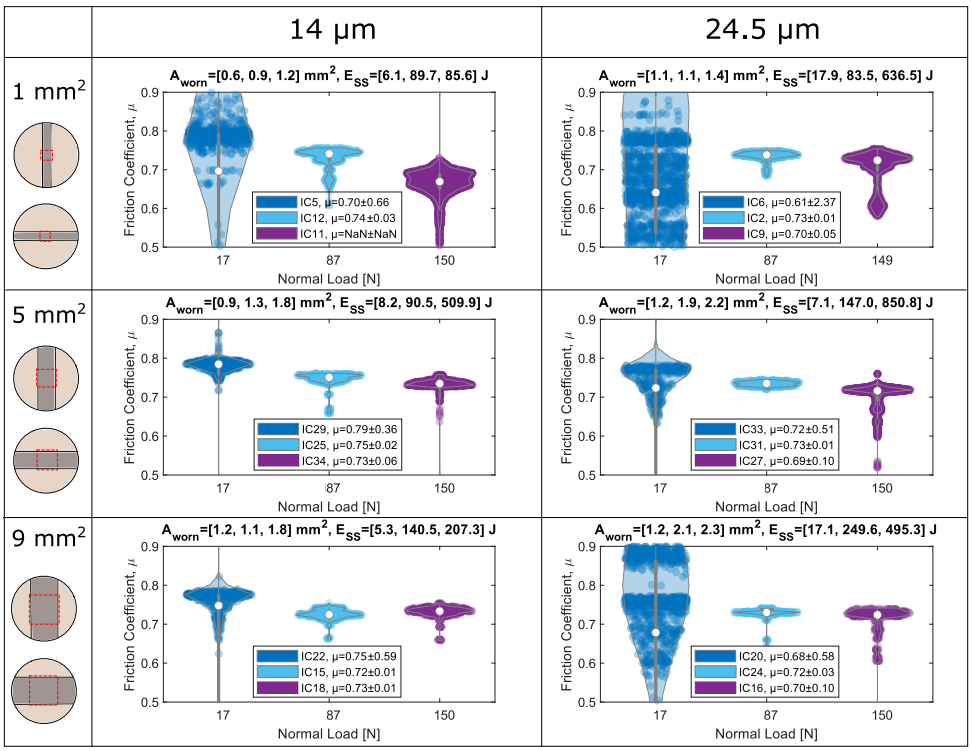


Figure 4.30: Violin plots of the steady state values of the friction coefficient of every round robin test on the Imperial friction rig. Each violin corresponds to a different test for one normal load, displacement amplitude and nominal area of contact. The legends indicate the mean and standard deviation of the steady state values of each test. The figure titles indicate the worn areas of the three tests and the energy dissipated when the steady state was reached. Chattering was often observed during tests at 17 N normal load and that is why the standard deviation is quite large in those tests.

Summary of Imperial hysteresis loop measurements

The round robin experimental measurements performed at Imperial have provided several insights into the physics of the contact parameters used as input in nonlinear dynamic analysis. The main outcomes are the followings:

- k_t increases with increasing normal load, as already well known from the existing literature. This increase is linked to the increase in the number and size of the individual contact spots at larger normal loads;
- k_t decreases with increasing displacement amplitudes. No explanations have been found in the existing literature and the reason for this behaviour has been here attributed to the ageing-induced velocity dependency;
- k_t increases with wear. This increase is linearly related to the increase in the worn area of contact and hence it is proposed that k_t should be normalised by the worn area of contact and not by the nominal area as it is commonly done in the literature. Experimentally, the worn area of contact should be measured at the end of the test for normalisation. If this is not possible, then the test should be run long enough so that the full nominal area is worn, and the k_t can be normalised by the nominal area;

- Also the normal load should be normalised by the worn area of contact since two tests performed with the same normal load but different worn areas will have different contact pressures and hence different normalised K_T according to Eq. 4.1;
- μ seems to not be affected by the loading conditions and shows an average value of 0.74 for the tested 304 stainless steel material at room temperature.
- μ increases quickly at the beginning of the test, within the first hundreds of cycles, from a very low value of 0.1 to a steady state value of 0.74. The rapid increase was associated with the removal of initial oxide layers on the unworn interfaces.

4.3 Measurements at Politecnico di Torino

This section shows a summary of the measurements performed on the PoliTO rig. As for the Imperial tests, also PoliTO tests were performed for each loading combination with new specimen pairs run for 2.5 hours. A general overview for every test is shown through Figs. 4.31-4.32-4.33. The Figures show the contact interfaces and the end-of-test hysteresis loops for all the loading combinations and specimens with nominal areas of contact of 5, 10 and 40 mm^2 respectively. Note that, in the rest of the chapter, tests performed at PoliTO are named consecutively TO1, TO2 etc.

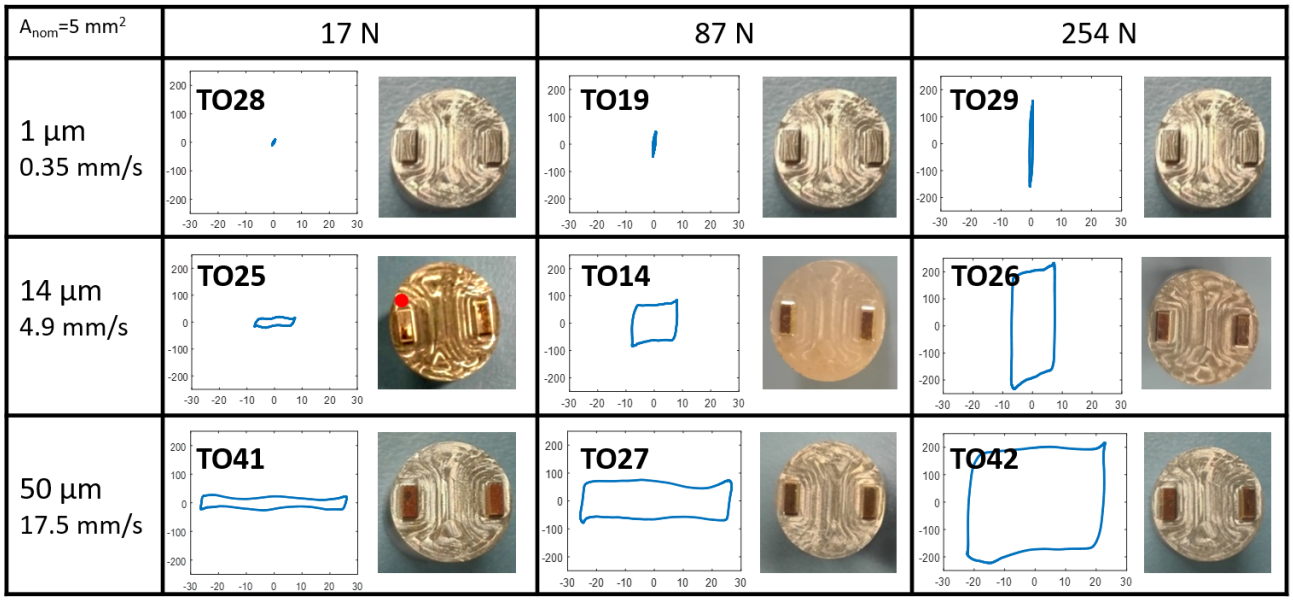


Figure 4.31: Overview of contact interfaces and hysteresis loops for tests conducted on specimens with a 5 mm^2 nominal area of contact at PoliTO. Columns are normal loads and rows are displacement amplitudes. The red dots indicate the position of the laser measurement location since the displacement could only be measured on one of the two contact legs during the experiment.

Hysteresis loops strongly change as displacement amplitude and normal load vary, in the same way as already observed with Imperial measurements. The main difference with Imperial measurements is that chattering does not appear during PoliTO measurements (see section 4.2.2). This probably occurs because the "static" block of the PoliTO rig is flexible due to the

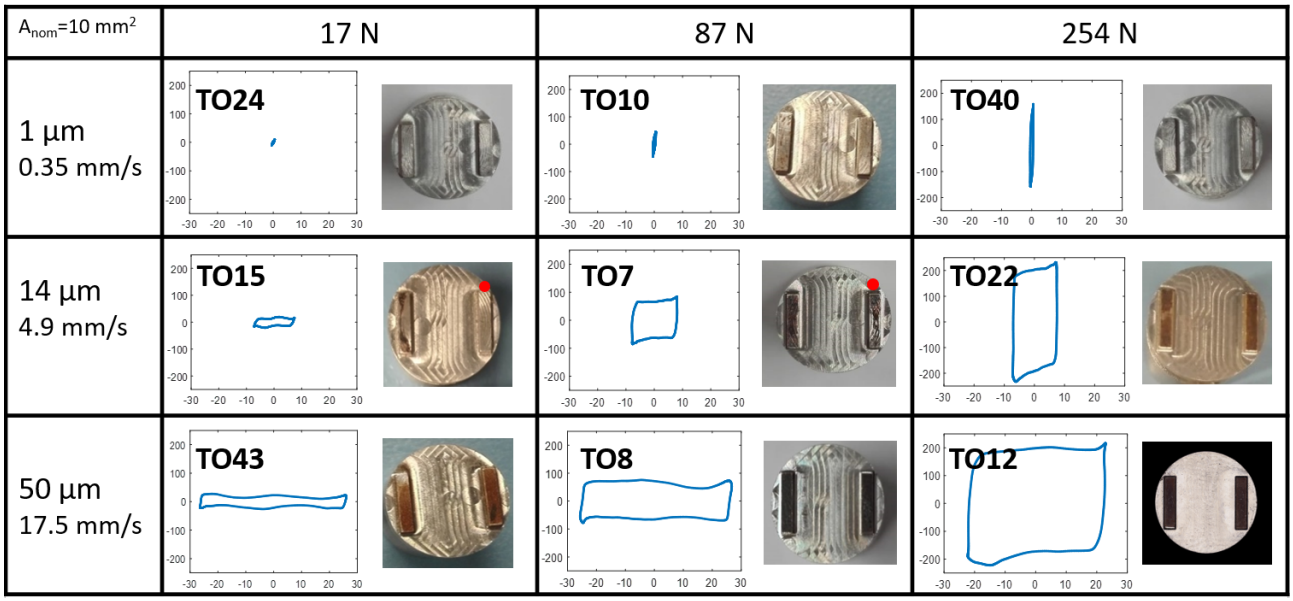


Figure 4.32: Overview of contact interfaces and hysteresis loops for tests conducted on specimens with a 10 mm^2 nominal area of contact at PoliTO. Columns are normal loads and rows are displacement amplitudes. The red dots indicate the position of the laser measurement location since the displacement could only be measured on one of the two contact legs during the experiment.

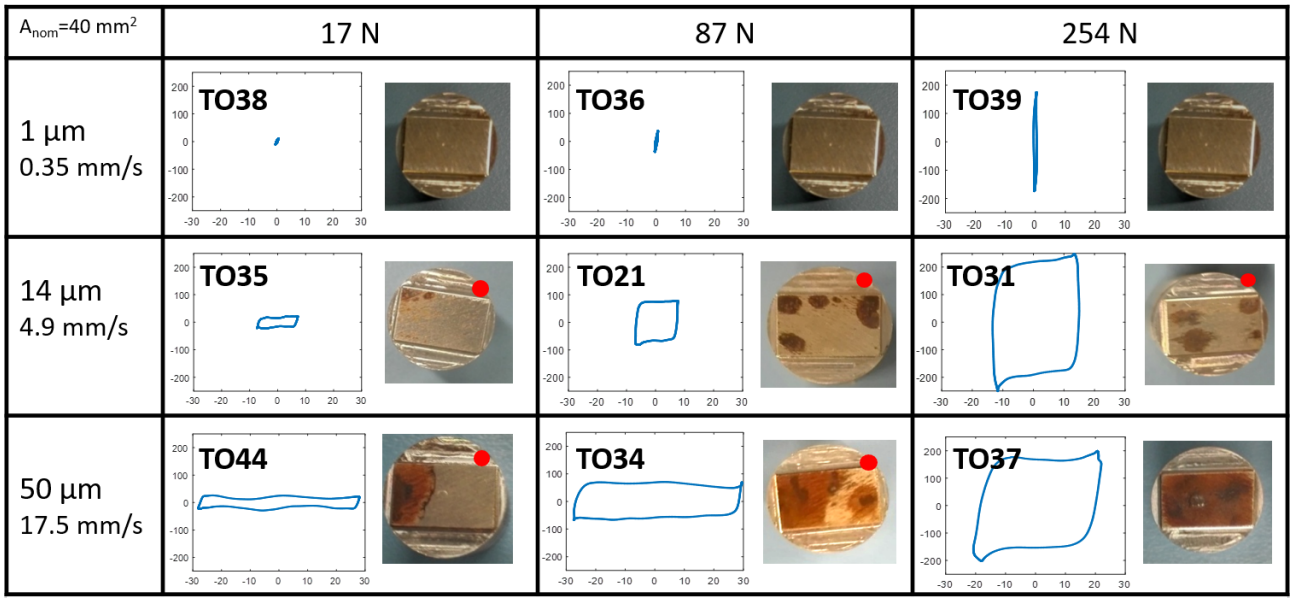


Figure 4.33: Overview of contact interfaces and hysteresis loops for tests conducted on specimens with a 40 mm^2 nominal area of contact at PoliTO. Columns are normal loads and rows are displacement amplitudes. The red dots indicate the position of the laser measurement location since the displacement could only be measured on one of the two contact legs during the experiment.

self-aligning contact approach and therefore it does not induce high-frequency vibrations due to its lower rigidity. Instead, the Imperial system is more rigid, thus increasing the possibility to develop chattering.

Figures 4.31-4.32-4.33 also show the contact interfaces at the end of each test. In the stick tests, 1 μm, the interfaces do not present any evident wear mark, suggesting that a negligible amount of energy is dissipated during the full stick regime, as already observed within the Imperial tests. At larger sliding distances, coloured spots appear indicating that worn areas have developed. Note that, within Imperial tests, a full worn area of contact was only reached in the specimens with the lowest 1 mm^2 nominal area of contact, while specimens with 5 and 9 mm^2 nominal areas never reached a full worn extension since those interfaces were too large and not enough energy was dissipated during the 2.5-hour tests. Instead, within PoliTO specimens, fully extended worn areas are also reached in some of the tests at larger nominal areas of contact (10 and 40 mm^2). This is probably due to the self-aligning system, which guarantees a more uniform contact and therefore higher wear rates. Another reason is that PoliTO specimen interfaces do not show the curvature observed in Imperial specimen interfaces, thus leading to a more distributed and extended contact to start with. In addition, PoliTO measurements were performed at a larger excitation frequency (175 Hz) than that of Imperial (100 Hz), thus leading to more energy dissipated during the same amount of time. In the case of the lowest 5 mm^2 nominal areas of contact, only the test performed at 14 N/μm and 17 N did not reach a fully extended worn area. In the case of the 10 mm^2 nominal areas of contact, also some tests at 87 did not reach a full worn area extension. Finally, in the case of the 40 mm^2 nominal areas of contact, only one test, performed at 50 N/μm and 254 N, reached a full worn area extension. With those large nominal areas of contact, wear marks usually developed at the edges of the contact first, where most of the slip is expected to occur according to contact mechanics predictions for nominally flat interfaces [264].

4.3.1 Evolution of the contact parameters with wear

The evolution of hysteresis loops over time for a typical test on the PoliTO rig is shown in Fig. 4.34 (Test n.TO14: 87 N normal load, 14 μm displacement amplitude and 5 mm^2 nominal area of contact - the trend is similar for other tests with loops in gross slip). The Figure shows a significant and rapid increase in μ at the beginning of the test, as already observed with the Imperial measurements, from an initial value of 0.04 to a steady state value of 0.81. The energy dissipated to reach the steady state was 120 J, which is on the same order of magnitude of tests at Imperial (hundreds of J on average, see Fig. 4.30).

With regards to k_t, it also reaches a steady state but it requires more energy dissipated (947 J of energy dissipated for the left k_t and 1847 J for the right). As a reminder, k_t left and right are referred to the contact stiffnesses extracted from the left and right stick portions of the hysteresis loops. Therefore, they represent the contact stick behaviour of the interface sliding along opposite directions (in one case the moving specimen goes forwards and in the other case backwards) and also in two different physical locations (since the interfaces have slid over tens of micrometres before reversing the motion during the stick regime). The amount of energy dissipated is similar to that observed in Imperial tests (see Fig. 4.23). However, while for Imperial measurements k_t left and right had very similar values and reached the steady state at the same energy for all tests (see e.g. Fig 4.12), they were in general different in PoliTO measurements. For example, in the case of the TO14 test, the k_t left reached the steady state at a value of around 500 N/μm and 947 J, while the k_t right reached the steady state at a value of around 360 N/μm and 1847 J.

The reasons for this discrepancy between left and right k_t are not well understood yet. A

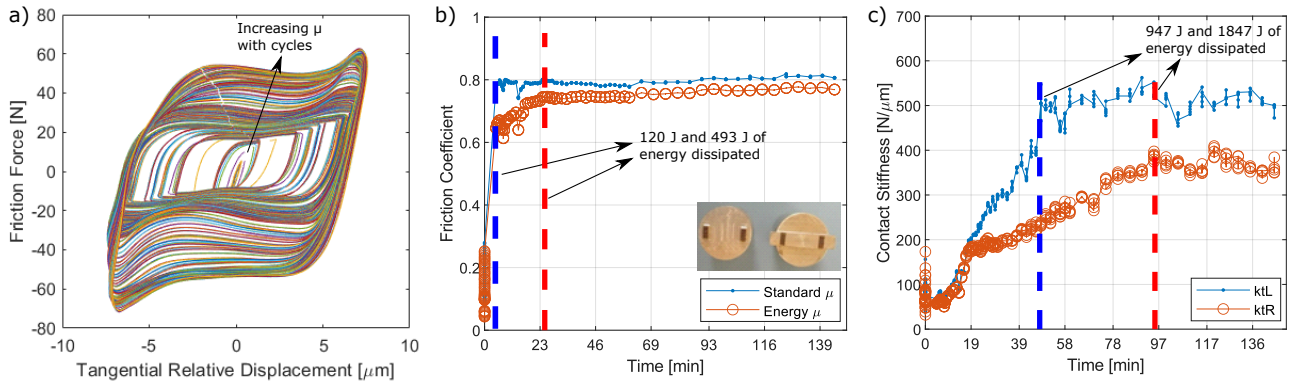


Figure 4.34: Typical evolution of contact parameters of PoliTO specimens: a) Hysteresis loops; b) Friction coefficient; c) Tangential contact stiffness (k_{tL} and k_{tR} are the contact stiffnesses of left and right stick portions of the hysteresis loops, as defined in section 3.2.1). Vertical lines indicate the beginning of the steady state; the photo shows the specimen interfaces at the end of the test with a full worn area of contact. Values for the Test n. TO14: 87 N normal load, 14 μm displacement amplitude, 5 mm^2 nominal area of contact, 175 Hz excitation frequency and 2.5 hours of running.

possible reason might be an asymmetry in the stiffness of the rig in the two different directions or the fact that such large measured k_t values are not very reliable due to the corresponding very low measured displacement (in the order of the nanometers). In fact, the other main difference with Imperial measurements is in the much larger k_t values obtained from PoliTO tests (up to 50 times larger values), which result from 50 times lower (and probably less reliable) measured relative displacements. The stick slope is so steep that even a slight change would lead to large variations in the values (i.e. results are very noise dependent as the slope approaches large values). These large values led to some inaccuracies in the post-processing as shown for example with Fig. 4.35, in which, even though the loops look similar through the test, slight changes in the slope led to massive changes in the estimated stiffness. Part of the reason for these large k_t values is that, at PoliTO, full worn areas of contact are often reached (at 5, 10 or 40 mm^2), which are much wider than the largest worn areas reached during Imperial tests (only up to 2 mm^2). When the k_t is normalised by the worn area, values become comparable, as discussed in more detail in the following sections. Hence, a first conclusion is that, to obtain more reliable k_t estimations, smaller nominal areas should be used since they lead to larger relative displacements that are less affected by post-processing issues.

Few other differences in the evolution of the contact interface and contact parameters with wear were observed in PoliTO tests, which were not observed in Imperial tests. Firstly, in a few tests, a steady state was reached even though a full worn area of contact was not reached, as observed with Test n. TO25 in Fig. 4.36. This test shows steady states in k_t left and right values after 200 J and 54 J of cumulative energy dissipated respectively. This energy dissipated is much lower than that usually observed in the other tests, see e.g. the more than 1000 J from Test n. TO14 in Fig. 4.34. The reason is that in Test n. TO25 the worn area "arrested", i.e. it stopped to grow although the test lasted for 2.5 hours (usually the full worn area is always reached within the first 50 minutes on average). It is thought that the worn area stopped growing because of a particular waviness or interface shape, or due to some alignment issues. This stop in the growth of the worn area is also confirmed by the fact that the apparent steady state in Fig. 4.36 is quickly reached after only 15 minutes since the time (and energy) required

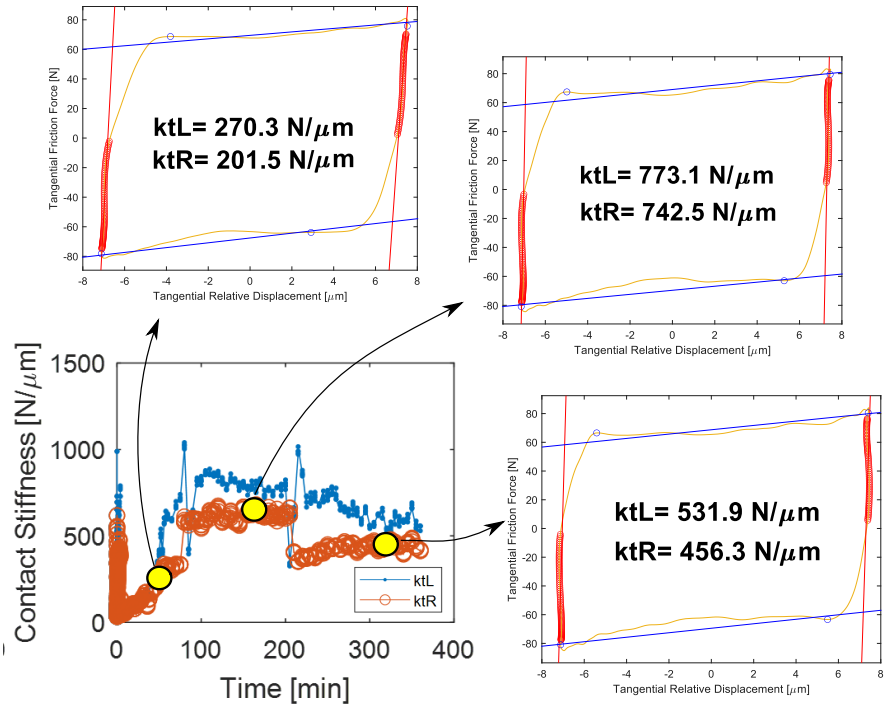


Figure 4.35: Example of post-processing issues in the k_t estimations occurring in few PoliTO tests with very large k_t (>300 N/μm). Test n. TO5: 87 N normal load, 14 μm displacement amplitude, 10 mm^2 nominal area of contact, 175 Hz excitation frequency and 6 hours of running.

to reach that small worn area is much lower than the time to reach the full worn area of Fig. 4.34b.

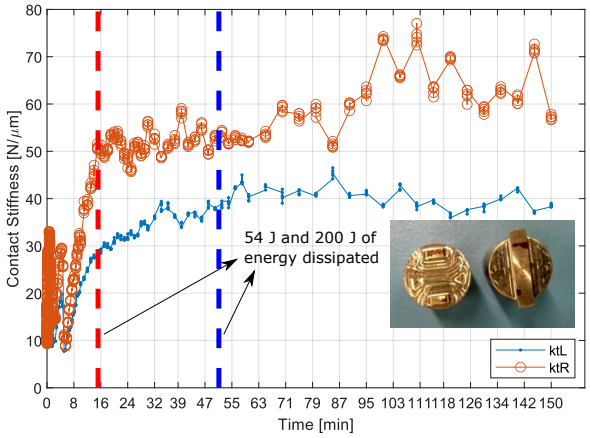


Figure 4.36: Tangential contact stiffness evolution for the Test n. TO25 (17 N normal load, 14 μm displacement amplitude, 5 mm^2 nominal area of contact, 175 Hz excitation frequency and 2.5 hours of running). Vertical lines indicate the beginning of the steady state for k_t left and right; the photo shows the specimen interfaces at the end of the test.

A second difference in the evolution of the contact parameters with wear, which was observed in PoliTO tests but not in Imperial tests, is the evolution of k_t during stick tests performed at 1 μm displacement amplitude. While stick tests performed at Imperial did not show any increases during time, as shown in Fig. 4.14, tests performed at PoliTO showed an increase in the k_t values even though they did not show any amount of wear on the contact interfaces at the end of the tests. This is shown for example with Test n. TO10 in Fig. 4.37. Fig. 4.37a shows that,

even though the displacement amplitude of the hysteresis loops is very small, they still dissipate a small amount of energy due to the area inside the loop. This amount of energy dissipated is not large enough to generate a worn area, but it is large enough to lead to an increase in the k_t, as shown in Fig. 4.14b, where a "steady state" in the k_t values is reached despite the quite low amount of energy dissipated (22 J and 7 J for k_t left and right respectively). The increase is here attributed to a plastic hardening of the asperities, which dissipate some energy during microslip loading and unloading cycles, hence increasing the stiffness of the contact and resulting in larger k_t estimations. Instead, Imperial hysteresis loops were almost straight lines without any energy dissipated and, therefore, did not show any evolution in the k_t values during the whole tests (see e.g. Fig. 4.14a). The reason why loops at PoliTO dissipate more energy than loops at Imperial is that PoliTO loops have larger k_t values (around 300 N/μm) compared to those observed in Imperial stuck tests (around 50 N/μm). For this reason, larger tangential loads are reached with lower displacement amplitudes, thus increasing the possibility to encounter microslip even at low displacement amplitudes such as 1 μm. Another feature from Fig. 4.37b is that the k_t left and right are quite different, especially at the end of the test. This difference is investigated in more detail in Fig. 4.37c, which shows the hysteresis loops measured after 5 and 50 minutes from the beginning of the test. The hysteresis loop at minute 50 is more asymmetric and its k_t left is much steeper than the k_t right. As mentioned at the beginning of the section, this is probably due to an asymmetry in the stiffness of the rig in the two different directions. In a first approximation, it is suggested to use the average of the two values as an estimation of the k_t.

4.3.2 Repeatability of the tests

This section investigates the repeatability in the PoliTO rig by presenting six tests performed under the same conditions (87 N normal load and 14 μm displacement amplitude). Three tests were performed for a 5 mm^2 nominal area of contact and three tests for a 40 mm^2 nominal area. Figs. 4.38 and 4.39 show the estimated μ and k_t for the two nominal areas respectively.

With regards to the friction coefficient, both energy and standard μ estimations are shown because they differ to a relatively large extent (while in the case of Imperial they were similar). Steady state values are shown in Table 4.3 and are reached for all tests within the first 15 minutes quite consistently. Standard μ has a mean of 0.8 and 0.78 for tests with 5 and 40 mm^2 respectively. For both sets of tests, values lie within a 6% range, which is slightly larger than the 4% observed in Imperial tests. Energy μ has a mean of 0.75 and 0.74 for tests with 5 and 40 mm^2 respectively. For both sets of tests, values lie within an 8% range. Although the scatter is in the same range, energy μ estimations are lower than the standard μ. This occurs because the microslip region in PoliTO tests is much more dominant than in Imperial tests, where instead the transition from stick to gross slip was sharper. The sharper the transition, the larger the energy μ estimations. A hysteresis loop with a sudden transition from stick to gross slip would have the same values of energy and standard μ. If a microslip transition state existed, the energy dissipated would have been lower, thus leading to a lower energy μ estimation, whilst maintaining the same standard μ estimation. More details on the differences between different μ estimation techniques can be found in the following review [167].

With regards to the k_t, measurements show a much larger scatter and less clear trends. End-of-test values are summarised in Table 4.3. The scatter is above 50% in most cases. k_{tL} has a mean of 358 N/μm and 244 N/μm for tests with 5 and 40 mm^2 respectively, while k_{tR} has a

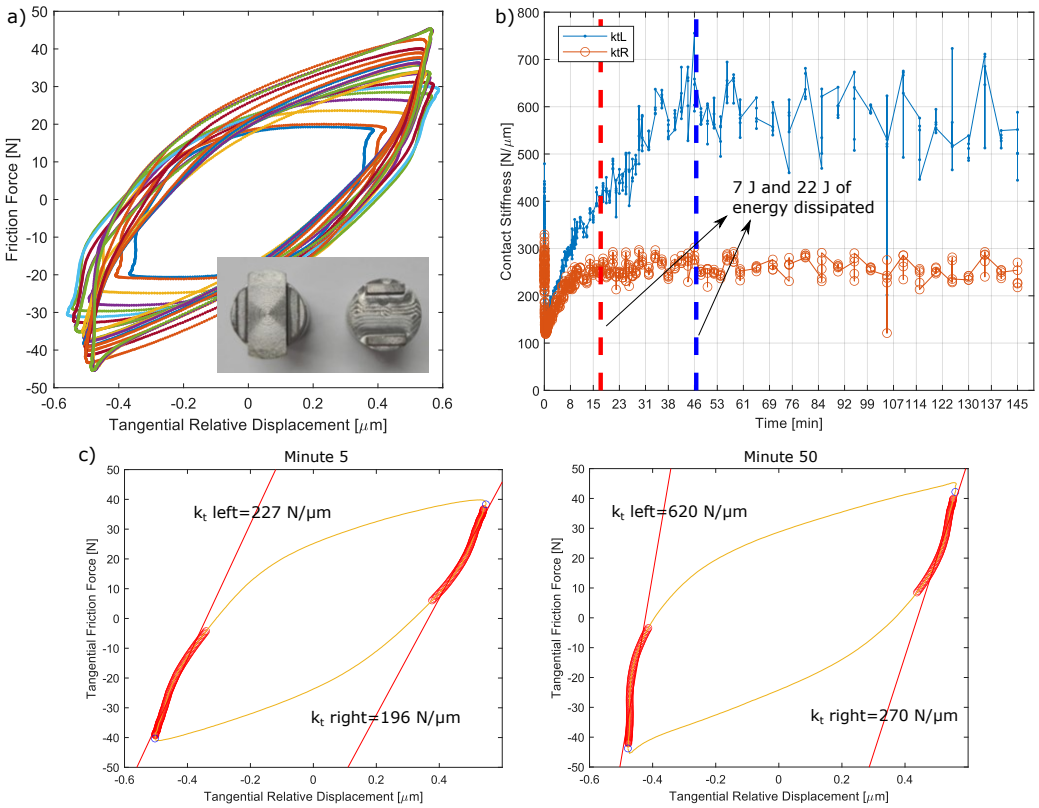


Figure 4.37: a) Evolution of hysteresis loops for the Test n. TO10 performed at 1 μm displacement amplitude on the PoliTO friction rig. The photo shows the specimen interfaces at the end of the test (no wear present); b) k_t evolution in time. Vertical lines indicate the beginning of the steady state (k_{tL} and k_{tR} are the contact stiffnesses of left and right stick portions of the hysteresis loops, as defined in section 3.2.1); c) Details of hysteresis loops at measured at different times to assess the difference between k_t left and right. Values for the Test n. TO10: 87 N normal load, 1 μm displacement amplitude, 5 mm^2 nominal area of contact, 175 Hz excitation frequency and 2.5 hours of running.

Table 4.3: μ and k_t steady state (or end of test) values of the three repeatability tests of Figs. 4.38 and 4.39.

	Energy μ	**Standard μ**	k_{tL} **[N/μm]**	k_{tR} **[N/μm]**
5 mm^2	[0.68, 0.77, 0.79]	[0.76, 0.80, 0.83]	[217, 490, 367]	[85 361 241]
40 mm^2	[0.78, 0.75, 0.68]	[0.82, 0.74, 0.77]	[266 360 105]	[238 49 87]

mean of 229 N/μm and 125 N/μm for tests with 5 and 40 mm^2 respectively. End-of-test values differ up to 60% for k_{tL} and up to 90% for k_{tR}, which is a larger scatter than the 25% observed in Imperial tests. This large scatter is probably due to the following reasons:

- The self-aligning contact approach leads to less repeatable experiments for different nominal areas of contact since the k_t is strongly kinematic dependent. This aspect will be further investigated in the following section 4.3.3;
- The very large k_t values become less reliable over a certain threshold (above 300 N/μm)

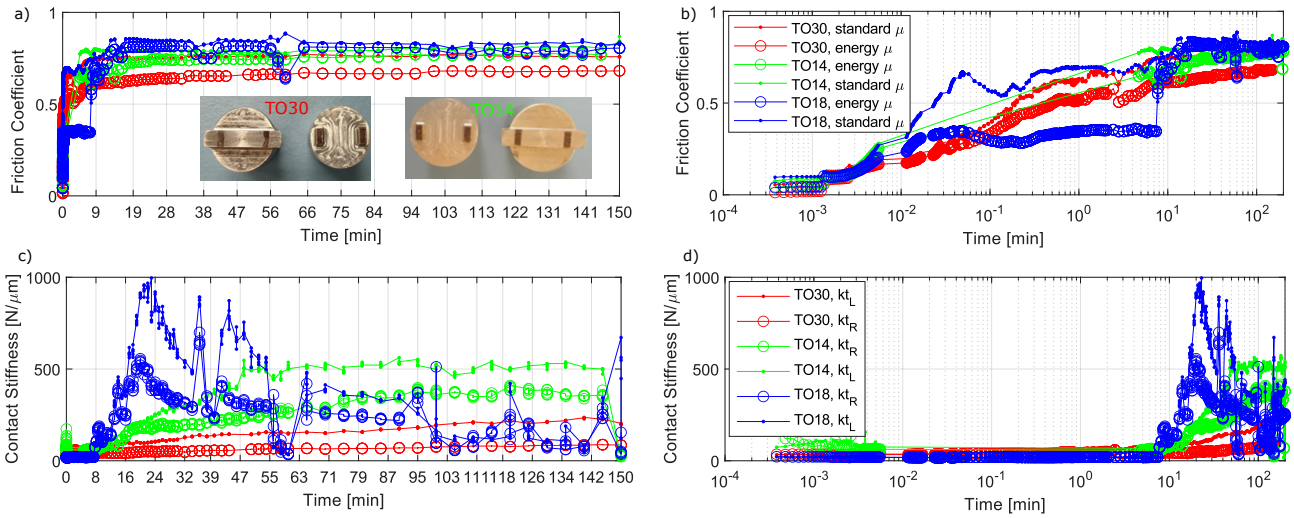


Figure 4.38: Repeatability study for specimens with 5 mm^2 nominal area of contact. Three tests performed with the same loading conditions but different specimen pairs: a-b) Friction coefficient, μ, (linear and log scale). The photos show the specimen interfaces at the end of the test with a full worn area of contact; c-d) Tangential contact stiffness, k_t, (linear and log scale). Values for the Tests n. TO30-14-18: 87 N normal load, 14 μm displacement amplitude, 5 mm^2 nominal area of contact, 175 Hz excitation frequency and 2.5 hours of running, total hysteresis cycles=1575000, material=stainless steel, temperature=25°C.

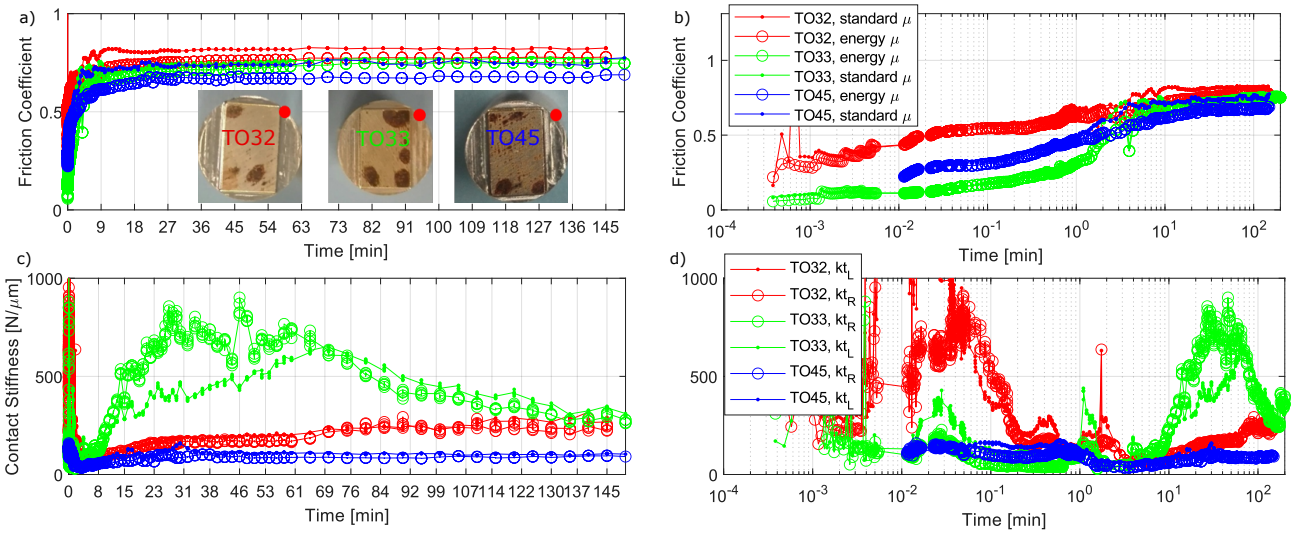


Figure 4.39: Repeatability study for specimens with 40 mm^2 nominal area of contact. Three tests performed with the same loading conditions but different specimen pairs: a-b) Friction coefficient, μ, (linear and log scale). The photos show the specimen interfaces at the end of the test (the red dots indicate the laser measurement location); c-d) Tangential contact stiffness, k_t, (linear and log scale). Values for the Tests n. TO32-33-45: 87 N normal load, 14 μm displacement amplitude, 40 mm^2 nominal area of contact, 175 Hz excitation frequency and 2.5 hours of running, total hysteresis cycles=1575000, material=stainless steel, temperature=25°C.

since even small variations in the measured displacements would lead to very large variations in the k_t estimations, as already discussed in the previous section.

In conclusion, this section has shown that PoliTO tests have a similar scatter, below 8%, in μ

estimations as compared to the Imperial tests. However, a much larger scatter is observed in k_t estimations, up to 90%. This aspect should be considered when comparing the end-of-test values of experiments performed at different loading combinations. The following two sections show detailed results of tangential contact stiffness and friction coefficient respectively, for all the loading combinations of the round robin test matrix.

4.3.3 Tangential contact stiffness

Figure 4.40a shows a summary of the steady state values of the tangential contact stiffness, k_t, for every loading combination (if a steady state was not reached, the end-of-test values were chosen instead). Details on the exact values and standard deviations are shown through violin plots in Fig. 4.41.

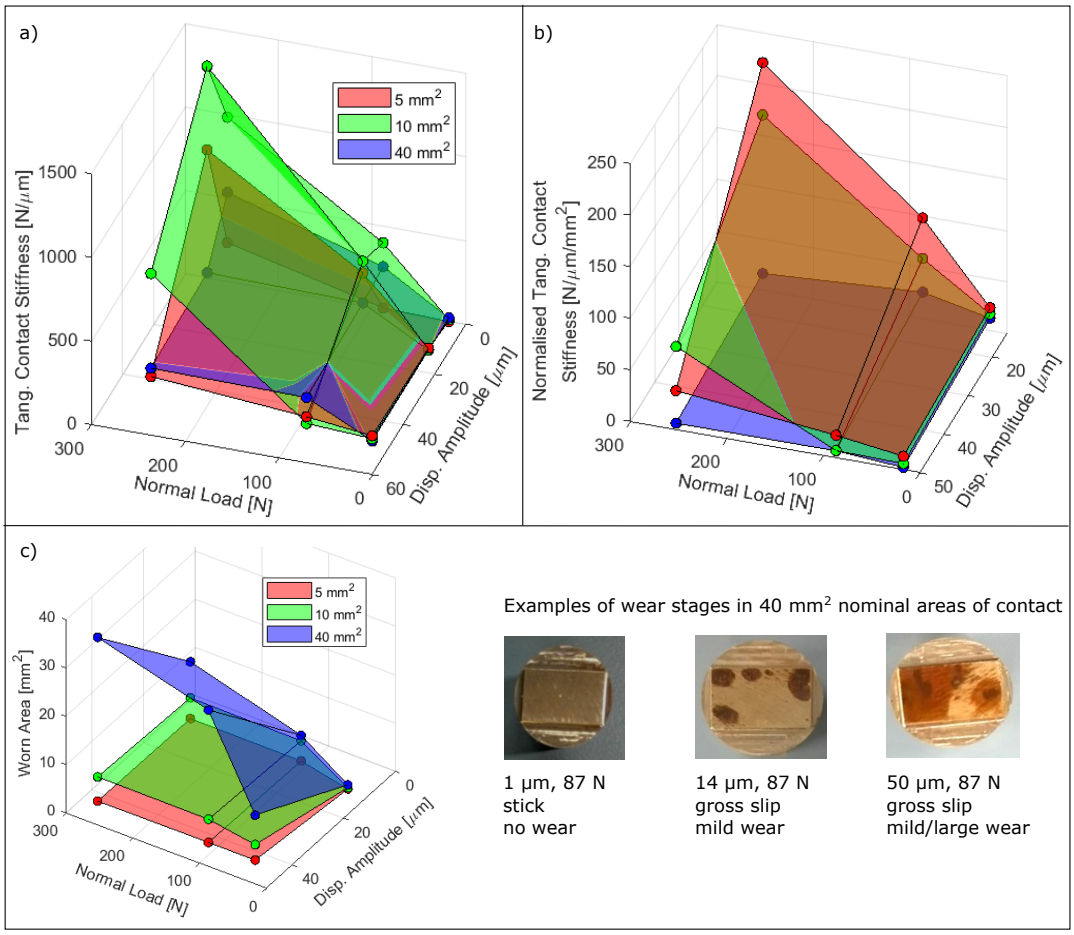


Figure 4.40: a) Tangential contact stiffness steady state values, k_t, of the round robin test on the PoliTO friction rig; b) Worn area normalised tangential contact stiffness steady state values, K_T; c) Worn areas of contact at the end of each test, plus photos of worn areas at the end of tests for the 40 mm^2 nominal area of contact case.

Firstly, it is clear that k_t strongly increases (up to fortyfold) with the normal load, with values rising from as low as 25 N/μm to 2000 N/μm when the normal load increases from 17 N to 254 N. This increase is much larger than the increase observed within Imperial tests (fourfold increase) and it is linked to the much larger worn areas of contact observed in each test, reached

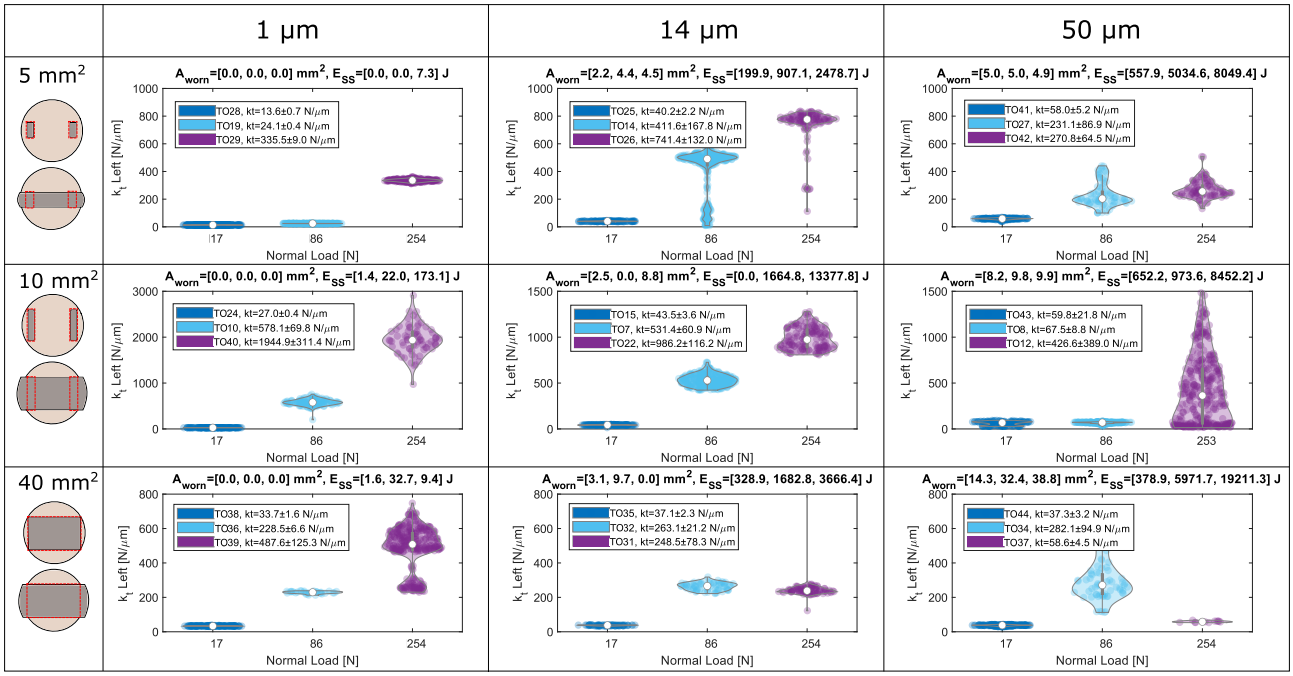


Figure 4.41: Violin plots of the steady state values of the tangential contact stiffness, k_t, of every round robin test on the PoliTO friction rig. Each violin corresponds to a different test for one normal load, displacement amplitude and nominal area of contact. The legends indicate the mean and standard deviation of the steady state values of each test. The figure titles indicate the worn areas of the three tests and the energy dissipated when the steady state was reached (note that in most of the tests the steady state was not reached, and the energy represents the energy towards the end of the test).

thanks to the self-aligning system but also to the larger displacement amplitudes and normal loads investigated. In fact, while during Imperial tests maximum extensions of 2.5 mm^2 were reached, during PoliTO tests extensions of up to 40 mm^2 were reached. In general, the relative standard deviation of the steady state values within the individual tests is below 8% for tests with low k_t values, while the relative standard deviation increases up to the 40% for tests with very large k_t values over 300 N/μm since, as already described in the previous sections, large k_t values are less reliable due to the very small relative displacements measured by the laser. For example, the test for a 10 mm^2 nominal area, 254 N normal load and 14 μm displacement amplitude, shows an extremely large k_t value around 1500 N/μm. This value results from very small relative tangential displacements below 100 nanometres, which are difficult to measure accurately and strongly affect the k_t estimation even for small deviations.

With regards to the k_t displacement dependency, it seems that the behaviour is strongly affected by the worn area extensions, as already observed in Imperial tests. Therefore, Fig. 4.40b shows the K_T normalised by the worn areas of contact, and details on the exact values are shown in Fig. 4.42 through violin plots. Normalised K_T values are in the range 10-250 N/μm/mm^2, which is wider than the range observed in Imperial tests, 20-80 N/μm/mm^2. The normalised K_T decreases as the displacement amplitude increases (almost twofold when the displacement amplitude decreases from 50 μm to 14 μm), thus confirming the trends already observed with Imperial measurements and explained with the velocity-dependent ageing concept. This decrease of K_T with the displacement amplitude has been confirmed by measuring hysteresis loops within the same test at different displacement amplitudes, as shown in Fig. 4.43. Results are

very similar to those obtained with the test performed at Imperial and shown in Fig. 4.26. The only difference is that, at PoliTO, it was possible to investigate larger displacement amplitudes at a larger excitation frequency (175 Hz), which resulted in much larger velocities, up to 21 mm/s, than velocities achieved during Imperial tests, maximum 4 mm/s. It is clear from the PoliTO test that, after a certain threshold (namely 20 μm displacement amplitude equal to roughly 7 mm/s, since the excitation frequency was 175 Hz), the k_t stops decreasing, indicating that no ageing occurs at velocities larger than 7 mm/s. More quantitative analyses will be performed in the future to confirm this hypothesis and understand what are the parameters that affect this threshold, such as supposedly the size of the asperities and the tendency to creep of the particular material.

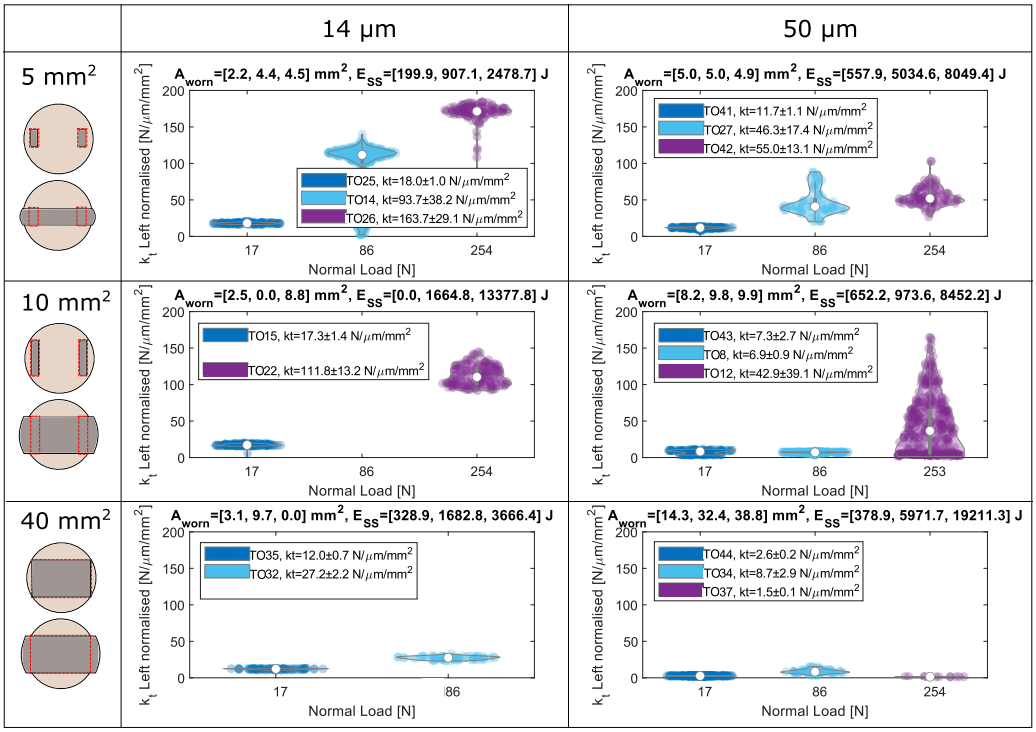


Figure 4.42: Violin plots of the steady state values of the worn area normalised tangential contact stiffness, K_T, of every round robin test on the PoliTO friction rig. Each violin corresponds to a different test for one normal load, displacement amplitude and nominal area of contact. The legends indicate the mean and standard deviation of the steady state values of each test. The figure titles indicate the worn areas of the three tests and the energy dissipated when the steady state was reached (note that in most of the tests the steady state was not reached, and the energy represents the energy towards the end of the test). Tests with unmeasured worn areas are not presented.

With regards to the nominal contact area, also this parameter affects the results, which however are different from what was observed during Imperial tests. In fact, in Imperial tests, the scatter was reduced between tests at different nominal areas of contact, when values were normalised by the worn area of contact. In PoliTO tests, trends are less clear and even the normalised K_T values show a large scatter when considering tests performed at the same displacement amplitude and normal load but different nominal areas of contact (see e.g. the three tests performed at 254 N normal load and 14 μm displacement amplitude in Fig. 4.40b). The reason for this behaviour is attributed to the fact that k_t probably does not depend only on the extension of the worn area, as previously shown with Imperial tests, but also on the

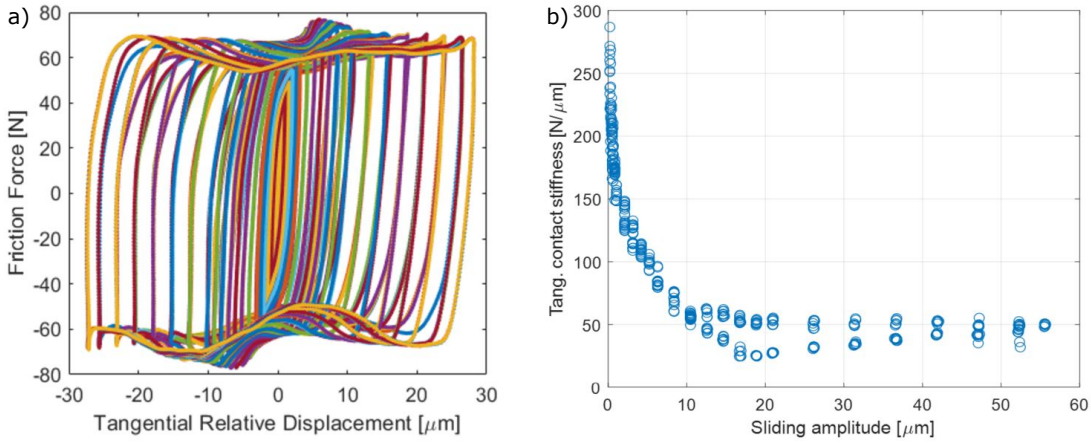


Figure 4.43: a) Hysteresis loops measured at different sliding distances at 175 Hz excitation frequency within the same test; b) k_t as a function of the displacement amplitude from hysteresis loops shown in a). Note that k_t is the slope measured right after the load reversal in each hysteresis loop. Test conditions: 87 N normal load, 10 mm^2 nominal area of contact, 175 Hz excitation frequency, steady state reached after 2.5 hours of running at 50 μm and then loops measured at different displacement amplitudes, material=stainless steel, temperature=25°C.

spatial distribution of the wear spots over the contact. The effect of the spatial distribution is explained and clarified here with some of the round robin tests. As an example, Fig. 4.44 represents an extreme case, the test TO6, in which one leg was not in contact at all due to an improper assembly of the specimens. The k_t measured in this test is very low (below 20 N/μm) if compared to the k_t from test TO3, which is performed under the same loading conditions but with the contact distributed on both legs. The red dots in the Figure indicate the location of the laser measurement. During the test TO6, the specimen was rotating around the leg in contact, while the displacement was measured on the opposite unsupported leg. As a result, a large displacement was measured, leading to much lower k_t estimations[5]. This example highlights that k_t estimations are strongly dependent on the kinematics of the contacting components and hence that it is important to accurately choose the most representative laser measurement locations for reliable k_t estimations. The displacement needs to be measured as close as possible to the actual spots of contact, which can be distributed in different locations if the nominal area is wide. Ultimately, the kinematic behaviour depends on where the interfaces get into contact. In other words, it strongly depends on the pressure distribution.

In order to further explore this concept, Fig. 4.45 compares the k_t estimations (y-axis) from different tests as a function of their worn area extension (x-axis). Fig. 4.45a shows three different tests performed under the same loading conditions. The contact is uniformly distributed over the two legs in all cases, and the k_t increases with the increasing worn area. Instead, trends are different in Figs. 4.45b-c, which show tests performed on specimens with different nominal areas of contact. For the cases at 5 mm^2 and 10 mm^2, k_t increases with the increasing worn area of contact. However, for the test at 40 mm^2 nominal area, even if the worn area is larger, the k_t is lower. The reason for this trend might be explained by the fact that k_t does not only

[5]Note that also the test previously shown in Fig. 4.38d showed very low values of k_t during the first few minutes of the experiment. The reason for those measured low values was that the contact was initially only on one leg also in that experiment. To measure larger (and expected) k_t values, the test was stopped after the first minutes to realign the specimens and get both legs in full contact. After the re-alignment, the measured k_t suddenly increased to larger values, as expected.

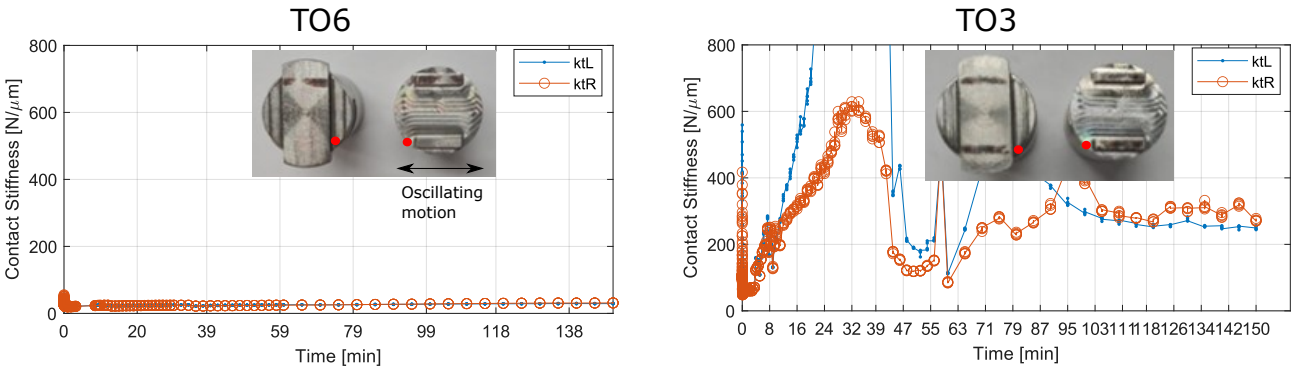


Figure 4.44: Evolution of the tangential contact stiffness of two tests performed on the PoliTO friction rig under the same loading conditions (87 N normal load, 14 μm displacement amplitude, 10 mm^2 nominal area of contact): a) Test n. TO6, k_t is very low because the displacement is measured on the leg not in contact (see red dot); b) Test n. TO3, k_t is larger because the contact is concentrated on the measured leg too. k_{tL} and k_{tR} are the contact stiffnesses of left and right stick portions of the hysteresis loops, as defined in section 3.2.1.

depend on the extension, but also on the spatial distribution of the wear spots in the contact. In fact, in the cases of 5 and 10 mm^2, the worn area is concentrated in the direction of the laser measurement (indicated by the red dots), see e.g. the test TO22 in Fig. 4.45c, which has a fully extended worn area of contact along the laser measurement direction. This concentration along the laser measurement location stiffens the contact in that direction. In the case of 40 mm^2 nominal areas, the worn area is not concentrated along the laser measurement direction, but it is more evenly distributed across the whole interface, and probably for this reason the measured k_t is lower. See e.g. the test TO31, which has an overall larger worn area of contact than test TO22, but only has two small worn circles along the laser measurement direction and could show some pivoting motion around the opposite worn areas with larger contact, similar to the one-leg contact seen before. Finally, Fig. 4.45d shows a test in which a full worn area is also reached for the 40 mm^2 nominal area case. In this case, k_t is still lower at 40 mm^2 probably because, even if it seems that the worn area is now evenly distributed, a closer look at the interface photo of test TO37 reveals that some portions of the worn area at 40 mm^2 are darker than others, indicating that the contact is dominant in some specific zones, and hence is not really uniformly distributed. This last observation suggests that, ideally, the displacement should be measured at different locations to quantify how strongly it varies and, eventually, to average it over the whole contact.

This example confirms again that k_t estimations are strongly dependent on the kinematics of the contacting components and hence on where the interfaces get into contact (namely on their pressure distribution). The importance of the spatial contact distribution, and not only of the overall extension, has been observed experimentally in the pioneering work of Kendall and Tabor [65], who described the effect of the position of contact spots on the k_t estimations (namely that contacts close to each other lead to lower k_t than contact spots further away from each other). The effect of the contact spots spacing has also been modelled numerically [63]. However, to the best of the author's knowledge, such observations are missing in more recent experimental studies despite this being a quite important piece of information, especially to measure and provide more accurate k_t estimations to be used in nonlinear dynamic analysis.

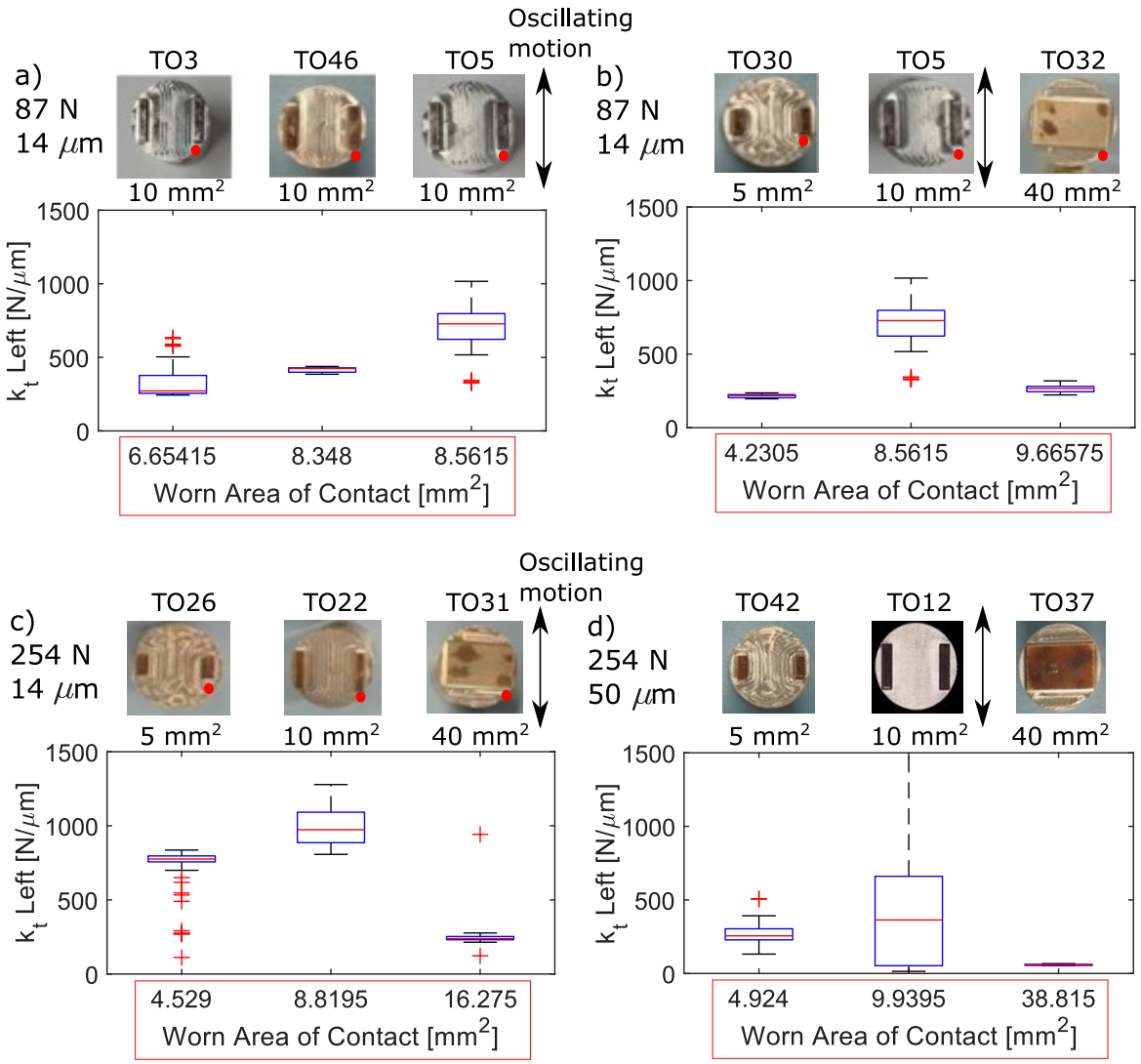


Figure 4.45: Boxplots of the tangential contact stiffness steady state (or end-of-test) values versus the worn areas of contact at the end of the tests on the PoliTO friction rig: a) Tests n. TO3-45-5 performed under the same loading conditions (87 N normal load, 14 μm displacement amplitude, 10 mm^2 nominal area of contact); b) Tests n. TO30-5-32 performed under the same loading conditions (87 N normal load, 14 μm displacement amplitude) and different nominal areas of contact (5, 10 and 40 mm^2); c) Tests n. TO26-22-31 performed under the same loading conditions (254 N normal load, 14 μm displacement amplitude) and different nominal areas of contact (5, 10 and 40 mm^2); d) Tests n. TO42-12-37 performed under the same loading conditions (254 N normal load, 50 μm displacement amplitude) and different nominal areas of contact (5, 10 and 40 mm^2). The red dots represent the location of the laser measurement.

4.3.4 Friction coefficient

The previous section has shown a summary of the k_t steady state values from the PoliTO measurements. This section shows instead the μ steady state values with Fig. 4.46. The Figure only shows results at 14 μm and 24.5 μm and not results at 1 μm displacement amplitude since loops at 1 μm were not in a fully-developed gross slip and therefore the friction limit was not reached. The friction coefficient decreases with increasing normal load, as was already observed in the Imperial tests. The average μ values and relative standard deviations are equal to 1.04

(14.2% std) at 17 N, 0.78 (3.0 % std) at 87 N and 0.75 (6.9% std) at 254 N. This decrease in μ is attributed to the fact that, at larger normal loads, a full established gross slip might not have been achieved within the relatively small investigated displacement amplitudes (14 μm and 50 μm). In addition, at the low 17 N normal load, very high μ values are measured, up to 1.24, probably because the very low normal load does not enable adequate conformity of the contact interfaces and, as a consequence, unstable hysteresis loops are recorded. As an example, Fig. 4.47a-b shows steady state hysteresis loops measured during a test performed under 50 μ displacement amplitude, and 17 N and 254 N normal load respectively. Relatively large oscillations appear in the friction force at 17 N normal load, which probably strongly affect the μ estimation. Instead, the 254 N normal load hysteresis loops are much more stable.

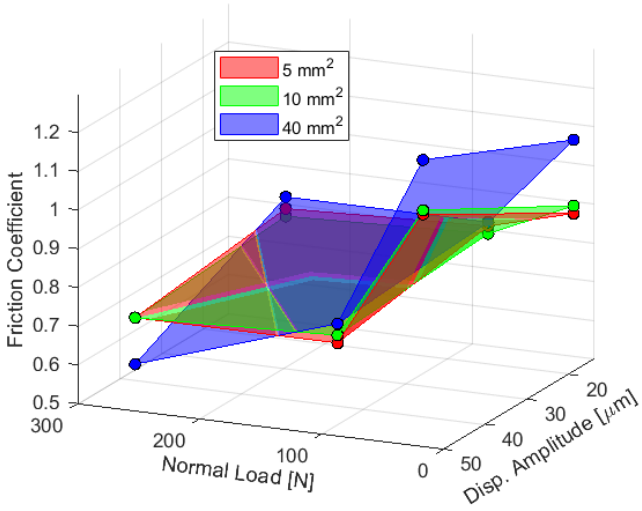


Figure 4.46: Friction coefficient steady state values of the round robin test on the PoliTO friction rig.

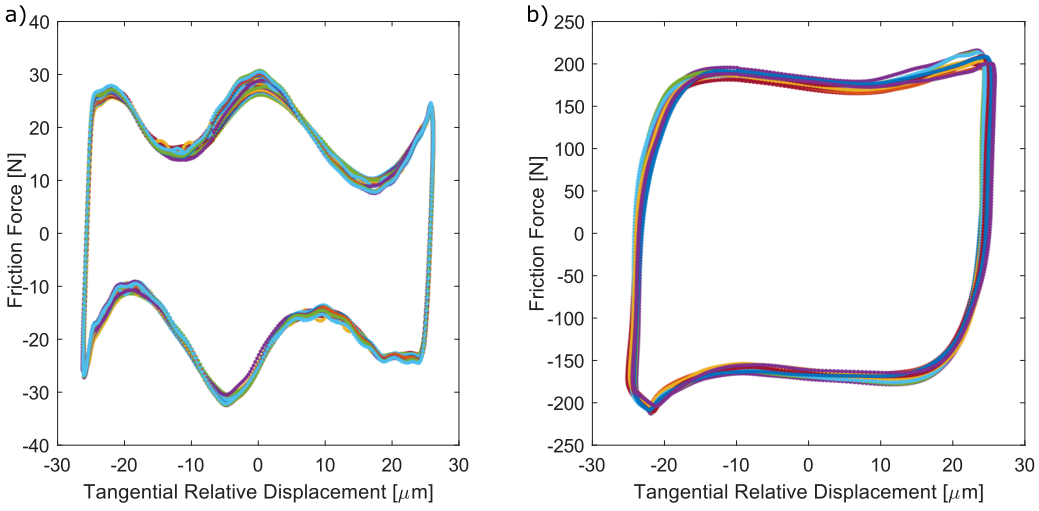


Figure 4.47: Steady state hysteresis loops measured on the PoliTO friction rig under 175 Hz excitation frequency, 50 μm displacement amplitude, room temperature and: a) 17 N normal load (Test n. TO44); b) 254 N normal load (Test n. TO37).

From Fig. 4.46, clear trends instead are not observable with regards to the different displacement amplitudes or nominal areas of contact, and this is in agreement with Imperial tests. The

absence of clear trends suggests that the differences and scatter might only be due to mounting and manufacturing uncertainties, which indeed were quantified to be below 8% in section 4.3.2. Details on the exact steady state μ values and standard deviations are shown in Fig. 4.48 through violin plots, where the normal load dependency is more evident. Also the relative standard deviation of the steady state values within the individual tests is in general below 8% for every test. This variability is slightly higher than the 4% variability observed within the individual Imperial tests.

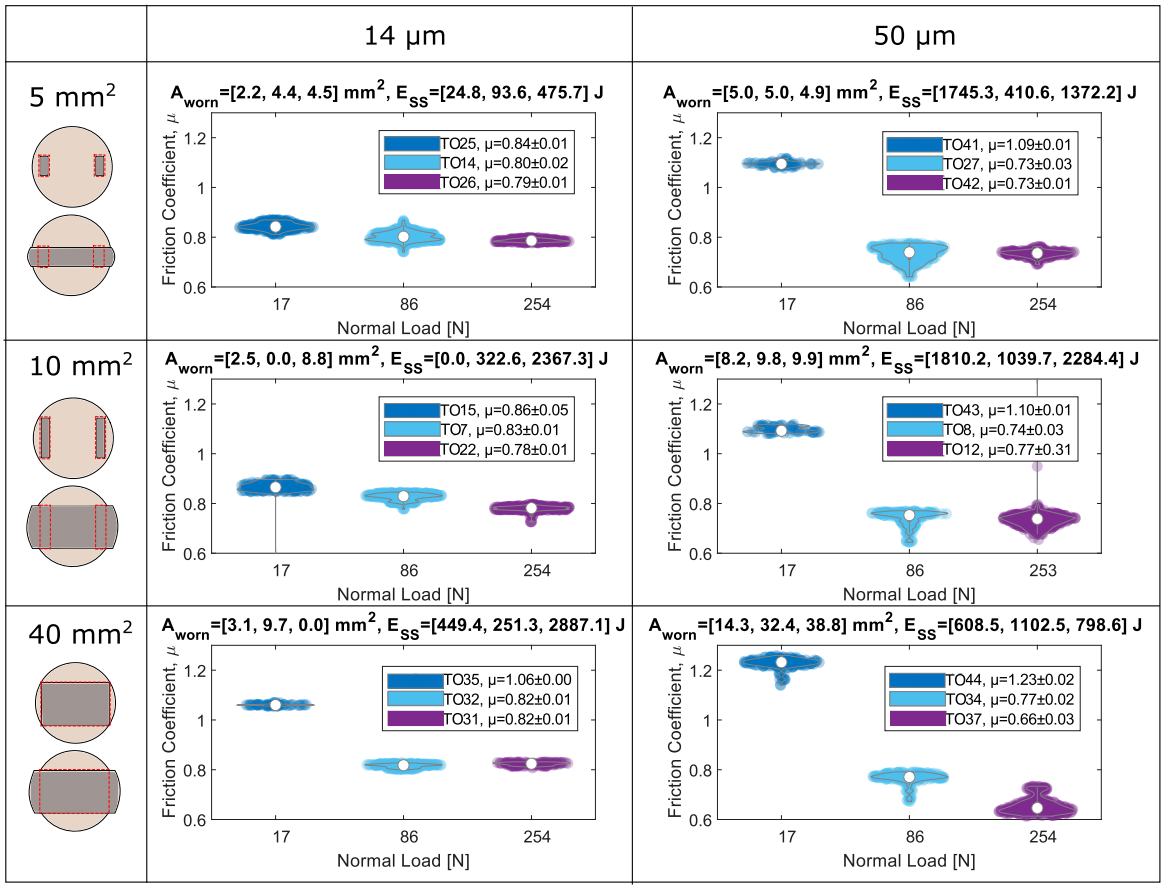


Figure 4.48: Violin plots of the steady state values of the friction coefficient of every round robin test on the PoliTO friction rig. Each violin corresponds to a different test for one normal load, displacement amplitude and nominal area of contact. The legends indicate the mean and standard deviation. The figure titles indicate the worn areas of the three tests and the energy dissipated when the steady state was reached.

Summary of PoliTO hysteresis loop measurements

The round robin experimental measurements performed at PoliTO have confirmed the main trends already observed within Imperial, for example that k_t increases with increasing normal load and it decreases with increasing displacement amplitudes. However, some differences were observed with regards to the k_t evolution with wear:
1) As observed in Imperial tests, k_t increases with wear because of the increase in the worn area of contact. Larger worn areas lead to more asperities and wear scars in contact which contribute to increasing the resistance to elastic deformation. However, it is here found that, in

addition to the extension, also the distribution of the worn area strongly affects the value of the contact stiffness by changing the kinematics of the contacting components. This indicates how important is the choice of the laser measurement locations for k_t estimations. The displacement needs to be measured as close as possible to the actual spots of contact and, therefore, smaller and single-patch contacts might provide more reliable measurements. These effects should also be captured accurately in Finite Element models by choosing, for example, appropriate and accurate pressure distributions in the contact.
2) In stick tests performed at 1 μm displacement amplitude, a running-in increase in k_t is observed although a worn area is not visible. It is hypothesized that the increase in k_t is due to a plasticity hardening process occurring at the asperities, which dissipate some energy during the microslip loading and unloading cycles. In fact, stick loops of PoliTO dissipate a small amount of energy due to microslip, on the contrary to the stick loops of Imperial, which are fully stuck and do not dissipate any energy nor show any running-in increases in k_t.

With regards to the friction coefficient, it is confirmed that μ seems to not be affected by the loading conditions, except a decrease with increasing normal loads. Also in PoliTO tests, μ increases quickly at the beginning of the test, within the first hundreds of cycles, from very low values around 0.1 to larger steady state values around 0.84.

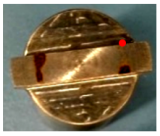
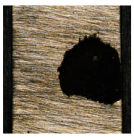
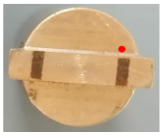
4.4 Comparison of results from the two friction rigs

This section compares results obtained from the two friction rigs, discussing matches and differences. To this purpose, Table 4.49 shows the end-of-test values for both Imperial and PoliTO tests performed under the same loading conditions and same nominal areas of contact. First, k_t and μ results are discussed and then the two rig designs are compared.

Tangential contact stiffness

Table 4.49 shows that tests conducted at 1 μm of displacement amplitude and 17 N normal load led to very similar and low k_t values, below 30 N/μm, at Imperial and PoliTO for both the nominal areas of 5 and 10 mm^2. For the 87 N case and 1 μm displacement amplitude, results are in general close, below 45 N/mum, except for the Test TO10 performed at 10 mm^2, whose k_t value is extremely large, 578 N/μm. The reason for this behaviour has already been described in section 4.3.1 with Fig. 4.37. The increase is due to a plasticity hardening process occurring at the asperities, which dissipate some energy during the microslip loading and unloading cycles (22 J much larger than the 0 J in the other stick tests). This microslip did not appear in Imperial fully-stuck hysteresis loops, whose very low initial k_t values were not large enough to give rise to microslip. It is concluded that stick tests performed at 1 μm displacement amplitude are very comparable between Imperial and PoliTO, except in cases where microslip is present, which leads to the energy dissipated with consequent increases in the k_t values. As a result, it is suggested to maintain displacement amplitudes as small as possible when measuring stuck hysteresis loops to avoid any potential microslip that may lead to an increase in stiffness due to plastic hardening.

With regards to tests performed at 14 μm of displacement amplitude, k_t values from the PoliTO rig are always larger than those from the Imperial rig. The difference is more evident in tests

A_{nom}=5 mm²	17 N		87 N	
	IC	PoliTO	IC	PoliTO
1 µm	Test IC28 k_t=17 N/µm, E_{kt}=0.0 J No worn area	Test TO28 k_t=14 N/µm, E_{kt}=0.0 J No worn area	Test IC30 k_t=42 N/µm, E_{kt}=0.2 J No worn area	Test TO19 k_t=24 N/µm, E_{kt}=0.1 J No worn area
14 µm	Test IC29 µ=0.79, E_μ=8 J k_t=31 N/µm, E_{kt}=76 J A_{worn}=0.9 mm² k_{norm}= 34 N/µm/mm² 	Test TO25 µ=0.84, E_μ=25 J k_t=40 N/µm, E_{kt}=200 J A_{worn}=2.2 mm² k_{norm}= 33 N/µm/mm² 	Test IC25 µ=0.75, E_μ=91 J k_t=58 N/µm, E_{kt}=1014 J A_{worn}=1.3 mm² k_{norm}=44 N/µm/mm² 	Test TO14 µ=0.80, E_μ=94 J k_t=490 N/µm, E_{kt}=907 J A_{worn}=4.4 mm² k_{norm}= 111 N/µm/mm² 

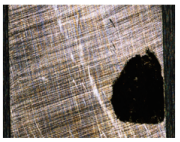
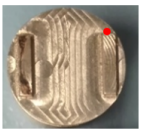
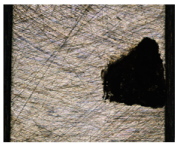
A_{nom}=10 mm²	17 N		87 N	
	IC	PoliTO	IC	PoliTO
1 µm	Test IC17 k_t=16 N/µm, E_{kt}=0.0 J No worn area	Test TO24 k_t=27 N/µm, E_{kt}=1.4 J No worn area	Test IC23 k_t=39 N/µm, E_{kt}=0.0 J No worn area	Test TO10 k_t=578 N/µm, E_{kt}=22 J No worn area
14 µm	Test IC22 µ=0.75, E_μ=5 J k_t=31 N/µm, E_{kt}=59 J A_{worn}=1.2 mm² k_{norm}= 26 N/µm/mm² 	Test TO15 µ=0.86, E_μ=N/A k_t=44 N/µm, E_{kt}=N/A A_{worn}=2.5 mm² k_{norm}=18 N/µm/mm² 	Test IC15 µ=0.73, E_μ=141 J k_t=63 N/µm, E_{kt}=1077 J A_{worn}=1.1 mm² k_{norm}=57 N/µm/mm² 	Test TO07 µ=0.83, E_μ=322 J k_t=531 N/µm, E_{kt}=1665 J A_{worn}=7.6 mm² k_{norm}=70 N/µm/mm² 

Figure 4.49: Steady state (or end-of-test) values for the 5 and 10 mm² nominal areas of contact. μ values refer to the standard friction coefficient and k_t values refer to the tangential contact stiffness of the left part of the hysteresis loops. The energy indicates the energy dissipated when a steady state in the contact parameter was reached. The worn areas of contact at the end of tests performed at 14 μm of displacement amplitude are also shown (red dots indicate the laser measurement location).

performed at 87 N normal load, in which the PoliTO k_t is even one order of magnitude higher than the Imperial k_t (for both nominal areas of contact). This mainly occurs because those values are not normalized by the worn area of contact, which indeed in PoliTO tests is much larger. After the normalization, K_T values become comparable, reaching the same order of magnitude with differences below 70%. This mismatch is reasonably acceptable considering that the two friction rigs have quite different designs and considering the inherent k_t measurement uncertainties, which have been previously quantified to be in the range of 25% for Imperial and 60% for PoliTO[6].

To further quantify the normal load dependency, Fig. 4.50a shows the worn area normalised K_T versus the normal load normalised by the worn area. Most of the PoliTO tests follow the trends of the Imperial tests, except a few tests that show much larger values. The large discrepancy

[6]Note that the scatter of PoliTO tests is higher mainly because the k_t estimations resulting from the wider worn areas of contact are larger than 300 N/μm. Above this value, issues appear in the displacement measurement and post-processing due to the very low relative displacements in the stick portion of the hysteresis loops. To reduce this scatter, smaller nominal areas should be used that lead to smaller, and easier to measure, k_t.

is probably due to the following reasons:

- As previously mentioned, un-normalised stiffness values above 300 N/μm are unreliable since even minimal changes in the measured displacement lead to major changes in the k_t estimated from the force-displacement slope (see e.g. Fig. 4.35, where a steep change in the estimated k_t is observed in the middle of the test purely due to post-processing). Indeed, the four outliers of Fig. 4.50a resulted from un-normalised k_t values above 500 N/μm (see Fig. 4.50c), which are unreliable due to displacement measurement and post-processing issues.
- PoliTO k_t estimations are expected to be slightly larger because of the different contact surface topographies with respect to Imperial specimens. Imperial specimen interfaces have a slight curvature that increases the compliance, while PoliTO specimens are flatter and, thus, expected to be stiffer.

This difference in the normalised K_T values gives an idea of the amount of uncertainty that different experimental setup and surface topographies can introduce into tests performed under the same loading conditions. This and other trends in the k_t are summarised in section 4.4.1, which provides clear guidelines and specific contact laws to be used for modelling contact interfaces in nonlinear dynamic analysis of jointed structures.

Friction coefficient

Figure 4.51 shows a comparison of the steady state μ estimations from Imperial and PoliTO rigs plotted versus the normal load. The Figure shows a decreasing trend of μ with respect to the normal load. The reason for this observed decrease is not clear yet and could be attributed to the fact that, at larger normal loads, a full established gross slip could have been not achieved within the relatively small investigated displacement amplitudes (14 μm and 50 μm). In addition, measurements at the lowest 17 N normal loads are in general less reliable, as shown with the chattering phenomenon previously described in section 4.2.2 or the unstable hysteresis loops of Fig. 4.47a. This lower reliability might also explain the large scatter shown in Fig. 4.51 between PoliTO and Imperial values at 17 N. The PoliTO μ values measured at 17 N normal load are quite large, up to 1.24, if compared to the Imperial 0.77 average μ at 17 N normal load. This relatively large difference of 35% is not attributable to the repeatability of the measurements, whose uncertainty was quantified to be below 4% for Imperial tests and below 8% for PoliTO tests performed under the same loading conditions. Instead, it is attributed to the very low conformity enabled by such low loading. In addition, at low normal loads, some inaccuracies might also appear in the normal load measurement. While the normal load is easy to check in the PoliTO rig since it is applied employing dead weights of known mass, in the case of the Imperial rig it is applied by means of a pneumatic actuator and measured with a strain gauge load cell. The strain gauge load cell could be inaccurate at low normal loads and this could be another reason for the observed differences. For all of the above reasons, it is concluded that measurements of the friction coefficient should be performed at normal loads large enough to guarantee adequate conformity that does not lead to separation phenomena, such as chattering and other instability effects.

With regards to the different displacement amplitudes and nominal areas of contact, trends are less clear, suggesting that these parameters do not affect μ estimations to a large extent.

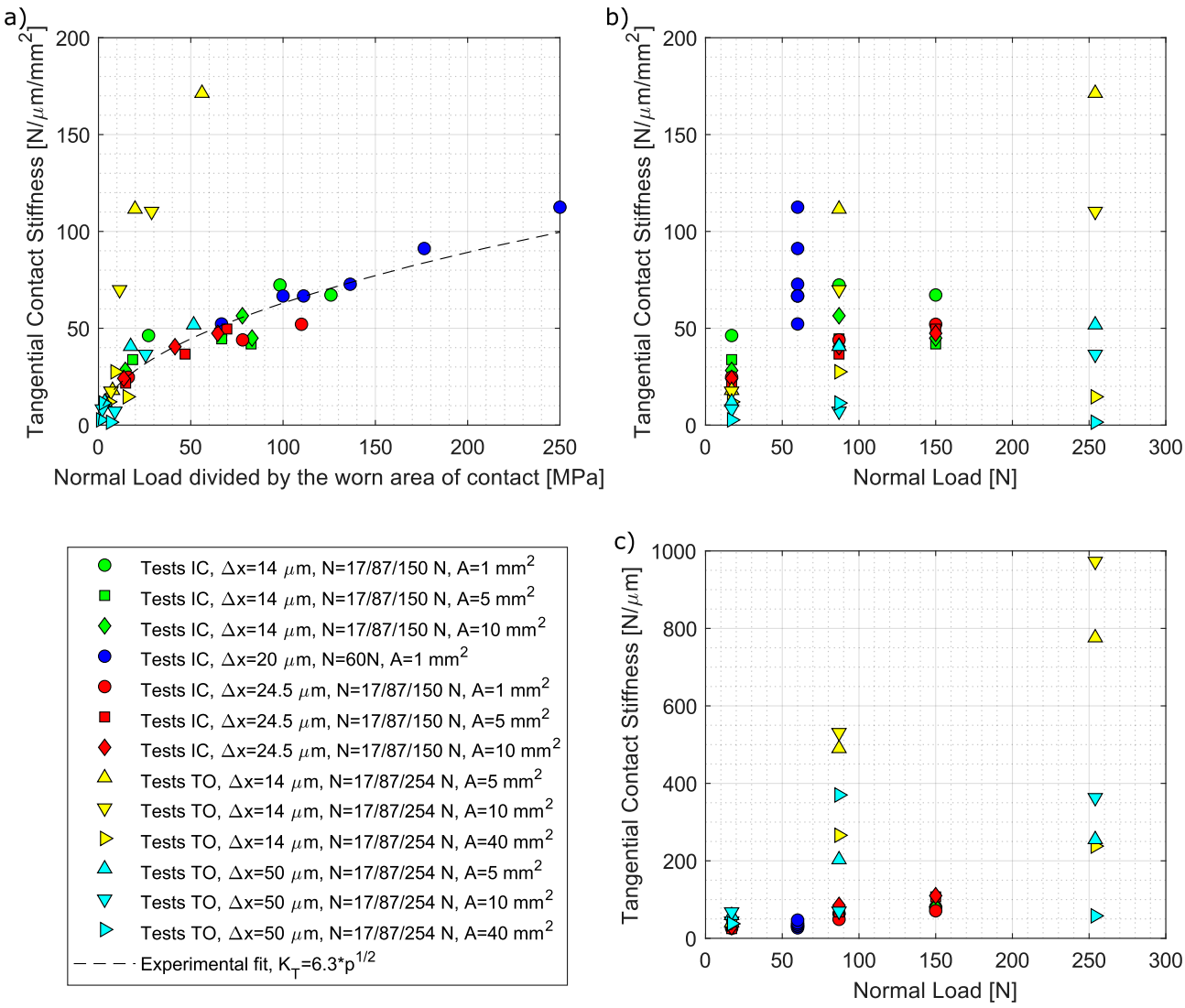


Figure 4.50: Tangential contact stiffness steady state values. Each point in the Figure corresponds to a different test of the round robin matrix with a different worn area of contact: a) Worn area normalised K_T versus contact pressure (normal load divided by the worn area). Note that, although some tests were performed with the same normal load, they have different contact pressures due to their different worn areas. The experimental fit on the Imperial tests is also shown (see Eq. 4.1); b) Worn area normalised K_T versus normal load; c) Un-normalised k_t versus normal load.

Finally, with regards to the evolution with wear, it was observed that the energy dissipated to reach a steady state was in general comparable between Imperial and PoliTO, although steady states were reached slower in tests performed at larger normal loads than in tests performed at lower normal loads. A possible hypothesis for this behaviour is that, at lower normal loads, the wear particles of the original oxide layer are ejected more easily from the contact.

Effect of rigs' design differences

Measured values of both μ and k_t show some differences between the two rigs. However, these differences are acceptable considering that the two friction rigs show some fundamental design

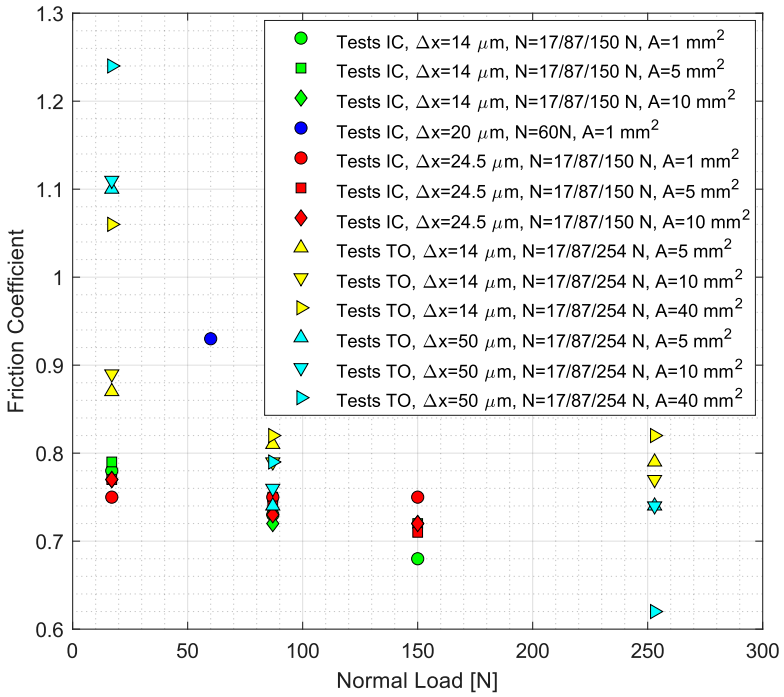


Figure 4.51: Friction coefficient steady state values plotted versus the normal load. Each point in the Figure corresponds to a different test of the round robin matrix.

differences, namely the self-alignment vs rigid alignment and the one-leg contact vs two-leg contact, which are described as follows:

Contact approach, i.e. self-alignment vs rigid alignment:
The two contact approaches employed in the two rigs present different advantages and disadvantages in terms of reliability and repeatability of the results. In the PoliTO rig, more variety of behaviour in the different tests was observed because the rig employed the self-alignment system that strongly depended on the contact surface topography and also because larger nominal areas were used, leading in some experiments to different spots for the initial contact and, consequently, to different distributions of the worn area of contact. This variability made it possible to gain insights into the kinematic dependency of the contact stiffness since different worn areas could be observed. Different spots of contact (i.e. different pressure distributions) led to different kinematic behaviour of the contacting components with consequent different k_t estimations. On the contrary, the Imperial specimens were rigidly fixed with slightly curved contact interfaces, and this allowed for better repeatability of the experiments, with similar worn areas of contact achieved after each test. However, because of this rigidity, the Imperial rig could not employ large areas of contact, because there would have been a larger risk of "edge contact" in the case of slightly inclined interfaces, which could not self-align properly. Instead, full worn areas were easily reached in the PoliTO rig as a result of the self-alignment, even with very large 40 mm^2 areas, while in the Imperial rig full worn area could be reached only for the smallest nominal area of contact of 1 mm^2 for the given 2.5 hours test length. In conclusion, the choice of whether to use a rigid or self-aligning system depends on the purpose of the test. If more repeatable tests are required, a rigid setup is preferable, at the cost of only testing smaller areas of contact and requiring larger testing times. Instead, if more complex and large interfaces are to be tested, a self-aligning system is to be used since it offers much higher flexibility to test.

Contact geometry, i.e. one-leg vs two-leg contact:
Two legs are required with a self-aligning system, to avoid tilting. In fact, with a single leg contact, the specimen would tilt unless rigidly fixed. The two-leg design might lead to setup and measurement challenges since the contact is prone to uneven load distribution on the two legs if not mounted accurately. In addition, different results can be obtained depending on which leg is measured and which leg is moving more. Consequently, great care is required during setup for this type of specimen, and some improvements in the displacement measurements may need to be considered to overcome the dependency on the measurement location. The one-leg setup is instead easier for mounting and leads to more repeatable results, although limitations exist on the size and topography of the tested interfaces.

4.4.1 Guidelines for providing accurate input contact parameters for nonlinear dynamic analysis of jointed structures

Values to be used in nonlinear dynamic analysis for steel on steel contacts are summarised in Table 4.4 based on the average between Imperial and PoliTO results. Those values were obtained for the following loading conditions: excitation frequency range 100-175 Hz, room temperature, displacement amplitudes below 50 μm, contact pressures below 250 MPa. The nominal areas of contact were below the 40 mm^2 either in a flat-on-flat arrangement or in a quasi-flat arrangement with relatively large curvatures, above 30 mm, if compared to the average contact width, which instead was in the order of the 2 mm. Based on the several insights gained within the round robin test, guidelines are provided in the following paragraphs for the use of μ and k_t as input for the nonlinear dynamic analysis of jointed structures.

Note that only room temperature was considered in this round robin in order to simplify the analysis of the results and reduce the complexity of the observed phenomena. However, turbomachinery components experience much higher temperatures (above 700 °C) and new physics could occur in those conditions. Measurements should be performed in future at higher temperatures to verify how the physics of the contact changes and, eventually, upgrade the contact laws accordingly since some of the uncovered effects might not be relevant at higher temperatures.

Table 4.4: μ and K_T values to be used in nonlinear dynamic analysis for steel on steel contacts plus uncertainty bands. p [MPa] is the normal load divided by the worn area of contact. Also K_T [N/μm/mm^2] is normalised by the worn area of contact. See Figs. 4.50 and 4.51 for the supporting data. See section 7.1 for the numerical modelling.

	Stuck/microslip loops	**Loops with gross slip**
K_T [N/μm/mm^2]	$31.5\sqrt{p}\pm11\sqrt{p}$	$6.3\sqrt{p}\pm2.2\sqrt{p}$
μ	0.79±0.06	0.79±0.06

Tangential contact stiffness:

- k_t has to be normalised by the worn area of contact (see sections 4.2.1, 4.2.3, 4.2.3, 4.3.3 and Fig. 4.50) rather than the nominal area of contact, as instead commonly

done in the structural dynamics community. The normalisation by the worn area of contact also requires the modelling of the evolution of the contact interfaces with wear. Some prelminiary studies exist in the literature that implemented the wear evolution in nonlinear dynamic analysis, see e.g. [141, 143], where the contact stiffness is updated as wear changes the contact interfaces.

- The normalised k_t, here named K_T, increases with increasing normal load (see sections 4.2.3, 4.3.3 and Fig. 4.50) and it reduces with increasing displacement amplitude (see sections 4.2.3 and 4.3.3). Both normal load and displacement amplitude dependency should be included in nonlinear dynamic analysis according to the laws summarised in Table 4.4. The displacement dependency can be included, in a first approximation, by considering K_T values in fully stuck loops 5 times larger than the K_T in loops with gross slip. The nonlinear dynamic solver should be able to switch between the two cases depending on the existence of gross slip or not. Since this approach might cause convergence issues, numerical analyses should be performed to test its feasibility. Note that values from Eq. 4.1 are considered as values for loops with gross slip and therefore they should be multiplied by 5 to get the contact stiffness of stuck loops.

- k_t is not only dependent on the extension of the worn area, but also on the distribution of the worn area over the contact (see section 4.3.3). A worn area distributed in a certain direction stiffens the contact when it moves in that direction mainly, and not in other directions. As a result, it is important to accurately choose the most representative laser measurement locations during experiments for reliable k_t estimations. Since the contact behaviour depends on where the interfaces get into contact, it consequently depends strongly on the pressure distribution. To account for this effect in nonlinear dynamic analysis, it is of high importance to accurately model the pressure distribution that is expected in the investigated structure. Depending on the pressure distribution, the k_t values will change according to Eq. 4.1 and, consequently, also the kinematic and vibrational behaviour of the contacting components will change. The pressure distribution can be obtained in different ways:

  - It can be predicted by numerical FE models, but only if the topographies of the contacting interfaces are realistically modelled. This requires the contact interfaces to be scanned with microscopes before the structure is assembled.
  - The pressure distribution can also be measured experimentally, for example with pressure films, which have to be placed between the two contacting structures.

- Measurements on the individual rigs for the same loading conditions show an uncertainty below 25% at Imperial (see section 4.2.2) and below 60% at PoliTO (see section 4.3.2). When normalised by the worn area, K_T shows reasonably similar values in both rigs, with differences below the 70% (see Fig. 4.49). These differences are due to the inherent experimental uncertainty and to the fact that the contact surface topography of Imperial and PoliTO specimens is slightly different. To account for the experimental uncertainty, it is suggested to run at least two sets of simulations with two k_t values differing by 70% within the investigated range.

- In stick regime conditions, a running-in increase in k_t is observed in PoliTO tests, although a worn area is not visible (see section 4.3.1). It was hypothesized that this increase in k_t, not due to the worn area of contact, is instead due to a plasticity hardening process occurring at the asperities since the stick loops of PoliTO dissipate energy due to the

presence of microslip despite the small displacement amplitudes. This increase with the energy dissipated during microslip can be accounted for by using contact models that include also microslip and not only the stick and gross slip conditions.

- A final comment is given on the normal contact stiffness k_n, which has not been investigated within this analysis. At a first approximation, it can be considered to be 1.25 times larger than the k_t, according to the Mindlin ratio defined by contact mechanics [63]. Future studies will be performed on the friction rig to also study this parameter, by measuring the relative normal displacements with the Digital Image Correlation technique, as briefly discussed in the Appendix B.

Friction coefficient:

- μ is very low (around 0.1) when the interfaces get into contact for the first time (see sections 4.2.1 and 4.3.1). As vibration begins, μ rapidly increases at the beginning of the test probably due to the removal of oxide layers, as already known in past literature. This aspect should be considered for the analysis of newly assembled structures, which will have very low friction coefficient values when their contact establishes for the first time. After a few runs, the friction coefficient will stabilise to an average value of 0.79. This reference value is valid for a stainless steel contact within the loading ranges analysed, namely 100-175 Hz excitation frequency at room temperature, 14-50 μm displacement amplitudes and 17-254 N normal loads corresponding to 5-125 MPa for the observed worn areas of contact.

- μ is mostly unaffected by the loading conditions, except for a slight normal load dependency (see sections 4.2.4, 4.3.4 and Fig. 4.51). It decreases by up to 15% with increasing normal loads. Since the reasons of this observed decrease are not clear yet, more tests should be performed in the future, under different loading conditions, to verify this trend.

- Measurements on the individual rigs for the same loading conditions are quite repeatable, uncertainty below 4% at Imperial (see section 4.2.2) and below 8% at PoliTO (see section 4.3.2). The PoliTO rig provides larger values than Imperial (on average 15% larger). This mismatch is probably due to inaccuracies in the normal load measurement in the rigs and should be a focus for any future improvements of the rigs. To account for the experimental uncertainty, it is suggested to run at least two sets of simulations with two μ values differing by 15% within the investigated range.

Guidelines for the use of the friction rigs and design of experiments:

- Scan the contact interfaces before and after the experiments with microscopes. Scans before the experiments provide information on the contact surface topographies, which are needed to predict the pressure distribution at the beginning of the tests. Interface scans at the end of the tests are required to measure the extension of the worn area of contact, which is needed to normalise the contact stiffness during the post-processing. If interface scans cannot be acquired at the end of the test, the test should be run long enough so that the full nominal area is worn, and the k_t can be normalised by the nominal area.

- A test length of a least 1.5 hours is required to reach (or at least approach) steady states in the measured hysteresis loops. This length is valid for experiments performed at excitation frequencies in the range of 100-200 Hz, displacement amplitudes larger than 14 μm and nominal areas below 40 mm^2.

- Hysteresis loops should be continuously recorded at the beginning of the test since significant changes occur in the first 10 seconds of the tests. After the first minutes, a lower recording rate can be adopted, since hysteresis loops will be more stable.

- Normal loads below 17 N lead to the chattering phenomenon if hysteresis loops are measured at excitation frequencies above 100 Hz and if one of the contacting components is particularly rigid. It is not suggested to perform measurements with such low normal loads if accurate input contact parameters estimations are needed for nonlinear dynamic analysis.

- A wide range of nominal areas was investigated, from 1 mm^2 up to 40 mm^2, to understand which experimental input values are best suited for nonlinear dynamic analysis. Based on the results shown in this chapter, the answer depends on the accuracy employed in the numerical simulation. If the Finite Element (FE) model is realistic and it accurately captures the real topography of the interface (i.e. its roughness, waviness and form), the pressure distributions will be well known from the FE predictions. By knowing the exact pressure distributions, accurate k_t estimations can be provided by performing simpler and more repeatable 1 mm^2 experiments with a rigid contact approach, at the required pressures. However, if the interface is numerically modelled as nominally flat with a simpler and not representative FE, it won't be possible to predict from the simple FE a realistic pressure distribution. Hence, experiments with larger areas of contact (of the same size as the investigated area and with similar surface topography) would be required to know beforehand the realistic pressure distribution. For larger areas, a self-aligning experimental setup is preferred, as already discussed in the previous sections.

  Note that, with larger areas of contact, also the k_t estimations will be larger. For values of k_t above 300 N/μm, issues appear in the displacement measurement and post-processing due to the very low relative displacements in the stick portion of the hysteresis loop. To reduce this scatter, smaller nominal areas should be used that lead to smaller, and easier to measure, k_t.

- The significant effect of the contact surface topography on the pressure distribution suggests that particular care should be taken in ensuring that contact interfaces are manufactured according to specifications. Geometric tolerances should be accurately specified in the technical drawings used to manufacture the components to be tested. An important tolerance parameter is the flatness of the contacting interfaces. The flatness is defined in the Geometric Dimensioning and Tolerancing (GD&T) standards [265] as the distance between two sets of parallel planes where the entire referenced surface must lie, expressed in mm. Therefore a flatness of 0.005 indicates that the whole interface should lie within two planes 5 μm apart. Note that the smallest flatness value defined in the standard ISO 2768 general tolerance specification is 0.02 [266], which corresponds to a 20 μm distance in the planes. This flatness definition would not be acceptable for the much more precise interface conditions required in this round robin test, which require even tighter values to guarantee a uniform pressure distribution at the beginning of the test. This relatively large flatness value defined in the standard tolerance specifications suggests that designers

should be aware of possible unwanted bumps and wavinesses in critical contact interfaces expected to be nominally flat during operation.

4.5 Conclusions

A round robin test campaign was performed on the high-frequency friction rigs at Imperial College London and Politecnico di Torino. The aim was to increase the confidence in the measurement of contact interface parameters used as input for nonlinear dynamic analysis of jointed structures. To this purpose, a test plan was designed to cover a wide experimental space by testing the friction rigs to their limits and measuring a multitude of hysteresis loops under a range of loading conditions at room temperature. Specimens had comparable sizes in nominal contact areas and were manufactured from the same batch of raw stainless steel.

Values of friction coefficient, μ, and tangential contact stiffness, k_t, were extracted and compared. Although the two friction rigs presented fundamental design differences, they provided similar values in the measurements. Measured μ agreed well, with differences below the 15%, probably coming from some uncertainty in the normal load measurements and specimen assembly procedures. Values of k_t were of the same order of magnitude, although showed discrepancies up to 70%. These differences were due to the inherent experimental uncertainty and to the fact that the contact surface topographies of the specimens of the two rigs were slightly different. To account for the experimental uncertainty, it is suggested to run at least two sets of simulations with two k_t values differing by 70% within the investigated range.

Measurements also demonstrated that the loading conditions strongly affect the interface contact states, namely stick, microslip and gross slip, and their effects must be included in nonlinear dynamic simulations for more reliable predictions. It was shown that k_t slowly increases during the test because of an increase in the worn area of contact. It is consequently necessary to normalise it by the worn area of contact, rather than by the nominal area of contact as often suggested in the literature. The normalised k_t, here named K_T, also increases with increasing normal loads, in agreement with previous studies that already showed how this is ultimately due to an increase in the number and size of the individual contact regions. Additionally, it is also found that K_T, evaluated right after the load reversal, is much lower in hysteresis loops with gross slip compared to fully stuck hysteresis loops at lower displacement amplitudes. This decrease in loops with gross slip is here attributed to a velocity dependence, which is induced by a reduced time for the ageing of the asperity contacts at higher velocities. The friction coefficient did not show a clear dependency on the loading conditions, except for a light decreasing dependency for increasing normal loads. Based on those findings, current contact models used for the nonlinear dynamic analysis of jointed structures should be updated to include the following effects:

- Worn area dependency of k_t by providing as input in contact models the normalised K_T values, but also including the evolution of the worn areas of contact in simulations.
- Normal load dependency of K_T by potentially including a square root dependency on the normal load divided by the worn area of contact;
- Displacement amplitude dependency (more exactly velocity dependency) of K_T by using fivefold higher K_T values in fully stuck loops than in hysteresis loops with gross slip;

- Include more accurate and realistic contact pressure distributions since those strongly affect the kinematics of the contacting components. This effect is often overlooked in current practices for nonlinear dynamic analysis.

Note that those guidelines are valid for stainless steel specimens tested at room temperature. More work is required in future to expand the test range of the round robin test and generalise the findings. Nevertheless, the results and guidelines presented in this chapter lay the basis for an improved understanding of contact, friction and wear, and provide useful information to develop more reliable contact models to be used in dynamic simulations. The author would also encourage other research groups to participate in this comparative study. By adding a further dataset, the statistical significance of the presented data can be increased. The addition of more friction rigs would show how measurements change with a different setup. For example, further investigations could be performed to quantify the effect of the distribution and size of worn areas of contact and, hence, to better understand how different contact surface topographies and pressure distributions affect the measurements. These and more measurements would eventually validate the proposed hypotheses and increase the confidence in measured contact parameters used as input for nonlinear dynamic analysis.

Chapter 5

Monitoring frictional hysteresis with the ultrasound technique

The previous chapter has presented a large range of friction hysteresis measurements and improved the physical understanding of the contact parameters used as input in contact models for nonlinear dynamic analysis. The main shortcoming of those measurements is that they only provide one-dimensional information from the outer edge of the contact interface, without providing any insight into the behaviour of the central part of the contact. The information on the central part of the contact is of importance for further validation of the contact models used for nonlinear dynamic analysis. These models can predict exactly what happens inside the contact by means of a very accurate discretisation of the interface. However since it is challenging to experimentally access the interface during vibration, predictions are usually only validated via global nonlinear vibration response measurements that are performed far from the contact. This experimental validation approach is not adequate when more detailed information on the contact is needed, for example for local contact predictions, wear or optimisation of interfaces. Experimental techniques are therefore needed to provide the missing validation data from the central part of vibrating contact interfaces.

In this chapter, the ultrasound technique is used to characterise the contact interfaces during vibration cycles to provide the required validation data. To this purpose, previously developed specimens are used that include ultrasonic transducers in their designs. The high-frequency friction rig is then used to enable a novel experimental method consisting of simultaneously acquiring ultrasonic measurements and friction hysteresis loops within the same test on the same contact interface. Large variability in the ultrasound reflection/transmission is observed within each hysteresis loop and is associated with stick/slip transitions, supported by numerical simulations of the ultrasonic wave propagation within the material. The measurement results reveal that the ultrasound technique can be used to detect stick and slip states in contact interfaces subjected to high-frequency shear vibration. This is the first observation of this type and paves the way towards real-time monitoring of vibrating contact interfaces in jointed structures, leading to a new physical understanding of the contact states and new validation data needed for improved nonlinear dynamic analysis. This research resulted in the following two publications in the journals Experimental Mechanics [201] and Mechanical Systems and Signal Processing [263], and in the awards of the first price in the 2020 “Young Stress Analyst Competition” by the British Society for Strain Measurement and the “Innovation in Tribology 2021 Award” by the Institute of Physics.

5.1 Experimental setup with ultrasound

The friction rig that measures hysteresis loops has been described in detail in chapter 3. Here, rig upgrades are shown that enable the simultaneous recording of ultrasonic measurements. Information on the physics of ultrasound has been given in section 2.5.2. 304 stainless steel specimens have been designed in a previous research [201] to accommodate a shear transducer (NOLIAC CSAP02) that generates and receives shear waves. Shear waves were preferred over longitudinal waves to enable a more accurate comparison with hysteresis loop measurements since shear waves provide tangential contact stiffness estimations, while longitudinal waves provide normal contact stiffness estimations. Here, these specimens are reused for the novel ultrasonic experimental campaign. The specimen is shown in Fig. 5.1 and consists of a 28 mm long cylindrical holder, with a 10 mm diameter, coupled with a threaded head on which the shear transducer is glued by using a two-parts Loctite Double Bubble epoxy resin capable of shear strength of 9 MPa. The specimen interface is nominally flat and is obtained by carefully hand polishing with two different grades of sandpaper: first, 800 grit for coarse and bulk material removal and then, 2500 grit for smooth and finer surface finish, leading to a final roughness value Ra of about 0.5 μm. The contact interface is 3 mm wide and approximately 10 mm long, and the two mating specimens are rotated by 90° to each other, hence obtaining a 3 by 3 mm square nominal area of contact as shown in Fig. 5.1c. The ultrasonic transducer has an area of 25 mm^2 that is larger than the area of the contact interface (9 mm^2), thus ensuring that the whole contact area is insonified with ultrasonic energy. The effects of this area mismatch need to be taken into account for the correct estimation of the reflection coefficient R at the interface, which is required as input in Eq. 2.13 to obtain the tangential contact stiffness. This was done via numerical simulations, as described in the Appendix D.

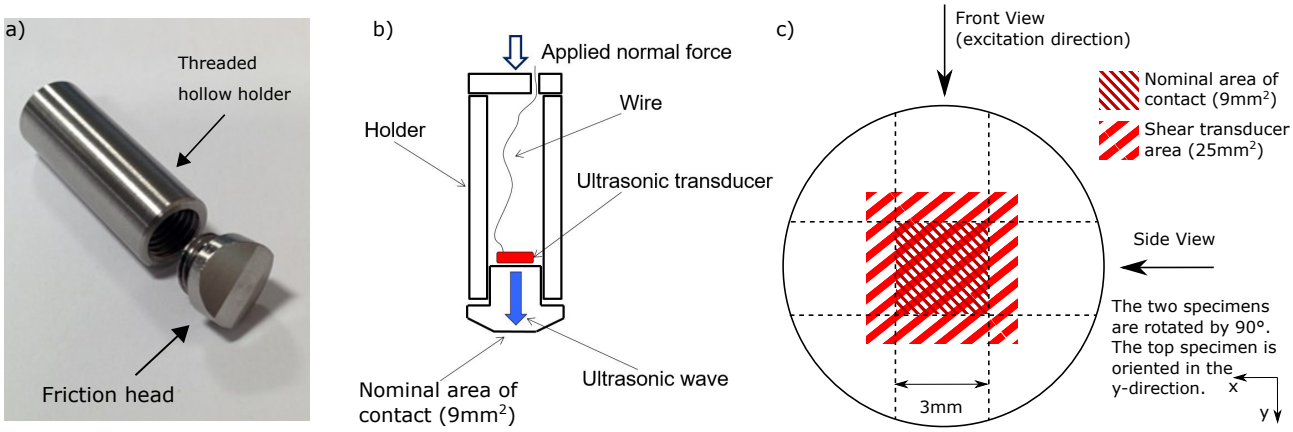


Figure 5.1: Specimen designed to accommodate an ultrasonic transducer: a) Photo; b) Scheme; c) Specimens' top view. Shear waves are polarized in the y-direction [263].

The experimental setup is schematically shown in Fig. 5.2a. Ultrasonic shear waves are sent to the contact interface by exciting a transmitting and receiving piezoelectric patch labelled T/R#1, which is installed on the moving specimen and operates in pulse-echo mode (i.e. signal sent and received by the same transducer). This transducer is paired with the second receiving patch labelled R#2, which is installed on the static specimen and acts only as a receiver, hence working in a pitch-catch mode (i.e. signal sent from a transducer and received by another). This setup allows for the simultaneous measurement of both reflection and transmission of the ultrasound signal amplitude across the frictional interface. The transducer T/R#1 needs an

input voltage signal to generate shear waves. The voltage signal is generated by the arbitrary function generator of a Handyscope HS5 (TiePie Engineering) which is amplified by an in-house linear 10x drive amplifier. The transducer generates a shear wave that travels from the top of the moving specimen down to the contact interface. When the wave reaches the interface, a portion of its energy is reflected back to the T/R#1 transducer, which also acts as a receiver, and a portion is transmitted to the R#2 transducer.

A typical signal recorded by the first transducer is shown in Fig. 5.2b. The handyscope generates a 3-cycle Hann windowed burst at 2 MHz (the resonance frequency of the transducer). After being generated and amplified, the burst is sent to the T/R#1 transducer. The first reflection from the contact interface arrives after 6 μs, and the second, much weaker, reflection is also seen after further 6 μs. This travel time depends on the length of the path between transducer and contact interface, and on the shear wave velocity which was determined to be 3060 m/s for the particular steel used by dividing the path length by the travel time. The receiver transducer R#2 receives the first and second transmission at the same time as the reflections that are picked up by T/R#1 since the travelling distance is the same for both specimens. In this investigation, multiple bursts are sent within a single hysteresis loop at a frequency of 10 kHz, while Pesaresi et al. [201] only sent one burst per loop. Consequently, the ultrasound variability within a single hysteresis loop can be observed, thus making it possible to assess whether the ultrasound behaviour depends on the changing friction regimes (stick, microslip and gross slip). In addition, ultrasound transmission and hysteresis loops are synchronised to localise where each burst lies within the hysteresis loop.

A 6th order digital Butterworth band-pass filter with cut-off frequencies of 1.5 and 2.5 MHz is applied to the ultrasonic signal to remove noise outside the signal bandwidth and identify the maximum peak in the signal. Next, a Hilbert transform is performed on the filtered signal. The Hilbert transform is a linear operator that generates the envelope of the amplitude of a time history as shown in Fig. 5.2b. This envelope is used to identify the exact peaks of the first reflection and transmission signal. These peaks are then used in the data analysis of the tests described in the following sections.

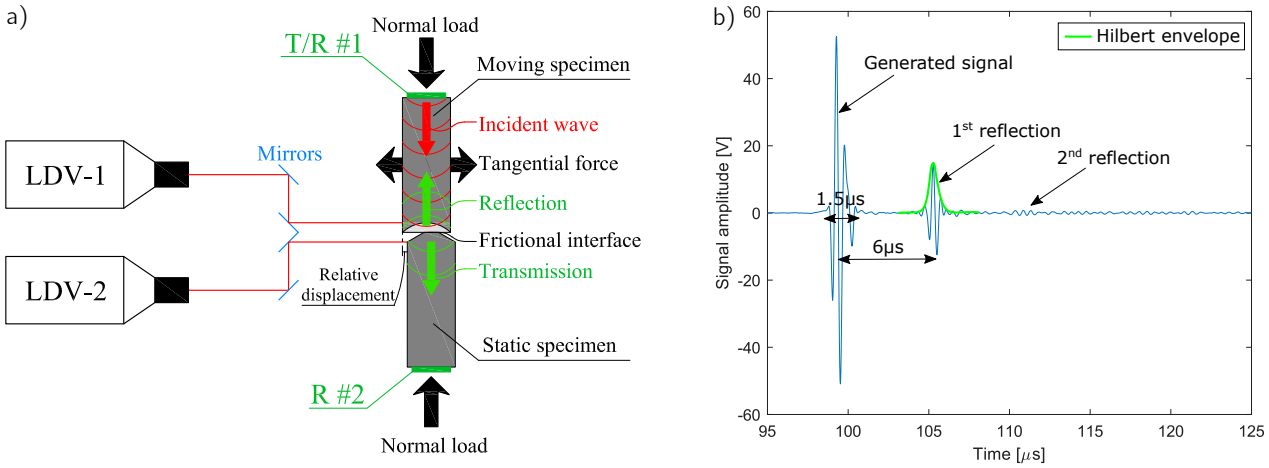


Figure 5.2: a) Simplified scheme of the ultrasonic experimental setup (note that the exact position of the ultrasonic transducers T/R#1 and R#2 is that shown in Fig. 5.1b); b) Incident signal characteristics [263].

5.2 Ultrasonic tests under stuck conditions and different normal loads

Before exploring the opportunity to identify stick and slip contact states, the ultrasonic measurements are used to extract tangential contact stiffness values to further validate the measurements presented in the previous chapter. As already described in detail in section 2.5.2, most of the previous ultrasonic studies improved the physical understanding of static contacts [195], providing e.g. detailed information on the contact stiffness [66,68,73,76,81,196–199], but only a few have attempted to use ultrasound to investigate sliding or dynamic contacts [65, 196, 201–204] and then compare results with hysteresis measurements [196]. The goal of the measurement campaign presented in this section is to assess the feasibility of the ultrasound technique to measure the tangential contact stiffness during vibration by means of a direct comparison with hysteresis measurements.

Vibration tests were conducted under a harmonic excitation of 100 Hz and hysteresis loops were recorded simultaneously with the ultrasound signals. The loops were recorded at a fixed displacement amplitude of 0.4 μm, which is small enough to obtain a stuck[1] regime without gross sliding and at different normal loads. Tests were conducted with the specimens initially not in contact (i.e. 0 N normal load), then increasing the normal load in multiple steps up to 400 N, and finally decreasing it in the same number of steps back to 50 N to check for repeatability (see the loading sequence in Table 5.1). For each normal load, 10 consecutive hysteresis loops were recorded and, at the same time, 100 ultrasound bursts equidistant in time were sent during each loop to investigate the ultrasound variability within the loop. Note that hysteresis loops were not recorded at the 0 N normal load case, since the specimens were not in contact; this scenario is associated with a null tangential contact stiffness.

5.2.1 Hysteresis loop measurements

The measured hysteresis loops from the friction rig are shown in Fig. 5.3a. All the loops are in the stuck regime with no-slip occurring because of the low relative displacement. As the normal load increases, the gradient of the hysteresis loops increases as well, indicating that the tangential contact stiffness, k_t, increases with the normal load. In fact, k_t is determined by fitting a line to the collapsed loop. Figure 5.3b shows the resulting mean k_t values over the normal load, where each error bar indicates two times the standard deviation (i.e. 95% of the values) of the 10 consecutive hysteresis loops measured at each normal load. As already observed in the previous chapter 2 and 4, the tangential contact stiffness increases with the normal load, approaching an asymptotic limit towards the higher loads, a behaviour that was also observed in previous studies [69, 70, 80, 267, 268]. Here, the stiffness increases by up to 10 times with the increasing normal load, from low values of 10 N/μm up to 100 N/μm. The relative standard deviation is in the range of 10-50%. In addition, loading and unloading steps in Fig. 5.3b follow roughly the same curve, highlighting the good repeatability of the measured contact stiffness.

[1] Please note that a full stuck regime is never achievable in practice since a small part of the contact interface will always exhibit microslip. However, at very low displacement amplitudes, the portion of the interface in microslip is assumed to be negligible compared to the major remaining portion of the interface in a stuck condition.

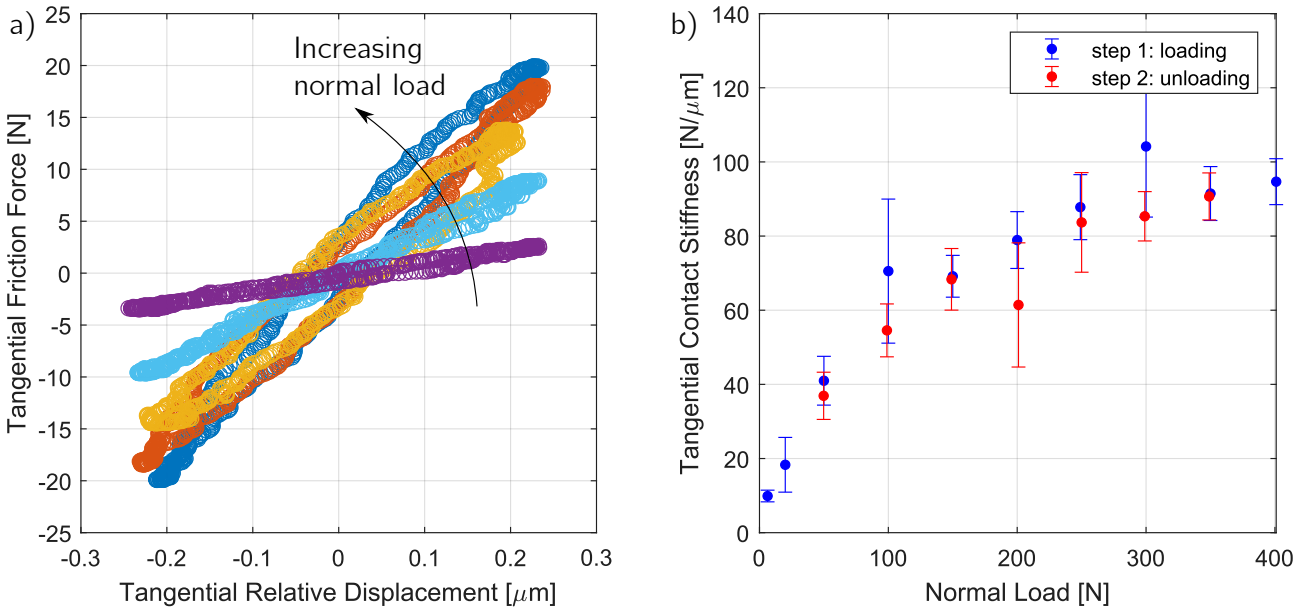


Figure 5.3: Vibration tests under stuck conditions: a) Hysteresis loops measured in stuck condition at different normal loads; b) Tangential contact stiffness extracted from hysteresis loops, k_t, as a function of the normal load [263].

Table 5.1: Summary of test loading conditions for the vibration tests under stuck conditions.

Test conditions	**Static normal load [N]**	**Displacement Amplitude [μm]**
Room temperature. 9 mm^2 flat nominal area of contact. 100 Hz harmonic excitation. 304 Stainless steel specimens.	0, 7, 20, 50, 100, 150, 200, 250, 300, 350, 400, 350, 300, 250, 200, 150, 100, 50	0.4

5.2.2 Ultrasonic measurements

Ultrasound bursts were sent every 100 μs, leading to 100 pulses per loop. The measurement was repeated for each of the 10 consecutive loops, leading to 1000 consecutive recorded bursts. The ultrasound measurements were synchronised with the hysteresis loop measurements of Fig. 5.3a so that the position of the bursts within each loop could be identified. Initially, a static test was conducted by only varying the normal load (with specimens not in motion), followed by the dynamic tests described in the previous section, to check if any difference in reflection/transmission appeared when specimens were still or in stuck vibration at 0.4 μm. Peaks in reflection and transmissions were computed following the procedure described in section 5.1, leading to the results shown in Fig. 5.4 for the different normal loads. The ultrasound measurements from static and stick tests give a nearly identical response in terms of mean values and noise.

Three observations can be made:
(i) the stuck transmission values of Fig. 5.4b remain constant throughout all 10 vibration cycles, and are very similar to the static measurements of Fig. 5.4a, suggesting that low displacement amplitudes do not affect the ultrasound transmission. This is probably because the asperities in contact do not slide and, consequently, the real contact area that affects the

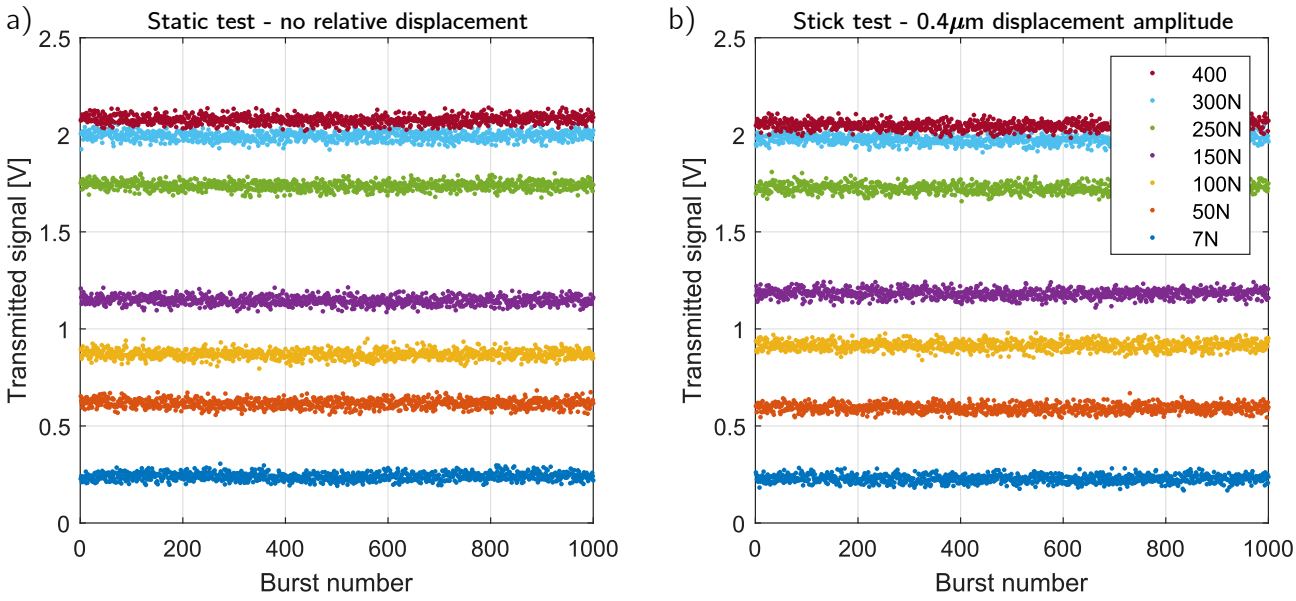


Figure 5.4: 1000 peaks in the transmitted signals: a) Static test; b) Stick test at 0.4 μm displacement amplitude for some normal loads from the measurements of Fig. 5.3 [263].

transmission remains unchanged during a vibration cycle. It can be concluded at this stage that the ultrasound technique cannot be used to detect if a contact is fully static or is undergoing elastic deformations in the stick regime. The same conclusions apply to the reflection, which is not shown for the sake of conciseness;

(ii) the ultrasound transmission increases with the normal load while the reflection decreases, confirming previously reported trends [65, 66, 68, 76, 79, 81, 199]. This is better illustrated in Fig. 5.5, where the mean of the peaks of the reflected and transmitted signals are plotted as a function of the normal load. Each error bar represents two times the standard deviation (i.e. 95% of the values) of the 1000 bursts that cover the 10 consecutive hysteresis loops recorded at each normal load. The transmitted signal follows a similar trend to that of the contact stiffness in Fig. 5.3b since the increasing number and size of the individual contact regions with the normal load lead to a higher ultrasound transmission along with an increase in the tangential contact stiffness. For the same reason, a weaker signal is reflected as the normal load increases. The relative standard deviation is in the range of 3-20%, which is more than three times lower than that observed during the hysteresis measurements, indicating that ultrasound measurements exhibit less noise than the hysteresis data when stick vibration tests are performed. The hysteresis measurement poorer performance is probably caused by the fact that two different time signals are needed (force and displacement) and hence uncertainty from both measurements is added, while for the ultrasound only a single time signal is needed, with a consequently reduced noise;

(iii) in Fig. 5.5b, the transmission at 200 N during the unloading is quite low (and conversely the reflection is larger). The same drop is also observed in the contact stiffness measured from the hysteresis loops as shown in Fig. 5.3b and might have occurred due to an unwanted drop in the normal load during the experiment. The drop has been captured by both measurement techniques, confirming the strong correlation between ultrasound, hysteresis measurements and normal load.

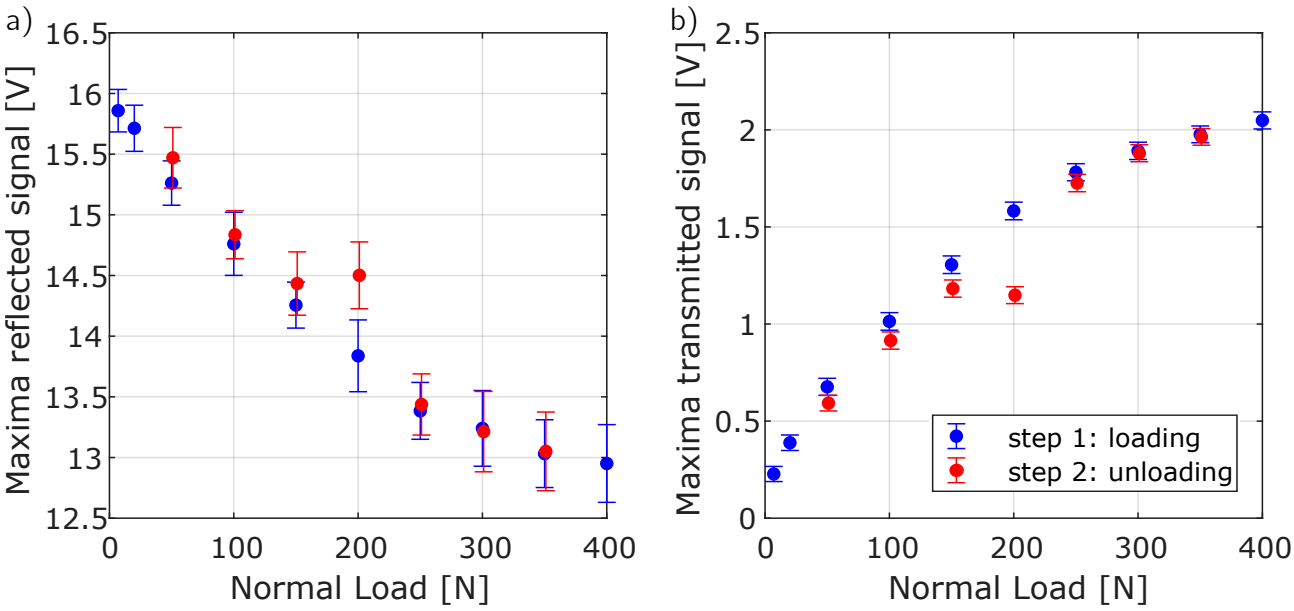


Figure 5.5: Vibration tests under stuck conditions: a) Reflected and b) Transmitted signals as a function of the normal load [263].

5.2.3 Comparison between contact stiffnesses obtained from hysteresis loops and ultrasonic measurements

To quantitatively analyse the correlation between contact stiffness extracted from the hysteresis loops, k_t, and the contact stiffness per unit area extracted from the ultrasonic measurements, K_{US}, Eq. 2.13 is used to obtain K_{US} from the experimental reflection coefficient. This coefficient is estimated with the methodology described in the Appendix D by using Eq. D.1. Figure 5.6a plots the reflection coefficient evaluated in this manner, showing that it drops with increasing normal load, following the identical trend of the reflected signal in Fig. 5.5a. The reflection coefficient seems to approach an asymptotic limit of R=0.75 at 400 N. In theory, the asymptote should be reached when a fully bonded contact is present, leading to a R=0 reflection coefficient as a result of a null reflection and maximum transmission. Since specimens are still in a fully elastic regime due to the relatively low loads (e.g. 400 N over 9 mm^2 equals a nominal mean pressure of 50 MPa at the bulk), the material is far from reaching a full contact, which only occurs when loads are so large that the material plastically deforms, and asperities flatten completely and merge. Consequently, the asymptote observed in Fig. 5.6a must have a different explanation.

Similar large asymptotic values in the reflection coefficient have been observed in previous studies [68, 269], and their origin has been attributed to the fact that the plastic flow occurred almost entirely within the first normal loading step [71, 76, 270], during which asperities flatten to a shape conformal with the opposing surface. In each subsequent loading and unloading step, the conformity was partially maintained even after the load removal, and the same points on each surface made contact again, thus leading asymptotically to the value previously reached with the largest load. In fact, during the first loading, measured trends were linear (i.e. no asymptote at the last loading step), but when subsequent unloading and reloading cycles were performed, an asymptote appeared [68, 269]. The same hysteretic behaviour was reported in studies that used optical measurements to estimate real areas of contact under increasing

normal loads [188, 271], all confirming existing elastoplastic descriptions of contact mechanics [76, 148, 270]. In the case of the measurements of Fig. 5.6a, a series of pre-loading and unloading cycles of the normal load were performed to initialise the experimental setup, during which the ultrasound transmission/reflection was not measured, and hence the results shown here were obtained for the already plastically deformed contact interface. It is worth mentioning that this plastic deformation is only induced by the applied static normal load, while the oscillating tangential load that generates hysteresis loops only leads to fully elastic displacements because of the very low displacement amplitudes. If the normal load were to be further increased, though this is not possible with the available test setup, new contact spots would appear and the asperities would further deform, thus increasing the contact stiffness and hence reducing the reflection coefficient until full contact is reached, eventually leading to a null reflection. This phenomenon is not commonly considered in nonlinear dynamics analyses of jointed structures subjected to vibration [3, 23], although it can lead to large variations in the system behaviour, especially during the first loading cycles.

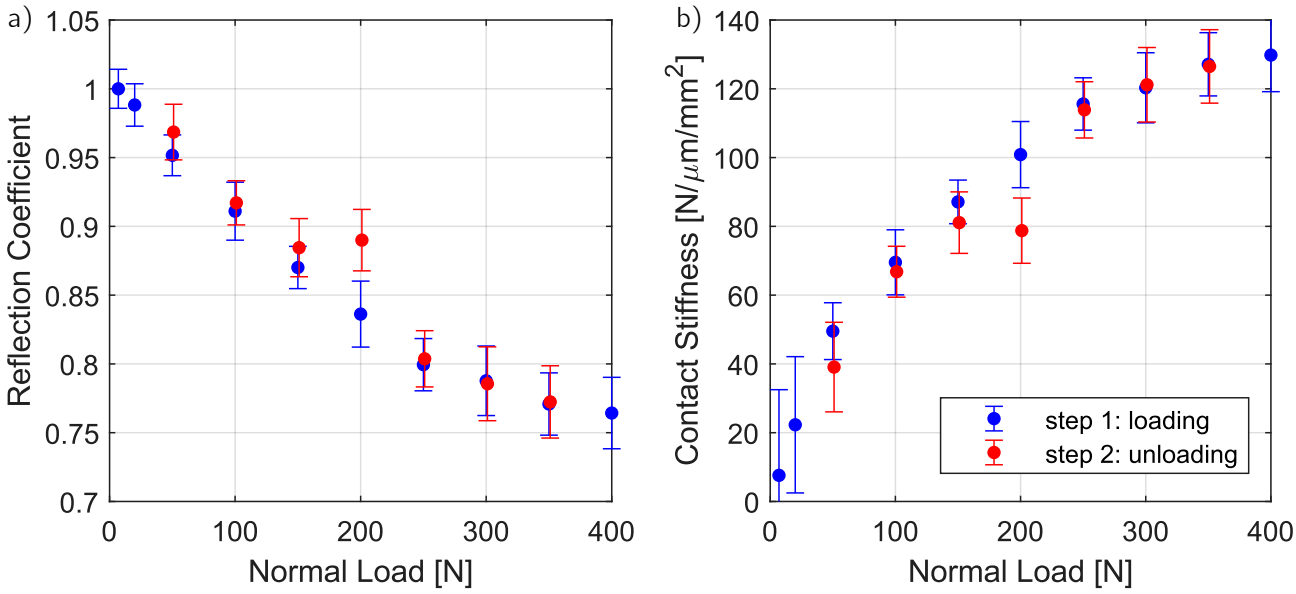


Figure 5.6: Vibration tests under stuck conditions: a) Reflection coefficients obtained from values of Fig. 5.5a; b) Tangential contact stiffness obtained from the reflection coefficient by using Eq. 2.13 (Tattersall formulation) [263].

Once the reflection coefficients were obtained, K_{US} values were calculated from Eq. 2.13 for different normal loads, with the ultrasonic wave frequency, f=2 MHz, the density, ρ=8000 kg/m^3 and the velocity, c=3060 m/s. Results are plotted in Fig. 5.6b, showing that K_{US} reaches a clear asymptote at around 400 N normal load, similarly to the contact stiffness, k_t, obtained from hysteresis measurements in Fig. 5.3b. It is worth noting that the K_{US} obtained from Eq. 2.13 is a stiffness per unit area expressed in N/μm/mm^2, while the k_t measured from hysteresis loops is expressed in N/μm. As described in the Appendix D, the reflection coefficient needed for the K_{US} calculation is estimated by taking as a reference the 9 mm^2 nominal area of contact, and therefore the resulting K_{US} is normalised by that nominal area of contact. By multiplying the K_{US} values by 9 mm^2, a k_{us} in N/μm is obtained (note that the latter is indicated in small letters to differentiate it from the K_{US} values expressed in N/μm/mm^2). The comparison between the ultrasonic k_{us} in N/μm and the hysteretic k_t is given in Fig. 5.7a, showing that k_{us} values are more than 10 times larger than those obtained from the hysteresis loops. This mismatch in values has also been observed in the only two previous studies [196, 201] in which a

direct experimental comparison between the two techniques was assessed. The large discrepancy can be most likely attributed to the fact that the contact stiffness obtained from hysteresis loops includes, in addition to the asperity contribution captured by the ultrasounds [71], also the bulk deformation between the laser measurement points. The FE analysis shown in the Appendix E helps in the validation of this hypothesis by estimating, at 361 N/μm, the stiffness solely due to the bulk deformation, k_{bulk}. Stiffnesses due to both bulk deformation and contact interfaces can be summed in series to estimate stiffness values that, at a first approximation, should be equivalent to those extracted from hysteresis loops according to:

$$k_{eq} = \left(\frac{1}{k_{bulk}} + \frac{1}{k_{us}} \right)^{-1} \tag{5.1}$$

Where k_{us} is in N/μm (see x-axis of Fig. 5.7a), and is obtained by multiplying the K_{US} values of Fig. 5.6b by 9 mm^2, which is the nominal area of contact of the specimens. It is worth stressing that k_{eq} can only be considered as an approximate value since this analytical formulation directly links static and dynamic phenomena occurring over a wide frequency range (static bulk stiffness, oscillations at 100 Hz and ultrasonic waves at several MHz). In addition, those stiffness values also depend on the spatial resolution (i.e. which scales do they represent and how much material is considered for their definition).

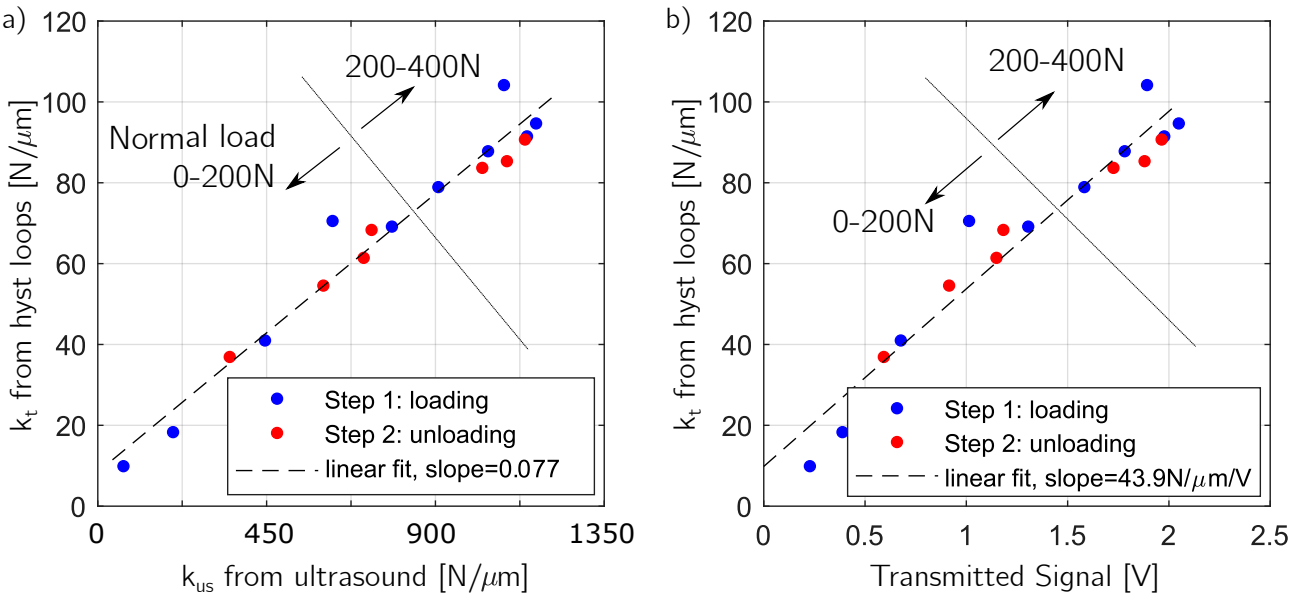


Figure 5.7: Vibration tests under stuck conditions - each point corresponds to a different normal load: a) k_t from hysteresis loops vs k_{us} from ultrasonic reflection or b) k_t from hysteresis loops vs ultrasonic transmitted signal [263].

The resulting k_{eq} from Eq. 5.1 is plotted in Fig. 5.8, where it is compared with the actual k_t measured from hysteresis loops (the same already shown in Fig 5.3b). The mismatch between k_t and this equivalent stiffness is now significantly reduced compared to the larger mismatch with the k_{us}, thus partially confirming that the bulk deformation term plays a key role in this comparison. However, the discrepancy is still relatively large, indicating that the specimen bulk deformation is not the only compliance missing in the ultrasonic stiffness. A further possible source of compliance would be the rotation of the test rig arms due to the bending, as previously described in section 3.3.1. The effect of this bending on the rotation-induced displacement was

therefore quantified, both numerically and experimentally, and found to be negligible (results not presented here for conciseness). Another reason for the stiffness mismatch can be that ultrasound might only be affected by the compliance due to the interface roughness, and not by the compliance coming from the interface waviness, which is at a slightly larger length-scale than that of the asperities (but at a smaller length-scale than that of the bulk, and therefore not captured by the FE model with ideal flat contacts). Part of this hypothesis has already been investigated in the previous chapter, for example with the discussion about Fig. 4.13. It was shown that the the contact interface started as a point contact at the beginning of the test (due to an initial curvature) and then evolved with wear in a fully distributed worn area of contact. When the fully distributed contact was developed, a steady state appeared in the contact parameters. To minimise this effect, all tests presented in this chapter have been therefore performed with the specimens already in a full worn steady-state condition.

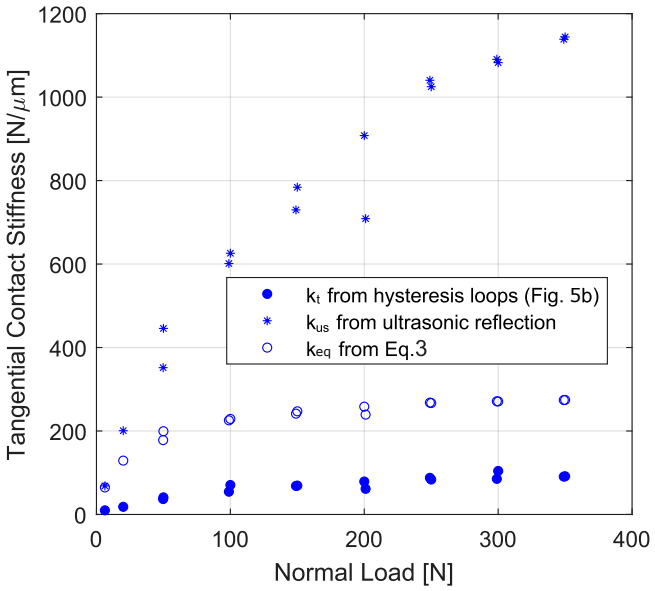


Figure 5.8: Vibration tests under stuck conditions: comparison of tangential contact stiffness from hysteresis loop, k_t; from ultrasonic reflection measurements, k_{us}; and from Eq. 5.1, k_{eq}, which includes the interface contribution (i.e. k_{us}) and the bulk deformation contribution (i.e. stiffness k_{bulk} obtained from the FE model of the Appendix E) [263].

Finally, note that K_{US} could also be computed from the transmission coefficient, T, by using Eq. 2.14 as suggested by Kendall and Tabor [65]. However, the transmission coefficient cannot be readily computed with Eq. D.1 as already done for the reflection coefficient. The ratio between "no contact" and "bonded contact" models (as described in the Appendix D) is undefined due to the absence of any received signal by the receiver installed in the "receiving" specimen when the two specimens are fully detached. Nevertheless, the transmitted signal can still provide information on the contact stiffness since it is linearly related to the transmission coefficient, which in turn is linearly related to the contact stiffness according to Eq. 2.14. This linear relationship is indeed confirmed by Fig. 5.7b, where the contact stiffness from the hysteresis loops is plotted against the ultrasonic transmitted signal for different normal loads. This is the first time, to the best of the author's knowledge, that such a direct comparison between hysteresis loops and transmission has been presented, further confirming the validity of the well-established Eq. 2.14.

Summary of vibration tests under stuck conditions

The results in this section have established a strong correlation between hysteresis measurements and ultrasound reflection/transmission measurements. An increase in the contact stiffness, obtained with both techniques, was observed as the normal load increased. This is in good agreement with existing literature. A direct comparison between contact stiffness values obtained from hysteresis measurements and ultrasound measurements showed a linear relationship, although the ultrasonic stiffness was roughly 10 times larger than that obtained from hysteresis loops. This mismatch was attributed to the bulk deformation that is included in the hysteresis measurements but is not captured by the ultrasonic measurements. This hypothesis was supported by FE simulations that estimated the bulk contributions. This bulk deformation effect suggests that current contact models used in dynamics simulations can use the contact stiffness obtained from hysteresis loops as long as the contact interface is not fully discretised, in order to account for the missing bulk deformation information in the FE model. By contrast, when the interface is more accurately discretised, e.g. waviness at a micrometre level is represented, the stiffness obtained from the ultrasound is the most suitable.

It was also observed that an asymptote in the reflection/transmission appeared at large normal loads. This is a plastic phenomenon that does not necessarily follow a continuous trend, but plateaux appear after the first loading cycles, having a potential impact for dynamic computations and experiments for engineering applications, where often the first loading effects are not taken into consideration and a constant tangential contact stiffness is assumed.

5.3 Ultrasonic tests under varying sliding conditions and fixed normal load

This campaign aims at assessing the feasibility of the ultrasound technique to detect stick, microslip and gross slip regimes at the contact interface during oscillating motion. For this purpose, hysteresis loops were recorded at varying relative displacements, while ultrasound bursts were simultaneously sent to the contact interface. The normal load was kept fixed at 100 N, which enabled the observation of a wide range of displacement amplitudes. Before starting the experimental campaign, specimens were run on the friction rig for 5 hours at 30 μm of displacement amplitude to reach a steady-state contact behaviour due to wear since it has been shown in chapter 4 that contact interfaces only stabilise when the wear is fully extended over the whole contact. Ultrasonic tests started then at a displacement of 30 μm, which was stepwise reduced to 0.4 μm, and then increased again to check for the repeatability (see the loading sequence in Table 5.2). Note that, at the voltage levels used in this study, the displacement amplitudes induced by the ultrasonic waves are in the nanometer range, which is two orders of magnitude lower than the displacement amplitudes of the measured hysteresis loops. Therefore, ultrasonic waves are not expected to perturb the hysteresis measurements at 100 Hz. This was confirmed by acquiring hysteresis loops with and without ultrasonic waves, and observing that they always retained the same hysteretic shape.

5.3.1 Hysteresis loop measurements

A typical set of measured hysteresis loops is shown in Fig. 5.9a. When the relative displacement is small, hysteresis loops are in the stuck regime and, as the displacement increases, they gradually enter microslip and eventually gross slip. For each relative displacement, 10 consecutive loops were recorded, and the contact stiffness was estimated for each loop from the gradient of the stick portion, considering the part from the point of motion reversal up to the 0 N friction force, as previously shown in Fig. 3.3. Figure 5.9b shows the mean contact stiffness extracted in this way, with each error bar indicating two times the standard deviation (i.e. 95% of the values) of the 10 consecutive hysteresis loops measured at each normal load. The contact stiffness reduces by approximately 50% over the 30 times increase in displacement amplitude, nearly reaching an asymptote at the largest tested amplitude. It has to be noted that this is the contact stiffness estimated right after load reversal, and has not to be confused with the "instantaneous" stiffness, which also decreases with increasing displacement amplitude, and becomes zero during gross slip (when the hysteresis loop shows a horizontal line). The drop in the tangential contact stiffness, evaluated after load reversal, with the increasing displacement amplitude agrees with what was already observed in the round robin test of chapter 4, as described in detail in section 4.2.3.

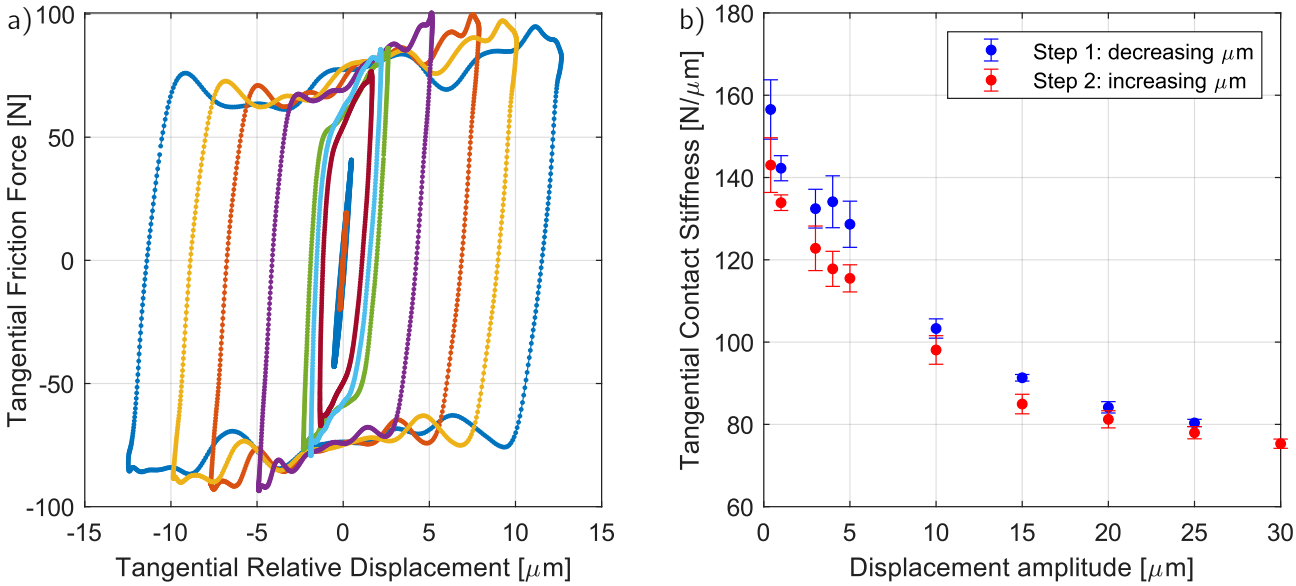


Figure 5.9: Tests under different displacement amplitudes and constant normal load: a) Hysteresis loops; b) Tangential contact stiffness extracted after load reversal for each hysteresis loop [263].

In that chapter, this observed behaviour was attributed to the so-called ageing phenomenon. The ageing results from the time of stationary contact during which the junction size at the asperity contact increases, induced by asperity creep and strengthening of bonding at asperity contacts [184, 260–262]. This concept can be applied to the present measurements by assuming that the stick condition is equivalent to a period of stationary resting contact. The ageing would lead to increased stiffness values during repeated (quasi-stationary) stick cycles at low displacement amplitudes (without any gross slip that would instead refresh the contact). Instead, at large displacement amplitudes, the asperities would be in stick conditions (i.e. a quasi-stationary contact) for shorter periods, thus reducing the amount of ageing and consequently resulting in lower contact stiffness. This hypothesis is well supported by the ultrasound

measurements shown in the next section.

Table 5.2: Summary of test loading conditions for the tests under different displacement amplitudes and constant normal load.

Test conditions **Test conditions**	**Static normal load [N]**	**Displacement Amplitude [μm]**
Room temperature. 9 mm^2 flat nominal area of contact. 100 Hz harmonic excitation. 304 Stainless steel specimens.	100	30, 25, 20, 15, 10, 5, 4, 3, 2, 1, 0.4, 1, 2, 3, 4, 5, 10, 15, 20, 30

5.3.2 Mean ultrasound values: dependence on relative displacement

100 ultrasound bursts were sent within each hysteresis loop over 10 consecutive loops, resulting in 1000 bursts, in the same way as already described in section 5.2.2. Transmission and reflection were recorded and, since they showed equal and opposite trends, only the transmission is presented here. Figure 5.10a shows the 1000 maxima of the transmitted signals at different displacement amplitudes, providing a series of interesting new insights into the mean signal values (described in this section) and their variability (described in the next section).

Figure 5.10a shows that the mean transmitted signal decreases with the increasing displacement amplitude. Following the previously introduced hypothesis of a reduced ageing, the larger displacement amplitude leads to a lower time of stationary contact and ,hence, a lower contact stiffness with consequently reduced transmission. The trend is better shown with Fig. 5.11, which plots the evolution of reflection and transmission as a function of the displacement amplitude where the error bars once more indicate the 95 percentiles of the 1000 ultrasound bursts maxima. The reflected signal follows the opposite trend of the contact stiffness evaluated from the hysteresis loops (see Fig. 5.9b), while the transmitted signal follows a similar trend as the contact stiffness since the drop in the stiffness due to the reduced ageing leads to more reflection and less transmission. This ultrasonic dependency on the displacement amplitude is a novel observation and confirms that the displacement amplitude is an important parameter to be considered in contact analyses.

Once the reflected signal was recorded, the (average) tangential contact stiffness was estimated from Eq. 2.13 by using reflection coefficients obtained with Eq. D.1 for different displacement amplitudes. The reference maximum value, V_{max}, needed in Eq. D.1 to estimate the reflection coefficient, was obtained from the test at 0 N normal load (i.e. no contact) from the previously shown measurements in stuck vibration. Detailed results of the contact stiffness are not shown here since they follow the same behaviour of the contact stiffness obtained from hysteresis loops, as discussed in sections 5.2.2 and 5.2.3. However, a comparison plot is shown in Fig. 5.12a, showing the relationship between the k_t from the hysteresis loops and the k_{us} from reflection (obtained by multiplying K_{US} by 9 mm^2). The slope of the best linear fit is very similar to that shown in Fig. 5.7a, suggesting that the same physical dependency holds when either changing the normal load or the displacement amplitude. Likely, this is again still driven by changes in the number and size of contact spots and overall real area of contact due to the varying

loading. Similarly to what presented with Fig. 5.7b, a comparison is also provided between the k_t from the hysteresis loops and the ultrasound transmission in Fig. 5.12b, showing that a linear relationship still exists between the two. The values of transmission are the mean values of the 1000 bursts. Although the slope is larger than that in Fig. 5.7b, the linear relationship still holds, even in the case of gross slip, confirming the strong correlation between contact stiffness and transmission.

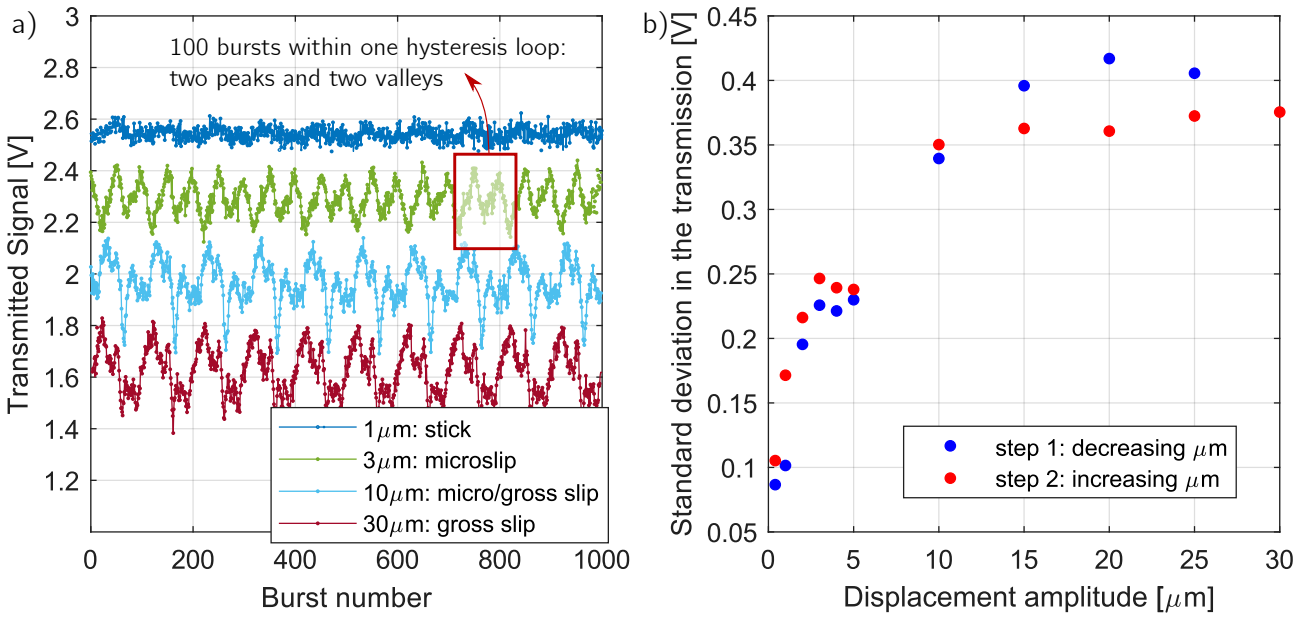


Figure 5.10: Tests under different displacement amplitudes and constant normal load - transmitted signal within hysteresis loops: a) Time history of the transmission within 10 consecutive hysteresis loops measured at different displacement amplitudes; b) Standard deviation from mean transmission within the hysteresis loops measured at different displacement amplitudes [263].

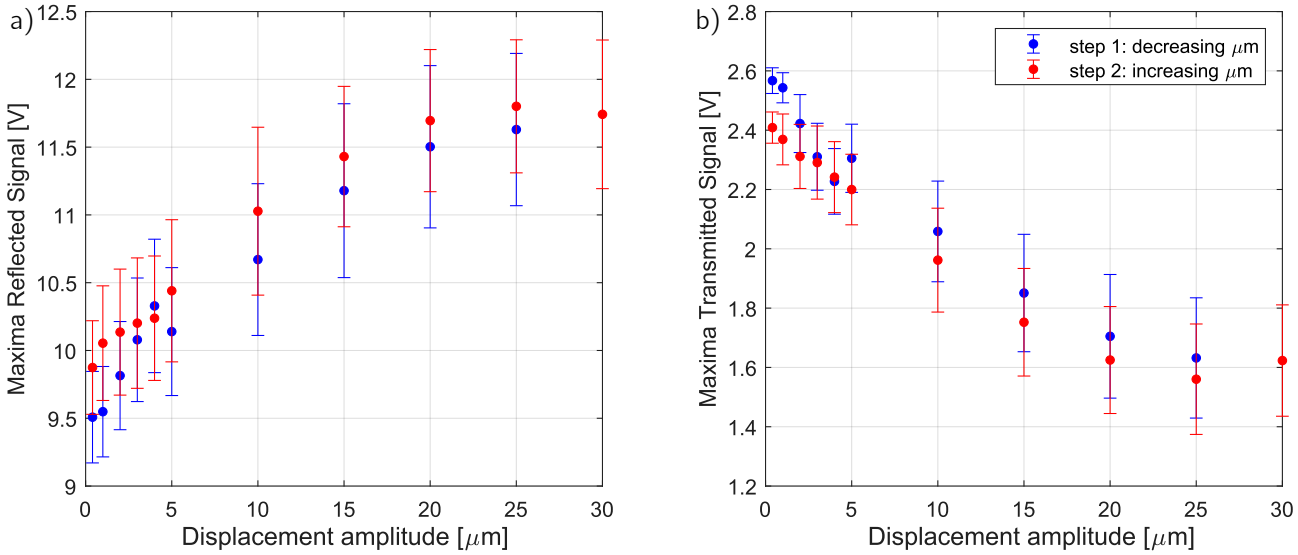


Figure 5.11: Tests under different displacement amplitudes and constant normal load: a) Reflected and b) Transmitted signals as a function of the displacement amplitude [263].

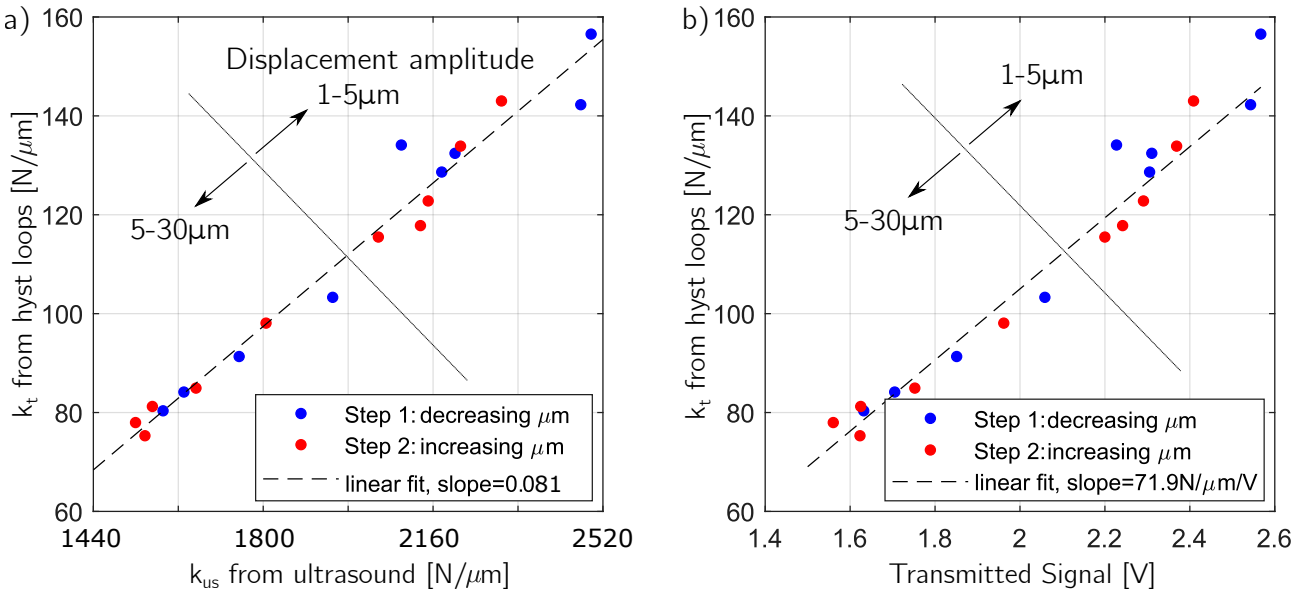


Figure 5.12: Tests under different displacement amplitudes and constant normal load - each point corresponds to different hysteresis loops with different displacement amplitudes: a) k_t from hysteresis loops vs k_{US} from ultrasound reflection or b) k_t from hysteresis loops vs transmitted signal [263].

5.3.3 Variations in the ultrasound measurement: effect of friction regimes

Figure 5.10a shows a large variability over the 1000 bursts as the displacement amplitude increases. Peaks and valleys appear around the mean transmission as the hysteresis loops go from the stick to the gross slip regime. There are almost no drops for the full stick case, while in the microslip regime there are small drops (0.2 V), and in gross slip there are larger drops (0.4 V). A closer look shows that there are two peaks and valleys per hysteresis loop. This ultrasound behaviour has never been reported before, and this novel observation suggests that the ultrasound variability in the transmission depends on the contact condition at the interface during the vibration cycle and consequently may be used to detect stick-slip changes at the contact.

Figure 5.10b quantifies this observed variability (i.e. the average signal drop in the transmitted signal) by plotting the standard deviation of the 1000 bursts. The variability increases with the displacement amplitude of the hysteresis loops, and it seems to reach a stable value for loops with more than 10 μm displacement amplitudes. It is interesting to note that 10 μm ($\pm 5\mu m$) is the threshold displacement amplitude after which the loops enter in full gross slip as shown in Fig. 5.9a, suggesting that the variation in the transmitted signal is (a) indicative of the ratio between stick and sliding at the contact, and (b) constant once the full contact enters in gross slip. In addition, the standard deviation in Fig. 5.11b increases with the relative displacement and is the same as that shown in Fig. 5.10b. The same trend is less evident in Fig. 5.11a because the ultrasound reflection is affected by other sources of noise as described in the Appendix D. This large variability has not been observed in the two previous studies in which ultrasound signals were acquired simultaneously with hysteresis loops [196, 201]. Mulvihill et al. [196] observed a constant reflection over the hysteresis loop, probably due to the quasi-static nature of their tests and relatively small relative displacements of only 2.5 μm. Pesaresi

et al. [201] only used one ultrasound burst for each loop, thus making it difficult to draw any valid conclusion about the variability within a loop.

To better understand the physical meaning of the observed variability, Fig. 5.13a plots the four different time histories from Fig. 5.10a on top of the respective hysteresis loops. The amplitude of the transmitted signal is shown as a colour variation to easily allocate the position of the peaks/valleys over the loops and help with their interpretation. Colorbars with the same range of variation of 0.4 V are used for the 4 loops, centred around each mean so that the colour change can be used as an indication of the actual variability within the loop. The ultrasound transmission is also plotted as a function of the relative displacement in Fig. 5.13b.

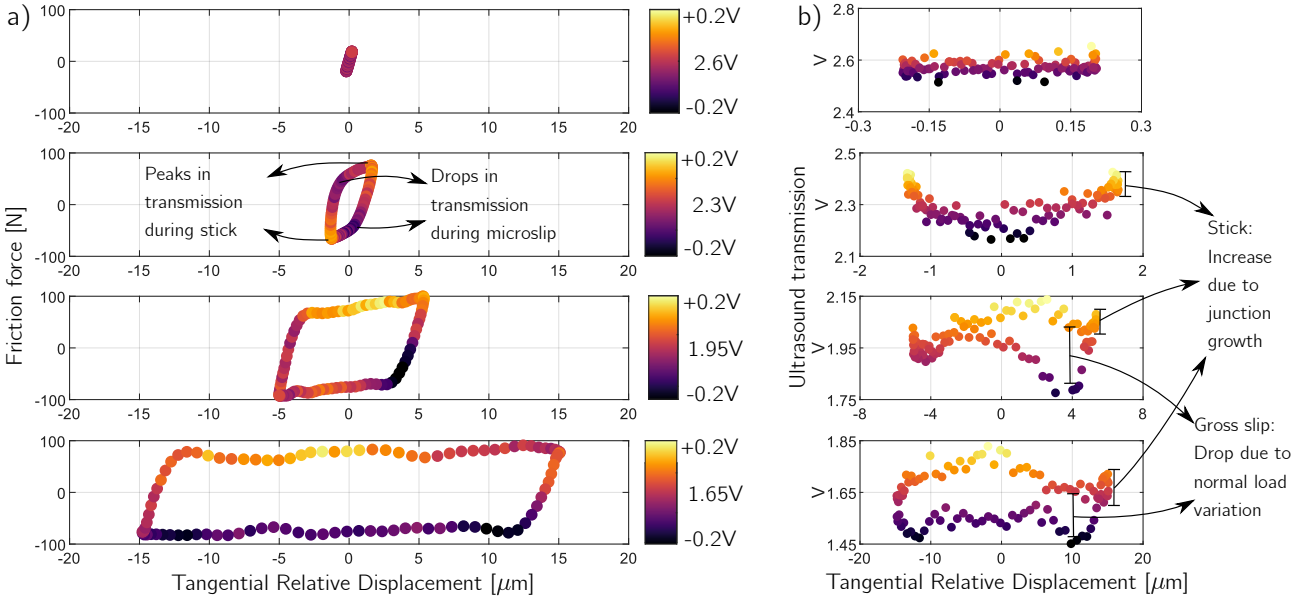


Figure 5.13: a) Ultrasonic transmission (in colorbar) within the hysteresis loops measured at different displacement amplitudes (1, 3, 10 and 30 μm respectively). The respective ultrasound time histories are shown in Fig. 5.10a; b) Ultrasonic transmission plotted versus the relative displacement to better identify peaks and drops [263].

Based on these plots, the following observations for the three friction regimes were made:

Stick regime (1 μm):
The transmission is mostly constant over the loop, as confirmed by Figs. 5.13b and 5.10a. The observed small variability is probably due to the measurement noise. This agrees with the time histories of loops measured at 0.4 μm from Fig. 5.4b).

Microslip regime (3 μm):
Peaks in the transmission appear at the beginning of the stick region, and they drop as microslip occurs. This suggests that, when the contact is slowly approaching the stuck condition, the conformity increases due to the ageing of the junctions, and hence the signal is transmitted to a larger extent. As soon as microslip starts, new asperities without any conformity attributed to the ageing enter in contact, while previously conformal asperities separate, and as a consequence the transmission drops. The two peaks and valleys in the transmission are visible in Figs. 5.13a and 5.10a and lead to U-shaped transmission curve in Fig. 5.13b for the case at 3 μm displacement, where the two peaks correspond to the stick region, and the central drop corresponds to the microslip region. The ageing hypothesis, here used to explain the observed

increase during stick and the decrease at the onset of slip/microslip, is strongly supported by optical measurements of the evolution real area of contact under shear loading [187, 189]. Those studies confirm that the real area of contact (and indirectly the contact stiffness) slowly increases at rest through ageing and drops at slip inception since already aged microjunctions gradually slip and are replaced by new, smaller microjunctions. Drops in the area of contact observed in those studies were as large as few tens of per cent, which are of the same order of magnitude of drops in transmission observed here (17% for the 0.4 V drop over the 2.3 V mean value shown in Fig. 5.13b from the 3 μm case). It is worth noting that the above-mentioned studies could only investigate transparent and soft materials because of the limitations of optical measurements. Here instead, opaque steel is used, revealing for the first time such evidence for metallic material.

Gross slip regime (10 and 30 μm):
A strong asymmetry of the transmitted signal is evident in Fig. 5.13a between the top friction limit of the loop and the bottom one. The transmission at the top friction limit is +0.2 V higher than the average, while in the bottom friction limit there is -0.2 V lower transmission. This dominant asymmetry was not attributed to contact states but was linked to a normal load variation in the test rig, caused by the bending moment of the rig when it moves along the two different sliding directions, as described in detail in section 3.3.1 with Abaqus FE structural simulations. From Fig. 5.5b, a transmission variation of $\pm$0.2 V around the 100N value would correspond to a $\pm$30 N normal load variation. This means that in the top friction limit the normal load would be 130 N (100 N plus 30 N) as a result of the measured +0.2 V increase, while 70 N (100 N minus 30 N) normal load would be acting on the bottom friction limit. This indicates that when the contact slides in one direction it has a lower normal load than when it slides in the opposite direction. It must be noted here that the above observations should result in two different friction limits, μN_0, given that they are directly proportional to the normal load, N_0, and assuming a constant friction coefficient, μ, over the loop. However, very similar friction limits in the measured hysteresis loops are observed at around 100 N (positive and negative) in the last plot in Fig. 5.13a. A possible explanation for this symmetric friction limit behaviour is attributable to the dynamic load transducers that measure the friction force. These transducers are designed to measure fast variations around a mean value and consequently cannot pick up steady offsets. The 30 N offset, generated by the normal load variation, acts as a constant value over the loop (the loop is shifted upwards by a 30 N offset), and consequently cannot be picked by the transducers. In fact, the transducers re-centre the loop around 0 N, effectively filtering out the 30 N offset. A further modification to the test rig will be required in the future to confirm this hypothesis. However, it is to be noticed that this normal load behaviour was already predicted in section 3.3.1 and has been successfully observed here with the ultrasonic technique. It is concluded that ultrasound is an alternative way to obtain a quantitative estimation of the normal load variation in the contact.

This observed normal load does not have a large impact on contact parameter estimations from the hysteresis loops. The friction coefficient is computed from the relative distance between the two friction limits, rather than their absolute values, see section 3.2. With regards to the contact stiffness, although it is normal load-dependent as highlighted by Fig. 5.3b, the stick regions in the two sliding directions have similar values of ultrasound transmission (see similar colours in the stick regions of the last loop of Fig. 5.13a), indicating that the normal load is similar in both directions, thus not affecting the two k_t values.

Overlaid to this asymmetry, four peaks are observable in the transmission in loops in gross

slip (see Fig. 5.13b), two major peaks in the centre of the gross slip (top and bottom), and two minor peaks during the initial stick phases. The minor peaks observed at the beginning of the stick region are linked to the increased ageing during the initial stick phase, as already observed in the microslip case at 3 μm. The major peaks in the middle of gross slip are most likely caused by additional changes in the normal load and/or global contact conditions at the interface due to the flexibility of the rig components. In addition, varying levels of specimen alignments and/or velocity may be responsible for some of the variation, but further refinement of the test setup will be required to confirm these results.

Overall, these results indicate that (a) the slip-stick behaviour is independent of the rig kinematics/dynamics, and more importantly (b) the hypothesised ageing behaviour that characterises the stick regime is still detectable in gross slip loops, making it the most promising indicator for slip-stick transitions at the contact interface.

Summary of vibration tests under varying sliding conditions

The results in this section provide novel insights into the physics of sliding contacts between non-transparent metallic materials. A reduction in the tangential contact stiffness measured from hysteresis loops, after the load reversal, was observed as the displacement amplitude increased. Following the same trend, the ultrasound transmission decreased with the increasing displacement amplitude while the reflection increased accordingly. It is here proposed that this behaviour is driven by the ageing phenomenon. The ageing results from the time of stationary contact during which the junction size at the asperity contact increases, induced by asperity creep and strengthening of bonding at asperity contacts. The ageing would lead to increased stiffness values during repeated (quasi-stationary) stick cycles at low displacement amplitudes (without any gross slip that would instead refresh the contact). Instead, at large displacement amplitudes, the asperities would be in stick conditions (i.e. a quasi-stationary contact) for shorter periods, thus reducing the amount of ageing and consequently resulting in lower contact stiffness. This dependency of the contact stiffness on the displacement amplitude is not commonly accounted for in current contact models for dynamics simulations, but the described stiffness reduction of more than half could have significant implications on the dynamic response and, consequently, updated contact models need to include this effect.

In addition, for the first time the ultrasound transmissibility was recorded at different time instances within a single high-frequency hysteresis loop and a large variability was observed during the vibration cycle. For loops with low relative displacements, i.e. only stick regime, the transmissibility was constant over the whole loop, making the contact indistinguishable from a non-vibrating contact. Hence, the ultrasound technique cannot be used to determine whether a contact is fully static or is undergoing low amplitude elastic vibrations, at least at these levels of ultrasonic measurement noise. When relative displacement was larger, and microslip and gross slip regimes occurred, peaks in the transmissibility appeared at the beginning of the stick regime (i.e. after the reversal of motion) while the transmission dropped once microslip occurred. The clear detectability of the "stick" peaks in the transmission highlights their potential to identify stick and slip transition in real-time in vibrating frictional contacts of non-transparent materials, which are of great interest for industrial applications. This technique can be extremely helpful when displacement measurements are not feasible in situ, e.g. in high pressure turbines equipped with underplatform dampers, where instead ultrasonic transducers could be mounted more easily. However, this ultrasound technique measures only one variable

(i.e. transmission/reflection), thus making it difficult to identify if changes are due to tangential or normal effects or even to wear. But, if used in conjunction with hysteresis measurements, it becomes a very powerful tool to accurately characterise the friction mechanisms at the interface and gain insights into the physics.

Finally, it is also revealed that high-frequency vibratory measurements might lead to normal load variations that cannot be detected by dynamic load cells since these exclude any static offset in the recording. This is an important observation for designers and users of high-frequency friction rigs. The ultrasound technique can be used to monitor such behaviour so to correctly interpret measured data and avoid erroneous conclusions.

5.4 Conclusions

This chapter proposes the novel use of ultrasonic shear waves to investigate the state of a dry metallic friction contact while it undergoes high-frequency shear vibration. The motivation of this novel application is to provide the missing validation data from the central part of contact interfaces during vibration to assess the reliability of contact models used in nonlinear dynamic analysis. Measurements are achieved by sending multiple ultrasound bursts into a high-frequency oscillating contact interface and acquiring them simultaneously with synchronized hysteresis loop measurements.

The results show that the tangential contact stiffness, evaluated from hysteresis loops right after load reversal, strongly correlates with the transmission/reflection of the ultrasonic signal, confirming previously obtained results by other researchers. When the bulk deformation effect is removed from the contact stiffness obtained from hysteresis measurements, values become comparable with those obtained from ultrasonic measurements. This highlights i) the importance of the bulk deformation in hysteresis measurement, as already anticipated in section 3.3 and ii) the fact that ultrasound gives physical information on the contact interfaces at a smaller length scale than the hysteresis measurements, which also include the larger-length-scale bulk deformation. In addition, the same conclusions as chapter 4 are here drawn with regards to the contact stiffness dependency on the normal load and displacement amplitude.

For the first time, a large variability is observed in the ultrasound transmission/reflection amplitude during the vibration cycle. Of particular interest is an increase in the transmissibility at the transition from gross slip to stick, and an opposite reduction at the transition from stick to microslip/gross slip. These variations in the transmissibility were present in all tests hence representing reliable indicators for the transitions between stick, microslip and gross slip regimes. This suggests that the ultrasonic technique can be used to detect spatially resolved changes in contact states during vibration cycles, for example, by mounting an array of ultrasonic transducers distributed in different regions of the contact area on the interface of interest (spatial resolutions down to 2-by-2 mm). This monitoring would be beneficial especially in structures where in situ displacement measurements are not feasible. The use of more transducers would provide real-time and spatially-resolved interface data required to validate the local contact predictions from nonlinear dynamic analyses of jointed structures. However, more investigations are required in the future to adapt this tool to industrial applications, with the aim of acquiring the missing validation data needed for improved nonlinear dynamic analysis.

Chapter 6

Effect of frictional hysteresis on the structural dynamics

The findings in the previous chapters have improved the physical understanding of the input contact parameters for nonlinear dynamic analysis. Here, this understanding is used to investigate the effect of such contact parameters on the dynamics. For this purpose, a detailed dynamic analysis of the friction rig was performed by employing impact hammer tests and shaker tests. The Imperial friction rig was used once more as a test case since it has its dynamic response in addition to the localised frictional contact, which makes it possible for a direct comparison with hysteresis measurements.

Recorded changes in damping and stiffness of the rig dynamic response were linked to variations in the hysteresis loops according to the friction measurements of the previous chapters. Several insights were obtained from the comparison of dynamics and friction measurements. There was some indication as to how certain nonlinear resonances of the system might strongly affect the frictional behaviour. In particular, it was observed that gross slip caused excitation of structural modes that in turn led to distortions in the measured hysteresis loops. This observation can be used to improve the reliability of hysteresis measurements in extracting input contact parameters for nonlinear dynamic analysis. The reliability of hysteresis measurements was also verified with the application of the dynamic substructuring technique to the friction rig. This technique was used to extract tangential contact stiffness values from system dynamics measurements and compare them against the tangential contact stiffness extracted from hysteresis measurements. The simultaneous use of the two experimental techniques provided further insights into the physics of the tangential contact stiffness, which are needed to improve current modelling and measuring approaches.

The findings resulting from those dynamics measurements confirm that the variations in the contact parameters observed in the previous chapters have a large impact on the dynamic response of the structure. The observed relationship between friction and dynamics highlights the necessity to include a detailed frictional description of contacting interfaces for a more accurate nonlinear dynamic analysis of jointed structures. Part of the measurements presented in this chapter resulted in the following three publications on Tribology International [20], Mechanical Systems and Signal Processing [272] and Proceedings of ASME Turbo Expo 2020 [169].

6.1 Description of the rig dynamic behaviour

The high-frequency friction rig was described in detail in chapter 3. Here, a detailed dynamics analysis of the rig is presented to understand its dynamics and link it to variations in the contact parameters. For this purpose, a hammer test campaign was performed because hammer tests are fast, easy to conduct and can capture instantaneously a large number of modes. The hammer test campaign is shown in Fig. 6.1. The test rig has been dismantled to measure it piece by piece for easier parameter identification. Hammer impacts at 100 N were performed on the back of the moving mass. Impacts were repeated three times to check for repeatability and, when impact forces were below 95 N or above 105 N, the impact was repeated. The response amplitude was recorded with accelerometers. A frequency resolution of 0.2 Hz was used for the data acquisition and the calculation of the Frequency Response Functions (FRFs). The campaign consisted of three phases shown in Fig. 6.1:

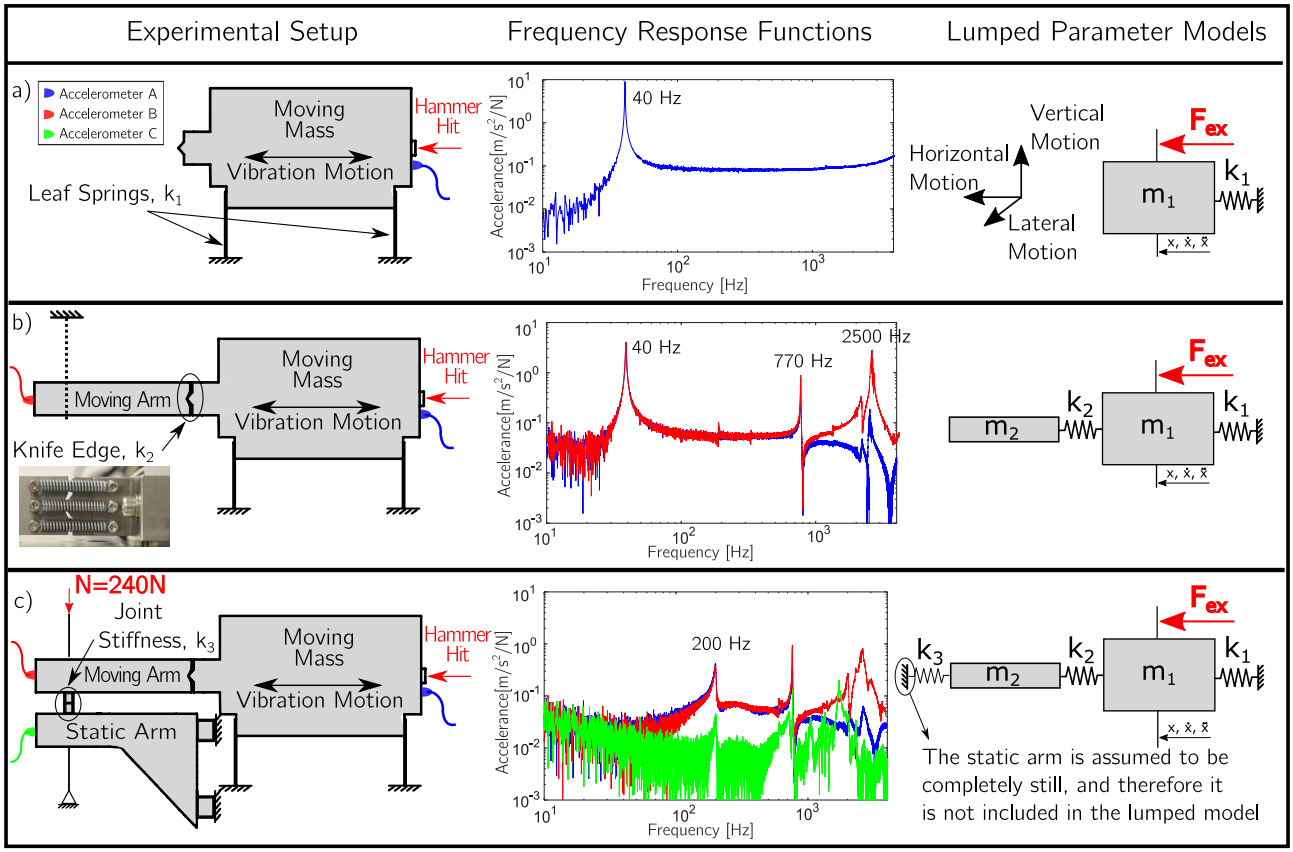


Figure 6.1: Hammer test campaign to evaluate the rig dynamic behaviour: a) moving mass alone; b) moving arm freely suspended on one end and attached to the moving mass on the other end; c) assembly with a very large normal load, which guaranteed a full stuck configuration [169].

Fig. 6.1a) The FRF of the moving mass solely with the leaf springs was experimentally obtained. Only a single mode appeared below 3000 Hz, suggesting that the moving mass could be modelled as a 1 degrees of freedom (DOF) lumped parameter system with a mass, m_1, due to the moving mass weight, and a stiffness, k_1, due to the deflection of the leaf springs, which were designed to allow large horizontal motions. The leaf spring stiffness was calculated from the experimental resonant frequency, f_1, and the known mass of the moving mass using the

following formula: $k_1 = m_1 \cdot (2\pi f_1)^2$. The damping ratio of this mode was obtained with the half-power bandwidth method [273] from the experimental FRF. Table 6.1 shows a summary of the lumped parameters obtained from the hammer test campaign, and Fig. 6.1a shows experimental setup, FRF and lumped model.

Fig. 6.1b) The moving arm was then attached to the mass using a spring-loaded knife-edge at one end, and on the other end was freely suspended via a fishing wire. A new impact test was performed, and three modes appeared in this new configuration, with two of them representing the in-phase (40 Hz) and out-of-phase (2500 Hz) horizontal motion of moving mass and moving arm. The mode at 770 Hz is an in-plane lateral rotation of the moving arm (see Fig. 6.1a for the nomenclature on the motion's convention). It was probably excited by a slight misalignment of the hammer impact location with respect to the rig axis in the lateral direction. The knife-edge stiffness, k_2, was obtained by fitting a 2 DOFs model to the modes at 40 Hz and 2500 Hz from the experimental FRF (keeping unchanged the known values m_1, m_2 and k_1). The damping ratio for this mode was obtained again with the half-power bandwidth method [273]. It is to be noted that a peak appears at 2000 Hz close to the out-of-phase mode. This peak might either correspond to another mode or be due to a weak nonlinearity probably induced by the knife-edge, which might be stiffer in one direction than the other[1]. This nonlinearity is small compared to the nonlinearity induced by the frictional contact and, for this reason, it is not accounted for in the 2 DOFs model.

Fig. 6.1c) The moving arm was then laid on the static arm and a large normal load of 240 N was applied to ensure that specimens would stay stuck together during the hammer impact at 100 N. No new modes appeared below 3000 Hz, and therefore the rig could still be modelled as a 2 DOFs system. The first mode however shifted from 40 Hz to 200 Hz. This increase in the resonant frequency was due to a stiffening of the system because of the connection to the static arm. The normal load stiffened the system due to the sticking of the top specimen with the bottom specimen of the static arm (i.e. hysteresis loops were completely stuck). This stiffening was modelled by adding a stiffness k_3 on the moving arm and by considering the static arm as the ground perfectly rigid. The static arm is considered as the ground in the lumped model since its response (green curve) is more than one order of magnitude lower compared to that of the moving arm, and therefore it can be neglected in the lumped model. The stiffness k_3 represents the overall stiffness of the contact and heavily depends on the shape of the hysteresis loop, as discussed in detail in the next section.

As a result of the hammer test campaign, it is concluded that the rig dynamics can be modelled employing a simple 2 DOFs lumped parameter model, which replicates the two main sliding modes of the friction rig. This model is a simple tool needed to facilitate the understanding of the effects of friction on the dynamics. A shortcoming of this simplified model is that it only includes the horizontal motion and does not account for the vertical motion, which might be relevant due to the bending moment induced by excitation and reaction forces, as it was previously described in section 3.3.1. To quantify the effect of the vertical motion, an updated 3 DOFs model was created that included the vertical motion and, since changes were negligible, it was decided not to include this effect [2].

[1] Note that the knife edge is connected to the moving arm via 12 springs that pre-load the knife edge with 400 N normal force, which is considered large enough to minimize the edge stiffness non-linearity potentially induced during vibration loading and unloading cycles, such that it can be assumed as a linear joint.

[2] The rig stiffness in the vertical direction was estimated with the Digital Image Correlation study shown in the Appendix B. The study showed that, for commonly-tested normal loads ranges of 50-100 N, the stiffness of the rig in the vertical direction is quite low (below 7 N/μm).

Table 6.1: 2 DOFs lumped model of the friction rig.

Moving mass	m_1	21.2 kg
Moving arm	m_2	1.2 kg
Leaf spring stiffness	k_1	1.4 N/μm
Knife-edge stiffness	k_2	273 N/μm
Damping ratio of 1^{st} mode	η_1	0.6 %
Damping ratio of 2^{nd} mode	η_2	1.5 %

6.2 Effects of hysteresis loops on the dynamics

This section aims to link the dynamic response of the friction rig to hysteresis loop variations at the contact interface. For this reason, hysteresis loops were measured for different loading conditions under a 100 Hz harmonic excitation coming from the shaker. After these hysteresis loop recordings, hammer tests were performed to get information on the rig's dynamic behaviour. The measured hysteresis loops were then associated with changes in the dynamic behaviour of the friction rig. The first mode (40-200 Hz) is analysed more in detail because it is expected to be the most affected by the frictional contact since it is in the sliding direction.

6.2.1 Effect of normal load

Chapters 4 and 5 have shown the large effect of the normal load on hysteresis loops and contact parameters. This section investigates the consequent impact on the dynamics. Hysteresis loops were measured at a 100 Hz harmonic excitation with a fixed displacement amplitude of 5 μm and varying normal loads. Specimens were made of stainless steel with a flat-of-flat square nominal contact area of 1 mm^2, as those previously shown in Figs. 3.1b and 4.5. Figure 6.2 shows that a transition in the friction regimes appears as the normal load changes, as already confirmed in the previous chapters. At low normal loads, loops are in the gross slip regime because the sliding limit is small enough to allow full sliding. As the normal load increases, the gross slip reduces until only microslip is present and loops go towards a full stick regime. It is known in existing literature that these changes in the friction regimes strongly affect the dynamic response, and the following dynamics measurements prove it.

Hammer tests were conducted with hammer impacts of 100 N on the back of the moving mass as shown in the experimental setup of Fig 6.1c. The response was measured with an accelerometer placed on the moving arm in the sliding direction and different normal loads were investigated. FRFs are shown in Fig. 6.3. For each normal load, 3 different impacts were performed to check the repeatability and when impact forces were below 95 N or above 105 N the impact was repeated. Measurements were repeatable in terms of both resonant frequencies and damping, despite the high degree of nonlinearity introduced by the frictional contact.

It is clear that the first mode shifts from 40 Hz at very low normal loads to 200 Hz at very high normal loads. This is due to the different friction regimes activated by the different normal loads:

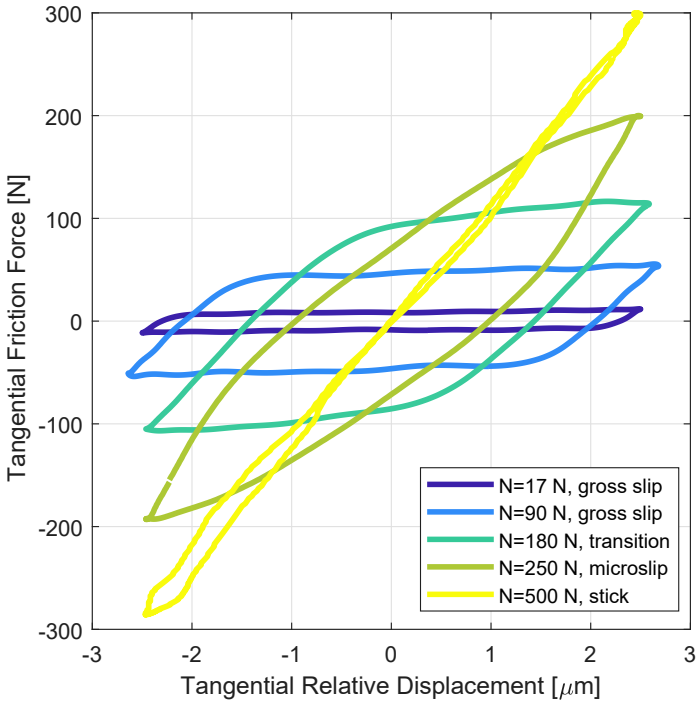


Figure 6.2: Effect of the normal load on hysteresis loops measured at a 100 Hz harmonic excitation. The transition from stick to microslip to gross slip is visible as the normal load decreases [169].

- At low normal loads ($N < 20$ N), the hammer impact (100 N) is large enough to ensure large sliding. However, the energy dissipated is reduced due to the small friction limit, thus resulting in small damping. The extreme case is achieved for a 0 N normal load that is the situation of no contact, with no dissipation at all, and hence a "free peak" at 40 Hz.

- At high normal loads (> 200 N), only microslip or full stick is present due to the large friction limit compared to the hammer impact (100 N). This leads to very small energy dissipated and hence almost no damping that results in a definite "stick peak" at 200 Hz. The resonant frequency increases because the contact is stiffer (as it is not sliding) and the whole system is thus stiffened. This stiffening is quantified with the concept of "equivalent" stiffness, k_{eq}, explained in the following section.

- At medium normal loads (40-120 N), the energy dissipation is maximised thus resulting in very high damping with almost no clear peaks visible in the FRFs.

The friction rig behaves exactly as expected and is similar to other frictional devices. These results confirm the existing knowledge that different friction regimes strongly affect both resonant frequency and damping of systems with friction joints. In particular:

- Large frequency shifts of more than 5 times are observed due to the friction regimes transitions. Also, damping changes are observed, with resonance amplitudes dropping by more than an order of magnitude due to friction energy dissipation.

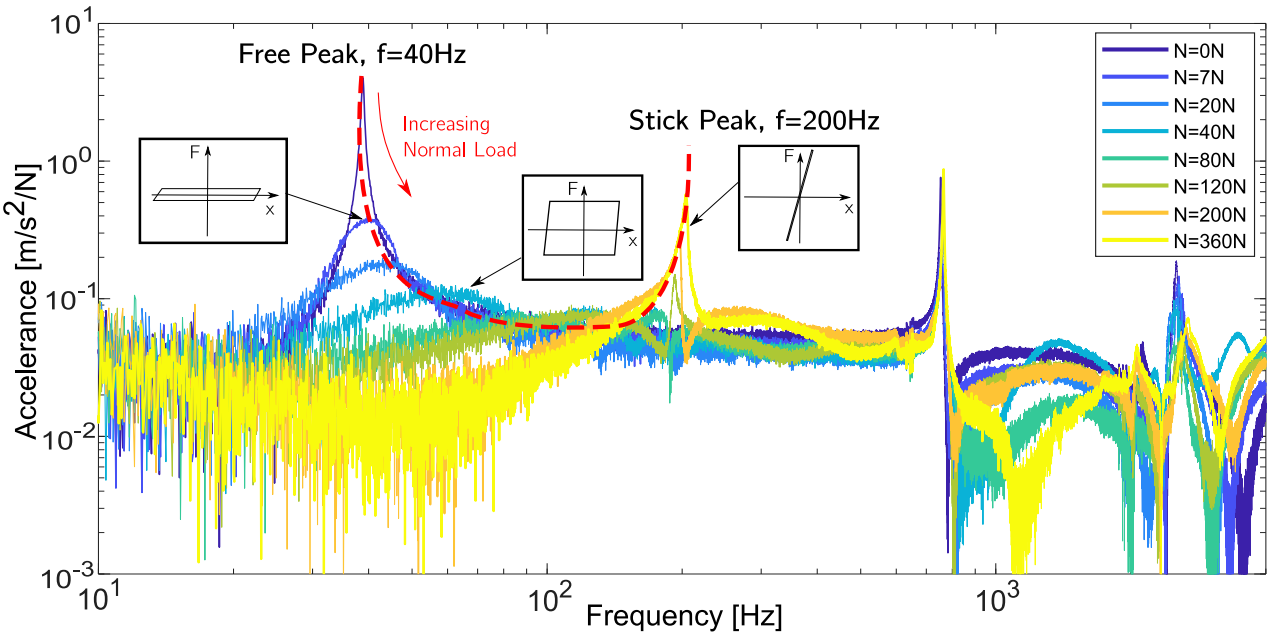


Figure 6.3: FRFs of the friction rig obtained from hammer tests performed at different normal loads and 100 N of excitation impacts [169].

- The shifts in frequency and damping are interestingly similar to the behaviour observed in friction dampers applied in turbine blades [19, 78, 99], as both friction rig and friction dampers exhibit the transition from a "free peak" to a "stick peak".
- The friction rig is used for hysteresis loop measurements usually recorded at a 100 Hz harmonic excitation. Before the dynamic analysis, it was thought that 100 Hz was an off-resonance value since the measured hysteresis loops were stable and easily controllable. However, from Fig. 6.3 it is clear that for some normal load conditions the rig resonance can be at 100 Hz, even though with a highly damped peak that indeed hides the resonance.

These results confirm the existing knowledge on the effects of the normal load on both hysteresis loops and dynamic response. The normal load is one of the main factors affecting friction and dynamics, but it is not the only one. Another important factor is the displacement amplitude, and its effects are discussed in the next section.

6.2.2 Effect of displacement amplitude and excitation force

Chapters 4 and 5 have also shown the large effect of the displacement amplitude on hysteresis loops and contact parameters. This section investigates the consequent impact on the dynamics. A second test was conducted for this purpose. Blue plots in Fig. 6.4 are hysteresis loops measured at a 100 Hz harmonic excitation with a fixed normal load of 40 N and varying displacement amplitudes. The relatively low normal load of 40 N was chosen to investigate hysteresis loops with all the contact states, from fully stuck to gross slip. During the hysteresis recordings, also the sinusoidal excitation force from the shaker was recorded and plotted versus the relative displacement (orange plots).

The orange plots give insights into the rig dynamics since they show the phase between the input excitation force and the output displacement. The phase can be visually estimated from the shape of the excitation force-displacement plots. In fact, since both excitation force and displacement are sinusoidal waves, they will generate a line if their phase is zero, a circle when the phase is 90° and another line (with opposite inclination) when the phase is shifted by 180°. In addition, for every plot in Fig. 6.4, the exact phase, φ, is shown, which has been extracted from the comparison between the time signals of excitation force and displacement.

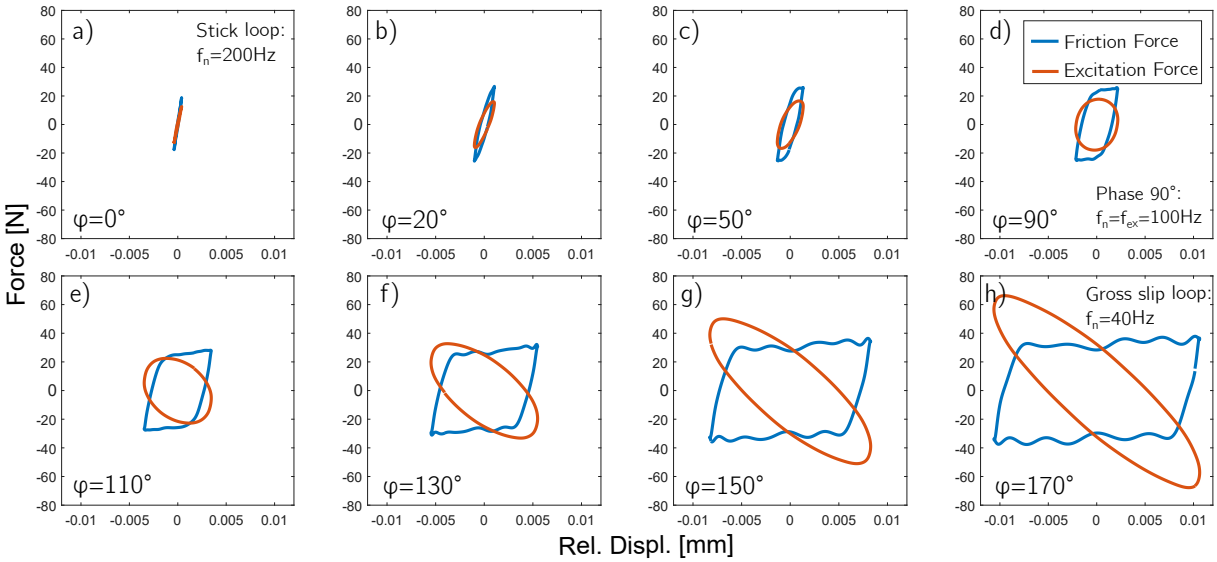


Figure 6.4: Effect of displacement amplitude on hysteresis loops (blue plots) and excitation force (orange plots). φ is the phase between the excitation force and the displacement. The resonant frequency of the first mode decreases from 200 Hz to 40 Hz as the displacement amplitude increases [169].

The trend of the phase of Fig. 6.4 is explained as follows:

- When the excitation is low, the orange plot is a line (Fig. 6.4a) and the phase, φ, between force and displacement is zero. Note that also the hysteresis loop (blue plot) is a line (i.e. full stuck condition).
- For a medium excitation, the orange plot becomes a circle (Fig. 6.4d), i.e. the axes of the phase orbit are oriented in the vertical direction. This means that force and displacement are phase-shifted by 90°. The hysteresis loop (blue plot) presents microslip.
- As the excitation increases even more, the friction hysteresis loop enters in the gross slip regime and the displacement gradually goes out of phase with the excitation force until they reach almost a 180° phase shift (Fig. 6.4h), i.e. the axes of the phase orbit are oriented towards left.

Such shifts between excitation force (input) and displacement (output) indicate that the system resonant frequency, ω_n, moves through the fixed 100 Hz excitation frequency, ω_{ex}. ω_n changes from 200 Hz to 40 Hz purely due to the increase in the excitation amplitude at the fixed 100 Hz ω_{ex}. Since ω_n changes, but ω_{ex} is constant, shifts in the phase occur. In particular, when

the hysteresis loop is in the stick regime, ω_n is 200 Hz, as shown in the "stick peak" of Fig. 6.3. Since in that case the 100 Hz ω_{ex} is below the 200 Hz ω_n, the excitation force goes in-phase with the displacement. On the contrary, in the case of full sliding, ω_n is at 40 Hz, as shown in the "free peak" of Fig. 6.3, and thus is below the 100 Hz ω_{ex}. This leads to a phase shift of 180° between force and displacement.

This experiment confirms that wider hysteresis loops soften the system because the system moves more and thus is less stiff. To validate this observation, an "equivalent" stiffness, k_{eq}, is defined for each hysteresis loop and used as input in the k_3 of the 2 DOFs model of the friction rig, which was shown in Fig. 6.1c. This k_{eq} represents the overall stiffness of the loop and is obtained by fitting the whole hysteresis loop to a straight line, as represented in the loops of Fig. 6.5. Of course, a more complex contact model that replicates hysteresis loops could have been used instead of the simplified k_{eq} approach. This more detailed modelling is presented in chapter 7, section 7.2.1, while here the aim is to show the effects of the joint equivalent stiffness alone.

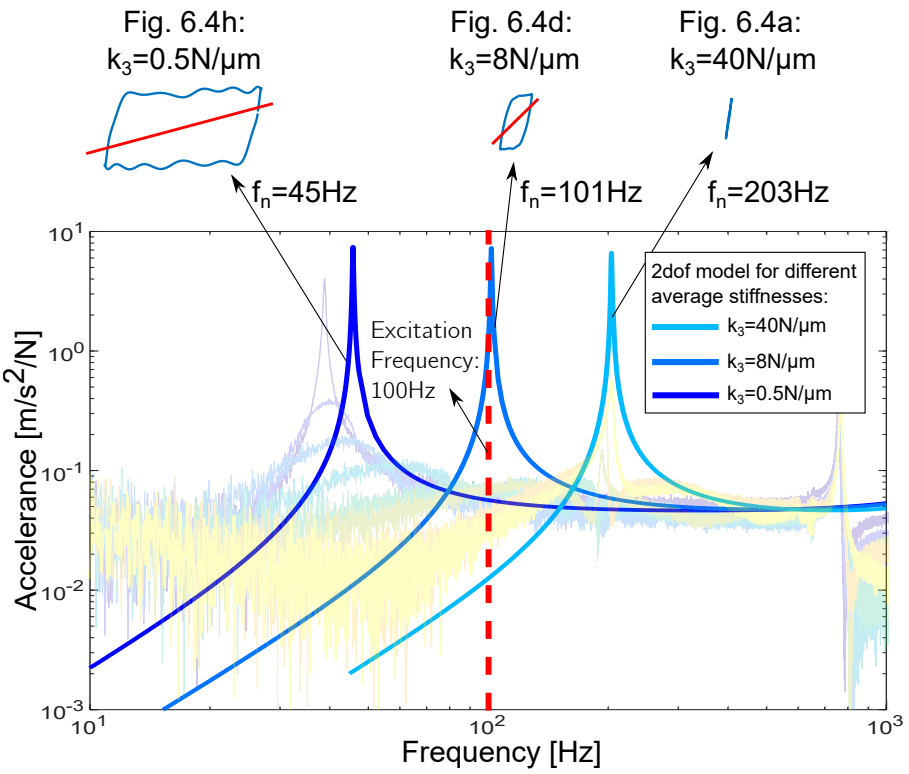


Figure 6.5: FRFs obtained from the linear 2 DOFs model of the friction rig shown in Fig. 6.1c. Different values of k_3 stiffness were obtained by fitting the hysteresis loops to straight lines. In the background, the experimental FRFs of Fig. 6.3 are shown to see the overlap of the resonant frequencies with those numerical [169].

Figure 6.5 shows the resonant frequencies of the 2 DOFs model for different k_3 values. When the loop is stuck (Fig. 6.4a), the k_{eq} of 40 N/μm leads to a ω_n quite close to the "stick peak" at 200 Hz. When the loop is in gross slip (Fig. 6.4h), the low k_{eq} of 0.5 N/μm leads to a ω_n very close to the "free peak" at 40 Hz. A peak at exactly 40 Hz would only be reached for a k_{eq} of 0 N/μm (i.e. a condition of separation with a 0 N friction force). This good agreement between predicted and measured ω_n confirms that, when the phase is 0°, the 100 Hz ω_{ex} is

below the 200 Hz ω_n. Instead, when the phase is 180°, the 100 Hz ω_{ex} is above the 40 Hz ω_n. Finally, the k_{eq} of the hysteresis loop of Fig. 6.4d is also calculated because this loop results in a phase of 90° and hence it should be the loop for which ω_{ex} equals ω_n. Indeed, the k_{eq} of this loop (8 N/μm) leads to a 100 Hz ω_n when substituted in k_3.

In conclusion, this investigation has confirmed that the displacement amplitude strongly affects the resonant frequency of the system and also quantified how changes in the k_{eq} cause the shifts in resonant frequencies. The last important parameter to consider for this dynamic analysis is wear, since chapter 4 highlighted its large effect on hysteresis loops and contact parameters.

6.2.3 Effect of wear

Section 4.2.1 showed that the contact parameters strongly changed with wear. The friction coefficient increased by almost an order of magnitude due to the removal of oxide layers at the beginning of the test and the tangential contact stiffness doubled depending on the extension of the worn area of contact. Since those changes will probably lead to changes in the dynamic response of the friction rig, an experimental plan was prepared to investigate how wear at the interfaces affected the dynamic response. The results here presented were obtained during a group project within the 2018 Nonlinear Dynamics of Coupled Structures and Interfaces (ND-CSI) Summer School organised at Imperial College [250] as part of the EXPERTISE programme, which funded this PhD project. The group was made up of five PhD students and everyone contributed equally to the work, including the author. Results of that project were published in [20] and are reported here in a brief summary.

During the group project, a wear test was performed on the Imperial friction rig by using a specimen pair at room temperature with the following loading conditions: 60 N normal load, 100 Hz excitation frequency, 14 μm displacement amplitude, 1 mm^2 nominal area of contact and a running time of 5.3 hours (i.e. almost two million hysteresis loops) to make sure that a fully worn interface could be established. Before and after the wear test, hammer tests were conducted to record the frequency response function (FRF) of the friction rig. The hammer hits were made at the excitation point in place of the shaker attachment as shown in Fig. 6.1c. Impacts with 50 N force were repeated three times to check for repeatability and, when impact forces were below 45 N or above 55 N, the impact was repeated. An accelerometer was placed on the moving arm to measure the friction rig response. In addition to the 60 N normal load, also the 7 N normal load condition was investigated with hammer tests because, when the pneumatic actuator was unloaded at the end of the test (or loaded at the beginning), a 7 N normal load resulted in the contact due to the self-weight of the moving arm that lay on the static arm. Therefore, an additional hammer test was conducted in this 7 N normal load condition, since it did not affect the wear test itself and could provide further insights on the effect of different normal loads under worn conditions.

Fig. 6.6a-b show the FRFs obtained at 7 N and 60 N of normal load respectively, in both cases before and after the wear test. The Figure shows that wear strongly affects both resonant frequency and damping of the first mode (the mode of interest since it is in the direction of sliding). For this mode, the main factor affecting damping and resonant frequency is the friction limit, μN, at which the contact starts to slide. The friction limit depends on the value of the friction coefficient, which is strongly affected by wear since it increases by almost 9 times with wear, as already shown in section 4.2.1, Fig. 4.15. The damping can either increase with wear

(Fig. 6.6a: peak amplitude of the first mode before wear is higher than the peak amplitude after wear) or decrease with wear (Fig. 6.6b: peak amplitude of the first mode before wear is lower than the peak amplitude after wear). These increases and decreases depend on whether the system raises or lowers its friction limit and, consequently, raises or lowers the amount of energy dissipated within each hysteresis loop. If the system before wear is already close to a fully stuck condition, then, after wear, the observed increase in the friction coefficient further reduces the tendency of the system to slip, thus resulting in a stiffer and less damped system due to the reduced dissipated energy (see Fig. 6.6b: μN before wear is 6.6 N and after wear is 54 N). In contrast, at low normal loads, it is more likely that the system is in gross slip and the increase in the friction coefficient over time would result in hysteresis loops having a larger area due to the increase in the friction limit, with the system still being far away from being stuck. The larger area results in more energy dissipated at the contact, which in turn increases the damping of the system over time (see Fig. 6.6a: μN before wear is 0.8 N and after wear is 6.3 N).

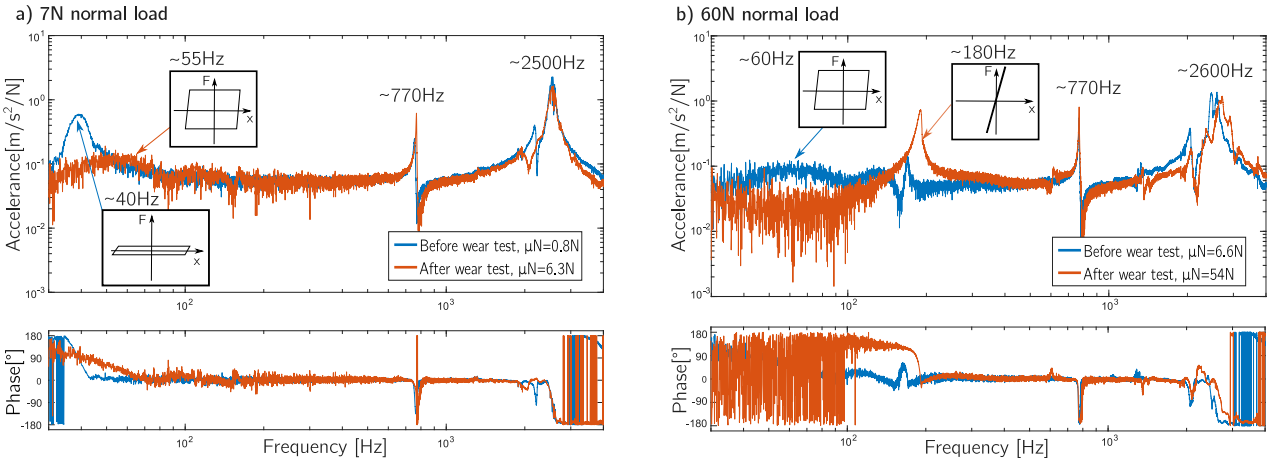


Figure 6.6: Evolution of the rig dynamics: a) 7N normal load; b) 60N normal load. Hysteresis loops are only indicative [20].

Because of the increase in the friction limit with wear, also the resonant frequency increases, in both normal load cases (from ∼40 Hz to ∼55 Hz for the 7 N normal load case and from ∼60 Hz to ∼180 Hz for the 60 N normal load). The increase in the resonant frequency is also attributable to the increase in the equivalent stiffness of the resulting hysteresis loops, as already discussed in section 6.2.2. Physically, these changes with increasing wear lead to higher conformity of the contact interfaces that are more inclined in being stuck rather than slipping.

It is also interesting to note that the FRF measured for the 7 N normal load case after wear (orange plot of Fig. 6.6a) is quite similar to the FRF measured at 60 N normal load before wear (blue plot of Fig. 6.6b). This similarity occurs since, in both cases, the friction limit is similar. At 7 N normal load, the after wear friction coefficient is 0.9, leading to a friction limit μN=6.3 N. At 60 N normal load, the before wear friction coefficient is 0.11, leading to a friction limit μN=6.6 N. The two similar friction limits lead to similar dynamic behaviour, confirming the significant effect of the amount of sliding on the dynamics of the system [3].

The wear does not seem to affect modes that are not linked to the interface sliding. For

[3] A last analysis was performed to extract the vibration amplitude dependency of both natural frequency and damping ratio of the first mode. This analysis is described in the Appendix C and confirms that both natural frequency and damping strongly vary as the amplitude of the vibration decays.

example, the second mode (i.e. lateral rotation of the moving arm at 770 Hz) is not affected by wear as shown in Fig. 6.6. The reason for this is not entirely clear, but probably this mode is characterized by a small relative sliding motion between the specimens and hence it is insensitive to the changes in the contact parameters of the contacting interfaces.

In summary, the presented results show that wear can strongly affect the dynamic behaviour of the system due to changes in the contact parameters. These changes lead to shifts in natural frequencies and damping, and have a particular influence on the modes that activate the contact mechanisms (i.e. the modes in the same direction of the vibratory sliding). To the best of the author's knowledge, the presented hysteresis measurements related, experimentally for the first time, the observed increase in the contact parameters with changes in the dynamic response, which however were already studied numerically in previous studies, e.g. in [141]. The next section shows that also the dynamic response can in turn have an impact on contact parameters and hysteresis loops, leading in some cases to distorted measurements.

6.3 Effects of the dynamics on hysteresis loops

In this section, the effects of the dynamics on the hysteresis loops are investigated. Previous results have shown massive changes in the dynamic response when different sliding regimes occurred, so vice versa it can be expected that the measured loops are being affected by the dynamic response of the system. The rig usually operates at 100 Hz, which is the most stable harmonic excitation as it is in the middle of the first resonant frequency transition between fully stuck and free vibration, where the damping of the rig is at its maximum. Even when the resonant frequency is 100 Hz and coincides with the excitation, the hysteresis loop shape is not affected, because the mode is heavily damped. As a result, the activated nonlinearity can be easily controlled and the extracted contact parameters, i.e. friction coefficient and tangential contact stiffness, will not be affected by this resonance transition.

However, higher and less damped modes might still affect the hysteresis loop shape. Oscillations in the gross slip region of the hysteresis loop are sometimes observed in high-frequency sliding tests across the literature [20, 175, 274], like those shown in the hysteresis loop of Fig. 6.7a. Here, a possible explanation for the origin of these oscillations is provided: it is hypothesized that such oscillations are not due to the frictional behaviour of the contact interface but to the dynamic behaviour of some of the test rig components.

Figure 6.7b shows the time signal of the friction force over the whole loop. The friction force is given by the sum of upper and bottom load cells that measure respectively the two friction force components, T_{up} and T_{bot}, as shown in the schematic of Fig. 6.7b. When looking at the total friction force, 17 peaks appear over the cycle, thus resulting in a frequency of 1700 Hz since the excitation frequency is 100 Hz. Instead, the upper and bottom force contributions, T_{up} and T_{bot}, present 7 oscillations over the cycle, thus resulting in a frequency of 700 Hz. Such oscillations are out of phase, indicating a possible bending or rocking mode of the static arm, in agreement with the bending described in section 3.3.1. It must be noted that several loops were also recorded at larger displacement amplitudes (here not shown) to check if these two frequencies changed. The number of peaks remained unchanged, thus indicating that these high frequencies are independent of the displacement amplitude. Therefore, these high-frequency oscillations might be due to the excitation of modes close to 700 Hz and 1700 Hz,

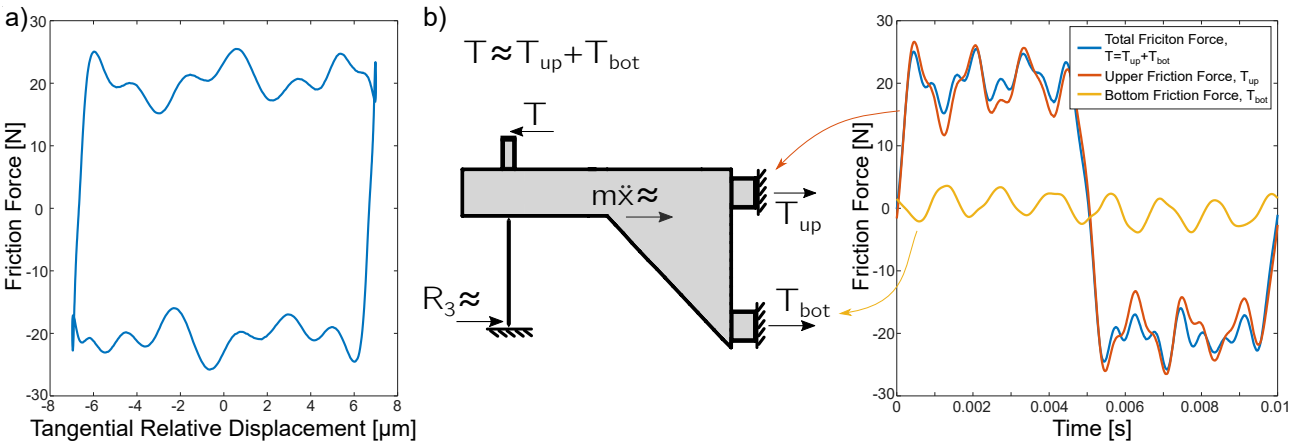


Figure 6.7: a) Typical hysteresis loop recorded at a 100 Hz harmonic excitation, 60 N normal load and 14 μm of sliding amplitude. Oscillations in the gross slip region are visible; b) friction force time signal and static arm scheme [169].

especially modes affecting the static arm, which is the only structure between the frictional contact and the load cells that measure the friction force. If the static arm vibrates, it could affect the force measured by such load cells.

To confirm this hypothesis, Fig. 6.8a shows the FRF of the static arm obtained from a hammer test at 60 N of normal load and 100 N of excitation impact. The impact was performed on the back of the moving mass and the response was measured with accelerometers in the horizontal direction as shown in Fig. 6.8b. No modes are present in the static arm up to 600 Hz, thus confirming that shaker experiments conducted at 100 Hz excitation should not excite any low-frequency modes of the static arm. However, the FRF shows two resonant frequencies (770 Hz and 1730 Hz), which are close within the 10% to 700 Hz and 1700 Hz. These two modes might be the cause of the high-frequency oscillations observed in the hysteresis loop. In fact, the friction force activates the odd superharmonics (700 Hz and 1700 Hz) of the excitation frequency (100 Hz), which in turn might excite these two modes. Note that the 770 Hz mode also appears in moving arm and moving mass, as already observed previously, see e.g. Fig. 6.6.

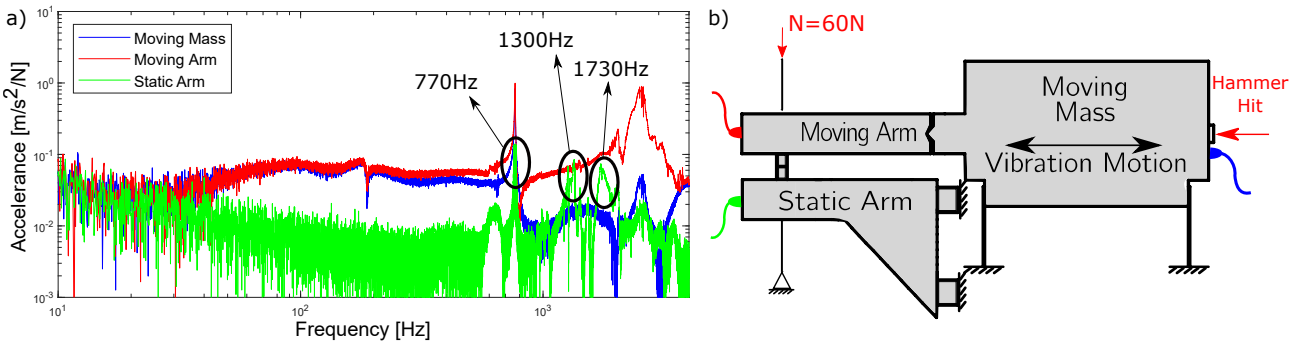


Figure 6.8: a) FRF of the static arm from an hammer test at 60 N of normal load and 100 N of excitation impact; b) experimental setup [169].

To verify this hypothesis, the harmonic excitation was slightly changed from 100 Hz to 95 Hz. In this second case, the closest odd harmonics to 770 Hz and 1730 Hz would be 665 Hz and 1615 Hz,

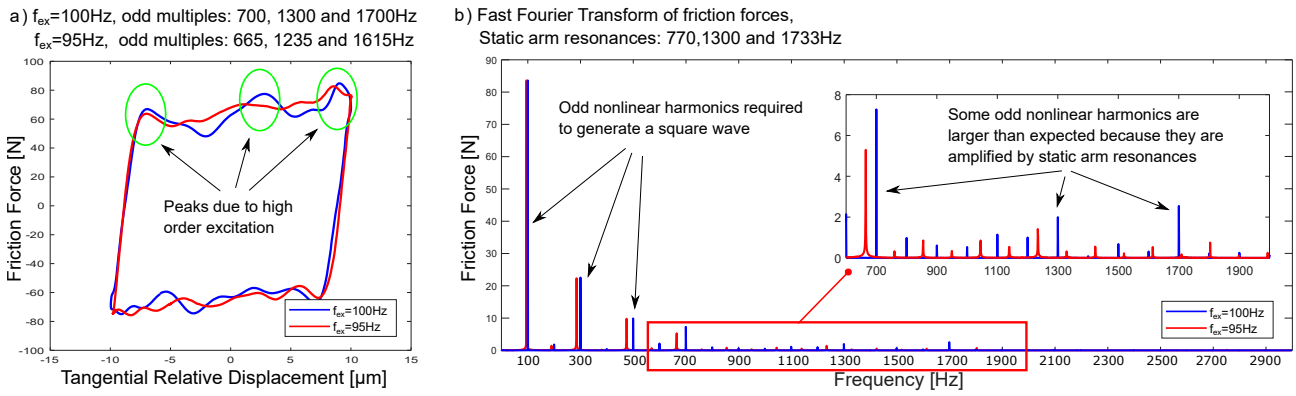


Figure 6.9: a) Hysteresis loops measured at two slightly different excitation frequencies; b) friction forces fft [169].

which are further away compared to the odd harmonics obtained for a 100 Hz excitation (700 Hz and 1700 Hz). Figure 6.9a shows two hysteresis loops measured at 100 Hz and 95 Hz respectively. In the second hysteresis loop, it seems that the oscillations at 700 Hz suddenly disappear, while only the higher frequency oscillations remain. To better quantify the change in the frequency content, a fast Fourier transform (fft) of the friction force time signal was performed as shown in Fig. 6.9b. This fft is used to quantify the frequency contributions. The first 3 odd harmonics have the largest contribution, which is required to generate a square wave (that is the shape of the friction force in time). A square wave is obtained by the infinite sum of odd harmonics with amplitude contributions inversely proportional to their harmonic number [275]. As a result, the subsequent odd harmonic contributions should be almost zero since the amplitude decreases hyperbolically. However, especially for the 100 Hz case, contributions at 700 Hz, 1300 Hz and 1700 Hz are larger than they should be. These contributions are probably amplified by a superharmonic resonance with the three modes highlighted in Fig. 6.8. In addition, it is notable that, for the 95 Hz case, such contributions are much reduced, because the corresponding odd superharmonics are further away from those modes.

This experiment confirms that friction excites the odd harmonics of the excitation frequency and, if such harmonics are close to some of the system resonant frequencies, then the system will respond with vibrations that might affect the contact behaviour and the dynamics at the interface. This investigation also suggests that, to capture such a high-frequency behaviour, a large number of harmonics should be used in current modelling approaches for more accurate predictions [21]. Finally, it is expected that such high-harmonic vibrations do not affect much the extraction of the friction coefficient, because on average they keep the friction limit constant. Unfortunately, they might affect the tangential contact stiffness estimation, as the slope in the stick portion of the hysteresis loop might be sensitive to the presence of a peak or valley due to such vibrations. In other words, the phasing of higher harmonics with respect to the hysteresis loop might affect the extraction of the tangential contact stiffness. To minimize such effects in hysteresis loop measurements and improve the reliability in contact parameters extraction, it is proposed to use excitation levels that do not trigger gross slip, and consequently do not lead to superharmonic excitations. Alternatively, a detailed dynamic analysis of the used rig should be performed to identify the excitation frequencies that do not excite higher modes with their odd superharmonic multiples.

6.4 Dynamic substructuring technique to extract tangential contact stiffness

The EXPERTISE programme, which funded this PhD project, involved several partner universities, including the Technical University of Munich (TUM). One of the TUM researchers involved in the EXPERTISE programme, Steven Klaassen from the research group of Prof. Daniel Rixen, was an expert in the Dynamic Substructuring (DS) technique [220]. This technique uses information from dynamics measurements to identify, amongst others, information on the joints in assembled structures, including contact stiffness estimations. This thesis author decided to collaborate with Steven Klaassen to apply the DS technique to the friction rig since the rig is also capable of measuring hysteresis loops and therefore a comparison could be attempted of the contact stiffness estimations from both techniques. The idea was to identify the contact stiffness from DS by measuring FRFs on the friction rig. Simultaneously with DS measurements, also hysteresis loops were measured and contact stiffness extracted from them. The advantage of this novel comparison would be to provide further insights into the physics of the contact stiffness and assess the reliability of both techniques in extracting tangential contact stiffness values. To do so, the author collaborated with Steeven Klaassen by choosing a master student from the TUM research group to carry out the DS study on the friction rig and extract contact stiffness values to be compared against the hysteresis measurements. This thesis author ideated the project and supervised the master student who came to Imperial to conduct the research activity. This section shows the main conclusions of that study, while a more detailed description of the work can be found in the resulting publication in the Mechanical Systems and Signal Processing journal [272].

The principle of dynamic substructuring is that it decomposes the assembly into several parts, the so-called substructures, which are somewhat easier to analyze than the assembly and are then combined to give information on the dynamic behaviour of the assembly [276]. In the context of contact parameter estimation and joint identification, it is assumed that the difference between the parts merged at their interfaces and the jointed assembly arises only due to the presence of the joints that combine the parts into the assembly, see e.g. Fig. 6.10. Thus, if the dynamic behaviours of the assembly and its parts are known, the joint properties can be identified without the need to directly access the interface. Nowadays, DS has attracted quite some attention for joint identification due to its potential ease of use in real structures [221–223, 277], as already described in section 2.5.3. Despite the several existing studies, it is as of yet not well understood how accurately DS can extract contact parameters since the technique is particularly sensitive to measurement noise. In addition, no direct validation has been yet reported of DS contact parameter estimations against local interface data or contact measurements, such as hysteresis loops.

In this study, a novel comparison was therefore attempted of DS with hysteresis measurements. FRFs were measured on the Imperial friction rig employing hammer tests and were used as input to the DS approaches for the extraction of contact stiffness values. Simultaneously, hysteresis loops were extracted from force and displacement time signals measured during the impact tests and tangential contact stiffness values were estimated. In this way, the same data set was used to extract contact stiffnesses with both techniques, thus improving the reliability of their comparison. The comparison showed that two kinds of contact stiffness could be determined:

- The contact stiffness of the stuck interface, k_t, as already described in the previous chap-

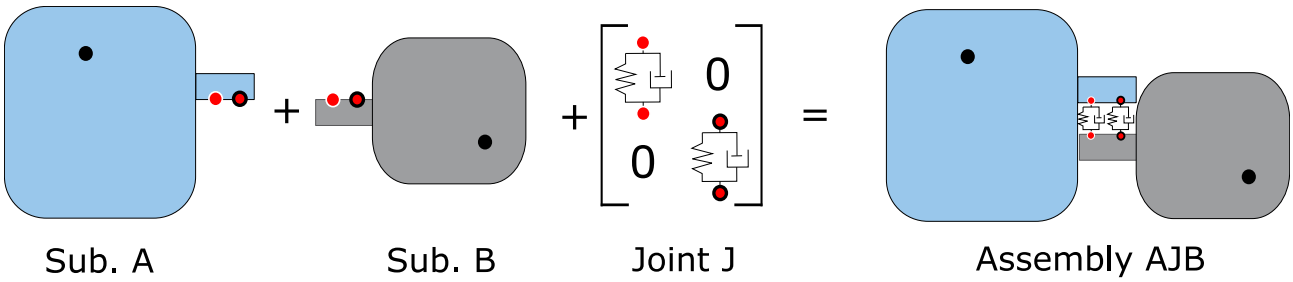


Figure 6.10: Visualisation of substructures coupling. The assembly AJB consists of two substructures A and B and the joint J. The two substructures are coupled with a flexible joint, indicating a "weak interface", e.g. the joint consists of springs and dampers and is assumed to be massless [272].

ters. This stiffness is due to the contact properties, e.g. joint type, surface topography, material pairing etc., and can be transferred from friction rig measurements to other structures having joints with the same contact properties.

- A softer equivalent stiffness, k_{eq}, which includes information on the dynamics of the interface and is a structure-specific property that needs to be determined on the structure of interest itself. This stiffness has already been described with the measurements in the previous section 6.2.2.

Hysteresis loop measurements could identify both types of stiffnesses, while, in this study, DS could only determine the softer k_{eq}. Fig. 6.11 shows the contact stiffness extracted with DS approaches. Note that, since hammer impacts provided data over an 800 Hz frequency range, contact stiffness values were extracted over that frequency range. The Figure shows a linear, almost constant, trend with frequency thus suggesting that the contact stiffness extracted from DS is independent of the frequency. Some variability is observed that was attributed to measurement uncertainties and led to the question of which frequency (range) should be used for the contact stiffness extraction. This is relevant considering that hysteresis loops (from shaker tests in standard rig configuration) are measured at distinct excitation frequencies and therefore provide stiffness values at these distinct frequencies. Instead, the investigated DS approach hardly allows doing so because of measurement noise and, therefore, it was decided to extract stiffness values over two different frequency ranges: 300 Hz-600 Hz and 100 Hz-800 Hz. The first range was chosen because it is narrow enough to provide more accurate and less noise polluted estimations. The second frequency range consists of the whole considered frequency range. The mean contact over these spectra and their standard deviations are:

- 27 N/μm (standard deviation of 4 N/μm) over the 300-600 Hz frequency range.
- 27 N/μm (standard deviation of 56 N/μm) over the 100-800 Hz frequency range.

These contact stiffness values are extremely low considering that experiments were performed with a relatively large normal load of 300 N, which instead led to measured contact stiffness from hysteresis loops of about 180 N/μm (not shown here but in agreement with the values higher than 120 N/μm at large normal loads shown in chapter 4, e.g. Fig. 4.22a).

It is thought that such low stiffness values estimated with the DS technique were due to a local resonance induced by the specimen clamping that was activated in the 192-218 Hz frequency

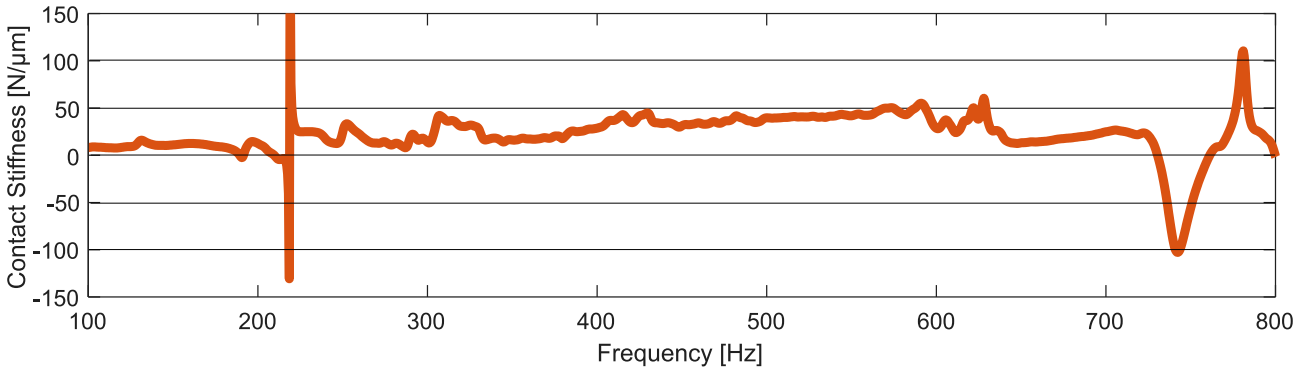


Figure 6.11: DS contact stiffness estimation over the investigated frequency range [272].

range (more details can be found in [272]). Although this clamping did not affect hysteresis measurements at 100 Hz, which is the measurement frequency used in this thesis, hysteresis loops measured in the 192-218 Hz frequency range were affected by the dynamics, showing elliptical shapes rather than the (expected) linear fully stuck shapes (see e.g. Fig. 6.12). The elliptical loops provided low contact stiffness estimations when fitted with straight lines. These estimations were not representative of the real k_t of the contact interface but included some dynamics effects due to the clamping that led to misleading contact stiffness estimations. In the case of DS estimation, this clamping dynamics effect was transferred over the whole frequency range, thus leading to very low stiffness estimations over the whole range. As a result, it was concluded that (hidden) joint resonances could lead to inaccurate estimations of the contact stiffness with either hysteresis or DS measurements. To overcome the measurement problems induced by local (hidden) joint resonances, it is strongly recommended to verify if such local joint resonances exist in the investigated frequency range. They can be recognized by checking if phase shifts exist in the measured displacements of the two contacting components. This check was done by observing the unexpected elliptical loops obtained during the low amplitude hysteresis measurements.

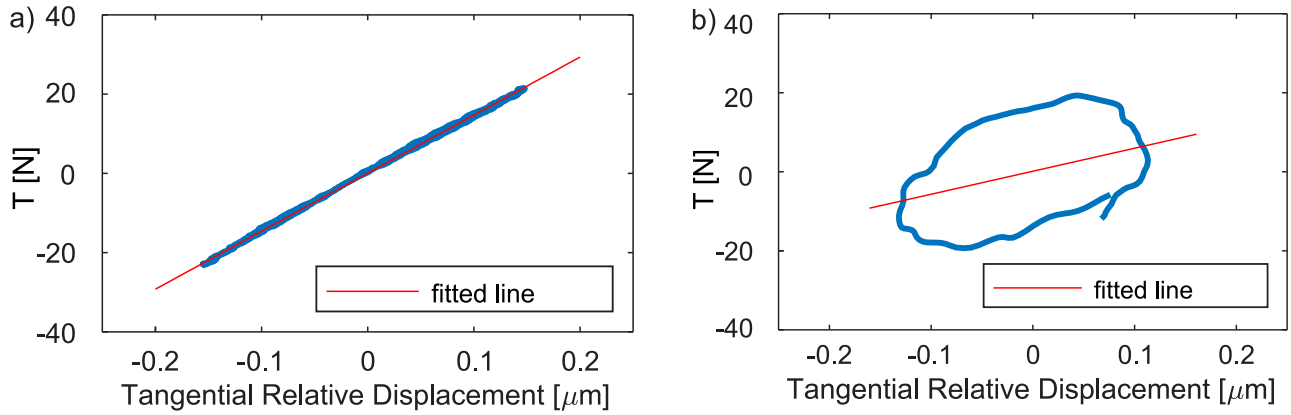


Figure 6.12: a) Fully stuck hysteresis loop at 100 Hz; b) Example of elliptical hysteresis loop measured in the 192-218 Hz frequency range [272].

These findings shine a new light on the reliability of those two measurement techniques to extract accurate k_t values. An improved understanding of the contact stiffness is also provided since, when local joint resonances are present, the estimated contact stiffnesses are much lower than the real contact stiffness of the contact interface. This aspect has to be taken into account when using such contact stiffness estimations as input in contact models used for the nonlinear

dynamic analysis of jointed structures. If such local resonances are included in the FE models (e.g. the clamping dynamics is captured in detailed FE models of the friction rig), then the k_t of the real contact interface should be used as input. Instead, if such local resonances are not captured in the FE models, the lower k_{eq} should be used since it would account for the missing dynamics in the FE models.

6.5 Conclusions

This chapter investigated experimentally the effects of friction on the dynamic response of the Imperial friction rig. The goals were to provide guidelines for improving existing measuring and modelling approaches for nonlinear dynamic analysis.

Effect of loading conditions on the dynamic response:
Normal load, displacement amplitude and wear lead to changes in the friction regimes (stick, microslip and gross slip), which in turn strongly affect resonant frequencies and damping. In particular, changes are observed with up to a five-fold increase in the resonant frequency and up to a ten-fold change in the damping due to different friction regimes and to changes in friction coefficient and tangential contact stiffness. Note that the presented hysteresis measurements related, experimentally for the first time, wear-induced changes of the contact parameters with changes in the dynamic response. This only occurs for vibration modes that excite the contact. Vibration modes that do not activate contact mechanisms (i.e. they are not in the sliding direction) seem not to be affected by the wear evolution of the interfaces. In addition, since wear leads to established contact conditions at the interface, it is suggested to run jointed structures for several vibration cycles before performing dynamics measurements since, during the first vibration cycles, contact parameters at jointed interfaces vary significantly thus leading to much different system dynamic responses.

Identification of implicit joint model stiffness:
An easy approach is proposed to obtain the implicit joint model stiffness (i.e. "equivalent" stiffness, k_{eq}) via hysteresis loop measurements. The k_{eq} can be directly obtained by fitting hysteresis loops to straight lines. Wider loops in gross slip have lower k_{eq}, and thus soften the system to a greater extent. As the displacement amplitude decreases, the k_{eq} of the loop increases, therefore stiffening the system. This k_{eq} can be used in joint implicit models as an input parameter to obtain estimations of the nonlinear resonant frequency. The k_{eq} could also be measured with the dynamic substructuring technique, without the need of measuring the friction force as required in hysteresis measurements. This was proved within a study supervised by the author in which dynamic substructuring was applied to the friction rig to extract the contact stiffness. The study showed that hysteresis loops could identify both contact stiffness and equivalent stiffness, while the dynamic substructuring techniques could only provide equivalent stiffness estimations. However, dynamic substructuring has the advantage that it can be applied potentially to any structure, while hysteresis loops require purposely built friction rigs to measure the friction force.

Choice of excitation frequency for accurate contact parameter estimation:
Thanks to the simultaneous recording of hysteresis and dynamics data, the origin of oscillations observed in the gross slip regime of some hysteresis loops was identified. Those oscillations were induced by the vibration of test rig components that were excited at their resonant frequencies

by the superharmonics generated by the nonlinear friction forces. It is thereby important for designers to consider that the operating excitation frequencies (and their odd superharmonics) might excite some resonances of the jointed structure, in turn affecting hysteresis loop measurements. This effect must be considered for the extraction of more reliable contact stiffness values. It is suggested to extract tangential contact stiffness from hysteresis loops in a full stuck regime, without gross slip, to make sure that the friction force does not excite odd superharmonics of the excitation frequency. Alternatively, if hysteresis loops in gross slip are to be measured, the high resonant frequencies of the investigated structure should be measured and, then, excitation frequencies should be chosen that are not sub-multiplies of those resonances. In the case of the friction rig, the 95 Hz excitation frequency led to cleaner loops than the usual 100 Hz since the 95 Hz excitation minimised the superharmonic excitation of higher modes.

The findings of this chapter experimentally validate the theory of structural dynamics of assemblies with friction contacts and improve the knowledge on the effect of wear on the structural dynamics. The novel comparison of hysteresis measurements with dynamic substructuring also cross-validates the reliability of both techniques. The strong relationship between friction and dynamics is confirmed, highlighting the necessity to include a detailed frictional description of contacting interfaces for more accurate modelling of the dynamics of jointed structures. This know-how is necessary to improve the current experimental and numerical capabilities for the nonlinear dynamic analysis of jointed structures.

Chapter 7

Validation of modelling approaches for nonlinear dynamic analysis: friction rig test case

Previous chapters have improved the understanding of the contact parameters used in nonlinear dynamic analysis and quantified their effect on the nonlinear dynamic response. As a result of the improved knowledge, guidelines have been proposed to improve current modelling methods, such as including realistic surface topographies in the models or including the normal load dependency of the tangential contact stiffness. The goal of this chapter is to include some of those guidelines in upgraded simulations of the friction rig and validate them against the previously obtained experimental data. In particular, three guidelines are validated: i) the use of more realistic surface topographies; ii) the inclusion of wear in simulations and iii) the normal load dependency of the contact stiffness. To verify the impact of those guidelines, two sets of simulations were performed:

1. Quasi-static contact simulations were performed to improve the modelling of the contact stiffness since it was observed in chapters 4 and 6 that this parameter has a major impact on the kinematic and dynamic response. For assessing the proposed improvements, Finite Element and Boundary Element methods were employed with the following upgrades:
    - Inclusion of realistic surface topographies, namely realistic roughness and waviness of contact interfaces. This is needed to understand how large is their effect on the contact stiffness predictions and to confirm the findings of chapter 4.
    - Inclusion of the effect of wear and worn area dependence, since it was shown in chapter 4 the large impact that it has on the contact stiffness, although the worn area dependence is not commonly included in current modelling approaches for nonlinear dynamic analysis.
2. Nonlinear dynamic simulations were performed to assess the effect of the proposed improvements on the predicted frequency response functions. Time integration and multi-harmonic balance solvers were employed with the following upgrades:
    - Inclusion of the effect of wear since chapter 6 showed that wear strongly affects the dynamic response due to the changes in the contact parameters.

- Inclusion of the contact stiffness normal load dependency since chapters 4 and 5 showed that the normal load strongly affects the contact stiffness, which in turn has a large impact on the dynamic response.
- Inclusion of the experimental measurement uncertainty since chapter 4 showed that measured contact parameters have some inherent uncertainty, which should be included in simulations to obtain a predicted range of possible dynamic responses.

Predictions from these simulations validate some of the hypotheses presented in the previous chapters and show the importance of the proposed upgrades for more accurate nonlinear dynamic analysis. Some of the results presented in this chapter were included in two publications in the journals Tribology International [20] and Mechanical Systems and Signal Processing [278].

7.1 Quasi-static contact simulations

Simulations presented in this section well replicate and validate the experimental observations presented in chapter 4 with regards to the k_t dependency on contact surface topography and wear. As a reminder, it was shown in section 4.2.1 that the k_t measured from the Imperial friction rig specimens increases as the worn area of contact increases. It was hypothesised that this increase resulted from a change in the surface topography from a point contact at the beginning of the test, due to the unworn curved contact interfaces, to a more distributed contact at the end of the test due to wear. The unworn and worn conditions are sketched in Fig. 7.1. The sketch also includes the stiffness k_{bulk} due to the deformation of the bulk material included between the laser measurement points. The effect of the bulk deformation was previously discussed in section 5.2.3, and is here briefly recalled. In the case of perfectly flat and fused interfaces, any applied tangential load would lead to relative tangential displacements purely due to the bulk material deformation. The resulting stiffness k_{bulk} can be considered as the upper bound of the tangential contact stiffness measured from hysteresis loops, k_t. In real applications, k_t is always lower than this upper bound because of the additional compliance introduced by asperities and waviness of real (non-smooth, non-flat) surface topographies [63, 279]. k_t can be hence approximated as the sum of two stiffnesses in series, as sketched in Fig. 7.1:

$$k_t \approx (1/k_{topography} + 1/k_{bulk})^{-1} \tag{7.1}$$

where k_t is the measured tangential contact stiffness measured from the slope of the stick portion of the hysteresis loop, $k_{topography}$ is the stiffness due to asperities and waviness of the real (non-smooth, non-flat) surface topography, and k_{bulk} and is the stiffness due to the bulk deformation of the (upper-bound) smooth and flat interface. Note that, at the highest extreme normal loads, all asperities would fully flatten and merge, giving a single area of contact equal to the nominal contact area. The resulting stiffness converges towards the smooth and flat interface stiffness, and the bulk material dominates the solution [63, 279]. Instead, at very low loads, the contact stiffness is dominated by the few asperities in contact that provide additional compliance to the bulk material deformation, thus reducing the measured stiffness k_t.

In this section, k_{bulk} and $k_{topography}$ are quantified by modelling unworn and worn contact interfaces through Finite Element and Boundary Element Methods (FEM and BEM). Predicted values are compared against the k_t measured from hysteresis loops. This is needed to validate

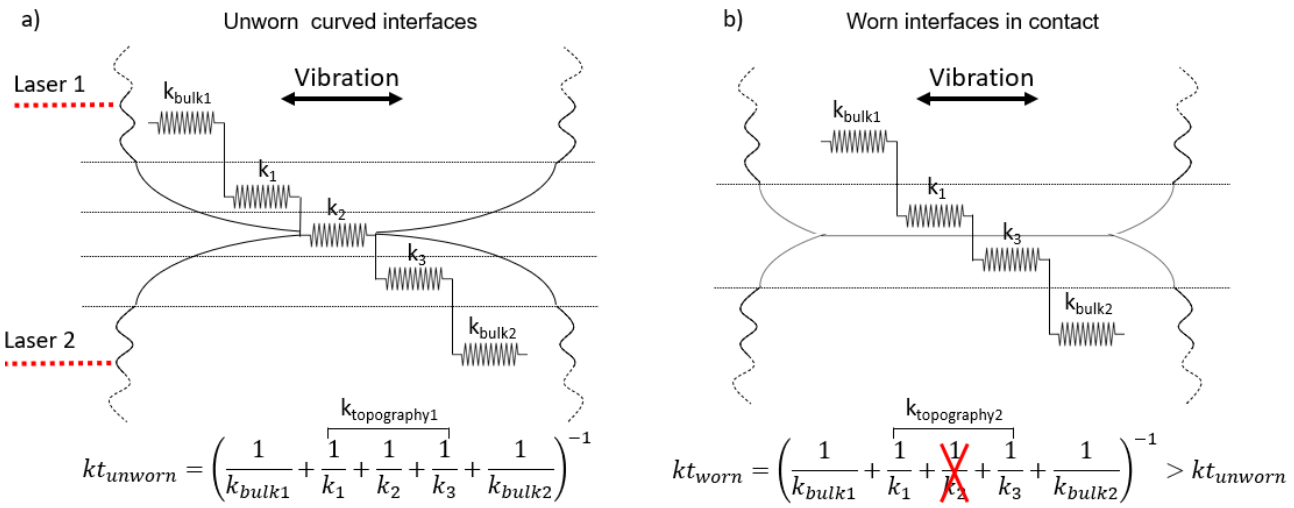


Figure 7.1: Typical evolution of the contact interface of Imperial specimens with wear: a) unworn contact and stiffness contributions; b) stiffness contributions in the worn contact. $k_{topography}$ is the stiffness due to asperities and waviness of the real (non-smooth, non-flat) surface topography; k_{bulk} is the stiffness due to the bulk deformation of the (upper-bound) smooth and flat interface.

the proposed hypothesis, to demonstrate that the same effect can be captured by models and, ultimately, to improve the modelling of the contact stiffness.

7.1.1 FEM simulations: effect of the bulk deformation

To estimate the (upper-bound) specimen bulk deformation of the smooth interface, a preliminary FE model of the specimens with perfectly flat and fused interfaces was created. The Imperial specimens have been described in chapter 4 and Fig. 7.2a shows a specimen photo. Only the tip of the specimen was modelled since a large portion of the specimen is rigidly held by two holders to the rig arms, as shown in Fig. 7.2b, and therefore it cannot deform significantly. Figure 7.2c shows the side view of the specimen with a zoom on the portion that sticks out of the holders. Only this portion was modelled, resulting in the model shown in Fig. 7.2d, which includes the two specimens with perfectly flat and fused interfaces of 1 mm^2 nominal square area. This model was meshed in SolidWorks using parabolic tetrahedral solid elements with an average size of 0.05 mm (~1.64 million elements in total, with a higher element density around the fused contact interface). Figure 7.2d also shows in red the two points that correspond to the experimental location of the laser used to measure the relative displacement during the hysteresis loop measurements. The bottom specimen was constrained at its base in all degrees of freedom, while the top specimen was only allowed to move along the sliding direction of tangential loading to best replicate the rig operating conditions.

A static tangential load of 100 N was applied to the top surface of the top specimen in the sliding direction. Figure 7.3 shows the displacement field of the deformed specimens under the 100 N tangential load. The Figure clearly shows that most of the bulk deformation occurs close to the fused contact (see highlighted red ellipse) while, further from the fused contact, the displacement field is more uniform. By dividing the applied load of 100 N by the relative displacement between two points on the two specimens, the stiffness solely due to the bulk deformation is obtained.

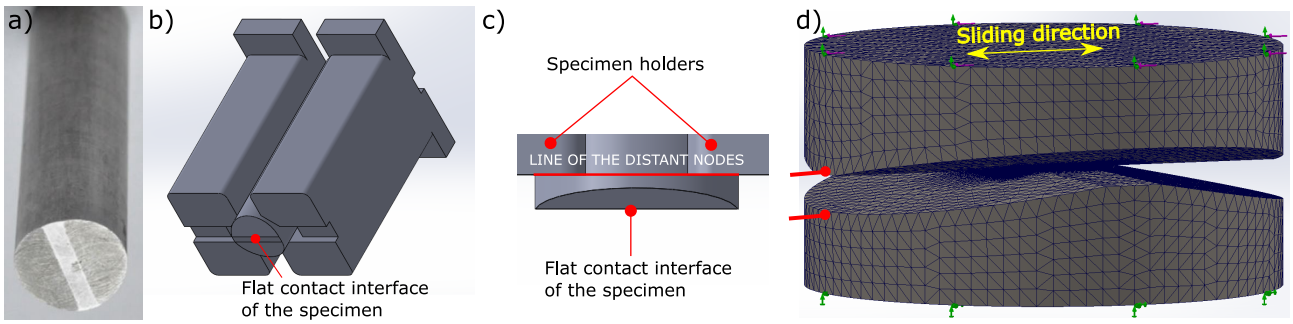


Figure 7.2: a) Photo of one specimen; b) Specimen held by the holders; c) Side view of the specimen close to the contact interface; d) FE mesh of the specimens and points of measured displacement.

This value is equal to 116 N/μm when laser points are at the minimum 0.6 mm distance as in the experiment (see laser locations of 7.2d). As a reference, the bulk stiffness is also shown between other different locations. As the point distance increases, the stiffness decreases since the relative tangential displacement is larger due to more bulk deformation.

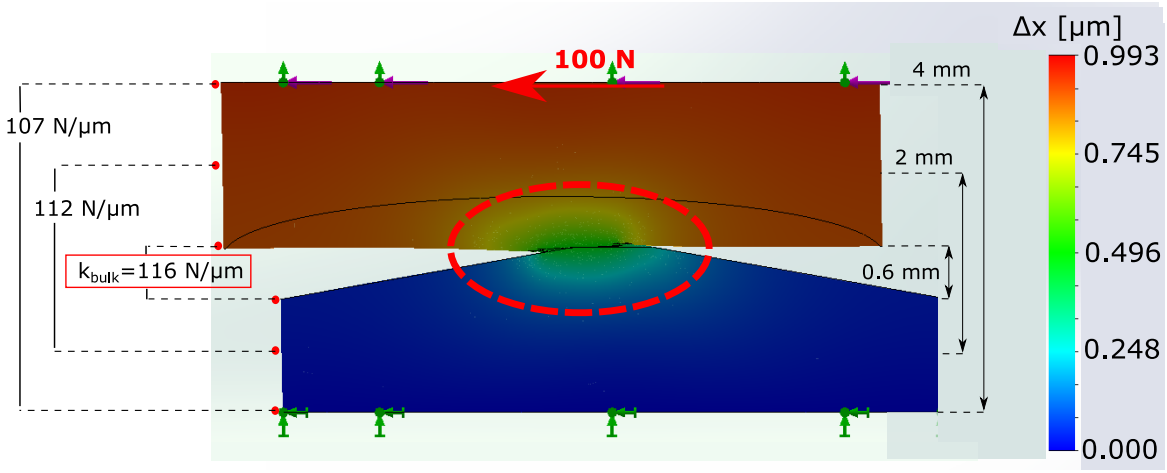


Figure 7.3: Displacement field of the deformed specimens under a 100 N tangential load (only the component in the sliding direction). Most of the deformation occurs in the portion highlighted with the red circle. Bulk stiffness values, k_{bulk}, are shown at different locations. The further the measurement points, the lower the k_{bulk}.

These values provide estimates of the value k_{bulk}, which defines the upper bound of the measured stiffness from hysteresis loops. The value of 116 N/μm (valid for a 1 mm^2 nominal area contact) is comparable to the measured contact stiffnesses from the hysteresis loops, which are in the order of 10-80 N/μm for different normal loads (see e.g. Fig. 4.23 - first row for a 1 mm^2 nominal area contact and different normal loads - from chapter 4). The measured values are lower than 116 N/μm because they also include the contribution of asperities and waviness due to the non-perfectly smooth real surface topography. This contribution can be estimated approximately by rewriting Eq. 7.1 as:

$$k_{topography} \approx (1/k_t - 1/k_{bulk})^{-1} \tag{7.2}$$

For a k_{bulk} equal to 116 N/μm and measured stiffnesses k_t in the range 10-80 N/μm, the $k_{topography}$ contribution due to asperities and waviness is in the range 11-258 N/μm. A similar

analysis on the bulk deformation was shown in the Appendix E to better understand the relation between k_t and the ultrasonic estimated stiffness, as previously described in section 5.2.3.

The preliminary FE analysis presented here suggests that care should be taken when choosing the contact stiffness values used as input in contact models for nonlinear dynamic analysis. If a finite element model with nominally flat interfaces is used, then the input contact stiffness for the nonlinear dynamic analysis should only include the effect of the asperities and waviness, $k_{topography}$, since the bulk deformation would already be included in the FE model itself. $k_{topography}$ can be approximated with Eq. 7.2 by measuring k_t from hysteresis loops and by estimating k_{bulk} from the FE model. This aspect is not commonly accounted for when providing measured contact stiffnesses as input in nonlinear dynamic analysis. Note that $k_{topography}$ depends on the surface topography and, therefore, measured specimens should have surface topographies similar to those of the actual contacting components of the jointed structure to be modelled or tested.

7.1.2 BEM simulations: effect of wear and surface topography

The FEM simulations of the previous section have investigated the effect of the bulk deformation, which leads to the upper bound of the measured contact stiffness. Here, an existing Boundary Element Method (BEM) solver is used to quantify the effect of the surface topography, which adds additional compliance and hence reduces the measured contact stiffness. Also the effect of wear is investigated with the BEM solver since it was shown in section 4.2.1 that the surface topography strongly changes with wear, resulting in consequent changes in the measured contact stiffness.

The BEM solver was previously developed at Imperial, as described in [144], but has not been used to investigate the variability of k_t with regards to surface topography and wear. The solver evaluates pressure distribution and rigid relative displacements of two contacting interfaces under normal and tangential loads imposed by the user. By plotting the tangential load versus the tangential relative displacement of the interfaces, the hysteresis loop is obtained and the tangential contact stiffness, k_t, can be extracted. The BEM solver needs as input the surface data of the contact interfaces in the form of heights matrices. The heights matrices can be either created manually by the user, as idealised shapes, or obtained from real optical scans of the actual interfaces taken with microscopes. Depending on the size of the matrices and hence on the detail of the interface mesh, different length scales can be modelled, from the micrometre asperity level to the millimetre macro-scale contact. Note that the BEM approach only solves the problem for the nodes on the contact interface by assuming an elastic half-space around the interface, in contrast to the FEM, which instead models the exact geometry of the bulk material around the contact interface. As a result, BEM approaches could provide inaccurate predictions in cases when the elastic half-space assumption does not apply to the investigated bulk geometry (i.e. when the size of the contact is comparable to the size of the surrounding bulk). However, BEM approaches are in general faster than FEM approaches since the latter require larger models that include information on the bulk geometry.

The BEM solver used in this study is described in detail in [144], and here only an overview is given on the formulation of the normal and tangential contact problems, which are solved by using the conjugate gradient method algorithm. The normal contact problem is solved first,

after defining the input height surface data and the applied normal load. For this contact problem, equations must be solved that satisfy the following three conditions:

- Compatibility of displacements: at any point in the potential contact area, the sum of elastic displacements, separation between the bodies and rigid bodies approach must be greater than or equal to zero.
- Displacement-force relationship: it must be satisfied according to the Boussinesq and Cerruti potentials [264], which are applicable since the BEM solver assumes the elastic half-space body description. The material of the contact bodies is assumed elastic and the deformations are small.
- Equation of equilibrium: the pressure distribution has to satisfy the Signorini-Fichera inequalities, namely that i) pressures must be larger than zero where nodes are in contact and ii) pressures must be equal to zero where nodes are not in contact.

The normal contact problem is solved by applying a given normal load and iterating on the pressure distribution and the area of contact until the three previous conditions are satisfied. Once the pressure distribution and the contact area have been defined, the tangential contact problem is solved, which is assumed to be uncoupled from the normal contact problem. The tangential contact problem is formulated assuming the Coulomb friction law, namely that the tangential force exchanged between two contact nodes cannot exceed the friction limit given by the friction coefficient multiplied by the normal load on those nodes. Starting from the user-imposed tangential load, nodal forces are calculated and, once the equilibrium is satisfied, the tangential contact problem is solved, giving as output the contact nodes in stick and slip condition and the rigid body tangential relative displacement. The rigid body tangential displacement is due to the local deformation of the elastic half-space around the contact interface. By plotting the user-imposed tangential load versus the rigid body tangential displacement, one force-displacement point of the hysteresis loop is obtained. By solving for different values of tangential loads (lower than the friction limit), the stick region of the hysteresis loop is plotted and the contact stiffness can be extracted from its slope.

Preliminary study with ideal interfaces

In chapter 4, section 4.1, it was shown that a slight curvature exists on the contact interfaces due to the interface sanding process (see Fig. 7.4a). This curvature was quantified by an equivalent radius of 33.2 mm. Even though this radius is relatively large compared to the small interface width of only 1 mm, it results in a bump of about 4 μm height that leads to an initial point contact rather than a uniformly distributed contact (the specimen interfaces could be associated to two crossed cylinders of radius 33.2 mm). With wear, the point contact develops in a fully distributed contact over the whole nominal area of contact, as shown with the sketch in Fig. 7.1b and confirmed with the experiments of section 4.2.1. To capture this behaviour and study its effects, a preliminary BEM analysis was performed by using "ideal" interface representations as input surface data. These ideal interfaces were created for a 1 mm*1 mm grid size with a 33.2 mm equivalent radius, but perfectly smooth and without any roughness, as represented in Fig. 7.4b. In addition, to represent the worn interface in an idealised manner, a flat portion at the tip was imposed as perfectly flat, as shown in Fig. 7.4c. The flat portion

represents the material removed due to wear. With this representation, the extreme idealised wear case is a perfectly flat 1 mm^2 interface without any curvature.

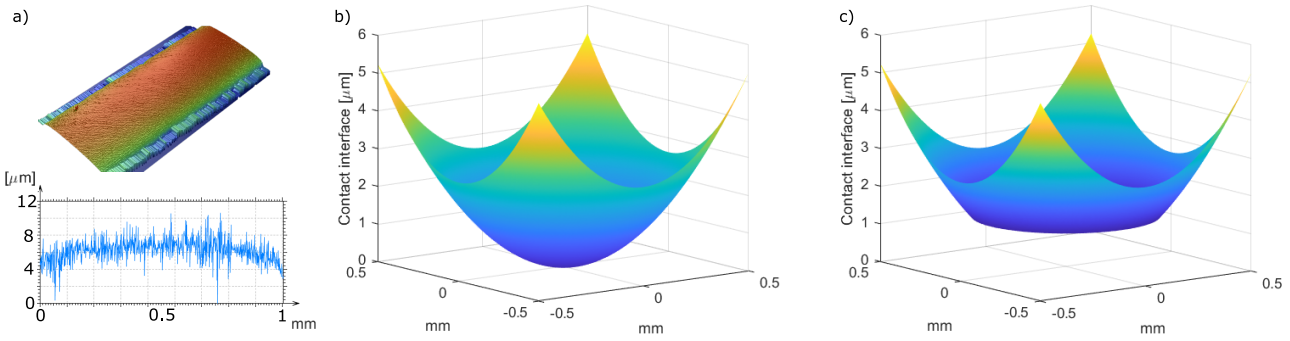


Figure 7.4: a) Curvature of the real specimen contact interface. When the mating specimen is oriented orthogonally, the resulting equivalent contact is a curved (spherical) contact; b) Rendering of the curved ideal unworn contact interface (33.2 mm curvature); c) Rendering of the curved contact interface with a 33.2 mm curvature and a flat portion at the tip that represents an ideal flat worn area of 0.34 mm^2.

Following this approach, six simulations were performed for the following worn interface extensions [0.24, 0.34, 0.44, 0.54, 0.6, 0.9] mm^2, which correspond to the worn areas of the tests shown in Fig. 4.16 within the round robin campaign presented in chapter 4. Those tests were performed with a 60 N normal load and hysteresis loops in gross slip. The same normal load was used as input to the BEM simulations together with a friction coefficient of 0.93 (same as that measured from those experiments) and a tangential load large enough to reach the friction limit and thus visualise the stick regime for the k_t extraction. Figure 7.5 shows the results for the ideal unworn interface of Fig. 7.4b and for the 0.34 mm^2 worn interface of Fig. 7.4c. For the unworn area (Fig. 7.5a-c), the normal and tangential pressures are highest at the centre of the contact and null at the extremes. This pressure distribution is expected since a point contact establishes with the mating interface, which is equivalent to a sphere-on-flat contact in accordance with the contact mechanics theory for spherical contacts [264]. The resulting force-displacement dependency is shown in Fig. 7.5c, with a k_t equal to 38.4 N/μm. For the worn interface, the pressure is null outside the contact, maximum at the edge and then again null at the centre. The k_t is equal to 57.9 N/μm. As expected, the k_t of the ideal worn interface is larger than the k_t of the unworn interface due to the reduced compliance resulting from the material missing at the centre of the contact.

Figure 7.6 shows the k_t predicted from the preliminary BEM analysis for the six "ideal" worn areas and compares them to the experimental values already shown in Fig. 4.16. Also the k_{bulk} obtained from the FE simulations presented in the previous section are shown for a comparison. First, BEM and FEM predictions are compared. The FEM predictions were obtained for fused specimens with a perfectly flat 1 mm^2 contact interface. Three different k_{bulk} were extracted from the FE model (see Fig. 7.3) for three different laser distances. Those k_{bulk} should be compared to the BEM k_t predictions for the 1 mm^2 worn area of contact, which also corresponds to a perfectly flat interface over the 1 mm^2 grid given as input to the BEM solver. The BEM k_t for such fully flat contact interface is equal to 99.6 N/μm, which is lower than the FEM k_{bulk} values, but in a similar range. Although BEM and FEM predictions are similar, as expected, they are not really comparable for the following two competing contributions:

- Material compliance: stiffnesses predicted from both methods result from the local deforma-

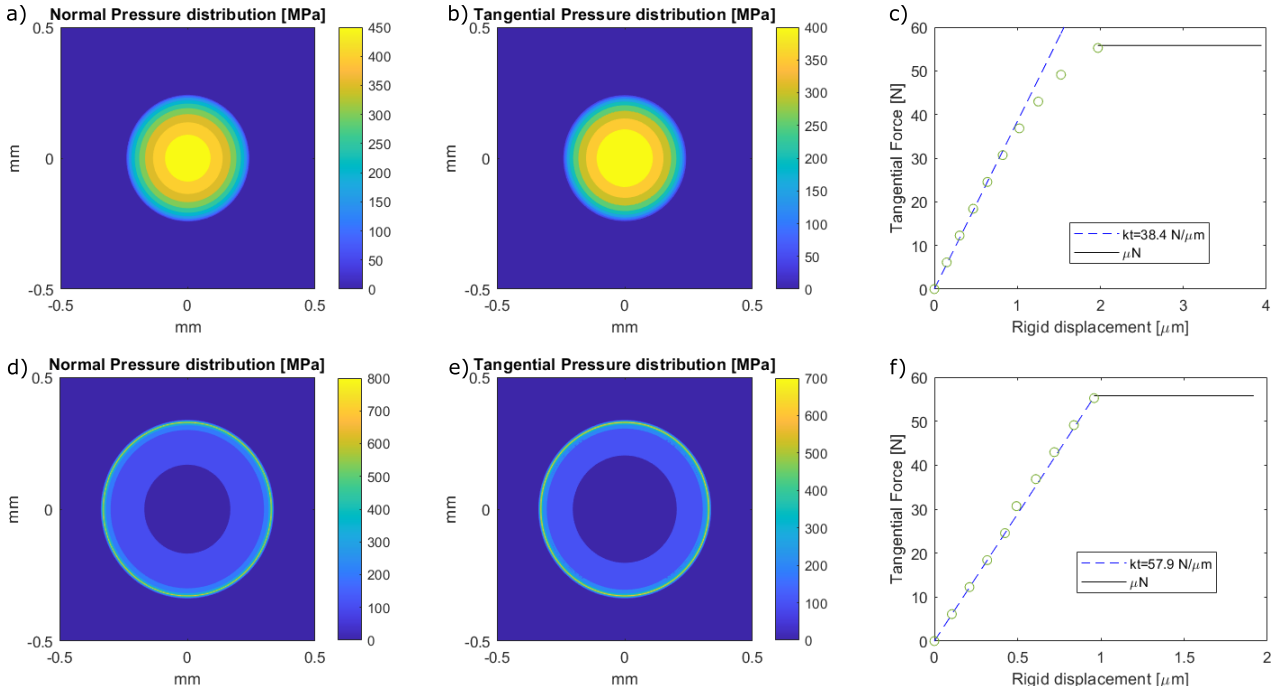


Figure 7.5: BEM predictions for the (a-b-c) ideal unworn interface and the (d-e-f) 0.34 mm^2 "ideal" worn interface: a-b/d-e) normal and tangential pressure distributions; c/f) Hysteresis loops.

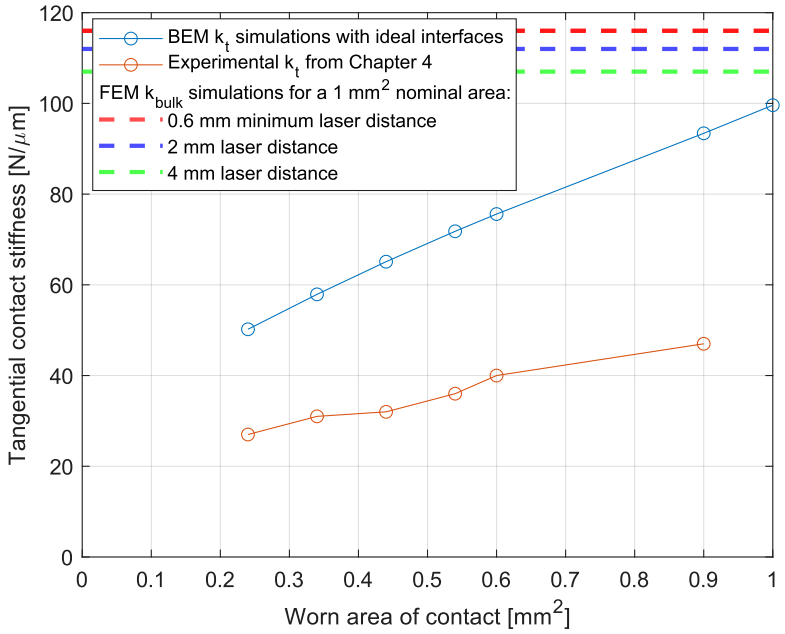


Figure 7.6: k_t versus worn areas of contact: comparison of experimental data from Fig. 4.16 and BEM predictions with ideal worn areas set up as in Fig. 7.4c. Also the k_{bulk} obtained from the FE simulation of Fig. 7.3 are shown.

tion of the material around the interface. In the case of BEM, the elastic half-space is assumed, which means that the 1 mm^2 contact interface is surrounded by a semi-infinite amount of elastic material that mostly deforms locally in proximity of the interface. Instead, FEM simulates the exact finite geometry of the specimen, which has less material than the infinitely extended half-space and, hence, deformes more and is less stiff. As a result, BEM should provide larger

stiffness predictions than the FEM bulk predictions.

• Displacement measurement points: in the case of BEM, the measurement points for the relative displacement are located, on the elastic half-space, infinitely far from the contact interface. The resulting relative tangential displacement between such infinitely far located points reaches a finite value asymptotically since most of the deformation occurs in proximity of the interface and not far from it. In the case of FEM, displacement measurement points were located 0.6, 2 and 4 mm far from the contact, as shown in Fig. 7.3. Because of this difference in the displacement measurement points, BEM should provide larger relative displacements, and hence lower stiffnesses, than FEM. In fact, BEM measures the (asymptotically-finite) tangential relative displacement at an infinite distance, while the FEM stiffness keeps decreasing as the measurement distance increases. To make results more comparable, the tangential relative displacements at 0.6, 2 and 4 mm distances should be extracted from the BEM solver, rather than using the relative displacement of infinitely far points. This extraction was not performed since it required further modifications in the existing BEM solver and, in addition, it was not required for the purpose of the study.

Those two contributions are competing and make the comparison of FEM and BEM predictions challenging. It is challenging to separate the effect of local deformation of the interface (or of the elastic half-space) from the deformation of the finite bulk modelled with FEM because it is not known where the deformation of the interface becomes negligible. In addition, those stiffness contributions depend on which scales they do represent and on how much material is considered for their definition. This is an important topic not only for simulations, but also for the interpretation of experimental measurements. For an accurate modelling, the scales that are missing in the FE models should be known and accounted for by using representative contact stiffness input values. Nevertheless, in the present study, values were comparable when considering the 1 mm^2 worn area BEM simulation.

Coming back to the comparison of BEM k_t with experimental data of Fig. 7.6, results are quite promising. The BEM k_t increases with larger worn areas, almost doubling as observed in the experiments. This occurs because, as previously discussed, less compliant curved material is present for the larger ideally flat worn interfaces. This k_t increasing trend with the worn area of contact confirms the experimental proposed hypothesis of the k_t wear induced increase due to a change in the surface topography, and more precisely a change in the waviness from a 33.2 mm radius curvature to a flatter condition[1]. It is worth mentioning that this BEM solver has been used to model the evolution of the contact interfaces with wear in a nonlinear dynamic analysis framework [141–143]. This was one of the few attempts found in the literature to include wear-induced evolution of contact interfaces into nonlinear dynamic solvers. More information about this approach was already given in section 2.4.

In the presented simulations, the increasing trend of k_t with the worn area of contact was in agreement with the experimental data. However, BEM predictions provided estimations larger than the experiments, almost twofold. This could occur because the worn interface was considered as "ideally" nominally flat, while the real worn interface presented roughness and wear scars as shown e.g. in Fig. 4.16c. Roughness and wear scars would almost certainly contribute to a softening of the contact and that is why they should be modelled to obtain more

[1]These results are in agreement with a similar FE analysis that investigated the effect of the surface topography on the k_t estimations. The FE analysis was performed within a Master Thesis project supervised by the author and is summarised in the Appendix F.

realistic contact stiffness estimations. To investigate this, a second set of BEM simulations was performed by using, as input surface data, the profiles of the real interfaces measured with a microscope.

Validation study with real interfaces

Real surface data obtained from an Olympius LEXT®OLS5000 3D Laser Confocal Microscope was used as input to the BEM solver to obtain more accurate predictions. The surface data was imported into MATLAB in the form of heights with a mesh size of 256x256 elements. This mesh size resulted in an average spatial resolution of 4 μm per element and was the best compromise between computational efficiency and accuracy based on a performed convergence study. Typical surface data is shown in Fig. 7.7a-b for a specimen pair. Material transfer spots due to wear are visible, suggesting that the dominant wear mechanism was adhesive. Although the matching in the two specimen interfaces is clear, their relative orientation needed to be slightly changed to obtain a perfectly matching grid, as shown in Fig. 7.7c for specimen B, where the wear marks are better aligned with those of the specimen A in Fig. 7.7a. Even though the specimens were manually positioned under the microscope for each scan, they could not always be perfectly aligned to the micrometre level to replicate the orientation observed during the experiment. To find the orientation that gave the best match, a MATLAB script was written to run a cross-correlation study that evaluated the degree of similarity of the two interfaces for several different relative orientations of the two surfaces. The cross-correlation function for the specimen pairs was determined using the *xcorr2* MATLAB function. Once the best orientation was found, as in Fig. 7.7c, two square matrices of the same size for both specimen interfaces were created, see Fig. 7.7d-e. The height difference of such matrices, shown in Fig. 7.7f, was used as input to the BEM solver. As a reference, the correlation coefficient of the two presented interfaces was 0.84 (a value equal to one indicates two perfectly matching interfaces and a value equal to zero indicates two unmatched interfaces).

Note that, during the experiments, specimens were mounted manually in the clampings, with the help of an aligning system, and could have been not perfectly perpendicularly aligned. This could be the reason why the specimens in Fig. 7.7d-e seem slightly rotated and not perfectly perpendicular. This uncertainty in the specimen assembly procedure has been experimentally quantified with the repeatability study previously shown in section 4.2.2, where the uncertainty induced by the specimen mounting procedure was quantified. It was found that differences in the measured tangential contact stiffness were always below the 25% when specimens were disassembled and reassembled in the clamping. This uncertainty might also explain why the experimental trend in Fig. 7.6 is not perfectly linear with the increasing worn area of contact.

Once surface data were obtained for the six specimen pairs of the experimental test shown in Fig. 4.16, BEM simulations were performed. Also in this case, a normal load of 60 N was used as input to the BEM solver together with a friction coefficient of 0.93 (same as that measured from those experiments) and a tangential load large enough to reach the friction limit and thus visualise the stick regime for the k_t extraction. Figure 7.8 shows the resulting k_t for all the specimen pairs. k_t values are much closer to those experimental if compared to the ideal interface simulations. Although this is a promising result, k_t values do not follow the expected increasing trend with the increasing worn area of contact. This may be because the worn specimens were cleaned soon after the test and therefore any wear debris had been removed before the optical measurements, thus leading to surface data with missing material. The wear

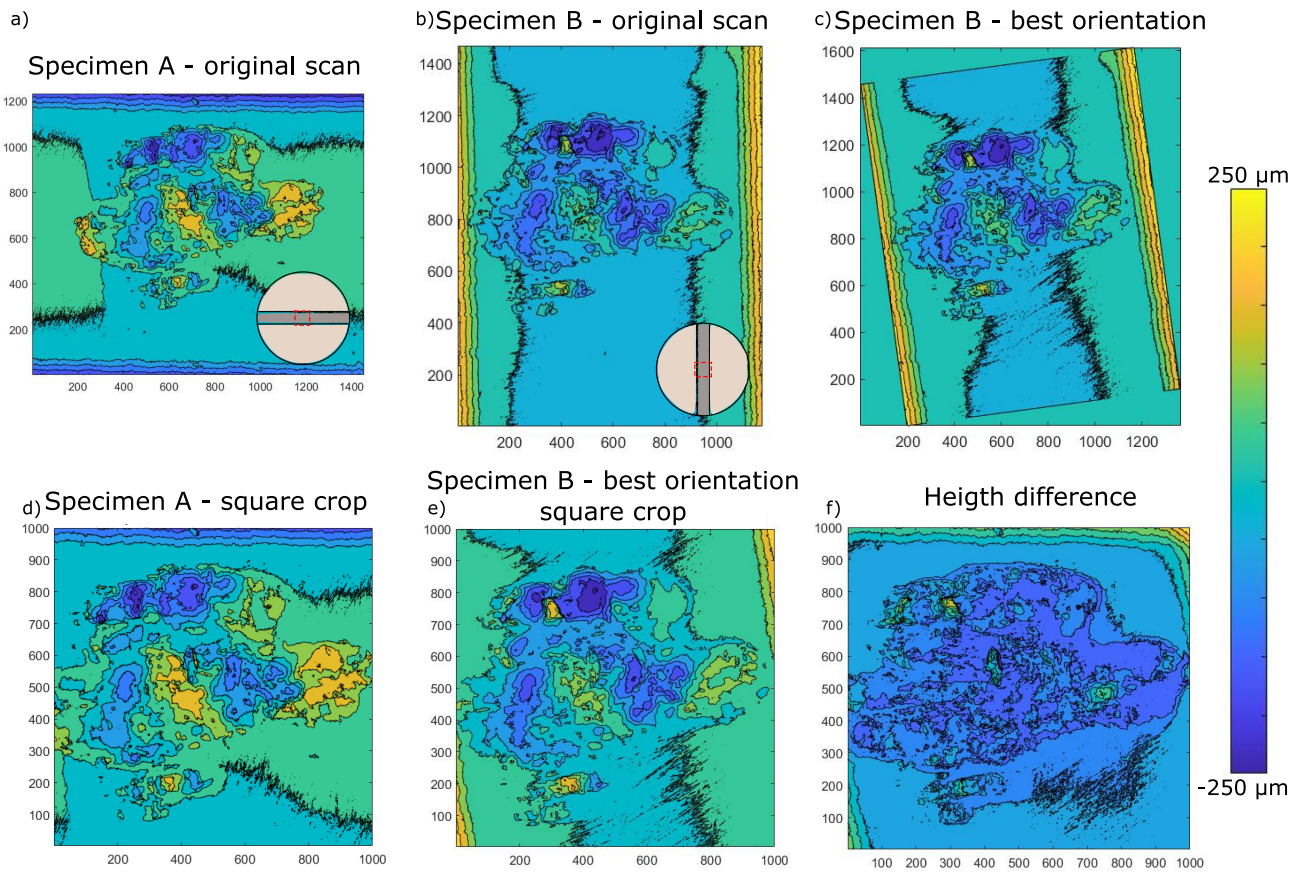


Figure 7.7: Real surface data: a-b) Specimens A and B; c) Specimen B with best orientation to match specimen A (correlation coefficient of 0.84 in this case); d-e) Specimens A and B after cross-correlation and cropping; f) Height difference of the two specimen interfaces used as input in the BEM solver.

debris size varies from as low as 0.5 μm to hundreds of μm [280] and it is expected to be an important contribution to the k_t estimations since during the test the debris is entrapped in the interface and it affects the compliance of the contact. Debris can either soften the contact when it generates a softer layer than the paired materials or stiffen the contact if it interlocks between the two paired materials.

To give an idea of the effect of the missing debris on the surface data, Fig. 7.9 shows the relative height of the two contact interfaces for the experimental test with a worn area of 0.44 mm^2. A reference plane is also plotted to show where the worn area would lie. The peaks and valleys that pass through the plane are in the order of the tens of μm and are probably the result of a wrong relative height calculation due to the absence of the wear debris in the surface data. If debris would have been scanned, a more evenly distributed worn area would have been obtained, probably leading to numerical trends more similar to those observed experimentally. This suggests that a potential improvement for the BEM technique is to include the effect of wear debris, for example by modelling the wear evolution, as performed in recent studies [166]. An alternative method would be to provide more accurate input surface data by scanning also the wear debris [280, 281], although it might be difficult to quantitatively measure it from experiments since, as soon as the contact is opened, most of this debris would detach from the contacting interfaces, thus making it challenging to verify its original location within the contact. Note also that the k_t predictions presented here did not show any time/velocity

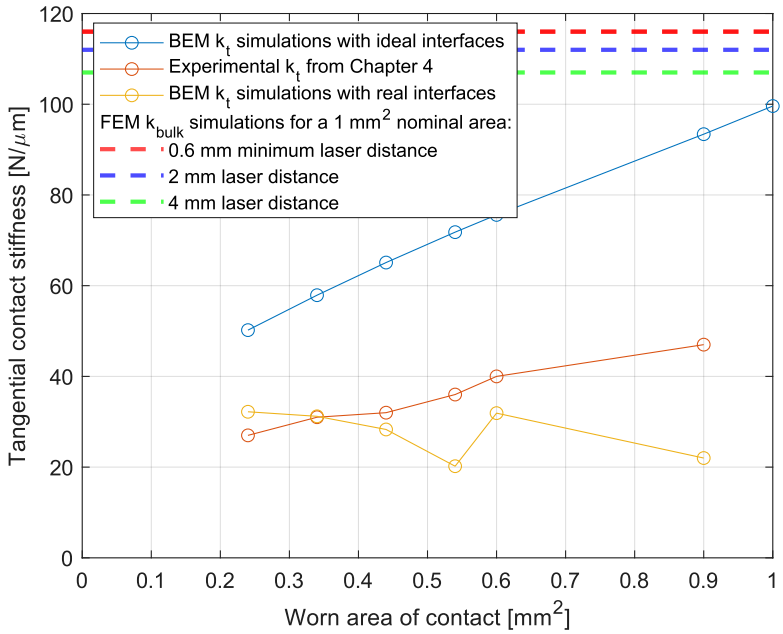


Figure 7.8: k_t versus worn areas of contact: comparison of experimental data from Fig. 4.16 and BEM predictions with ideal and real worn areas.

dependence, although ultrasonic measurements in chapter 5 demonstrated that the contact stiffness strongly depends on the time of static contact because of the ageing phenomenon. This effect should also be considered when comparing high-frequency hysteresis measurements with quasi-static contact simulations.

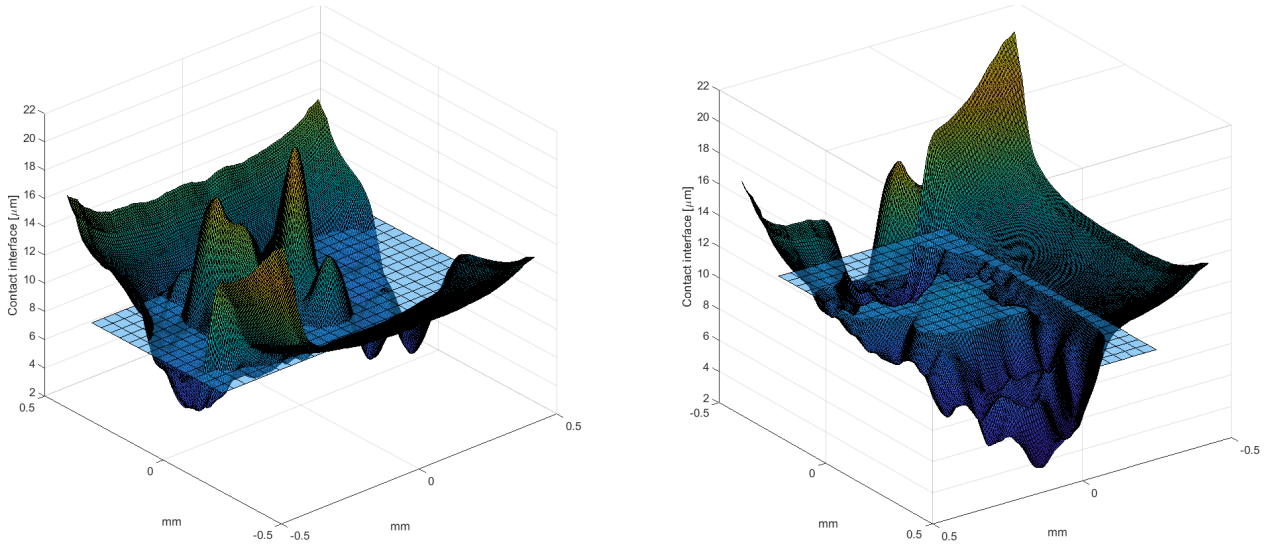


Figure 7.9: Relative height of the two contact interfaces for the test with a 0.44 mm^2 worn area of contact. A reference plane is plotted to show where the worn area would lie. The peaks and valleys that pass through the plane are probably due to missing wear debris that leads to a wrong relative height calculation.

In conclusion, this section provided further evidence that the global (waviness) and local (wear scar) geometry play a significant role in the obtained contact stiffness, although this aspect is often neglected in nonlinear dynamic analysis. The initial experimentally-based hypothesis

regarding the significant effect of surface topography and wear on the k_t estimations is hence confirmed. In addition, the BEM approach showed high potential in modelling the contact stiffness of contacting interfaces, although more work is needed to include more accurate descriptions of the interfaces, for example by including the effects of wear debris. Taking these features into account in the modelling is challenging and this limits the accuracy of the current modelling approaches.

7.2 Nonlinear dynamics simulations

The quasi-static contact simulations presented in the previous section validated some of the hypotheses on the contact mechanisms proposed in chapter 4 and showed that the same effects can be captured by existing models. This section assesses the effects of such contact mechanisms on the nonlinear dynamic response of systems with friction. To do so, two different test cases are investigated: the Imperial friction rig and the Imperial underplatform damper rig.

7.2.1 Imperial friction rig: effect of wear

Section 6.2.3 has shown how strongly wear affected the dynamic response of the Imperial friction rig, leading to significant variations in natural frequencies and damping. Here, the two degrees of freedom (DOFs) lumped model of the friction rig, previously presented in section 6.1, is used to numerically assess the effect of wear. This is done by proposing an improved physically-based, wear evolving Bouc-Wen model in conjunction with a time integration code that solves the nonlinear dynamic problem. The results here presented were obtained during a group project within the 2018 Nonlinear Dynamics of Coupled Structures and Interfaces (ND-CSI) Summer School organised at Imperial College [250] as part of the EXPERTISE programme, which funded this PhD project. The group was made up of five PhD students and everyone contributed equally to the work, including the author. Results of that project were published in [20] and are reported here in a summary.

Description of the modelling approach and improved contact model

A detailed description of the modelling approach can be found in [20], and a summary is given here for completeness. A Newmark time integration scheme [31] was used to solve the following dynamic equilibrium equation that describes the rig vibration:

$$M\ddot{\mathbf{x}}(t) + C\dot{\mathbf{x}}(t) + K\mathbf{x}(t) = \mathbf{F_{ex}}(t) + \mathbf{F_{nl}}(t, \mathbf{x}, \dot{\mathbf{x}}) \tag{7.3}$$

where M, C and K are respectively the mass, damping and stiffness matrices of the lumped model. $\ddot{\mathbf{x}}, \dot{\mathbf{x}}, \mathbf{x}$ are the acceleration, velocity and displacement of the degrees of freedom of the lumped model, $\mathbf{F_{ex}}$ is the input excitation force and $\mathbf{F_{nl}}(t, \mathbf{x}, \dot{\mathbf{x}})$ is the nonlinear friction force. The known variables are the matrices M, C and K and the excitation force, which was taken from the exact time signals measured during the hammer test campaign described in section 6.2.3. The unknowns of the equation of motion are the displacements (velocities and accelerations) and the friction force. The friction force can be predicted by using any of the

existing contact models in the literature, such as Jenkins or Bouc-Wen models as described in section 2.3. Here, the Bouc-Wen model is chosen since it could capture also microslip. The Bouc-Wen model was used to obtain hysteresis loops by taking as input a cyclic displacement and other contact parameters. This model is described in detail in section 2.3.2, where a physically-based formulation is presented that is particularly useful in friction problems.

One shortcoming of the existing physically-based Bouc-Wen formulation is that it does not include the wear evolution. To account for this, the proposal of Ma et al. [282] was followed. They modified the original Bouc-Wen formulation to account for the degradation of the hysteresis loops, defining a function to represent the degradation of the other parameters in the model. Here, this idea is introduced to the physically-based model of Eq. 2.9 by defining a set of wear functions that describe how the physical parameters evolve in time. These evolving parameters are the contact stiffness k_t, the slope during gross slip (if present) k_p and the friction coefficient μ, and they are all pre-multiplied by their respective wear functions. The wear functions, called f_μ, f_{k_p} and f_{k_t}, can take any form which is in agreement with experimental curves (i.e. a fitting is required unless the wear laws are known for the considered material and geometry), as those previously shown in Fig. 4.12, and they can be formulated as a function of time but also of the dissipated energy. The resulting modified Bouc-Wen model that takes the evolution of wear into account is formulated as:

$$\begin{cases} \mathbf{F_{nl}}(\mathbf{x}, \dot{\mathbf{x}}) = f_{k_p}(E) k_p \boldsymbol{\Delta x} + f_\mu(E) \mu N \boldsymbol{\xi}(\boldsymbol{\xi}, \boldsymbol{x}, \dot{\boldsymbol{x}}) \\ \dot{\xi} = \frac{f_{k_t}(E) k_t - f_{k_p}(E) k_p}{f_\mu(E) \mu N} (1 - (\sigma \mathrm{sgn}(\dot{x}\xi) + 1 - \sigma) \left|\xi\right|^n) \dot{x} \end{cases} \tag{7.4}$$

where a typical wear function for the considered contact parameters, based on the best fit of the experimental trends, can be written as:

$$f(E) = 1 + a\ e^{-\frac{b}{E}} \tag{7.5}$$

where a and b depend respectively on the maximum amplitude and the speed at which the steady state is reached. When $E = 0$, then $f(E) = 1$ and therefore the initial value of the parameter is obtained since it becomes just pre-multiplied by 1. When $E \to \infty$, $f(E) = a + 1$, which leads to the steady state observed experimentally and a is, therefore, the normalized change of amplitude of the contact parameter. This newly modified Bouc-Wen formulation has been used to obtain the numerical results. Please note that the wear functions can be applied to any contact model whose evolution of the contact parameters with wear is known. For example, this formulation is also valid for Jenkins elements [89, 90] or a Valanis model [108].

To simulate the evolution of wear with increasing numbers of cycles, the Newmark time integration scheme [31] was used to solve Eq. 7.3 and the friction force F_{nl} was calculated by solving Eq. 7.4 from the modified Bouc-Wen model. At each time step, the energy dissipated was computed and the contact parameters (μ, k_t and k_p) were updated. Once the equation was solved, it was possible to plot the frequency response function (FRF) of the moving arm and compare it to the experimental FRF. Additionally, also the hysteresis loops were obtained since they were given by the friction force plotted versus the displacement of the moving arm.

Numerical results and comparison with experiments

The experimental test described in section 6.2.3 is used as a reference for the simulations. The test was performed with a 60 N normal load and displacement amplitude of 14 μm and an excitation frequency of 100 Hz. Figure 7.10c and d show the experimental evolution with wear of the friction coefficient μ and the contact stiffness k_t respectively. The contact stiffness (i.e. the slope of the stick portion of the loops) increases with wear, as well as the friction coefficient. The Figure also shows the wear functions used to fit such data, which are summarised in Table 7.1 for future references for Bouc-Wen parameters applications. Figure 7.10a shows the evolution of the numerical hysteresis loops with wear resulting from such wear functions. Several of these curves were superimposed with the experimental, as shown in Fig. 7.10b. The match confirms that the proposed method correctly uses the experimentally-fitted equations to simulate the evolution of wear in frictional contacts.

Table 7.1: Bouc-Wen parameters used to replicate experimental trends of the test of section 6.2.3.

	Value	Wear Function	Parameters
μ	0.11	$f_\mu(E) = 1 + b \cdot log(aE + 1)$	a=1.3e^9; b=0.26
k_t	27.3	$f_{k_t}(E) = 1 + a\ e^{-\frac{b}{E}}$	a=1.32; b=150
k_p	0.88	$f_{k_p}(E) = 1 + aE$	a=0.24
σ	0.5	/	/
n	2	/	/

As described in section 6.2.3, FRFs were also measured on the friction rig, before and after the wear test, at two different norma loads, 7 N and 60 N. The time integration code was used to predict such FRFs in order to address a comparison with the experimental shown in Fig. 6.6. The input excitation force used for the numerical simulation was the same as that measured during the hammer test. The FRF was obtained by plotting the acceleration (from the solution of Eq. 7.3) over the input force, for the range of frequency of interest. In Fig. 7.11 the numerical FRFs are shown. The results are quite promising since they follow the same trend of the experimental FRFs shown in Fig. 6.6. For both normal loading conditions, the natural frequency of the first peak increases after wear, resulting in a stiffer system. This stiffening is due to the increases in friction coefficient, friction limit and contact stiffness. Damping is also well replicated since the peak after wear is more damped than the peak before wear for the 7 N normal load case. The opposite occurs for the 60 N normal load case again in accordance with the experimental data. This confirms the reliability of the numerical approach but also highlights the good quality of the experimental measurements that fed the friction model. More on the physical origin of these behaviours have already been discussed in section 6.2.3.

The very good agreement between the trends of experimental FRFs of Fig. 6.6 and numerical FRFs of Fig. 7.11 is a promising result since i) a simple 2 DoFs model was used to represent the friction rig and ii) only one calibration was performed for the modelling, namely matching the experimental evolution of friction coefficient and contact stiffness with the numerical evolution through the wear functions. Although the evolution of these contact parameters corresponded to a wear experiment conducted at 60 N normal load, the model performed well even outside of the calibrated regime of 60 N, predicting the correct trend of the FRFs also for the 7 N normal load case. Therefore, the newly proposed wear formulation has shown a very good capability

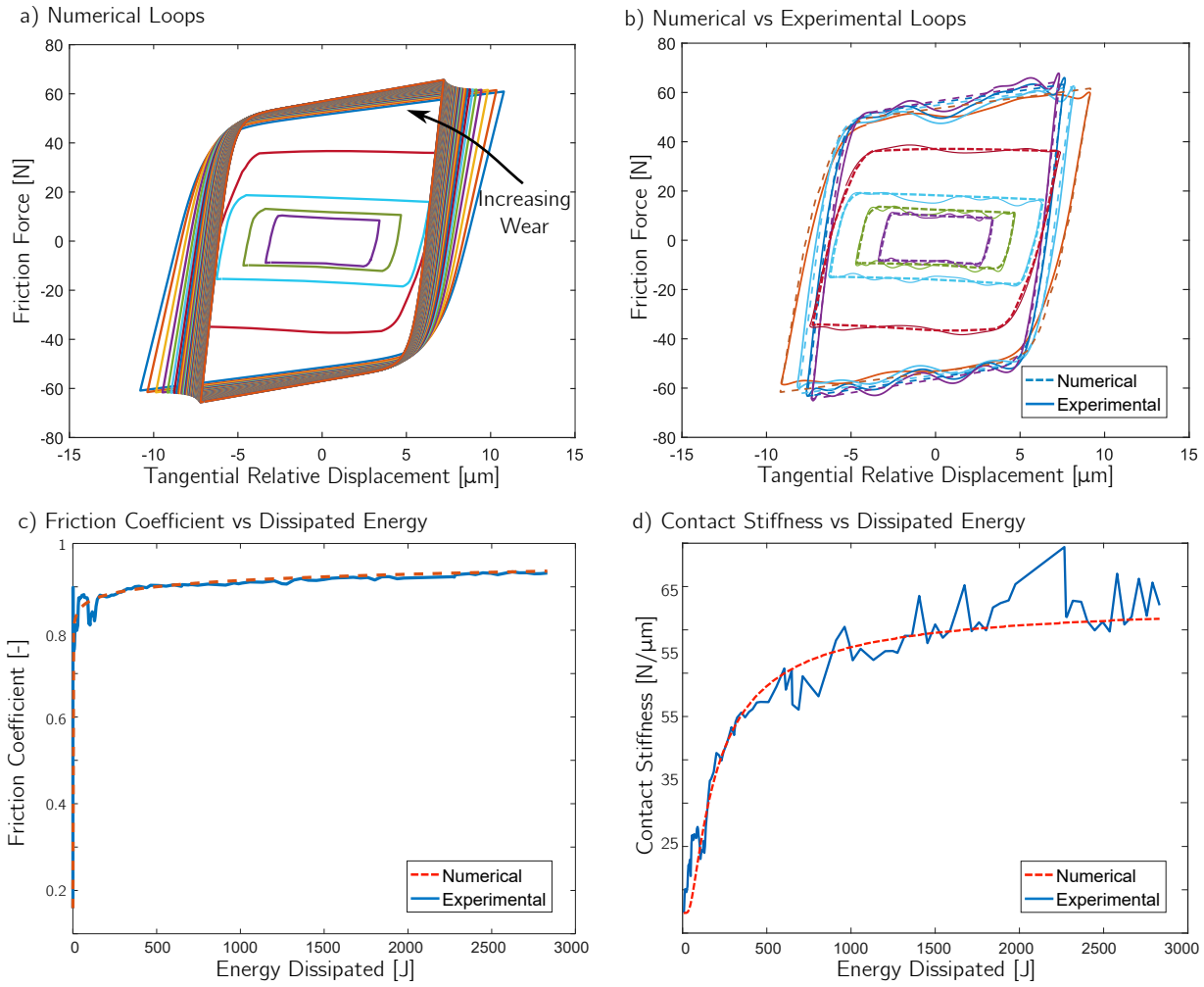


Figure 7.10: Comparison between numerical and experimental results for the test of section 6.2.3: a) numerical loops; b) numerical loops vs experimental loops; c) friction coefficient vs energy dissipated (wear function defined in Table 7.1); d) contact stiffness vs energy dissipated (wear function defined in Table 7.1) [20].

in representing the evolution of both hysteresis loops and system dynamics and highlighted the importance of including the effects of wear in nonlinear dynamic analysis.

7.2.2 Underplatform damper rig: effect of contact stiffness load dependency and uncertainty quantification

The previous section has shown how to include the effect of wear in nonlinear dynamic analysis and how important its effects are for accurate predictions of the dynamic response of the system. This section shows other improvements for nonlinear dynamic analysis focused on the choice of more accurate values of contact stiffness, k_t, and friction coefficient, μ. This is done by implementing some of the suggested guidelines from the round robin test, namely the k_t load dependency and the uncertainty in μ and k_t, in an existing modelling approach by using an in-house developed nonlinear dynamic solver. The test case for this study is the underplatfrom damper rig that was designed and built at Imperial and described in detail in [19]. The rig consists of two simplified turbine blades equipped with an underplatform damper (UPD) as

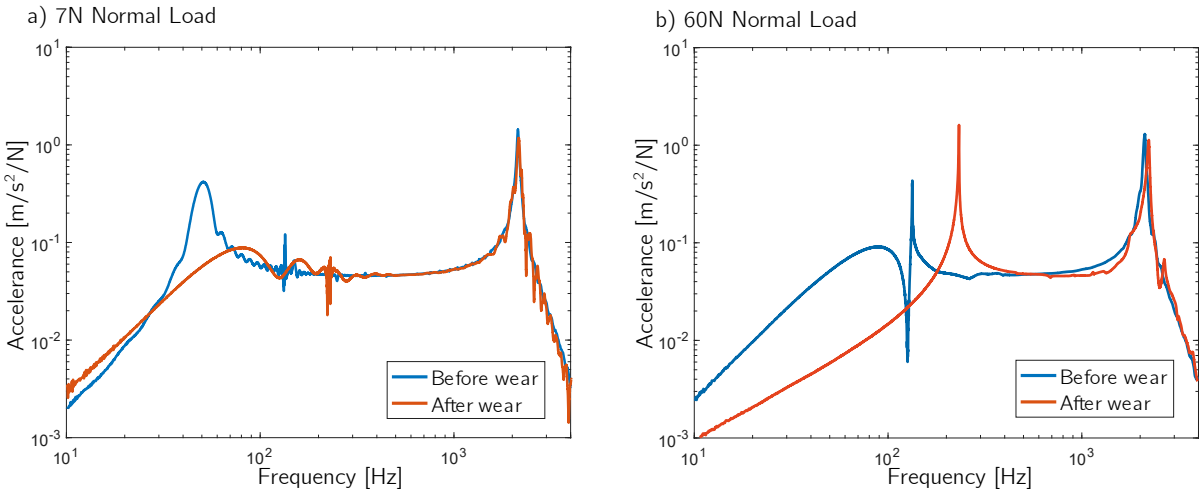


Figure 7.11: Numerical FRFs, before and after wear, based on the input hammer excitation of the test 1: a) 7 N normal load; b) 60 N normal load. Compare with the experimental FRFs in Fig. 6.6 [20].

shown in Fig. 7.12. The UPD is pulled against the blade platforms by means of a pulley system. An electrodynamic shaker is attached to the base of one of the blades and excites harmonically the whole system. Displacements of damper and blades are measured with laser doppler vibrometers.

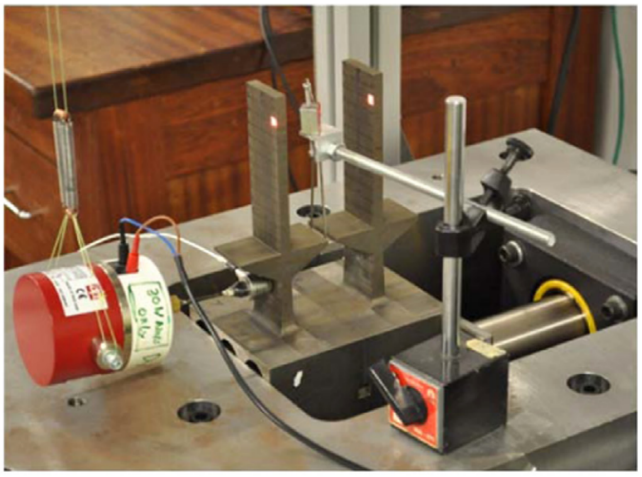


Figure 7.12: Photo of the underplatform damper rig [19].

A set of FRF measurements was originally shown in [19] concerning the first two modes of the rig, which are the in-phase and out-of-phase bending modes of the two blades. Experimental FRFs of those modes have been compared against FRFs predicted with a multi-harmonic balance-based solver. The predicted FRFs were in very good agreement with the experimental FRFs of the out-of-phase mode, while the in-phase mode was less accurately captured. Some hypotheses were proposed for this lower accuracy and this section attempts at verifying those hypotheses by improving the simulations and implementing some of the guidelines suggested in the previous chapters, such as the contact stiffness normal load dependency.

Description of modelling approach and multi-harmonic balance-based solver

The FRFs were predicted by following the standard approach for the nonlinear dynamic analysis of jointed structures already described in section 2.1. The approach consists of modelling the individual components (blades and damper in this case) with Finite Elements and connecting their contacting interfaces employing contact elements that predict the exchanged friction forces. Once the contact elements are defined over the discretised contact interfaces of the components, the nonlinear dynamic analysis can be performed. In the present study, the multi-harmonic balance-based solver FORSE (FOrce Response SuitE) is used for such analysis. The solver has been developed by the Vibration University Centre at Imperial and is described in detail in [97]. This solver is used due to its computational efficiency as compared to the time integration code described in the previous section. The higher computational efficiency is needed since the input FE models used here are much larger than the simplified 2 DoFs model used in the previous section.

A short overview of the FORSE solver is given here. The solver predicts the FRFs by finding the solution to the dynamic equilibrium equation described before (Eq. 7.3). The problem represented by Eq.7.3 is expressed in the time domain. By applying the Multi-Harmonic Balance Method (MHBM), it is possible to turn the initial system of time-domain nonlinear second-order differential equations into a set of frequency-domain non-linear algebraic complex equations, obtaining sensible reductions in the computational times. This transformation from time to frequency domain is possible because the external excitation $\mathbf{F}_{ex}$ is periodic in the investigated experiments, while in the previous section a (non-periodic) hammer impact excitation was used. As a result of the periodic excitation, also the displacements $\mathbf{x}$(t) and the nonlinear friction forces $\mathbf{F}_{nl}$ are periodic[2] and, therefore, they can be approximated by truncated Fourier series with n harmonics as expressed below:

$$\mathbf{x}(t) = \mathbf{Q}_0 + \sum_{j=1}^{n} \mathbf{Q}_j^c \cos(j\omega t) + \mathbf{Q}_j^s \sin(j\omega t) \tag{7.6}$$

where $\mathbf{Q}_0$ is the 0^{th} order harmonic coefficient, $\mathbf{Q}_j^c$, $\mathbf{Q}_j^s$ are the j^{th} harmonic coefficients for each DOF, and ω is the excitation frequency. This system of algebraic equations is solved with a Newton-Raphson method for the harmonic coefficients, as described in detail in [97].

The solutions obtained by the FORSE solver (i.e. the displacements of all the DOFs) strongly depend on the estimations of the friction forces arising at the contact between damper and platforms. As previously mentioned, such friction forces are estimated for each contact node pair by means of contact models. In the case of the present study, the contact models used to connect the node pairs were the 3-directional Jenkins elements, which are described in detail in section 2.3, Fig. 2.9. Jenkins elements were used to be consistent with the original UPD study presented in [19], which modelled the contacting interfaces with those contact elements. Those elements need three inputs: i) the cyclic relative displacement between the contacting node pairs; ii) values for tangential and normal contact stiffnesses; iii) value for the friction limit at which sliding occurs, defined by the friction coefficient multiplied by the normal load acting on the contact nodes. Reliable input contact parameters, i.e. k_t and μ, are required

[2]Only the steady state response of the system is periodic, while the transient response is not periodic, since it is not dependent on the external forces. Consequently, the MHBM can only compute the steady state response of the system and not the transient.

for accurate friction force estimations and hence accurate solutions to the nonlinear dynamic problem. The next two sections investigate the effects of such contact parameters on the FRF predictions. Blades and damper FE models used in the simulations were the same as those used and validated in the original study [19], in which the blade/damper contact interfaces were discretised with 146 Jenkins elements.

Effect of the contact stiffness load dependency

The original study on the UPD rig [19] showed a very good agreement between experimental and numerical FRFs for the out-of-phase (OOP) mode. A good match was achieved in the resonant frequency since the experimental resonance (435.5 Hz) was similar to the numerical (440 Hz), difference of only 1%. Instead, the in-phase (IP) mode did not have such a good agreement in the resonant frequency, since the experimental resonance (390 Hz) was lower than the numerical (424 Hz) by almost 10%. The simulations predicted a stiffer system (i.e. higher resonant frequency) than the experiments. The reason for this stiffening has been attributed, in that study, to the use of a constant input contact stiffness, independent of the normal pressure. The use of a constant contact stiffness was more limiting for the in-phase mode, which involved rotations of the damper during vibration with consequent significant normal load variations.

Here, a new set of simulations is performed to improve the match by including the contact stiffness normal load dependency as suggested in chapter 4. The chapter highlighted the large influence of the normal load on the k_t and suggested accounting for this dependency by using the experimental law given in Table 4.4. In the original simulations [19], a constant K_T value of 60 N/μm/mm^2 was used based on the experimental measurements available at that time (capital letters are used here for K_T since it is normalised by the area of contact). According to the experimental law given in Table 4.4, a K_T of 60 N/μm/mm^2 would be given by a pressure of 90 MPa (see also Fig. 4.24). However, the average contact pressures at the UPD/blade platform interfaces are further below, in the range of 0.1-1.5 MPa, given the applied normal load and the damper nominal area of contact [19]. The experimental law given in Table 4.4 indicates that the corresponding K_T values for this pressure range are below 7 N/μm/mm^2, which are almost an order of magnitude lower than the constant K_T originally used in [19]. Therefore, a new set of simulations was performed with updated K_T values and compared against experiments.

Figure 7.13a-b shows the experimental measurements from [19], which were performed for different excitation amplitudes to assess the effect of the friction nonlinearity. In the Figure, the experimental resonance of the 0.96 N excitation amplitude case is highlighted, as a reference, in green and red dashed lines for the IP and OOP modes respectively. Figure 7.13c shows a summary of the new simulations, which were performed for three different stiffness values and different excitation amplitudes. The Figure also shows the experimental resonances with dashed lines. The IP mode is strongly affected by the k_t variations, with changes in the resonant frequency up to 10%. The best match with the experimental resonance is obtained for a stiffness value of 1.4 N/μm/mm^2, which is within the expected stiffness range for the blade/damper contact pressure. The worst case is for the originally used stiffness value of 60 N/μm/mm^2. The OOP mode shows a less marked stiffness dependency, with the best match in resonance being for a stiffness value between 1.4 and 6.5 N/μm/mm^2. It is thus concluded that the upgrade and use of lower stiffness values led to better representations of the dynamic behaviour of the system.

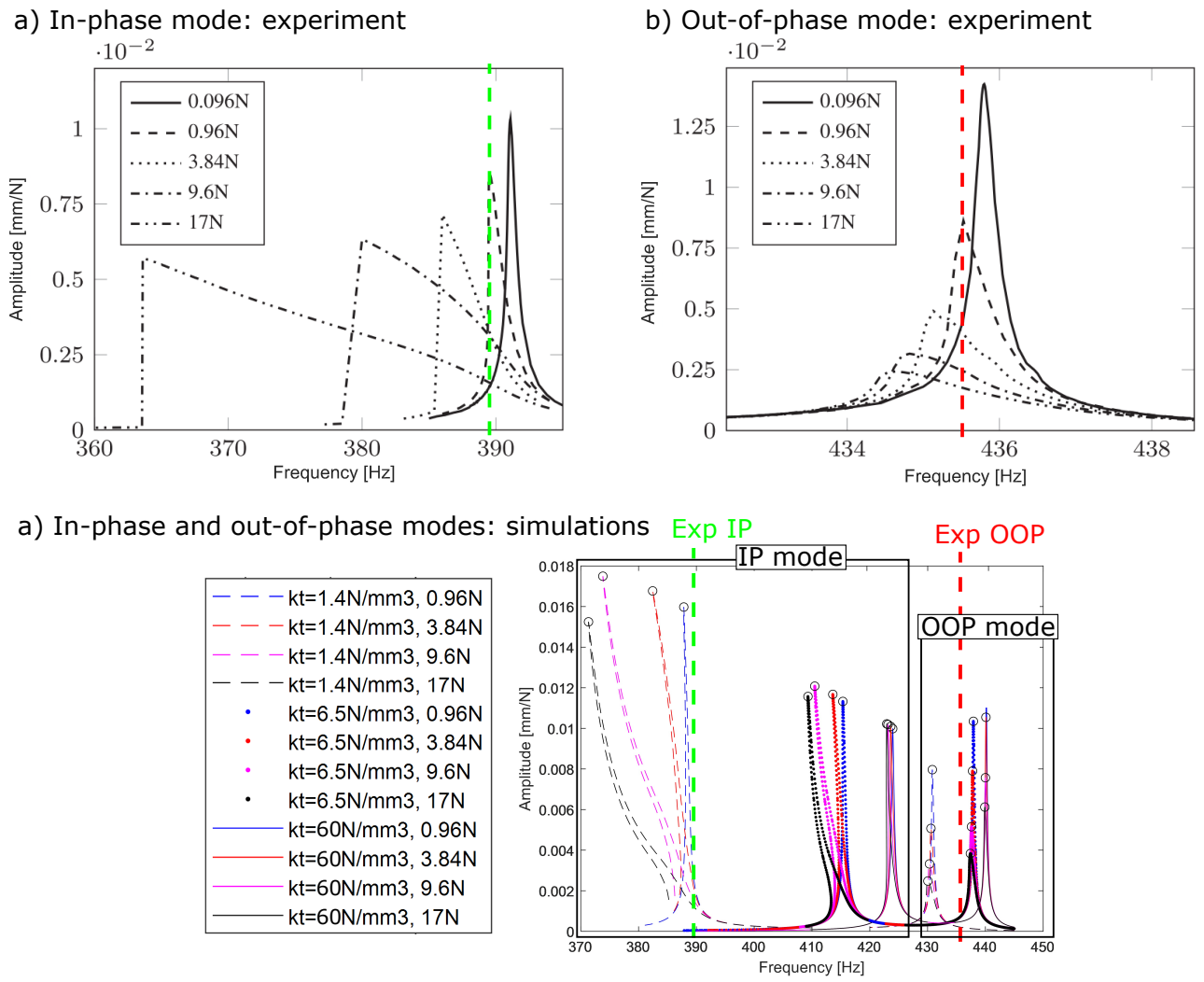


Figure 7.13: Comparison of experimental FRFs [19] and numerical FRFs predicted for different k_t on the UPD rig.

These simulations highlight the need to accurately attribute the correct contact stiffness to each contact element and also increase the confidence in the experimentally k_t laws proposed in chapter 4. A limitation of the performed simulations is that they only used the same k_t value for each contact element. A first improvement would be to assign a different k_t value to each contact element depending on its exact contact pressure. In addition, the used k_t values were considered constant and did not vary during the individual vibration cycles. However, the normal load will vary within a vibration cycle and, consequently, the k_t is expected to vary too. A future improvement in the FORSE solver could be to include the k_t load dependency within the individual vibration cycles, rather than maintaining it at a constant value over the whole simulation. The last comment is given on the fact that the experimental laws proposed in chapter 4 also include a range of variability in the values due to the experimentally observed uncertainty. The next section shows an investigation performed to include such uncertainty in the nonlinear dynamic simulations.

Effect of the experimental uncertainty

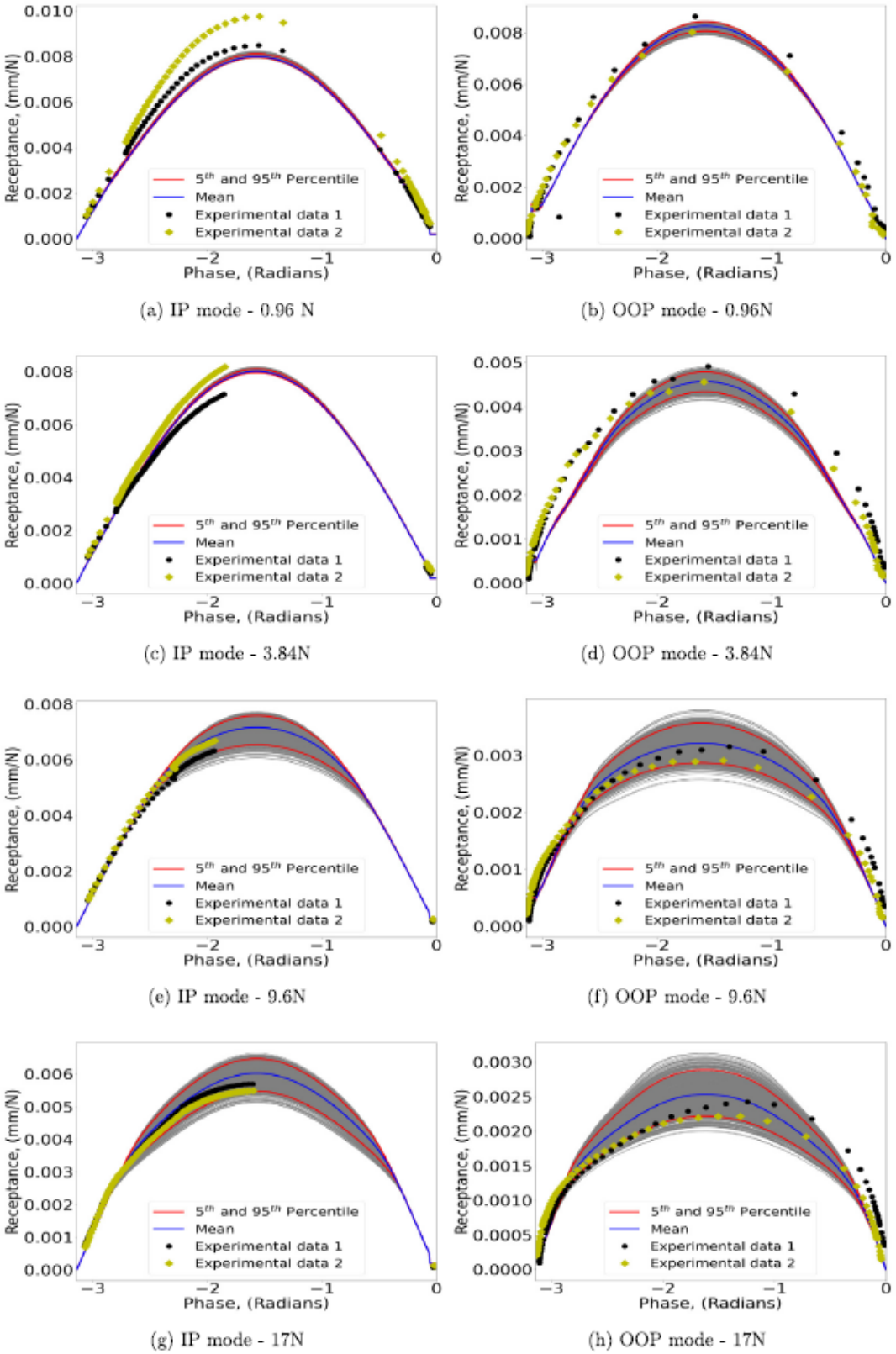
One of the guidelines proposed in chapter 4 to improve the nonlinear dynamic analysis of jointed structures was to include in the simulations the experimental uncertainty observed in μ and k_t. This uncertainty would lead to a large scatter in the predicted FRFs, as shown for example in the previous section. Several methods exist to account for such uncertainty in a computationally efficient framework [283–285]. Here, it was decided to quantify the effect of such experimental uncertainty employing a probabilistic approach, based on the Polynomial Chaos Expansion (PCE) theory [286, 287], which is capable of estimating uncertainty bands of FRFs rather than individual FRFs. The approach was not implemented by the author, but it was implemented within a collaborative project in the author research group to which the author contributed by providing experimental uncertainty bands in the contact parameters. The work is briefly presented here to show how the experimentally measured uncertainty was used for the numerical analyses and more details can be found in the resulting publication in the Mechanical Systems and Signal Processing journal [278].

The work consisted of generating 50 different combinations of μ and k_t obtained with a Latin Hypercube Sampling (LHS) strategy [288] and assuming a Gaussian distribution for both contact parameters with mean values and standard deviations defined as in Table 7.2. These values were chosen based on the experimental uncertainty observed during the round robin test of chapter 4, namely 4% uncertainty in μ and 25% uncertainty in k_t. Then, for each μ and k_t combination, nonlinear dynamic simulations of the UPD Imperial rig were performed by using the FORSE multi-harmonic balance solver described in the previous section. Four different excitation amplitudes [0.96, 3.84, 9.6, 17] N were used leading to a total of 200 nonlinear dynamic simulations. Given that one simulation lasted about 45 minutes, the whole set required about 150 hours to complete.

μ	mean: 0.88, relative std: 5%
k_t $[N/mm^3]$	mean: 44000, relative std: 30%
k_n $[N/mm^3]$	mean: 1.25*k_t, relative std: 30%

Table 7.2: Uncertainty parameters used for the LHS based on the experimental data from chapter 4.

Starting from the 200 predicted FRFs, four surrogate models were created for the four excitation amplitudes by using the PCE stochastic approach, which consists in projecting a stochastic solution on an orthogonal polynomial basis [286, 287]. More details on the approach are given in [278] since the focus of this section is not to describe the model, but to show what is the effect of the experimental contact parameter uncertainty on the prediction of the FRFs. The surrogate models were used to generate a new set of 1000 FRFs for 1000 new μ and k_t combinations. This was possible thanks to the very low computational cost required to obtain the approximate solutions from the surrogate models. Results were provided in less than 5 minutes, while a much larger computational time, of more than four weeks, would have been required to run the 1000 simulations with the standard nonlinear dynamic approach. Once the 1000 FRFs were obtained, their vibration amplitudes were plotted in the form of receptances versus the phase, for the in-phase (IP) and out-of-phase (OOP) modes, leading to 90% confidence uncertainty bands, which are shown in Fig. 7.14. The Figure also plots two sparse experimental FRFs for each excitation amplitude (in yellow and black dots). These FRFs were previously measured to represent the experimental uncertainty in the blade response amplitude.



(a) IP mode - 0.96 N (b) OOP mode - 0.96N

(c) IP mode - 3.84N (d) OOP mode - 3.84N

(e) IP mode - 9.6N (f) OOP mode - 9.6N

(g) IP mode - 17N (h) OOP mode - 17N

Figure 7.14: Comparison of amplitude response from the updated PCE models and experimental data from the UPD rig [278].

For the IP mode, the experimental response could not be measured over the whole phase range, because of the softening effects in the IP forced response, as explained in [19]. At high

excitation levels, 9.6 N and 17 N, the 90% confidence bands predicted from the PCE surrogate models were able to include the sparse experimental FRFs. Instead, at the low excitation levels of 0.96 N and 3.84, the 90% confidence bands predicted from the PCE surrogate models did not include the amplitudes of the two experimental FRFs, which differed up to the 20% in the resonance regions. Such a disagreement could be due to the uncertainties related to the variation in the normal load across the interface. In fact, the IP mode is dominated by contact separation conditions and, therefore, it is more sensitive to the variation in the normal load, whose variability was not included in this preliminary uncertainty analysis. For the OOP mode, the majority of the experimental data points lied within the 90% confidence interval identified from the PCE surrogate models, especially at 3.84 N to 17 N.

Excluding the low excitation amplitudes for the IP mode, a good agreement could be achieved between the uncertainty bands predicted from PCE surrogate models and the sparse experimental FRFs. This agreement suggests that the distribution of the contact parameters was correctly quantified from the experiments presented in chapter 4 and should be included in the simulations, since it leads to variations in the nonlinear dynamic response, with changes in the amplitudes up to the 40%.

7.3 Conclusions

The goal of this chapter was to apply some of the guidelines proposed in the previous chapters to improve simulations for the nonlinear dynamic analysis of jointed structures. To show the impact of the proposed guidelines, existing modelling tools were used, partly in collaboration within the author research group. Two sets of simulations were performed: quasi-static contact simulations and nonlinear dynamic simulations.

The quasi-static contact simulations were performed by using Finite Element (FE) and Boundary Element (BE) methods to model the Imperial specimens and predict accurate values of tangential contact stiffness. The contact stiffness must be predicted accurately because it has a major impact on the dynamic response. The FE analysis showed that the bulk deformation has a significant impact on the measured contact stiffness. This bulk deformation should therefore be removed from measurements so that they only include the effect of the surface topography, i.e. asperities and waviness. In addition, when measuring input contact stiffnesses for the nonlinear dynamic analysis of a jointed structure, the surface topography of the tested specimen interfaces must be similar to that of the modelled jointed structure. In addition to the surface topography, also the wear is important for simulations since it strongly affects the evolution of the surface topography as vibration proceeds. The effects of the surface topography and wear on the contact stiffness were quantified with a new set of Boundary Element simulations that took as input the real surface data obtained from optical scans of the specimen interfaces. When realistic surface topographies and wear conditions were included in the simulations, the contact stiffness predictions were in very good agreement with experiments in contrast to the original simulations that did not model in detail the realistic conditions. This improved agreement confirms the experimental observations from the previous chapters about the strong dependence of k_t on surface topography and wear, and highlights the need to include those factors in simulations, although they are often overlooked in current modelling approaches for nonlinear dynamic analysis.

The second set of simulations was used to predict frequency response functions (FRFs) and to understand how different contact conditions affect the predictive capability of existing nonlinear dynamic modelling tools. First, the effect of wear was included in simulations since chapter 6 showed how wear strongly affected the dynamic response of the Imperial friction rig, leading to significant variations in natural frequencies and damping. A novel and simple formulation was proposed to account for wear in contact models by using wear-evolving, physically-based contact laws of frictional hysteresis. A time integration solver was used with the new contact laws to predict FRFs of the friction rig at different wear conditions. Both resonant frequencies and damping were in very good agreement with experimental measurements when the effect of wear was included. The novelty in the presented study was the double experimental validation against both local contact data (hysteresis loops) and global vibration data (measured FRFs). The validation highlighted the importance of including the effects of wear in contact models to correctly capture the dynamics of jointed structures over the lifetime of the system. In addition to simulations on the friction rig, also another structure was investigated, an underplatform damper (UPD) rig that consisted of two blades equipped with a UPD. A harmonic balance based solver was used to predict the FRFs of the rig and compare them against existing experimental measurements. The simulations included updated normal load-dependent k_t values, since chapter 4 quantified the strong dependence of k_t on the normal load. The use of updated k_t values led to a great improvement in the predictions if compared to the original predictions, thus showing how sensitive the dynamic response is to k_t variations. Also the effect of uncertainty was investigated since chapter 4 showed that measured contact parameters have some inherent uncertainty. This experimental uncertainty was provided by the author as input to an existing probabilistic approach based on the Polynomial expansion theory. Based on the provided contact parameter uncertainty, uncertainty bands of FRFs were predicted within a collaborative project and compared to experimental FRFs, which in general lied within the predicted FRF uncertainty bands. This last set of simulations showed how large is the impact of the contact parameters measurement uncertainty.

In conclusion, predictions presented in this chapter strongly support some of the hypotheses presented in the previous chapters and show the importance of accurate interface modelling and other proposed upgrades for more accurate nonlinear dynamic analysis of jointed structures.

Chapter 8

Validation of modelling approaches for nonlinear dynamic analysis: industrial test case

The previous chapter focused on the improvement of existing modelling approaches for the nonlinear dynamic analysis of jointed structures. Although the improved simulations were in a much better agreement with experimental data, simulations were only performed on academic test rigs, which are less complex than real industrial structures. Indeed, most of the validation studies available in the literature have been carried out on small-scale experimental rigs, but there does not seem to be any detailed information on how the predictions of these approaches compare to real and complex turbomachinery, such as aero-engines.

This chapter shows predictions of a real industrial case, an aero-engine from Rolls-Royce plc, on which the author worked during a 3-month secondment conducted at Rolls-Royce plc within the final year of his PhD project. The aim of the secondment was twofold: i) gain a better understanding of industrial-scale problems and apply the developed research understanding; ii) transfer research understanding to the company. To do so, the chosen industrial test case was a first stage high-pressure (HP) bladed disk consisting of turbine blades equipped with underplatform dampers. Nonlinear frequency response functions were predicted with existing state-of-the-art approaches and some of the guidelines proposed in the previous chapters were implemented. Simulations results were compared against existing measurement data, obtained during a previous aero-engine strain gauge test campaign. A much-improved agreement could be achieved with experiments when realistic pressure distributions were included in the simulations. In addition to the different contact pressure distributions, other factors were also investigated based on the findings of previous chapters, such as updated values of input contact parameters and different densities of contact nodes to find the optimal interface discretisation.

8.1 Industrial test case: aero-engine turbine bladed disk sector

This section describes the test case used in this study, a high-pressure stage turbine bladed disk of a Trent aero-engine [6]. Since details of the model cannot be specified because of intellectual property restrictions, a de-featured representation of the disk sector is shown in Fig. 8.1a. The model has been previously created with an in-house FE solver used in the company and consists of about 2 million 10-node tetrahedral elements, leading to about 5 million nodes and 30 million degrees of freedom (DOFs). Although the model represents only one disk sector, the full bladed disk was replicated by imposing cyclic symmetry as is commonly done with cyclic symmetric structures [289].

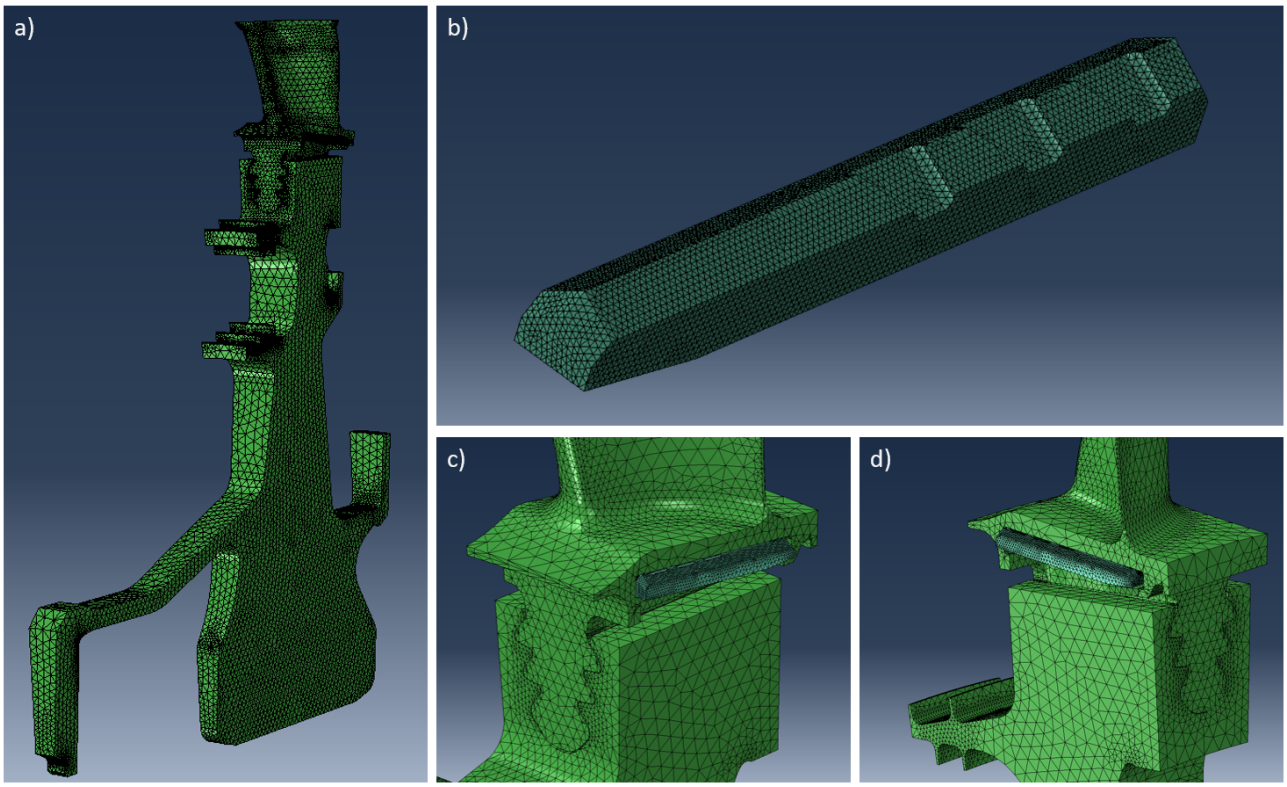


Figure 8.1: a) FE model of the high-pressure turbine bladed disk sector used in the analysis (IP-free version); b) FE model of the damper (IP-free version); c-d) Close-up of the blade-damper assembly.

The focus of this study is on the vibration of the blades because blades are the components with the highest risk of high cycle fatigue failures due to the small, but high-frequency, excitation coming from the gas flows. To reduce vibrations, underplatform dampers are used in the assembly as shown in Fig. 8.1b-d[1]. The damper has some slots that are needed for cooling. These slots divide the potential contact area into more independent nominally flat areas, as shown in Fig. 8.1b. The mesh of such interface areas is relatively dense (1 FE node every 0.05 mm^2) to guarantee accurate modelling of the interface contact mechanisms. Four modes of interest of the blade were investigated in this study: mode 1, the first flap mode (1F) consisting

[1]Note that beneficial damping also comes from the blade root interaction with the disk. This contribution is neglected in this study by modelling blade and disk as a single component.

of the blade moving left and right; mode 2, the first edge-wise mode (1E) consisting of the blade moving backwards and forward; mode 3, the first torsional mode (1T); and mode 4, the second flap mode (2F). Resonant frequencies and vibration amplitudes of those modes were predicted with a state-of-the-art nonlinear response solver, which is extensively used in the company for the design of robust turbine blades and for assessing high-cycle fatigue endurance levels. Although the solver is predictive, its accuracy is still affected by factors such as machining tolerances and wear, which cannot easily be included in the models. Therefore, the confirmation of resonant frequencies is still heavily reliant on engine strain gauge tests.

This study proposes upgrades in the nonlinear dynamic modelling approach based on the guidelines of the previous chapters, such as including realistic surface topographies and pressure distributions. To this purpose, the real contact bedding patterns at the blade/damper interfaces are observed after the experimental tests and replicated in simulations, instead of assuming a uniformly distributed contact over the whole contact interface, as currently done. Previous studies on academic test structures have in fact demonstrated the importance of using correct interface models [19, 290], and here it is shown that this knowledge is highly relevant for real engines as much as it was for the academic cases.

Strain gauge test and contact bedding patterns analysis

Numerical predictions of this chapter are compared to existing experimental measurements from a ground engine strain gauge test. The ground engine strain gauge test is one of the standard testing methods of aero-engines in the company. The test considered in this study consisted of running the engine on the ground over three consecutive days, each day with several slow acceleration/deceleration manoeuvres up to the maximum engine speed. During each acceleration/deceleration manoeuvre, the vibration of each blade was measured by means of strain gauges previously mounted on the blades at different locations, as illustrated in Fig. 8.2. Those locations were chosen to best represent the strains of the four modes of interest. The same locations were used in the blade FE model to extract strain data information from the simulations and assess a comparison with experimental data. After the test, strain data at the strain locations were available over the full range of engine rotational speed. Although the rotational speed of the engine did not exceed 15000 rpm (i.e. 250 Hz), frequencies much larger than 250 Hz could be excited due to the effect of higher engine orders (EO). The EO is an integer number indicating the number of times each blade is excited during one complete rotation of the disk. As a result of the EO excitation, the bladed disk will respond in an equivalent nodal diameter (ND) number equal to the EO[2]. For instance, if the excitation is caused by the gas flow coming from the upstream stator wakes, the EO is equal to the number N of stator wakes since the gas flow is divided into as many sub-flows, which all impact the individual blades during a complete rotation, thus leading to that N^{th} EO excitation. The bladed disk will consequently respond with its N^{th} ND.

In general, each mode is excited only by one particular EO. For example, it was found experimentally that modes 3 and 4 are excited by a high EO equal to the number N of high-pressure nozzle guide vanes (N is not stated here due to intellectual property restrictions). This means

[2]The number of nodal diameters of a mode shape is the number of nodal lines crossing the centre of the cyclic symmetric structure along which the modal quantities (displacements, strains, stresses, etc.) are equal to zero.

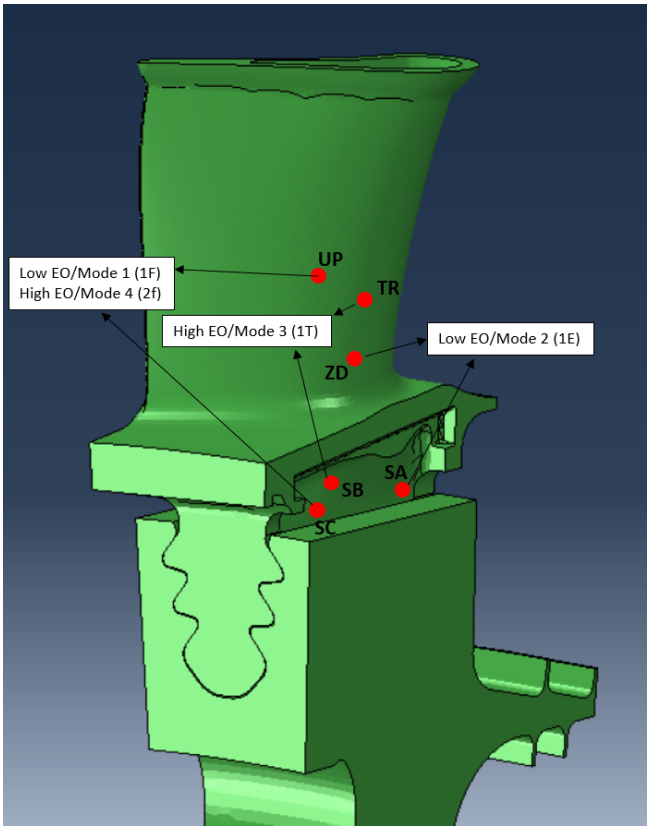


Figure 8.2: Strain gauge locations for the vibration test and corresponding mode shapes.

that, during each complete rotation, the blade underwent N perturbations that excited the mode. The excitation frequency for that mode is then given by multiplying the rotational speed in Hz by the EO number N. Experiments showed that instead modes 1 and 2 are excited at a lower EO (below 20) due to the presence of some gas fluid interaction relevant to this engine type.

Since the measured data contains contributions from several different EO excitations, data were post-processed to be presented in a tracked-engine order format, which means that, for each strain gauge dataset, individual EO contributions were extracted. In this way, it was possible to isolate the different modes depending on the chosen tracked EO contribution. Range responses in the form of tracked-engine order data are shown in Fig. 8.3 for each mode of interest. Both amplitudes and frequencies are normalised to the resonant values to protect intellectual property. This kind of tracked-engine order data format could directly be superimposed on the numerical predictions, since also numerical predictions are performed, for each mode, under the exact EO excitation that excites that particular mode.

After the test campaign, photos were taken of the contact interface of each blade/damper pair to investigate the most common contact bedding patterns, which could be identified by dark bedding marks. Figure 8.4a shows a simplified sketch of the most common type of bedding pattern seen on the tested dampers, which consists of marks on the outer edges of the damper. It is here assumed that the dark bedding marks correspond to the actual location of the blade/damper contact, thus indicating that contact occurred only at the outer edges of the damper. Indeed, the contact at the outer edges of the damper is expected since, due to the centrifugal load, the damper is pushed upward leading to the lifting of the blade platforms as

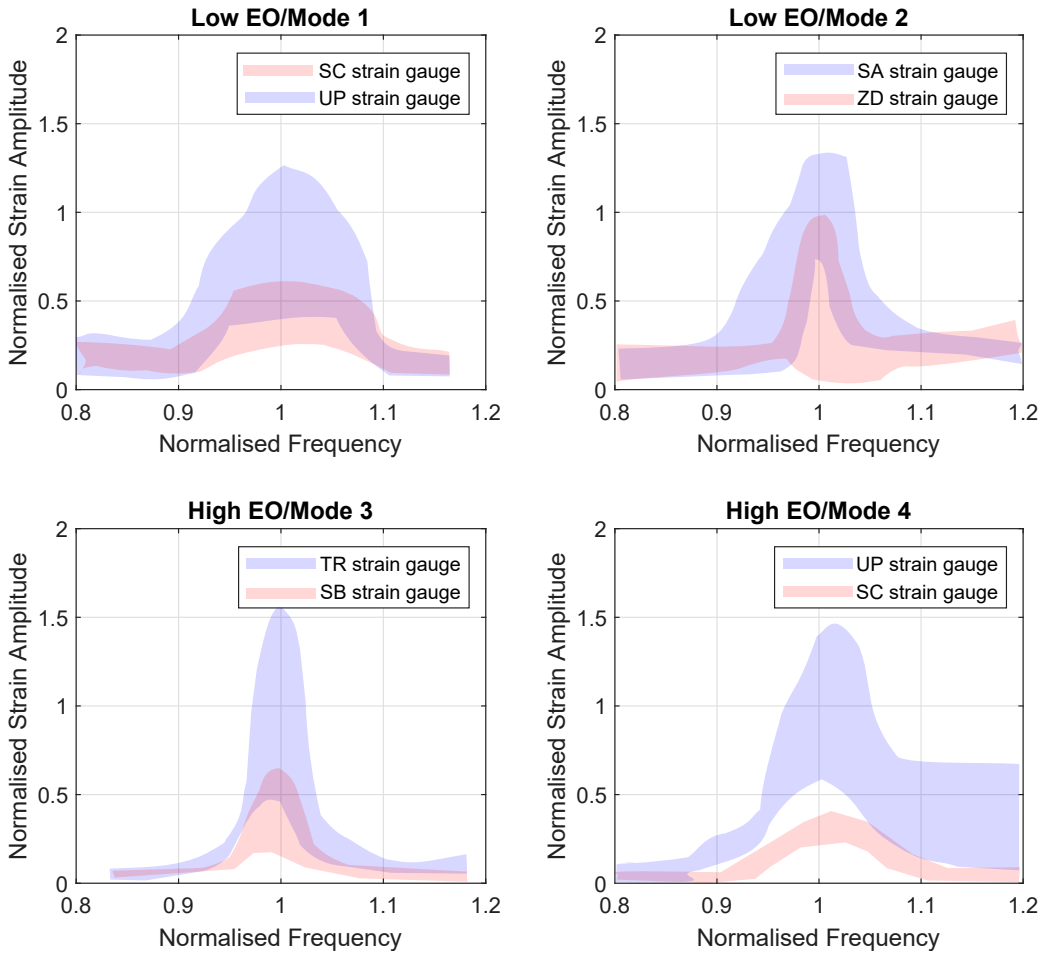


Figure 8.3: Engine order components of strain gauge experimental data for the four modes of interest.

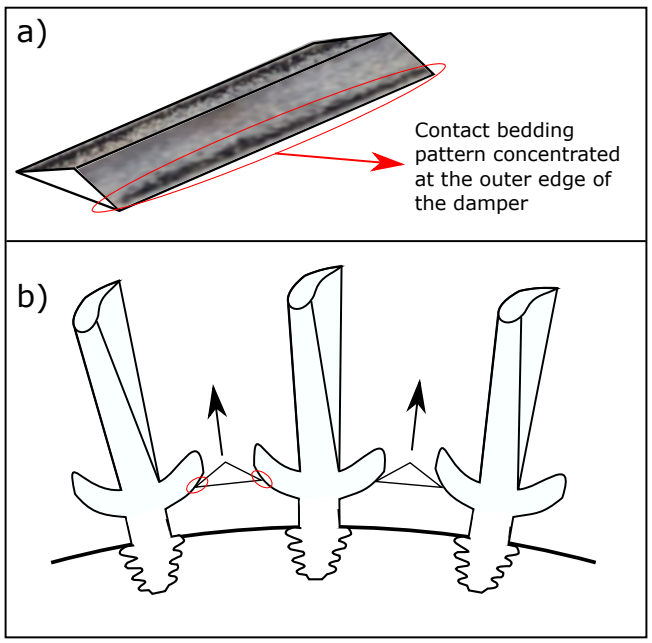


Figure 8.4: a) Most common contact marks on the damper; b) kinematics blade/damper due to the centrifugal load.

shown in Fig. 8.4b, thus concentrating the contact at its outer edges. The following sections describe how the effect of those bedding marks was included in the simulations.

Finally, to enrich the information of the ground engine strain gauge tests, notice that the aero-engine used in the strain gauge test did not undergo a large amount of running, which instead can be observed from service engines at the end of their lives. Hence, the tested engine might not be representative of the worn operating engines at the end of their lives. To further investigate this, photos were also analysed of a service engine at the end of its life. In the case of that engine, 60% of the dampers had the outer edge bedding marks, while 40% of them had bedding marks extended over the full contact interface, indicating that, with a larger number of operating cycles, the load distributes over a larger portion of the damper rather than only at the damper outer edges. This observation is relevant as it indicates that the contact condition may evolve during operation due to wear and can therefore affect also the dynamic response.

8.2 Modelling approach

A large number of numerical simulations was performed to predict frequency response functions (FRFs) to be compared against the measurements from the ground engine strain gauge test. The FRFs were predicted by following the standard approach for the nonlinear dynamic analysis of jointed structures already described in section 7.2.2, based on the use of the FORSE multi-harmonic balance-based solver. Please refer to that section for the method description.

The focus of this study is on the more accurate modelling of the contact at the blade/damper interfaces. The datum approach to model the blade/damper contact is to uniformly distribute the contact elements over the whole contact interface and apply the same pressure on each node pair based on the damper centrifugal load and its nominal contact area. However, Fig. 8.4a showed that uniform pressure distribution is not representative of the real case since the most common contact bedding pattern is that with the contact concentrated only at the outer edges of the damper with no contact on the remaining portions. Therefore, it was decided to investigate the effect of more realistic pressure distributions on the dynamic response by designing a matrix of simulations that include six different contact interface descriptions resulting from different contact bedding patterns. In addition to the "outer edge" pressure distribution observed in the real dampers, other distributions are investigated with new possible patterns not observed in operation, which could be useful for new designs of better dampers. The six different bedding patterns are shown in Fig. 8.5. Each bedding pattern is modelled by imposing the contact only on certain "retained" blade/damper node pairs and leaving the remaining nodes in a no-contact condition. This is done by excluding such nodes from the nonlinear analysis and only connecting the "retained" nodes of the damper with the corresponding blade nodes.

Each bedding pattern is modelled with three different node grid densities that result in different numbers of contact nodes per pattern/grid combination as detailed in Table 8.1. The number of contact nodes strongly affects the computational time needed to complete the simulations, since the resulting larger models have more DOFs to be solved (6 DOFs for each contact node pair) and require more time. Although the computational time increases, the fidelity of the prediction is higher when more contact nodes are used to discretise the interface. Different grid densities were therefore investigated to find the optimal number of contact nodes (i.e., the minimum number for which there is convergence in the predictions).

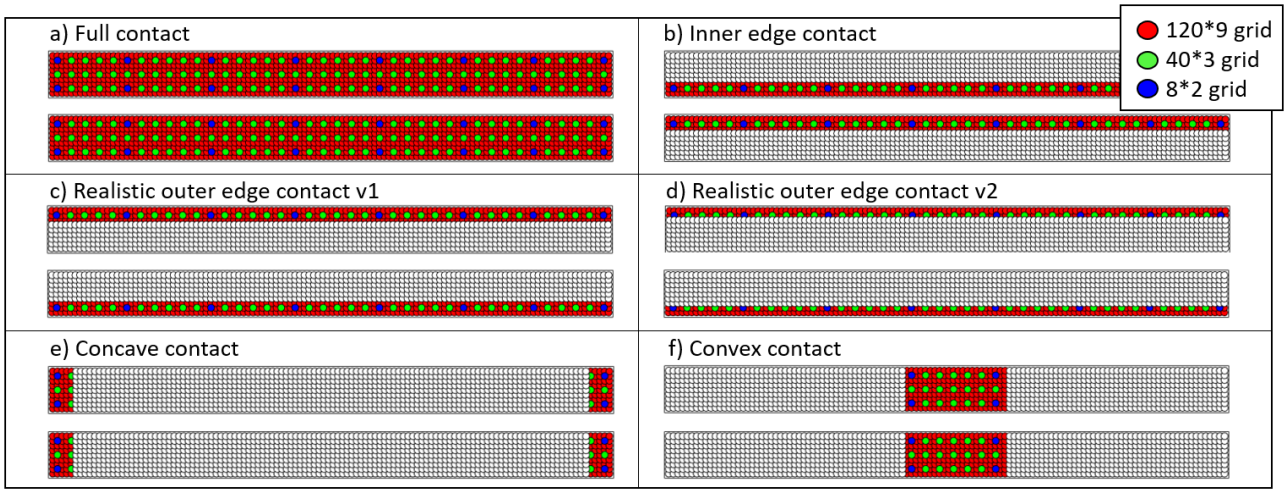


Figure 8.5: Six contact bedding patterns used in the simulation and three grid densities (shown in different colours – red, green and blue).

Table 8.1: Number of nodes for each combination of bedding patterns and grid densities. The table also shows the information on the nominal areas, which is needed for the caclulation of the normal load distribution, as discussed in section 8.2.1.

	8*2		40*3		120*9		
Contact bedding pattern type	Number of nodes	Area per node [mm^2]	Number of nodes	Area per node [mm^2]	Number of nodes	Area per node [mm^2]	Area tot
Full contact	40	3.09	239	0.52	2098	0.06	100%
Outer edge contact1	20	2.27	85	0.53	766	0.06	36.7%
Outer edge contact2	18	1.59	74	0.39	489	0.06	23.3%
Inner edge contact	20	1.77	75	0.47	609	0.06	28.7%
Concave contact	12	1.24	34	0.44	266	0.06	12.1%
Convex contact	12	1.79	41	0.52	383	0.06	17.4%

The six patterns are shown in Fig. 8.5, with the three different colours indicating the three grid densities. The full contact case with a grid 40*3 (i.e., 40 columns * 3 rows of nodes) is the approach considered as a datum in this study and is shown in Fig. 8.5a, with green coloured nodes. The other gird densities are shown in red (120*9) and blue (8*2). On each contact node pair, a Jenkins element is applied with the contact parameters shown in Fig. 2.9, section 2.3. Figure 8.5c and d show two versions of the (realistic) outer edge contacts since, from the analysis of the experimental patterns, those versions best represent most of the contacts. Figure 8.5b shows the inner edge contact case. Finally, the concave and convex contact are two non-observed cases, which are however included for the completeness of the analysis.

The external loads used as input in the simulations are the static centrifugal load, resulting from the damper centrifugal force, and the modal excitation on the blades coming from the gas flow. Representative blade temperatures are also included in the simulations based on the resonant speed point as well as material property differences due to temperature. In addition, the designed simulation matrix investigates not only the effect of different pressure distributions but also the effect of three different contact stiffness laws based on the findings of chapter 4. Details on those parameters are provided in the following sections.

8.2.1 Normal load distribution and nominal area of contact

Each pair of contact nodes is coupled by a Jenkins element, which requires as input four contact parameters: normal load, friction coefficient and tangential and normal contact stiffnesses. This section describes how the normal load is estimated for each node pair. The normal load distribution on the contact interface depends on the damper centrifugal load, which pushes the damper upwards against the blade platforms. The centrifugal load, F_c, is a quadratic function of the disk rotational speed defined as follows:

$$F_c = r * m * 4 * \pi^2 * f^2 \tag{8.1}$$

Where r [m] is the radial distance of the damper centre of gravity from the rotational axis, m [kg] is the damper mass and f [Hz] is the rotational speed. This load distributes on the two faces of the damper[3], which are in contact with the platforms of two adjacent blades, according to [291]:

$$N_{face} = \frac{F_c}{2(cos(\alpha) + \mu * sin(\alpha))} \tag{8.2}$$

Where N_{face} is the load on each of the two damper contacting faces, α is the damper angle and μ is the friction coefficient. Note that N_{face} is the normal load on the two damper faces, not to be confused with the centrifugal load. The normal load on each contact node is then obtained by dividing N_{face} by the total number of nodes of each face. This leads to a uniform load distribution on the contact nodes since they all have equal normal loads. This uniform load distribution is a simplification compared to the more realistic approaches in which non-uniform normal load distributions are obtained via a quasi-static nonlinear analysis [19,27] but, in this case, it was assumed that the use of different contact bedding patterns with uniform load distributions was already well representative of the experimental non-uniform distributions. Please note that those loads are expressed in N. However, the nonlinear dynamic solver requires pressures [N/mm^2] as input, and therefore the normal load must be divided by the nominal area of each contact node, which is shown in Table 8.1. Fig. 8.6a shows how the contact pressure on each damper face evolves with rotational speed according to Eq. 8.1 and Eq. 8.2 for the different contact bedding patterns. The full contact bedding pattern has the lowest pressure since, according to Table 8.1, it has the largest nominal area and therefore the normal load is more evenly distributed.

8.2.2 Friction coefficient and contact stiffness load dependence

A friction coefficient of 0.3 was used in the simulations based on existing experimental measurements performed on the Imperial friction rig for the blade/damper material combination (Nickel- and Cobalt-base superalloys) at the high temperatures encountered during operation (>700 °C) [85]. To account for some of the experimental uncertainty, a sensitivity analysis on the effect of the friction coefficient was performed and is shown in section 8.3.3.

With regards to the contact stiffness, measured values at the high temperatures representative of the testing conditions are shown in Fig. 8.6b (Test 3, red dots) for the blade/damper material

[3]The UPD is also in contact on its shorter inclined end, which takes 10% of the centrifugal load according to previously performed quasi-static analyses. This contact was included in the simulations but not shown in the de-featured damper representation of Fig. 8.1b

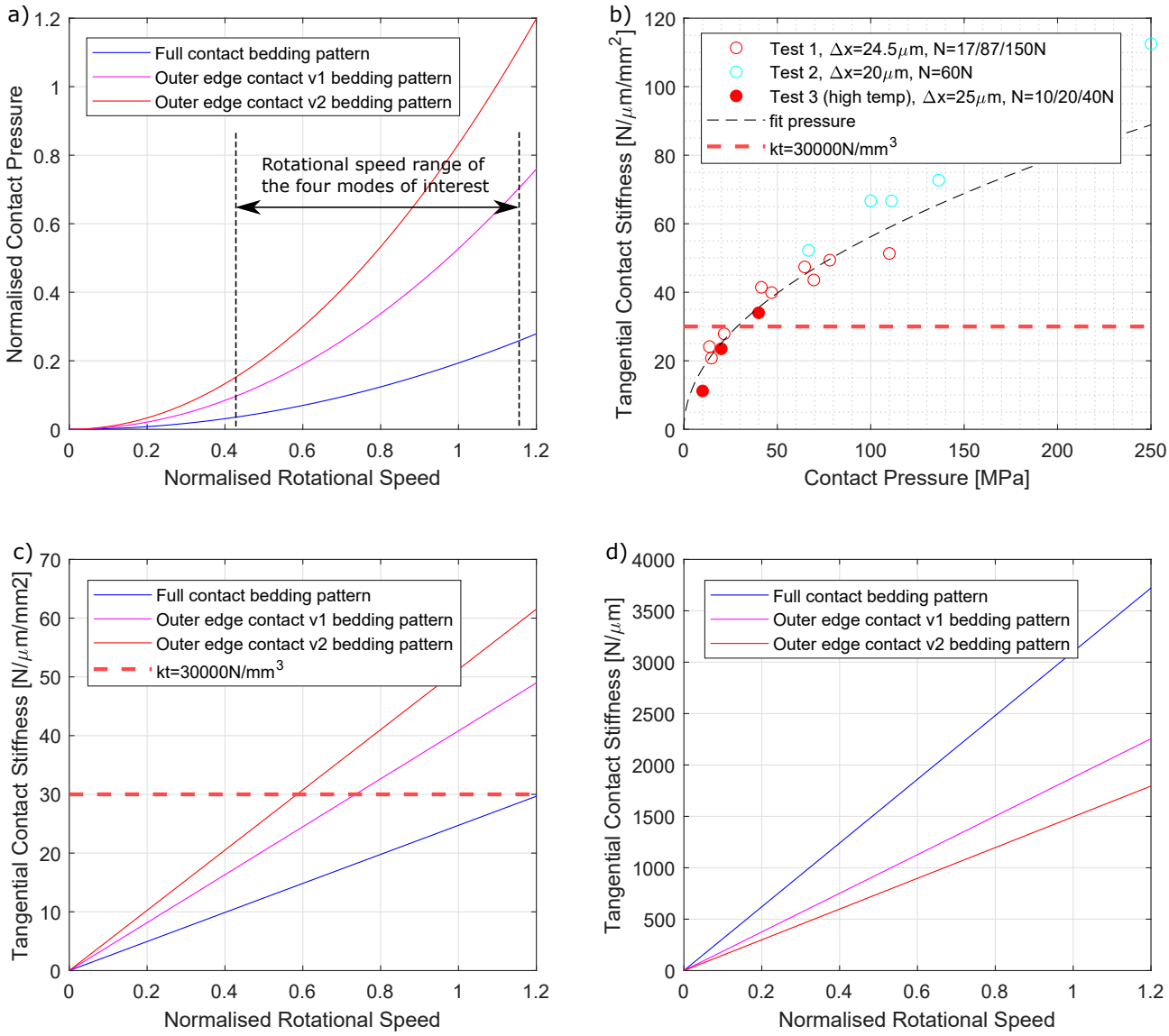


Figure 8.6: a) Contact pressure on each damper face as a function of the rotating speed; b) tangential contact stiffness dependency on the contact pressure, measurements from chapter 4 and ref. [85]; c) tangential contact stiffness as a function of the rotational speed; d) global contact stiffness as a function of the rotational speed.

combination. The tangential contact stiffness increases as the contact pressure increases from 10 MPa to 40 MPa. A value of 30000 N/mm^3 was used in the simulation as a datum approach according to previous measurements [85]. However, a more physically representative approach is the use of normal load-dependent contact stiffness, based on the evidence in chapter 4. Figure 8.6b shows the square fit of the K_T vs normal pressure proposed in chapter 4 together with three different tests performed on the Imperial friction rig: tests 1 and 2, which were those performed on stainless steel specimens at room temperature within the round robin of chapter 4, and test 3 that was performed for the blade/damper material combination at high temperature [85]. The square fit coefficient is 6.3, which gives a stiffness [N/μm/mm^2] when multiplied by the square root of the contact pressure [MPa]. Although this fit was obtained from tests performed on stainless steel at room temperature, it captures quite well even the behaviour of the blade/damper material combination, although those materials are different from the stainless steel used in the round robin and were performed at much higher

temperatures. The match gives some confidence that the fit law obtained in chapter 4 can be also applied to that material combination tested at a larger temperature, although more experiments should be performed in future to validate this assumption.

Based on the pressure evolution in Fig. 8.6a, the K_T was evaluated as a function of the disk rotational speed by using the square fit of Fig. 8.6b. The resulting stiffness vs rotational speed relation is linear and is shown in Fig. 8.6c. The relation is linear because the pressure scales up by the power of two with the speed while the stiffness increases with the pressure square root. The Figure highlights that the constant 30000 N/mm^3 value used as a datum approach in this study might not be representative of the whole speed range. Contact bedding patterns with lower nominal areas have larger stiffnesses since these were obtained at larger contact pressures. Finally, Fig. 8.6d shows the global k_t [N/μm] not normalised by the area of contact, obtained by multiplying the K_T of Fig. 8.6c in [N/mm^3] by the nominal area of contact [mm^2] of each damper face. This global k_t represents the global stiffness of contact, which ultimately affects the resonance frequency of the modes of interest since larger values will lead to a stiffer system with higher resonances.

In the result section, simulations with both stiffness laws (constant and load-dependent) are presented and compared. Since each contact bedding pattern has a different nominal area, which leads to a different global k_t in [N/μm], it was decided to run a third set of simulations with a global k_t value fixed to 3701 N/μm, which is the value of the global k_t for the full contact bedding pattern with a normalised K_T of 30000 N/mm^3. With this last set of simulations, it has been possible to evaluate the effect of the contact bedding patterns alone, without the superimposed effect of the different k_t. The global 3701 N/μm value was obtained by adapting the input stiffnesses in N/mm^3 so that, when multiplied by the nominal area of contact of the investigated bedding pattern, their total contribution was 3701 N/μm.

Finally, it is to be noted that for both K_T load-dependent simulations and k_t fixed to 3701 N/μm simulations, the normal contact stiffness k_n was considered to be 1.25 times larger than the tangential contact stiffness, according to previous contact mechanics studies [63].

Modal excitation from gas flow unsteady pressures

Turbine blades are excited by a periodic excitation coming from the unsteady pressures of the gas flow. Those unsteady pressures were predicted with the in-house CFD solver commonly used in the company for such predictions. Each of the four analysed modes had a different set of excitation unsteady pressures, evaluated by the CFD solver at the rotational speed and engine order corresponding to the resonance of the analysed mode. These sets of unsteady pressures change with the rotational speed since larger rotational speeds lead to more gas impacting on the blades and thus higher pressures. Representative blade temperatures were also included in the simulations based on the resonant speed point as well as material property differences due to temperature.

As mentioned before, modes 3 and 4 are excited by a high engine order (EO) excitation, coming from the high-pressure nozzle guide vanes upstream of the analysed rotor. CFD simulations were performed to estimate unsteady pressures at this engine order. However, simulations could not be performed for low EO excitations (i.e. those exciting modes 1 and 2) since there is no validated prediction capability for non-specific low EO excitation. Therefore, for the low

EO assessment, unsteady pressure amplitudes were arbitrarily chosen to match predicted and experimental strain response amplitudes.

8.3 Simulation results

This section shows a summary of the predicted dynamic responses of the investigated engine turbine blades. Resonance frequencies and strain amplitudes of vibration are compared against strain gauge data.

8.3.1 Frequency shift predictions - Effect of contact bedding patterns and k_t sensitivity

Predicted resonant frequencies are compared here versus strain gauge data resonances. All results are plotted for a node located on the blade tip. Simulations were performed for the six different contact bedding patterns and the different k_t laws described in the previous section. Each mode of interest is analysed separately with figures plotting the following:

- A dashed green line, which is the undamped response (i.e. the vibrational response of the blade without the damper).
- A thick blue line, which is the benchmark reference response obtained with the datum approach, i.e. full contact bedding pattern with a K_T=30000 N/mm^3 and grid density 40*3.
- All other coloured lines show the damped responses for the remaining contact bedding patterns.
- In the legends, frequency shifts from the undamped case (green dashed line) are shown. Amplitude percentages refer to the difference from the amplitude of the benchmark case (thick blue line). The global k_t in [N/μm] is also shown for each case.
- The strain gauge experimental resonances are shown via frequency bands (for the raw EO-tracked data see Fig. 8.3. Strain amplitudes are instead compared in section 8.3.2.

To protect intellectual property, all frequency data have been normalised by the resonance of the undamped mode (i.e. blade free without damper), while amplitudes were normalised by the peak amplitude of the full bedding pattern damped mode.

Low EO/Mode 2 (1E)
Modal family 2 represents the first edge-wise mode shape (blade moving backwards and forwards). The low EO excitation (equal to the number of high-pressure vane pairs and combustor fuel-spray nozzles) is here analysed because, during the engine test, the largest measured resonant response for this modal family occurred at that particular EO. Figure 8.7a shows the simulations for the datum approach, i.e. 30000 N/mm^3 constant K_T case (with the thick blue line being the reference full contact case). The reference full contact case over-predicts the experimental resonance frequency, while a much-improved match is obtained for four contact

bedding patterns, namely outer edges v1 and v2, convex and concave patterns. In particular, the reference case has a resonance shift of +42.4% compared to the undamped case, while the outer edge bedding patterns (more realistic according to the real pressure distributions) have a resonance shift of around +26%, which is significantly lower and within the experimental resonance range. This improved match for the low EO/mode 2 highlights how important is the identification of realistic bedding patterns to achieve more accurate simulations.

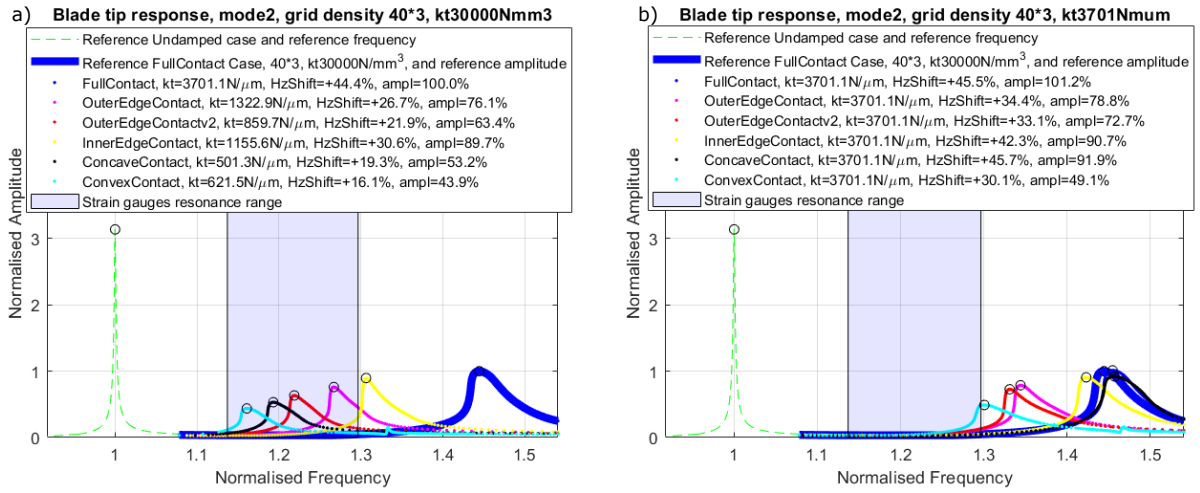


Figure 8.7: Low EO/mode 2 (1E) simulations for the six bedding patterns and the node grid density 40*3: a) K_T=30000 N/mm^3 for all the bedding patterns – this leads to lower global k_t for bedding patterns with lower nominal areas of contact; b) k_t=3701 N/μm for all the bedding patterns – this case is needed to investigate the effect of the patterns alone.

Figure 8.7b shows simulations with a constant global k_t equal to 3701 N/μm for every bedding pattern. These simulations were run to investigate the effect of the pattern alone by using the same "artificial" global k_t for every test. This is done because each bedding pattern would have a different global k_t resulting from the different nominal areas[4]. The global k_t in [N/μm] directly affects the resonance frequency, and therefore, by keeping it constant, it is possible to investigate the effect of the different bedding patterns alone, without the superimposed effect of the different area-dependent global k_t. Figure 8.7b shows that the patterns that most soften the system are the outer edge v1 and v2, and the convex pattern. It is expected that patterns with non-full contact bedding result in softer assemblies, as compared to the full contact bedding, because fewer contact nodes are constrained and therefore, both blade and damper, have more freedom to move. The inner edge bedding pattern does not show a significant softening, although its area is small. The reason for this might be that the nodes constrained in this pattern experience large relative motions and therefore the fact that they are included in the analysis, and put into contact with the corresponding blade nodes, did not lead to the large softening observed for the other non-full contact bedding patterns. While Figure 8.7b shows the effect of the patterns only, Fig. 8.7a also shows the further softening induced by the lower k_t in [N/μm] at each pattern (the reduced global k_t values are indicated in the legend). From a comparison of Fig. 8.7a and b, it seems that the different bedding patterns contribute to half of the reduction in the frequency, while the other half of the reduction results from the lower k_t values due to the lower nominal areas of the new bedding patterns.

[4]As a reminder, the global k_t is obtained by multiplying the nominal area of contact by the K_T in [N/mm^3], as shown in Fig. 8.6c-d.

Finally, Fig. 8.8a shows simulations for the k_t load-dependent case. Trends are very similar to the 30000 N/mm^3 K_T case because the range of K_T for the load-dependent case is still around 30000 N/mm^3. The thin blue line slightly differs from the thick blue line because the first has a global k_t lower than the global k_t for the K_T=30000 N/mm^3 reference case.

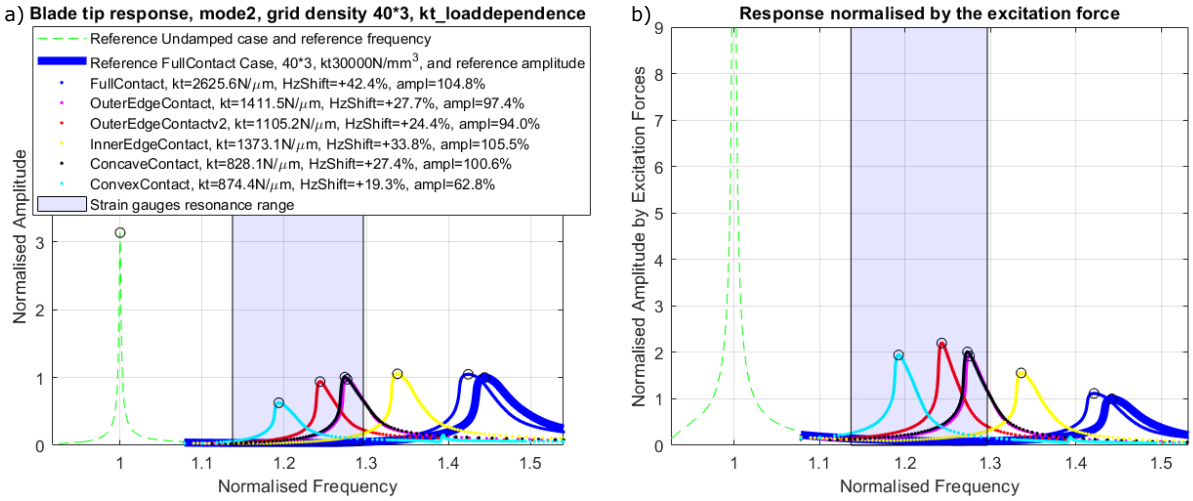


Figure 8.8: Low EO/mode 2 (1E) simulations for the six bedding patterns and the node grid density 40*3: a) k_t load dependence case; b) k_t load dependence case and response normalised by the scaling factor of exciting forces.

With regards to the amplitudes, it seems from Fig. 8.8a that softer patterns result in lower amplitudes. This might occur because, at lower frequencies, also the excitation amplitude is lower since it decreases with the rotational speed thus leading to lower responses. To investigate this, Fig. 8.8b shows the amplitudes normalised by the excitation. This normalisation is not correct to a full extent since the system is nonlinear and different excitations might lead to different nonlinear system responses. However, for the considered speed/frequency range, the variation in the excitation amplitude is small and thus the nonlinear change is considered acceptable. Figure 8.8b shows that amplitudes of the softer patterns are in general larger.

To understand why the amplitudes are different, a detailed analysis of the contact condition and energy dissipated at the contact was performed. Figure 8.9 shows the contact states of three different bedding patterns for the k_t load-dependent simulations (each colour represents a different contact state). The figure shows that the full contact bedding case has the largest number of contact nodes in slip condition (41%) compared to the other two patterns[5]. This larger slip percentage probably occurs because the full contact pattern has a larger resonance, and therefore is excited by larger excitation forces since they scale up with the rotational speed. The larger amount of nodes in slip in the full contact bedding pattern is reflected in the larger amount of energy dissipated, which is shown in Figure 8.10. The top plots show, with colour bars, the amount of energy dissipated on each node at resonance. On the figure titles, information is given on the exact amount of energy dissipated per second over the whole contact. The evolution of the total energy over the frequency range is instead presented in the plots below, which show that the peak in the energy dissipated is reached at resonance, different for every bedding pattern. From the figure, it is clear that the full contact pattern dissipates the largest amount of energy (4.4 J/s) and, for this reason, has also the lowest amplitude in

[5]Note that a contact node is considered in slip condition if, at any point during the vibration cycle, slip occurs even if for only a very small time and short distance.

response (when looking at the normalised plot in Figure 8.8b). In fact, the more the energy dissipated, the larger the damping in the system.

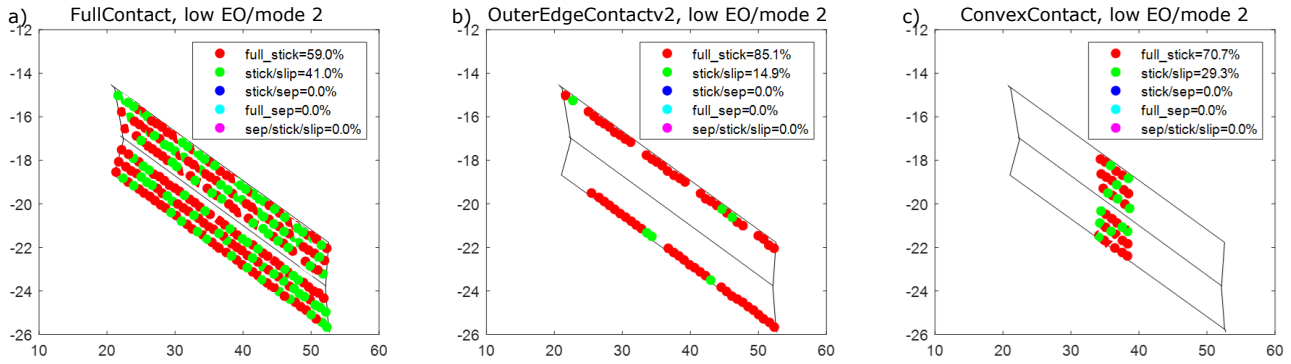


Figure 8.9: Low EO/mode 2 (1E) contact states at resonance for the k_t load-dependent simulations with grid density 40*3: a) Full contact bedding pattern; b) OuterEdgeContactv2 bedding pattern; c) Convex contact bedding pattern. Note that the 2D damper view is deformed to protect intellectual property.

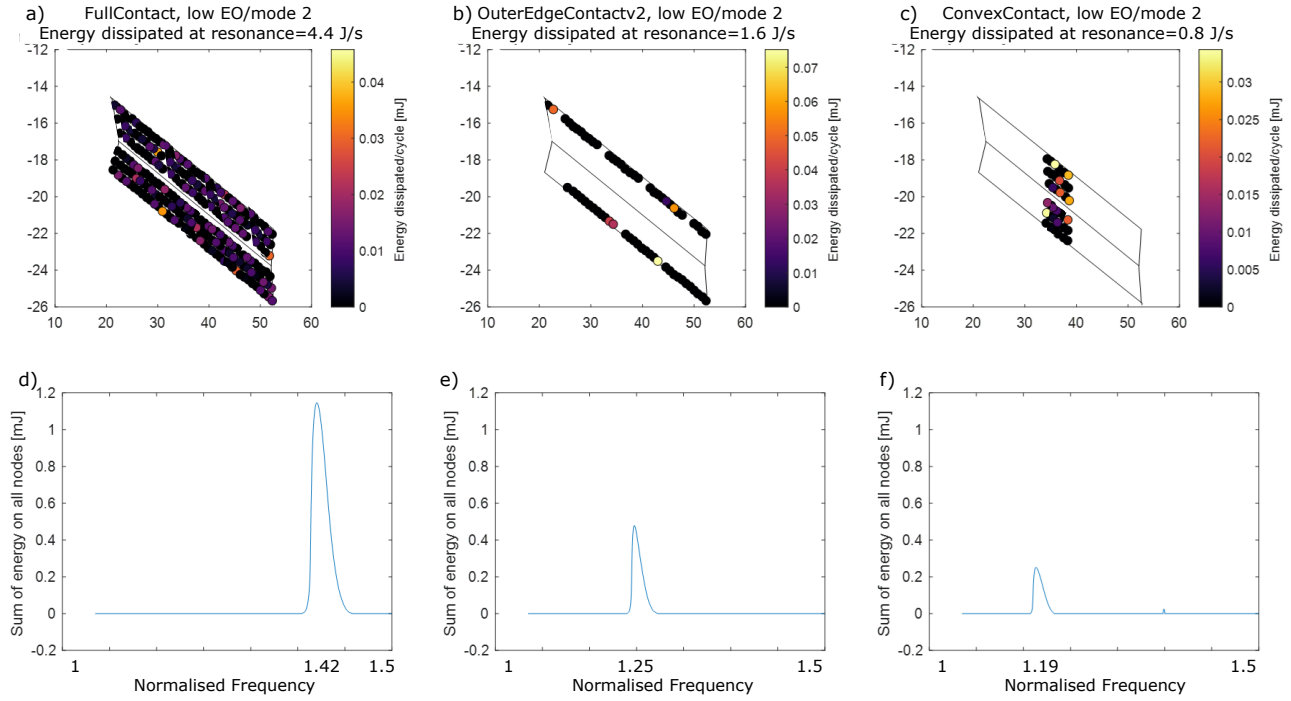


Figure 8.10: Low EO/mode 2 (1E) energy dissipated at resonance for the k_t load-dependent simulations with grid density 40*3: a) Full contact bedding pattern; b) Real contact bedding pattern v2; c) Convex contact bedding pattern. Energy dissipated over frequency range: d) Full contact bedding pattern; e) OuterEdgeContactv2 bedding pattern; f) Convex contact bedding pattern. Note that the 2D damper view is deformed to protect intellectual property.

In conclusion, this analysis on the resonance frequencies has shown how important is the accurate modelling of the contact bedding patterns and, consequently, of the pressure distribution and contact parameters. The best prediction is obtained for the realistic bedding pattern, outer edge contact in this case, which captures very well the experimental resonance frequency. Instead, the uniform full contact, which is the datum approach in most of the existing studies, led to over predictions in the resonances, by more than 20% compared to those experimental. With

regards to the k_t choice, the best results are obtained for the load-dependent contact stiffness, although the constant K_T also leads to similarly good predictions since, for the considered simulations, the chosen constant value was within the range of the load-dependent values. In addition, the usage of a normalised K_T, in N/mm^3, is necessary to obtain accurate contact representations instead of the k_t in N/μm.

The same analysis was performed for the other modes, which are described in detail in the Appendix G. A summary is given here: i) for the low EO/mode 2, the outer edge contact cases v1 and v2 and the convex case best represent the experimental behaviour compared to the full contact case; ii) for the high EO/mode 3 the outer edge contact cases v1 and v2, inner edge and concave contact cases best represent the experimental behaviour compared to the full contact case; iii) in contrast to the previous two modes, for the high EO/mode 4, the full contact case seems the best approximation for the experimental behaviour, although other patterns provide similar predictions. This last result indicates that there is not an individual pattern that works for all modes, suggesting that bedding patterns might be mode dependent. This is possible considering that all the studied modes occurred at a different rotational speed and, hence, the blade platforms might vibrate differently at those rotational speeds thus activating different contact bedding patterns. Nevertheless, for two of the three modes, the most representative pattern is the outer edge bedding pattern, which indeed is the pattern most present in the tested dampers as described in section 8.1. Table 8.2 shows a summary of all data presented in this section and the Appendix G.

Table 8.2: Summary of frequency shifts with respect to the undamped case (simulations and experiments) and contact conditions for modes low EO/mode 2, high EO/mode 3 and high EO/mode 4, for the full contact case and outer edge contact case v2, both with the grid density 40*3 and k_t load-dependence.

Mode	Full contact at resonance			Outer Edge Contact v2 at resonance			Experimental
	Freq. shift	Contact state [%stick/%slip]	Energy [J/s]	Freq. shift	Contact state [%stick/%slip]	Energy [J/s]	frequency shift range
Low EO/Mode 2	+44.5%	59.0/41.0	4.4	+24.4%	85.1/14.9	1.6	+[13.5-29.5]%
High EO/Mode 3	+6.3	43.5/56.5	17.7	+3.2%	77.0/23.0	19.0	+[2-6.5]%
High EO/Mode 4	+24.9%	12.1/87.9	219.0	+19.0%	32.4/67.8	148.4	+[21-31]%

8.3.2 Amplitude predictions - Comparison with strain gauge data

The previous section has shown a comparison of predicted and experimental resonance frequencies from strain gauge tests. Those simulations also provided information on the strain amplitudes of the material at the locations where the strain gauges were mounted. This section presents a comparison between predicted and measured strain amplitudes, for each mode and relevant contact bedding patterns. For each simulation, a numerical strain is extracted by averaging the strain of the nodes at the strain gauge locations. For each mode, two different strain gauge locations are considered, as shown in Fig. 8.2, to get also information on how the mode shape changes by evaluating the strain amplitude ratios.

Figure 8.11 shows predicted and experimental strain amplitudes for the low EO/mode 2 (1E). Experimental data is shown in the same format already described with Fig. 8.3. Predicted strain amplitudes are shown with thick blue and red lines for the benchmark reference responses

obtained with the datum approach (full contact bedding pattern with a K_T=30000 N/mm^3 and grid density 40*3). Blue and red colours correspond to the two gauge locations. Thin blue and red lines show the predicted damped responses for the outer edge bedding pattern with a k_t load dependency since this is the best combination of pattern and k_t law as shown in the previous section. In the legends, amplitude % changes from the amplitude of the benchmark case (thick blue line) are shown. Strain amplitude ratios of the two gauges are also shown (calculated from the ratios of the amplitudes at resonance). To protect intellectual property, all frequency data are normalised by the resonance of the experimental strain data, as well as the amplitudes, which were normalised by the average strain amplitude at resonance for the SA gauge. In respect to the amplitude comparison that follows, it is important to mention the following:

- Due to instrumentation capacity limits, only a small sample of the total number of measured blades had two gauges fitted that provided reliable data. Therefore, the data sample size is relatively small and might not be indicative of the average behaviour.
- In some cases, the measured gauge amplitudes are relatively low and so the measured results could be influenced by the noise floor.

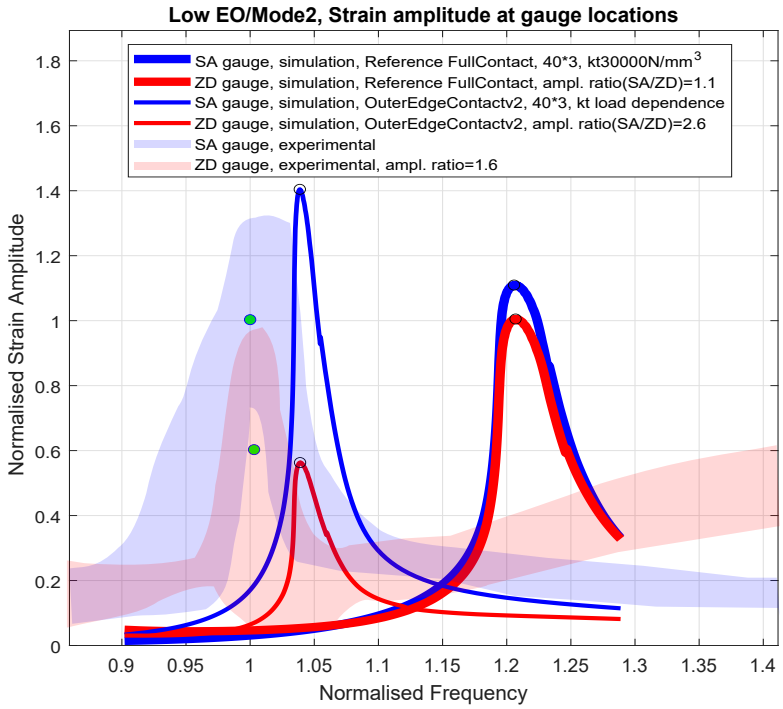


Figure 8.11: Low EO/mode 2 (1E) strain amplitudes. Comparison between strain gauge data and simulations for three bedding patterns with node grid density 40*3.

Figure 8.11 shows that the reference full contact case (thick lines) has a higher resonance frequency than the experimental (as already shown in the previous section), while the outer edge contact v2 case with k_t load dependence has a better match. With regards to the amplitudes, it is to be noted that, only for this low EO excitation mode, the excitation used in the simulations was scaled in such a way that numerical strain amplitudes became similar to the experimental, since no validated prediction capability is available to predict low EO excitation, as already discussed in section 8.2.2. Therefore, the amplitude comparison is only indicative of the real behaviour. However, the numerical amplitude ratio (between the two strain gauges SA and

ZD) can still be compared with the experimental ratio, since the same excitation amplitude was used for every simulation. It seems that the full contact case has a ratio (1.1) closer to the experimental (1.6) than the outer edge case (ratio=2.6). This comparison must be treated with caution because of the following reasons: 1) all predictions are for a tuned rotor, whereas measurements are made on a real (mistuned) rotor. Therefore, for the absolute prediction of amplitude, an agreement is not expected when compared against individual gauge/blade measurements, since other blades might have different ratios due to mistuning and measurement noise; 2) strain measurements are noisy and, in this case, the measured values were close to the noise floor. The experimental ratio was approximately estimated by calculating the ratio of the two green dots shown in figure 8.11. Still, the figure provides two interesting insights: 1) numerical ratios strongly change depending on the contact bedding pattern, by almost three times. This indicates that the mode shape has changed; 2) strain amplitudes strongly vary depending on the contact bedding pattern. For example, the SA maximum strain predicted for the outer edge contact v2 case is 27% larger than the reference full contact case. This relatively large variation is relevant for evaluations of high cycle fatigue risks since it highlights how different contact bedding patterns might lead to different amplitude predictions.

The same analysis was performed for the high EO modes 3 and 4. For those modes, the excitation pressures were predicted with CFD simulations, and therefore no tuning was performed to match numerical and experimental amplitudes. A summary of the results is given here, while more details are shown in the Appendix G. For the high EO/mode 3, simulations showed lower strain amplitudes than those measured (by roughly 20%), with the outer edge contact v2 being closer to experimental values. Also in this case, the maximum predicted strain for the outer edge contact case is larger than that for the reference full contact case (by 33%), suggesting that the full contact case might not be the most conservative case for strain predictions. This large variation must be considered for more accurate evaluations of high cycle fatigue risks. Numerical amplitude ratios were also estimated, showing a strong dependence on the contact bedding pattern (almost two times difference). This bedding pattern dependency indicates that the mode shape has changed. With regards to the high EO/mode 4, simulations showed larger strain amplitudes than those experimentally measured (by up to 30%), with the full contact case being closer to experimental values. Strain amplitudes also vary depending on the contact bedding pattern, with the maximum predicted strain for the outer edge contact case being 10.6% higher than the reference full contact case. For this mode, on the contrary of what was observed previously, the numerical ratios are equal for both contact bedding patterns. This indicates that the mode shape of this second flap mode is not affected by the different bedding patterns.

In conclusion, the analysis of the three modes showed that the outer edge contact always leads to larger strain amplitude predictions than those predicted by the full contact case (except for the ZD strain gauge of low EO/mode2), meaning that this is a more conservative case for evaluations against high cycle fatigue risks, for this type of analysed engine. Table 8.3 shows a summary of predicted and experimental amplitude ratios, including also the ratio of the undamped model (blade alone without damper). Notice once again that the experimental ratios are not fully reliable, since they are based on measurements on a single blade, and not averaged over the whole test set. In addition, amplitude ratios (either full contact or outer edge contact) are in general different from the undamped ratios of the blade alone (except for high EO/mode 4), indicating that the mode shape changes, as expected, when the damper is included in the simulations.

Table 8.3: Summary of normalised strain amplitudes of two strain gauges for each mode. The experimental amplitudes are not directly comparable, since they are based on measurements of a single blade, and not averaged over the whole test set.

	Strain	Undamped	Full contact			Outer Edge Contact v2			Experimental		
Mode	gauges	ratios	SG1	SG2	ratio	SG1	SG2	ratio	SG1	SG2	ratio
Low EO mode 2	SA and ZD	1.17	1.1	1.0	1.1	1.4	0.55	2.6	1	0.6	1.6
High EO mode 3	SA and ZD	1.17	0.7	0.15	4.7	0.93	0.36	2.6	1	0.37	2.7
High EO mode 4	SA and ZD	1.17	1.75	0.65	2.7	1.9	0.7	2.7	1	0.3	3.3

The last mention is given to the modal family 1, which represents the first flap mode (blades moving left and right). This modal family is excited at a low EO and it is studied with a different set of simulations since it requires a combined analysis with the high EO/mode 4. Both modes occur at similar engine rotational speeds, as observed experimentally, and therefore they interact with each other. Since the high EO/mode 4 has very large damping, it strongly damps also the low EO/mode 1. The combined analysis is shown in the Appendix G. It is shown that the analysis with both modes included led to a much-improved agreement with experimental measurements than when the low EO/mode 1 was modelled alone. Both modes were included in the simulation by using as input excitation both low EO and high EO excitation. The improved match indicates that the inclusion of more modes in the same simulation is of extreme importance if i) they occur in the same rotational speed range (although at different EOs) and ii) if one of them (mode 4 in this case) presents a large amount of damping, which might damp the other mode response.

8.3.3 Effect of the friction coefficient

This section investigates the effect of the friction coefficient on the forced response. A friction coefficient of 0.3 was used in the simulations based on previous measurements for the particular blade-damper material combination at the operational high-temperatures [85]. However, chapter 4 showed that a degree of uncertainty exists in the measured values of the friction coefficient. Therefore, a sensitivity study was performed with four different μ values: 0.03, 0.1, 0.3 and 0.5. The realistic outer edge contact v2 case with grid density 40*3 was used for this analysis since it is the most representative case as shown in the previous sections. Figure 8.12 shows the forced responses for low EO/mode 2, high EO/mode 3 and high EO/mode 4. For all modes, the amplitude of vibration strongly increases with the increasing friction coefficient, while the resonance frequency changes less markedly, with variations below 6%, thus negligible compared to the larger effects on the amplitude. Legends show the percentage amplitude change to the reference case with μ=0.3. In the range of μ=0.1-0.5, the amplitude changes from 43% to 135% of the nominal amplitude for the low EO/mode 2, from 50% to 140% of the nominal amplitude for the high EO/mode 3 and from 38% to 158% of the nominal amplitude for the high EO/mode 4. These strong variations in the amplitude confirm that the friction coefficient is an important parameter to consider in simulations. Although not investigated here, similar behaviour is expected for the different bedding patterns.

Chapter 4 has also shown how the friction coefficient strongly changes with wear, especially during the first vibration cycles when the components are assembled for the first time. This information is relevant since it is known from industrial experience that the first/second runs

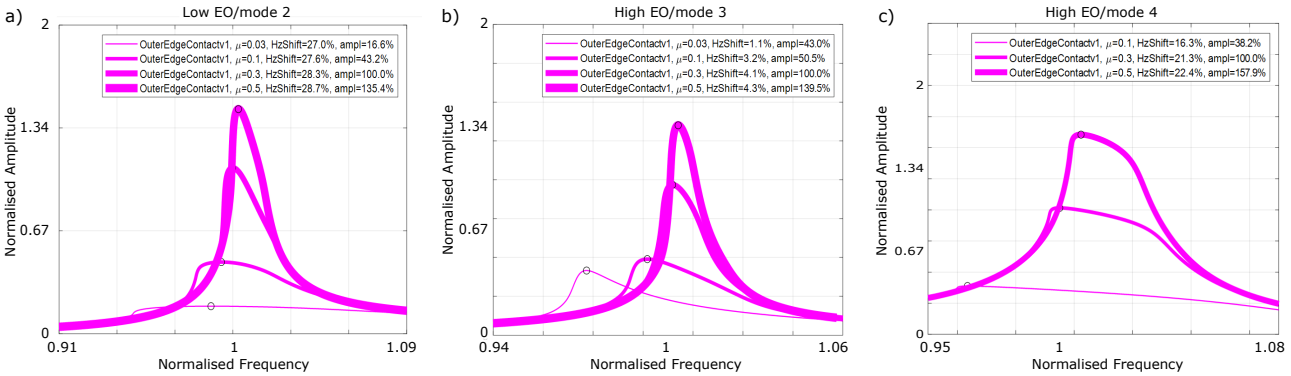


Figure 8.12: Friction coefficient sensitivity: simulations for the three modes (a-b-c) and outer edge contact v2 case, grid density 40*3, k_t load-dependence.

in strain gauge tests tend to exhibit different measured amplitudes than those at later runs when amplitudes settle to a consistent value. This change might be due to a different friction coefficient at the beginning of the test when a bedding-in of the contact has not occurred yet, according to the findings of the previous chapters (see e.g. Fig. 4.12b in section 4.2.1 and Fig. 6.6 in section 6.2.3). This aspect should be further investigated in future industrial measurements and simulations.

The contact states were also analysed for each mode. Figure 8.13a-c shows the contact conditions for the low EO/mode2 (the behaviour is similar for the other modes). As expected, when the friction coefficient is low (0.1), more contact nodes are in slip condition (50.5%), while when the friction coefficient is maximum (0.5), fewer contact nodes are in slip condition (19.6%)[6]. Figure 8.13d-f shows the corresponding energy dissipated. Although the case with μ=0.5 has the lowest percentage of contact nodes in slip, the energy dissipated is the largest (2.8 J/s). This might occur because the friction limit (μ*N) is larger, and therefore each hysteresis loop dissipates more energy although fewer nodes slip. When the energy dissipated is the largest, there should be the maximum damping and therefore the lowest amplitude of vibration. However, the case with μ=0.5 does not have the lowest amplitude, but the largest. The reason for this observed incongruence is not clear yet and could be attributed to the fact that the mode shape changes when more contact pairs are in a fully stuck condition, thus resulting in a different vibration behaviour. Simulations should be performed in future to further investigate this behaviour.

In summary, this sensitivity study highlighted the strong effect that the coefficient of friction has on the response amplitude, as already observed in the previous chapters. Up to 62% amplitude reductions were observed if the coefficient of friction was reduced from 0.3 to 0.1. Up to 58% amplitude increases were observed if the coefficient of friction was increased from 0.3 to 0.5. No major changes in the resonance frequency were instead observed (changes in the resonance frequency below the 6%).

[6]Note that a contact node is considered in slip condition if, at any point during the vibration cycle, slip occurs, even if for only a very small time and short distance.

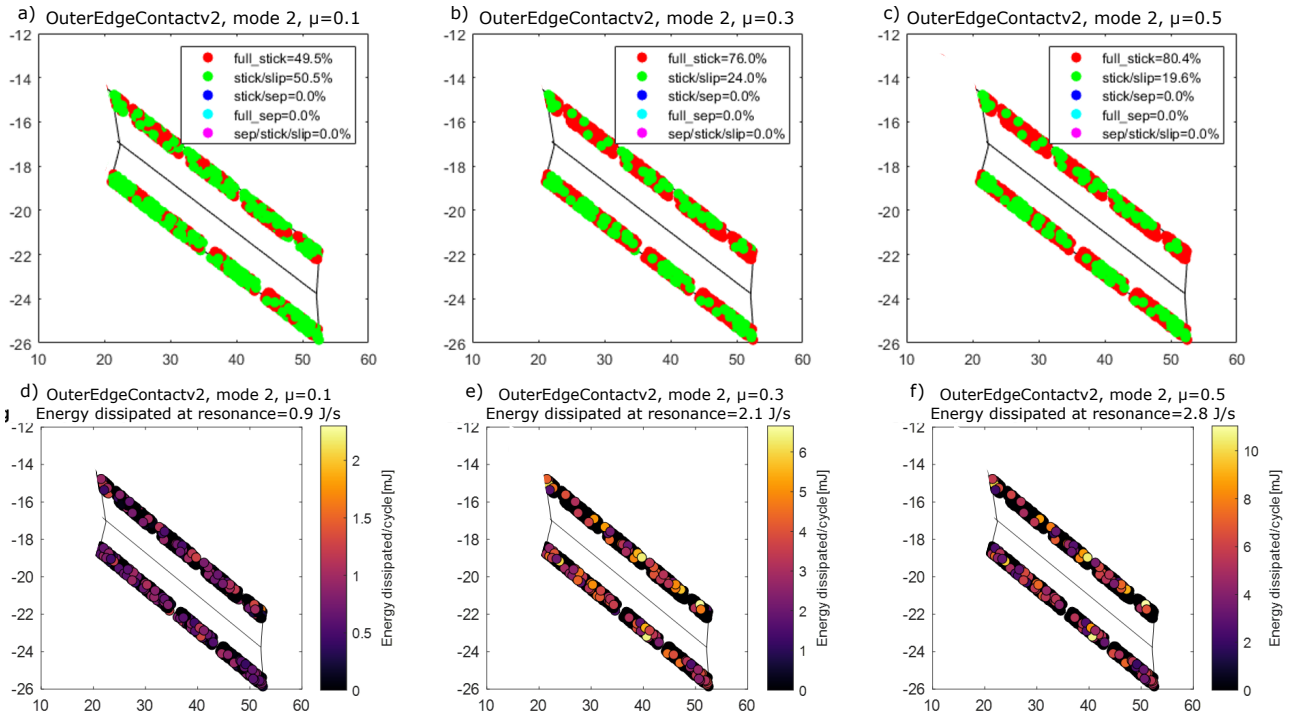


Figure 8.13: Friction coefficient sensitivity for low EO/mode2, outer edge contact v2 case, grid density 40*3, k_t load-dependence: a-c, Contact conditions; d-f, Energy dissipated. Note that the 2D damper view is deformed to protect intellectual property.

8.3.4 Effect of the grid density of contact nodes

This section investigates the effect of the density of contact nodes used in the simulations. As described in section 8.2 with Fig. 8.5, this study investigated three different node grid densities: the grid 40*3 (i.e. 40 columns * 3 rows of nodes, resulting in roughly 0.5 mm^2 per contact node) that is the datum approach of this study; the grid 120*9 (roughly 0.06 mm^2 per contact node) and the grid 8*2 (roughly 2 mm^2 per contact node).

Figure 8.14 shows a comparison of the three grid densities for two different bedding patterns and different modes (conclusions are similar for other bedding patterns). In general, results for 40*3 and 120*9 grid densities are similar (difference in Hz-shifts below 1% and amplitudes below 1%), while results for the 8*2 grid density differ in terms of Hz-shifts (below 3%) and amplitudes (below 10%). It can be concluded that the 8*2 density is not accurate enough, while the 40*3, which is the datum approach used in all the simulations presented in the previous sections, leads to results reasonably close to the denser 120*9 case, which is the most accurate.

With regards to the computational time, Table 8.4 shows a summary of the computational time required for simulations with different grid densities. The computational time increases roughly quadratically with the increasing number of nodes included in the simulation. The lowest grid density (8*2) led to the shortest computational times, up to 36 times faster than the 40*3 datum approach. The largest grid density (120*9) led to much larger computational times, up to 70 times more than the 40*3 datum approach, with the full contact simulation even aborting due to the very large number of contact nodes (>2000). It is concluded that the datum approach, 40*3 grid density with an average of 0.5 mm^2 per contact node, is the most appropriate compromise between accuracy and computational time.

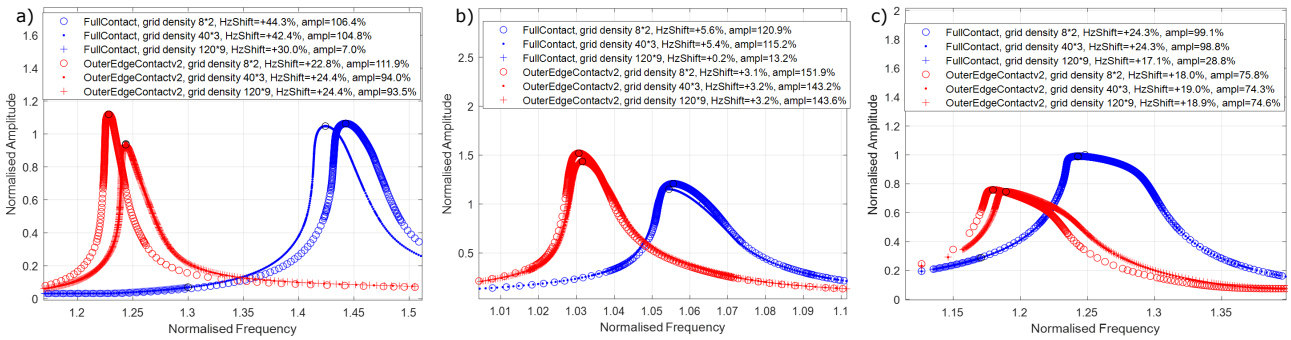


Figure 8.14: Grid density sensitivity. Full contact and outer edge contact v2 cases with k_t load dependence. Hz shifts are referred to the undamped resonance, while amplitudes are referred to the full contact bedding pattern with K_T=30000 N/mm^3.

Table 8.4: Computational time for different grid densities and contact bedding patterns. The computational time is normalised to the datum approach – 40*3 full contact case - and refers to simulations of the high EO/mode 3 with the k_t load dependence law as those shown in the Appendix G. Note that the two shown bedding patterns have a different total number of nodes, for the same grid density, as a result of their different nominal areas of contact, as shown in Table 8.1.

	Full contact		Outer edge contact v2	
Grid density	Number of nodes	Computational time normalised	Number of nodes	Computational time normalised
8*2 (2 mm^2/node)	40	0.028	20	0.009
40*3 (0.5 mm^2/node)	239	1	85	0.082
120*9 (0.06 mm^2/node)	2098	>70, aborted	766	18.14

8.4 Summary of results

This section summarises the results of the performed simulations and shows how the findings from the previous chapters were applied to improve the accuracy of the predictions. The main improvement was the modelling of different contact bedding patterns, which led to major changes in resonant frequencies and strain amplitudes predictions as follows:

- Different contact bedding patterns strongly affect the resonance frequency with up to 30% frequency shifts. In general, realistic patterns (outer edge contacts in this industrial case) led to an improved match with measured data, thanks to a softening in the response. This softening is due to the larger vibration freedom of blade and damper (since they are less constrained compared to the full contact case) and to the fact that lower nominal contact areas lead to an overall lower global contact stiffness. The improved match, obtained when modelling realistic bedding patterns, confirms the observations of the previous chapters concerning the importance of correctly modelling realistic pressure distributions in simulations (see e.g. sections 4.3.3 and 7.1.2). For the considered engine test industrial case, the outer edge pattern is the dominant contact condition and, when accurately modelled, simulations show an improved match with experimental measurements.

- The comparison between experimental and predicted strain amplitudes was more difficult to assess due to the noise in the experimental strain amplitude data. For this reason, it was not possible to identify the best bedding patterns to be used for strain amplitude predictions. In general, for each bedding pattern, the agreement changed based on the considered mode, with the largest differences below the 80%. When the realistic outer edge pattern is modelled, larger amplitudes are predicted than those predicted by the full contact pattern by up to 35%. This probably occurs because, with the outer edge contact, fewer contact nodes are constrained and therefore the structure has more freedom to vibrate. As a result, the full contact simulations (datum approach) provide less conservative estimations to be used for high cycle fatigue risk evaluation. It is therefore suggested to use the realistic outer edge bedding pattern since it provides more conservative predictions. This finding can be extended to other structures by constraining fewer contact nodes, thus giving the assembly more freedom to vibrate.

- Previous chapters have highlighted the importance of wear and wear-related changes in the contact interfaces. This effect must be considered in the presented study for a better interpretation of the results. Strain gauge tests presented in this chapter may not exhibit the same wear as end-of-life service engines since, during operation, the contact pattern might evolve from the smaller outer edge to the extended full contact. This wear-induced change in the bedding pattern could lead to some evolution of the dynamic characteristics in service confirming the importance of including the effect of wear in simulations. Examples of wear inclusions in simulations were presented in chapter 7 but also in previous studies, such as [141]. A simpler approach would be to model the two extreme cases, which in the present study are the outer edge contact and full contact. For example, after a short test such as the strain gauge test here presented, most contact evidence would be on the damper outer edges, but after longer running (with lots of exposure) the contact may appear more uniform. Simulations should be run with both full contact and outer edge contact, as these two contact conditions represent suitable bounding cases that are also consistent with hardware observation.

- A further summary is proposed in the Appendix G in a mode by mode format since it was found that, depending on the blade/damper kinematic of each mode, the agreement with experimental data varied for the investigated bedding patterns. This suggests that the actual contact condition might be mode/speed-dependent, probably due to the different blade kinematics, i.e. at different engine speeds, different mode-shapes are activated and might lead to different contact patterns. The understanding of the kinematics for each mode shape is therefore important since it might lead to different bedding patterns and hence different responses. In the case of the aero-engine turbine disk sectors, it is suggested to look at the kinematics of two consecutive blades, at different nodal diameters, to understand how damper and structure move, and how the damper contact evolves through the vibration cycle.

8.5 Conclusions

This chapter presented the nonlinear dynamic analysis of a real high-pressure turbine bladed disk sector from an industrial aero-engine test case. Simulations of the dynamic response of the turbine blades, equipped with underplatform dampers, were performed and compared against

experimental data obtained during engine tests. The simulations were performed by following some of the guidelines and improvements proposed in the previous chapters. The aim was to validate the proposed improvements on a real industrial test case since, in the literature, most of the experimental validations are only performed on small-scale academic test cases.

The main improvement was the modelling of realistic contact conditions at the interfaces. This was done by identifying from experiments the real contact bedding patterns at the blade/damper interfaces and replicating them in the simulations. For the studied blade/damper contact interfaces, the most common observed bedding pattern was the contact concentrated at the damper outer edges. This concentrated contact was modelled in the simulations leading, in general, to a much-improved match in resonance frequencies against measured data. As a result of the improvement, the main recommendation is that a contact sensitivity analysis should be included in current approaches for nonlinear dynamic analysis of jointed structures. A range of representative contact conditions should be assessed to evaluate the range of responses. As well as modelling a uniformly distributed contact, as commonly done, it is strongly recommended to enforce the contact at the actual locations observed in the real hardware for example by looking at worn interfaces of jointed structures to understand where the contact occurred. This guideline agrees with what was already proposed in the previous chapters.

As suggested in chapter 4, the effect of k_t and μ variations was also included in the simulations. Simulations showed a better match when a k_t load-dependency was included in the contact models, with changes in the resonant frequencies up to 20%. The friction coefficient also had a large impact on the nonlinear dynamic response, especially in terms of predicted amplitudes (up to threefold changes) rather than resonance frequencies (changes up to 8%). Also a sensitivity analysis on the best contact node density to be used was performed. The best compromise between accuracy and computational time was obtained for a grid density of 0.5 mm^2 per contact node, which agrees with other similar studies in the literature. The last mention is given to the mode coupling, which must be considered in simulations of rotating structures, when resonances of more modes occur at similar rotational speeds (although at different engine orders).

Although the proposed improvements led to better predictions, their validation against real engine measurements is fraught with challenges and uncertainty in the measurements. It is recommended to invest in an intermediate rig test capability that can bridge the significant gap that currently exists between idealised academic small-scale test rigs and real engine testing. A rotating full-scale component rig within a well-controlled environment would address this. At the same time, this work highlighted the sensitivity of damper functioning and turbine dynamic characteristics to contact conditions at the damper-to-blade interface. This indicates that there may be benefits to alternative damper design styles, which present contact interfaces that are robust to the effects of geometric tolerance, through life wear, mode-shape etc. All these aspects should be the basis for future research directions.

Chapter 9

Guidelines for improved nonlinear dynamic analysis

In this chapter, the findings of the previous experiments and simulations are discussed and compared. First, guidelines are proposed to increase the reliability of the measuring approaches employed in this work for the extraction of the contact parameters. Then, guidelines are proposed to improve modelling approaches for nonlinear dynamic analysis based on the improved knowledge from the performed experiments and simulations.

9.1 Guidelines for improving measuring approaches

To achieve the thesis goals, an extensive experimental investigation was performed by applying different experimental methods to the same test case, the high-frequency friction rig of Imperial College described in chapter 3. The employed experimental methods were hysteresis measurements, ultrasound measurements and dynamics measurements. Their comparison is challenging since they all investigate different aspects of the frictional phenomena and it is hard to apply them simultaneously on the same structure for cross-validation. Indeed, only a few studies have attempted to use these experimental methods simultaneously and detailed comparisons are missing. Based on their comparison performed in this PhD research, guidelines are proposed for the industry and the joint mechanics research community to improve the experimental methods for providing more accurate input data to nonlinear dynamic simulations. These guidelines are summarised in the following sections, in author's ranking. In addition, the advantages and disadvantages of the three experimental methods are summarised in Table 9.1.

Effect of displacement measurement location

In hysteresis measurements, the laser measurement location strongly affects the measured displacement and, consequently, the estimated contact stiffness. If displacements are measured close to a region where the components are not in contact, the measured displacement would be large, leading to lower (and misleading) contact stiffness estimations, see e.g. the measurements of section 4.3.3. To account for this effect in experimental displacement measurements,

Table 9.1: Summary of experimental methods.

	Advantages	**Disadvantages**
Hysteresis measurements	Provide results in the format needed for nonlinear dynamic analysis; Provide both friction coefficient and contact stiffness estimations;	Provide information only on the edge of the contact, and not on the central part; Require purposely designed friction rigs to record force and displacement signals; Information only on the tangential direction if laser is used instead of digital image correlation; Include the effect of the bulk deformation;
Ultrasonic measurements	Fast setup since do not require purposely designed friction rigs; Access to the central part of the interface; Can provide information on the normal load at the contact;	Sensors needs to be close to the contact interface; Difficult to distinguish between normal and tangential load effects; Do not provide friction coefficient estimations;
System dynamic response measurements	Easy setup; Do not require access to the contact interfaces; Provide information on the dynamic response;	Noise sensitive; Only provide indirect estimations of the contact parameters; Difficult to obtain accurate estimations and validation of the interface mechanisms;

it should be verified that the chosen displacement measurement locations are representative of the real contact spot distribution. Inappropriate laser measurement locations will lead to wrong contact stiffness estimations that, when used in simulations, might have a significant impact on the predicted dynamic responses. As an example, Fig. 4.44 from section 4.3.3 is recalled here, showing how the displacement measurement location depends on the contact spots in the measured interfaces. To the best of the author's knowledge, this effect has not been yet reported in existing hysteresis measurements.

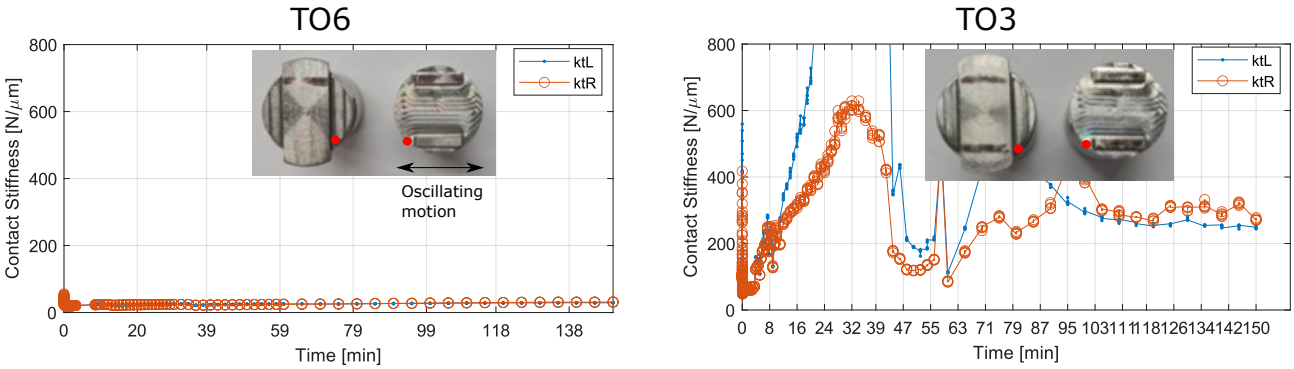


Figure 4.44: Evolution of the tangential contact stiffness of two tests performed on the PoliTO friction rig under the same loading conditions (87 N normal load, 14 μm displacement amplitude, 10 mm^2 nominal area of contact): a) Test n. TO6, k_t is very low because the displacement is measured on the leg not in contact (see red dot); b) Test n. TO3, k_t is larger because the contact is concentrated on the measured leg too. k_{tL} and k_{tR} are the contact stiffnesses of left and right stick portions of the hysteresis loops, as defined in section 3.2.1.

Another important factor to consider for accurate displacement measurements is the bulk deformation of the structure. To minimise the measured bulk deformation, the laser measurement

location needs to be extremely close to the contact interface (less than tens of micrometres from it), especially in the case of very flexible structures. The effect of the bulk deformation was quantified in section 5.2.3 by comparing the contact stiffnesses extracted from hysteresis and ultrasonic measurements performed simultaneously on the same specimens. With the aid of finite element simulations, it was concluded that ultrasonic data give physical information on the contact interfaces at a smaller length scale than the hysteresis measurements, which also include the larger-length-scale bulk deformation. This finding confirms the only previous study that compared both measurement techniques [196], but only for quasi-static contacts. Here, the hypothesis is quantified and confirmed also for high-frequency vibration experiments. The bulk deformation effect must be taken into account in current contact models used for nonlinear dynamic analysis, even though laser measurement points are only a few tens of micrometres from the contact interface. The contact stiffness obtained from hysteresis loops can be used in contact models as long as the contact interface is not fully discretised in the FE model, e.g. the interface is modelled as nominally flat without any waviness. In that case, the FE model would not include the bulk deformation information. By contrast, when the interface is more accurately discretised, e.g. the waviness at a micrometre level is represented, the contact stiffness obtained from the ultrasound is the most suitable.

Effect of surface topography

Also the distribution of the contact spots is of importance since contact spots distributed in a certain direction mainly stiffen the contact when it moves in that direction, and not in other directions, as shown in section 4.3.3. As a result, the contact stiffness depends on the contact spot distribution, which ultimately depends on the topography of the contacting interfaces. It is therefore suggested to only use contact stiffness estimations to model the contact interfaces of structures with surface topographies similar to those of the tested specimens. For example, if the contact interface of an underplatform damper or a turbine blade root has a curvature with an equivalent radius of 50 mm, contact stiffness estimations should be taken from specimens with an equivalent radius of 50 mm. To the best of the author's knowledge, there is not any existing formulation in the literature that could transform measurements taken on individual surface topographies to other different surface topographies.

Other guidelines to account for the surface topography should be followed when performing experimental measurements on contacting interfaces. First, optical scans of the contact interfaces should be performed before and after the experiments. Scans before the experiments provide information on the contact surface topographies, which are needed to predict the pressure and contact spot distribution at the beginning of the tests. Interface scans at the end of the tests are required to measure the extension of the worn area of contact, which is needed to normalise the measured contact stiffness, as discussed in the following section on the effect of wear.

Second, to ensure higher predictability of contact interface behaviours, contacting components should be designed with a predefined curvature. In this way, the contact spot is less dependent on the manufacturing uncertainties since the contact would occur most likely at the peak of the curvature. Instead, in the case of a nominally flat interface, the contact spot would be highly dependent on the uncertainty in the surface topography resulting from manufacturing. Although similar recommendations were already proposed in some recent studies [290], measurements on the two different types of specimens tested within the round robin test of chapter 4 could confirm and highlight the importance of such a design guideline.

Effect of wear

The round robin test has shown the large impact of wear on the contact parameters (see e.g. sections 4.2.1 and 4.3.1). When components are assembled for the first time, the contacting interfaces are characterised by very low values of the contact parameters, especially the friction coefficient, which will increase with wear once high-amplitude vibration begins. It is therefore suggested to verify that the structure has approached the steady state before finishing the experiment. The steady state can be verified either by looking at fully worn contact interfaces or by verifying that the measured contact parameters do not vary as the test progresses. In the case of the investigated friction rig, a test length of a least 1.5 hours was required to reach the steady state in the measured hysteresis loops. This length was valid for experiments performed on stainless steel specimens with nominally flat contact interfaces smaller than 40 mm^2 at excitation frequencies in the range of 100-200 Hz and gross slip displacements of 14 μm at least.

Dynamics measurements performed on the rig simultaneously with hysteresis measurements related, experimentally for the first time, the observed increase in the contact parameters with significant changes in the dynamic response, see e.g. section 6.2.3. Because of such significant changes, the verification of the steady state becomes extremely important when the dynamic response of structures is investigated. If the structure is assembled for the first time, several wear cycles should be performed to ensure that the contact interfaces have settled down. This guideline is extremely relevant for industrial aero-engine testing since tested engines might have not undergone many flight cycles when they get tested. As a result, contact interfaces might remain unworn thus leading to measured dynamic responses not representative of those observed in operating worn conditions. The significance of this guideline was confirmed with the aero-engine simulations shown in chapter 8, which were validated against existing experimental engine data.

Novel use of the ultrasound technique

If the target of a dynamics or hysteresis measurement is to fully validate the nonlinear modelling of a jointed structure, the simultaneous use of the ultrasound technique represents a reliable and comprehensive way to provide additional insights into the contact mechanisms. For example, vibration tests (similar to traditional nonlinear dynamic testing) can be performed to study complex assembled structures while ultrasonic waves are sent through the contact. At first, low-level excitations can be imposed, which would lead to constant ultrasonic transmissibility under stuck conditions. Then, the excitation can be gradually increased, leading to changes in the transmitted signal. In this way, excitation amplitudes that trigger microslip/gross slip can be found, thus helping engineers to quantify the damping effect of friction on structures, to monitor the wear evolution of the contact interfaces as the test progresses and to potentially help in the prediction of unexpected changes in the dynamic response of the structure. This novel use of the ultrasound is possible thanks to the unprecedented insights gained during the simultaneous acquisition of ultrasonic and high-frequency hysteresis data shown in chapter 5.

Additionally, refined spatial validations can be achieved by mounting multiple ultrasonic transducers distributed in different regions of the contact area. The use of more transducers would lead to experimental refined grids that can validate the spatially-resolved predictions of the

numerical models used for dynamics simulations. Such a use of the ultrasound has never been proposed before for the monitoring of contact interfaces, such as those in underplatform dampers or turbine blade roots. This monitoring is needed to develop more predictive capabilities that could lead to better component designs and more accurate high cycle fatigue risk evaluations.

However, this ultrasound technique measures only one variable (i.e. transmission/reflection), thus making it difficult to identify if changes are due to tangential or normal effects or even to wear. But, if used in conjunction with hysteresis measurements, it becomes a very powerful tool to accurately characterise the friction mechanisms at the interface and gain insights into the physics.

Effect of force misalignments

High-frequency friction rigs should be designed to have the excitation force on the same axis of the measured force. This is needed to avoid unwanted bending moments that might lead to load variations in the contact during the vibration cycle. Load variations in the contact can induce a large uncertainty in the extraction of the friction coefficient and the tangential contact stiffness, thus providing inaccurate input contact parameters for the nonlinear dynamic analysis. In already existing rigs with asymmetry of excitation and reaction forces, ultrasonic sensors might be mounted to monitor the load variation within the vibration cycle and assess the accuracy of the extracted contact parameters, as done in the experiments of section 5.3.3. The ultrasonic measurements showed that indeed the normal load changed during the vibration cycle. Those normal load variations could not be quantified with the hysteresis measurements, indicating that the use of the ultrasound technique can be of support to hysteresis measurements to correctly interpret measured data and avoid erroneous conclusions.

Effect of high-frequency resonances

Thanks to the simultaneous recording of hysteresis and dynamics data, several dynamics phenomena could be explained such as the origin of unexpected oscillations observed in the gross slip regime of some hysteresis loops (see e.g. section 6.3). Those oscillations were induced by the dynamic excitation of the investigated structure. If contact parameters are to be extracted, the excitation frequency should be chosen carefully, since certain excitation frequencies might excite some resonances of the structure thus generating the unwanted oscillations. Such oscillations distort the measurements, ultimately leading to inaccurate contact parameter estimations with consequences on the reliability of the dynamics simulations that use those input parameters. To avoid such events, the high resonant frequencies of the investigated structure should be first measured and, then, excitation frequencies should be chosen that are not sub-multiplies of those resonances.

9.2 Guidelines for improving modelling approaches

The findings drawn from the three experimental techniques were used to define guidelines for improving modelling approaches for nonlinear dynamic analysis. To assess the significance of

such guidelines, several simulations were performed of the friction rig (see chapter 7) and of a real aero-engine (see chapter 8). Such guidelines are ranked below in author's ranking.

Effect of wear, normal load and displacement amplitude

Nonlinear dynamic simulations of jointed structures should include the effect of wear, normal load (i.e. pressure distribution) and displacement amplitude to achieve more accurate contact parameter estimations. This is one of the highest priorities since hysteresis and ultrasonic measurements have shown that contact parameters may vary up to 20 times due to those varying conditions. They have a large impact on the dynamic response in terms of changes in predicted resonant frequencies and vibration amplitudes, as observed from the dynamics measurements and simulations, which were in accordance with the existing literature. The contact parameter dependencies are defined by the following experimentally-based guidelines:

Effect of wear. The round robin test results (see section 4.2.1) showed that the contact stiffness has to be normalised by the worn area of contact and not by the nominal area of contact as commonly done in state-of-the-art approaches. Larger worn areas lead to more asperities and wear scars in contact which contribute to increasing the resistance to the elastic deformation. This should be accounted for in nonlinear dynamic simulations by including the evolution of the contact interfaces with wear and by updating the contact stiffness with the new developed worn areas of contact, as done in recent preliminary studies available in the literature [141, 143].

If numerical codes that model the wear evolution of the contact interfaces are not available, customised experimental laws that include wear can be used in simulations. For example, a new set of dynamics simulations was shown in section 7.2.1 that included the wear-evolving contact stiffness based on the findings of the hysteresis measurements of chapter 4. The dynamic responses predicted before and after wear were compared with those experimental, showing a promising agreement in both resonance frequencies and damping of the investigated vibration modes. This agreement confirms the importance of including the wear evolution of contact parameters in nonlinear dynamic analysis.

Effect of normal load. The simultaneous acquisition of ultrasonic and hysteresis data confirmed that the tangential contact stiffness, evaluated from hysteresis loops right after load reversal, strongly correlates with the transmission/reflection of the ultrasonic signal, as previously observed by other researchers [196]. An increase in the contact stiffness was observed as the normal load increased (see e.g. sections 4.2.3 and 5.2). This is in agreement with previous studies that revealed how this increase is ultimately due to an increase in the number and size of the individual contact regions [65].

The normal load dependency of the tangential contact stiffness can be included via the experimental Eq. 4.1 from section 4.2.3 (obtained for steel specimens with nominally flat contact interfaces) and recalled here:

$$K_T = K_1 * p^{\frac{1}{2}} = 6.3 * p^{\frac{1}{2}} \tag{9.1}$$

where K_T is the contact stiffness in [N/μm/mm^2] normalised by the worn area of contact and p is the normal load normalised by the worn area in [MPa].

The normal load-dependent contact stiffness was included in nonlinear dynamic simulations

and led to a much-improved agreement with experimental data on both academic test cases (see the underplatform damper rig of section 7.2.2) and industrial cases (see the aero-engine simulations of chapter 7).

Effect of displacement amplitude. The simultaneous acquisition of ultrasonic and hysteresis data provided novel insights on the displacement dependency of the tangential contact stiffness. A reduction in the tangential contact stiffness measured from hysteresis loops, after the load reversal, was observed as the displacement amplitude increased (see e.g. sections 4.2.3 and 5.3.1). Following the same trend, the ultrasound transmission decreased with the increasing displacement amplitude (see section 5.3.3). This decrease was attributed to a reduced time for the ageing of the asperity contacts occurring at large displacement amplitudes. Such a hypothesis could be proposed thanks to the novel synchronisation of ultrasonic measurements with hysteresis measurements during vibration. The dependency of the contact stiffness on the displacement amplitude has been observed in few previous studies [20, 24, 209, 259], but no physical explanation has been provided so far. Consequently, this dependency is not accounted for in current contact models for nonlinear dynamic analysis, although it might have significant implications on the dynamic response.

The displacement dependency of the tangential contact stiffness can be included, in a first approximation, by considering the contact stiffness values in fully stuck loops fivefold higher than the values in loops with gross slip. The nonlinear dynamic solver should be able to switch between the two cases depending on the existence of gross slip or not. Note that values from Eq. 9.1 are considered as values for loops with gross slip and therefore they should be multiplied by 5 to get the contact stiffness of fully stuck loops.

The previous guidelines regarded the tangential contact stiffness. With regards to the friction coefficient, a constant value of 0.79 should be used in nonlinear dynamic analyses of 304 stainless steel structures at room temperatures. This is one of the materials most commonly encountered in academic test benches. The friction coefficient is mostly unaffected by the loading condition, except for a slight normal load dependency. It strongly changes with wear since it is very low (around 0.1) when the interfaces get into contact for the first time. After only a few vibration cycles, it rapidly increases to the steady-state value. In case the behaviour of the structure (when it is first assembled) is of interest, simulations should be performed with a very low value of 0.1. This is relevant, for example, in cases in which hammer impact tests are performed on newly assembled structures that did not undergo any loading cycles.

All of these guidelines were obtained for stainless steel specimens under the following loading conditions: excitation frequency range 100-175 Hz, room temperature, displacement amplitudes below 50 μm, contact pressures below 250 MPa. The nominal areas of contact were below the 40 mm^2 either in a flat-on-flat arrangement or in a quasi-flat arrangement with relatively large curvatures. Although the displacement amplitude and contact pressure ranges are representative of the aero-engine operating conditions, the room temperature and excitation frequency range are not. In addition, the tested stainless steel might not be representative of the whole range of industrial metallic materials. Hence, the presented guidelines could be more reliably applied when loading ranges are closer to those tested here. Nevertheless, these guidelines were applied to the industrial aero-engine turbine blade sector shown in chapter 8. Simulations of the blade dynamic response were strikingly matching experimental data for some of the investigated modes after implementing some of the proposed improvements. This proves that the fundamental understanding gained with the experimental measurements could be also applicable to industrial cases out of the tested operational ranges.

Effect of surface topography

As already discussed in section 9.1, the surface topography strongly affects the kinematics and vibrational behaviour of the jointed structure by influencing the contact spot distribution and, consequently, the pressure distribution. Therefore, to improve the modelling accuracy and reliability, realistic surface topographies should be included in simulations. This aspect has been already discussed in recent studies [19, 290], but the common practice in existing modelling approaches is still to model contact interfaces as nominally flat, although the flat condition is rarely encountered in real interfaces.

In this thesis, the importance of the surface topography was highlighted with the simulations performed on the friction rig specimens (see section 7.1) and on a real aero-engine (see chapter 8). The simulations performed on the friction rig specimens included a realistic waviness measured from optical scans of the interfaces, leading to a very good match with experimental data. This good match could not be achieved by modelling the interfaces as nominally flat, as instead is commonly done in the literature. However, realistic surface topographies are not easy to implement in finite element (FE) or boundary element models since a large computational power and very fine meshes would be required to model the actual topography of the contacting interfaces (i.e. roughness, waviness and form). In addition, it is often challenging to access the contact interfaces for optical scans with microscopes. If optical scans are not available nor the FE model can be adequately refined, the interfaces could be modelled as nominally flat but, then, non-uniform realistic pressure values should be imposed on the FE nodes. In fact, real interfaces will have only a few spots of contact leading to non-uniform pressures distributions [290]. Realistic pressure distributions can be measured experimentally, for example with the ultrasound technique as described in the previous paragraphs or with pressure films, which have to be placed between the two contacting components. If ultrasonic data or pressure films are not available, estimates of the pressure distributions can be obtained by looking at the worn contacting interfaces at the end of the test to understand where the contact occurred.

This approach was used in the simulations presented in chapter 8, where the industrial aero-engine turbine bladed disk sector equipped with underplatform dampers was investigated. Nonlinear dynamic simulations of the blade dynamic response were compared against existing strain gauge experimental measurements. Simulations were improved by identifying, from experiments, the real contact bedding patterns at the blade/damper interfaces. Such bedding patterns were replicated in the simulations by imposing non-zero contact pressures only in a few spots of the interface, where the actual contact occurred. By using such non-uniformly distributed contact pressures, a much-improved agreement with measured data could be achieved in the predicted resonance frequencies of the investigated vibration modes. For some of the modes, the agreement between numerical and experimental resonances improved strikingly, with differences between predictions and experiments below the 2% (see section 8.3.1). If instead the (commonly-used) uniform pressure was modelled, differences were up to 30%.

The improved match obtained when modelling realistic bedding patterns confirms the importance of correctly modelling realistic pressure distributions in simulations. If realistic pressure distributions are not known, a range of representative pressure distributions should be modelled to evaluate the range of responses, as performed for example in a very recent study [292].

Effect of structural flexibility

The large differences mentioned in the previous section of up to 30% in the predicted resonance frequencies, for the different bedding patterns, are partly due to changes in the structural flexibility. Indeed, simulations of chapter 8 showed that bedding patterns with smaller and/or fewer spots of contact lead to a softening in the response. This softening is due to the larger vibration freedom of the contacting components since fewer contact nodes are constrained and therefore the structure has more freedom to vibrate. The increased flexibility also affects the vibration amplitude leading, in general, to larger predicted amplitudes than those predicted with a uniform contact pattern (differences up to 35% as shown in section 8.3.2). As a result, the full contact pattern simulations, commonly performed in the literature, provide less conservative estimations to be used for high cycle fatigue risk evaluation. It is therefore suggested to constrain fewer contact nodes in nonlinear dynamic analyses to explore the effect of different, and less conservative, contact conditions, which give the assembly more freedom to vibrate.

The aero-engine simulations also showed that the kinematics of each mode shape might lead to different bedding patterns and hence different dynamic responses. It is therefore important to study the kinematics of the mode shapes to predict how the contact will change during the vibration cycles. By designing the structure to have certain kinematics during vibration, it would be possible to control the contact behaviour advantageously to achieve better damping performances. The effect of different contact bedding patterns has only been investigated in few studies in the existing literature [19, 290], and such effect of the flexibility has not been reported before to the best of the author's knowledge.

Previous paragraphs have also highlighted the importance of wear and wear-related changes in the contact bedding patterns. This effect must be considered in simulations since the contact pattern might evolve from the small non-uniformly distributed contact to the extended full contact. This wear-induced change in the bedding pattern could lead to changes in the flexibility of the structure with consequent evolution of the dynamic characteristics in service.

Effect of experimental uncertainty

Even if each of the previous loading conditions will be included in the simulations, uncertainty might still exist in the contact parameter estimations due to the uncertainty coming from the experimental inaccuracy. Variations were observed during the round robin test up to 70% in the measured contact stiffness and up to 15% in the friction coefficient, for the same loading conditions. The uncertainty in the contact stiffness is due to the inherent experimental uncertainty and to the fact that the contact surface topography of Imperial and PoliTO specimens is slightly different. The uncertainty in the friction coefficient is probably due to inaccuracies in the normal load measurement in the rigs and should be a focus for any future improvements of the rigs. This observed uncertainty should be accounted for in nonlinear dynamic analysis since it could lead to a large scatter in the predicted dynamic responses. This could be done by performing more simulations with different values of contact parameters, as shown with the simulations performed in section 7.2.2 or in the aero-engine test case of chapter 8. Possibly, the contact parameter lower and upper bounds within the 70% and 15% ranges should be tested. Then, the most critical predicted response should be used as a conservative benchmark for the design of the component to obtain high cycle fatigue risk evaluations. In the presented

simulations, resonance frequencies changed up to 10% for changes in the contact stiffnesses of 50%, while vibration amplitudes varied to 10% for changes in the friction coefficient of 15%. This effect of the friction coefficient was also observed experimentally with the experiments presented in section 6.2.3.

Summary

The guidelines summarised above do not require major changes in current modelling and measuring approaches for nonlinear dynamic analysis. State-of-the-art modelling approaches, based on the replication of hysteresis loops, can be used already now, although the input values of contact parameters should be updated depending on the loading conditions (most importantly the normal load) and sensitivity studies should be performed for different pressure distributions. Measuring techniques such as hysteresis and dynamics measurements seem also adequate, although the real spots of contact should be known before (and after) testing. This is needed to choose the most appropriate measurement setup and hence avoid unwanted measurement inaccuracies. In addition, the novel use of the ultrasound technique is recommended as a support to the existing experimental techniques, since it can provide additional insights through the real-time monitoring of the contact during vibration.

All these guidelines take a step towards the ultimate goal of the joint mechanics community to provide fully-validated and predictive modelling tools for the nonlinear dynamic analysis of turbomachinery assemblies. Such predictive modelling tools are needed in the industry to improve design processes and provide products with improved safety, efficiency and reliability. Improvements will guarantee economic benefits resulting from reduced maintenance requirements, reduced physical testing and less late-cycle product re-designs. This PhD research helps in advancing the knowledge in this direction, although more work is needed in the future dozens of years to achieve such predictive capabilities.

Chapter 10

Conclusions and future work

The control of vibrations is a key challenge to designing safer and more efficient engineering assemblies, such as aero-engines and other turbomachinery. If excessive, vibrations might lead to loss of performance, higher maintenance and large stresses in components, which compromise the structural integrity. Accurate dynamics predictions are therefore needed to achieve safer designs. However, predicting the dynamics of the assembly is quite challenging, partly due to the presence of friction between the thousands of components in contact. Despite the considerable research efforts over the past decades, the effects of friction on the dynamics are not yet fully understood due to the complex mechanisms that govern the interface behaviour. As a result, fully-validated and predictive modelling approaches are not available, and expensive physical testing is still required to assess the performance and reliability of new designs.

This research addressed this issue by improving the current understanding of friction mechanisms and their effects on the dynamic response of jointed structures. An extensive round robin test was performed on two high-frequency friction rigs of different institutions (Imperial College London and Politecnico di Torino) to measure a wide range of hysteresis loops (chapter 4). Although measurement results provided many insights on the friction mechanisms, they were based on information coming only from the outer edge of the contact, where the displacement was measured. The behaviour of the central part of the contact was instead unknown, thus limiting the completeness of the measurements. Therefore, another experimental method was used to access the central part of the contact during vibration: the ultrasound technique, which was used simultaneously with the hysteresis measurements to monitor the vibrating contact in real time (chapter 5).

Based on the results of both measurement techniques, novel insights were provided on the physics of the contact parameters (friction coefficient and tangential contact stiffness) used as input in contact models for nonlinear dynamic analysis. It was shown that the tangential contact stiffness slowly increases during the test because of an increase in the worn area of contact. It is consequently necessary to normalise it by the worn area of contact, rather than by the nominal area of contact as instead commonly suggested by the literature. The contact stiffness also increases with increasing normal loads, in agreement with previous studies that already showed how this is ultimately due to an increase in the number and size of the individual contact spots. Measurements showed that not only the number and size of contact spots are important, but also their distribution, which strongly affects the kinematics of the contacting components and, consequently, the contact parameter estimations. Additionally, it was discovered that

the tangential contact stiffness, evaluated right after the load reversal, is much lower when hysteresis loops are measured at large displacement amplitudes. This decrease in loops at large displacement amplitudes was attributed to a reduced time for the ageing of the asperity contacts, which enhances the conformity of the contacting interfaces with time. The friction coefficient showed instead a milder dependency on the loading conditions. Other unprecedented insights on the contact behaviour were obtained by using the ultrasound in synchronisation with hysteresis measurements. For example, large variability was observed in the ultrasound transmissibility at different time instances within individual high-frequency hysteresis loops. This variability was linked to stick-slip transitions at the contact, highlighting the potential of the technique to identify stick and slip transitions in real time in vibrating frictional contacts.

Based on those findings, the following guidelines were proposed to improve measuring and modelling approaches for the nonlinear dynamic analysis of jointed structures:

- Include the normal load dependency of the tangential contact stiffness, k_t, by means of a square root dependency on the contact pressure. This guideline is known in existing literature but it is often overlooked in current practices for nonlinear dynamic analysis;
- More accurate and realistic contact pressure distributions should be used in simulations. This can be achieved by using realistic finite element models of the manufactured contact interfaces or by imposing non-uniform pressure values on the finite element nodes of the contacting interfaces. This effect is often overlooked in current practices for nonlinear dynamic analysis. In addition, the real contact distribution should be known during experiments to properly choose displacement measurement locations that are representative of the contacting interfaces. Inappropriate measurement locations might in fact lead to misleading measurements with consequent inaccurate contact parameter estimations;
- Include the displacement amplitude dependency of k_t by using k_t values of fully stuck loops fivefold higher than those of hysteresis loops with gross slip. This effect is not included in current practices for nonlinear dynamic analysis;
- Include the worn area dependency of k_t by providing as input in contact models the k_t normalised by the worn area of contact and not by the nominal area of contact, as commonly suggested in the literature. The importance of wear is also emphasised for more reliable experimental measurements. It should be verified that the contacting interfaces of the investigated structure have fully settled to a steady state, especially soon after the first assembly, otherwise, measurement results would not be representative of the operating conditions.
- If the target of a dynamics or hysteresis measurement is to fully validate the nonlinear modelling of a jointed structure, the simultaneous use of the ultrasound technique represents a reliable and comprehensive way to provide additional insights into the contact mechanisms. The novel use of the ultrasound technique proposed here makes it possible to monitor, in real time during vibration, the contact interfaces of non-transparent materials, otherwise inaccessible, which are of great interest for industrial applications. This real-time monitoring can also provide the interface data needed to validate interface predictions from nonlinear dynamic analysis and monitor jointed structures in real time to prevent unwanted high cyclic stresses.

After improving the understanding of the friction mechanisms and proposing guidelines, dynamics measurements were performed to improve the understanding of the effects of friction on the dynamics (chapter 6). It was shown that the changes in the contact parameters had a large impact on the dynamic response in terms of changes in predicted resonant frequencies and vibration amplitudes, in agreement with existing literature. These changes were also confirmed with a new set of simulations. In fact, the proposed guidelines were integrated into nonlinear dynamic simulations leading to an improved agreement between predictions and experiments. Simulations were performed not only on academic test cases (chapter 7) but also on a real turbine blade sector from an industrial aero-engine (chapter 8). Also in that case, the inclusion of the proposed guidelines led to a much-improved agreement between simulations and experimental data from aero-engine testing. The achieved agreement confirmed the significance of the proposed guidelines even in the case of complex and realistic industrial cases.

Suggestions for future work

The work in this PhD research has made some major contributions towards improving the understanding of friction and its effects on the dynamic response of jointed structures. The proposed guidelines take a step towards the ultimate goal of the joint mechanics community to provide fully-validated and predictive modelling tools for the nonlinear dynamic analysis of jointed structures. However, current modelling approaches are not fully predictive yet and more work is needed in the future dozens of years to achieve such predictive capabilities and higher levels of accuracy and reliability. Based on the limitations of this work, some research directions are defined for the short- and long-terms.

Short-term research directions:

- Expand the round robin test dataset:
  - Experiments were performed at room temperature and provided a fundamental understanding of the contact mechanisms at those temperatures. However, turbomachinery components experience much higher temperatures (above 700 °C) and new physics could occur in those conditions. Measurements should be performed at higher temperatures to verify how the physics of the contact changes and, eventually, upgrade the contact laws accordingly since some of the uncovered effects might not be relevant at higher temperatures.
  - Only the stainless steel material pairing was tested. Although the stainless steel is assumed to be representative of other metallic material pairings, a range of typical metallic materials used for engineering applications should be tested to investigate how generally applicable the round robin findings are. In addition, the values of the contact parameters should be measured for the exact material pairing used for the given industrial application. A more detailed set of tests should be performed to investigate the behaviour of coatings, which will probably behave differently than metallic materials. The experimental guidelines proposed during the round robin test are also applicable to coatings and will strongly benefit both testing and result interpretation.

  - Experiments were performed at high frequencies and, thus, were affected by the dynamics of the friction rigs. It is suggested to measure the contact parameters statically under the same tested normal load and displacement amplitude ranges and observe if any differences appear in the measured values. If differences appear, further investigations should be performed to separate the dynamic behaviour from the contact behaviour.
  - To better understand how different contact surface topographies and pressure distributions affect the measurements, further investigations should be performed that quantify the effect of the distribution and size of worn areas of contact. New specimens should be manufactured with different surface topographies and be tested following the designed round robin test matrix. In this way, more detailed contact laws can be defined for different surface topographies and pressure distributions. In addition, also different initial roughnesses should be investigated to quantify if and how they influence the wear evolution of both contact parameters and contact interfaces.
  - In some tests, in which there was energy dissipation, the contact stiffness increased although the worn area of contact remained constant. It was assumed that a plastic hardening occurred at the asperities. This phenomenon should be investigated in more detail in future, for example by measuring the hardness of the asperities at the end of those tests and comparing it with the pre-test one.
  - In this round robin test, two different friction rigs were included, from Imperial College London (Imperial) and Politecnico di Torino (PoliTO). In future, more friction rigs from other institutions could be added to the round robin to increase the statistical significance of the measurements. The addition of more friction rigs would show how measurements change with a different setup, eventually validating the proposed hypotheses and further increasing the confidence in measured contact parameters. For example, different test rigs could measure hysteresis loops at displacement amplitudes larger than 50 μm. Such measurements are needed to validate the hypothesis on the dependency of the friction coefficient on the normal load. The reason for the observed decrease in the friction coefficient with increasing normal loads was attributed to the fact that, at larger normal loads, a full established gross slip was not achieved within the relatively small investigated displacement amplitudes (14 μm and 50 μm). Tests at larger displacement amplitudes could verify this hypothesis.

- This thesis investigated in detail the physics of the tangential contact stiffness, but not that of the normal contact stiffness. Although it is assumed in the literature that the normal contact stiffness has similar values [63], few studies exist that measured both at the same time under high-frequency vibrations. It is suggested to use the digital image correlation technique to measure relative normal displacements during hysteresis measurements. In this way, normal contact stiffness values can be measured and compared to the tangential contact stiffness to verify that the hypotheses presented in this thesis also apply to the normal contact stiffness.

- To further investigate the physics in the normal direction, a new system would be needed to harmonically excite the rig in the normal direction, for example by using piezo actuators. Such a system that varies the normal load can be also used to counterbalance the dynamic normal load variations observed in the Imperial rig during the vibration cycles. This counterbalancing can remove the measuring issues related to the normal load vari-

ations but can also potentially help to understand why friction coefficient measurements at Imperial and PoliTO were slightly different. It was in fact assumed that the difference arose from inaccuracies in the applied normal load.

Long-term research directions:

- This thesis showed simulations performed on academic test cases and also on a realistic industrial test case. Although simulations on the industrial test case could provide many insights, experimental data were not enough since they required very expensive physical testing to be obtained. It is therefore suggested to invest in an intermediate test rig capability that can bridge the significant gap that currently exists between idealised academic small-scale test rigs (underplatform damper rigs, blade roots etc.) and real engine testing. This intermediate test rig capability would make it possible to perform tests under a more realistic framework but also at a much-reduced cost than real engine testing. Hypotheses on the effects of contact on the dynamics behaviour could be tested without the simplifications present in the academic test rigs (e.g. realistic centrifugal loads due to rotation instead of pulling loads applied through wires, or realistic airflow excitation instead of electrodynamic shaker excitation).

- Chapter 8 showed a detailed contact sensitivity analysis performed to model the dynamic response of aero-engine turbine blades equipped with underplatform dampers. The results of that analysis suggested that, there may be benefits in testing alternative underplatform damper designs, which present contact interfaces that are robust to the effects of geometric tolerance, through life wear, mode-shape etc. For example, the effect of different tolerance specifications could be assessed by manufacturing multiple dampers within tolerances and testing them to verify their repeatability. Then, the most robust dampers against manufacturing tolerances could be identified and used for industrial applications. In this way, the experimental uncertainty could be reduced and, thus, the predictive capabilities of existing modelling approaches could be easily increased. Another factor to consider in future analyses is the position of the damper, which is always considered to be fixed in the finite element models of the existing literature (and in this thesis as well). However, the initial position in real operation might be slightly different from the nominal position. The effect of slightly different damper initial positions should be therefore investigated, both numerically and experimentally.

- This research proposed the novel use of the ultrasound technique to monitor non transparent contact interfaces, in real time, during vibration. It is recommended to explore the use of ultrasonic arrays for real-time monitoring of industrial test cases. Refined spatial validations can be achieved by mounting multiple ultrasonic transducers distributed in different regions of the contact area. The use of more transducers would lead to experimental refined grids that can validate the spatially-resolved predictions of the interfaces discretised with finite element models. Ultrasonic transducers can be as small as 2 by 2 mm. This size is comparable to the mesh grids used in FE models for nonlinear dynamic analysis (0.5 by 0.5 mm elements generally are used to discretise the contacting interfaces). These validations are needed to develop more predictive capabilities that lead to better component designs and more accurate high cycle fatigue risk evaluations. Ultrasonic arrays can also be used to monitor wear at the interface and hence study the degradation of the joints.

- Boundary element simulations of the contact interface behaviour showed a promising agreement with experimental data. In addition, the real contact interface could be modelled and tested with a relatively small computational effort. However, the accuracy of the simulations strongly depended on the quality of the optical scan of the real interfaces. The quality of the scans was in turn affected by the presence of wear debris, which could be accidentally removed when the interfaces were opened at the end of the tests. The boundary element method (BEM) should be updated to take this effect into account. Then, it should be included in nonlinear dynamic analysis routines to substitute the very dense finite element interface meshes, which lead to very large computational requirements. The inclusion of the BEM in modelling approaches could lead to a significant reduction in the computational time and a higher accuracy given by the realistic representation of the contacting interfaces.

Bibliography

[1] "PM speech at COP 26 Launch: 4 February 2020," *GOV.UK, Feb 2020.*

[2] "DECARBONISATION ROAD-MAP: A PATH TO NET ZERO. A plan to decarbonise UK aviation," *Report from Sustainable Aviation, Feb 2020.*

[3] M. R. Brake, *The Mechanics of Jointed Structures: Recent Research and Open Challenges for Developing Predictive Models for Structural Dynamics.* Springer International Publishing, 2018.

[4] L. Gaul and R. Nitsche, "The Role of Friction in Mechanical Joints," *Applied Mechanics Reviews*, vol. 54, no. 2, p. 93, 2001.

[5] G. Kerschen, K. Worden, A. F. Vakakis, and J.-C. Golinval, "Past, present and future of nonlinear system identification in structural dynamics," *Mechanical Systems and Signal Processing*, vol. 20, no. 3, pp. 505–592, 2006.

[6] "Rolls-Royce Trent XWB [Internet]. Available from: https://www.rolls-royce.com/media/Files/R/Rolls-Royce/documents/civil-aerospace-downloads/High-Res-posters/High-Res-poster-Trent-XWB.pdf [Accessed: 2018-06-10]."

[7] D. J. Segalman, L. A. Bergman, and D. J. Ewins, "Report on the SNL / NSF International Workshop on Joint Mechanics," *Arlington, VA, 16-18 October 2006, Technical Report SAND2007-7761*, 2007.

[8] D. J. Segalman, L. A. Bergman, and D. J. Ewins, "Report on the SNL/AWE/ NSF International Workshop on Joint Mechanics," *Dartington, UK, 27-29 April 2009, Technical Report SAND2010-5458*, 2010.

[9] M. J. Starr, M. R. Brake, D. J. Segalman, L. A. Bergman, and D. J. Ewins, "Proceedings of the Third International Workshop on Jointed Structures," *Chicago, IL, 16-17 August 2012, Technical Report SAND2010-5458*, 2013.

[10] M. R. Schroeder, *Fractals, Chaos, Power Laws, Minutes from an Infinite Paradise.* W.H. Freeman and Company, New York, 1991.

[11] L. Pesaresi, J. Armand, C. W. Schwingshackl, L. Salles, and C. Wong, "An advanced underplatform damper modelling approach based on a microslip contact model," *Journal of Sound and Vibration*, vol. 436, pp. 327–340, 2018.

[12] C. Gastaldi and M. M. Gola, "On the relevance of a microslip contact model for underplatform dampers," *International Journal of Mechanical Sciences*, vol. 115-116, pp. 145–156, 2016.

[13] L. Panning, W. Sextro, and K. Popp, "Spatial Dynamics of Tuned and Mistuned Bladed Disks with Cylindrical and Wedge-Shaped Friction Dampers," *International Journal of Rotating Machinery*, vol. 9, no. 3, pp. 219–228, 2003.

[14] D. J. Ewins, *A Survey of Contact Hysteresis Measurement Techniques.* Cham: Springer International Publishing, 2018.

[15] A. V. Srinivasan, "Flutter and Resonant Vibration Characteristics of Engine Blades," *Journal of Engineering for Gas Turbines and Power*, vol. 119, no. 4, p. 742, 1997.

[16] S. Zucca, C. M. Firrone, and M. M. Gola, "Numerical assessment of friction damping at turbine blade root joints by simultaneous calculation of the static and dynamic contact loads," *Nonlinear Dynamics*, vol. 67, pp. 1943–1955, feb 2012.

[17] S. Schwarz, L. Kohlmann, A. Hartung, *et al.*, "Validation of A Turbine Blade Component Test with Frictional Contacts by Phase-Locked-Loop and Force-Controlled Measurements," *Journal of Engineering for Gas Turbines and Power*, 2019.

[18] D. Botto, C. Gastaldi, M. M. Gola, and M. Umer, "An Experimental Investigation of the Dynamics of a Blade With Two Under-Platform Dampers," *Journal of Engineering for Gas Turbines and Power*, vol. 140, no. 3, p. 032504, 2017.

[19] L. Pesaresi, L. Salles, A. Jones, J. S. Green, and C. W. Schwingshackl, "Modelling the nonlinear behaviour of an underplatform damper test rig for turbine applications," *Mechanical Systems and Signal Processing*, vol. 85, pp. 662–679, 2017.

[20] A. Fantetti, L. Tamatam, M. Volvert, *et al.*, "The impact of fretting wear on structural dynamics: Experiment and simulation," *Tribology International*, vol. 138, pp. 111–124, 2019.

[21] C. W. Schwingshackl, E. P. Petrov, and D. J. Ewins, "Effects of Contact Interface Parameters on Vibration of Turbine Bladed Disks With Underplatform Dampers," *Journal of Engineering for Gas Turbines and Power*, vol. 134, no. 3, p. 032507, 2012.

[22] S. Zucca, C. M. Firrone, and M. M. Gola, "Modeling underplatform dampers for turbine blades: A refined approach in the frequency domain," *Journal of Vibration and Control*, vol. 19, no. 7, pp. 1087–1102, 2013.

[23] M. Krack, L. Salles, and F. Thouverez, "Vibration Prediction of Bladed Disks Coupled by Friction Joints," *Archives of Computational Methods in Engineering*, vol. 24, no. 3, pp. 589–636, 2017.

[24] K.-H. Koh, J. H. Griffin, S. Filippi, and A. Akay, "Characterization of Turbine Blade Friction Dampers," *Journal of Engineering for Gas Turbines and Power*, vol. 127, no. 4, p. 856, 2005.

[25] M. H. Jareland and G. Csaba, "Friction Damper Mistuning of a Bladed Disk and Optimization with respect to Wear," in *Proceedings of ASME Turbo Expo 2000*, 2000.

[26] P. Vargiu, C. M. Firrone, S. Zucca, and M. M. Gola, "A reduced order model based on sector mistuning for the dynamic analysis of mistuned bladed disks," *International Journal of Mechanical Sciences*, vol. 53, pp. 639–646, aug 2011.

[27] J. Groß and M. R. Brake, "A Standard Practice for Modeling Bolted Joints in a Finite Element Package," in *The Mechanics of Jointed Structures* (M. R. W. Brake, ed.), pp. 415–426, Cham: Springer International Publishing, 2018.

[28] M. R. Brake, "An Overview of Constitutive Models," in *The Mechanics of Jointed Structures* (M. R. W. Brake, ed.), pp. 207–221, Cham: Springer International Publishing, 2018.

[29] C. M. Firrone and S. Zucca, "Modelling Friction Contacts in Structural Dynamics and its Application to Turbine Bladed Disks," *Numerical Analysis - Theory and Application*, pp. 301–334, 2011.

[30] D. J. Segalman, "Modelling joint friction in structural dynamics," *Structural Control and Health Monitoring*, vol. 13, pp. 430–453, jan 2006.

[31] N. M. Newmark, "A method of computation for structural dynamics," *Journal of the engineering mechanics division*, vol. 85, no. 3, pp. 67–94, 1959.

[32] J. R. Dormand and P. J. Prince, "A reconsideration of some embedded Runge-Kutta formulae," *Journal of Computational and Applied Mathematics*, vol. 15, no. 2, pp. 203–211, 1986.

[33] J. M. Fine, "Low order practical Runge-Kutta-Nyström methods," *Computing*, vol. 38, no. 4, pp. 281–297, 1987.

[34] A. Cardona, T. Coune, A. Lerusse, and M. Geradin, "A multiharmonic method for non-linear vibration analysis," *International journal for numerical methods in engineering*, vol. 37, no. 9, pp. 1593–1608, 1994.

[35] K. Sanliturk and D. Ewins, "Modelling Two-Dimensional Friction Contact and Its Application Using Harmonic Balance Method," *Journal of Sound and Vibration*, vol. 193, no. 2, pp. 511–523, 1996.

[36] E. P. Petrov and D. J. Ewins, "Analytical Formulation of Friction Interface Elements for Analysis of Nonlinear Multi-Harmonic Vibrations of Bladed Disks," *Journal of Turbomachinery*, vol. 125, no. 2, p. 364, 2003.

[37] E. P. Petrov and D. J. Ewins, "State-of-the-art dynamic analysis for non-linear gas turbine structures," *Proceedings of the Institution of Mechanical Engineers, Part G: Journal of Aerospace Engineering*, vol. 218, no. 3, pp. 199–211, 2004.

[38] P. Deuflhard, *Newton Methods for Nonlinear Problems: Affine Invariance and Adaptive Algorithms*, vol. 35. Berlin: Springer Science & Business Media, 2011.

[39] M. R. Brake, "Historical Perspective on Numerical Techniques for Modeling Joints," in *The Mechanics of Jointed Structures* (M. R. W. Brake, ed.), pp. 397–413, Cham: Springer International Publishing, 2018.

[40] M. R. Brake, J. Groß, R. Lacayo, *et al.*, "Reduced Order Modeling of Nonlinear Structures with Frictional Interfaces," in *The Mechanics of Jointed Structures* (M. Brake, ed.), ch. 24, pp. 427–450, Cham: Springer International Publishing, 2018.

[41] R. Lacayo, L. Pesaresi, J. Gross, *et al.*, "Nonlinear modeling of structures with bolted joints : a comparison of two approaches based on a time-domain and frequency-domain solver," *Mechanical Systems and Signal Processing*, no. 114, pp. 413–438, 2019.

[42] M. H. Müser, W. B. Dapp, R. Bugnicourt, *et al.*, "Meeting the Contact-Mechanics Challenge," *Tribology Letters*, vol. 65, no. 4, 2017.

[43] J. Greenwood and J. Williamson, "Contact of nominally flat surfaces," *Proceedings of the Royal Society London A*, vol. 1442, no. 295, pp. 300–319, 1966.

[44] J. J. O'Connor and K. L. Johnson, "The role of surface asperities in transmitting tangential forces between metals," *Wear*, vol. 6, no. 2, pp. 118–139, 1963.

[45] M. R. Brake, *Introduction to Research on the Mechanics of Jointed Structures*, pp. 3–10. Cham: Springer International Publishing, 2018.

[46] D. Dowson, *History of tribology*. Professional Engineering Publishing, London, 1998.

[47] E. McCurdy, *The Notebooks of Leonardo da Vinci, Vol. 1*. Reynal and Hitchcock, New York, 1938.

[48] G. Amontons, "De la resistance causee dans les machines," *Memoires de l'Academie Royale des Sciences*, vol. MIT Press, pp. 206–226, 1699.

[49] L. Euler, "Sur la frottement des corps solides," *Memoires de l'Academie des Sciences de Berlin*, no. 4, pp. 122–132, 1750.

[50] S. K. Kotelnikov, *A book containing the doctrine on equilibrium and motion of bodies*. St. Petersburg: Naval Nobel Cadet Corps., 1774.

[51] R. Holm, "The friction force over the real area of contact," *Wiss. Veroff. Siemens-Werk*, vol. 17, no. 4, pp. 38–42, 1938.

[52] F. P. Bowden and D. Tabor, "The area of contact between stationary and between moving surfaces," *Proceedings of the Royal Society of London. Series A. Mathematical and Physical Sciences*, vol. 169, no. 938, pp. 391–413, 1939.

[53] H. Ernst and M. E. Merchant, "Surface friction of clean metals: a basic factor in the metal cutting process," in *Proc. Special Summer Conf. on Friction and Surface Finish*, pp. 76–101, MIT Press, 1940.

[54] C. Coulomb, "Theorie des machines simples, en eyant egard au frottement de leurs parties et a la roideur des cordages," *Memoires de Mathematique et de Physique de l'Academie Royale*, pp. 161–342, 1785.

[55] J. T. Desaguliers, *A Course of Experimental Philosophy, Vol.1, with thirty-two copper plates*. London: W. Innys, 1734.

[56] F. P. Bowden, "BBC broadcast," 1950.

[57] F. P. Bowden and D. Tabor, "Mechanism of metallic friction," *Nature*, vol. 150, pp. 197–199, 1942.

[58] F. P. Bowden and D. Tabor, *The friction and lubrication of solids. Vol. 2*. OUP, 1964.

[59] N. P. Suh and H. C. Sin, "The genesis of friction," *Wear*, vol. 69, no. 1, pp. 91–114, 1981.

[60] M. Godet, "The third-body approach: A mechanical view of wear," *Wear*, vol. 100, pp. 437–452, 1984.

[61] J. Denape, "Third body concept and wear particle behavior in dry sliding conditions," *Tribological aspects in modern aircraft industry*, pp. 1–12, 2014.

[62] A. I. Vakis, V. A. Yastrebov, J. Scheibert, *et al.*, "Modeling and simulation in tribology across scales: An overview," *Tribology International*, vol. 125, no. February, pp. 169–199, 2018.

[63] S. Medina, D. Nowell, and D. Dini, "Analytical and numerical models for tangential stiffness of rough elastic contacts," *Tribology Letters*, vol. 49, no. 1, pp. 103–115, 2013.

[64] R. D. Mindlin and H. Deresiewicz, "Elastic Spheres in Contact Under Varying Oblique Forces," *Journal of Applied Mechanics*, vol. 20, pp. 327–344, 1953.

[65] K. Kendall and D. Tabor, "An Ultrasonic Study of the Area of Contact between Stationary and Sliding Surfaces," *Proceedings of the Royal Society A: Mathematical, Physical and Engineering Sciences*, vol. 323, pp. 321–340, dec 1971.

[66] J. Krolikowski and J. Szczepek, "Prediction method of contact parameters using ultrasonic method," *Wear*, vol. 148, pp. 181–195, 1991.

[67] M. Hashimoto, E. Marui, and S. Kato, "Estimation of contact stiffness at interfaces in machine structures by a beam model on an elastic foundation," *Tribology International*, 1994.

[68] B. W. Drinkwater, R. S. Dwyer-Joyce, and P. Cawley, "A study of the interaction between ultrasound and a partially contacting solid-solid interface," *Proceedings of the Royal Society A: Mathematical, Physical and Engineering Sciences*, vol. 452, pp. 2613–2628, 1996.

[69] P. Berthoud and T. Baumberger, "Shear stiffness of a solid-solid multicontact interface," in *Procedures Royal Society London*, no. 454, pp. 1615–1634, 1998.

[70] T. Fujimoto, J. Kagami, T. Kawaguchi, and T. Hatazawa, "Micro-displacement characteristics under tangential force," *Wear*, vol. 241, no. 2, pp. 136–142, 2000.

[71] R. S. Dwyer-Joyce, B. W. Drinkwater, and A. M. Quinn, "The Use of Ultrasound in the Investigation of Rough Surface Interfaces," *Journal of Tribology*, vol. 123, no. 1, p. 8, 2001.

[72] J. Szwedowicz, M. Kissel, B. Ravindra, and R. Kellerer, "Estimation of Contact Stiffness and its Role in the Design of a Friction Damper," *ASME Turbo Expo*, pp. 1–8, 2001.

[73] A. Baltazar, S. I. Rokhlin, and C. Pecorari, "On the relationship between ultrasonic and micromechanical properties of contacting rough surfaces," *Journal of the Mechanics and Physics of Solids*, vol. 50, no. 7, pp. 1397–1416, 2002.

[74] S. Filippi, A. Akay, and M. M. Gola, "Measurement of Tangential Contact Hysteresis During Microslip," *Journal of Tribology*, vol. 126, no. 3, p. 482, 2004.

[75] R. S. Dwyer-Joyce and M. Gonzalez-Valadez, "Ultrasonic determination of normal and shear interface stiffness and the effect of Poisson's ratio," in *Proceedings of the 30th Leeds-*

Lyon Symposium on Tribology, vol. 43, pp. 143–149, 2004.

[76] J. Y. Kim, A. Baltazar, and S. I. Rokhlin, "Ultrasonic assessment of rough surface contact between solids from elastoplastic loading-unloading hysteresis cycle," *Journal of the Mechanics and Physics of Solids*, vol. 52, no. 8, pp. 1911–1934, 2004.

[77] X. Shi and A. A. Polycarpou, "Measurement and Modeling of Normal Contact Stiffness and Contact Damping at the Meso Scale," *Journal of Vibration and Acoustics*, vol. 127, no. 1, p. 52, 2005.

[78] C. Siewert, L. Panning, A. Schmidt-fellner, and A. Kayser, "The estimation of the contact stiffness for directly and indirectly coupled turbine blading," in *Proceedings of ASME Turbo Expo 2006: Power for Land, Sea and Air*, 2006.

[79] M. Gonzalez-Valadez, A. Baltazar, and R. Dwyer-Joyce, "Study of interfacial stiffness ratio of a rough surface in contact using a spring model," *Wear*, vol. 268, no. 3-4, pp. 373–379, 2010.

[80] M. E. Kartal, D. M. Mulvihill, D. Nowell, and D. A. Hills, "Measurements of pressure and area dependent tangential contact stiffness between rough surfaces using digital image correlation," *Tribology International*, vol. 44, no. 10, pp. 1188–1198, 2011.

[81] G. Starzynski and R. Buczkowski, "Ultrasonic Measurements of Contact Stiffness Between Rough Surfaces," *Journal of Tribology*, vol. 136, 2014.

[82] A. Soom and C. I. Serpe, "Normal stiffness and damping at lightly loaded rough planar contacts," *Tribology International*, vol. 100, pp. 171–177, 2016.

[83] M. Kreider and C. W. Schwingshackl, "Experimental evaluation of pressure dependent tangential contact stiffness," in *International Conference on Noise and Vibration Engineering*, 2018.

[84] X. Shi and A. A. Polycarpou, "Investigation of Contact Stiffness and Contact Damping for Magnetic Storage Head-Disk Interfaces," *Journal of Tribology*, vol. 130, no. 2, p. 021901, 2008.

[85] C. W. Schwingshackl, E. P. Petrov, and D. J. Ewins, "Measured and estimated friction interface parameters in a nonlinear dynamic analysis," *Mechanical Systems and Signal Processing*, vol. 28, pp. 574–584, 2012.

[86] M. Lavella and D. Botto, "Fretting wear characterization by point contact of nickel superalloy interfaces," *Wear*, vol. 271, no. 9-10, pp. 1543–1551, 2011.

[87] M. Lavella, "Contact Properties and Wear Behaviour of Nickel Based Superalloy René 80," *Metals*, vol. 6, no. 7, p. 159, 2016.

[88] A. Mathis, N. N. Balaji, R. Kuether, *et al.*, "A Review of Damping Models for Structures with Mechanical Joints," *Applied Mechanics Reviews*, jul 2020.

[89] G. Jenkins, "Analysis of the stress-strain relationships in reactor grade graphite," *British Journal of Applied Physics*, vol. 13, no. 1, pp. 30–32, 1962.

[90] J. H. Griffin, "Friction Damping of Resonant Stresses in Gas Turbine Engine Airfoils," *Journal of Engineering for Power*, vol. 102, no. 2, pp. 329–333, 1980.

[91] C.-H. Menq, J. H. Griffin, and J. Bielak, "The Influence of a Variable Normal Load on the Forced Vibration of a Frictionally Damped Structure," *Journal of Engineering for Gas Turbines and Power*, vol. 108, pp. 300–305, 1986.

[92] C. H. Menq, P. Chidamparam, and J. H. Griffin, "Friction damping of two-dimensional motion and its application in vibration control," *Journal of Sound and Vibration*, vol. 144, no. 3, pp. 427–447, 1991.

[93] C. H. Menq and B. D. Yang, "Non-linear spring resistance and friction damping of frictional constraint having two-dimensional motion," *Journal of Sound and Vibration*, vol. 217, no. 1, pp. 127–143, 1998.

[94] B. D. Yang, M. L. Chu, and C. H. Menq, "Stick-slip-separation analysis and non-linear

stiffness and damping characterization of friction contacts having variable normal load," *Journal of Sound and Vibration*, vol. 210, no. 4, pp. 461–481, 1998.

[95] B. D. Yang and C. H. Menq, "Characterization of 3D Contact Kinematics and Prediction of Resonant Response of Structures Having 3D Frictional Constraint," *Journal of Sound and Vibration*, vol. 217, no. 5, pp. 909–925, 1998.

[96] C. Siewert, L. Panning, J. Wallaschek, and C. Richter, "Multiharmonic Forced Response Analysis of a Turbine Blading Coupled by Nonlinear Contact Forces," *Journal of Engineering for Gas Turbines and Power*, vol. 132, no. 082501, pp. 1–8, 2010.

[97] E. P. Petrov, "A High-Accuracy Model Reduction for Analysis of Nonlinear Vibrations in Structures With Contact Interfaces," *Journal of Engineering for Gas Turbines and Power*, vol. 133, no. 10, p. 102503, 2011.

[98] M. Krack, A. Herzog, L. Panning, *et al.*, "Multiharmonic Analysis and Design of Shroud Friction Joints of Bladed Disks Subject to Microslip," in *Proceedings of the ASME 2012 International Design Engineering Technical Conferences and Computers and Information in Engineering Conference*, 2012.

[99] A. Fantetti, C. Gastaldi, and T. Berruti, "Modelling and testing flexible friction dampers : challenges and peculiarities," *Experimental Techniques*, vol. 42, no. 4, pp. 407–419, 2018.

[100] W. D. Iwan, "A Distributed-Element Model for Hysteresis and Its Steady-State Dynamic Response," *Journal of Applied Mechanics*, vol. 33, no. 4, pp. 893–900, 1966.

[101] D. J. Segalman, "A Four-Parameter Iwan Model for Lap-Type Joints," *Journal of Applied Mechanics*, vol. 72, no. 5, pp. 752–760, 2005.

[102] R. Bouc, "A Mathematical Model for Hysteresis," *Acustica*, vol. 24, no. 1, pp. 16–25, 1971.

[103] Y.-K. Wen, "Method for Random Vibration of Hysteretic Systems," *Nanotechnology*, vol. 8287, pp. 142–145, 1976.

[104] P. R. Dahl, "Solid Friction Damping of Mechanical Vibrations," *AIAA Journal*, vol. 14, no. 12, pp. 1675–1682, 1976.

[105] C. Canudas de Wit, H. Olsson, K. Astrom, and P. Lischinsky, "A new model for control of systems with friction," *IEEE Transactions on Automatic Control*, vol. 40, no. 3, pp. 419–425, 1995.

[106] F. Preisach, "Über die magnetische Nachwirkung," *Annalen der Physik*, vol. 94, pp. 277–302, 1935.

[107] V. Aleshin and K. Van Den Abeele, "Preisach analysis of the Hertz-Mindlin system," *Journal of the Mechanics and Physics of Solids*, vol. 57, no. 4, pp. 657–672, 2009.

[108] K. C. Valanis, "Fundamental consequences of a new intrinsic time measure: Plasticity as a limit of the endochronic theory," *Arch. Mech. Stos.*, vol. 32, pp. 171–191, 1980.

[109] M. Oldfield, H. Ouyang, and J. E. Mottershead, "Simplified models of bolted joints under harmonic loading," *Computers and Structures*, vol. 84, no. 1-2, pp. 25–33, 2005.

[110] K. Guo, X. Zhang, H. Li, H. Hua, and G. Meng, "A New Dynamical Friction Model," *International Journal of Modern Physics B*, vol. 22, no. 08, pp. 967–980, 2008.

[111] K. C. Valanis, "A theory of viscoplasticity without a yield surface," *Archive Mech*, vol. 23, no. 4, pp. 517–551, 1971.

[112] L. Gaul and J. Lenz, "Nonlinear dynamics of structures assembled by bolted joints," *Acta Mechanica*, vol. 125, no. 1-4, pp. 169–181, 1997.

[113] J. Abad, F. J. Medel, and J. M. Franco, "Determination of Valanis model parameters in a bolted lap joint: Experimental and numerical analyses of frictional dissipation," *International Journal of Mechanical Sciences*, vol. 89, pp. 289–298, 2014.

[114] H. Hertz, "Über die Berührung fester elastischer Körper," *Jnl. reine und angewandte Mathematik*, vol. 92, pp. 156–171, 1882.

[115] A. W. Bush, R. D. Gibson, and T. R. Thomas, "The elastic contact of a rough surface," *Wear*, vol. 35, no. 1, pp. 87–111, 1975.

[116] J. A. Greenwood, "A simplified elliptic model of rough surface contact," *Wear*, vol. 261, no. 2, pp. 191–200, 2006.

[117] G. Carbone and F. Bottiglione, "Asperity contact theories: Do they predict linearity between contact area and load?," *Journal of the Mechanics and Physics of Solids*, vol. 56, no. 8, pp. 2555–2572, 2008.

[118] M. Ciavarella, J. A. Greenwood, and M. Paggi, "Inclusion of "interaction" in the Greenwood and Williamson contact theory," *Wear*, vol. 265, no. 5-6, pp. 729–734, 2008.

[119] M. Paggi and M. Ciavarella, "The coefficient of proportionality κ between real contact area and load, with new asperity models," *Wear*, vol. 268, no. 7-8, pp. 1020–1029, 2010.

[120] V. A. Yastrebov, J. Durand, H. Proudhon, and G. Cailletaud, "Rough surface contact analysis by means of the Finite Element Method and of a new reduced model," *Comptes Rendus - Mecanique*, vol. 339, no. 7-8, pp. 473–490, 2011.

[121] C. Cattaneo, "Sul Contatto di due Corpi Elastici: Distributione Locale Degli Sforzi," *Reconditi dell'Academia Nazionale dei Lincei*, vol. 27, pp. 342–348, 434–436, 474–478, 1938.

[122] R. D. Mindlin, "Compliance of Elastic Bodies in Contact," *Journal of Applied Mechanics*, vol. 16, pp. 259–268, 1949.

[123] K. L. Johnson, "Surface Interaction between Elastically Loaded Bodies under Tangential Forces," *Proceedings of the Royal Society A: Mathematical, Physical and Engineering Sciences*, vol. 230, no. 1183, pp. 531–548, 1955.

[124] S. Akarapu, T. Sharp, and M. O. Robbins, "Stiffness of Contacts Between Rough Surfaces," *Physical Review Letters*, vol. 106, no. 085001, 2011.

[125] C. Campañá, B. N. J. Persson, and M. H. Müser, "Transverse and normal interfacial stiffness of solids with randomly rough surfaces," *Journal of Physics Condensed Matter*, vol. 23, no. 085001, 2011.

[126] D. Dini and D. A. Hills, "Frictional Energy Dissipation in a Rough Hertzian Contact," *Journal of Tribology*, vol. 131, no. 2, p. 021401, 2009.

[127] S. Medina, D. Dini, A. V. Olver, and D. A. Hills, "Fast Computation of Frictional Energy Dissipation in Rough Contacts under Partial Slip," in *Proceedings of the STLE/ASME International Joint Tribology Conference*, pp. 1–3, 2008.

[128] B. N. J. Persson, "Theory of rubber friction and contact mechanics," *The Journal of Chemical Physics*, vol. 115, no. 8, pp. 3840–3861, 2001.

[129] B. N. J. Persson, F. Bucher, and B. Chiaia, "Elastic contact between randomly rough surfaces: Comparison of theory with numerical results," *Physical Review B*, vol. 65, no. 18, p. 184106, 2002.

[130] C. Yang and B. N. Persson, "Contact mechanics: Contact area and interfacial separation from small contact to full contact," *Journal of Physics Condensed Matter*, vol. 20, no. 21, 2008.

[131] C. Campañá, M. H. Müser, and M. O. Robbins, "Elastic contact between self-affine surfaces: Comparison of numerical stress and contact correlation functions with analytic predictions," *Journal of Physics Condensed Matter*, vol. 20, no. 35, 2008.

[132] A. Papangelo, N. Hoffmann, and M. Ciavarella, "Load-separation curves for the contact of self-affine rough surfaces," *Scientific Reports*, vol. 7, no. 1, pp. 4–10, 2017.

[133] V. A. Yastrebov, G. Anciaux, and J. F. Molinari, "From infinitesimal to full contact between rough surfaces: Evolution of the contact area," *International Journal of Solids*

and Structures, vol. 52, pp. 83–102, 2015.

[134] P. K. Banerjee, P. K. Banerjee, and R. Butterfield, *Boundary element methods in engineering science*. McGraw-Hill Book Co. (UK), 1981.

[135] O. Zienkiewicz and R. Taylor, *The finite element method: solid mechanics*. Butterworth-Heinemann, 2000.

[136] E. Fermi, J. Pasta, and S. Ulam, "Studies of Nonlinear Problems, I," Tech. Rep. No. LA - 1940, Los Alamos Scientific Laboratory, N. Mex., 1955.

[137] V. K. Tewary, "Green-function method for lattice statics," *Advances in Physics*, vol. 22, no. 6, pp. 757–810, 1973.

[138] T. Andersson, "The Boundary Element Method applied to Two-Dimensional Contact Problems with Friction," in *Boundary Element Methods* (C. A. Brebbia, ed.), (Berlin, Heidelberg), pp. 239–258, Springer Berlin Heidelberg, 1981.

[139] A. Bemporad and M. Paggi, "Optimization algorithms for the solution of the frictionless normal contact between rough surfaces," *International Journal of Solids and Structures*, vol. 69-70, pp. 94–105, 2015.

[140] S. Medina, A. V. Olver, and D. Dini, "The Influence of Surface Topography on Energy Dissipation and Compliance in Tangentially Loaded Elastic Contacts," *Journal of Tribology*, vol. 134, no. 1, p. 011401, 2012.

[141] J. Armand, L. Pesaresi, L. Salles, and C. W. Schwingshackl, "A Multi-Scale Approach for Nonlinear Dynamic Response Predictions With Fretting Wear," *Journal of Engineering for Gas Turbines and Power*, vol. 139, no. 022505, pp. 1–7, 2017.

[142] J. Armand, L. Pesaresi, L. Salles, C. Wong, and C. W. Schwingshackl, "A modelling approach for the nonlinear dynamics of assembled structures undergoing fretting wear," *Proc. R. Soc. A*, vol. 475, no. 2223, p. 20180731, 2018.

[143] J. Armand, L. Salles, C. W. Schwingshackl, D. Süß, and K. Willner, "On the effects of roughness on the nonlinear dynamics of a bolted joint: A multiscale analysis," *European Journal of Mechanics, A/Solids*, vol. 70, no. February, pp. 44–57, 2018.

[144] J. Armand, L. Salles, and C. W. Schwingshackl, "NUMERICAL SIMULATION OF PARTIAL SLIP CONTACT USING A SEMI-ANALYTICAL METHOD," tech. rep., 2015.

[145] S. K. Chan and I. S. Tuba, "A finite element method for contact problems of solid bodies-Part II. Application to turbine blade fastenings," *International Journal of Mechanical Sciences*, vol. 13, no. 7, pp. 627–639, 1971.

[146] S. K. Chan and I. S. Tuba, "A finite element method for contact problems of solid bodies-Part I. Theory and validation," *International Journal of Mechanical Sciences*, vol. 13, no. 7, pp. 615–625, 1971.

[147] S. Hyun, L. Pei, J. F. Molinari, and M. O. Robbins, "Finite-element analysis of contact between elastic self-affine surfaces," *Physical Review E - Statistical Physics, Plasmas, Fluids, and Related Interdisciplinary Topics*, vol. 70, no. 2, pp. 026117(1–12), 2004.

[148] L. Pei, S. Hyun, J. F. Molinari, and M. O. Robbins, "Finite element modeling of elasto-plastic contact between rough surfaces," *Journal of the Mechanics and Physics of Solids*, vol. 53, no. 11, pp. 2385–2409, 2005.

[149] B. J. Alder and T. E. Wainwright, "Studies in molecular dynamics. I. General method," *The Journal of Chemical Physics*, vol. 31, no. 2, pp. 459–466, 1959.

[150] J. Jones, "On the determination of molecular fields. II. From the equations of state of a gas," *Procedures Royal Society London*, vol. 106, pp. 463–477, 1924.

[151] P. M. Morse, "Diatomic molecules according to the wave mechanics. II. Vibrational levels," *Physical Review*, vol. 34, pp. 57–64, 1929.

[152] C. Campañá and M. H. Müser, "Practical Green's function approach to the simulation of

elastic semi-infinite solids," *Physical Review B - Condensed Matter and Materials Physics*, vol. 74, no. 7, pp. 1–15, 2006.

[153] L. T. Kong, G. Bartels, C. Campañá, C. Denniston, and M. H. Müser, "Implementation of Green's function molecular dynamics: An extension to LAMMPS," *Computer Physics Communications*, vol. 180, no. 6, pp. 1004–1010, 2009.

[154] J. P. Ewen, C. Gattinoni, F. M. Thakkar, *et al.*, "Nonequilibrium Molecular Dynamics Investigation of the Reduction in Friction and Wear by Carbon Nanoparticles Between Iron Surfaces," *Tribology Letters*, vol. 63, no. 3, 2016.

[155] R. D. Mindlin, W. P. Mason, T. F. Osmer, and H. Deresiewicz, "Effects of an Oscillating Tangential Force on the Contact Surfaces of Elastic Spheres," *Proceedings of the first U.S. National Congress of Applied Mechanics*, vol. 18, no. 3, p. 331, 1952.

[156] L. E. Goodman; and C. B. Brown, "Energy Dissipation in Contact Friction: Constant Normal and Cyclic Tangential Loading," *Journal of Applied Mechanics*, vol. 29, no. 1, pp. 17–22, 1962.

[157] M. Burdekin, N. Back, and A. Cowley, "Experimental Study of Normal and Shear Charatestics of Machined Surfaces in Contact," *Journal Mechanical Engineering Science*, vol. 20, no. 3, pp. 129–132, 1978.

[158] S. Fouvry, P. Kapsa, and L. Vincent, "Analysis of sliding behaviour for fretting loadings: determination of transition criteria," *Wear*, vol. 185, no. 1-2, pp. 35–46, 1995.

[159] J.-W. Liang and B. F. Feeny, "Dynamical Friction Behavior in a Forced Oscillator With a Compliant Contact," *Journal of Applied Mechanics*, vol. 65, no. 1, p. 250, 1998.

[160] V. Fridrici, S. Fouvry, and P. H. Kapsa, "Fretting wear behavior of a Cu-Ni-In plasma coating," *Surface and Coatings Technology*, vol. 163-164, pp. 429–434, 2003.

[161] V. Lampaert, F. Al-Bender, and S. J., "Experimental Characterization of Dry Friction at Low Velocities on a Developed Tribometer Setup for Macroscopic Measurements," *Tribology Letters*, vol. 16, no. 1, pp. 95–105, 2004.

[162] M. Eriten, A. A. Polycarpou, and L. A. Bergman, "Development of a Lap Joint Fretting Apparatus," *Experimental Mechanics*, vol. 51, no. 8, pp. 1405–1419, 2011.

[163] J. Hintikka, A. Lehtovaara, and A. Mäntylä, "Normal displacements in non-Coulomb friction conditions during fretting," *Tribology International*, vol. 94, pp. 633–639, 2016.

[164] W. Lu, P. Zhang, X. Liu, *et al.*, "Influence of surface topography on torsional fretting wear under flat-on-flat contact," *Tribology International*, vol. 109, pp. 367–372, 2017.

[165] H. Lee and S. Mall, "Investigation into effects and interaction of various fretting fatigue variables under slip-controlled mode," *Tribology International*, vol. 39, pp. 1213–1219, 2006.

[166] V. Done, D. Kesavan, M. Krishna R, *et al.*, "Semi analytical fretting wear simulation including wear debris," *Tribology International*, vol. 109, pp. 1–9, 2017.

[167] I. Llavori, A. Zabala, A. Aginagalde, *et al.*, "Critical Analysis of Coefficient of Friction Derivation Methods for Fretting under Gross Slip Regime," *Tribology International*, vol. 143, mar 2020.

[168] D. Infante-García, M. Marco, A. Zabala, *et al.*, "On the Role of Contact and System Stiffness in the Measurement of Principal Variables in Fretting Wear Testing," *Sensors*, vol. 20, p. 4152, jul 2020.

[169] A. Fantetti and C. Schwingshackl, "Effect of Friction on the Structural Dynamics of Built-up Structures: An Experimental Study," in *Proceedings of the ASME Turbo Expo 2020: Turbomachinery Technical Conference and Exposition. Volume 11: Structures and Dynamics: Structural Mechanics, Vibration, and Damping; Supercritical CO2*, 2020.

[170] M. Lavella, D. Botto, and M. M. Gola, "Design of a high-precision, flat-on-flat fretting test apparatus with high temperature capability," *Wear*, vol. 302, no. 1-2, pp. 1073–1081, 2013.

[171] A. Cabboi, T. Putelat, and J. Woodhouse, "The frequency response of dynamic friction: Enhanced rate-and-state models," *Journal of the Mechanics and Physics of Solids*, vol. 92, pp. 210–236, 2016.

[172] T. Hoffmann, L. Panning, and J. Wallaschek, "Analysis of Contacts in Friction Damped Turbine Blades Using Dimensionless Numbers," *Journal of Engineering for Gas Turbines and Power*, vol. 141, dec 2019.

[173] A. R. Warmuth, P. H. Shipway, and W. Sun, "Fretting wear mapping: The influence of contact geometry and frequency on debris formation and ejection for a steel-on-steel pair," *Proceedings of the Royal Society A: Mathematical, Physical and Engineering Sciences*, 2015.

[174] J. Hintikka, A. Lehtovaara, and A. Mäntylä, "Fretting-induced friction and wear in large flat-on-flat contact with quenched and tempered steel," *Tribology International*, vol. 92, pp. 191–202, 2015.

[175] C. H. Hager, J. H. Sanders, and S. Sharma, "Characterization of mixed and gross slip fretting wear regimes in Ti6Al4V interfaces at room temperature," *Wear*, vol. 257, no. 1-2, pp. 167–180, 2004.

[176] F. Hild and S. Roux, "Digital Image Correlation : from Displacement Measurement to Identification of Elastic Properties – a Review," *Strain*, vol. 42, pp. 69–80, 2006.

[177] J. de Crevoisier, N. Swiergiel, L. Champaney, and F. Hild, *Identification of In Situ Frictional Properties of Bolted Assemblies with Digital Image Correlation*, vol. 52. 2012.

[178] L. Pesaresi, M. Stender, V. Ruffini, and C. Schwingshackl, "DIC Measurement of the Kinematics of a Friction Damper for Turbine Applications," in *Conference Proceedings of the Society for Experimental Mechanics Series*, no. Dic, 2017.

[179] J. Juoksukangas, A. Lehtovaara, and A. Mäntylä, "Applying the digital image correlation method to fretting contact for slip measurement," in *Proceedings of the Institution of Mechanical Engineers, Part J: Journal of Engineering Tribology*, vol. 231, pp. 509–519, SAGE Publications Ltd, apr 2017.

[180] W. Chen, M. Jin, I. Lawal, M. R. Brake, and H. Song, "Measurement of slip and separation in jointed structures with non-flat interfaces," *Mechanical Systems and Signal Processing*, vol. 134, p. 106325, dec 2019.

[181] M. Brøns, T. A. Kasper, G. Chauda, *et al.*, "Experimental investigation of local dynamics in a bolted lap joint using digital image correlation," *Journal of Vibration and Acoustics*, pp. 1–24, jul 2020.

[182] W. Chen, D. Jana, A. Singh, *et al.*, "Measurement and identification of the nonlinear dynamics of a jointed structure using full-field data, Part I: Measurement of nonlinear dynamics," *Mechanical Systems and Signal Processing*, vol. 166, mar 2022.

[183] C. H. Scholz, "Earthquakes and friction laws," tech. rep., 1998.

[184] Q. Li, T. E. Tullis, D. Goldsby, and R. W. Carpick, "Frictional ageing from interfacial bonding and the origins of rate and state friction," *Nature*, vol. 480, pp. 233–236, dec 2011.

[185] A. Ovcharenko, G. Halperin, I. Etsion, and M. Varenberg, "A novel test rig for in situ and real time optical measurement of the contact area evolution during pre-sliding of a spherical contact," *Tribology Letters*, vol. 23, pp. 55–63, jul 2006.

[186] E. Diaconescu and M. L. Glovnea, "Visualization and measurement of contact area by reflectivity," *Journal of Tribology*, vol. 128, pp. 915–917, oct 2006.

[187] O. Ben-David, S. M. Rubinstein, and J. Fineberg, "Slip-stick and the evolution of frictional strength," *Nature*, vol. 463, no. 7277, pp. 76–79, 2010.

[188] B. A. Krick, J. R. Vail, B. N. Persson, and W. G. Sawyer, "Optical in situ micro tribometer for analysis of real contact area for contact mechanics, adhesion, and sliding experiments," *Tribology Letters*, vol. 45, pp. 185–194, jan 2012.

[189] R. Sahli, G. Pallares, C. Ducottet, *et al.*, "Evolution of real contact area under shear and the value of static friction of soft materials," *Proceedings of the National Academy of Sciences of the United States of America*, vol. 115, pp. 471–476, jan 2018.

[190] J. H. Dieterich I and B. D. Kilgore, "Direct Observation of Frictional Contacts: New Insights for State-dependent Properties," Tech. Rep. 3, 1994.

[191] C. Ferrer, F. Salas, M. Pascual, and J. Orozco, "Discrete acoustic emission waves during stick-slip friction between steel samples," *Tribology International*, vol. 43, pp. 1–6, jan 2010.

[192] Z. Geng, D. Puhan, and T. Reddyhoff, "Using acoustic emission to characterize friction and wear in dry sliding steel contacts," *Tribiology International*, vol. 134, pp. 394–407, 2019.

[193] N. A. Emira, H. T. Mohamad, and M. S. Tahat, "Stick-slip detection through measurement of near field noise," Tech. Rep. 3, 2011.

[194] C. L. Jiaa and D. A. Dornfeld, "Experimental studies of sliding friction and wear via acoustic emission signal analysis," *Wear*, vol. 139, no. 2, pp. 403–424, 1990.

[195] R. S. Dwyer-Joyce, "The application of ultrasonic NDT techniques in tribology," oct 2005.

[196] D. M. Mulvihill, H. Brunskill, M. E. Kartal, R. S. Dwyer-Joyce, and D. Nowell, "A Comparison of Contact Stiffness Measurements Obtained by the Digital Image Correlation and Ultrasound Techniques," *Experimental Mechanics*, vol. 53, no. 7, pp. 1245–1263, 2013.

[197] J. Baik and R. B. Thompson, "Ultrasonic Scattering from Imperfect Interfaces: A Quasi-Static Model," tech. rep., 1984.

[198] H. Xiao and Y. Sun, "An improved virtual material based acoustic model for contact stiffness measurement of rough interface using ultrasound technique," *International Journal of Solids and Structures*, 2018.

[199] M. B. Marshall, R. Lewis, R. S. Dwyer-Joyce, U. Olofsson, and S. Björklund, "Experimental characterization of wheel-rail contact patch evolution," *Journal of Tribology*, vol. 128, pp. 493–504, jul 2006.

[200] H. G. Tattersall, "The ultrasonic pulse-echo technique as applied to adhesion testing," *Journal of Physics D: Applied Physics*, vol. 6, no. 7, pp. 819–832, 1973.

[201] L. Pesaresi, A. Fantetti, F. Cegla, L. Salles, and C. Schwingshackl, "On the Use of Ultrasound Waves to Monitor the Local Dynamics of Friction Joints," *Experimental Mechanics*, vol. 60, no. 1, pp. 129–141, 2020.

[202] A. Takeuchi, "Detection of Operational Abnormality of Ball Bearing with Ultrasonic Technique," *Key Engineering Materials*, vol. 270-273, pp. 252–257, mar 2009.

[203] H.-S. Ahn and D.-I. Kim, "In situ evaluation of wear surface by ultrasound," tech. rep., 2001.

[204] H. Brunskill, A. Hunter, L. Zhou, R. Dwyer Joyce, and R. Lewis, "An evaluation of ultrasonic arrays for the static and dynamic measurement of wheel–rail contact pressure and area," *Proceedings of the Institution of Mechanical Engineers, Part J: Journal of Engineering Tribology*, 2020.

[205] M. Eriten, C. H. Lee, and A. A. Polycarpou, "Measurements of tangential stiffness and damping of mechanical joints: Direct versus indirect contact resonance methods," *Tribology International*, vol. 50, pp. 35–44, 2012.

[206] G. Zhao, Z. Xiong, X. Jin, L. Hou, and W. Gao, "Prediction of contact stiffness in bolted interface with natural frequency experiment and FE analysis," *Tribology International*, vol. 127, pp. 157–164, 2018.

[207] H. Ahmadian and H. Jalali, "Identification of bolted lap joints parameters in assembled structures," *Mechanical Systems and Signal Processing*, vol. 21, pp. 1041–1050, feb 2007.

[208] D. Nouira, D. Tonazzi, A. Meziane, L. Baillet, and F. Massi, "Numerical and Experimental Analysis of Nonlinear Vibrational Response due to Pressure-Dependent Interface Stiffness," *Lubricants*, vol. 8, p. 73, jul 2020.

[209] J. Wang, T. Chen, X. P. Wang, and Y. Xi, "Dynamic identification of tangential contact stiffness by using friction damping in moving contact," *Tribology International*, 2019.

[210] H. A. Sherif and K. S. S., "Relationship between normal and tangential contact stiffness of nominally flat surfaces," *Wear*, vol. 151, pp. 49–62, 1991.

[211] Z. Fuadi, T. Takagi, H. Miki, and K. Adachi, "An experimental method for tangential contact stiffness evaluation of contact interfaces with controlled contact asperities," *Proceedings of the Institution of Mechanical Engineers, Part J: Journal of Engineering Tribology*, 2013.

[212] P. Cawley and D. L. R. Clayton, "A vibration technique for the measurement of contact stiffness," *Mechanical Systems and Signal Processing*, vol. 1, no. 3, pp. 273–283, 1987.

[213] H. T. Zou and B. L. Wang, "Investigation of the contact stiffness variation of linear rolling guides due to the effects of friction and wear during operation," *Tribology International*, 2015.

[214] T. Butlin, G. Spelman, P. Ghaderi, W. J. Midgley, and R. Umehara, "Predicting response bounds for friction-damped gas turbine blades with uncertain friction coupling," *Journal of Sound and Vibration*, vol. 440, pp. 399–411, feb 2019.

[215] K. Sanliturk, A. B. Stanbridge, and D. J. Ewins, "Friction Dampers Measurement, Modelling and Application to Blade Vibration Control," in *Proceeding of Design Engineering Technology Conferences*, 1995.

[216] J. Szwedowicz, S. Slowik, A. Mahler, and C. J. Hulme, "Nonlinear Dynamic Analyses of a Gas Turbine Blade for Attainment of Reliable Shroud Coupling," in *Proceedings of GT2005 ASME Turbo Expo 2005: Power for Land, Sea and Air*, 2005.

[217] C. Gastaldi, A. Fantetti, and T. Berruti, "Forced Response Prediction of Turbine Blades with Flexible Dampers: The Impact of Engineering Modelling Choices," *Applied Sciences*, vol. 8, no. 1, 2017.

[218] H. Dastani, D. Botto, and M. Glorioso, "Experimental and Numerical Investigation of Contact Parameters in a Dovetail Type of Blade Root Joints," *Applied Sciences*, vol. 11, p. 12008, dec 2021.

[219] Y. Ren and C. F. Beards, "Identification of 'Effective' Linear Joints Using Coupling and Joint Identification Techniques," *Journal of Vibration and Acoustics*, vol. 120, no. 2, p. 331, 1998.

[220] D. de Klerk, D. J. Rixen, S. N. Voormeeren, *et al.*, "General Framework for Dynamic Substructuring: History, Review and Classification of Techniques," *AIAA Journal*, vol. 46, pp. 1169–1181, may 2008.

[221] Z. Saeed, S. W. Klaassen, C. M. Firrone, T. M. Berruti, and D. J. Rixen, "Experimental Joint Identification Using System Equivalent Model Mixing in a Bladed-Disk," *Journal of Vibration and Acoustics*, pp. 1–29, may 2020.

[222] J. Brunetti, W. D'Ambrogio, and A. Fregolent, "Dynamic coupling of substructures with sliding friction interfaces," *Mechanical Systems and Signal Processing*, vol. 141, jul 2020.

[223] e. Tol and H. N. Özgüven, "Dynamic characterization of bolted joints using FRF decoupling and optimization," *Mechanical Systems and Signal Processing*, vol. 54, pp. 124–138, 2015.

[224] C. W. Schwingshackl, "Measurement of friction contact parameters for nonlinear dynamic analysis," *Topics in Modal Analysis I*, vol. 5, pp. 167–177, 2012.

[225] M. Umer and D. Botto, "Measurement of contact parameters on under-platform dampers coupled with blade dynamics," *International Journal of Mechanical Sciences*, vol. 159, pp. 450–458, aug 2019.

[226] A. Fantetti, C. Pennisi, D. Botto, S. Zucca, and C. Schwingshackl, "Comparison of contact parameters measured with two different friction rigs for nonlinear dynamic analysis," in *International Conference on Noise and Vibration Engineering*, 2020.

[227] "Available from: https://github.com/bastibe/Violinplot-Matlab [Accessed: 2020-01-20].."

[228] J. L. Hintze and R. D. Nelson, "Violin Plots: A Box Plot-Density Trace Synergism," Tech. Rep. 2, 1998.

[229] D. M. Mulvihill, M. E. Kartal, A. V. Olver, D. Nowell, and D. A. Hills, "Investigation of non-Coulomb friction behaviour in reciprocating sliding," *Wear*, vol. 271, no. 5-6, pp. 802–816, 2011.

[230] C. Navas, M. Cadenas, J. M. Cuetos, and J. de Damborenea, "Microstructure and sliding wear behaviour of Tribaloy T-800 coatings deposited by laser cladding," *Wear*, vol. 260, no. 7-8, pp. 838–846, 2006.

[231] H. Lee and S. Mall, "Effect of dissimilar mating materials and contact force on fretting fatigue behavior of Ti-6Al-4V," *Tribology International*, vol. 37, no. 1, pp. 35–44, 2004.

[232] X. Huang and R. W. Neu, "High-load fretting of Ti-6Al-4V interfaces in point contact," *Wear*, vol. 265, no. 7-8, pp. 971–978, 2008.

[233] Y. Berthier, M. Godet, and M. Brendle, "Velocity accommodation in friction," *Wear*, vol. 125, pp. 25–38, 1988.

[234] J. Ding, G. Bandak, S. B. Leen, E. J. Williams, and P. H. Shipway, "Experimental characterisation and numerical simulation of contact evolution effect on fretting crack nucleation for Ti-6Al-4V," *Tribology International*, vol. 42, pp. 1651–1662, 2009.

[235] N. M. Everitt, J. Ding, G. Bandak, *et al.*, "Characterisation of fretting-induced wear debris for Ti-6Al-4 V," *Wear*, vol. 267, pp. 283–291, 2009.

[236] S. Toumi, S. Fouvry, and M. Salvia, "Prediction of sliding speed and normal force effects on friction and wear rate evolution in a dry oscillating-fretting PTFE Ti-6Al-4V contact," *Wear*, vol. 376-377, pp. 1365–1378, 2017.

[237] B. Van Peteghem, S. Fouvry, and J. Petit, "Effect of variable normal force and frequency on fretting wear response of Ti-6Al-4V contact," *Wear*, vol. 271, no. 9-10, pp. 1535–1542, 2011.

[238] M. E. Kartal, D. M. Mulvihill, D. Nowell, and D. A. Hills, "Determination of the Frictional Properties of Titanium and Nickel Alloys Using the Digital Image Correlation Method," *Experimental Mechanics*, vol. 51, no. 3, pp. 359–371, 2011.

[239] S. Fouvry, P. Duó, and P. Perruchaut, "A quantitative approach of Ti-6Al-4V fretting damage: Friction, wear and crack nucleation," *Wear*, vol. 257, no. 9-10, pp. 916–929, 2004.

[240] K. J. Kubiak, T. Liskiewicz, and T. Mathia, "Surface morphology in engineering applications influence of roughness on sliding and wear in dry fretting," *Tribology International*, vol. 44, pp. 1427–1432, 2011.

[241] C. H. Hager, J. Sanders, S. Sharma, and A. Voevodin, "Gross slip fretting wear of CrCN, TiAlN, Ni, and CuNiIn coatings on Ti6Al4V interfaces," *Wear*, vol. 263, no. 1-6 SPEC. ISS., pp. 430–443, 2007.

[242] A. L. Mohd Tobi, W. Sun, and P. H. Shipway, "Evolution of plasticity-based wear damage in gross sliding fretting of a Ti-6Al-4V non-conforming contact," *Tribology International*, vol. 113, pp. 474–486, 2017.

[243] M. R. Hirsch and R. W. Neu, "A simple model for friction evolution infretting," *Wear*, vol. 301, pp. 517–523, 2013.

[244] W. D. Milestone and J. T. Janeczko, "Friction between steel surfaces during fretting," *Wear*, vol. 18, pp. 29–40, 1971.

[245] I. R. McColl, J. Ding, and S. B. Leen, "Finite element simulation and experimental validation of fretting wear," *Wear*, vol. 256, pp. 1114–1127, 2004.

[246] Y. Shen, D. Zhang, and S. Ge, "Effect of fretting amplitudes on fretting wear behavior of steel wires in coal mines," *Mining Science and Technology*, vol. 20, pp. 803–808, 2010.

[247] P. I. Hurricks, "The mechanism of fretting - a review," *Wear*, vol. 15, pp. 389–409, 1970.

[248] D. K. Zhang, S. R. Ge, and Y. H. Qiang, "Research on the fatigue and fracture behavior due to the fretting wear of steel wire in hoisting rope," *Wear*, vol. 255, pp. 1233–1237, 2003.

[249] T. Yue and M. Abdel Wahab, "Finite element analysis of fretting wear under variable coefficient of friction and different contact regimes," *Tribology International*, vol. 107, pp. 274–282, 2017.

[250] "ND-CSI Summer School 2018 [Internet]. https://www.imperial.ac.uk/dynamics/nd-csi-2018/ [Accessed: 2021-12-30],"

[251] O. Jin and S. Mall, "Effects of independent pad displacement on fretting fatigue behavior of Ti-6Al-4V," *Wear*, vol. 253, pp. 585–596, 2002.

[252] A. L. Mohd Tobi, J. Ding, G. Bandak, S. B. Leen, and P. H. Shipway, "A study on the interaction between fretting wear and cyclic plasticity for Ti-6Al-4V," *Wear*, vol. 267, pp. 270–282, 2009.

[253] R. S. Magaziner, V. K. Jain, and S. Mall, "Wear characterization of Ti-6Al-4V under fretting-reciprocating sliding conditions," *Wear*, vol. 264, pp. 1002–1014, 2008.

[254] S. Fouvry, P. Arnaud, A. Mignot, and P. Neubauer, "Contact size, frequency and cyclic normal force effects on Ti–6Al–4V fretting wear processes: An approach combining friction power and contact oxygenation," *Tribology International*, vol. 113, pp. 460–473, 2017.

[255] S. Fouvry, P. Kapsa, and L. Vincent, "Quantification of fretting damage," *Wear*, vol. 200, no. 1-2, pp. 186–205, 1996.

[256] N. M. Kinkaid, O. M. O'Reilly, and P. Papadopoulos, "Automotive disc brake squeal," oct 2003.

[257] W. Nack, Y. Yuan, and F. Chen, "Engineering Mechanics in 1982, an ME in Solid Mechanics in 1985, and a PhD in Structural Engineering in 1989," tech. rep., 2005.

[258] T. Butlin and J. Woodhouse, "Friction-induced vibration: Model development and comparison with large-scale experimental tests," *Journal of Sound and Vibration*, vol. 332, pp. 5302–5321, oct 2013.

[259] J. Wu, R. Yuan, Z. He, D. Zhang, and Y. Xie, "Experimental study on dry friction damping characteristics of the steam turbine blade material with nonconforming contacts," *Advances in Materials Science and Engineering*, 2015.

[260] E. Rabinowicz, "The nature of the static and kinetic coefficients of friction," *Journal of Applied Physics*, vol. 22, no. 11, pp. 1373–1379, 1951.

[261] T. Baumberger and C. Caroli, "Solid friction from stick-slip down to pinning and aging," *Advances in Physics*, vol. 55, pp. 279–348, may 2006.

[262] Y. Bar-Sinai, M. Aldam, R. Spatschek, E. A. Brener, and E. Bouchbinder, "Spatiotemporal dynamics of frictional systems: The interplay of interfacial friction and bulk elasticity," *Lubricants*, vol. 7, oct 2019.

[263] A. Fantetti, S. Mariani, L. Pesaresi, *et al.*, "Ultrasonic monitoring of friction contacts during shear vibration cycles," *Mechanical Systems and Signal Processing*, vol. 161, p. 107966, dec 2021.

[264] K. L. Johnson, *Contact Mechanics*. Cambridge: Cambridge University Press., 1985.

[265] "Flatness description [Internet]. Available from: https://www.gdandtbasics.com/flatness/ [Accessed: 2021-05-26]."

[266] "ISO 2768 [Internet]. Available from: https://www.plianced.com/compliance-wiki/iso-2768-general-geometrical-tolerances-and-technical-drawings/ [Accessed: 2021-05-26]."

[267] D. J. Dickrell III and W. G. Sawyer, "Lateral Contact Stiffness and the Elastic Foundation," *Tribology Letters*, vol. 41, pp. 17–21, 2011.

[268] S. M. Lee, M. W. Shin, W. K. Lee, and H. Jang, "The correlation between contact stiffness and stick-slip of brake friction materials," *Wear*, vol. 302, pp. 1414–1420, 2013.

[269] R. Thomas, B. W. Drinkwater, and D. Liaptsis, "The reflection of ultrasound from partially contacting rough surfaces," *The Journal of the Acoustical Society of America*, vol. 117, pp. 638–645, feb 2005.

[270] F. P. Bowden and D. Tabor, *The friction and lubrication of solids. Vol. 1.* Clarendon, Oxford, 1950.

[271] S. M. Rubinstein, G. Cohen, and J. Fineberg, "Contact area measurements reveal loading-history dependence of static friction," *Physical Review Letters*, vol. 96, no. 25, 2006.

[272] V. Gimpl, A. Fantetti, S. W. Klaassen, C. W. Schwingshackl, and D. J. Rixen, "Contact stiffness of jointed interfaces: A comparison of dynamic substructuring techniques with frictional hysteresis measurements," *Mechanical Systems and Signal Processing*, vol. 171, p. 108896, may 2022.

[273] D. J. Ewins, *Modal testing: theory and practice*. Mechanical engineering research studies: Engineering dynamics series, Vol. 15. Letchworth: Research studies press, 1984.

[274] C. Gastaldi and M. M. Gola, "A random sampling strategy for tuning contact parameters of underplatform dampers," in *Proceedings of ASME Turbo Expo 2015: Turbine Technical Conference and Exposition*, pp. 1–12, 2017.

[275] R. B. Randall, *Frequency Analysis (Bruel and Kjaer)*. Preventative maintenance program handbook (IRD Mechanalysis), 1987.

[276] M. Van der Seijs, *Experimental Dynamic Substructuring Analysis and Design Strategies for Vehicle Development*. PhD thesis, 2016.

[277] M. Haeussler, S. Klaassen, and D. Rixen, "Experimental twelve degree of freedom rubber isolator models for use in substructuring assemblies," *Journal of Sound and Vibration*, vol. 474, may 2020.

[278] J. Yuan, A. Fantetti, E. Denimal, *et al.*, "Propagation of friction parameter uncertainties in the nonlinear dynamic response of turbine blades with underplatform dampers," *Mechanical Systems and Signal Processing*, vol. 156, 2021.

[279] K. S. Parel, R. J. Paynter, and D. Nowell, "Linear relationship of normal and tangential contact stiffness with load: Contact Stiffness Relationship with Load," *Proceedings of the Royal Society A: Mathematical, Physical and Engineering Sciences*, vol. 476, no. 2243, 2020.

[280] A. M. Kirk, P. H. Shipway, W. Sun, and C. J. Bennett, "Debris development in fretting contacts – Debris particles and debris beds," *Tribology International*, 2019.

[281] A. M. Kirk, P. H. Shipway, W. Sun, and C. J. Bennett, "The effect of frequency on both the debris and the development of the tribologically transformed structure during fretting wear of a high strength steel," *Wear*, vol. 426-427, pp. 694–703, apr 2019.

[282] F. Ma, H. Zhang, A. Bockstedte, G. C. Foliente, and P. Paevere, "Parameter Analysis of the Differential Model of Hysteresis," *Journal of Applied Mechanics*, vol. 71, no. 3, p. 342, 2004.

[283] X. Delaune, E. de Langre, and C. Phalippou, "A Probabilistic Approach to the Dynamics of Wear Tests," *Journal of Tribology*, vol. 122, pp. 815–821, 2000.

[284] S. Ghosh, P. Pandita, S. Atkinson, *et al.*, "Advances in Bayesian Probabilistic Modeling for Industrial Applications," *ASCE-ASME J Risk and Uncert in Engrg Sys Part B Mech Engrg*, vol. 6, mar 2020.

[285] T. Butlin, P. Ghaderi, G. Spelman, W. J. Midgley, and R. Umehara, "A novel method for predicting the response variability of friction-damped gas turbine blades," *Journal of Sound and Vibration*, vol. 440, pp. 372–398, feb 2019.

[286] N. Wiener, "The Homogeneous Chaos," Tech. Rep. 4, 1938.

[287] D. Xiu, G. E. Karniadakis, and S. J. Sci Comput, "THE WIENER-ASKEY POLYNOMIAL CHAOS FOR STOCHASTIC DIFFERENTIAL EQUATIONS *," Tech. Rep. 2, 2002.

[288] B. Sudret, "Global sensitivity analysis using polynomial chaos expansions," jul 2008.

[289] D. L. Thomas, "DYNAMICS OF ROTATIONALLY PERIODIC STRUCTURES," tech. rep., 1979.

[290] C. Gastaldi, T. Berruti, and M. M. Gola, "The effect of surface finish on the proper functioning of underplatform dampers," *Journal of Vibration and Acoustics*, pp. 1–30, apr 2020.

[291] E. P. Petrov and D. J. Ewins, "Advanced modeling of underplatform friction dampers for analysis of bladed disk vibration," *Journal of Turbomachinery*, vol. 129, pp. 143–150, jan 2007.

[292] C. Gastaldi, J. Gross, M. Scheel, T. M. Berruti, and M. Krack, "Modeling complex contact conditions and their effect on blade dynamics," *Journal of Engineering for Gas Turbines and Power*, vol. 143, jan 2021.

[293] D. Proprentner, *Friction , wear and tangential stiffness of metal surfaces under fretting conditions*. PhD thesis, Imperial College London, 2012.

[294] "DICE software available from: https://github.com/dicengine [Accessed: 2020-04-01]."

[295] A. Ramalho and J. C. Miranda, "The relationship between wear and dissipated energy in sliding systems," *Wear*, vol. 260, pp. 361–367, 2006.

[296] M. Z. Huq and J. P. Celis, "Expressing wear rate in sliding contacts based on dissipated energy," *Wear*, vol. 252, pp. 375–383, 2002.

[297] S. Fouvry, T. Liskiewicz, P. Kapsa, S. Hannel, and E. Sauger, "An energy description of wear mechanisms and its applications to oscillating sliding contacts," *Wear*, vol. 255, no. 1-6, pp. 287–298, 2003.

[298] B. D. Leonard, *Head of the Graduate Program Date An Experimental and Numerical Investigation of the Effect of Coatings and the Third Body on Fretting Wear Doctor of Philosophy*. PhD thesis, Purdue University, 2012.

[299] O. Vingsbo and S. Söderberg, "On fretting maps," *Wear*, vol. 126, pp. 131–147, 1988.

[300] S. R. Pearson and P. H. Shipway, "Is the wear coefficient dependent upon slip amplitude in fretting? Vingsbo and Söderberg revisited," *Wear*, no. 330-331, pp. 93–102, 2015.

[301] M. Jin, M. R. Brake, and H. Song, "Comparison of Nonlinear System Identification Methods for Free Decay Measurements with Application to Jointed Structures," *Journal of Sound and Vibration*, vol. Accepted, pp. 268–293, aug 2019.

[302] S. D. Stearns and N. Ahmed, "Digital signal analysis," *IEEE Transactions on Systems, Man, and Cybernetics*, no. 10, p. 724, 1976.

[303] M. Feldman, *Hilbert transform applications in mechanical vibration*. John Wiley and Sons, 2011.

[304] H. Sumali and R. Kellogg, "Calculating damping from ring-down using hilbert transform and curve fitting," in *4th International Operational Modal Analysis Conference, IOMAC 2011*, 2011.

[305] M. W. Sracic, M. S. Allen, and H. Sumali, "Identifying the Modal Properties of Nonlinear Structures Using Measured Free Response Time Histories from a Scanning Laser Doppler Vibrometer," in *30th International Modal Analysis Conference (IMAC XXX)*,

(Jacksonville, FL), 2012.

[306] P. Huthwaite, "Accelerated finite element elastodynamic simulations using the GPU," *J. Comput. Phys.*, vol. 257, pp. 687–707, 2014.

[307] F. Moser, L. Jacobs, and J. Qu, "Modeling elastic wave propagation in waveguides with the finite element method," *NDT & E Int*, vol. 32, no. 4, pp. 225–234, 1999.

[308] R. Courant, K. Friedrichs, and H. Lewy, "On the partial difference equations of mathematical physics," *IBM J*, vol. 11, no. 2, pp. 215–234, 1967.

[309] A. Raghavan and C. E. Cesnik, "Finite-dimensional piezoelectric transducer modeling for guided wave based structural health monitoring," *Smart materials and structures*, vol. 14, no. 6, 2005.

[310] D. Botto and M. Lavella, "A numerical method to solve the normal and tangential contact problem of elastic bodies," *Wear*, vol. 330-331, pp. 629–635, may 2015.

[311] R. R. Craig and M. C. Bampton, "Coupling of substructures for dynamic analyses," *AIAA Journal*, vol. 6, no. 7, pp. 1313–1319, 1968.

Appendices

Appendix A

High-frequency friction rigs to measure hysteresis loops

This Appendix gives a short description of the high-frequency friction rigs used in other research groups (Politecnico di Torino and University of Oxford) for the measurement of input contact parameters for nonlinear dynamic analysis. The friction rig of Imperial College is instead described in detail in chapter 3, since it is the focus of the present PhD research. The main features of these rigs are summarized in Table A.1.

Table A.1: Main features of the Imperial, Politecnico and Oxford friction rigs.

	Imperial Chapter 3	**Politecnico 1** Fig. A.1a	**Politecnico 2** Fig. A.1b	**Oxford 1** Fig. A.2	**Oxford 2** Fig. A.3
Type of contact	Flat-on-flat	Sphere-on-flat	Flat-on-flat	Flat-on-flat	Flat-on-flat
Nominal Contact Area	1 - 25 mm^2	Point contact	5 - 50 mm^2	25 - 100 mm^2	90 - 170 mm^2
Excitation Frequency	$< 300Hz$	$< 100Hz$	$< 300Hz$	$< 10Hz$	$< 10Hz$
Sliding amplitude	$< 150\mu m$	$< 250\mu m$	$< 150\mu m$	$< 20 - 500\mu m$	$< 1300\mu m$
Contact pressure	$< 500MPa$	$10 - 250N$	$< 30MPa$	$20 - 200MPa$	$30 - 70MPa$
Temperature Range	$< 800°C$	$< 1000°C$	$< 1000°C$	$< 900°C$	Room condition

Politecnico di Torino. The research group at Politecnico di Torino built two test rigs for hysteresis measurements with different contact arrangements: sphere-on-flat and flat-on-flat.

Sphere-on-flat rig: This test rig was developed in 2000 [74] for measuring hysteresis loops of sphere-on-flat contact arrangements. It was later improved in 2007 to perform fretting tests [86]. The rig is shown in Fig. A.1a together with its typical measured loops. The moving specimen has a flat contact interface and is attached to an oscillating beam excited by means of a shaker. The static specimen has a hemispherical contact interface and is constrained by two force transducers, which measure the friction force. Contact is ensured by applying a constant normal load on the specimens during the wear test. The relative displacement between the specimens is measured with two laser Doppler vibrometers (LDVs). The rig works at high temperatures up to 1000 °C by means of induction heating. Preliminary measurements conducted for Nickel

alloy specimens showed that both friction coefficient and contact stiffness reached a steady state (0.4 and 20 $N/\mu m$ respectively) after about $3 * 10^6$ cycles at 32 N of normal load and 60 μm of relative displacement. This number of cycles corresponds to a cumulated sliding distance of 240 meters and a total energy dissipated of 2400 J. In addition, the evolution of the contact stiffness was investigated with an increasing normal load. The experimental results agreed very well with the theoretical predictions obtained using the contact mechanics theory for elastic contact of non-conformal smooth surfaces [121, 122, 264].

Flat-on-flat rig: The second rig was developed in 2010 [170], after many years of experience, for measuring hysteresis loops of flat-on-flat contact arrangements. The novelty of the rig is the adoption of a free approach for the contact interfaces. This kind of approach allows for a self-alignment of the contact interfaces, which can be disassembled after wear cycles and then reassembled together with minimal perturbations. The rig is shown in Fig. A.1b and consists of a moving block excited by means of a shaker. The friction force is measured with force transducers attached to the static side of the rig, and two LDVs measure the relative displacement. Contact is constantly ensured by applying a normal load, and the temperature is controlled with an induction heating system. This friction rig is used with the Imperial friction rig within the Round-Robin test campaign, described in chapter 4 to assess the repeatability of the hysteresis measurements and to compare the rigs' capabilities.

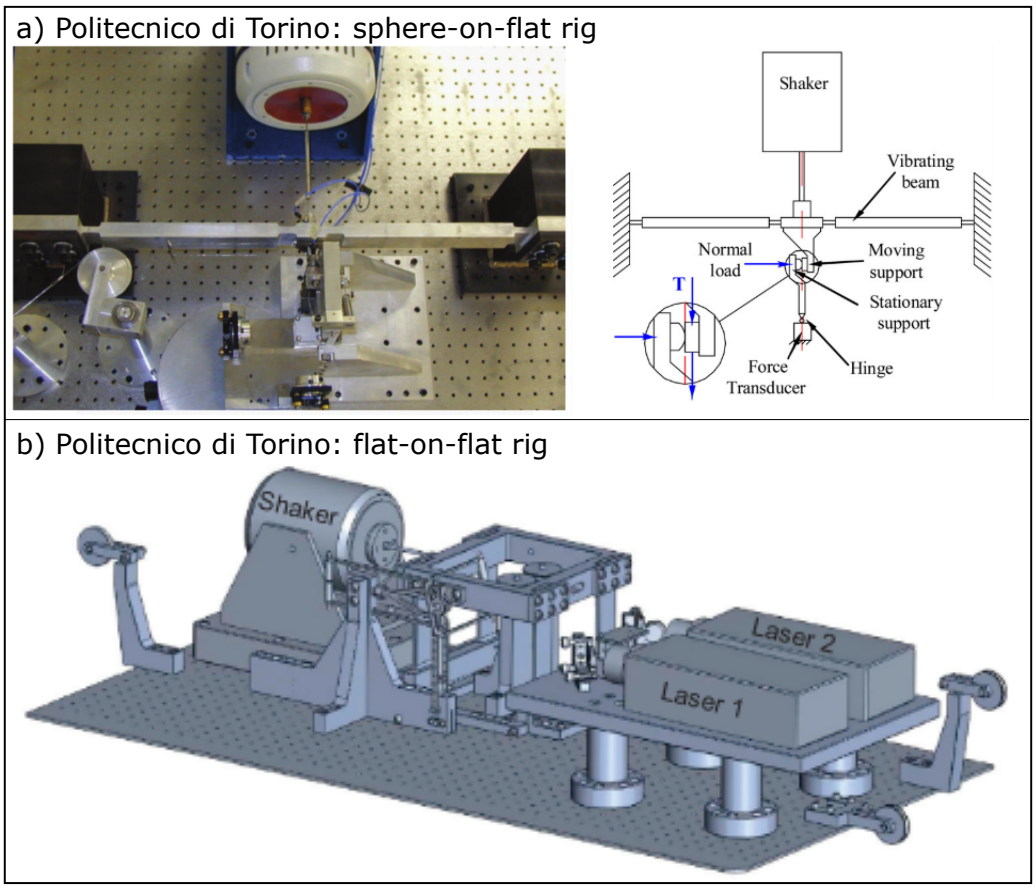


Figure A.1: Politecnico di Torino friction rigs: a) sphere-on-flat test rig [14, 86]; b) flat-on-flat test rig [170].

University of Oxford. The research group at the University of Oxford developed two test rigs for hysteresis measurements of flat-on-flat contact arrangements with two kinds of sliding

motions: linear and torsional motion.

Linear motion rig: This rig was developed in the late 1990s [80, 238] and consists of a moving block actuated by an hydraulic actuator as shown in Fig. A.2a. Two specimens are pushed on the sides of the moving block and generate contact areas between 25 and 100 mm^2. Forces are measured with a load cell, while the relative displacement is measured either with a linear variable differential transformer (LVDT) or with a digital image correlation technique (DIC). DIC is a well established technique to measure displacement fields [176] and is preferable to LVDT as it is a non-contact measuring technique and it provides more accurate measurements.

Results from this rig show that the contact stiffness is higly dependent on both normal load and nominal contact area [80]. The relationship with the contact area is linear, while the relationship with the normal load is approximately proportional to the normal pressure raised to the power of 0.64. This trend was compared with the predictions of the analytical model proposed by Medina et al. [63] and the comparison showed a reasonably good agreement with the experimental results. It is also interesting to note that for low normal loads the contact stiffness remained constant as the fretting cycles increased, while it only evolved with the fretting cycles for higher normal loads. This behaviour was thought to be caused by the more severe fretting wear that occurs at higher pressures. This rig was also used within A PhD project [293] to investigate the evolution of contact interfaces with fretting cycles. The project was conducted mainly using the Imperial College friction rig, but comparisons were made also with the Oxford rig. Results showed that one of the major mechanisms occurring at the interfaces during fretting cycles is the oxidation, which leads to the formation of oxide layers that change material properties. Debris detaching from these layers act as third bodies in the contact. In addition, as fretting cycles increase, both roughness and conformity of the interfaces vary considerably suggesting that existing contact models should account for this evolving conformity.

Lastly, it was noted that hysteresis loops often showed the so-called "hook" feature, which is a rise in the friction force at the end of the sliding region, before the reversal of motion (see Fig. A.2b). Since this feature only appeared after some wear cycles, it was assumed to be due to wear-scar interactions generated during fretting [229]. These wear-scars increase the resistance in sliding and can be of the two kinds represented in Fig. A.2c: scar interactions localized at the contact edges or scar interactions distributed along the whole contact interfaces. In order to investigate this effect, a torsional rig was designed and built by the same research group and is described below.

Torsional motion rig: This friction rig [229] was designed to investigate the "hook" feature. The rig is shown in Fig. A.3 and generates a torsional motion between two specimens kept in contact by applying a constant normal load. The top specimen can have two configurations: continuous annular area or segmented annular area. With the segmented configuration, wear-scars at the edge of the contact might generate, while with the continuous circular configuration only distributed wear-scars generate. A comparison between the loops measured with the two different configurations is shown in Fig. A.3. Since the "hook" is present also in the continuous annular configuration, which has only wear scars distributed along the whole contact interfaces, it was concluded that the rise in the friction force is not due only to the wear scars at the contact edges.

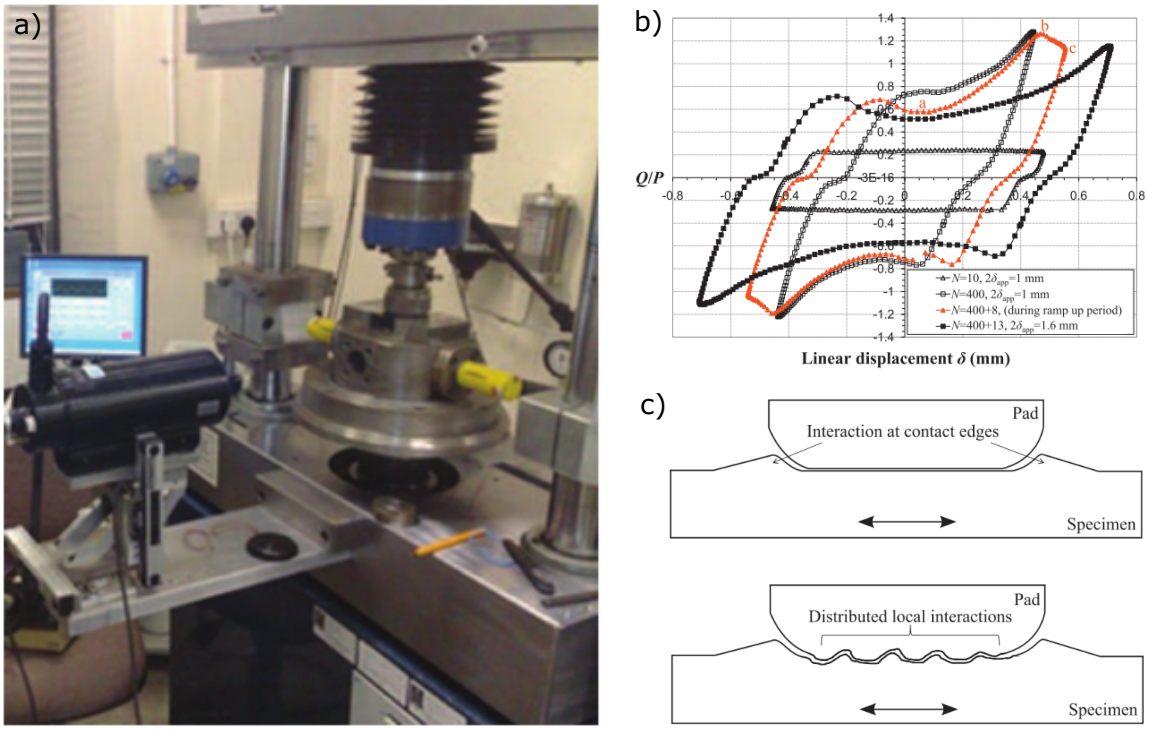


Figure A.2: a) University of Oxford - Linear motion test rig [80]; b) "Hook" feature in the hysteresis loops [229]; c) Schematic diagram of wear–scar interaction types [229].

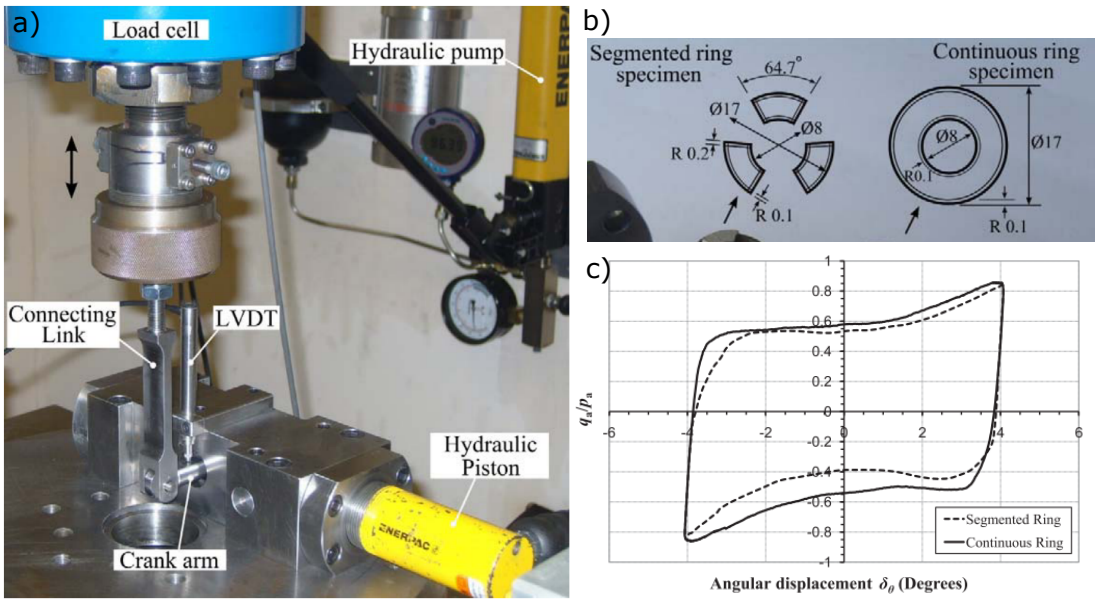


Figure A.3: a) University of Oxford - Torsional motion test rig [229]; b) Two contact configurations; c) Hysteresis loops for the two contact configurations [229].

Appendix B

Digital Image Correlation to investigate the stiffness of the friction rig in the normal direction

From the measurement of hysteresis loops, friction coefficient and tangential contact stiffness can be extracted, but information on the normal contact stiffness cannot be extracted since data on the relative normal displacement cannot be measured with the Laser Doppler Vibrometers. For this reason, it was decided in this research to design a system to excite the Imperial friction rig in the normal direction by means of piezo actuators and measure the normal displacements with a high speed camera placed on the side of the rig.

A preliminary study was performed to investigate the stiffness of the friction rig in the normal direction by means of the Digital Image Correlation (DIC) technique, which consists in taking photos of the rig at different loading and estimating the relative displacement. A photo camera (FUJIFILM X-T1) was mounted on the side of the rig that captured photos as that shown in Fig. B.1a. Different static normal loads were applied and one photo was taken at each load. Then, photos were post-processed with the DICE software [294] to estimate the relative displacement at each different normal load. As an example, Fig. B.1c shows the rig deformation for three different normal loads (visualised with a 500 scaled displacement magnification, since with the nominal scale it is not possible to see the difference). From the plots, the bending is visible as already discussed in section 3.3. Normal displacement were estimated for each normal load so that the rig stiffness in the normal direction could be estimated by dividing the change in normal load by the change in normal displacement. The trend of the rig stiffness in the normal direction is shown in Fig. B.1b as a function of the normal load. The Figure shows that the stiffness of the rig increases with the normal load and is relatively low ($<$20 N/mum) compared to the expected normal contact stiffness, which should be on the same order of magnitude of the tangential contact stiffness whose values are shown in chapters 4 and 5 and are 10 times larger. This stiffness value can also be used to improve the rig simplified dynamic model shown in chapter 6, section 6.1. As expected, the bottom portion of the rig (green point/plot in Fig. B.1a-b) has a larger stiffness than the top portion (red point/plot in Fig. B.1a-b). This is due to the fact that between the two portions there are components which increase the compliance thus reducing the stiffness.

In future, the normal contact stiffness will be extracted with the DIC technique and also a

dynamic normal load will be applied by means of a piezo exciting system designed during this PhD, but not mounted due to delays related to the Covid pandemic during the year 2020/21.

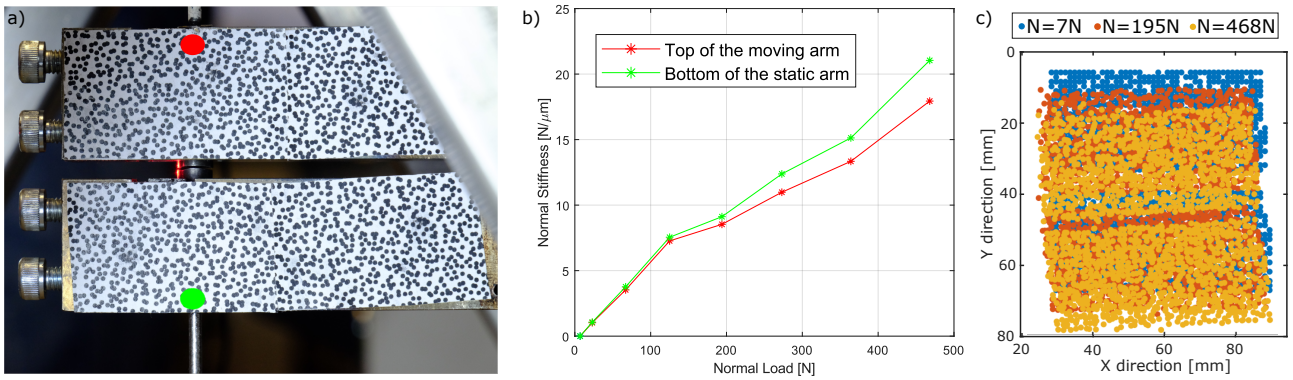


Figure B.1: a) Typical photo of the side view of moving and static arms used for the DIC study. In blue and orange highlighted the point locations used for the analysis; b) Normal stiffness on the point locations highlighted in a); c) Rig deformation for three different normal loads visualised with 500 scaling magnification.

Appendix C

Evolution of contact interfaces with wear

This section supports the experiments shown in section 4.2.1, Fig. 4.17, to investigate the evolution of the contact interfaces with wear. As mentioned before, those experiments were performed within the 2018 Nonlinear Dynamics of Coupled Structures and Interfaces (ND-CSI) Summer School organised at Imperial College [250] as part of the EXPERTISE programme, which funded this PhD project. Here, a further analysis is presented to investigate the amount of worn material generated during the tests. The wear volume was calculated by superimposing the optical interferometer images before and after wear tests, and then taking the difference in 3D topography. The result of this calculation is illustrated in Fig. C.1, where the relationship is shown between the wear volume and the energy dissipated at the contact for different excitation amplitudes. The relationship is almost linear for the tests conducted at 22 μm of displacement amplitude, confirming the previous findings from the literature [87, 236, 237, 239, 242, 253, 254, 295–297]. The linear relationship is defined by a wear coefficient α that is the linear slope of wear volume versus cumulative energy dissipated as defined in [297]. In the case of tests at 22 μm of displacement amplitude, this coefficient is roughly α $\sim$1500 $\mu m^3/J$, and is of the same order of magnitude of the ones found in studies investigating ductile materials [297, 298] or one order of magnitude lower compared to other studies [166, 236, 242, 253, 254]. The two tests conducted at 14 μm of displacement amplitude showed an almost similar wear volume, 4.3 and 5.2 $\mu m*mm^2$ respectively, since they dissipated almost the same amount of energy. The variability is below the 20% and this relatively small difference gives an idea of the measurements variability and could be due to the difficulty in measuring the wear volume accurately due to such small quantities and irregular worn area distributions.

Additionally, the wear volume of tests 1 and 2 (conducted at 14 μm) is lower than that obtained for the same energy dissipated but with a larger displacement amplitude (test 4 at 22 μm) and this would lead also to a lower wear coefficient. This is in accordance with the fretting maps concept proposed by Vingsbo and Söderberg [299], who observed that, in gross sliding, the wear coefficient increases with larger displacement amplitudes. This means that, for the same cumulative energy dissipated, the wear volume is larger if also the displacement amplitude is larger. Fouvry et al. [239] described this behaviour by considering (i) the energy required to generate the debris (that contributes to the wear volume) and (ii) the energy successively required to expel such debris from the contact interface. The higher the displacement amplitude, the faster the debris is ejected and the lower is the energy required for expelling it. Therefore,

for a larger displacement amplitude, less energy is required to expel the debris and, as a result, more energy is left to increase the wear volume. In other words, if the displacement amplitude is very small it is more likely that wear debris remains trapped under the surface and less new debris is generated. However, in a more recent study, Pearson and Shipway [300] argued that the wear coefficient is not dependent on the displacement amplitude. It is expected that for the same cumulative energy dissipated, the wear coefficient, and hence the wear volume, are equal regardless of the displacement amplitude. The current results seem to match better the first hypothesis, but future experiments will hopefully clarify this dependency of the wear coefficient on the displacement amplitude.

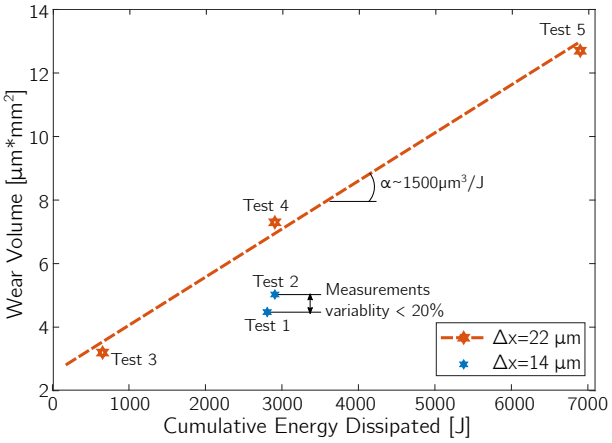


Figure C.1: Wear volume as a function of energy dissipated at the contact. Test conditions: excitation frequency=100Hz, normal load=60 N, nominal area of contact=1mm^2, material=Stainless Steel, temperature=25°C.

Evolution of the rig dynamics with wear

Within the 2018 ND-CSI Summer School, dynamics measurements were also performed to investigate the effect of wear on the dynamic response. These measurements are described in section 6.2.3. At the end of those measurements, it was decided to perform another wear test to extract the vibration amplitude dependency of both natural frequency and damping ratio of the first mode, which is the mode of interest since it is in the direction of sliding. The new wear test was performed with the same loading conditions as before, but for 9 consecutive hours. The rig was stopped every 2.5 hours for allowing the shaker to cool. When the rig was stopped, hammer tests were conducted and the normal load was maintained fixed at 60 N. During the hammer tests, time histories of the moving arm response were recorded and an existing code [301] was used to extract the vibration amplitude dependency of both natural frequency and damping ratio from those time histories. The code first extracted, from the raw signal of the acceleration, information on the first mode by applying a 3rd order digital Butterworth band-pass filter [302], with cut-off frequencies below and above 15% of the resonant frequency, see Fig. C.2a. Subsequently, a Hilbert transform [303–305] was performed on the filtered signal. The Hilbert transform is a linear operator that generates the envelope of the amplitude of a decaying time history as shown in Fig. C.2b. This envelope was then used to obtain the natural frequency and damping ratio as functions of the vibration amplitude, see Fig. C.2c-d.

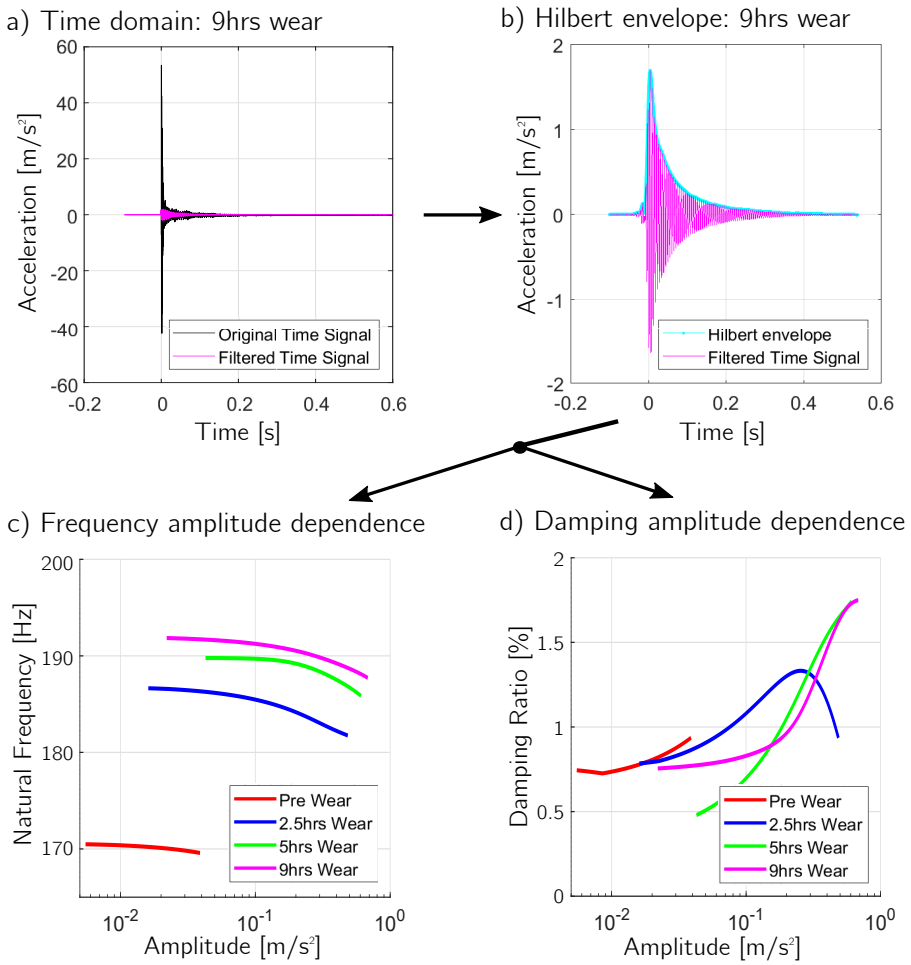


Figure C.2: Hilbert analysis to capture the evolution of the first natural frequency during test 5: a) Time signal at the end of the test; b) Hilbert envelope of the filtered signal; c-d) Amplitude dependencies of natural frequency and damping ratio obtained from the Hilbert envelopes [20].

As expected, both natural frequency and damping are not constant and strongly vary as the amplitude of the vibration decays. The natural frequency increases with wear, due to the increase in both friction coefficient and contact stiffness, and it seems to be not much affected by the acceleration amplitude (and therefore the by sliding distance) of the moving arm. Instead, the damping increases with the amplitude. This is not surprising since at larger accelerations (and therefore larger sliding) hysteresis loops become wider, resulting in higher energy dissipated and therefore higher damping. Moreover, the damping ratio reduces as the test goes on, meaning that the system dissipates less energy as wear increases. This trend is in accordance with Fig. 6.6b since, after wear, the peak is less damped because the increases in both friction coefficient and contact stiffness reduce the tendency of the system to slip.

Appendix D

FE analysis to characterize the ultrasonic wave propagation

The work presented in this Appendix was performed within a collaborative project with the Non Destructive Evaluation group at Imperial College by Dr. Stefano Mariani. For completeness, that work can also be found in [263]. A finite element model of the specimens was created to characterize the ultrasonic wave propagation in the material. This characterization is needed because, as shown in section 5.1, the area covered by the shear transducer is larger than the nominal area of contact (see Fig. 5.1c). This mismatch needs to be considered to correctly estimate the reflection coefficient R at the contact interface, which is required as input in Eq. 2.13 to obtain the ultrasonically estimated contact stiffness per unit area, K_{US}, since the wave components not directly reaching the area of contact are unaffected by the contact conditions. R can be measured as:

$$R_i = \frac{V_i - V_{min}}{V_{max} - V_{min}} = \frac{V_i - V_{max}/\zeta}{V_{max} - V_{max}/\zeta} \tag{D.1}$$

where V_i is the measured voltage envelope peak in the reflection at any test i in which the specimens are at an unknown compressive contact state, V_{max} and V_{min} are the measured voltage envelope peaks for a fully detached specimen and for specimens in full contact, respectively, and ζ is the ratio between V_{max} and V_{min}. While V_{max} can be obtained simply by measuring the reflection in a single specimen not in contact (since the whole signal would be fully reflected), it is less trivial to measure V_{min}. In fact, V_{min} is different than zero when two specimens are bonded in full contact since part of the waves emitted by the sensor are inevitably reflected back by faces other than the contact interface between the two specimens. Finite element (FE) analyses can be used to estimate the ratio ζ by simulating tests performed on a single specimen and on two fully connected specimens. Such ratio ζ depends fundamentally on the position of the transducer footprint within the specimen and on the geometry of the two specimens. In fact, those two determine the fraction of signal directly reaching the contact area versus the fraction impinging on the other geometrical boundaries of the excited specimen. Once ζ is estimated, V_{min} can be substituted by V_{max}/ζ in Eq. D.1, so that the reflection coefficient can be obtained by experimentally measuring V_i, and then used in Eq. 2.13 to estimate the contact stiffness from ultrasound.

Simulations were performed with Pogo, which is a well-suited software to solve wave propagation problems involving a large number of elements [306]. A 3D model of the two specimens in full contact (Fig. D.1a) was generated using linear tetrahedral elements with edges of 0.05 mm

nominal length (∼23M elements in total). This model is referred to as "model with bonded contact". Care was taken to form a smooth boundary at the interface between the two specimens (i.e. impeding element faces from crossing it), so that a single specimen model could be simply obtained by deleting the bottom specimen elements. The single specimen is referred to as "model with no contact". To reach the required accuracy, it is generally recommended to include at least 20 elements per shortest propagating wavelength [307]. In this model, 30 elements are offered to discretize a 2 MHz shear wavelength, hence safely meeting the accuracy requirement. For stability, the Courant-Friedrichs-Lewy condition dictates that the fastest wave-front must not travel more than one element in a single time-step [308]. The fastest waves that propagate through the model are longitudinal waves, which are generated alongside the input shear waves due to the finite extent of the transducer active surface and due to mode-conversion of shear waves reflected from the specimen boundaries; by setting the simulation time-step to 1ns a longitudinal wave travelling at about 5.7 km/s takes more than 8 time-steps to travel through a single element, hence safely satisfying the stability condition.

The actuator stage of the transducer was modelled by applying a shear force, in the y-direction, to the nodes lying within the footprint of the actual piezoelectric surface on the top surface of the top specimen, as shown in the red square patch of Fig. D.1a. Similarly, the wave sensing stage was simulated by averaging the displacements measured on the same nodes at each simulation time. The grade 304 steel was modelled as an isotropic medium, whose material properties were first assigned within the ranges of values found in literature and then refined by comparing the results from the "no contact" model to an experimental signal acquired on a single specimen (Fig. D.2a). This process resulted in setting a density of 8000 kg/m^3, an elastic modulus of 193 GPa and a Poisson's ratio of 0.29, for which a satisfactory agreement between experimental and simulation results was obtained, as seen in Fig. D.2a. Note that a perfect match between the two signals can hardly be obtained, since the exact RF shape of the wave transmitted by the actual sensor is inevitably different than the supplied voltage excitation signal, due to the specific "transfer function" exerted by the sensor assembly and the bonding adhesive, which is difficult to measure experimentally [309].

Figure D.1b-c display the magnitude of displacements measured after 3 μs of simulation time for the model with bonded contact on two section cuts passing through the middle of the specimens either (b) in the direction of shear polarization (side view in Fig. 5.1c) or (c) in the orthogonal direction (front view in Fig. 5.1c). As seen in the figures, the largest fraction of shear wave amplitude is effectively directed toward the interface between the two specimens, with a wave-front essentially parallel to the interface itself; also, at 3μs the first part of the excited tone burst has already entered the bottom specimen. However, a smaller fraction of shear amplitude hits the lower boundary of the top specimen outside the contact patch, from which it is totally reflected towards the top sensor active surface (except for negligible losses into the air). The various reflected components interfere within each other and arrive at the transducer at slightly different times depending on the exact length of the travelled path, producing the black signal of Fig. D.2b. This contribution to the actual received voltage was already defined V_{min} in Eq. D.1 and is virtually unaltered at any compressive contact state. By contrast, in the model with no contact the shear wave impinging on the contact patch is entirely reflected back toward the sensor (again, excluding negligible losses into the air) producing the red signal in Fig. D.2a-b. Note that in Fig. D.2b both signals are normalized to unity at the peak of the red envelope, and the ratio between the predicted peaks of the "no contact" and "bonded contact" model envelopes is $\zeta = 4.5$.

As explained above, this estimated value of ζ can be used to compute the reflection coefficient R_i that characterizes any test in which the specimens are at an unknown compressive state via Eq. D.1, i.e. by using the measured voltage envelope peak V_i and by expressing V_{min} as a function of V_{max}, which can be readily measured by testing a single specimen before pressing the specimens in contact to each other. Clearly, V_i will represent an "averaged" indication of the contact condition over the entire contact patch, since the wave front reaching the interface is larger than the interface itself, as seen in the FE solutions of Fig. D.1b-c. The estimated R_i can then be used in Eq. 2.13 to compute the ultrasonically estimated contact stiffness per unit area, K_{US}, for the entire contact patch.

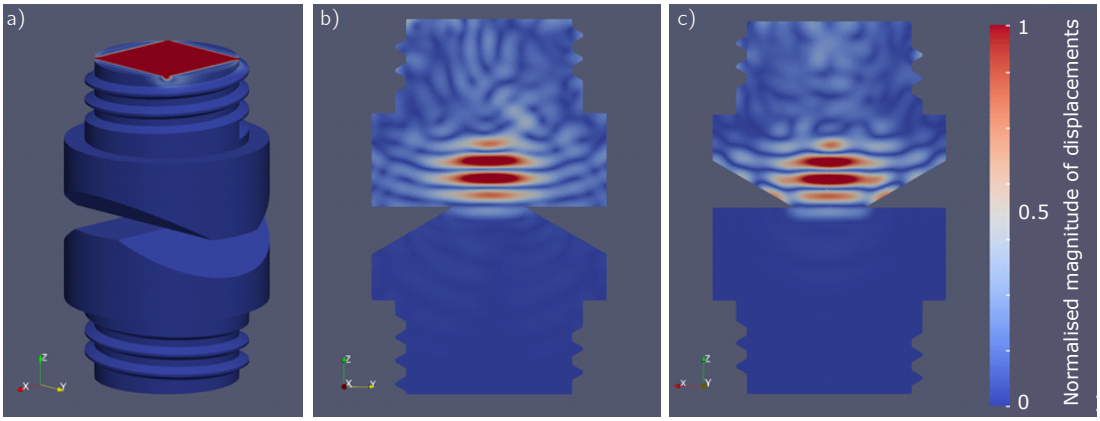


Figure D.1: Colour-coded magnitude of displacements measured at two simulation times for the "bonded contact model". a) The red area shows the extent of the modelled sensor patch. b-c) Section cuts in the y-z and z-x planes, respectively, after 3μs from the wave being generated.

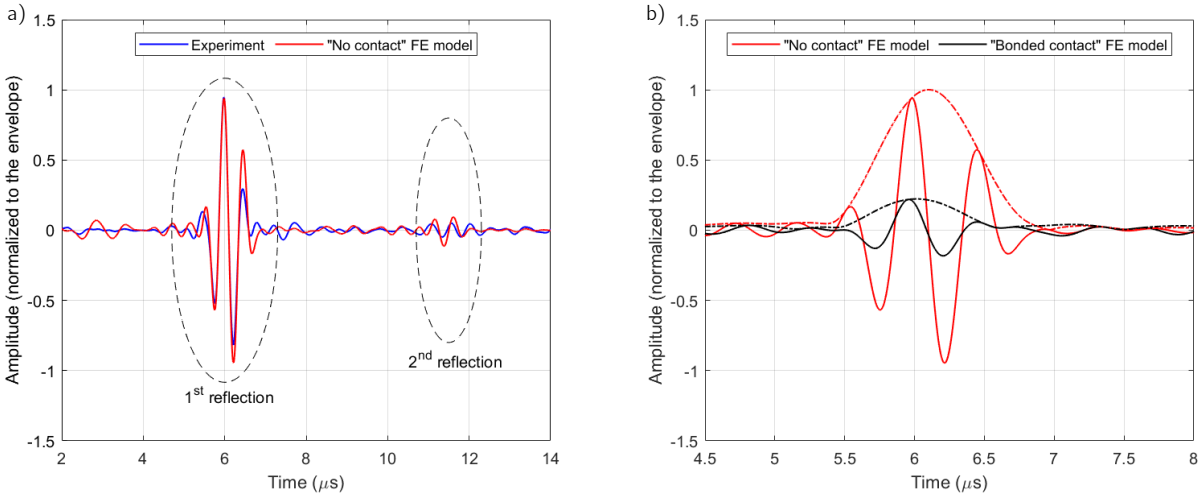


Figure D.2: a) Comparison between experimental and numerical signals obtained for the "no contact model" (both signals normalized to the peak of their envelopes). b) Comparison between numerical signals obtained for "no contact" (same as red signal in (a)) and "bonded contact" models, both signals being normalized to the envelope peak of the former.

Appendix E

FE analysis to estimate the specimen tangential bulk deformation

A finite element model of the specimens of the Imperial friction rig was created to estimate the specimen bulk deformation induced by applied tangential loads. This analysis is needed to quantify how much the measured stiffness from the hysteresis loops is affected by the bulk deformation (see section 3.3), but also to assess the difference between the contact stiffness obtained from ultrasound measurements, which only include the interface compliance, and that obtained from hysteresis loops, which include the bulk deformation in addition to the interface compliance (see section 5.2.3).

Two different FE models of the specimens were created: one representing the standard 8mm-diameter specimens as those shown in Fig. 3.1a, and one representing the modified 10-mm diameter specimens used for the ultrasonic measurements (see Fig. 5.1 and Appendix D). Fig. E.1a shows the model of the latter (same applies to the 8-mm diameter specimen), in which the highlighted points correspond to the experimental location of the laser points used to measure the relative displacement of the hysteresis loop. Since the specimen FE models have perfectly flat and fully bonded interfaces, the relative displacement between the two highlighted points only gives the compliance due to the bulk deformation of the specimens, while the compliance due to the interface is null (i.e. infinite stiffness of the bonded contact). By estimating the bulk deformation contribution from the FE model, the sole information of interface compliance can be then extracted from hysteresis measurements (to validate the study of section 3.3) and compared to that obtained from the ultrasound by using Eq. 5.1 as described in the study presented in section 5.2.3.

The specimens' model was meshed in Solidworks using linear tetrahedral elements with an average size of 0.5 mm (∼70k elements in total). A static tangential load was applied on the top surface of the top specimen. The thread of the bottom specimen was constrained in all degrees of freedom, while the top specimen was only allowed to move along the direction of excitation to best replicate the rig operating conditions. By dividing the applied load by the relative displacement between the two points of displacement measurement, the stiffness solely due to the bulk deformation was obtained. Fig. E.1b shows the bulk stiffness between different locations. As the point distance increases, the stiffness decreases since the relative tangential displacement is larger. The mid-points are those closer to the real laser measurement points, and they result in a bulk stiffness value of 361 N/μm, which is used in section 5.2.3

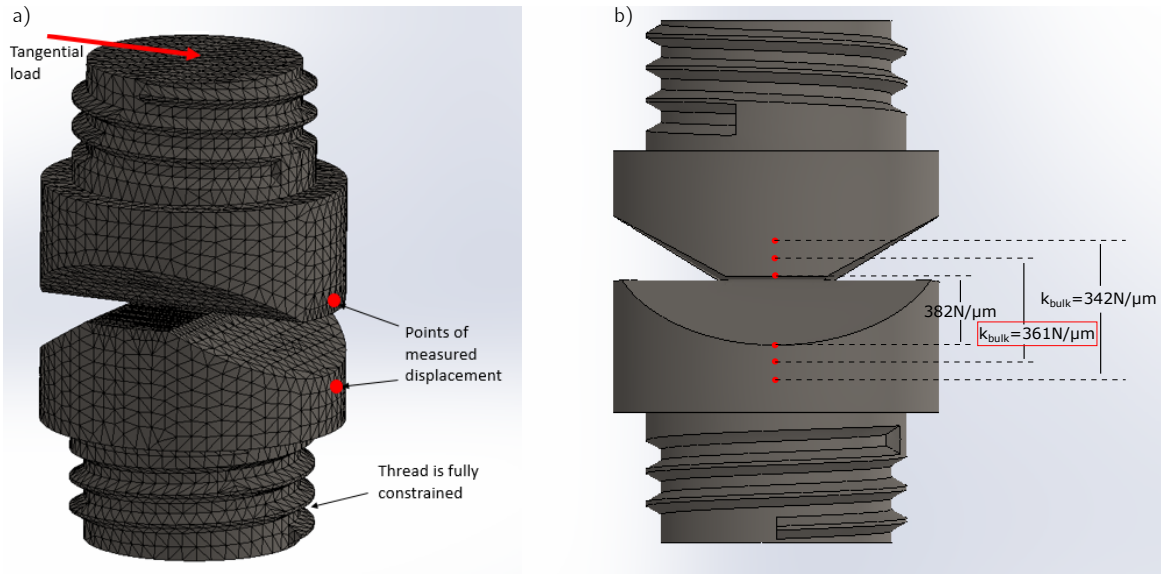


Figure E.1: a) FE mesh of the specimens and points of measured displacement; b) Bulk stiffness values, k_{bulk}, at different locations. The further the measurement points, the lower the k_{bulk}.

for the comparison between contact stiffness values obtained from ultrasound and hysteresis measurements. The same simulation was performed for the standard 8-mm diameter specimens, leading to a bulk stiffness of 116 N/μm, whose value should be accounted for when the contact stiffness is extracted from hysteresis loops to differentiate bulk and interface contributions as discussed in section 3.3.

Appendix F

FE simulations to quantify the effect of the surface topography

This Appendix shows supplementary finite element simulations to quantify the effect of the bulk deformation on the contact stiffness estimation. These supplementary simulations support the Boundary Element simulations shown in section 7.1.2, chapter 7. During the 3-month secondment at Politecnico di Torino to perform round robin tests, as part of the EXPERTISE programme that funded this PhD research, the author collaborated with Daniele Botto and Mario Lavella from Politecnico who had previously developed an FE solver to model the contact of elastic bodies under normal and tangential loads [310]. The author wanted to use this code to predict contact stiffnesses and compare them against experimental measurements. A master student was chosen in Politecnico di Torino to use this FE solver within a master thesis project formulated by the author. The author wishes to acknowledge the work of the student, Mr. Luca Ciuffreda, who created the FE models presented in this appendix and set up the FE simulations.

The FE solver simulates the fretting wear between two oscillating bodies in contact and it evaluates the normal and tangential pressure distributions and the worn area of contact as a result of a cyclic tangential displacements imposed by the user. By plotting the tangential force versus the tangential displacement, the hysteresis loop is obtained and the tangential contact stiffness k_t can be extracted. In addition to hysteresis loops and k_t estimations, the code also predicts the evolution of the area of contact with wear. This code is used in this study to predict the k_t values and worn areas of contact of the Imperial specimens. Predictions from the code are compared against the experimental data presented in chapter 4 and are used to confirm some of the hypotheses presented in that chapter.

The FE solver needs as input the stiffness matrices of the contact bodies, which are modelled with finite elements. Different length scales can be modelled (asperity level, waviness or macro scal contact), depending on the detail of the interface mesh. A lossless reduction method is applied to the stiffness matrices to reduce the size of the problem. After the reduction, the contact problem is solved, normally and tangentially, by imposing a user-defined displacement and evaluating the contact area and iterating until convergence. The code is computationally efficient thanks to the lossless reduction of the stiffness matrices, while its accuracy relies on the accuracy of the FE models themselves. The code is described in detail in [310], and here only an overview is given on the formulation of the contact problem. The main assumptions of

the FE solver are the following:

- The material of the contact bodies is elastic and the deformations are small.
- The friction model is the Amonton-Coulomb model with a constant friction coefficient.
- The normal and tangential contact problems are assumed to be uncoupled, with the normal contact problem being solved before the tangential one.

The normal contact problem is formulated by imposing equations that satisfy the following three conditions:

- Compatibility of displacements: at any point in the potential contact area, the sum of the elastic displacements, of the separation between the bodies, and of the rigid bodies approach must be greater than or equal to zero.
- Displacement-force relationship: it must be satisfied and it is given by the stiffness matrices obtained from the FE models.
- Equation of equilibrium: the pressure distribution has to satisfy the Signorini-Fichera inequalities, namely that i) pressures must be larger than zero where nodes are in contact and ii) pressures must be equal to zero where nodes are not in contact.

The normal contact problem is solved by applying a given rigid body approach and iterating on the pressure distribution and the area of contact until the three previous conditions are satisfied. Once the pressure distribution and the contact area have been defined, the tangential contact problem is solved. This problem is formulated assuming the Coulomb friction law, namely that the tangential force exchanged between two contact nodes cannot exceed the friction limit given by the friction coefficient multiplied by the normal load on those nodes. Starting from the user-imposed tangential displacement, forces are calculated and, once the equilibrium is satisfied, the tangential contact problem is solved, giving as output the contact nodes in stick and slip condition and their corresponding tangential forces. By summing the tangential forces of all the contact nodes, the total tangential force is obtained. By plotting the total tangential force versus the user-imposed tangential displacement, hysteresis loops are obtained. The numerical code can also predict the effect of wear by taking as input wear coefficients that define the amount of material lost due to the energy dissipated during sliding. The area of contact is thus updated as the simulation proceeds. More details on the algorithm and its equations can be found in [310].

The main differences with the BEM solver presented in section 7.1.2 are the following:

- Input: Surface data obtained from the laser confocal microscope are used as input to the BEM solver in the form of heights matrices, while FE models were required for the FE solver presented here. FE models are in general larger than the matrices originated from the microscope surface data and thus BEM is in general faster. However, the BEM approach only solves the problem for the nodes on the contact interface, in contrast to the FEM which also model the exact bulk geometry.

- In the case of the BEM solver, the relationship between force and displacements is given by the Boussinesq and Cerruti potentials [264] since the BEM solver assumes the elastic half-space body description. Instead, the FE solver does not assume the elastic half-space and therefore it accepts as input the stiffness matrices extracted from the FE models of the contacting bodies.

As a result of these assumptions, the main difference is that the FEM solver should provide more accurate contact stiffness estimations since it models the exact bulk geometry, while BEM only assumes an elastic half-space. As long as the exact bulk geometry can be approximated as an elastic half-space, the two methods should provide similar results (which is the case in the presented simulations).

Description of the FE model

The Imperial specimens have been described in chapter 4. Figure F.1a shows that, due to the interface sanding process, a slight curvature appears on the contact interfaces. This curvature was quantified by a radius of 50 mm. Even though this radius is relatively large compared to the small interface width of only 1 mm, it results in a bump of about 2 μm that leads to an initial point contact rather than a uniformly distributed contact. In order to capture this behaviour and study its effects, two different FE models of the specimens were created: specimens with nominally flat interfaces and specimens with curved interfaces with a 50 mm radius. Figure F.1b shows the flat interface FE model, which was created in Ansys with 8-node brick elements (solid 185). A density of 11 by 11 nodes was chosen for the contact area, leading to a total of 121 contact nodes. The same applies to the curved model and Fig. F.1c shows a rendering of the curved contacting interfaces, with the z-axis magnified to show the imposed curvature.

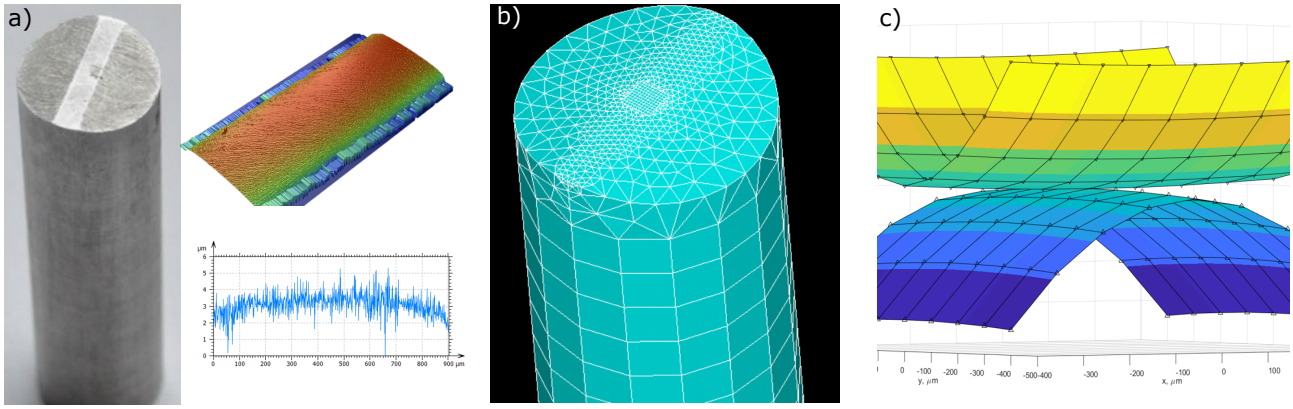


Figure F.1: a) Specimen photo and surface data to show the curvature; b) Specimen FE model; c) Rendering of the curved contact interfaces of the two specimens in contact.

As mentioned in the previous section, the full FE model is reduced to obtain smaller stiffness matrices for faster computations. The Craig-Bampton reduction method [311] was used to reduce the FE model. Two sets of nodes were retained, namely the 121 contact nodes and a set of "distant nodes", which are nodes far from the contact area used to define the rigid-body approach and also used as a reference to determine the k_t. These nodes where defined according to Fig. F.2a-b, which shows the specimens held by the holders. The set of "distant nodes" is selected on the circumference located where the specimen sticks out of the holders. The full

and reduced models are shown in Fig. F.2c-d respectively. In the reduced models, 121 contact nodes and 16 distant nodes were retained.

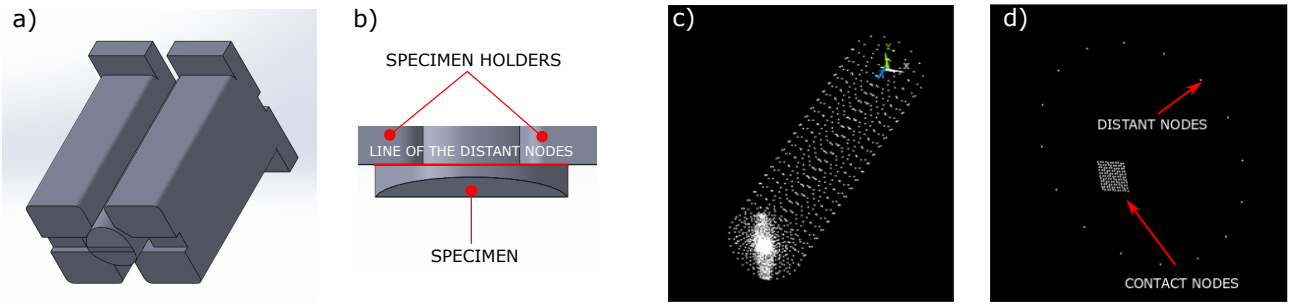


Figure F.2: a) Specimen held by the holders; b) Side view of the specimen close to the contact interface; c) Full set of FE nodes; d) Reduced set of FE nodes.

Contact stiffness predictions

Once the stiffness matrices of the reduced FE models were extracted, they were used as input to the FE solver. Simulations were run using the same loading conditions used for the round robin test presented in chapter 4, namely four different normal loads (17, 87, 150 and 254 N) and a displacement amplitude of 14 μm. Note that only one displacement amplitude was investigated since the FE solver does not include any contat stiffness displacement dependency. Different displacement amplitudes would have only led to wider/shorter hysteresis loops thus leading to more/less energy dissipation and consequent faster/slower wear. The friction coefficient used as input was 0.93, which is the mean value obtained from the tests shown in Fig. 4.16 within the round robin campaign presented in chapter 4. A wear coefficient of 1500 $\mu m^3/J$ was used to model the material removal due to wear and energy dissipated, according to measurements in previous studies for the same stainless steel material [20].

Figure F.3 shows the results of the simulations for the flat interface specimens with a 87 N of normal load. When the interfaces are unworn, the pressure distribution is maximum at the edges and minimum at the centre of the contact, in accordance with the contact mechanics theory for a nominally flat contact [264]. After 30000 hysteresis cycles at 14 μm displacement amplitude, energy is dissipated mainly at the edges of the contact and therefore material is firstly removed there, as shown in the specimen interface representation. This material removal leads to a smoothing of the contact pressure. The same behaviour occurs at larger number of cycles. Figure F.4 shows the evolution of the k_t as a function of the number of cycles for the four normal loads. In contrast to what was observed experimentally, see e.g. Fig. 4.16b, the k_t does not increase during the test but it slightly decreases from an initial value of about 110 N/μm to a value of about 100 N/μm. This slight decrease is probably due to the fact that, at the beginning of the test, the whole area is in contact for these perfectly flat interfaces while, as the test proceeds, the contact interfaces become rounded thus reducing the effective area of contact and hence resulting in a lower k_t. Note that the initial value of the perfectly flat nominal interface is in agreement with the SolidWorks simulations of the nominally flat and bonded specimens shown in section 7.1.1, thus cross-validating both simulations.

To investigate the effect of the surface topograhpy, Fig. F.5 shows the results of the simulations for the curved interface specimens with a 87 N of normal load. Due to the curvature, the contact

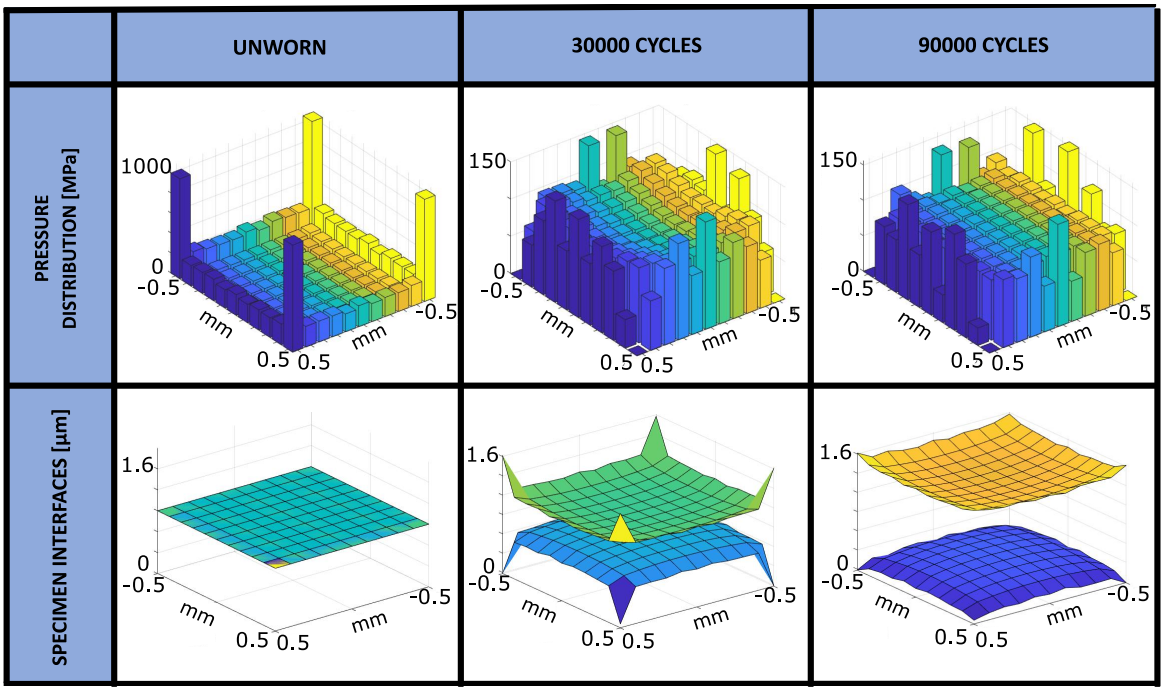


Figure F.3: Pressure distribution and specimen interfaces for the nominally flat specimens at 87 N normal load and 14 μm displacement amplitude. Results given at different wear cycles.

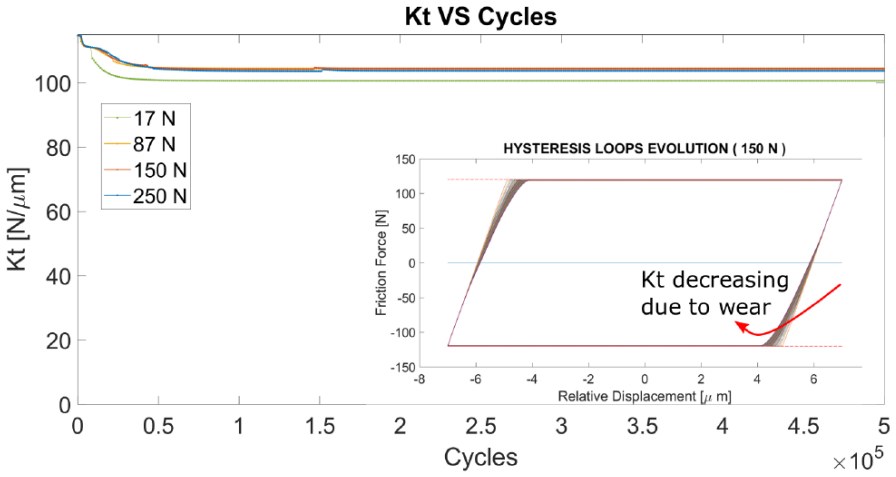


Figure F.4: k_t as a function of the number of cycles for the nominally flat specimens and different normal loads.

at the beginning of the test is like a sphere-on-flat and therefore the pressure distribution is maximum at the centre and minimum at the edges, in accordance with the contact mechanics theory for elliptical/spherical contacts [264]. As the simulation proceeds, the contact area gradually increases with wear and energy is dissipated mainly at the edges of the contact, where the normal pressure is lower, slip occurs and therefore material is firstly removed there. Also in this case, the material removal leads to a smoothing of the contact pressure. Figure F.6 shows the evolution of the k_t as a function of the number of cycles for the four normal loads. In contrast to what was observed with the flat interface, k_t increases during the test from low initial values around 40-60 N/μm to steady state values at 110 N/μm. This behaviour is in accordance with the experimentally observed trend (see e.g. Fig. 4.16b), where k_t increases with wear as a result of an increase in the worn area of contact. In fact, while at the beginning of

the test a point contact leads to low k_t estimations, as the test proceeds the contact interfaces become more conformal thus leading to an increase in the k_t estimations. This simulation further confirms the hypothesis presented in chapter 4, namely that the increase in the k_t with wear was due to a shift from an initial point contact to a more distributed contact.

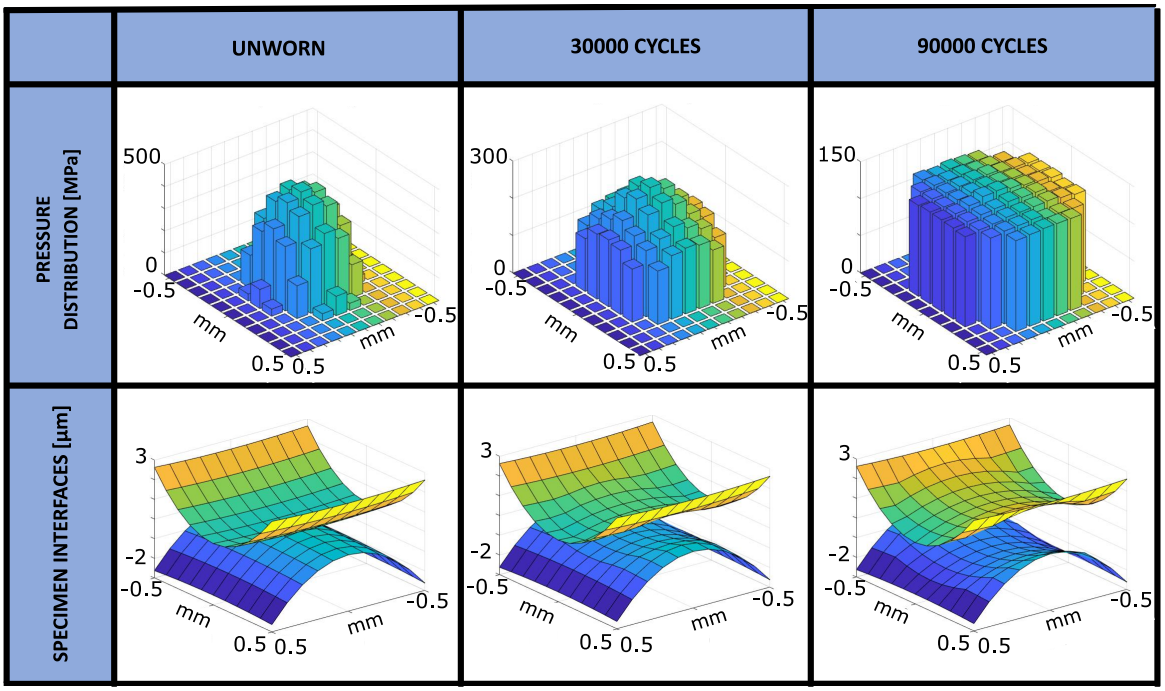


Figure F.5: Pressure distribution and specimen interfaces for the curved specimens at 87 N normal load and 14 μm displacement amplitude. Results given at different wear cycles.

As the normal load increases, the steady state is reached earlier, since each hysteresis loop dissipates more energy thus leading a faster material removal. Figure F.6b shows the same values plotted versus the energy dissipated rather than the hysteresis cycles. In this case, the steady state is reached for the same amount of energy dissipated (around 600 J) for all normal loads. This energy value is comparable to the experimentally observed energy dissipated at steady state (see e.g. Fig. 4.16b). Finally, note that the normal load does not have a large influence on the k_t estimations in terms of amplitudes, since most of the values are around the 110 N/μm with a slight normal load dependency, which instead is much more evident in the experimental data presented in chapter 4 (see e.g. Fig. 4.24). This might be due to the fact that the FE model does not include the roughness but only the waviness. Hence, for the considered specimens, the normal load dependency might be mainly driven by the roughness (μm scale) rather than by the waviness (μm-mm scale). For the same reason, the k_t predicted with FEM is larger (almost double) than the k_t measured experimentally.

The results of this Appendix confirm the strong effect that the surface topography has on both experiments and simulations, and it confirms how important is to include realistic surface topographies in simulations, although this aspect is often neglected in nonlinear dynamic analysis. A shortcoming of the presented FE models is that they do not model the roughness, but only the waviness. In order to investigate the effect of roughness, the Boundary Element Method (BEM) solver was used to perform a new set of simulations as discussed in section 7.1.2.

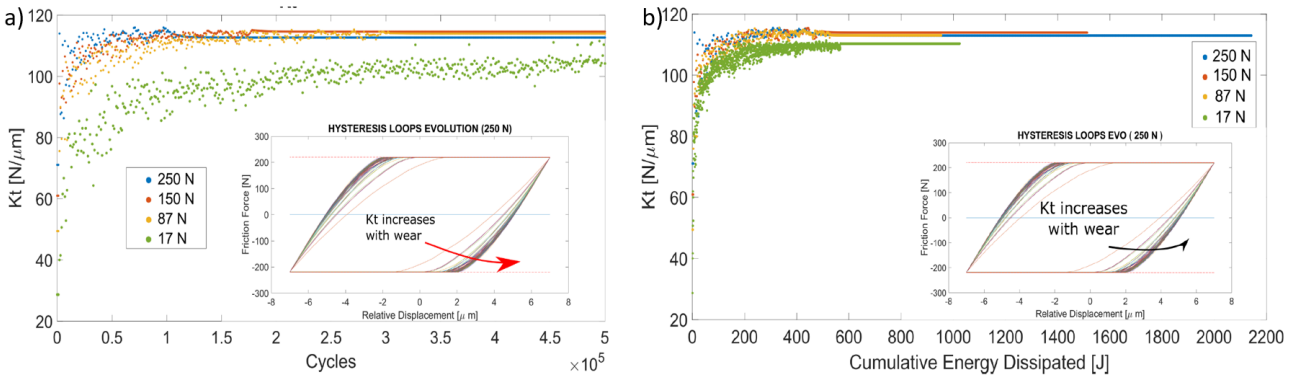


Figure F.6: a) k_t as a function of the number of cycles for the curved specimens and different normal loads; b) k_t as a function of the energy dissipated for the curved specimens and different normal loads.

Appendix G

Supplementary data for the simulations of chapter 8

This Appendix shows supplementary information and simulations of the aero-engine industrial case described in chapter 8.

High EO/Mode 3 (1T) – Frequency shift predictions

This section shows simulations on the frequency response of the modal family 3, which represents the first torsional mode shape. For more details on the simulation method please refer to sections 8.2 and 8.3.1. The high EO excitation (resulting from the high-pressure nozzle guide vanes) is here analysed because this is the exciting EO observed experimentally for this modal family within the service speed range. Figure G.1a shows the simulations for the 30000 N/mm^3 constant K_T case (with the thick blue line showing the reference full contact case). For this mode, the reference case lies at the higher edge of the experimental resonance range, while a slightly improved match is obtained for all the other contact bedding patterns. The outer edge v1 and the concave contact seem to give the best match with the experimental resonance range. Instead, the convex bedding pattern under-predicts the resonance, while it well predicted the resonance for the low EO/mode 2. Excluding this pattern, all the other patterns lie within a 2% frequency shift range, which is a much smaller range than that observed for mode 2, in which those cases laid within an 18% frequency shift range. This smaller frequency shift range suggests that this mode is less influenced by the contact bedding patterns than the low EO/mode 2, probably because the torsional mode shape leads to less movement on the blade platform.

Also for this mode, k_t=3701 N/μm simulations were performed. Results are shown in Fig. G.1b, which indicates that the pattern that most softens the system is the convex pattern. Figure G.1a shows the further softening induced by the lower total k_t in N/μm at each pattern (the reduced global k_t values are indicated in the legend). From a comparison of Figure G.1a and b, it seems that, also for this mode, the different bedding patterns contribute to half of the reduction in the frequency (with respect to that predicted by the reference case), while the other half of the reduction results from the lower k_t values due to lower nominal areas of contact.

Finally, Fig. G.2 shows k_t load-dependent simulations. As for low EO/mode 2, they only slightly differ from the 30000 N/mm^3 constant K_T case because the range of K_T for the load-dependent case is still around 30000 N/mm^3, although the full contact case shows a better softening when a kt load dependence is used. In fact, in the k_t load-dependent case, even the full contact bedding pattern is within the experimental resonance range. This slightly improved match indicates that the full contact bedding pattern is partly representative of the EO40/mode 3 since this mode occurs at a different rotational speed than the low EO/mode 2. In fact, at different rotational speeds, blades vibrate slightly differently depending on the modal contributions and thus slightly different kinematics might affect the blade/platform contact.

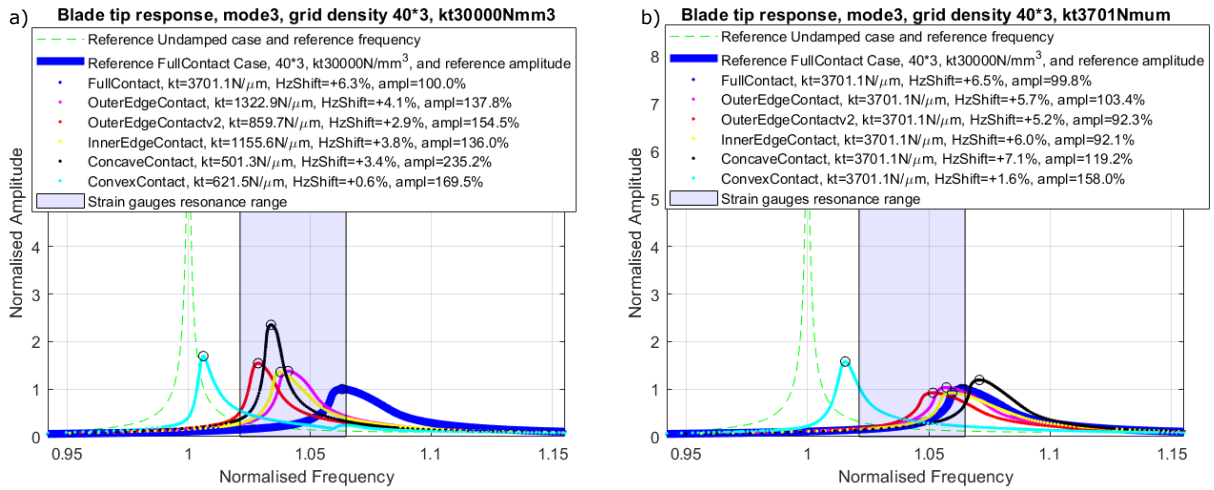


Figure G.1: High EO/mode 3 (1T) simulations for the six bedding patterns and node grid density 40*3: a) k_t=30000 N/mm^3; b) k_t=3701 N/μm (case needed to investigate the effect of the patterns alone).

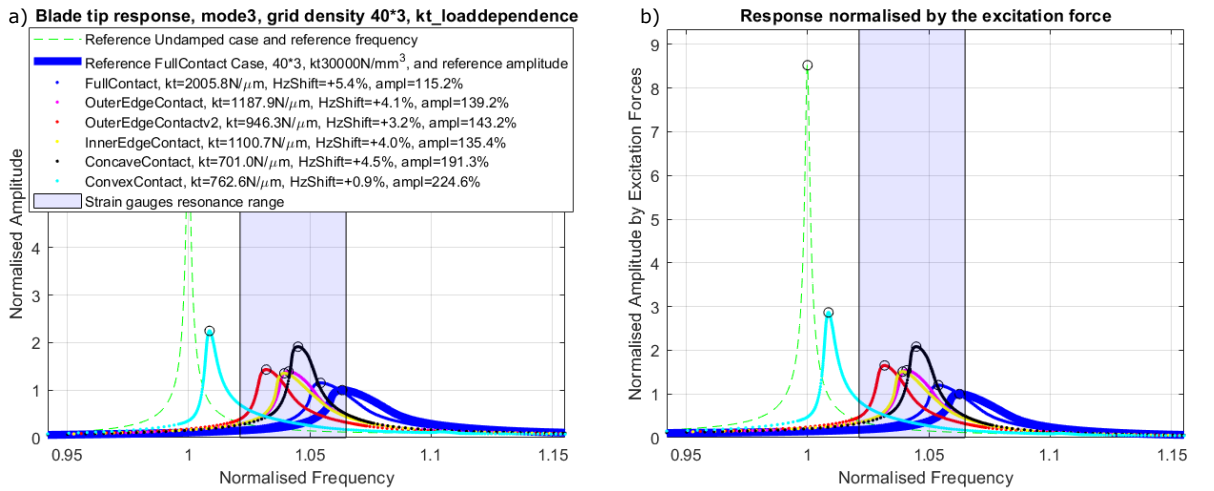


Figure G.2: High EO/mode 3 (1T) simulations for the six bedding patterns and node grid density 40*3: a) k_t load dependence case; b) k_t load dependence case and response normalised by the scaling factor of exciting forces.

With regards to the amplitudes, they seem to increase with decreasing resonant frequency, except for the concave pattern case. Figure G.2b shows the amplitudes normalised by the excitation amplitude. In this case, the normalisation does not have a large effect since all

resonances occur at similar frequencies (i.e. similar rotational speeds). The observed increase in the amplitude with reduced frequency is in agreement with what was observed for the low EO/mode 2. The contact states were also analysed and shown in Figure G.3. As already observed for the low EO/mode 2, the full contact bedding pattern has the largest percentage of nodes in slip condition. However, on the contrary of what was observed for mode 2, the energy dissipated for the full contact bedding pattern (17.7 J/s) is lower than the energy dissipated for the convex contact pattern (22.8 J/s), although the convex contact pattern has a larger amplitude of vibration at resonance (almost double of the full contact bedding pattern case). It is expected that larger energy dissipated leads to a lower vibration amplitude. This aspect should be investigated more in detail in future, for example by performing new simulations at different excitation amplitudes or by comparing the dissipated energy with the global strain energy, which was not obtained during the presented simulations. It is also interesting to notice that the average energy dissipated for EO40/mode 3 (∼19 J/s) is much higher than that dissipated for low EO/mode 2 (∼2J/s), probably due to the much larger excitation force coming from the high EO excitation coming from the nozzle guide vanes.
These results are compared with those of the other modes in sections 8.3.1 and 8.4 of chapter 8.

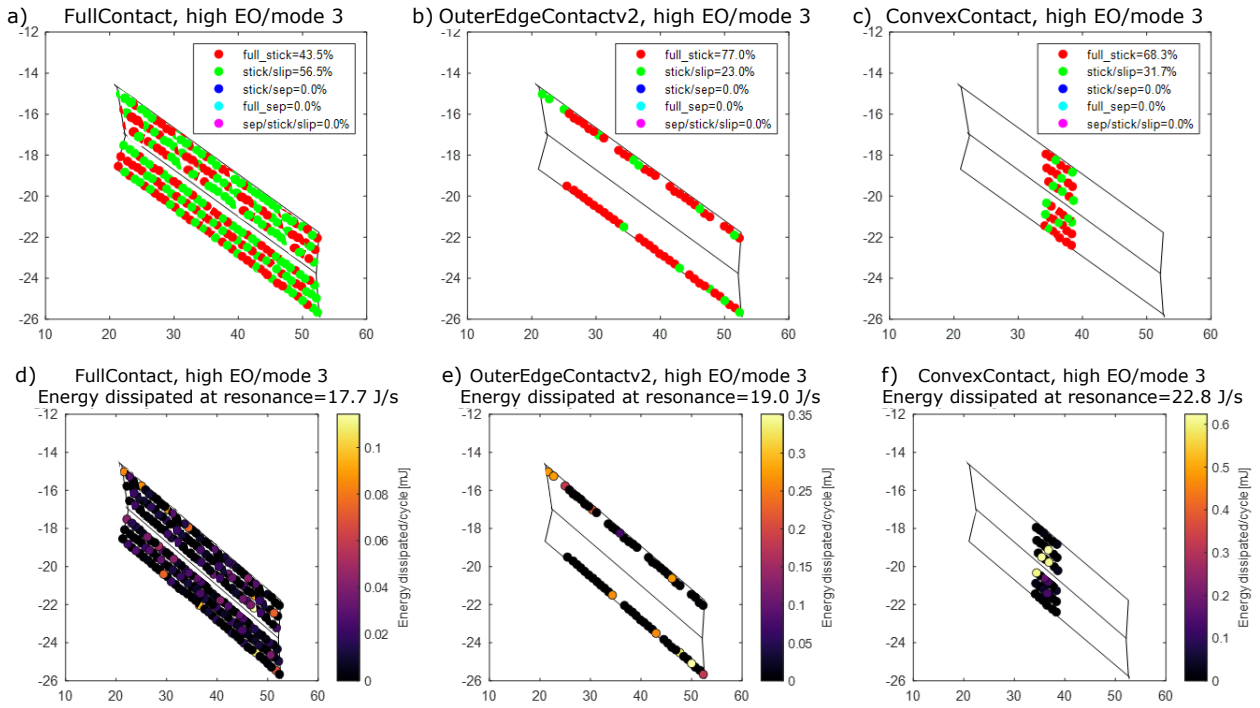


Figure G.3: High EO/mode 3 (1T) contact states at resonance for the k_t load dependent simulations with grid density 40*3: a) Full contact bedding pattern; b) OuterEdgeContactv2 bedding pattern; c) Convex contact bedding pattern. Energy dissipated at resonance for: d) Full contact bedding pattern; e) OuterEdgeContactv2 bedding pattern; f) Convex contact bedding pattern.

High EO/Mode 4 (2F) – Frequency shift predictions

This section shows simulations on the frequency response of the modal family 4, which represents the second flap mode shape (blades moving left and right). For more details on the

simulation method please refer to sections 8.2 and 8.3.1. The high EO excitation (resulting from the high-pressure nozzle guide vanes) is here analysed because this is the most critical excitation within the service speed range observed experimentally for this modal family. Figure G.4a shows the simulations for the 30000 N/mm^3 constant K_T case (with the thick blue line showing the reference full contact case). For this mode, the full contact case lies in the middle of the experimental resonance range, while a slightly worst match is obtained for all the other contact bedding patterns, on the contrary of what was observed for the low EO/mode 2 and high EO/mode 3. In particular, the outer edge v1 and v2 pattern resonances lie slightly outside the lower part of the experimental resonance range, thus indicating that they are not the most representative bedding patterns for the rotational speed at which the high EO/mode 4 occurs. It is possible that, depending on the rotational speed, blades vibrate differently and hence also their platforms vibrate differently, thus leading to possible different contact bedding patterns for the modes that occur at different rotational speeds. Excluding the concave pattern, which is the least representative, the other patterns lie within a 6.5% frequency shift range, which is smaller than the 18% frequency shift range observed for mode 2, but larger than the 2% frequency shift range for mode 3.

Also in this case, simulations were performed for a constant global k_t equal to 3701 N/μm. Results are shown in Fig. G.4b, which indicates that the bedding patterns do not have a large effect on the resonances. This is probably because, for this mode, most of the contact nodes are in slip conditions (see Fig. G.6) and therefore their distribution does not affect the response to a large extent, since the damper slips to a large extent with every bedding pattern. Figure G.4a shows the further softening induced by the lower total k_t in N/μm at each pattern (the reduced global k_t values are indicated in the legend). From a comparison of Figure G.4a and b, it seems that also the reduced stiffness does not affect the resonances to a large extent, further confirming that this mode is dominated by the nodes in slip condition rather than by the contact stiffness (which mainly affects the stick regime).
Finally, k_t load-dependent simulations are shown in Fig. G.5a. They are slightly stiffer than those from the 30000 N/mm^3 constant K_T case, even though the difference is not significant, as already observed for modes 2 and 3.

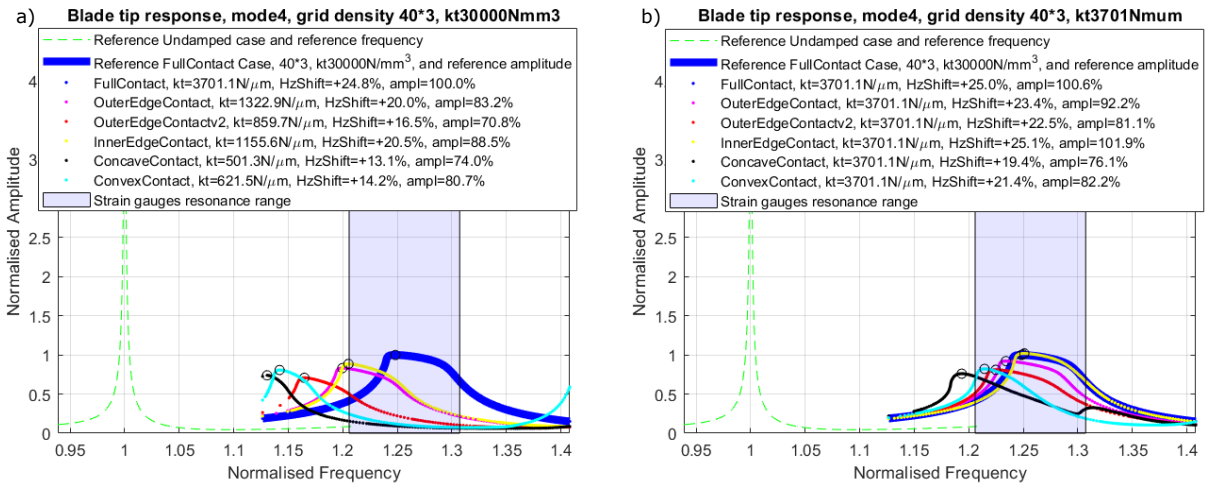


Figure G.4: High EO/mode 4 (2F) simulations for the six bedding patterns and node grid density 40*3: a) k_t=30000 N/mm^3; b) k_t=3701 N/μm (case needed to investigate the effect of the patterns alone).

With regards to the amplitudes, Figure G.5b shows that the normalised amplitudes seem to

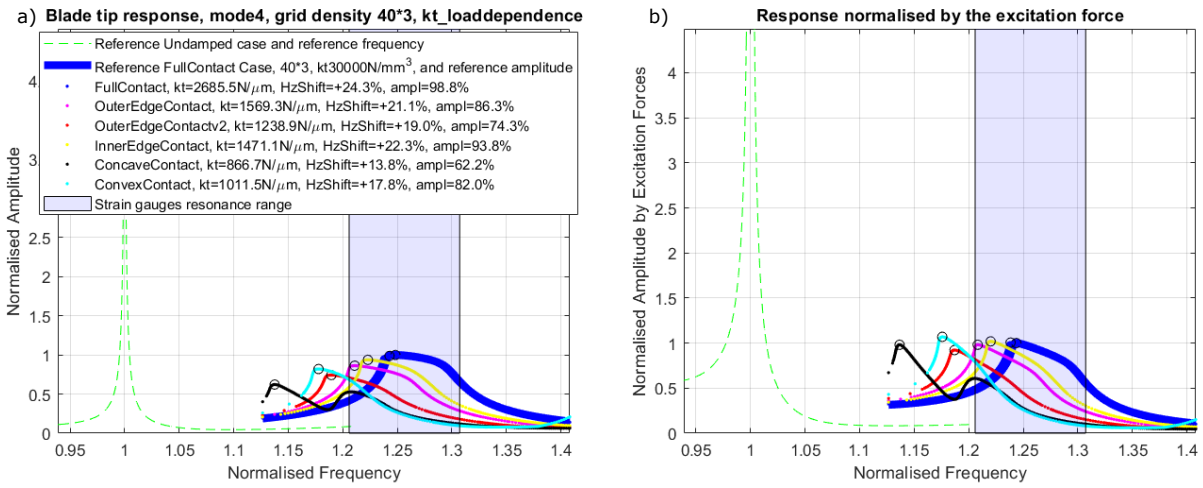


Figure G.5: High EO/mode 4 (2F) simulations for the six bedding patterns and node grid density 40*3: a) k_t load dependence case; b) k_t load dependence case and response normalised by the scaling factor of exciting forces.

be around the same values, with lower variations than those observed in modes 2 and 3. Also for this mode, the contact states were analysed and shown in Fig. G.6. As already observed for modes 2 and 3, the full contact bedding pattern has a larger percentage of nodes in slip conditions. It is also evident that for this mode, a much larger percentage of the contact nodes are in slip states compared to previous modes. This is probably due to the larger excitation due to the large rotational speed at which this mode occurs – as a reference, the rotational speed of this mode is roughly 37% larger than the rotational speed at which the high EO/mode 3 occurs. With regards to the energy dissipated, values are in the range 150-220 J/s, which are up to 10 times larger than those observed in modes 2 and 3. This is again in agreement with the larger excitation and large percentage of nodes in slip state. In this mode, the full contact bedding pattern has the largest amount of energy dissipated at resonance (almost double than the convex contact), although the amplitude vibration for this bedding pattern is not much lower than the convex contact case when normalised, as shown in Figure G.5b. The reason for this unexpected behaviour will be investigated in more detail in future, for example by performing new simulations at different excitation amplitudes or by comparing the dissipated energy with the global strain energy, which was not obtained during the presented simulations. These results are compared with those of the other modes in sections 8.3.1 and 8.4 of chapter 8.

High EO/Mode 3 (1T) – Amplitude predictions

Figure G.7 shows strain amplitude predictions and comparisons against experiments for the high EO/mode 3 (1T). For more details on the amplitude predictions, refer to section 8.3.2. For this mode, the excitation pressures were predicted with CFD simulations, and therefore no tuning was performed to match numerical and experimental amplitudes. The Figure shows that the reference full contact cases (thick lines) have a slightly higher resonance frequency than that experimental, while the outer edge contact v2 has a slightly lower frequency (as also shown in Appendix G). With regards to the amplitudes, both simulations show lower strain

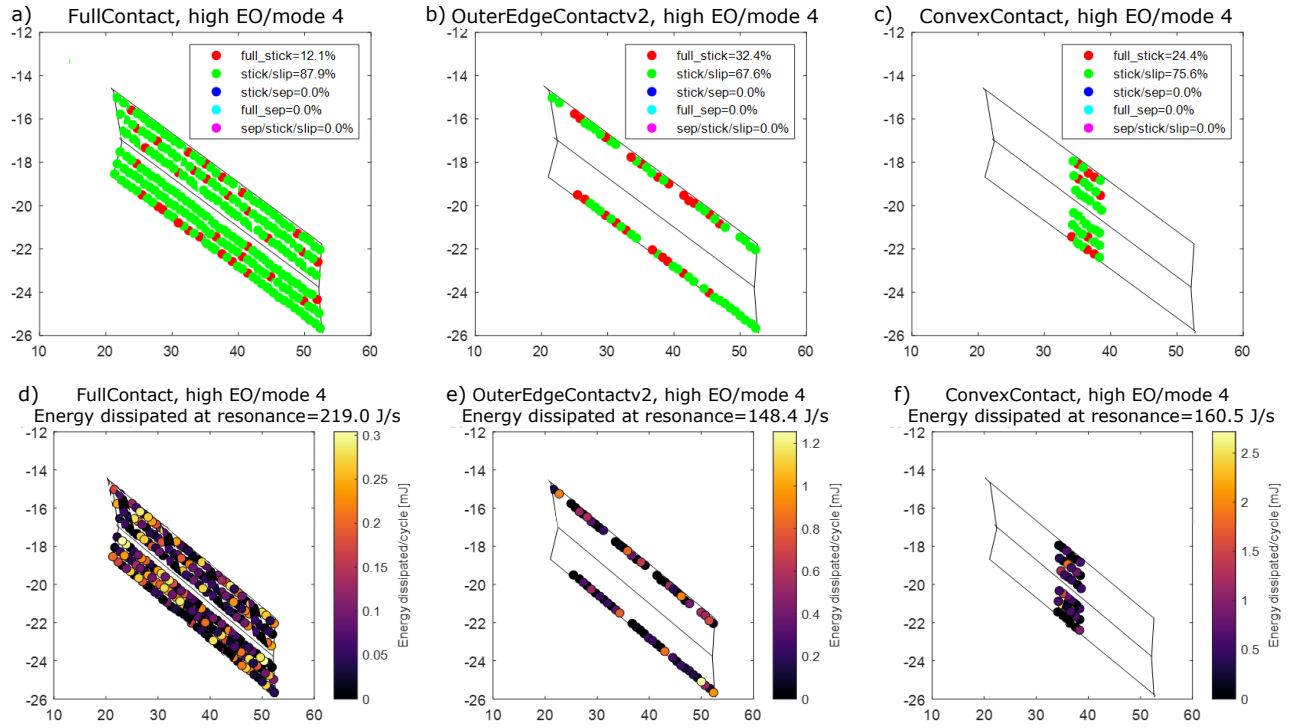


Figure G.6: High EO/mode 4 (2F) contact states at resonance for the k_t load dependent simulations with grid density 40*3: a) Full contact bedding pattern; b) OuterEdgeContactv2 bedding pattern; c) Convex contact bedding pattern. Energy dissipated at resonance for: d) Full contact bedding pattern; e) OuterEdgeContactv2 bedding pattern; f) Convex contact bedding pattern.

amplitudes than those measured, with the outer edge contact v2 being closer to experimental values. Numerical amplitude ratios (between the two strain gauges TR and SB) were also estimated for a comparison with the experimental ratio. The full contact case has a ratio of 4.7, which is larger than that experimental (2.7), while the outer edge case shows a better match (ratio=2.6). The figure shows that numerical ratios strongly change depending on the contact bedding pattern (almost two times difference), indicating that the mode shape has changed. Strain amplitudes also strongly vary depending on the contact bedding pattern. The maximum TR predicted strain for the outer edge contact case is 33% larger than the reference full contact case, suggesting that the full contact case might not be the most conservative case for strain predictions. This large variation must be considered for more accurate evaluations of high cycle fatigue risks.

High EO/Mode 4 (2F) – Amplitude predictions

Figure G.8 shows strain amplitude predictions and comparisons against experiments for the high EO/mode 4 (2F). For more details on the amplitude predictions, refer to section 8.3.2. The reference full contact case (thick lines) has a resonance frequency matching with the experimental one, while the outer edge contact v2 has a lower frequency (as already shown in the Appendix G). With regards to the amplitudes, also in this case, excitation unsteady pressures were predicted with CFD simulations, and therefore no tuning was performed to match

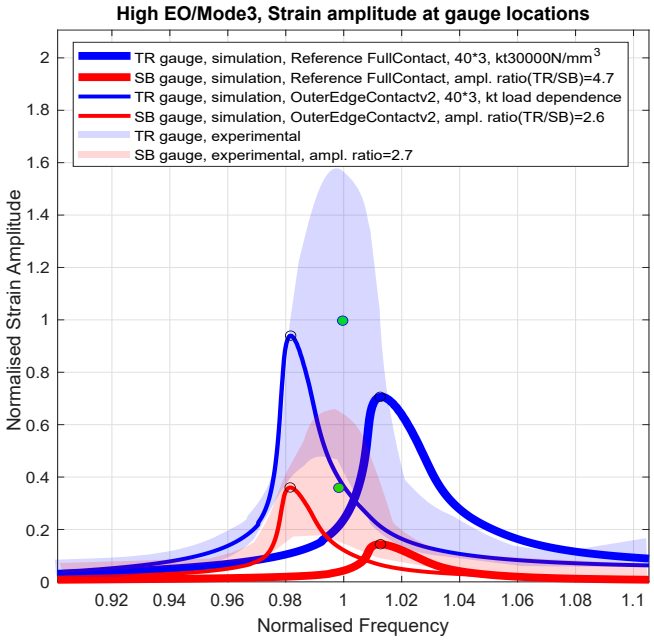


Figure G.7: High EO/mode 3 (1T) strain amplitudes. Comparison between strain gauge data and simulations for two bedding patterns with node grid density 40*3.

numerical and experimental amplitudes. Both simulations show larger strain amplitudes than those experimentally measured, with the full contact case being closer to experimental values. Numerical amplitude ratios (between the two strain gauges TR and SB) were also estimated for a comparison with that experimental. The full contact case has a ratio of 2.7, which is the same as the outer edge contact case, and smaller than that experimental (3.3). For this mode, on the contrary of what was observed previously, the numerical ratios are equal for both contact bedding patterns. This indicates that the mode shape of this second flap mode is not affected by the different bedding patterns. Finally, strain amplitudes also vary depending on the contact bedding pattern. The maximum UP predicted strain for the outer edge contact case is 10.6% larger than the reference full contact case.

Effect of Combined Mode Analysis: low EO/mode 1 (1F) + high EO/mode 4 (2F)

Section 8.3.2 and Appendices G-G have shown a detailed analysis of modes 2, 3 and 4. This Appendix shows a detailed study of the low EO/mode 1 (1F), which is the first flap mode (blades moving left and right), and requires a different analysis since experimental data showed that it occurs at a similar rotational speed to that of the high EO/mode 4, and therefore might be strongly affected by the highly damped mode 4. To include the effect of the high EO/mode 4 in the simulation, the high EO excitation has to be included in addition to the low EO excitation. In fact, the high EO excitation excites mode 4, while the low EO excitation excites mode 1, as observed during the engine test. Both high and low EO excitations are present at the same time during the engine operation since the high EO excitation results from the stator vanes that divide the gas flow into several sub-flows, while the low EO excitation results from a general non-axisymmetry in the circumferential pressure field upstream of the blade.

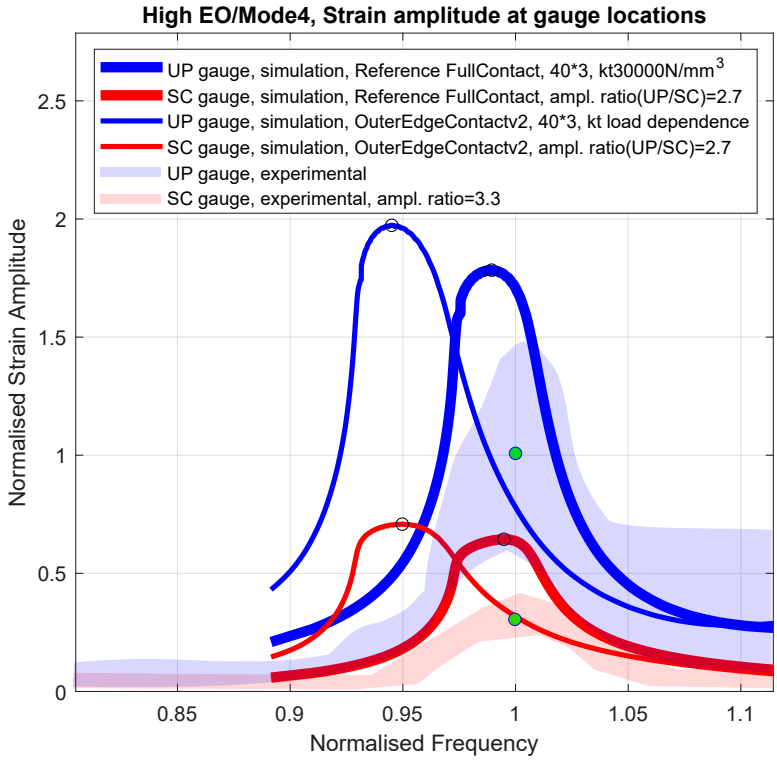


Figure G.8: High EO/mode 4 (2F) strain amplitudes. Comparison between strain gauge data and simulations for two bedding patterns with node grid density 40*3.

Figure G.9 shows predicted and experimental strain amplitudes of the low EO/mode 1 with the only low EO contribution included. This is done for the reference full contact and outer edge v2 contact cases with grid density 40*3. Since the low EO contribution could not be predicted with the available software capabilities, as discussed in section 8.2.2, it was arbitrarily scaled so that predicted strain amplitudes matched measured amplitudes. The Figure shows that even though amplitudes are matching, the damping is not. Experimental data appear to be heavily damped with a wide peak, while numerical data indicates low damping with a sharp peak. To better investigate this aspect, Fig. G.9b shows the contact conditions at resonance. All contact nodes are in the stuck contact condition, thus confirming that the damper contact is not adding any damping to the system. A possible explanation for this low damping is that most of the damping observed experimentally comes from the high EO/mode 4 since this mode occurs at a similar rotational speed to that of the low EO/mode 1 and therefore might affect its response. Fig. G.6 showed that the high EO/mode 4 has a large percentage of contact nodes in slip condition, which might damp the low EO/mode 1.

Therefore, it was decided to run a simulation that included both modes. The high EO/mode 4 was included by using the corresponding high EO contribution as input excitation in addition to the low EO contribution. In fact, the high EO contribution activates mode 4. After running the simulation, the low EO component was extracted to represent it in a tracked-engine order format, as done for the experimental data of each mode, whose exact EO components were extracted as discussed in section 8.1. The low EO contribution is shown in Fig. G.10 with yellow and green curves for the two gauge locations respectively. The new response is heavily damped, with almost 30 times lower amplitude than the original simulation with only the low

EO excitation (a close-up is shown in Fig. G.10b). This large damping is introduced by the high EO/mode 4 (activated by the high EO excitation), which affects the low EO/mode 1. With this combined analysis, the numerical response is much lower than the experimental and therefore the amplitude of the low EO contribution exciting mode 1 was increased to match again numerical and experimental strain amplitudes. Figure G.11 shows the new simulations with the larger low EO contribution, which was increased by roughly 50 times. This increase produced a better match between numerical and experimental strain amplitudes. The new response (thick green and yellow lines) has more damping and is more similar to measured data, although it presents two peaks. The double peak is probably induced by the strong system nonlinearity or internal resonance. Figure G.11b shows the contact conditions at resonance, highlighting that when mode 4 is included in the simulation (and the excitation of mode 1 is increased), almost all contact nodes (85%) enter in slip conditions, thus explaining the observed damping in the response. This improved match indicates that the inclusion of more modes in the same simulation is of extreme importance if i) they occur in the same rotational speed range (although at different EOs) and ii) if one of them (mode 4 in this case) presents a large amount of damping, which might damp the other mode response.

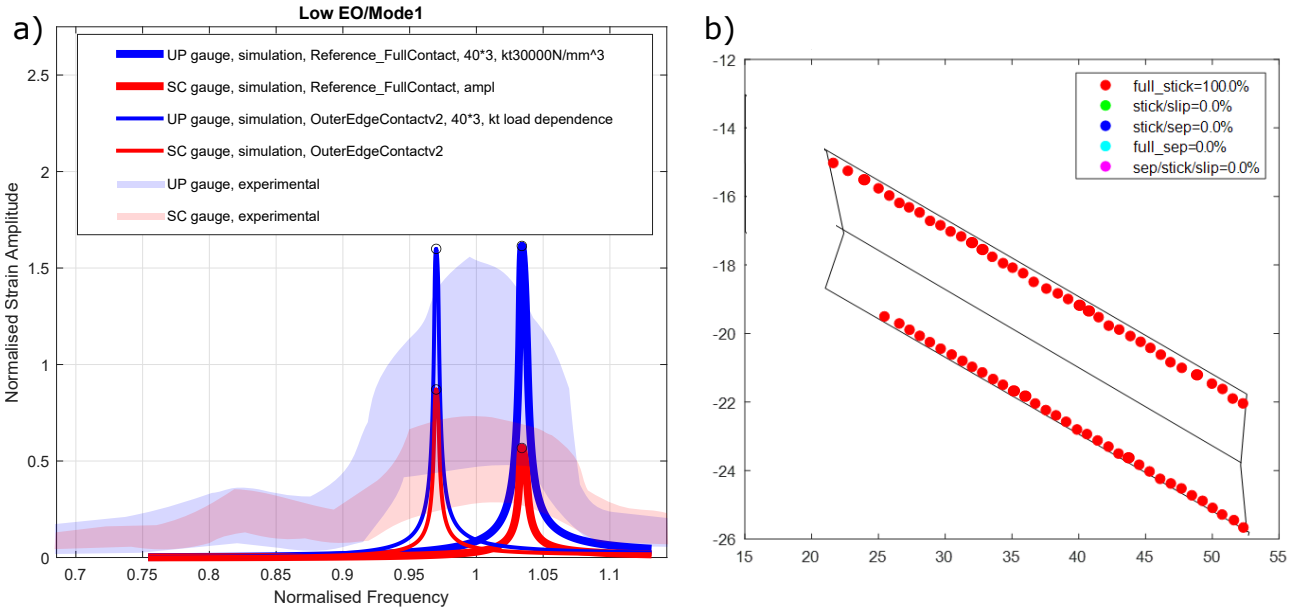


Figure G.9: Low EO/mode 1 (1F) strain amplitudes: a) Comparison between strain gauge data and simulations. The outer edge bedding pattern has node grid density 40*3 and k_t load dependence; b) the contact conditions at resonance.

Finally, Figure G.12 shows the effect of the low EO/mode 1 on the high EO/mode 4. The plot was obtained by extracting the high EO component from the previous simulation. The strain amplitudes in this case increase by 6-7% compared to the case when the low EO/mode 1 is not included. It is concluded that mode 1 does not have a large impact on mode 4, even though the 7% increase in amplitude might be relevant for more accurate endurance ratio predictions.

Summary for all the modes

A summary is proposed below in a mode by mode format since it was found that, depending on the blade/damper kinematic of each mode, the investigated bedding patterns have different

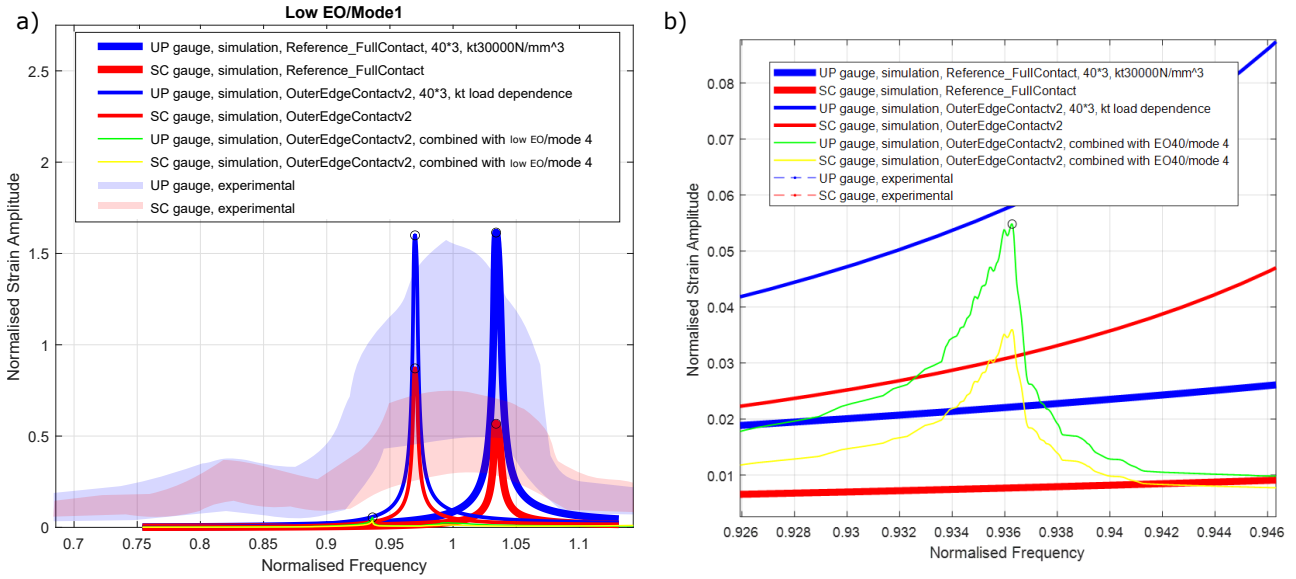


Figure G.10: Combined analysis of low EO/mode 1 (1F) and high EO/mode 4 (2F). a) Comparison between strain gauge data and simulations for the outer edge bedding pattern with node grid density 40*3 and k_t load dependence; b) Close-up of the combined analysis simulation resonance.

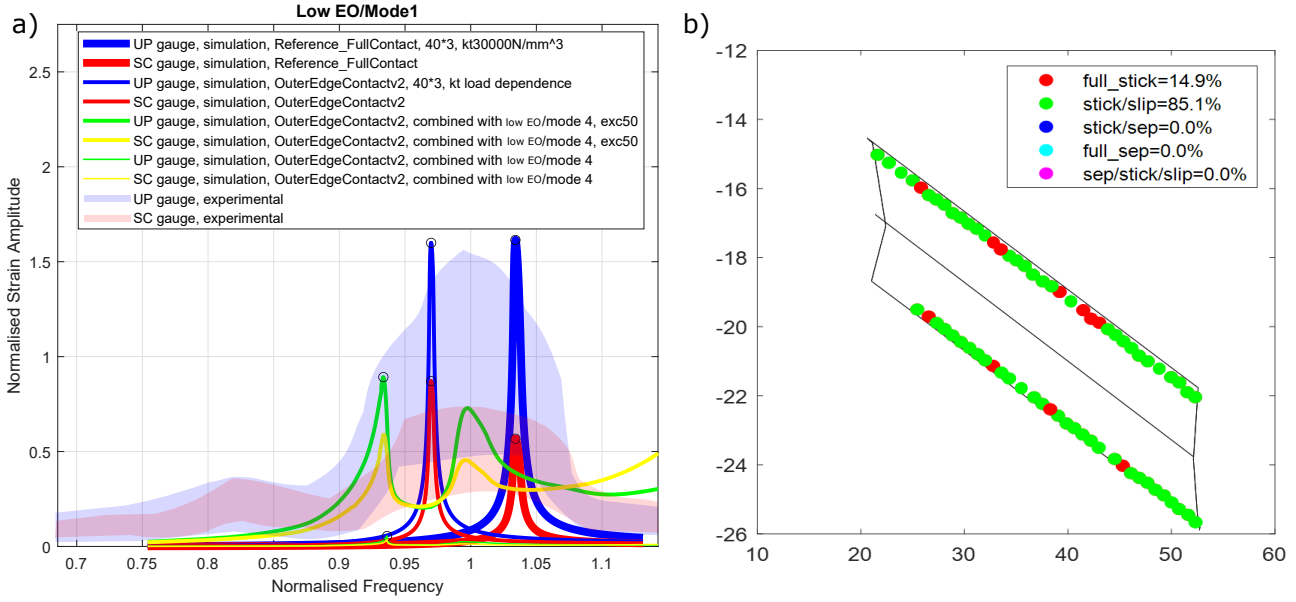


Figure G.11: a) Combined analysis of low EO/mode 1 (1F) and high EO/mode 4 (2F), with excitation 50 times larger than what was used in Figure 37; b) contact conditions at resonance.

effects on the dynamic response:

- Low EO/Mode 1 (1F, first flap mode - blade moving left and right): For this mode, simulations were performed with the high EO/mode 4 coupled, since it was found experimentally that the two modes occur at a similar engine rotational speed (although at different EOs), and therefore they might interact. The coupled prediction is performed by including both low and high EO excitation in the simulations. Results are in better agreement with the experimental measurements than those uncoupled. This is thanks to the damping introduced by the high EO/mode 4, which strongly damps the response of

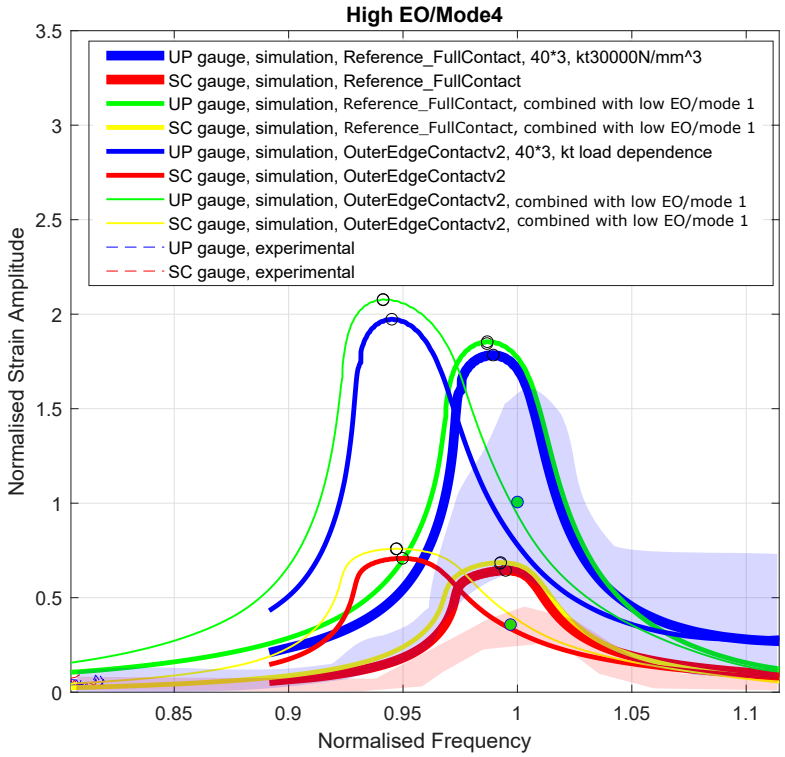


Figure G.12: Combined analysis of low EO/mode 1 (1F) and high EO/mode 4 (2F). Effect on high EO/mode 4.

the low EO/mode 1, making it more similar to the measured response. Instead, if the high EO/mode 4 is not included in the simulation, there is no additional damping in the response and the contact is fully stuck. This analysis highlights the importance of including more modes (excited by different EO) if they occur at the same engine rotational speed.

- Low EO/Mode 2 (1E, first edge-wise mode - blade moving backwards and forwards): The resonant frequency of this mode is over-predicted when using the datum approach full contact bedding pattern (the frequency is roughly 23% larger than that experimental). Instead, when using the more realistic outer edge contact bedding pattern, the resonance drops to resonances strikingly close to those observed experimentally. This highlights the importance of correctly capturing the real interface conditions, confirming the findings and guidelines suggested in the previous chapters. The different bedding patterns significantly affect the dynamic response of this mode, with resonances varying by up to 25% for the different cases. In addition, the damped resonant frequency increases by up to 40% when compared to the undamped case, where the damper is not present, meaning that the addition of the damper significantly stiffens this mode. Conclusions cannot be drawn with regards to the strain amplitude predictions, since unsteady pressures could not be predicted for the low EO exciting this mode. Finally, this mode has the lowest amount of contact nodes in slip conditions, probably due to the low relative displacement between blade and damper during the edge-wise motion. This also results in the lowest energy dissipated ($\sim$2 J/s) compared to the other modes.

- High EO/Mode 3 (1T, first torsional mode): this mode is the least sensitive to the contact stiffness and bedding patterns in terms of resonance frequencies (differences below 5% when different patterns are modelled). In addition, this mode shows the lowest frequency

shift when compared to the undamped case (only up to +5% increase in the resonant frequency), meaning that the addition of the damper does not stiffen this mode shape to a large extent. Instead, with regards to the amplitudes, changes are more significant when different bedding patterns are modelled. The outer edge bedding pattern leads to the best match with experimental data, while the datum approach full contact case predicts lower amplitudes, by 33%, which are therefore less conservative for high cycle fatigue risk evaluations. This mode has a medium amount of contact nodes in slip conditions as compared to other modes and energy dissipated of about 19 J/s.

- High EO/Mode 4 (2F – second flap mode): the different bedding patterns do not change much the resonance frequency of this mode, with shifts below 10%. However, it has the largest frequency shift compared to the undamped case (up to 24% increase in the resonant frequency), meaning that the addition of the damper stiffens this mode shape. With regards to the strain amplitudes, this mode is the least sensitive to the contact stiffness and bedding patterns changes. Variations in strain amplitudes are below 10% for the different bedding patterns, probably because of the very large percentage of contact nodes in slip conditions (dissipated energy up to 220 J/s), which slip regardless of the contact stiffness value or bedding pattern. Conversely, this mode is the most sensitive to friction coefficient variation, probably because most of the contact nodes are in slip condition.